Revealing Porosity and Structure of Ni-based Catalysts for Dynamic CO_2 Methanation with Hard X-rays

Zur Erlangung des akademischen Grades eines

DOKTORS DER NATURWISSENSCHAFTEN

(Dr. rer. nat.)

von der KIT-Fakultät für Chemie und Biowissenschaften

des Karlsruher Instituts für Technologie (KIT)

genehmigte

DISSERTATION

von

M. Sc. Sebastian Weber
aus Friedrichroda

1. Referent: Prof. Dr. Jan-Dierk Grunwaldt
2. Referent: Prof. Dr. Holger Kohlmann
Tag der mündlichen Prüfung: 21. Juli 2022



This document is licensed under a Creative Commons
Attribution-Non Commercial 4.0 International License (CC BY-NC 4.0):
https://creativecommons.org/licenses/by-nc/4.0/deed.en

Abstract

A holistic understanding of materials applied in heterogeneous catalysis is a requirement for a knowledge-based catalyst design leading to materials with enhanced performance or stability. The heterogeneously catalyzed CO_2 methanation is a reaction in the scope of Power-to-X concepts to store excess energy from fluctuating renewable sources, which can lead to dynamic catalyst/reactor operation. The reaction itself and especially dynamic process operation thereof as a result of fluctuating energy supply, poses challenges regarding the catalyst stability due to hot-spot formation or thermal runaway behavior of the reactor. Therefore, new catalyst designs with improved stability are required, which are ideally based on a fundamental understanding. As heterogeneous catalysis by its nature is a multiscale time and space phenomena, spatially- and time-resolved characterization, ideally under *in situ* or *operando* conditions, is important to retrieve structure-function relationships. In this respect, different hard X-ray imaging techniques are valuable tools, which can provide various textural and structural information. In this thesis, Ni-based catalysts applied in CO_2 methanation were thoroughly investigated by a variety of hard X-ray techniques, focusing on expanding the current understanding of such materials by advanced characterization. This included an industrial Ni/Al_2O_3 reference catalyst (SPP2080-IMRC), a hierarchically porous Ni/Al_2O_3 catalyst (Ni/Al_2O_3-h) and a systematically designed series of Ni/ZrO_2 catalysts.

In the first part of this thesis, different imaging methods are presented to reveal the structure of methanation catalysts in 3D. As part of that, the SPP2080-IMRC was thoroughly characterized by X-ray microtomography (µ-XCT), X-ray nanotomography and electron tomography (ET) to cover length scales ranging from whole catalyst pellets (mm) down to mesopores (nm). The porosity characterization with these advanced imaging methods revealed significant presence of macropores in the catalyst. Those could not be identified by conventionally applied pore characterization methods, thus highlighting the advantage and requirement in performing advanced spatially-resolved catalyst characterization. Furthermore, it is shown how quantitative electron density information from ptychographic X-ray computed tomography (PXCT) can be used to retrieve sub-resolution information on the mesoporosity of the catalyst.

This is followed by the textural characterization of designed core-shell particles based on the Ni/Al_2O_3 reference catalyst as active core using µ-XCT. The designed core-shell catalysts exhibit an inert shell introducing mass transport limitations, which allow less temperature sensitivity of the catalyst particles. In this way, a more stable dynamic process operation is possible as suggested by literature simulation studies by avoiding excessive hot-spot formation or thermal

runaway. µ-XCT was applied to analyze the shell thickness depending on synthesis coating duration as an important design parameter for the mass transport properties of the shell and can unveil whether the shell is homogeneously closed. Contrary to the desired mass transport limitations in the shell, the active core should ideally exhibit no mass transport limitations.
Therefore, the first part is complemented by introducing a hierarchically meso-/macroporous Ni/Al_2O_3 catalyst with potentially enhanced mass transport properties. The synthesis together with its general characterization suggested incorporation of Ni into the $\gamma-Al_2O_3$-like structure requiring high reduction temperatures for Ni activation. Further, the combination of PXCT and electron tomography allowed to confirm the true presence of a hierarchical pore structure and to derive mass transport descriptors, i.e., porosity and average pore sizes. The latter were applied in initial simulations of the catalyst effectiveness factor indicating improved performance of the catalyst compared to a purely mesoporous sample.
In the second part, hard X-ray methods were applied for a detailed understanding of the synthesis of the hierarchically porous Ni/Al_2O_3-h catalyst focusing on the calcination as final synthesis step. The combination of *in situ* 2D X-ray ptychography and *ex situ* PXCT is presented to unravel the evolution of the pore structure from the dried gel to the calcined state of the catalysts. The *in situ* 2D experiments allowed to follow the morphological changes almost in real time highlighting that the macropore network was present already in the dried gel state and did not collapse during calcination. Complementary, PXCT on identical particles in the dried gel and calcined states of the catalyst could quantify a decrease of the macropore diameter and apparent mesoporosity, while the macroporosity was almost unchanged.
As general characterization suggested the incorporation of Ni into the $\gamma-Al_2O_3$-like structure of the Ni/Al_2O_3-h, the calcination step was additionally investigated by *in situ* X-ray total scattering experiments. The powder X-ray diffraction (PXRD) and pair distribution function (PDF) analysis revealed two phase transformations during calcination: Starting from a $\gamma-AlO(OH)$-like structure in the dried gel, upon heating formation of an amorphous intermediate phase with only short-range order and a final $\gamma-Al_2O_3$-like structure were identified. Furthermore, additional indication of the Ni incorporation into the $\gamma-Al_2O_3$-like structure was found by Rietveld analysis.
In the first two parts of the thesis, the focus was on understanding the structure and texture as well as the synthesis of the catalysts. The final part highlights the application of hard X-ray methods to unravel catalyst deactivation phenomena. Coking and thermal deactivation were investigated as potential deactivation pathways for CO_2 methanation over Ni-based catalysts. For activated and artificially coked catalysts with a hierarchical (Ni/Al_2O_3-h) and a purely mesoporous pore structure, PXCT was examined to reveal coke formation in 3D with sub-100 nm resolution. The quantitative electron density contrast of PXCT allowed to identify the formation of coke and estimation of its location in the catalyst particles. The formed coke was found in mesopores of the catalysts with a dominant location at the particle exterior.
In addition to coking, thermal deactivation was systematically investigated using a designed Ni/ZrO_2 catalyst series of tailored thermal stability. The catalysts differed mainly by the textural

properties of the support material, while exhibiting similar Ni nanoparticles as confirmed by laboratory characterization and testing in CO_2 methanation. *Operando* synchrotron PXRD experiments during artificial thermal aging cycles enabled to follow the structural and textural evolution of the catalysts. Thereby, it was possible to deconvolute different deactivation mechanisms, i.e., dominant support or Ni particle sintering depending on the initial support properties of the catalysts. This allowed to derive clear structure-deactivation relationships.
In summary, the present thesis showcases the great potential in applying various hard X-ray methods to understand the structure and texture of catalysts. Especially X-ray ptychography is presented as a powerful X-ray nanoimaging method to unravel catalyst pore structures and changes thereof. Furthermore, combining different hard X-ray methods allows to cover length scale from the atomic (sub-nm) to the catalyst pellet (mm) scale. Their application enables a detailed understanding of the catalyst structure as well as synthesis and deactivation mechanisms. This opens the path towards a more holistic understanding of catalysts as a requirement for a future knowledge-based design of catalyst materials.

Kurzfassung

Für eine wissensbasierte Verbesserung von Katalysatoren in der heterogenen Katalyse ist ein detailliertes Verständnis der verwendeten Materialien nötig. Dies gilt insbesondere hinsichtlich der Katalysatoraktivität oder -stabilität. Die katalytische Methanisierung von CO_2 ist eine Reaktion im Rahmen der Power-to-X Konzepte. Diese umfassen die chemische Energiespeicherung überschüssiger fluktuierender erneuerbarer Energien in Form chemischer Moleküle, in diesem Fall Methan. Durch die volatile Stromerzeugung bedürfen diese Konzepte allerdings der Möglichkeit einer dynamischen Prozessführung. Dabei treten Herausforderungen bezüglich der Stabilität der verwendeten Katalysatoren auf, welche auf die exotherme Reaktion selbst, aber auch die dynamische Prozessführung zurückzuführen sind. Insbesondere die Ausbildung von "Hot-Spots" im Katalysatorbett oder das thermische Durchgehen des Reaktors sind hier eine Herausforderung, die durch die volatile Betriebsweise noch verstärkt werden kann. Aus diesem Grund sind neuartige Katalysatorkonzepte oder stabilerer Materialien notwendig, welche idealerweise basierend auf grundlegendem Wissen entwickelt werden. Die heterogene Katalyse ist von Grund auf, sowohl in zeitlicher als auch räumlicher Hinsicht, ein Multiskalen-Phänomen. Um Struktur-Eigenschafts-Beziehungen ableiten zu können bedarf es deshalb orts- und zeitaufgelöster Charakterisierungsmethoden, idealerweise unter *in situ* und *operando* Bedingungen. Dabei sind verschiedene bildgebende harte Röntgenmethoden wertvolle Werkzeuge um diverse strukturelle und texturelle Eigenschaften von Katalysatoren abzuleiten. In dieser Arbeit werden Ni-Katalysatoren mit möglicher Anwendung in der Methanisierung von CO_2 mittels diverser harter Röntgenmethoden detailliert untersucht. Der Fokus liegt dabei in einer Charakterisierung der Materialien über die Möglichkeiten konventioneller Methoden hinaus. Die untersuchten Systeme sind hierbei ein industrieller Ni/Al_2O_3-Referenzkatalysator (SPP2080-IMRC), ein hierarchisch poröser Ni/Al_2O_3-Katalysator (Ni/Al_2O_3-h) sowie eine konstruierte Serie von Ni/ZrO_2-Katalysatoren.

Im ersten Teil der Dissertation werden verschiedene 3D-bildgebende Verfahren zur Untersuchung der Struktur von Methanisierungskatalysatoren vorgestellt. Hierbei wird zunächst anhand des SPP2080-IMRC die Multiskalen-Charakterisierung mittels Röntgenmikrotomographie (µ-XCT), Röntgennanotomographie und Elektronentomographie (ET) präsentiert. Diese Kombination ermöglichte es Längenskalen vom Katalysatorpellet (mm) bis zu den Mesoporen (nm) zu überbrücken, was für die Analyse der Porenstruktur sowie der texturellen Eigenschaften notwendig ist. Durch die Multiskalen-Tomographieanalyse wurde dabei die signifikante Anwesenheit von Makroporen im SPP2080-IMRC festgestellt. Im Vergleich dazu versagten konventionelle Methoden zur

Porencharakterisierung (Gas-Sorption oder Hg-Intrusion) in der Analyse dieser Makroporen. Dies zeigt den Vorteil und die Notwendigkeit in der Anwendung fortgeschrittener räumlich-aufgelöster Analysetechniken für die Porositätsuntersuchung von Katalysatoren. In diesem Zusammenhang wird die Verwendung der ptychographischen Röntgen-Computertomographie (PXCT) zur Bestimmung der Mesoporosität des Katalysators vorgestellt. Durch die Auswertung der durch PXCT erhaltenen quantitativen Elektronendichteinformation war es möglich Informationen zur Mesoporösität unterhalb der erreichbaren räumlichen Auflösung zu erlangen.
Anschließend werden auf dem SPP2080-IMRC basierende Kern-Schalen-Katalysatoren vorgestellt. Diese bestehen aus einem aktiven Kern (SPP2080-IMRC) und einer inerten stofftransportlimitierenden Schale. Das Katalysatordesign besitzt eine geringere thermische Sensitivität in Hinblick einer dynamischen Betriebsweise der CO_2-Methanisierung, da der Stofftransport der limitierende Schritt der Reaktion ist. Dieses optimierte Verhalten wurde in Simulationsstudien in der Literatur gezeigt und "Hot-Spots" oder thermisches Durchgehen können somit vermieden werden. Die Dicke und das Vorliegen einer homogen geschlossenen inerten Schale sind hierbei entscheidende Parameter. Mittels µ-XCT wurden beide Eigenschaften abhängig von der Beschichtungszeit während der Herstellung der Schale in einem Wirbelschichtreaktor untersucht. Dabei zeigte sich, dass eine gewisse Beschichtungsdauer nötig ist um eine geschlossene Schale und somit die gewünschten stofftransportlimitierenden Eigenschaften zu erhalten. Im Gegensatz zur Schale sollen im Kern dieses Katalysatordesigns möglichst keine Stofftransportlimitierungen vorliegen. Aus diesem Grund ist die Entwicklung von Katalysatoren mit optimierten Porensystemen notwendig. In Anbetracht dessen wird in dieser Dissertation ein vielversprechender hierarchisch meso-/makroporöser Ni/Al_2O_3-Katalysator (Ni/Al_2O_3-h) vorgestellt. Der Ni/Al_2O_3-h Katalysator wurde mittels Sol-Gel-Synthese hergestellt. Dabei zeigten konventionelle Charakterisierungsmethoden den Einbau von Ni in die $\gamma-Al_2O_3$-artige Struktur. Dies hat eine hohe Aktivierungstemperatur zur Reduzierung der Ni-Spezies zur Folge, was nachteilig für eine praktische Anwendung des Katalysators ist. Die hierarchische Porenstruktur konnte durch kombinierte PXCT und ET Experimente bestätigt werden. Zusätzlich abgeleitete Informationen aus den Tomographiedaten zur Porosität und den durchschnittlichen Porendurchmessern wurden folgend in Simulationsstudien des Katalysatorwirkungsgrades verwendet. Letztere zeigten verbesserte Stofftransporteigenschaften des hierarchischen Porensystems im Vergleich zu einem rein mesoporösen Material.
Im zweiten Teil der Arbeit wurde der Einfluss der Kalzinierung als finaler Syntheseschritt des hierarchisch porösen Ni/Al_2O_3-h mit Hilfe von harten Röntgenmethoden untersucht. Die Kombination von *in situ* 2D-Röntgenptychographie und *ex situ* PXCT ermöglichte es die Evolution der Porenstruktur vom getrockneten Gel zur kalzinierten Probe zu verfolgen. Die *in situ* 2D-Röntgenptychographie erlaubte morphologische Änderungen nahezu in Echtzeit zu verfolgen. Das Makroporennetzwerk konnte dabei schon im getrockneten Gel beobachtet werden und blieb während der Kalzinierung intakt. Komplementär zu den 2D-Untersuchungen wurden 3D-PXCT Studien an identischen Partikeln im getrockneten und kalzinierten Zustand durchgeführt. Dabei

konnten die Abnahme der Makroporendurchmesser sowie der Mesoporösität quantifiziert werden, während die Makroporösität nahezu unverändert blieb.
Der durch generelle Charakterisierung vorhergesagte Einbau von Ni in die $\gamma-Al_2O_3$-artige Struktur wurde mittels *in situ* Röntgentotalstreuungs-Experimente näher untersucht. Die Röntgenpulverbeugungs- und der Paarverteilungsfunktionsanalyse zeigten zwei Phasenübergänge während der Kalzinierung. Beginnend von einer $\gamma-AlO(OH)$-ähnlichen Struktur bildete sich unter Temperaturerhöhung zunächst eine nahgeordnete amorphe Struktur aus, die sich wiederum zur finalen $\gamma-Al_2O_3$-artigen Struktur umwandelte. Rietveld-Verfeinerung der Beugungsdaten bestätigte zusätzlich die Indikation des Einbaus von Ni in die $\gamma-Al_2O_3$-artige Struktur.
Die ersten beiden Teile der Dissertation fokussierten sich auf das Verständnis der multiskaligen Katalysatorstruktur sowie der Katalysatorsynthese. Im finalen Abschnitt der Arbeit wurden verschiedene Desaktivierungsphänomene untersucht. Für die CO_2-Methanisierung wurden dabei die Verkokung und thermische Alterung als wahrscheinliche Desaktivierungsmechanismen von Ni-basierten Katalysatoren ausgewählt. Die Möglichkeiten und das Potential von PXCT zur Aufklärung der Koksbildung in 3D mit sub-100 nm Auflösung wurden für aktivierte und künstlich verkokte Katalysatoren mit hierarchisch poröser (Ni/Al_2O_3-h) und rein mesoporöser Porenstruktur beleuchtet. Der quantitative Elektronendichtekontrast der PXCT-Analyse ermöglichte die Identifizierung des gebildeten Koks und erlaubte eine anfängliche Abschätzung der Lokalisierung innerhalb der Katalysatorpartikel. Die Koksspezies waren vorwiegend in den Mesoporen lokalisiert, wobei eine dominante Verteilung hin zur Außenseite des Partikels gefunden wurde.
Zusätzlich zur Verkokung wurde die thermische Desaktivierung einer konstruierten Ni/ZrO_2-Katalysatorserie systematisch untersucht. Die Katalysatoren unterschieden sich vorwiegend durch die texturellen Eigenschaften der Trägermaterialien. Während ähnliche Ni-Nanopartikel durch konventionelle Charakterisierungsmethoden und Labortestung in der CO_2-Methanisierung bestätigt wurden. *Operando* Synchrotron-Röntgenpulverbeugung ermöglichte es texturelle und strukturelle Änderungen der Katalysatoren während künstlicher thermischer Desaktivierungszyklen zu verfolgen. Dabei gelang es zwischen der Desaktivierung durch dominantes Sintern des Trägers oder der Ni-Partikel abhängig der anfänglichen Trägereigenschaften zu unterscheiden. Dies erlaubte die Ableitung von Struktur-Desaktivierungs-Beziehungen für die Katalysatorserie.
Zusammenfassend zeigt die vorliegende Arbeit das enorme Potential harter Röntgenmethoden zum Verständnis der texturellen und strukturellen Eigenschaften von Katalysatoren auf. Insbesondere wird die Röntgenptychographie als leistungsstarke bildgebende Röntgenmethode für den nm-Bereich vorgestellt. Durch diese sind detaillierte Untersuchungen von Porenstrukturen und deren Änderung möglich. Außerdem kann die Kombination verschiedener harter Röntgenmethoden Längenskalen von atomaren Strukturen (sub-nm) bis hin zu Katalysatorpellets (mm) abdecken. Deren Anwendung erlaubt es, die Katalysatorstruktur sowie die Katalysatorsynthese und -desaktivierung im Detail zu verstehen. Dies öffnet den Weg zu einem ganzheitlichen Verständnis von Katalysatoren, was eine eminente Grundlage für eine wissensbasierte Katalysatorentwicklung darstellt.

Contents

Abstract iii

Kurzfassung vii

1 Introduction 1

1.1 Dynamic Conditions and Operation of Catalysts in a Future Renewable Energy Scenario . . . 1

1.1.1 Renewable and Fluctuating Supply of Electrical Energy . . . 1

1.1.2 Chemical Energy Storage - Power-to-X . . . 3

1.2 Overview on the CO_2 Methanation Reaction as a Power-to-X Example . . . 6

1.2.1 Suitable Catalysts for CO_2 Methanation . . . 6

1.2.2 Proposed Mechanism for CO_2 Methanation . . . 8

1.2.3 Potential Deactivation Phenomena Associated with CO_2 Methanation . . . 10

1.2.4 Dynamic Process Operation of the CO_2 Methanation . . . 14

1.2.5 Control of Methanation Reactors by Designed Catalyst Particles . . . 15

1.3 Length Scales in Heterogeneous Catalysis and Challenges for Spatially-Resolved Characterization . . . 18

1.4 Catalyst Porosity and Conventional Analysis Methods . . . 20

1.5 3D-Spatially-Resolved Characterization in Heterogeneous Catalysis . . . 23

1.5.1 Suitable X-ray Probes for Spatially-Resolved Studies . . . 23

1.5.2 Resolution vs. Sample Size – a Trade-off in Catalyst Characterization . . . 27

1.5.3 Chemical Imaging of Catalysts in 3D . . . 34

1.5.4 Tomography Studies of Catalysts at Work . . . 37

2 Scope of the Thesis 43

3 Methods and Experimental 47

3.1 Catalyst Synthesis . . . 48

3.1.1 Industrial Ni/Al_2O_3 Reference Catalyst and Core-Shell Catalysts . . . 48

3.1.2 Hierarchically Porous Catalysts . . . 49

3.1.3 Deposition Precipitation Ni/ZrO_2 Catalysts . . . 50

3.1.4 Overview Catalyst Samples . . . 52

3.2 Conventional Catalyst Characterization . . . 53

3.3 Catalyst Treatment and Testing . . . 56
3.3.1 Tubular Quartz Glass Reactor . . . 56
3.3.2 Stainless Steel Tubular Fixed-bed Reactor . . . 57
3.3.3 Quartz Glass Microreactor Setup and Artificial Coking Studies . . . 59
3.4 Imaging Experiments . . . 62
3.4.1 Overview Tomography Experiments . . . 62
3.4.2 Electron Microscopy Experiments . . . 63
3.4.3 X-ray Microtomography . . . 65
3.4.4 Sample Preparation for X-ray Nanoimaging . . . 66
3.4.5 *In Situ* 2D X-ray Ptychography . . . 68
3.4.6 Ptychographic X-ray Computed Tomography at cSAXS . . . 71
3.4.7 Ptychographic X-ray Computed Tomography at I13-1 . . . 73
3.4.8 Holographic X-ray Computed Tomography . . . 74
3.4.9 Image Analysis of Tomography Data . . . 76
3.5 Synchrotron X-ray Diffraction Experiments . . . 83
3.5.1 *Operando* Synchrotron Powder X-ray Diffraction . . . 83
3.5.2 *In Situ* X-ray Total Scattering . . . 84
3.5.3 (S)PXRD, Rietveld and PDF Analysis . . . 85

4 Porosity and Textural Characterization of Catalysts by Imaging on Different Length Scales 89
4.1 Conventional vs. Imaging Methods for Pore Structure Analysis . . . 90
4.1.1 Introduction . . . 90
4.1.2 Conventional Porosity Characterization . . . 91
4.1.3 Tomography-Based Porosity Characterization . . . 93
4.1.4 Comparison of Conventional and Tomography-Based Porosity Characterization . . . 97
4.1.5 Particle Size from Transmission Electron Microscopy . . . 99
4.1.6 Conclusions . . . 100
4.2 Shell Thickness Analysis of Designed Core-Shell Catalysts . . . 101
4.2.1 Introduction . . . 101
4.2.2 Shell Thickness Analysis . . . 101
4.2.3 Conclusions . . . 106
4.3 Hierarchically Porous Catalysts for CO_2 Methanation . . . 108
4.3.1 Introduction . . . 108
4.3.2 Synthesis and Structural Characterization . . . 109
4.3.3 Catalytic Measurements . . . 112
4.3.4 Tomographic Studies . . . 113
4.3.5 Porosity Analysis . . . 116

4.3.6 Macrokinetics . . . 121
4.3.7 Conclusions . . . 123

5 Understanding the Synthesis of Catalysts with Tailored Pore Structures 125
5.1 Following the Porosity Evolution by X-ray Ptychography . . . 126
5.1.1 Introduction . . . 126
5.1.2 Synthesis and Characterization of Hierarchically Porous Nickel Alumina Catalysts . . . 127
5.1.3 *In Situ* X-ray Ptychography . . . 129
5.1.4 *Ex Situ* Ptychographic X-ray Computed Tomography . . . 131
5.1.5 3D Pore Structure Characterization by PXCT Image Analysis . . . 132
5.1.6 Electron Density Analysis of PXCT Data . . . 137
5.1.7 Pore Structure Evolution During Calcination . . . 140
5.1.8 Conclusions . . . 141
5.2 Resolving Structural Changes During Calcination by X-ray Total Scattering . . . 143
5.2.1 Introduction . . . 143
5.2.2 *In Situ* Calcination Followed by PXRD . . . 143
5.2.3 *In Situ* Calcination Followed by PDF . . . 146
5.2.4 Discussion of Structural Analysis by PXRD and PDF . . . 148
5.2.5 Conclusions . . . 149

6 Revealing Catalyst Deactivation with Hard X-rays 151
6.1 Coke Localization Unraveled by X-ray Ptychography . . . 152
6.1.1 Introduction . . . 152
6.1.2 Artificial Coking Treatment and Raman Spectroscopy . . . 153
6.1.3 Ptychographic X-ray Computed Tomography Analysis . . . 155
6.1.4 Electron Density Analysis to Reveal Coke Location . . . 156
6.1.5 Conclusions . . . 159
6.2 Deconvolution of Thermal Deactivation Phenomena by X-ray Diffraction . . . 160
6.2.1 Introduction . . . 160
6.2.2 Synthesis of Catalysts with Varying Support Texture . . . 161
6.2.3 Catalyst Testing Results . . . 165
6.2.4 *Operando* Synchrotron Powder X-ray Diffraction Experiments (SPXRD) . . . 166
6.2.5 Crystallite Size Changes During *Operando* SPXRD . . . 168
6.2.6 Correlation of Crystallite Size and Thermal Deactivation . . . 171
6.2.7 Overall Discussion of the Thermal Deactivation . . . 173
6.2.8 Conclusions . . . 175

7 Conclusions and Outlook 177

Bibliography **185**

8 Appendix A **215**

8.1 Conventional vs. Imaging Methods for Pore Structure Analysis 216
8.2 Shell Thickness Analysis of Designed Core-Shell Catalysts 219
8.3 Hierarchically Porous Catalysts for CO_2 Methanation 220
8.4 Following the Porosity Evolution by X-ray Ptychography 224
8.5 Resolving Structural Changes During Calcination by X-ray Total Scattering . . . 234
8.6 Coke Localization Unraveled by X-ray Ptychography 237
8.7 Deconvolution of Thermal Deactivation Phenomena by X-ray Diffraction 245

Appendix B **I**

Acknowledgments II
Curriculum Vitae V
Measurement Campaigns at Synchrotron Radiation Facilities VII
List of Publications Related to this Thesis IX
List of Further Publications X
List of Conference Contributions XI
Eidesstattliche Erklärung XV

1 Introduction

1.1 Dynamic Conditions and Operation of Catalysts in a Future Renewable Energy Scenario

The hottest years since beginning of temperature recordings have been noticed in the 21^{st} century. From a scientific point of view this observation is mainly related to anthropogenic climate change. This is predominantly caused by green house gas (GHG) emissions, like carbon dioxide, methane, ozone or nitrous oxide, while the major role is attributed to CO_2.[1–3] Challenges and problems associated with human made climate change are enormous. The influence on many areas is discussed and expected, e.g., environment, plants and crops, the financial system, geopolitics, human health or our energy systems.[2–8] In order to mitigate or at least reduce consequences of global warming, the "Paris Agreement" from 2015 aims to limit the increase of the average global temperature to 2.0 °C or ideally 1.5 °C.[2, 9] In 2019, the global CO_2 emissions were in total about 34.2 Gt CO_{2eq} according to the International Energy Agency.[10] Electricity and heat generation accounted for 14.0 Gt CO_{2eq}, transport for 8.2 Gt CO_{2eq} and industry for 6.3 Gt CO_{2eq}.[10] Those sectors together might be in general considered as energy systems, which currently heavily rely on fossil fuels. In 2019, the global primary energy supply was 606.5 EJ, from which only 13.8 % were covered by renewables.[11] Although the share of renewables is constantly increasing, the enormous numbers show the challenges lying ahead for our global society in replacing fossil fuels by renewables. In the following two sections challenges associated with renewable energy production will be discussed in more detail and connected with the potential role of chemistry in solving those.

1.1.1 Renewable and Fluctuating Supply of Electrical Energy

In 2019, Germany produced 42.1 % of the electrical energy (244.3 TWh) and 17.4 % of the primary energy using renewables.[12] The aim of the current German government is to increase the share in electricity production in 2030 to 80 % and reach carbon neutrality by 2045.[13] However, to reach these ambitious and important goals several challenges regarding the supply of renewable energies have to be solved. A major problem of renewable power production is the fluctuating nature of the main sources - wind and solar. To illustrate this issue, the average weekly electricity production in Germany in 2021 is shown in Figure 1.1. The average week data illustrates the fluctuating demand and production of electrical power, while the volatile nature of renewables on

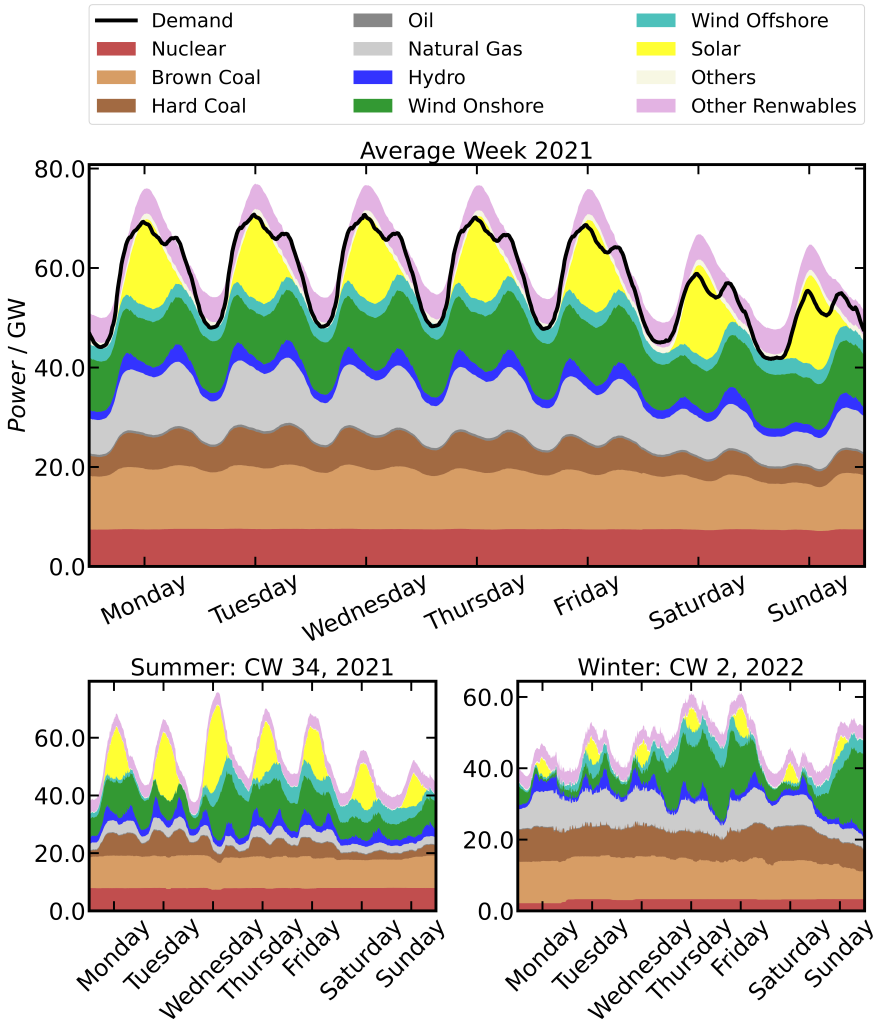


Figure 1.1: Power production according to its source in Germany. Average weekly data for the year 2021 from Fraunhofer ISE[14] (top) and data for an exemplary summer 2021 (bottom left) and winter 2022 (bottom right) week with data from entsoe Transparency Platform[15].

a daily base can be observed. However, also seasonal differences have to be considered as shown for an exemplary summer week of 2021 and winter week of 2022 in Figure 1.1. In the summer week especially solar energy production during daytime is strong, while the fluctuation between day and night increases. On the other hand, in the winter week there are two days of almost no power production from wind or solar sources and generally the amount of solar sources is low. On a side note, the comparison of the summer and winter week also shows the much lower share of nuclear energy in Germany due to the withdrawal from nuclear energy decided after the Fukushima incident in 2011.

The installed capacity of renewable energy production in Germany increased from 27.9 GW in 2005 to 123.4 GW in 2019.[16] Theoretically, the average electrical energy demand shown in Figure 1.1 could be covered twice if all production capabilities would be available. However, the

volatile nature of wind and solar sources results in above illustrated fluctuations with periods on the hourly, daily, weekly or even seasonal time scale (Figure 1.1). As a consequence, there is a requirement for an effective energy system capable of handling unsteady energy supply, either by flexible demand or buffering/storage. In the following section, the possibilities to store electrical energy during peak times by chemical energy storage will be highlighted.

1.1.2 Chemical Energy Storage - Power-to-X

Due to the fluctuating nature of wind and solar sources a multiscale energy storage strategy of different systems is required.[17–19] It can be distinguished between different time and capacity scales that are required as illustrated in Figure 1.2. The shown storage options might be very

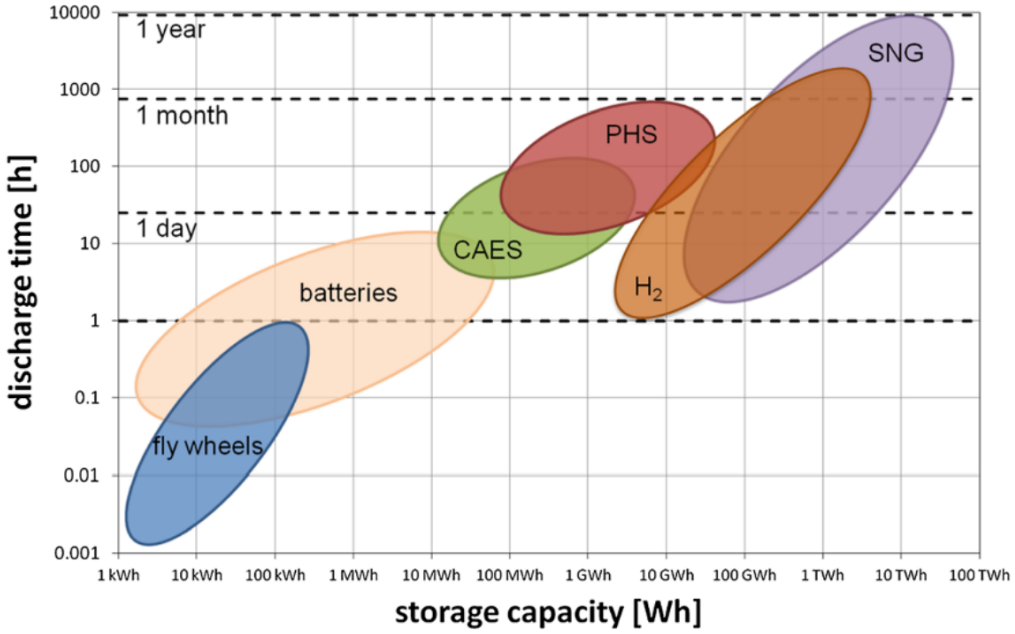


Figure 1.2: Different possible energy storage systems sorted by their charge/discharge time and capacity. CAES: compressed air energy storage, PHS: pumped hydro storage, SNG: substitute natural gas. With permission from ref.[20] Available under the terms and conditions of the Creative Commons Attribution 4.0 license (CC BY 4.0, `https://creativecommons.org/licenses/by/4.0/`), Copyright ©2014.

roughly distinguished into mechanical/thermal (fly wheels, compressed air energy storage and pumped hydro storage) and chemical systems (batteries, hydrogen and substitute natural gas (SNG)). Considering the time scales of the fluctuations, chemical systems have the possibility of covering almost all relevant periods. Here, one might differentiate in intraday storage, which is very well suited for batteries, while in a realistic scenario they cannot reasonably cover seasonal periods.[17–19] For the latter purpose, hydrogen, SNG or other small organic compounds are feasible.[17–19, 21, 22] The storage of excess electrical energy in form of chemical molecules is also often referred to as Power-to-X technologies, which might be further divided into, e.g.,

Power-to-Gas, Power-to-Fuel and Power-to-Liquid or even very specific as Power-to-Hydrogen or Power-to-Methane.[23–26] The chemically stored electrical energy during surplus periods can then be used to buffer fluctuations, in case not enough renewable energy can be produced.
The general concept of Power-to-X is schematically shown in Figure 1.3, with the additional option of direct conversion of solar energy into chemicals without the intermediate step of electricity generation. The first step of all Power-to-X processes is the generation of electrical

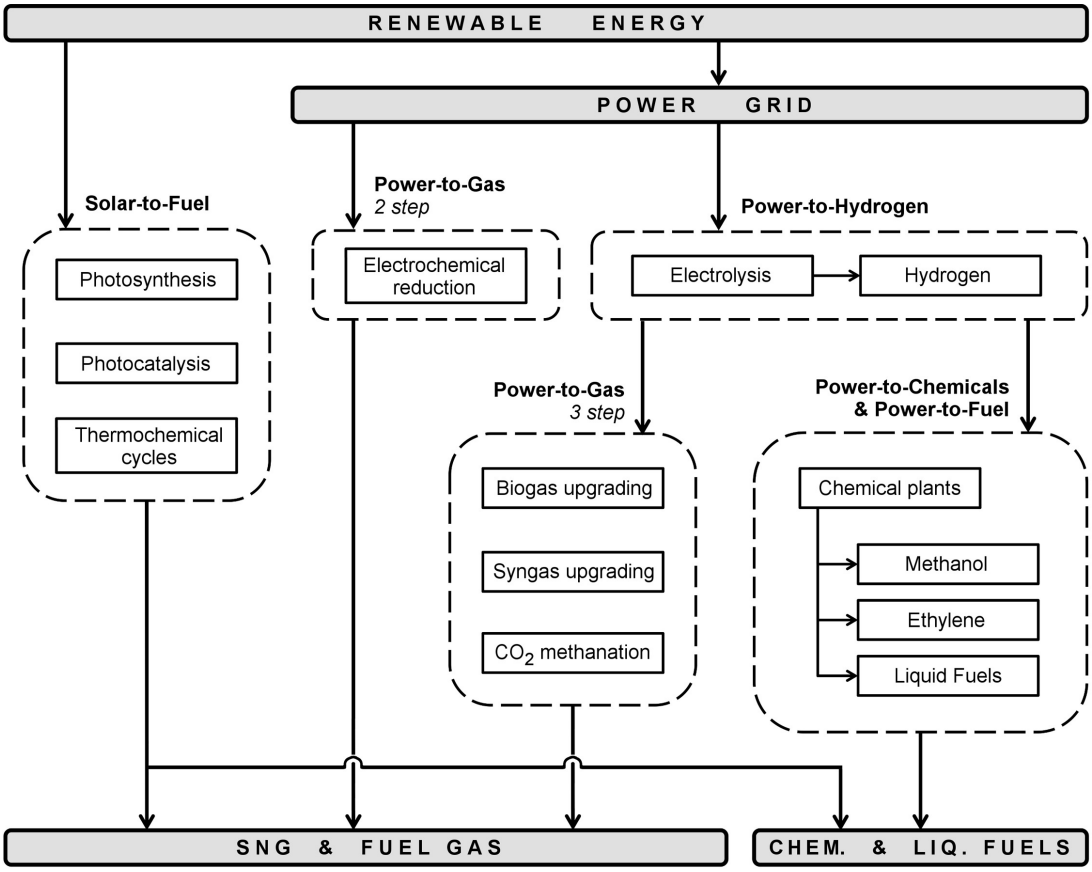


Figure 1.3: Flowchart illustrating different Power-to-X technologies. Reprinted from *Renew. Sust. Energ. Rev.*, *69*, M. Bailera, P. Lisbona, L. M. Romeo, S. Espatolero, "Power to Gas projects review: Lab, pilot and demo plants for storing renewable energy and CO_2", 292-312, Copyright 2017, with permission from Elsevier.[26]

energy from renewable sources, which are especially solar and wind. The second optional step is the distribution of the produced electricity *via* the power grid as shown in Figure 1.3, while also modular solutions of Power-to-X exist, which can be directly applied at or in vicinity of the power production.[22, 27] Typically, the electrical energy is first used to produce H_2 (Power-to-Hydrogen) via electrolysis of water. There are also approaches for direct conversion of H_2O with e.g. CO_2 via electrochemical reduction,[28, 29] which are not the focus of the present thesis. The produced H_2 from Power-to-Hydrogen can be either directly utilized or used as feedstock for Power-to-Gas or Power-to-Chemicals/Fuels technologies. Here, the focus will be

on the additional Power-to-Gas pathway, which converts the produced H_2 into SNG. For this purpose a carbon source is required, which might be CO_2, CO, a mixture of both or syngas streams (CO/H_2 mixture). In general, one might consider that the production of H_2 and also following steps have to be able to deal with certain fluctuations and thus a dynamic operation might be required.[30] That means that the reactor is not operated in a steady-state, but rather different load-changes or start-ups/shut-downs have to be performed, which will be discussed more detailed in the later section 1.2.4.
As all transformation processes suffer from efficiency losses, the question might raise why H_2 is not used directly. This can be answered from different points of view. First, as also shown for the storage capacity and duration in Figure 1.2, SNG can be stored in larger capacities and for longer duration. While improvements of H_2 storage can be expected, also its distribution might be a challenge on a grid scale across Germany or Europe.[31–33] For SNG, there is an existing large scale storage and distribution infrastructure of underground storage and pipeline systems. This existing infrastructure cannot be directly used for a complete substitution of SNG by H_2, while mixtures of SNG with up to 10 vol.% of H_2 are expected to be feasible without any adaption.[31–33] Therefore, conversion of H_2 into SNG is an option to avoid expensive large scale infrastructure investments on the grid and storage systems. However, research in this field is ongoing and the feasibility of different approaches might also strongly depend on political decisions.
A second aspect in the conversion of H_2 in Power-to-Gas or Power-to-Chemicals/Fuels might be the search for alternative carbon sources than fossil ones. In this respect CO_2 from different point sources or the atmosphere might be used as a carbon source. These concepts are often also discussed in the framework of Carbon Capture and Utilization (CCU).[34, 35] Ideally, CO_2 is obtained from point sources of large scale processes that emit CO_2 as secondary product, e.g., steel production, cement industry or chemical processes like ethylene oxidation, that are not related to energy production using fossil resources.[34, 35] One of the CCU approaches and also a Power-to-Gas concept is the direct methanation of CO_2, which is the reaction of focus of this thesis and will be discussed more detailed in the next section.
In a short summary, Power-to-X concepts can address different challenges towards a more sustainable society and have attracted large political, societal and research interests in the last years. The concepts can be used to balance fluctuations from renewable energy production or allow the use of non-fossil carbon sources and can be expected to be a pillar of our future energy and resource systems. However, by nature of the renewable power sources Power-to-X strategies have to allow for dynamic process operation, which might present certain challenges as discussed later in section 1.2.4 for CO_2 methanation as an example.

1.2 Overview on the CO_2 Methanation Reaction as a Power-to-X Example

1.2.1 Suitable Catalysts for CO_2 Methanation

As discussed in the previous section, the CO_2 methanation reaction might be applied as one of the Power-to-X concepts, i.e., Power-to-Gas. This process is additionally illustrated in the flowchart shown in Figure 1.4a. The reaction itself traces back to the hydrogenation studies of Sabatier and Senderens using Ni as a catalyst in the early 20^{th} century.[36] As Sabatier reflects in his 1912 Noble Prize lecture:"Carbon monoxide and carbon dioxide are both changed immediately into methane, which can therefore be synthesized with the greatest ease".[37] Today, more than

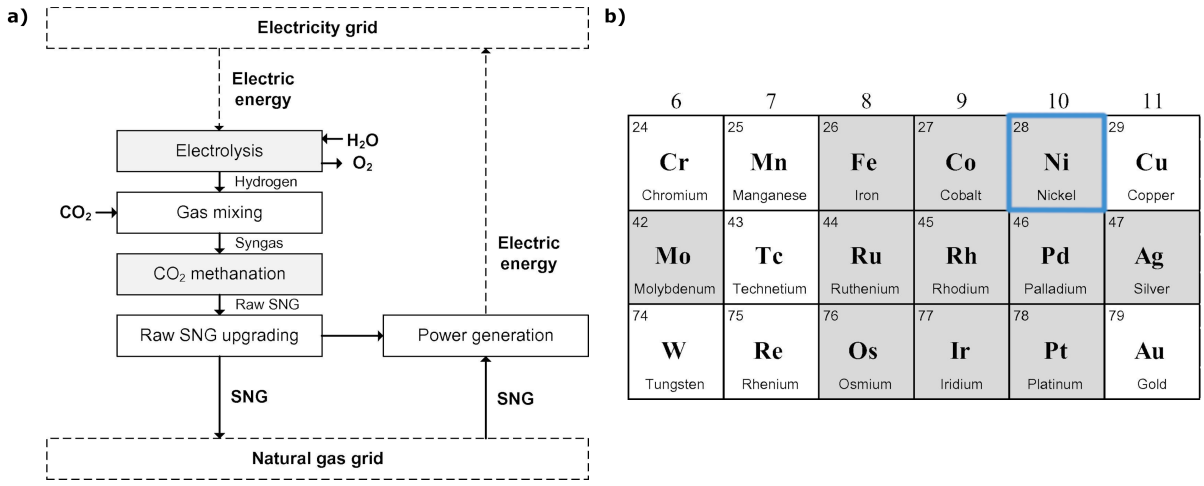


Figure 1.4: (a) Flowchart illustrating the CO_2 methanation as a Power-to-gas concept. (b) Overview of various active transition metals considered as potential catalyst materials (grey) with Ni highlighted as the element of focus of this thesis. Reprinted from *Fuel*, *166*, S. Rönsch, J. Schneider, S. Matthischke, M. Schlüter, M. Götz, J. Lefebvre, P. Prabhakaran, S. Bajohr, "Review on methanation – From fundamentals to current projects", 276-296, Copyright 2016, with permission from Elsevier.[38]

100 years later, Ni is still one of the most often applied active elements in catalysts for this exothermic reaction (eq. 1.1).[38–44]

$$CO_2 + 4H_2 \rightleftarrows CH_4 + 2H_2O \quad \Delta H = -164\,\mathrm{kJ\,mol^{-1}} \text{ at } 298\,\mathrm{K} \tag{1.1}$$

Besides the CO_2 methanation reaction also two possible side reactions have to be considered, which are the exothermic methanation of CO (eq. 1.2) and the endothermic reverse water-gas shift (RWGS) reaction (eq. 1.3).

$$CO + 3H_2 \rightleftarrows CH_4 + H_2O \quad \Delta H = -206\,\mathrm{kJ\,mol^{-1}} \text{ at } 298\,\mathrm{K} \tag{1.2}$$

$$CO_2 + H_2 \rightleftarrows CO + H_2O \quad \Delta H = +41\,\mathrm{kJ\,mol^{-1}} \text{ at } 298\,\mathrm{K} \tag{1.3}$$

As the CO_2 methanation is an exothermic reaction the reaction temperature should be as low as possible according to the principle of Le Chatelier. Additionally, an increase of pressure also favors the formation of CH_4. However, for sufficient activity the reaction is typically performed at higher temperatures from 523 K to about 773 K and pressures can range from 1 to 100 bar.[38–40, 45] Starting from 573 K, the RWGS starts to play a more dominant role at pressures of 1 bar, which results in decreasing selectivity towards CH_4 as shown in detailed analysis of the thermodynamics by Gao *et al.*[45] Hence, a strong drop in CH_4 selectivity is only observed starting at 673 K.[45] Therefore, according to thermodynamics lower reaction temperatures and higher pressures should be favored.

Besides Ni, many other elements, especially transition metals, as shown in Figure 1.4b, might be used for CO_2 methanation.[38–42] Generally, Ru and Rh are reported to be more active than Ni, while Ni is considered as more selective.[40] Despite being less active, Ni is more abundant and much cheaper than the other two metals and thus applied most often. As the amount of studies on CO_2 methanation and possible catalysts is enormous, the focus in this thesis is limited to few selected Ni-based systems. A recent search in the Web of Science™ database for the keywords "(Ni) AND (methanation) AND (CO2)" results in more than 900 publications only on Ni based catalysts.[46] Typically, those are supported Ni nanoparticles on different metal oxides. The support materials studied in literature include, e.g., Al_2O_3 (most often in the γ-Al_2O_3 modification), ZrO_2 (tetragonal and monoclinic), CeO_2, Ce−ZrO_2, SiO_2, MgO, TiO_2 or zeolites as reviewed in different studies.[38–42] As part of this thesis the focus will be on Al_2O_3 and ZrO_2 as support materials. Applied catalysts usually exhibit Ni loadings in the range from 5 to 30 wt.% with Ni particle sizes from two up to tens of nm.[39, 41, 44]

There are various synthesis methods described for the preparation of Ni/Al_2O_3 and Ni/ZrO_2 catalysts, e.g., impregnation,[47–50] (co-)precipitation,[51–54] or sol-gel methods,[55–58].[39–41, 43, 44] The research focuses mainly on tuning the particle size of the supported metal, adding promoters or changing the acid/base properties of the support. Furthermore, the preparation of bi- or multimetallic Ni-based catalysts strongly developed over the last years with the Ni−Fe system being very prominent as reviewed by Tsiotsias *et al.*[59] Based on the current literature knowledge,[30, 43, 44] the following main challenges in the development of Ni-based methanation catalysts might be identified:

- Increase of the low-temperature activity (below 573 K).
- Increase of catalyst stability, especially towards deactivation caused by sintering.
- Development of new catalyst materials (support, promoters, synthesis methods).
- CO_2 methanation under dynamic process operation.
- More detailed understanding of the reaction mechanism and catalyst performance (role of active metal, support or metal-support interactions).

In the following sections, the state of the art of selected open challenges will be shortly summarized. This includes a brief overview on the different proposed mechanisms for CO_2 methanation (section 1.2.2), possible deactivation phenomena (section 1.2.3) and challenges upon dynamic operation (section 1.2.4).

1.2.2 Proposed Mechanism for CO_2 Methanation

There are two major mechanisms discussed for Ni-catalyzed CO_2 methanation in the literature. Different studies that investigated those were discussed and summarized in several reviews.[39, 41, 43, 60] While there is no clear consensus in the research community about the preferred mechanism, it appears that the active compound and support both have an influence. The first one as shown in Figure 1.5a involves the adsorption of CO_2 and subsequently formed formate or carbonate species on the catalysts surface, while the second mechanism is characterized by a CO intermediate and subsequent CO methanation Figure 1.5b. The first mechanism is often referred to as the associative and the second as dissociative mechanism.[39, 41, 43, 60] The dissociative

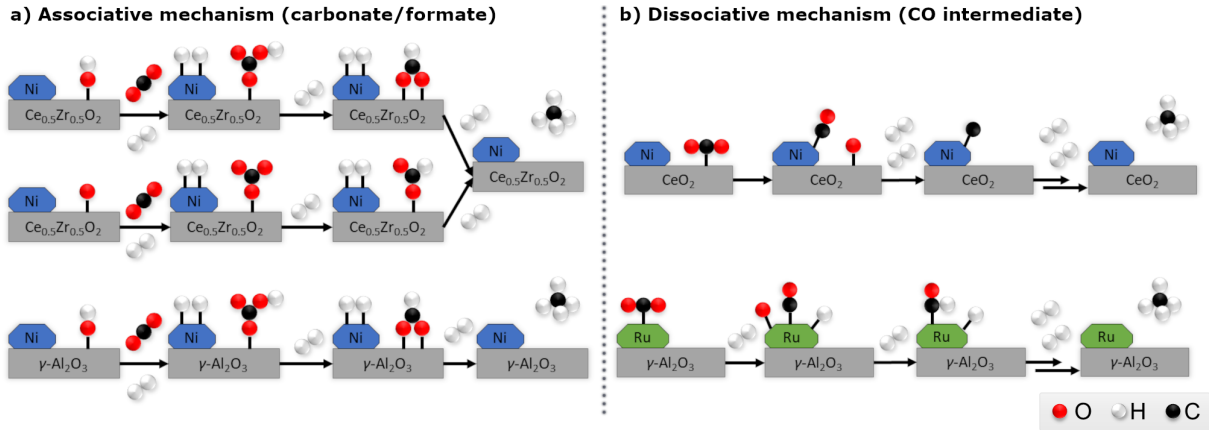


Figure 1.5: Overview on different general proposed CO_2 methanation mechanisms. The associative mechanism (a, left) and dissociative mechanism (b, right). Atom colors: white (H), red (O), black (C); support material (grey), nanoparticles blue (Ni), green (Ru). For simplification H_2O as reaction product is not shown. Figure prepared according to ref.[50] and ref.[60]

pathway involves the adsorption of CO_2, followed by formation of CO, which subsequently either dissociates into adsorbed C or a formyl intermediate as shown in Figure 1.5b. This mechanism is typically found for noble metal based catalysts, but is also discussed for some Ni based catalysts.[43, 44, 60–62] Westermann *et al.* proposed this mechanism for Ni/USY catalysts with a USY zeolite support.[61] Similar, Miguel *et al.* suggested the dissociative mechanism for an industrial Ni calcium aluminate catalyst.[62] In case of surface carbonyl species, the formation of $Ni(CO)_4$ could be possible under certain conditions, especially at low-temperature applications as well known for CO methanation.[63]

The associative pathway is characterized by adsorption of CO_2 and H_2 on the catalyst surface, which is followed by hydrogenation of the adsorbed carbonate/formate or intermediate species as

found for different catalysts and illustrated in Figure 1.5a.[50, 57, 64–66] Schild *et al.* reported that the associative pathways mainly proceeds via formate intermediates on Ni/ZrO_2 catalysts.[64] In the study of Ussa Aldana *et al.* on different $Ni/Ce{-}ZrO_2$ catalysts, it is proposed that carbonates are formed on the support and subsequently form formates and methoxy species before CH_4 is formed.[57] Similar results were also found by Solis-Garcia *et al.* on such catalysts.[66] Additionally, it is proposed that CO_2 activation mainly takes place on the support, while metallic Ni is responsible for H_2 dissociation.[57, 66] Muroyama *et al.* further investigated the role of different support materials and found an activity increase in the order: $Ni/La_2O_3 < Ni/Al_2O_3 < Ni/CeO_2 < Ni/ZrO_2 < Ni/Sm_2O_3 < Ni/Y_2O_3$ attributing the observations to the basic properties of the catalysts.[67] They proposed that moderate basic sites are preferred for high activity, while they also found differences in the reaction mechanism depending on the support material. For Ni/Al_2O_3 the dissociative pathway is proposed, while for the others formation of various carbonate and formate species are discussed.[67] The role of the same oxides as promoters in Ni/Al_2O_3 catalysts was also investigated by Guilera *et al.* showing the benefit of increased number of basic and thus CO_2 adsorption sites.[68] In DFT studies, Pan *et al.* showed for Ni/Al_2O_3 catalysts that surface hydroxyl groups on the alumina can influence the mechanism by shifting from the formate route to the dissociative route when the surface is hydroxylated.[69] These selected examples clearly highlight the importance of the role of the support material and its properties and not only the Ni nanoparticles.
In addition to the influence of support material, the Ni particle size might play an important role on the mechanism as shown by Vogt *et al.*[70] On a series of Ni/SiO_2 catalysts with Ni particle sizes ranging from 1 to 7 nm, they found an optimal activity at 2 nm that was associated with an optimum amount of adsorbed CO species. At smaller particle sizes they conclude that CO adsorbs too weakly, while at larger particle sizes the adsorption becomes too strongly forming a monolayer on the catalyst.[70] Additional complexity to the mechanism of CO_2 methanation might be observed for promoted or event bimetallic catalyst systems. As shown by Serrer *et al.* for $Ni{-}Fe/Al_2O_3$ catalysts, FeO_x clusters can promote the CO_2 dissociation and thus leading to higher activity.[71]
For the present thesis the following main conclusions for the presented selected examples and hypotheses about the CO_2 methanation mechanism over Ni based catalysts can be drawn:

- Multiple reaction mechanisms are possible, which might be sorted into the associative and dissociative pathway.

- The support can play an important role by offering adsorption sites for CO_2, especially with presence of medium basic sites.

- Surface properties of the support (e.g. hydroxilation) might alternate the reaction mechanism.

- In case of the dissociative pathway, the formation of $Ni(CO)_4$ might have to be considered, which can lead to volatile or mobile Ni species. Additionally, if surface carbon species are present formation of coke species could occur.
- The reaction mechanism can be dependent on the Ni nanoparticle size, especially in the case of small particles.

Based on the summarized conclusions on the CO_2 reaction mechanisms, it is obvious that certain deactivation mechanisms have to be considered for Ni-based methanation catalysts. Furthermore, it is difficult to assume a single occurring mechanism, in reality an interplay of different mechanisms might be the case, which eventually has to be analyzed for each system by its own. Following, different potential deactivation effects for CO_2 methanation catalysts will be discussed in section 1.2.3.

1.2.3 Potential Deactivation Phenomena Associated with CO_2 Methanation

There are several reported scenarios, which can influence the stability of Ni-based catalysts in CO_2 methanation reaction. Potential deactivation phenomena are illustrated in Figure 1.6 and were summarized in some literature reviews, e.g., in ref.[38, 40, 60] The deactivation can either mainly affect the metal nanoparticles, the support material or both together, but this also strongly depends on the exact reaction conditions, e.g., the used feed or temperature range. One might roughly distinguish the different deactivation mechanisms in poisoning or chemical reaction of the catalytic active sites (chemical deactivation, Figure 1.6,grey), which also includes redox, fouling (coking or mechanical blocking of active sites, Figure 1.6,green) as well as thermal degradation, including sintering, morphological changes and reaction between the support and metal nanoparticles (Figure 1.6,orange).[72, 73] For an industrial application also attrition or crushing are relevant, but out of the scope of the present thesis.[38]

Poisoning is mainly discussed due to sulfur containing feeds, which leads to formation of metal sulfides like NiS.[38, 60, 74, 75] In respect to CO methanation, Legras *et al.* showed that ppm and ppb levels in the synthesis gas mixture are already sufficient for deactivation of the applied $Ni/\gamma{-}Al_2O_3$ catalysts.[75] Erekson *et al.* and Fitzharris *et al.* report that especially the formation of surface sulfide layers deactivate the catalysts most severely.[76, 77] In addition to rather bulk species of sulfides, also blocking of active sites by chemisorption of the sulfur species can be possible. This was shown for CO methanation over Ni-based catalysts, as it was concluded that CO and the sulfur species compete for the same geometric sites, specifically step sites.[78, 79] While the selected examples are for CO methanation, the findings can also be translated towards CO_2 methanation.[38, 40, 60]

In addition to sulfur poisoning, also formation of volatile $Ni(CO)_4$ species might be possible. This would lead to dissolution and loss of active Ni species. However, as already discussed as part of the CO_2 methanation mechanism, this process is highly unlikely at temperatures above

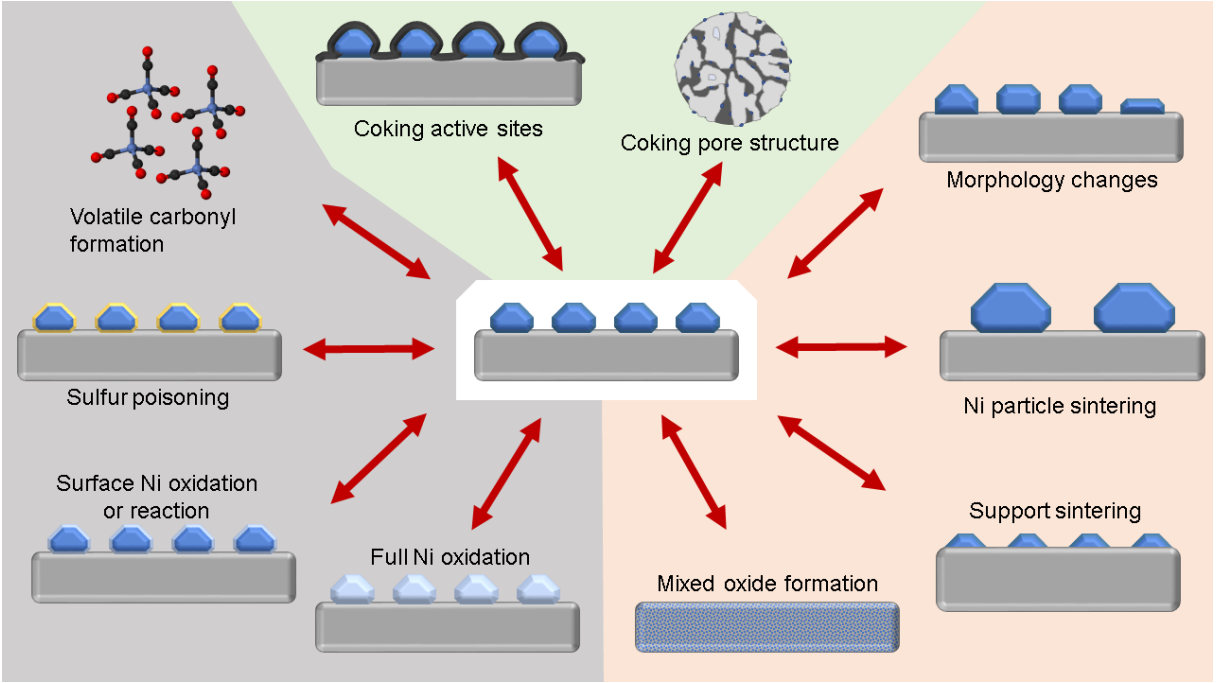


Figure 1.6: Overview on general possible deactivation phenomena of supported Ni-based CO_2 methanation catalysts, illustrated model of Ni nanoparticles (blue), support material (grey). Phenomena are sorted by deactivation due to poisoning/chemical reaction (grey area), fouling/coking (green area) and thermal degradation (orange area). Prepared based on information from ref.[30, 38, 40, 60]

573 K.[63] In addition, for CO_2 methanation, most probably it is strongly dependent on the actual reaction mechanism, and probably only relevant for the dissociative pathway or in case of mixed CO/CO_2 methanation.

Another possible deactivation pathway can be the deactivation by (partly) irreversible oxidation of the Ni nanoparticles towards NiO. This process was investigated in studies by Mutz *et al.* and Serrer *et al.* for a scenario of H_2 dropouts.[54, 71, 80–82] Depending on the length of the dropouts, the following reaction or reactivation conditions, either a complete oxidation or only surface oxidation as illustrated in Figure 1.6 is possible.

Additionally to the poisoning/chemical reaction type deactivation, fouling processes can cause deactivation of CO_2 methanation catalysts. More specifically, the focus is on coking of the catalysts (Figure 1.6,green). Coking can generally lead to different effects, i.e., chemisorption and thus blocking of active sites, encapsulation of nanoparticles or plugging of micro- and mesopores.[72, 73] The exact type of formed coke can strongly depend on reaction conditions, like temperature, amount of H_2O or reactants as reviewed by Bartholomew for coking on Ni-based catalysts applied in steam reforming and methanation reactions.[83] During deactivation different types of coke might be formed, which was exemplary shown by McCarty *et al.* for Ni/Al_2O_3 catalysts applied in CO methanation revealing the formation of either atomic carbon, amorphous carbon, carbide formation or crystalline graphitic carbon.[84] They showed that only amorphous

carbon and graphitic carbon were stable, while the other carbon deposits easily react also to desired products. As shown by Czekaj *et al.* also the formation of carbon whiskers might be possible, which can cause a detachment of Ni nanoparticles.[85] In general, for CO methanation catalyst deactivation by coking is widely observed as reviewed in ref.[38, 40, 60, 72, 73, 83] However, this is different for CO_2 methanation as shown by *operando* Raman spectroscopy studies of Mutz *et al.*[86] Significant coking could only be observed under artificial coking conditions, i.e., pyrolysis/carbonization of a diluted CH_4 gas stream at 673 K.[86] Therefore, in the specific case of CO_2 methanation, coking appears to be not a major deactivation cause, but might be relevant for mixed feeds of CO and CO_2 as well as under certain operating conditions and position of the catalyst particle in the reactor.

The above discussed deactivation pathways strongly depend on applied reaction conditions or are not very common for pure CO_2 methanation. The main deactivation in CO_2 methanation is thought to be due to thermal degradation, which can be associated to the strong exothermic nature of the reaction itself and a typical operation in a temperature range of 523 to 673 K.[38–40, 45, 87] Due to the exothermic nature of the reaction, it is prone to form hot-spots inside chemical reactors, especially in industrial large scale applications, where heat management is more difficult to achieve compared to smaller laboratory testing setups, e.g., glass capillaries. The potential hot-spot formation for Ni-based methanation catalysts is exemplary shown in Figure 1.7. Serrer *et*

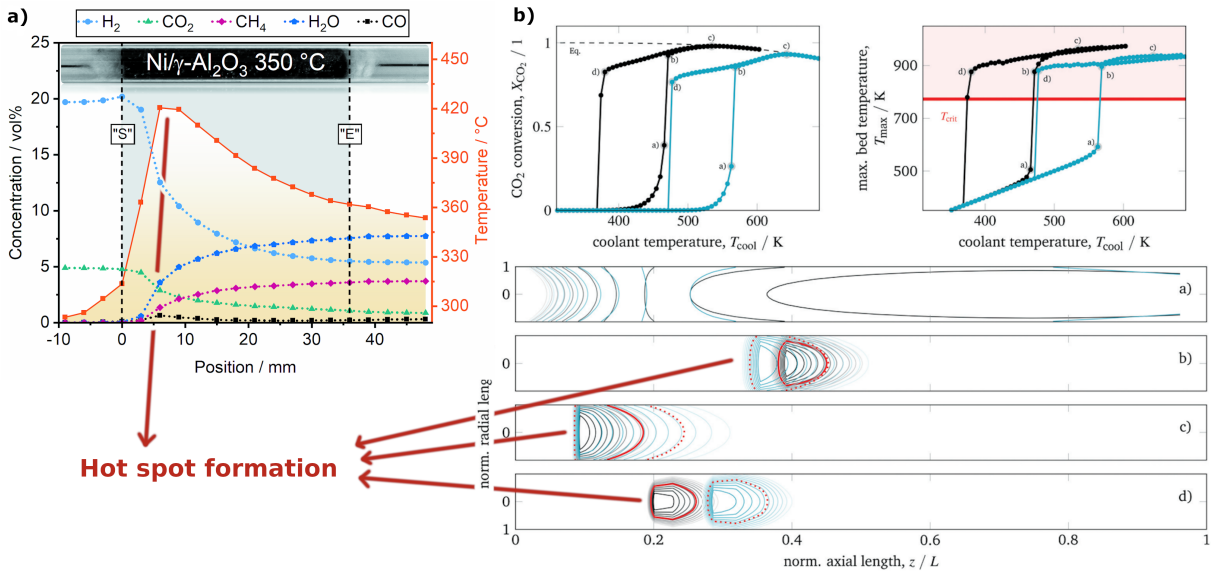


Figure 1.7: (a) Hot-spot formation during CO_2 methanation over a Ni/$\gamma-Al_2O_3$ catalyst revealed using a capillary setup for axially resolved reactor profiles. Available under the terms and conditions of the Creative Commons Attribution 4.0 license (CC BY 4.0, `https://creativecommons.org/licenses/by/4.0/`), Copyright ©2021.[88] (b) Simulation results showing the hot-spot formation for different kinetic models of a more active (black) and less active (blue) Ni-based catalyst in an industrial scale reactor. Available under the terms and conditions of the Creative Commons Attribution 3.0 license (CC BY 3.0, `https://creativecommons.org/licenses/by/3.0/`), Copyright ©2019.[89]

al. showed the hot-spot formation in a spatially-resolved laboratory capillary setup with a reactor diameter of 6 mm for a Ni/$\gamma-Al_2O_3$ catalyst during CO_2 methanation (Figure 1.7a).[88] Despite the catalyst was diluted 1:4 with SiC, the hot-sport reached almost 700 K at a controlled furnace temperature of 623 K.[88] Similarly, Bremer *et al.* showed in simulation studies strong hot-spot formation of even higher temperatures up to ≈900 K in typical industrial reactors as shown in Figure 1.7b.[89] For calculations they used different kinetic models available from literature, the one from Koshany *et al.*[51] (Figure 1.7b,black) and Xu and Froment[90] (Figure 1.7b,blue). The observed differences in Figure 1.7b mainly reflect the different activities of the catalyst used to retrieve the kinetics. Therefore, hot-spot formation and probably thermal degradation is much more severe for very active catalysts.[89]

As illustrated in Figure 1.6, thermal degradation can be associated to different reasons. For the four different deactivation mechanisms some selected examples are presented. Abello *et al.* and Koshany *et al.* showed long-term deactivation for co-precipitated Ni/Al_2O_3 catalysts, which were tested at 673 K and 653 K, respectively.[51, 91] They showed that the tested catalysts show a slow decline in activity and reaching only a constant activity after several hundreds of hours.[51, 91] In addition to their findings, Beierlein *et al.* studied similar catalysts in rapid ageing tests under hydrothermal conditions at 873 to 973 K.[87] All three studies attribute the deactivation of the catalysts mainly towards sintering of the Ni nanoparticles.[51, 87, 91] Additionally, Beierlein *et al.* found an influence of support structure changes based on slight decrease in the specific surface area and pore volumes derived from N_2 sorption measurements.[87] In general, Ni particle sintering is known to be enhanced under high temperatures and hydrothermal (steam) conditions,[92–94] which are present due to the H_2O formed in the methanation reaction. Furthermore, Beierlein *et al.* discussed the possibility of surface restructuring of Ni nanoparticles leading to morphological changes and thus influence on the activity.[87] Finally, they could also reveal that hydrothermal conditions at high temperature might lead to oxidation of Ni towards NiO showing that thermal degradation and chemical effects are strongly related to each other.[87] Similar results were found by Mebrahtu *et al.* elucidating the influence of nickel hydroxide species formed during hydrothermal conditions, concluding an enhanced sintering and formation of mixed oxides, e.g., $NiAl_2O_4$ or related defect spinel structures.[95] Due to the structural similarity of the crystal structures of $NiAl_2O_4$ and $\gamma-Al_2O_3$, the latter generally described as a defect spinel structure, the formation of mixed oxides is frequently observed.[92, 96–100] An additional example are the studies from Ewald *et al.*, investigating the long term deactivation of co-precipitated Ni/Al_2O_3 catalysts.[101] They report a complex interplay of different thermal degradation effects, i.e. Ni particle sintering, textural changes of the support (support sintering) by loss of specific surface area and thus medium basic sites.[101] As discussed in the previous section 1.2.2, a loss in medium basic site can reduce the number of CO_2 adsorption sites and thus lower the activity in case of the associative mechanism. Furthermore, similar to Mebrahtu *et al.* and Beierlein *et al.*, they found mixed oxide formation, which they attribute to Ni incorporation into $\gamma-Al_2O_3$ or partial formation of $NiAl_2O_4$.[101] Ewald *et al.* summarized their results as that the amount

and variety of changes makes it challenging to clearly determine, which of those has the main impact on the deactivation of the catalyst or whether all effects contribute significantly.[101] This demonstrates that support and Ni nanoparticle changes upon (hydro)thermal degradation might have a strong effect on the catalyst stability. The deconvolution of the different phenomena, which were discussed before, is challenging especially as catalyst changes are typically only investigated *post mortem* (i.e. after the deactivation occurred) and *ex situ*. For a detailed understanding of deactivation and catalyst function, *in situ* or *operando* techniques are required, which are sensitive to possible sample changes.[102–104] The applied technique(s) should be able to reveal textural and structural changes of the studied catalysts, and a combination of different techniques might be required for a complete picture. Based on the discussed examples for the deactivation of Ni-based methanation catalysts the following conclusions for the present thesis can be drawn:

- Different deactivation effects affecting the metal nanoparticles or the support material have to be considered.
- (Hydro)thermal degradation is considered as the main deactivation pathway, because of the exothermic nature of the reaction.
- Fouling and specifically coking might only be relevant for specific reaction conditions.
- Poisoning or formation of volatile compounds is not expected under relevant reaction conditions of this thesis.
- Advanced characterization methods are required to unravel the multitude of effects responsible for catalyst deactivation.

1.2.4 Dynamic Process Operation of the CO_2 Methanation

As already discussed in section 1.1.1 and shown in Figure 1.1 a scenario of fluctuating power supply can be associated to the use of renewable energy sources. If the CO_2 methanation is used in the frame of Power-to-X concepts to store surplus energy in form of CH_4, it can be expected that the reaction might have to be performed under dynamic process conditions.[30, 105] The reason for this is that intermediate buffer tanks for CO_2 and H_2 should be reduced in size and amount due to cost reasons, which is especially the case in a small scale and delocalized application of the CO_2 methanation reaction, e.g., close to the renewable power generation. As discussed as part of potential deactivation effects in section 1.2.3, a H_2 dropout scenario was studied which led to (partly) irreversible oxidation of Ni during longer dropout times (min scale).[54, 71, 80–82] However, in a practical application the dropout of a single feed component is not a realistic scenario. Rather load changes of the reactor or many startup and shutdown cycles instead of a constant operation are more relevant.[105]

Considering tubular fixed-bed reactors, simulation studies showed that for undiluted feeds the hot-spot formation cannot be avoided under conventional steady-state operation of these reactors.[106, 107] The importance of heat management during dynamic load changes or reactor startup to minimize hot-spot formation and thermal runaways of the reactor was shown by Bremer *et al.*[89, 108] As hot-spot formation and thermal runaway can be directly associated to thermal degradation of the employed catalysts, they have to be avoided or at least minimized for an industrial application. Furthermore, the thermal runaway has to be avoided due to safety aspects of an uncontrolled reactor behavior. Therefore, alternative concepts in the dynamic operation of fixed-bed reactors for CO_2 methanation have to be found to ensure save and longtime operation of the reactor and catalysts.

1.2.5 Control of Methanation Reactors by Designed Catalyst Particles

As discussed previously for the dynamic process operation in terms of load changes of the CO_2 methanation reaction, new catalyst reactor concepts might be required. In this respect, the control of the reactor in terms of its temperature can be optimized by tuning the interplay of mass transport, heat transport and the reaction rates on a catalyst particle scale.[106] As one can imagine, tuning those parameters allow for a large parameter space with many degrees of freedom for catalyst design. This could include tailored pore structures to adjust mass transport properties, tuned activity of the active sites or spatial distribution within the macroscopic catalyst particles, among many others. However, prediction of a certain function is not trivial and challenging due to the complex interplay. For example, "egg-yolk" like catalyst particles, i.e., active sites concentrated in the center and not at the exterior of the macroscopic particles, were shown to prevent thermal runaway behavior in Fisher-Tropsch synthesis.[109] Furthermore, Wu *et al.* reported the influence of the metal distribution inside catalyst particles for CO methanation on selectivity and carbon deposition.[110, 111] But not only the active site distribution can influence the performance, also distribution of heat and mass transport capabilities inside a catalyst particle can be a design parameter.[112, 113]
For the CO_2 methanation reaction Zimmermann *et al.* proposed an improved catalyst particle design, which allows for load flexible operation of fixed-bed reactors.[114, 115] The possible catalyst particle design is shown in Figure 1.8a,d as a selected example to control the dynamic behavior of reactors for CO_2 methanation. In a first study, Zimmermann *et al.* introduced a catalyst particle design with an active core and inert shell (blue and red, Figure 1.8a) and compared it to a uniform active particle (black, Figure 1.8a).[114] The core-shell concepts can be differentiated as a distinct shell (blue) and a radial gradient towards the inner core (red). In their simulations, they showed that the permeability (mass transport properties) of the catalyst particle is a decisive parameter for the particle-reactor model. All three designs could be optimized for a stable steady-state operation with CO_2 conversions above 90 % as shown in Figure 1.8b. However, in dynamic simulation studies they found that the uniform particle (black)

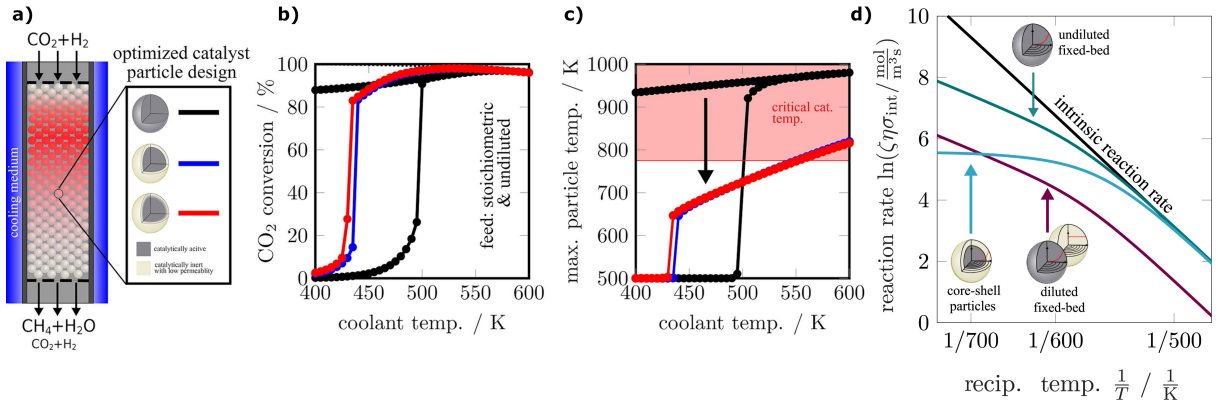


Figure 1.8: (a) Catalyst particle designs studied for an optimized dynamic operation of a fixed-bed CO_2 methanation reactor. (b) Simulated corresponding conversion levels depending on the cooling temperature. (c) Illustrated thermal sensitivity depending on the coolant temperature. (d) Arrhenius plots showing the induced mass transport limitations of the core-shell catalyst concept. (a-c) Available under the terms and conditions of the Creative Commons Attribution 4.0 license (CC BY 4.0, `https://creativecommons.org/licenses/by/4.0/`), Copyright ©2020.[114] (d) Available under the terms and conditions of the Creative Commons Attribution 4.0 license (CC BY 4.0, `https://creativecommons.org/licenses/by/4.0/`), Copyright ©2021.[115]

exhibits a wrong-way behavior, especially during shutdown, which means a thermal runaway. Furthermore, this uniform particle design was found to be very sensitive towards parameter changes, e.g., coolant temperature (thermal sensitivity, Figure 1.8c), reactor pressure and feed velocity. The two designs with an inert shell were identified to be much less sensitive as no wrong-way behavior could be observed and the reactor allows much faster dynamic operation changes. The particle design of an inert shell (blue) was found as the optimum also from the practical point of preparation compared to a controlled gradient system. This optimized core-shell particle allows to operate the reactor under stoichiometric undiluted feed with conversion higher than 95 %. Furthermore, the thermal sensitivity is strongly reduced and fast startup and shutdown of the reactor is possible.[114]

In a second study, Zimmermann *et al.* compared the optimized catalyst particle design with a diluted reactor bed of inert and active particles as well as solely the uniform active particles (Figure 1.8d).[115] They confirmed the previous simulations that the core-shell particle design is an optimum for load-flexible operation of the methanation reaction. It is reported that also the diluted catalyst bed does not necessarily prevent the thermal runaway behavior of the uniform particles. As shown in the Arrhenius plot in Figure 1.8d, it was found that the reduced sensitivity of the core-shell particle can be attributed to mass transfer limitations by the inert shell, which "control" the activity of the overall particle as rate limiting steps. By design of the pore structure of the inert shell or its thickness, this mass transport properties can be optimized.[115]

Based on this selected example, the following conclusions can be made:

- Innovative catalyst particle design concepts may allow for a safe and efficient dynamic operation of fixed-bed CO_2 methanation reactors.
- Tuned mass transport properties are crucial to reduce thermal sensitivity of the reactor by activity control via mass transfer limitations.
- Heterogeneous catalyst particle concepts seem promising allowing for many degrees of freedom in optimal particle design.

1.3 Length Scales in Heterogeneous Catalysis and Challenges for Spatially-Resolved Characterization

As illustrated in the previous sections, there is a multitude of scales that has to be considered in catalysis research. In the following and as part of this thesis, the focus is on relevant length scales from the atomic to the reactor level in heterogeneous catalysis. However, spatial and temporal effects might be connected to each other, but have different requirements for spatial-, time- or spatiotemporal resolved characterization.[116, 117] Different relevant length scales in heterogeneous catalysis are illustrated in Figure 1.9 for a Ni/Al_2O_3 catalyst applicable in the CO_2 methanation. It can be observed that relevant length scales in heterogeneous catalysis range

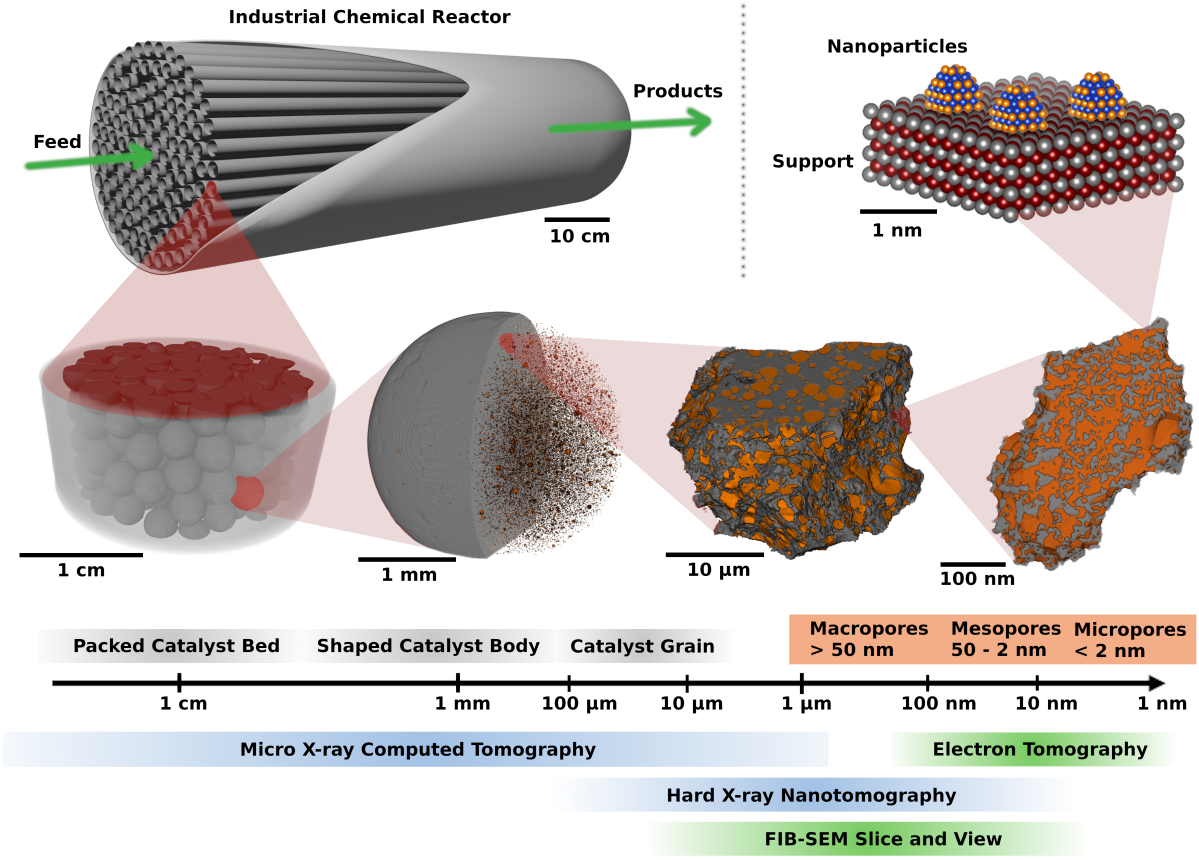


Figure 1.9: Relevant length scales for a selected Ni/Al_2O_3 catalyst employed in CO_2 methanation. From large to small: industrial scale multitubular fixed-bed reactor, micro X-ray computed tomography of a selected volume of a single tube, micro X-ray computed tomography of a single catalyst particle/body, X-ray nanotomography of a selected catalyst grain, electron tomography volume of an even smaller grain, illustration of an support surface (atoms color: white Al, red O) with metal (oxide) nanoparticles (atoms color: blue Ni, orange Ni/(O)). The highlighted red shadowed areas show the respective volumes which were investigated by the different techniques highlighting the multi-scale challenge of catalyst characterization. Available under the terms and conditions of the Creative Commons Attribution 4.0 license (CC BY 4.0, `https://creativecommons.org/licenses/by/4.0/`), Copyright ©2022.[118]

from m to cm in case of the reactor, down to Å(100 pm) in case of the active catalytic sites bridging about 10 orders of magnitude. In comparison to the required storage capacities in the Power-to-X discussion (Figure 1.2), a single process in heterogeneous catalysis has a similar high complexity.
The different length scales can be associated to different phenomena:[117, 119]

- Reactor scale (single tube in the present example): pressure drop, heat management, overall product formation and integration in a larger network of processes.
- Catalyst particle/body scale: heat and mass transport properties, but also mechanical stability of the single particle.
- Single catalyst grains or regions inside a particle/body: different mass transport phenomena, like convex flow or types of diffusion.
- Active sites: actual reaction, which involves adsorption and desorption of the molecules on the active site and the actual chemical reaction.

Considering the previous discussions about catalyst deactivation (section 1.2.3) or the design of catalyst particles (section 1.2.5), different length scales are relevant to understand catalyst performance (activity, stability) as well as in the design space for the core-shell materials. In terms of deactivation, not only the active site might be affected, but also the support material or the catalyst pores or even mechanical failure of whole particles can occur. The core-shell design (section 1.2.5) showed that on a particle scale, both activity with related heat management and mass transport might interact closely and affect the overall reactor behavior.
Therefore, different characterization methods are required to bridge the different length scales as reviewed in a couple of articles to obtain a multiscale understanding of catalytic processes.[104, 116, 117, 119–121] From Figure 1.9, it is obvious that there is no single method, which can directly cover all relevant length scales at once. This is further complicated, if one is not only interested in resolution related information like morphology, texture or similar, but also chemical information are required. As in an example reviewed by Buurmans and Weckhuysen, there is a multidimensional room of spatially-resolved characterization methods in terms of sample size, sample complexity, spatial resolution or chemical information content.[104] This space might easily be further extended, e.g., by availability or costs of certain methods, especially in an industrial application perspective. The challenge of the possible sample size, which can be investigated by a certain method is also illustrated in Figure 1.9, which might also raise the question how representative results from certain characterization methods are. Due to this complexity, the main focus of spatially-resolved characterization in this thesis is limited to pore structures and related morphological and textural properties. In the following, first catalyst porosity and the conventional characterization of the pore structure will be reflected. This is complemented by reviewing spatially-resolved characterization methods to understand catalysts in 3D over multiple length scales, with a focus on hard X-ray tomography methods.

1.4 Catalyst Porosity and Conventional Analysis Methods

As shown in the previous section 1.2.5, the mass transport properties of catalysts can strongly influence, if not even determine, the catalyst performance. The mass transport takes place in the pores or void space of catalysts. Based on the IUPAC recommendation, pores can be distinguished into micro- (< 2 nm), meso- (2-50 nm) or macropores (> 50 nm).[122] Additionally, one might describe porous features of catalysts qualitatively according to their characteristics as shown in Figure 1.10a. For example, one can distinguish in (a) closed pores, (b) ink-bottle shaped pores, (c) open pores, (d) funnel shaped pores, (e) through pores, (f) blind pores or (g) roughness of the external surface.[122] As one can see, pores might be differentiated by their

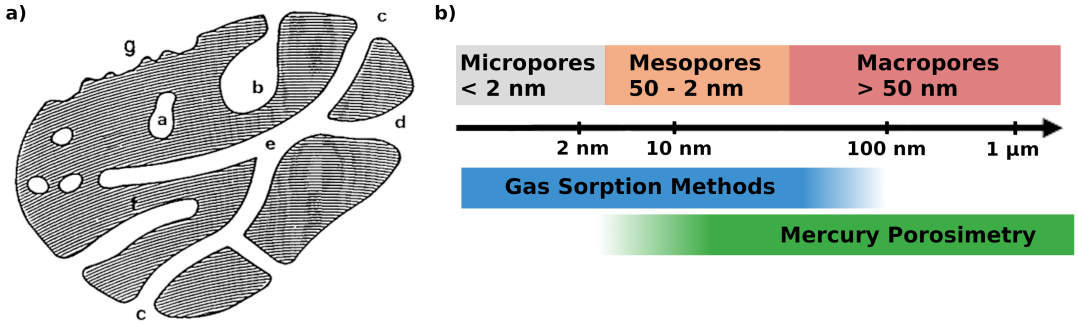


Figure 1.10: (a) Overview on different qualitative descriptions of pores inside a porous catalyst. a: closed pores, b: ink-bottle shaped pores, c: open pores, d: funnel shaped pores, e: through pores, f: blind pores or g: roughness of the external surface. From J. Rouquerol, D. Avnir, C. W. Fairbridge, D. H. Everett, J. H. Haynes, N. Pernicone, J. D. F. Ramsay, K. S. Sing, K. Unger, "Recommendations for the characterization of porous solids", *Pure Appl. Chem.* **1994**, *66*, 1739–1758, ©1994 IUPAC.[122] (b) Definition of pore sizes according to IUPAC[122] with conventional methods to study porosity in those length scales.

shape or whether they are connected to the outer surface and how. Already this simple schematic model illustrates the potential complexity of pore structures in catalysts.
The core-shell particle design (section 1.2.5) showed how strongly mass transport, which is mainly defined by the pore structure of catalysts, can influence the reactor scale performance. For that example, enhanced mass transport limitation were found as promising.[114] However, in case of coking or especially for undesired mass transport limitations inside the active core of this design concept, a tailored pore structure providing improved mass transport might be desired. Hierarchical pore structures with a combination of different pore sizes of micro-, meso- or macropores compared to uniform ones are a promising approach for this purpose.[123–128] In the following, the focus will be on meso-/macroporous systems with predominant Knudsen diffusion in mesopores and molecular diffusion or convective flow in macropores.[124] In this respect, the introduction of macropores into a uniform mesopore network can allow for higher mass transfer velocity.[123, 124, 129] Such hierarchical structures are also often present in our environment, especially for transport processes, e.g., modern designed road networks or our

respiratory system.[130, 131]
The conventional routine characterization of pore structures in catalysts is performed by gas sorption or intrusion methods.[122, 132, 133] For gas sorption mostly N_2 sorption is applied, while for intrusion methods mercury porosimetry is most common. The correct assessment of hierarchical porosity is an existing challenge, as shown by Schlumberger *et al.* and Cychosz *et al.* for the application of gas sorption and Hg porosimetry as routine methods to study hierarchical pore structures.[134, 135] As illustrated in Figure 1.10b, a single method of the two is not sufficient to investigate all relevant length scales of pores in hierarchically porous catalysts. In case of meso-/macroporous catalysts, the combination of Hg porosimetry (macro- and mesopores down to 4 nm), and Ar- or N_2-sorption applied for smaller mesopores is required.[122, 132–135] A challenge for both methods is that they hardly provide direct information about complex pore network information, e.g., the connectivity or shape of individual pores as well as the whole pore network. Additionally, gas sorption usually requires an initial thermal degassing step, which might change fragile or intermediate sample stages and in such a case being an invasive method.[133–135] Hg porosimetry is also an invasive technique, as it is likely that after intrusion not all Hg can be removed from the sample. Furthermore, the high pressure required during intrusion to investigate especially small mesopores can easily break fragile samples.[132, 134, 135]
Considerable progress in the synthesis and design of meso-/macroporous materials with promising applications in adsorption or catalysis was achieved in the last two decades as reflected in several reviews.[125, 127, 136–145] There is a multitude of proposed synthesis strategies, e.g., post processing (often leaching), templating or self-assembly methods, each of those enables certain control over porosity, particle shape and applicability for certain material classes.[125, 145] Among those, modified sol-gel synthesis is one strategy to obtain meso-/macroporous materials in form of spheres, membranes or monoliths.[141, 143, 145, 146] This method can be described by five essential steps: (1) sol formation by hydrolysis and partial condensation, (2) gel formation via polycondensation, (3) aging of the gel, (4) drying of the gel and (5) stabilization (usually calcination), while each of the steps can influence the texture and structure of the final material.[143, 146, 147] Detailed understanding of this synthesis approach is difficult due to the various steps and parameters involved and an optimization of the synthesis is often based on "trial and error". Besides structure-directing or phase separation agents (i.e. polymers), the final pores structure might be strongly influenced by the solvent and its removal during drying and calcination.[143, 146] The final calcination can change the porosity, pore sizes or induce crystallization, sintering, partial or even complete structural collapse.[127, 143, 146] A more detailed understanding and control of those effects should be obtained in order to allow for a rational design of hierarchical meso-/macroporous materials.
As discussed before, conventional methods do not allow to understand those changes while they are happening, as they are apllied *ex situ* and *post mortem*. Furthermore, intermediate steps involving fragile sample stages, might not be investigated at all without introducing sample changes. For example, the thermal outgassing step for N_2 sorption might already change a dried

gel sample before calcination. Therefore, comparing the exact dried gel and related final state is hardly possible. In addition, the conventional methods can hardly allow for detailed insights into the pore structure evolution by *in situ* experiments. This requires the application of other more advanced characterization methods to study pore structure changes while they occur. Therefore, the following state-of-the art and challenges can be concluded:

- Conventional porosity characterization is usually performed by gas sorption (mainly N_2 sorption) and Hg porosimetry methods, which both can be considered as invasive, especially for intermediate or fragile samples / sample structures.
- As mass transport properties strongly determine catalyst performance, improving these is a crucial design parameter. Tailored hierarchically porous catalyst structures are a promising strategy in this direction.
- Proving true hierarchical structures in catalyst materials is challenging with conventional methods as they only probe the bulk sample and usually only provide 0D/1D information in terms of porosity or pore size distribution. Furthermore, only basic pore structure models might be reasonably derived.
- Understanding of porosity and structural formation steps of synthesis procedures towards hierarchically porous materials are often very premature, which results in often "trial and error" based tailoring of the synthesis.
- Due to their invasive nature and missing *in situ* possibilities, conventional methods cannot directly unravel the porosity formation steps as they occur, which requires new alternative characterization tools to understand pore structure evolution.
- Besides the understanding of the textural evolution during catalyst synthesis, knowledge about structural transformation processes is equally important for a future tuning of the preparation method.

1.5 3D-Spatially-Resolved Characterization in Heterogeneous Catalysis

Keeping in mind the multidimensional nature of heterogeneous catalysis in terms of length scales (Figure 1.9) and characterization of hierarchically porous materials by conventional methods (section 1.4), advanced spatially-resolved methods might overcome these challenges. In this section, general aspects and examples of spatially-resolved characterization in heterogeneous catalysis are presented. A main focus is lying on sample size and resolution of the method in order to be able to address all length scales as previously shown in Figure 1.9. In this respect, different hard X-ray tomography methods will be presented as key tools to retrieve spatially-resolved information from different length scales. Furthermore, some examples are provided to show potentials of chemical imaging using hard X-rays, which is complemented by an outlook towards *in situ* and *operando* imaging methods.

1.5.1 Suitable X-ray Probes for Spatially-Resolved Studies

The advantage of X-ray imaging compared to other types of electromagnetic radiation or particles, i.e., electrons, are their high penetration depth in matter. This is crucial for imaging of extended objects, e.g., whole catalyst pellets or larger catalyst grains, where the penetration depth of the applied probe (used radiation) has to be high enough to significantly transmit the whole sample volume. The Lambert law can be applied to describe the absorption of electromagnetic radiation generally as:

$$I(z) = I_0 e^{-\mu(E)z} \tag{1.4}$$

with $I(z)$ as the transmitted radiation intensity through the sample, I_0 as the incident radiation intensity, z as sample thickness and $\mu(E)$ as the energy dependent attenuation coefficient. In case of X-rays $\mu(E)$ is often referred to as the linear X-ray attenuation coefficient, which depends on the X-ray energy, the chemical elements and compounds of those with values available in databases, e.g. the "XCOM: Photon Cross Sections Database".[148] Regarding the X-ray energy, one might differentiate roughly between soft ($\lessapprox 2400\,\mathrm{eV}$) and hard (tens to hundreds of keV) X-rays with no exact boundary.[149–152] The penetration depth of X-rays generally increases with higher energy. Therefore, especially hard X-rays allow to image extended objects, e.g., the full human body in medicinal application of X-ray computed tomography (CT). Contrary to that, soft X-rays only allow to investigate thin samples in 3D, usually $< 1\,\mu\mathrm{m}$ in thickness. As the main interest here is on spatially-resolved studies of samples with larger dimensions (particle or grain scale), the following focus is on hard X-ray imaging.

Despite the general high penetration depth of X-rays, synchrotron-based X-ray radiation offers many additional advantages.[149] This includes greater brightness and flux compared to laboratory X-ray sources, which is important for focusing X-rays.[149, 150] Therefore, high intensity micro- or nanofocused beams are currently mainly related to synchrotron-based instruments, although

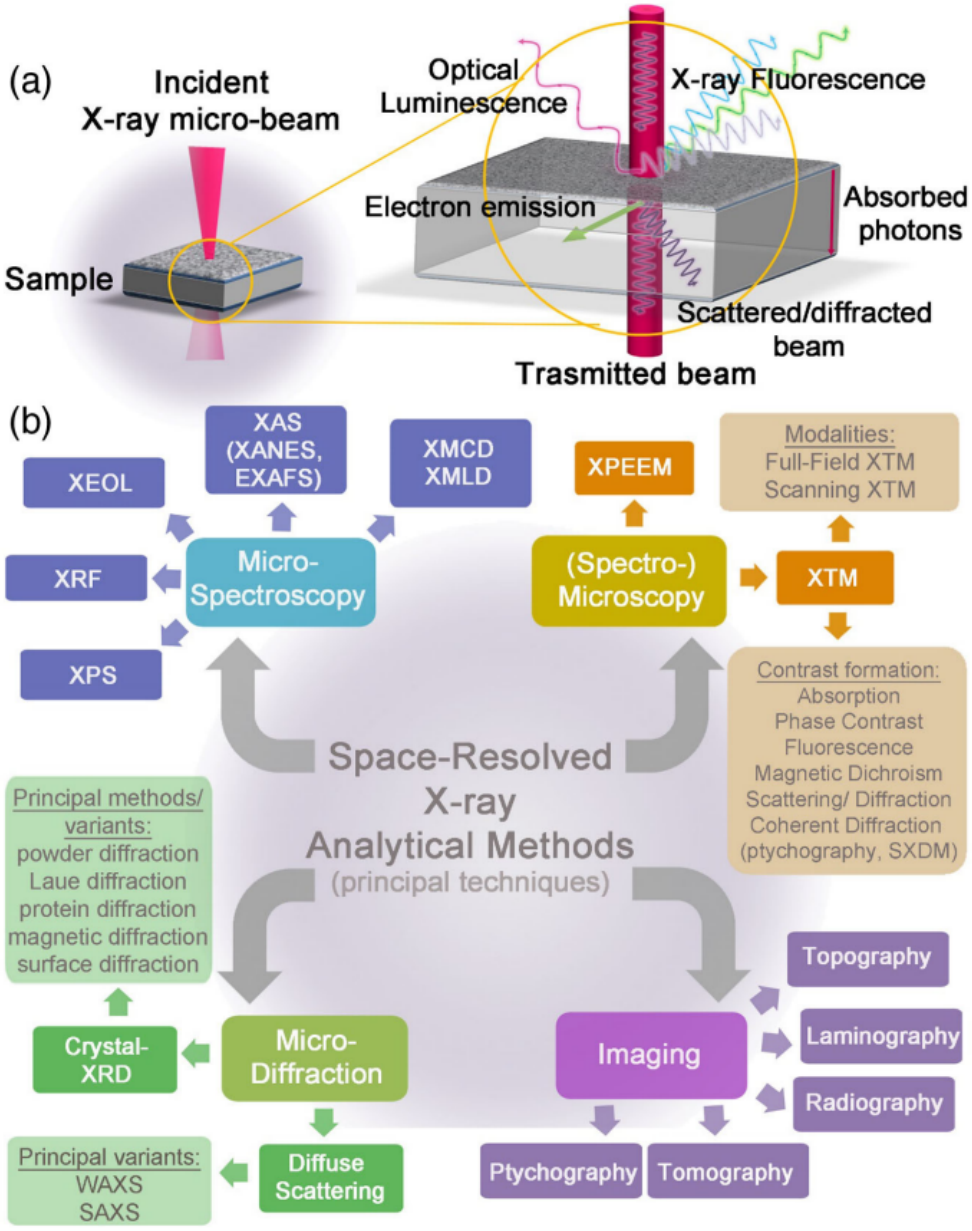


Figure 1.11: Overview on different possible synchrotron X-ray probes for spatially-resolved analysis. The illustration highlights the multitude of contrast modes available with X-rays to study materials.[149] Reprinted with permission from: L. Mino, E. Borfecchia, J. Segura-Ruiz, C. Giannini, G. Martinez-Criado, C. Lamberti, *Rev. Mod. Phys.*, *90*, 25007, **2018**. Copyright 2018 by the American Physical Society.

laboratory methods are also developing.[149, 150] A further advantage of synchrotron-based X-rays is that several complementary contrast modes can be applied as illustrated in Figure 1.11.[149] As visible in Figure 1.11, the contrast modes can provide different information about the studied sample as very roughly distinguished following:[149]

- Elemental contrast: X-ray fluorescence (XRF).
- Information about the local atomic structure of materials: X-ray absorption near edge spectroscopy (XANES) and extended X-ray absorption fine structure (EXAFS).
- Medium or long range atomic structure: powder X-ray diffraction (PXRD) and wide angle X-ray scattering (WAXS).
- Short range order on the material scale: small angle X-ray scattering (SAXS).

The previously listed contrast modes might be generally grouped as chemical imaging. Additionally, there are imaging contrast modes with no direct chemical information, e.g., phase or pure absorption contrast. In general, all the methods can be employed as spatially-resolved techniques, i.e., in tomography mode, to characterize catalysts in 3D as summarized in multiple reviews.[104, 116, 117, 149, 153–155]
According to Mino *et al.*, the different tomography modes might be distinguished into full-field imaging or scanning X-ray microscopy.[149] The full-field imaging mode can be compared with a classical optical microscope or camera system. In this respect the sample is illuminated via a condenser optic and an objective lens produces a magnified projection of the sample, usually acquired by charge-coupled device (CCD) camera systems. A series of angular distributed 2D projections of the sample allows then for tomographic reconstruction of the sample volume. This mode can be easily implemented for absorption or phase contrast methods.[149] Scanning X-ray microscopy mode is the most common and straightforward way for chemical imaging. A micro- or nanofocused X-ray beam is raster scanned over the sample to create 2D maps of the sample. By acquisition of those 2D maps from different angles of the samples again tomographic reconstructions are feasible.[149] A short comparison of the two scanning and full-field modes shows that they kind of complement advantages and disadvantages. Generally, full-field imaging is much faster on a cost of usually a higher dose on the sample, because the objective lenses strongly limit the efficiency. Furthermore, complementary contrast information is challenging to obtain. The scanning mode on the other hand easily allows to acquire different contrast modes simultaneously at a lower dose. However, the scanning requires much more time and scanning stages might influence the final resolution, especially for highest-resolution imaging.
There are mainly three different tomography methods, which allow for routine resolution down to 100 nm: (1) absorption contrast based (scanning) transmission X-ray microscopy ((S)TXM), (2) phase contrast based full-field imaging, i.e., X-ray holotomography or other variants of full-field phase contrast tomography and (3) coherent X-ray diffraction imaging based methods.[149, 154,

156–158] The possibilities for heterogeneous catalysis are briefly presented for each technique in the following.
(S)TXM is a straightforward method, which provides tomograms based on the absorption contrast of the sample, however due to raster scanning of a focused beam over the sample it is essentially limited to the focus size of the incident X-ray beam.[158] On the other hand, this directly allows for complementary contrast modes, e.g., XRF. However, as discussed by Dierolf *et al.* with increasing X-ray energy, which is required to study larger samples, the absorption decreases to the fourth power.[156] This ultimately leads to only small contrast variations, which might be hard to quantify and analyze. In addition, (S)TXM with absorption contrast does not directly provide quantitative information about the electron density of the sample.[157]
Contrary to the absorption contrast, X-ray phase changes are much more pronounced (orders of magnitude higher), especially for weakly absorbing samples.[156] However, it is difficult to directly retrieve phase shifts.[156] One example technique to study phase changes is X-ray holotomography. Here, principally for each angular projection of the sample images at different sample to detector distances are acquired, which allows to retrieve the phase shift.[159] The phase contrast enables to obtain direct quantitative information about the electron or mass density of the studied sample.[156, 157, 159] However, the full-field X-ray holotomography approach is limited by the X-ray focusing optics.
Here, coherent diffractive imaging (CDI) allows for much less stringent requirements. CDI is also sometimes referred to as "lensless X-ray imaging", describing that there is no direct need for strong focusing high quality lenses.[158] Therefore, CDI related methods offer the possibility to overcome resolution limits especially related to the possibility of focusing the X-ray beam.[158] In the CDI approach, essentially far-field Fraunhofer diffraction patterns are acquired that provide information about the scattering vectors of a sample.[158] Only a bit more than a decade ago, X-ray ptychography and its 3D counterpart ptychographic X-ray computed tomography (PXCT) were presented as a combination of CDI and STXM.[156, 158] Here, the sample is raster scanned with an overlapping illumination and diffraction patterns are acquired at each sampling point. An iterative algorithm then retrieves absorption and phase shift information from the diffraction patterns and reconstructions for the 2D projection of the sample.[158, 160–163] The method combines the advantages and overcomes disadvantages of STXM and CDI. The resolution of X-ray ptychography is not limited to the beam size as for STXM.[158]
In summary, especially synchrotron-based hard X-rays provide a large toolbox of different methods, which allow µm to nm resolution for spatially-resolved catalyst characterization. Possibilities of 3D spatially-resolved hard X-ray imaging in catalysis research will be presented on selected examples in the following three subsections.

1.5.2 Resolution vs. Sample Size – a Trade-off in Catalyst Characterization

As shown in Figure 1.9, multiple length scales have to be considered in the characterization of solid catalysts. Due to limitations of different methods there is a general trade-off between sample size and achievable resolution. Ideally, the studied sample should be as large as possible to ensure a good representation of the overall sample. As discussed previously for the different X-ray probes, hard X-rays allow to penetrate large sample volumes, especially compared to soft X-rays or electrons. Therefore, they are ideal for imaging of large sample volumes. In the following, different hard X-ray tomography techniques and studies are presented with a focus on resolution and sample size, which is complemented with electron tomography. This includes mainly absorption and phase contrast methods, as chemical imaging will be discussed in section 1.5.3.

Reactor scale

The following review of examples will start from the reactor over the pellet to the grain size sample scale according to Figure 1.9. µ-XCT experiments are commonly applied for this large sample length scales, which are also commonly accessible by laboratory instruments. For example, Caulkin *et al.* investigated the packing of catalyst pellets inside fixed-bed reactors with inner diameters up to 290 mm. They could retrieve information about the overall bulk density of the bed, derive local packing density profiles or information about pellet orientation. A specific focus was to obtain information about the influence of particle-particle and particle-wall interactions and to verify simulation models that are commonly applied to simulate packing of catalyst beds.[164] Similar, Seckendorff *et al.* studied the formed void space of fixed-bed reactors containing spherical catalyst particles with different reactor to particle diameter ratios. By determination of the bed porosity they determined the influence of different ratios on the pressure drop behavior of the reactor as an important design parameter.[165]

Furthermore, there are examples of different catalytic foams studied by µ-XCT, where the tomography data was used to create 3D models for heat transport simulations.[166–169] Bianchi *et al.* focused there especially on the heat transport between reactor walls and different aluminum foams.[166, 167] Sinn *et al.* investigated different sponge materials for CO_2 methanation and performed CFD simulations of the heat transport based on the µ-XCT data.[168] In addition to simulations, Sadeghi *et al.* compared µ-XCT model based simulation of mass transport on the reactor scale with experimental data based on magnetic resonance velocimetry.[169] The application of µ-XCT to retrieve 3D models to simulate mass transport behavior on the reactor scale was also shown by Kočí *et al.*. They transformed the µ-XCT data of a coated catalytic filter for exhaust gas treatment into a 3D mesh that could be used for simulations in OpenFOAM.[170] A rather rare application was shown by Joss *et al.*, who could retrieve information about gas adsorption by µ-XCT at low resolution (voxel size 0.234 mm x 0.234 mm x 1 mm) by performing µ-XCT measurement under different gas atmospheres (He and CO_2) and different CO_2 pressures,

which allowed to observe differences in gas adsorption for a zeolite/activated carbon adsorbent bed.[171] The structure of SiC foam ceramics could be analyzed regarding its porosity and tortuosity by Ou *et al.* with voxel sizes of $13.6^3\,\mu m^3$ for a 20 x 20 x 20 mm sized sample.[172]

Pellet Scale

Very early studies employing synchrotron based µ-XCT on the catalyst pellet scale trace back to the early 90's studying the polymerization of polyolefin particles.[173, 174] With far less quality of the tomograms than today's laboratory instruments they could achieve a voxel size of around $3^3\,\mu m^3$.[173, 174] However, in comparison to nowadays studies, those examples might be rather seen as proof of concept studies mostly providing only a qualitative discussion of the tomograms, but setting the path for a future development of the field. µ-XCT on the catalyst pellet scale is often performed to study macroscopic sample features. For example, Grundwaldt *et al.* studied the impregnation of $\gamma-Al_2O_3$ pellets with $CuCl_2$ solution depending on the impregnation time as shown in Figure 1.12.[175] In the cross sections of the tomograms one can clearly observe the

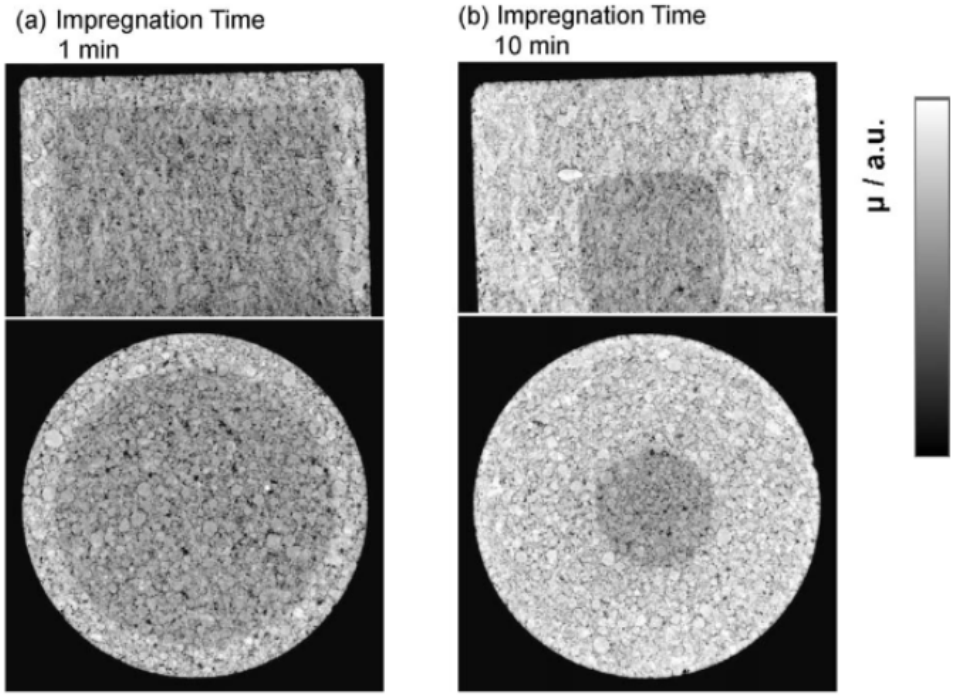


Figure 1.12: µ-X-ray computed tomography showing the impregnation of a $\gamma-Al_2O_3$ pellet with a $CuCl_2$ solution depending on different impregnation times. Reprinted from *Catal. Today*, *145*, J. D. Grunwaldt, B. Kimmerle, A. Baiker, P. Boye, C. G. Schroer, P. Glatzel, C. N. Borca, F. Beckmann, "Catalysts at work: From integral to spatially resolved X-ray absorption spectroscopy", 267–278, Copyright 2009, with permission from Elsevier.[175]

processing of the $CuCl_2$ solution from the pellet exterior to the interior based on the difference in absorption contrast. However, a direct determination of the Cu concentration depending on the absorption contrast is not possible, but the process could be followed qualitatively.[175] Similarly,

Gibson *et al.* studied the distribution of Mo species during impregnation and drying of Mo/Al_2O_3 catalysts by µ-XCT. They could observe more absorbing hot-spots, which were assigned to regions with higher Mo concentration inside the 3 mm sized $\gamma-Al_2O_3$ pellets. Additionally, they could verify that additions of H_3PO_4 as acid to the impregnation solution lead to a more uniform and homogeneous Mo distribution.[176] Another example studying impregnation processes is provided by Silva *et al.* They could qualitatively reveal the location of Fe−Ni species after impregnation of $\gamma-Al_2O_3$ spheres and found depending on the synthesis parameters egg-white, egg-shell or uniform distribution of Fe−Ni. In addition, the egg-shell type catalysts were found to perform better in ammonia decomposition than the other catalyst types.[177]
Pura *et el.* studied sections of a PdNi gauze for ammonia oxidation and could reveal morphological changes of the wire from the fresh to the spent state. They found a significant decrease of the wire diameter, which was about 80 µm in diameter in the initial state.[178] Catalyst aging was also studied by Hofmann *et al.* employing µ-XCT. They investigated a cross section of a single channel of a Pt/Al_2O_3 exhaust gas monolith with 1.27^3 µm^3 voxel size. Between acquisition of µ-XCT the sample underwent a thermal treatment to study the aging behavior. They found the formation of µm-sized Pt particles in the washcoat during aging, which was also validated by complementary electron probe micro analysis of a cross section.[179] Similarly, Becher *et al.* studied changes of the pore sizes in the washcoat of a monolith cross section of a Pt/Al_2O_3 catalyst during hydrothermal aging. They found an increase of the pore sizes during aging.[180] Recently, the coking of a $NiMo/Al_2O_3$ catalyst applicable in the catalytic upgrade of heavy crude oil was studied by Hart *et al.* using µ-XCT and complementary Hg porosimetry and N_2 sorption. The authors identified larger parts of coking inside of the catalyst extrudates, but did not perform detailed quantitative image analysis and discussed the coking identified by µ-XCT only qualitatively.[181] Bridging length scales from the reactor to the pellet scale, Kaltner *et al.* compared µ-XCT on the pellet scale of hollow sphere metal structures with a Pt-impregnated Al_2O_3 washcoat by neutron tomography on packed beds of those spheres. The catalyst has a potential application in the oxidation of NO. With µ-XCT (1 cm sample size with 10 µm pixel size) they were able to study the washcoat thickness, while neutron tomography (sample size up to 30 cm with 50 to 100 µm pixel size) allowed to study the packing density of the overall bed, similar to studies reviewed for the reactor scale.[182]

Grain Scale

To investigate catalysts on the single grain scale (sample size ≈5 to 100 µm) with possible resolution below 100 nm mainly X-ray nanotomography methods are suited. Selected examples of catalysts studied by STXM, X-ray holotomography or PXCT are following presented, while the application and the methods are relatively new. Fore example, the first reported PXCT on a bone sample was 2010 by Dierolf *et al.* showing about 150 nm resolution on a 25 µm sample.[156] PXCT here provides a direct quantitative information about the electron and mass density.[156, 157] The currently reported record solution for PXCT are 16 nm for a porous glass with a thin

Ta_2O_5 layer on a 6 µm sample cylinder.[183]
Based on this high resolution, PXCT was applied by da Silva *et al.* to study a cylindrical section of a fluid catalytic cracking (FCC) catalyst particle (8 µm diameter) and investigated the pore structure. They compared the results from PXCT with conventional Hg porosimetry analysis and complementary phase contrast µ-XCT on a frequency base. This revealed the limits of the two imaging methods in terms of resolution, but provided proof that PXCT is suited to study pores with tens of nm in size. Especially, close to the resolution limit PXCT and µ-XCT showed potentially enhanced artifacts in the pore size distributions, which might be related to the frequency and not volume weighted analysis. Furthermore, they could assign clay and zeolite domains in the 3D volume based on the electron density contrast of PXCT.[184] FCC catalyst particles were also studied by Ihli *et al.* during different deactivation stages. With resolutions of about 35 nm on sample diameters of about 30 µm they could assign pores, clay and zeolite similar to the previous study based on the electron density as shown in Figure 1.13. Figure 1.13a shows cross sections of the electron density contrast and a zoom-in highlighting the fine structural details along with an overview volume rendering of one of the studied samples. In Figure 1.13b,c the theoretical electron density contrast of the assigned material and the measured electron density distribution are highlighted. The finally obtained segmented PXCT into pores (blue), clay (orange) and zeolite (red) is presented in Figure 1.13d. Additionally, the authors quantified the spatial distribution of those segmented labels through the volume an could find increased clay location at the exterior with increasing catalyst deactivation.[185] By performing a similar experiment below and above the Fe absorption edge, Ihli *et al.* could further use PXCT to elucidate the Fe location inside FCC catalyst particles. This approach called "resonant X-ray ptychography" combines the high spatial resolution with chemical contrast.[186] Fam *et al.* showed the potential to study the pores of nanoporous gold using PXCT. They could study larger mesopores (around 30 nm) as well as macropores (around 200 nm) using PXCT with a resolution of about 23 nm.[187] Changes of the macropores of a Pt/Al_2O_3 exhaust gas monolith upon aging were studied by Becher *et al.* The authors found an increase in the diameter of the macropores upon thermal and hydrothermal aging. Furthermore, changes of the electron density distribution during aging were observed.[180] Weissenberger *et al.* studied hierachically porous TS-1 zeolites with PXCT. They were able to study the macropores in single zeolite grains and could differentiate between pores inside of the grain and pores directly connected to the exterior. On a particle of 3 µm in diameter they could obtain a resolution of about 47 nm only sufficient to directly analyze the macropores. Furthermore, they compared the macroporosity obtained from PXCT with electron tomography (ET), which was in agreement.[188] The hierarchical structure of hydrodesulfurization catalysts was investigated using PXCT by Ihli *et al.* They studied the structure of the pure Al_2O_3 support and compared it with low (5 wt.% Mo) and high metal loading (10 wt.% Mo with 2.3 wt.% Ni) of the impregnated catalysts. With the electron density contrast they could identify different matrices existing in the Al_2O_3, which exhibited also differences in the uptake of the metal species as associated to increased electron density.[189]

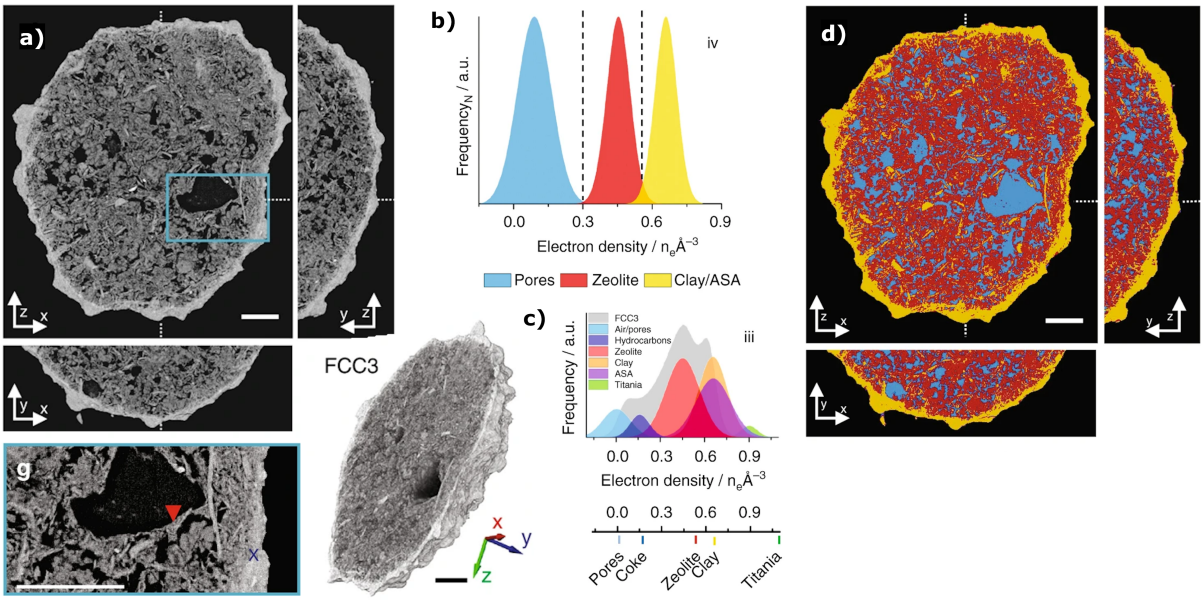


Figure 1.13: (a) Electron density contrast cross-sections of a FCC catalyst particle studied by PXCT together with the studied particle volume. (b) Calculated electron density distribution for air/pores, clay and zeolite. (c) Electron density distribution obtained for the FCC catalyst with potential phases. (d) Segmentation of (a) into pores (blue), zeolite (red) and clay (orange) according to the electron density. Available under the terms and conditions of the Creative Commons Attribution 4.0 license (CC BY 4.0, `https://creativecommons.org/licenses/by/4.0/`), Copyright ©2017.[185]

TXM tomography was shown by Meirer *et al.* to be suitable to study 50 µm sized FCC catalyst particles with voxel sizes of 64 to 320 nm. By performing TXM tomography at different energies at the Fe and Ni edges they were additionally able to localize the distribution of the metals. They found that Fe and Ni accumulate at the outer layers of the particles.[190, 191] In addition, the authors performed permeability calculations for subvolumes to simulate mass transport properties of the catalysts.[190] The application of TXM nanotomography data for diffusion simulation was further presented by Yamada *et al.* They investigated porous Al_2O_3 pellets and simulated the diffusion properties based on the 3D images of the 60 µm sized samples with voxel sizes of 35 nm. Additionally, they performed ET and Hg porosimetry experiments to complement and verify the porosity analysis results, respectively.[192] Besides hard X-ray TXM, soft X-rays have the potential for further information, but on more limited sample volumes. Aramburo *et al.* used STXM based soft X-ray nanotomography on small particles with diameters of about 2 µm to identify 4-fold or 6-fold coordination of Al inside of zeolites. This is possible by performing STXM at different energies around the Al-K-edge.[193] In a different study, Wu *et al.* studied the location of ZnO and Al_2O_3 in a Al_2O_3 aerogel, which was coated with ZnO. They applied soft X-ray STXM and PXCT at different energies and were able to reveal the co-localization of both species along with a non-uniform coating. Furhermore, they could show the advantage of PXCT in terms of resolution compared to STXM with 16 nm vs. 40 nm, respectively.[194]

Recently, Ziegler-type polymerization catalysts were studied by the Weckhuysen group employing hard X-ray holotomography or PXCT.[195, 196] With X-ray holotomography they could show differences in fragmentation of $MgCl_2/TiCl_4$ catalysts depending on the reaction stages. For a field of view of 90 x 90 x 81 µm they could achieve a resolution of 246 nm on the single particles. However, they found that single particle scans might not be representative for the complex fragmentation pathways of those polymerization catalysts.[195] Addressing the issue of representativity, they studied more than 400 differtent particles in a capillary by PXCT with a resolution of 74 nm for a field of view of 120 x 120 x 20 µm. This enables to investigate the heterogeneity of the particles regarding their fragmentation, which was analyzed by a k-means clustering analysis.[196]
In the future, spectro-nanotomography methods or multi-scale combination of different methods will likely be a strongly evolving research area. Spectro-nanotomography includes here approaches like resonant X-ray ptychography as well as STXM and X-ray holotomography at different X-ray energies to allow for a chemical contrast in addition to the high resolution.[186, 190, 191, 193, 194, 197–199] For example, Hirose *et al.* showed the possibility to differentiate Ce oxidation states in $Pt/Ce_2Zr_2O_x$ three way catalysts, by performing PXCT at different energies.[198] Additional combination with other contrasts, like XRF can reveal elemental distributions at lower resolution, which can be combined with high-resolution phase contrast methods.[197, 200] Vesely *et al.* could reveal coking in FCC catalyst particles by comparing the spent and regenerated state of an identical particle by holotomography. The electron density contrast here could reveal the coking with resolution of 200 nm. Additional XRF tomography could then reveal the location of Ni, Fe and La and could correlate this to the coking with lower resolution of 540 nm.[197] Ultimately, a combination of different contrast modes might also lead to more efficient acquisition approaches, like sparsity techniques.[199] This was shown in an example by Gao *et al.* for the combination of PXCT with X-ray transmission near-edge spectrotomography with 30 nm resolution on VPO type catalysts. The approach allows for high-resolution chemical and structural sensitivity, e.g., revealing V concentration and oxidation states in the VPO catalysts.[199] In addition to the development of synchrotron-based methods, also laboratory nano-CT is developing. As shown by Apeleo Zubiri *et al.*, Wirth *et al.* or Zhang *et al.*, this allows for more routine porosity studies using hard X-ray nanotomography.[201–203] However, due to mostly fixed beam energy, lower flux and rather inflexible instrumentation it is not as powerful as synchrotron methods.

Electron Tomography Scale

For even lower length scales, ET studies allow for routine resolution below 10 nm, however the sample sizes are limited to few hundreds of nm.[204, 205] Generally, ET can provide information about mesopores of catalysts.[180, 187, 204, 206, 207] As illustrated in Figure 1.14a, Stoeckel *et al.* studied meso-/macroporous silica materials with ET and FIB-SEM. FIB-SEM was applied to image the macropores of the systems, while ET allowed to investigated the mesopores. Based on the imaging results they could retrieve pore network models, which can be used for mass transport

simulations.[206] In several studies on mesoporous silicas, i.e., SBA-15 materials, further potential

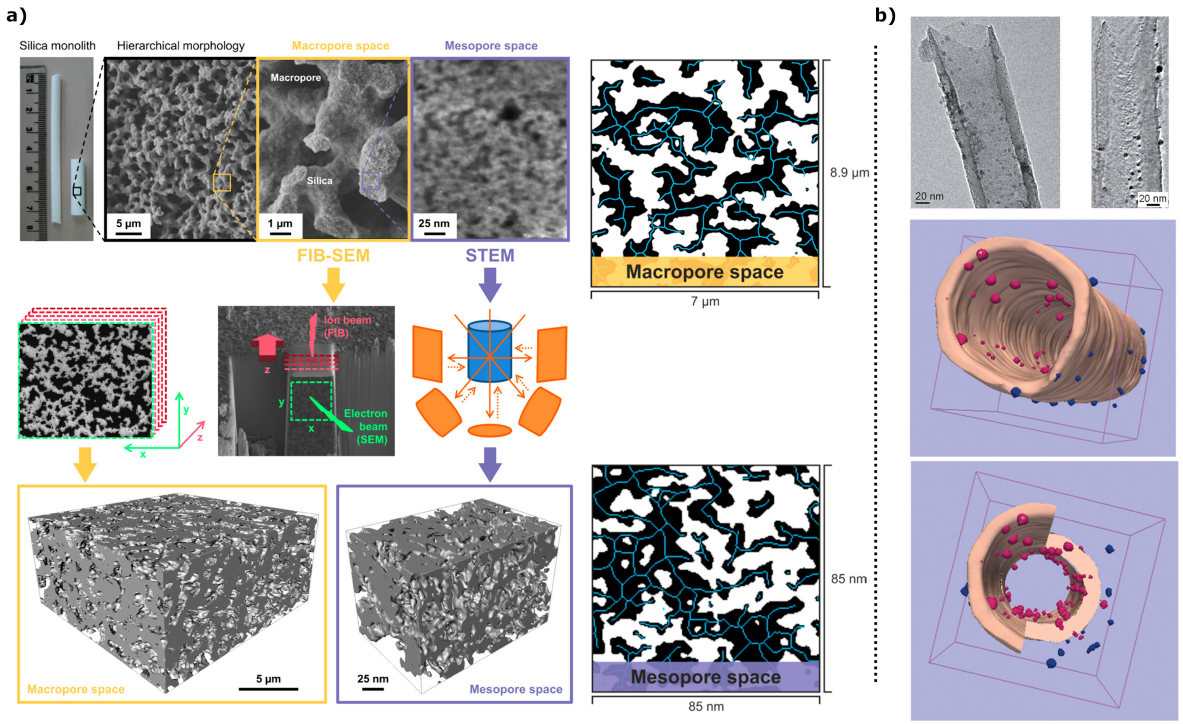


Figure 1.14: (a) Example of the FIB-SEM and ET investigation of a hierarchically porous silica-alumina monolith. The macropore space could be investigated by FIB-SEM and the mesopores by ET allowing to retrieve pore network models for both pore scales. Reprinted with permission from D. Stoeckel, C. Kübel, K. Hormann, A. Höltzel, B. M. Smarsly, U. Tallarek, "Morphological analysis of disordered macroporous-mesoporous solids based on physical reconstruction by nanoscale tomography", *Langmuir* **2014**, *30*, 9022–9027. Copyright 2014 American Chemical Society.[206] (b) location of Ni nanoparticles inside (red) and outside (blue) of carbon nanotubes as revealed by ET. Adapted with permission from J. P. Tessonnier, O. Ersen, G. Weinberg, C. Pham-Huu, D. S. Su, R. Schlögl, "Selective deposition of metal nanoparticles inside or outside multiwalled carbon nanotubes", *ACS Nano* **2009**, *3*, 2081–2089. Copyright 2009 American Chemical Society.[208]

of ET for small length scales could be shown. For example, the pore corrugation in SBA-15 was studied by Gommes *et al.*[207] While Daoura *et al.* and Prieto *et al.* could reveal the location of Ni or Cu nanoparticles within the pores of SBA-15,respectively.[209, 210] Similar, the location of Ni inside of carbon nanotubes was investigated by Tessonier *et al.* as shown in Figure 1.14b. Nevertheless, a big challenge for ET is the represenativity of the method due to the small sample volume as illustrated in Figure 1.9.

Combination of Scales

Due to the limitations of the different methods in terms of possible sample size and resolution, often a combination of length scales is required for a complete picture as illustrated in Figure 1.9. There are few early studies on porous catalysts, which report why a combination of different methods like micro X-ray computed tomography (µ-XCT), X-ray nanotomography methods,

focused-ion beam slice and view (FIB-SEM) or electron tomography (ET) are required.[180, 187, 188, 201, 211, 212] For example, Tariq *et al.* showed the combination of µ-XCT, FIB-SEM and ET to study bimodal pore structures of silica-alumina catalysts. They were also able to show that conventional methods might fail to correctly resolve macroporosity at large length scales.[211, 212] However, pore scales from 1 µm down to larger mesopores could only be studied by FIB-SEM, which is an invasive method and therefore alternative methods are required to cover those scales. Becher *et al.* showed the combination of µ-XCT, PXCT and ET to study exhaust gas monoliths and changes upon aging on the different length scales with a very basic porosity analysis.[180] Similar, Fam *et al.* applied complementary PXCT, FIB-SEM and ET analysis on a model system of nanoporous gold and highlighted the limitation of the different methods in terms of possible sample sizes vs. resolution.[187]
Especially, for samples with hierarchical porosity the combination of different techniques is inevitable. However, this was so far only reported for model systems (nanoporous gold) or bimodal pore structures. Furthermore, the porosity analysis of the tomograms in reported multiscale experiments is often of premature, which limits the comparison with conventional porosity characterization.

1.5.3 Chemical Imaging of Catalysts in 3D

Additionally to the resolution-based imaging in the previous section, spatially-resolved information about chemical properties of catalyst in 3D are important. As already presented in section 1.5.1, synchrotron-based hard X-ray methods offer a large toolbox for this purpose. Those might be applied in combination with the resolution focused techniques as already mentioned for the study of Bossers *et al.* The results of the combination of PXCT and XRF tomography are shown in Figure 1.15. XRF tomography is able to provide an additional information to the high-resolution from PXCT, here the elemental distribution and concentration of Ti and Cl inside the fragmented catalyst (Figure 1.15c,d).[200] In general, XRF tomography is powerful to retrieve the elemental distribution in catalyst particles. For example, in FCC catalysts Bare *et al.* and Kalirai *et al.* could provide information about the location of Ni, Ti, Fe, V, La, Zn or Ca.[213, 214] However, XRF contrast is usually applied in combination with other contrast modes as it can be often obtained on the side.
The use of different contrast modes is often referred to as multimodal chemical imaging. Price *et al.* investigated Mo promoted Pt/carbon catalysts by µ-XANES-CT and µ-XRF-CT. They could reveal the elemental distribution of Pt and Mo mainly by XRF and could distinguish between metallic and Pt/Cl_x species using XANES.[215] Multicomponent Bi−Mo−Fe−Co oxides were studied by combined holotomography, XRF-CT and absorption contrast imaging by Sprenger *et al.* on a fresh and spent catalyst. They could reveal the location of the different elements and found indications for a complex interplay of different possible phases being present.[216] The effect of Ni poisoning in FCC catalyst particles was studied by Gambino *et al.* by a

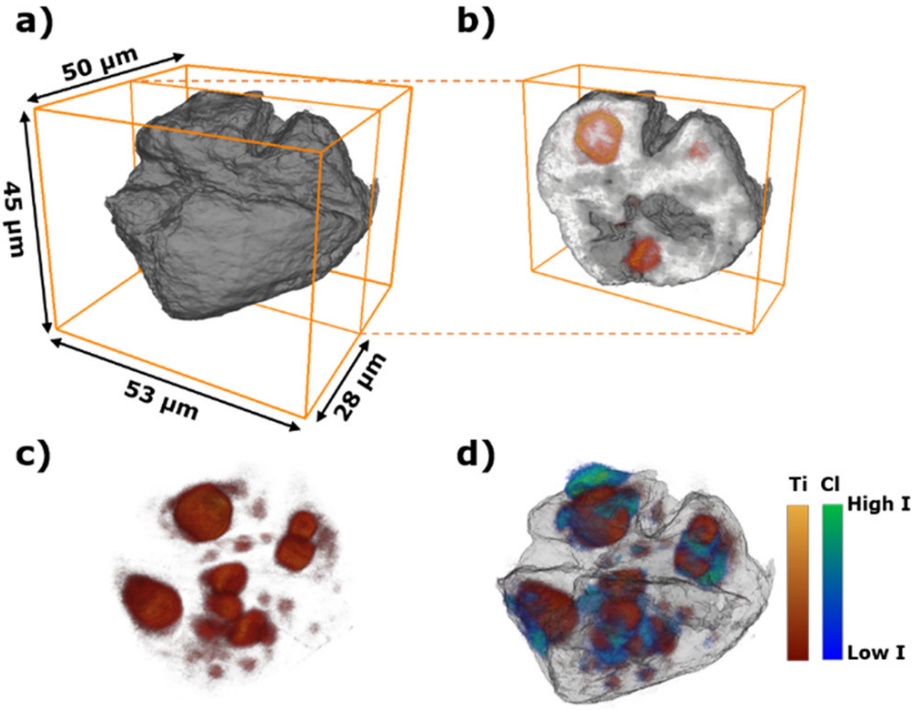


Figure 1.15: Example for XRF tomography on a Ziegler-type polymerization catalyst. PXCT and XRF are combined, with XRF being able to identify the location of Ti and Cl within the catalyst particles and PXCT provides high resolution. Available under the terms and conditions of the Creative Commons Attribution 4.0 license (CC BY 4.0, `https://creativecommons.org/licenses/by/4.0/`), Copyright ©2020.[200]

combination of XRF-, XRD-, and XAS-CT. By the complementary techniques they could reveal the interaction of Ni with Al_2O_3 forming spinel like phases, and that hydrothermal deactivation might be associated with dealumination of the zeolite phase.[217] The combination of STXM with XRF- and XRD-CT allowed Sheppard *et al.* to study the influence of oxidizing and reducing atmospheres on $Cu/ZnO/Al_2O_3$@ZSM−5 core shell catalysts applied in the conversion of synthesis gas to dimethyl ether. They could reveal the location of different crystalline phase in the core and shell. Furthermore, different Cu species could be identified depending on the atmosphere.[218] For a different synthesis gas conversion catalyst, a Rh/Mg/Al hydrotalcite type catalyst co-precipitated on a FeCr alloy foam, Ho *et al.* were able to reveal the location of crystalline phases by XRF- and XRD-CT. They found that a $MgAl_2O_4$ spinel phase was acting as a crucial stabilizing interaction layer between the coating and the foam.[219]
To obtain more detailed knowledge about different chemical structures, e.g., XAS-CT can be used as early shown by Schroer *et al.*. By XANES tomography at the Cu-K-edge they could reveal the presence of Cu and Cu_2O in CuO/ZnO catalysts.[220] Even more detailed information can be retrieved by XRD-CT and following spatially-resolved Rietveld refinement.[155] Wragg *et al.* performed Rietveld refinements on a SAPO-34 zeolite catalyst bed as a proof of principle study and to identify potential coking of the catalyst bed.[221] For a more detailed understanding of

catalyst synthesis and deactivation, O'Brien *et al.* studied the evolution of different Ni precursors after the impregnation of mm sized Ni/Al_2O_3 catalyst bodies applied in CO methanation. After calcination and following activation in H_2, they found differences in the Ni crystallite size depending on the location of the Ni particles.[222] Similarly, Jacques *et al.* followed the phase evolution of Ni/Al_2O_3 catalysts upon thermal activation with XRD-CT. They could unravel different phase formation processes along with variation of crystallite sizes.[223] Even more powerful might be the combination of XRD- and PDF-CT as shown for Pd/Al_2O_3 catalysts by Jacques *et al.* PDF is here the pair distribution function, which can be obtained from high energy X-ray diffraction experiments and allows to also analyze short and medium rang order of structure in addition to the long range order covered by XRD. They were able to reveal the location of PdO and Pd inside the catalyst bodies in calcined and reduced states. The advantage of PDF-CT is that also small X-ray amorphous metal particles can be found as presented in Figure 1.16. XRD-CT only significantly found the roughly 4.5 nm sized Pd particles at the exterior of the catalyst body. On the other hand, PDF-CT could also reveal smaller ≈1.4 nm sized Pd nanoparticles in the center of the body.[224]

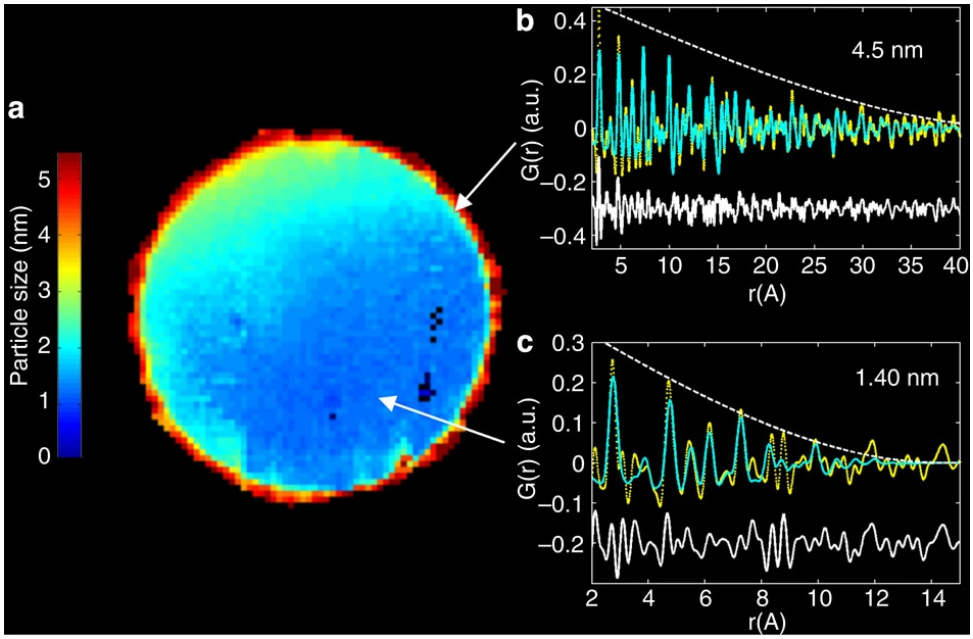


Figure 1.16: Results of the PDF-CT refinements for a Pd/Al_2O_3 catalyst in reduced state. (a) Spatial distribution of the particle size. Respective PDF refinements for the exterior (b) and interior (c) parts of the body highlighting differences of the Pd particle size. Reprinted by permission from Nature Publishing Group, a division of Macmillan Publishers Limited: Springer Nature, *Nat. Commun.* "Pair distribution function computed tomography", S. D. Jacques, M. Di Michiel, S. A. Kimber, X. Yang, R. J. Cernik, A. M. Beale, S. J. Billinge, ©2013.[224]

1.5.4 Tomography Studies of Catalysts at Work

The previously presented examples of resolution or chemical imaging of catalysts focused mainly on *ex situ* studies of catalyst materials. This already showed the potential of the variety and amount of information that can be revealed by spatially-resolved methods in order to derive structure-function relationships. Although, a further step would be to understand catalysts under well-defined gas and temperature conditions (*in situ*) or while they are actually performing their task with acquisition of catalytic data (*operando*).[102, 121, 225] This would enable to not only understand catalysts along different length scales (Figure 1.9), but allows for spatiotemporal knowledge that is essential for a true understanding of structure-function relations.[104, 116, 117, 153, 154, 226]

Following, some selected examples for progress in the development of *in situ* and *operando* methods for high-resolution and chemical imaging of catalysts with hard X-rays will be provided. True *in situ* tomography studies of catalysts were pioneered recently by Vamvakeros *et al.* with XRD-CT experiments.[227–229] In a study in 2018, they showed XRD-CT of a $Ni{-}Pd/CeO_2{-}ZrO_{2/}Al_2O_3$ catalyst applied in methane reforming. With performed Rietveld analysis they could retrieve information from the Å̃(crystalline structure) to µm scale. Selected results of the refinements, i.e., crystallite size of different phases, are shown in Figure 1.17. With the Rietveld analysis they could reveal the presence and evolution of different phases in the catalyst bed depending on different reaction conditions, e.g., gas composition or temperature. As shown in Figure 1.17 detailed information like the evolution of the crystallite size can be obtained while the catalyst is performing the reaction. For example, they found the formation of $NiAl_2O_4$ spinel depending on temperature and applied conditions, which might be valuable to understand catalyst deactivation. However, the used instrumental setup is not perfectly gas-tight, which might starts the dispute whether the study is true *operando* or *in situ*.[227] In a comparable study, they investigated the oxidative coupling of methane over a $Mn{-}Na{-}W/SiO_2$ catalyst and a La promoted variant. In addition to XRD-CT, also XRF-CT and absorption contrast were acquired on a single particle level allowing for multimodal imaging, while on the reactor scale only XRD-CT is feasible. The La promotion of the catalyst was found to be due to formation of a $NaLa(WO_4)_2$ phase and other mixed metal oxide phases. In the study, the advantages of multimodal and *in situ*/*operando* tomography characterization is highlighted to study complex catalytic systems and the interplay of different effects.[228] Their developed setup can also be applied to study other reactor geometries, e.g., membrane type reactors. Here they could follow the phase evolution of a variety of mixed metal oxide phases under controlled gas and temperature conditions.[229]

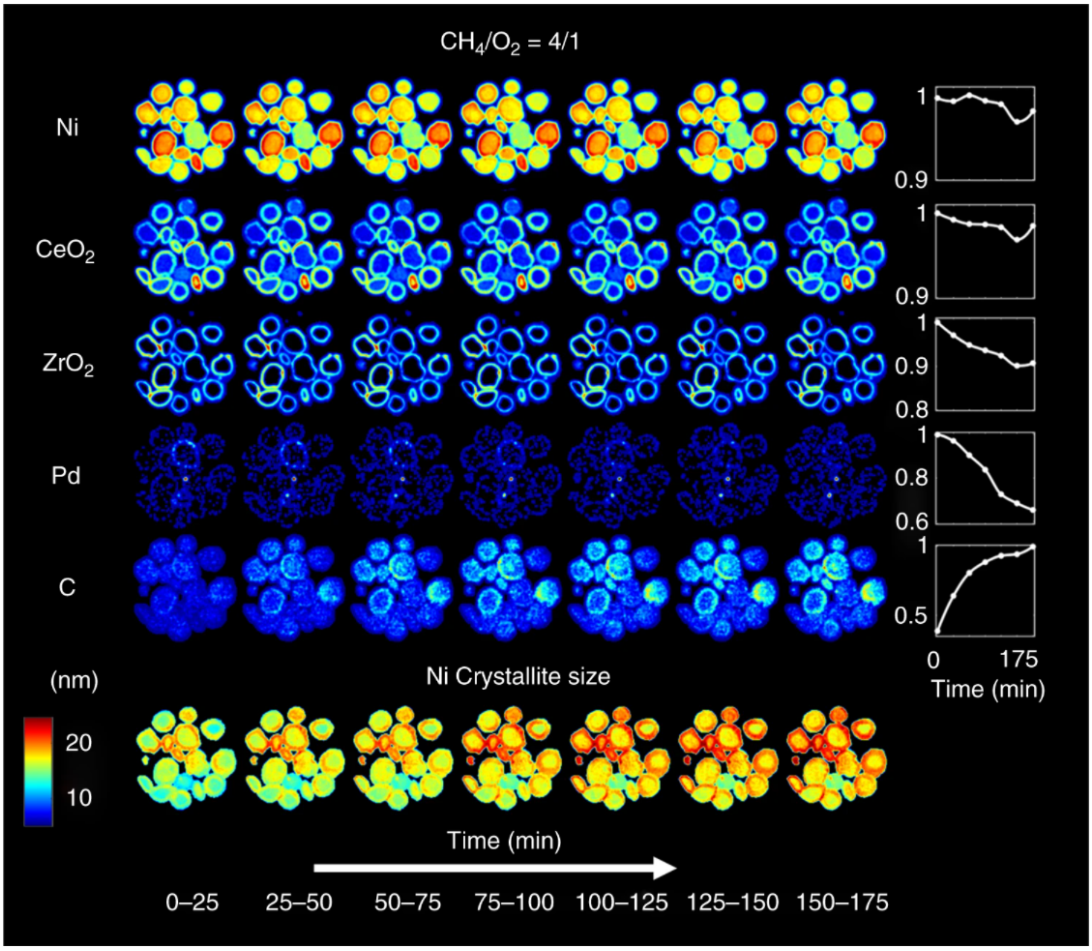


Figure 1.17: "Chemical evolution of the catalyst during partial oxidation of methane. Phase distribution maps of Ni, CeO_2, ZrO_2, Pd and C (graphite) corresponding to the normalised scale factors of these phases derived from the Rietveld analysis of the XRD-CT data collected during the POX experiment. Bottom: maps of crystallite sizes of Ni under [partial oxidation of methane] reaction conditions (colour bar axes in nm). Scale bar corresponds to 1 mm." Available under the terms and conditions of the Creative Commons Attribution 4.0 license (CC BY 4.0, `https://creativecommons.org/licenses/by/4.0/`), Copyright ©2018.[227]

A big step towards true *operando* imaging in 3D was achieved by Becher *et al.* by developing a complete gas-tight reaction cell allowing tomography studies.[230, 231] The cell was shown to enable *operando* XANES tomography of a Cu-SSZ-13 catalyst for the ammonia SCR reaction with quantitative product analysis. In the *operando* experiments at different temperatures as shown in Figure 1.18a-d, Cu(I) and Cu(II) species and thus the coordination environment of Cu inside the washcoat of a catalyst monolith could be studied. Essentially, each pixel in the tomographic cross sections represents a single XANES spectrum. Along the washcoat a gradient of the Cu oxidation state could be revealed as shown in Figure 1.18e-h.[230] Even more progress can be expected in the upcoming years on the development of spatially- and time-resolved chemical imaging of catalysts in 3D. However, as most of the chemical imaging methods are scanning microscopy variants, there is a huge trade-off between resolution and scanning time.[149] Therefore, resolutions on larger sample scales (reactor, pellet) are rather expected in the tens of µm range.

In addition to the above discussed progress for chemical imaging of catalysts in 3D, true *in situ* and *operando* X-ray nanotomography of catalysts might be even more challenging, especially regarding the development of suitable reactor setups.[232] Recently, Baier *et al.* developed an *in situ* cell for X-ray ptychography and showed the possible application in catalysis research. However, the cell is limited to perform 2D imaging studies, e.g., on the sintering of nanoporous gold at different temperatures or changes of a $CuO/ZnO/Al_2O_3$ core and zeolite shell catalyst under different gas atmospheres and temperatures. The possibility of this approach to study morphological changes of the samples during *in situ* imaging was presented.[233] This setup was further developed by Fam *et al.* to allow for a limited angle tomography mode ($\pm 35°$). The cell allowed to follow the sintering of nanoporous gold up to temperatures of 1573 K, while a 2D resolution of 23 nm could be obtained. The setup further allows for complementary TEM experiments on the sample.[234] One challenging point for *operando* X-ray nanoimaing is the small sample volume, which is basically limited by the imaging method, and thus difficult quantitative gas analysis.

For the current state of X-ray imaging in heterogeneous catalysis research the following open challenges and questions can be summarized for section 1.5:

- Moving from model systems towards applied catalysts and exploitation of the methodological limits thereby.
- Improving feasible sample sizes and imaging resolution for X-ray nanoimaging methods to approach electron microscopy length scales on more representative sample volumes.
- Transition from *ex situ* towards *in situ* and *operando* X-ray nanoimaging, which is mainly related to reactor and experimental setup developments.
- True *operando* X-ray imaging on the microscale with combined contrast modes.

- Flexible multipurpose imaging methods, which allow for combination of different contrast modes and resolutions.
- Development of more efficient data analysis paths and reporting of the data – making full use of the available information of the tomography experiments.
- Increasing availability and application of the advanced experimental techniques together with checks for representativity.

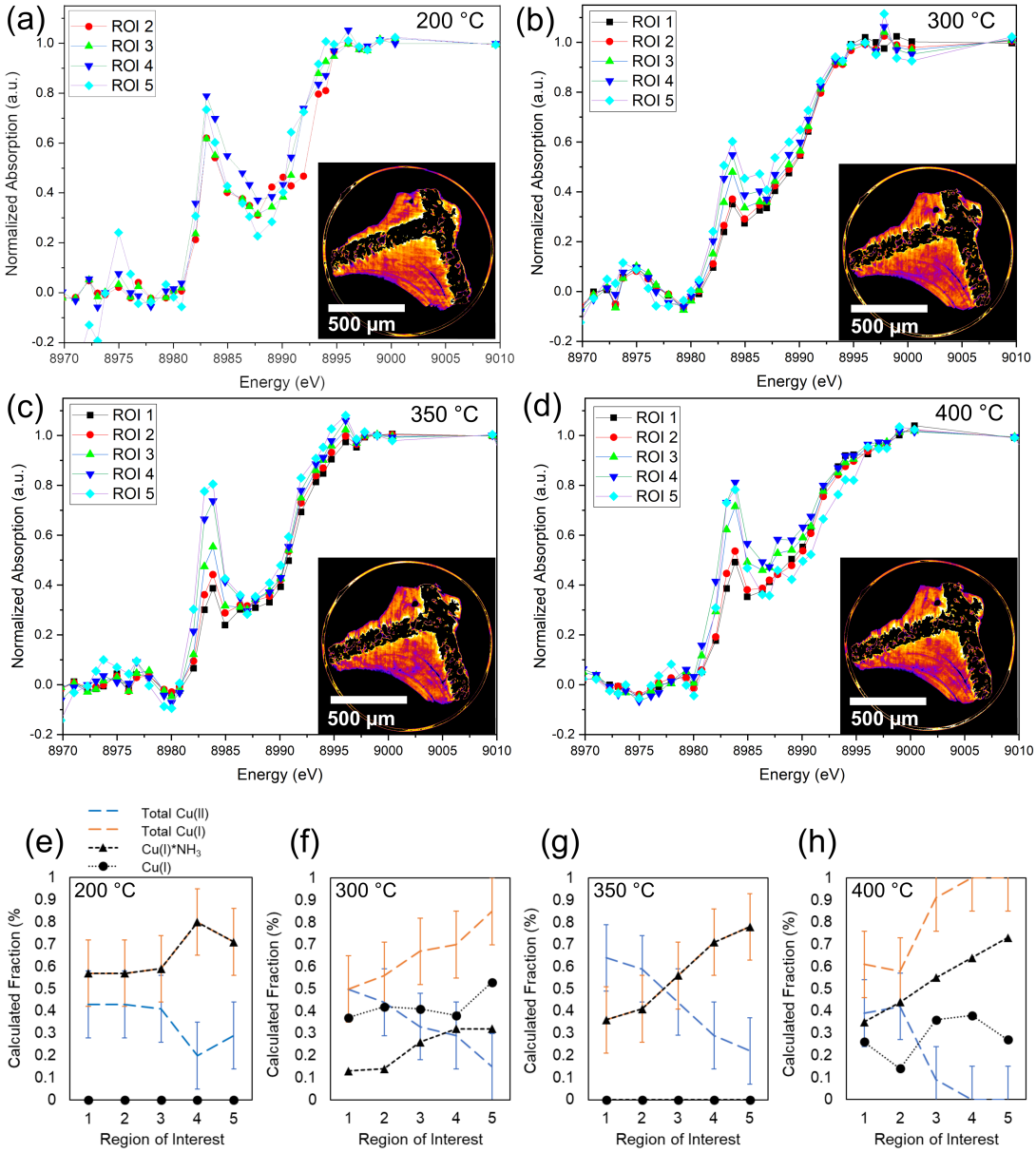


Figure 1.18: "Revealing the chemical state of Cu in a Cu-SSZ-13 washcoat. a–d, Normalized Cu K-edge XANES spectra in an identical sample slice at 200, 300, 350 and 400 °C (a–d, respectively), showing visible gradients of the feature at 8,983 eV from ROI 1–5 (inset: fitted slice with colour coding corresponding to intensity of the XANES feature at 8,983 eV). e–h, Fitted fractions of Cu(I), Cu(I)⋆NH_3 and Cu(II) in the XANES spectra at 200, 300, 350 and 400 °C (e–h, respectively) showing gradients from ROI 1–5. Error bars represent the maximum uncertainty reported by the linear combination analysis subroutine of the software package Athena 0.8.056. a.u., arbitrary units." Reprinted by permission from Springer Nature Limited: Springer Nature, *Nat. Catal.* "Chemical gradients in automotive Cu-SSZ-13 catalysts for NOx removal revealed by operando X-ray spectrotomography" J. Becher, D. F. Sanchez, D. E. Doronkin, D. Zengel, D. M. Meira, S. Pascarelli, J. D. Grunwaldt, T. L. Sheppard, ©2021.[230]

2 Scope of the Thesis

Detailed knowledge about structure-function relationships in heterogeneous catalysis is of fundamental importance for a future tailoring or design of improved catalysts. As heterogeneous catalysis is generally a multidimensional process (*c.f.* Figure 1.9), spatially-resolved characterization of catalysts is important. In this regard, imaging methods play an important role and one could even postulate that it is more convenient to understand a catalyst if one can visualize its structure according to the slogan "seeing is believing". The aim of this thesis is to present a toolbox of various available modern hard X-ray techniques to retrieve different information about Ni-based catalysts applied in CO_2 methanation. Due to the many different properties that have to be probed to understand the function of catalysts, there is no single method that allows to holistically understand the catalyst and its function. The general structure of this thesis is illustrated in Figure 2.1, providing a brief overview on the discussed topics and studied catalyst systems.

The chapter 4 (Figure 2.1, green) highlights and discusses multiscale challenges in the spatially-resolved characterization of porous catalysts. In section 4.1, an industrial Ni/Al_2O_3 reference catalyst (SPP2080-IMRC) is thoroughly studied by a combination of X-ray microtomography, X-ray nanotomography and electron tomography, to cover relevant length scales from the whole catalyst pellet (mm) down to mesopores (nm). The focus is to highlight the challenge of imaging methods to achieve the right sample size vs. resolution trade-off. Furthermore, conventional and advanced imaging techniques for porosity characterization of the SPP2080-IMRC are compared to show limitations of the conventional methods in revealing the true pore structure of catalysts. Additionally, perspectives of advanced X-ray nanotomography are exploited in providing sub-resolution information on the porosity based on quantitative electron density information that can be obtained from X-ray ptychography. In the following section 4.2, designed core-shell catalyst particles based on the SPP2080-IMRC are investigated for their textural properties. The core-shell catalysts reflect an optimized catalyst design for a dynamic process operation of the CO_2 methanation. An inert shell around the active SPP2080-IMRC core artificially introduces mass transfer limitations controlling the overall catalyst performance. Here, especially the shell thickness is an important design parameter, which is studied by X-ray microtomography. Furthermore, X-ray microtomography is used to investigate whether a homogeneously closed shell was obtained. The chapter is complemented by section 4.3, introducing a tailored hierarchically porous catalyst (Ni/Al_2O_3-h) with potentially enhanced mass transport and application in CO_2

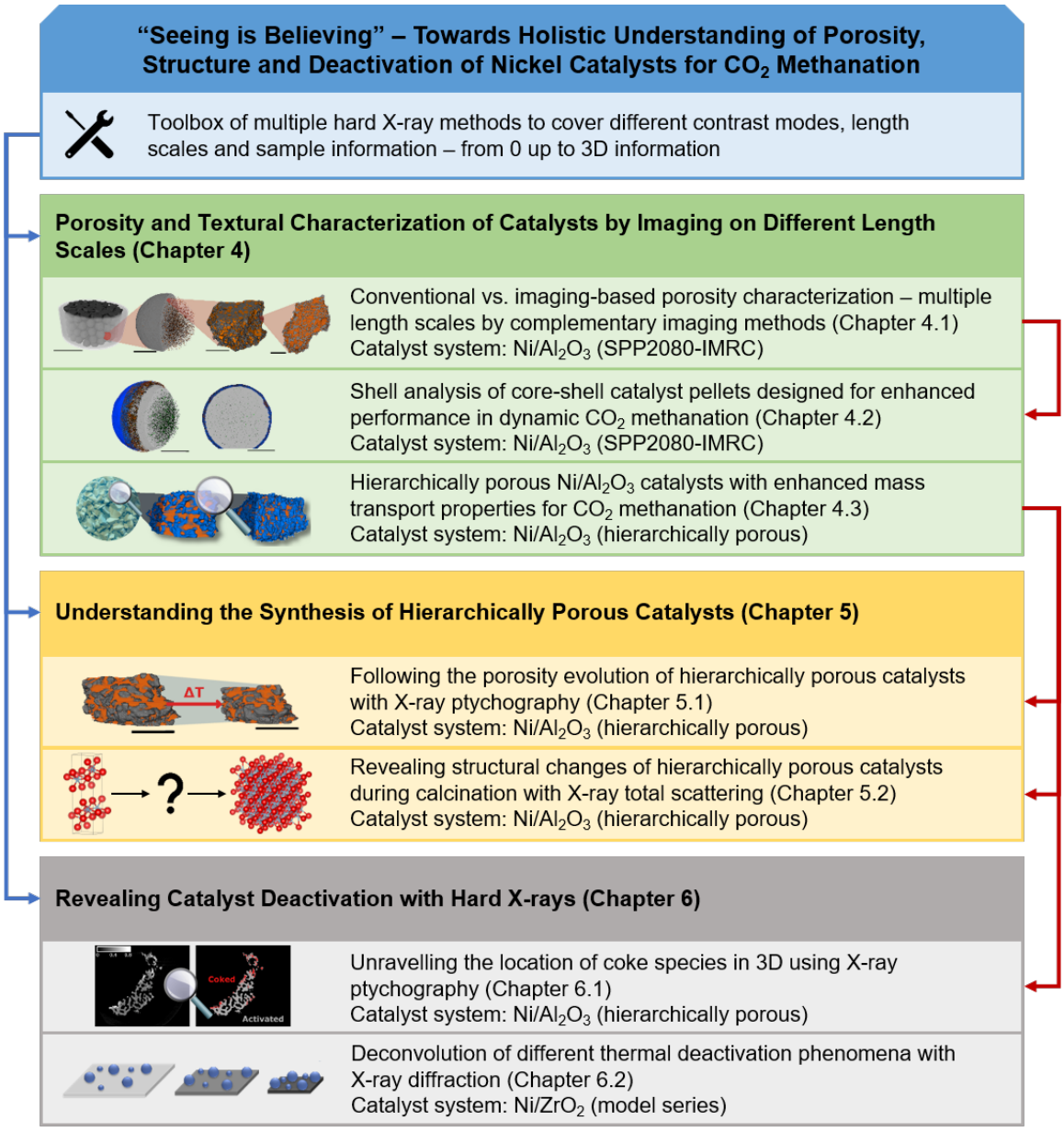


Figure 2.1: Overview on the different topics and general catalyst systems discussed as part of this thesis. The red arrows indicate chapters investigating related catalyst systems.

methanation. The material synthesis via modified sol-gel synthesis is shown together with general characterization and catalytic testing results. The hierarchical pore structure is further studied by combined X-ray nanotomography and electron tomography to cover relevant meso- and macropore length scales. The pore characterization results are used for macrokinetic simulations to uncover the potentially beneficial mass transport properties.
In chapter 5 (Figure 2.1, orange), hard X-ray methods are applied for a detailed understanding of the calcination step during the sol-gel synthesis of the hierarchically porous catalyst introduced in section 4.3. The aim is to reveal structural and textural transformation processes during calcination of the dried gels of the hierarchically porous Ni/Al_2O_3-h, which are the basis for a fundamental understanding of the catalyst preparation. First in section 5.1, the evolution of the porosity from the dried gel towards the calcined samples is followed using X-ray ptychography *in situ* in 2D and *ex situ* in 3D. In this respect, the potential of X-ray ptychography to study intermediate sample states during calcination and to reveal pore structure changes while they occur is exploited. The investigation of such changes is hardly possible by conventional porosity characterization methods due to their invasive nature. In the following section 5.2, the calcination of the same dried gel is investigated by X-ray total scattering experiments, which provide access to information about the atomic structure. This allows to follow potential phase transformation processes during calcination, which includes crystalline and amorphous structures.
The last part of the thesis deals with the understanding of the deactivation of Ni-based CO_2 methanation catalysts in chapter 6 (Figure 2.1, grey). Coking and thermal deactivation are selected as potentially relevant deactivation phenomena for CO_2 methanation (*c.f.* Figure 1.6). In section 6.1, the artificial coking of the Ni/Al_2O_3-h is investigated and compared to a different mesoporous Ni/Al_2O_3 catalyst. As coking is often referred to blockage of the pore system, the location of coke has to be unraveled in a spatially-resolved way. For this purpose, ptychographic X-ray computed tomography is applied on activated and coked catalysts particles. The quantitative electron density information from X-ray ptychography is then investigated as a suitable contrast mode to estimate the location of coke in 3D. In section 6.2, this is complemented by systematic thermal deactivation studies on a Ni/ZrO_2 catalyst series. The designed catalyst series essentially differs by the textural properties and thermal stability of the support material. *Operando* synchrotron powder X-ray diffraction is performed to deconvolute different thermal deactivation mechanisms with a focus on metal nanoparticle vs. support changes during CO_2 methanation. Chapter 6 provides detailed methodological insights into coking and thermal deactivation pathways. Potential structure-deactivation relationships can support future catalyst design with improved stability.
Overall, this thesis aims to provide an overview on the powerful application of modern hard X-ray techniques to understand the structure and texture of Ni-based catalysts applied in CO_2 methanation from zero to multidimensional information. Principally, the chosen X-ray contrast modes are suitable for *in situ* or *operando* experiments in general and allow 2D and 3D spatially-resolved investigations. A basic requirement for the chosen X-ray methods was that sample sizes

of minimum tens of µm in size should be feasible to allow for certain representativity. Potentials and limitations of the different applied methods are highlighted as well as compared and discussed towards conventional methods. Ultimately, combination of modern X-ray methods might allow to derive detailed structure-function relationships to unravel catalyst function, synthesis and deactivation as a basis for a future knowledge-based catalyst design – the "holy grail" in catalysis research.

3 Methods and Experimental

In the following section the relevant experimental details are provided. This includes information about the synthesis of the materials in section 3.1. Furthermore, the general catalyst characterization methods are reported in section 3.2. This is followed by the description of relevant catalytic testing experiments as part of this thesis in section 3.3. Then, the performed imaging studies and analysis of those are explained in section 3.4. Finally, *in situ* and *operando* X-ray diffraction experiments are described in section 3.5. More detailed information is provided in the appendix sections of the relevant discussion chapters as referenced. Unless stated otherwise, the experiments or analysis of the results was performed by myself.

3.1 Catalyst Synthesis

In the following subsections 3.1.1, 3.1.2 and 3.1.3, the synthesis of the different catalysts discussed as part of this thesis is introduced. Furthermore, a summarized overview of all catalyst samples and the relevant sections, where they are applied, is provided in subsection 3.1.4.

3.1.1 Industrial Ni/Al_2O_3 Reference Catalyst and Core-Shell Catalysts[1,2]

An industrial Ni/Al_2O_3 catalyst (denoted as SPP2080-IMRC) is used as a reference material for application in CO_2 methanation in the DFG priority program SPP2080 and in this thesis. The material was provided by the group of Prof. Kai Sundmacher (Otto von Guericke University Magdeburg and Max Planck Institute for Dynamics of Complex Technical Systems Process Systems Engineering, Magdeburg). Influences of the synthesis pathway on material properties can be reduced to a minimum due to the kilogram single batch preparation of the catalyst, which is an advantage in the application as a reference material distributed among many research groups. The catalyst had a Ni loading of 8.6 wt.%. The whole catalyst spheres and crushed powder thereof are shown in Figure 3.1.

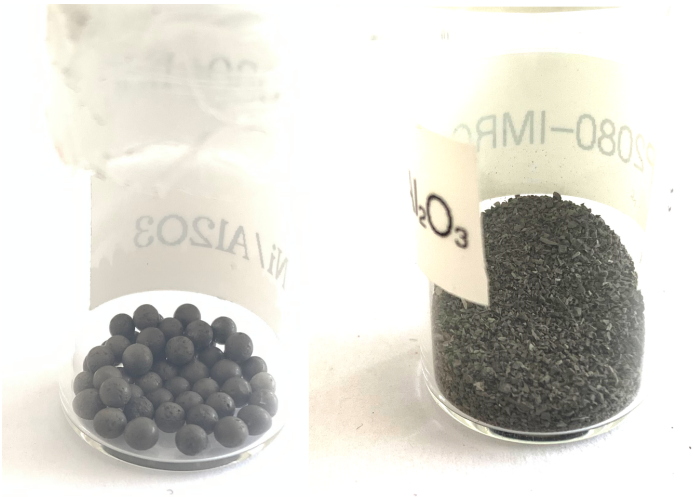


Figure 3.1: Pictures of the SPP2080-IMRC whole catalyst particles (left) and crushed powder (right).

The SPP2080-IMRC catalyst pellets were further used as basis for core-shell catalyst particles as suggested in simulation studies by Zimmermann *et al.*[114, 115], with the SPP2080-IMRC serving as the active core. The core-shell catalysts were prepared and provided by Ronny T.

[1]Parts of section 3.1.1 are adapted and taken from: R. T. Zimmermann, S. Weber, J. Bremer, V. Idakiev, R. Pashminehazar, T. L. Sheppard, L. Mörl and K. Sundmacher, "Core-Shell Catalyst Pellets for Effective Reaction Heat Management", *Chem. Eng. J.*, **2023**, *457*, 140921.[235]

[2]The SPP2080-IMRC is provided by the group of Prof. K. Sundmacher, core-shell catalyst were prepared and provided by R. Zimmermann, J. Bremer and V. Idakiev.

Zimmermann, Dr. Jens Bremer and Dr.-Ing. Vesselin Idakiev from the groups of Prof. Kai Sundmacher (Otto von Guericke University Magdeburg and Max Planck Institute for Dynamics of Complex Technical Systems Process Systems Engineering, Magdeburg) and Prof. Lothar Mörl (Otto von Guericke University Magdeburg). "Spherical Ni/Al_2O_3 catalyst pellets (SPP2080-IMRC) are coated with an inert shell. For this purpose an aluminum oxide suspension is prepared. At first, polyvinyl alcohol (PVA, Mowiol(R) 8-88, Kuraray Europe GmbH) is stirred into distilled water at 343 K. After complete dissolution of PVA, pseudo-boehmite powder (Disperal P2W (R), Sasol Germany GmbH) is added and vigorously stirred for 30 min. Subsequently γ-alumina powder (1.65 µm, BA-2, xtra GmbH) is added and stirred for another 90 min, before coating of the particles begins. In total, the mass fractions in the suspension are 5 wt.% pseudo-boehmite powder, 10 wt.% γ-alumina powder, 1.5 wt.% polyvinyl alcohol and 83.5 wt.% distilled water. As the catalysts pellets' availability is limited, 0.15 kg thereof is diluted with 1.35 kg inert γ-alumina pellets (2.5 mm, Sasol Germany GmbH) and put into the fluidization chamber of a fluidized bed coating pilot plant. The suspension is dosed into the fluidization chamber of a pilot plant by a bottom-spray two-fluid nozzle (Mod. 940, Düsen-Schlick GmbH, Germany). A peristaltic pump conveys the solution from a tank to the nozzle. The fluidization chamber itself is cylindrical with an inner diameter of 200 mm and is made of temperature resistant borosilicate glass. Additionally, ambient air is sucked in by a pressure blower and heated up, before entering the fluidized bed chamber through perforated disk. After passing the fluidized bed, the air enters a calming zone and overspray particles are separated via a cyclone and a filter. Every 10 min samples are taken and the coated catalyst pellets are separated from the inert pellets into ceramic dishes for calcination in a furnace. The furnace is heated from ambient conditions to 823 K with a heating rate of $1\,K\,min^{-1}$, to remove the organic binder and to calcine the applied pseudo-boehmite. After 823 K is reached, the temperature is held for 3.5 h and subsequently the particles were cooled down to ambient temperature in the closed furnace. Samples taken after 0 min (calcined catalyst particles without coating), 10 min, 30 min, and 50 min process time are investigated in detail."[235] The core shell catalysts are denoted as SPP2080-IMRC-0min, SPP2080-IMRC-10min, SPP2080-IMRC-30min and SPP2080-IMRC-50min according to their respective coating duration.

3.1.2 Hierarchically Porous Catalysts[3,4]

As a second sample system a sol-gel synthesized hierarchically porous Ni/Al_2O_3-h catalyst is discussed in this thesis. The materials were prepared in the group of Prof. Roger Gläser by Ken Luca Abel (Universität Leipzig). "Chemicals used were aluminum chloride hexahydrate

[3]Parts of section 3.1.2 are adapted and taken from: S. Weber, K. L. Abel, R. T. Zimmermann, X. Huang, J. Bremer, L. K. Rihko-Struckmann, D. Batey, S. Cipiccia, J. Titus, D. Poppitz, C. Kübel, K. Sundmacher, R. Gläser and T. L. Sheppard, "Porosity and Structure of Hierarchically Porous Ni/Al_2O_3 Catalysts for CO_2 Methanation", *Catalysts*, **2020**, *10*, 1471[236] and S. Weber, A. Diaz, M. Holler, A. Schropp, M. Lyubomirskiy, K. L. Abel, M. Kahnt, A. Jeromin, S. Kulkarni, T. F. Keller, R. Gläser, T. L. Sheppard, "Evolution of Hierarchically Porous Nickel Alumina Catalysts Studied by X-ray Ptychography", *Adv. Sci.*, **2022**, *9*, 2105432.[237]

[4]The synthesis of the hierarchically porous catalysts was performed by K. L. Abel.

($AlCl_3 \cdot 6\,H_2O$, 99 %, AlfaAesar), nickel(II) chloride hexahydrate ($NiCl_2 \cdot 6\,H_2O$, 98 %, AlfaAesar, Ward Hill, MA, USA), polyethylene glycol MW 900,000 (PEG-900k, no purity given, AlfaAesar, Ward Hill, MA, USA), (±)-propylene oxide (PO, 99.5 %, Acros Organics, Fair Lawn, NJ, USA), ethanol (EtOH, for gelation: absolute, VWR, Radnor, PA, USA; for solvent exchange: 99.5 % denaturated with 1 % butan-2-one, VWR, Radnor, PA, USA; and nickel(II) oxide nanopowder (99.8 %, Aldrich, St. Louis, MO, USA). The synthesis of Ni/Al_2O_3-h was adapted from Herwig *et al.*[238] 2.88 g $NiCl_2 \cdot 6\,H_2O$, 12.53 g $AlCl_3 \cdot 6\,H_2O$, and 0.200 g PEG-900k were dissolved in an EtOH-H_2O-mixture to give a molar ratio of $n_M\,/\,n_{EtOH}\,/\,n_{H_2O} = 1\,/\,5.4\,/\,30.1\,/\,3.5 \cdot 10^{-6}$, with $n_M = n_{Ni} + n_{Al}$. The masses of $NiCl_2 \cdot 6\,H_2O$ and $AlCl_3 \cdot 6\,H_2O$ were calculated for a target Ni mass fraction of 20 wt.%. The solution was cooled in an ice bath to 274 to 276 K. Then, 11.52 g of propylene oxide (PO), representing a molar ratio of $n_M\,/\,n_{PO} = 3.1$, were added rapidly under vigorous stirring (600 rpm). The solution was stirred for 3 min in the ice bath, followed by 7 min of stirring at room temperature. The container was then sealed and stored at 323 to 328 K for 24 h. Afterwards, the gel was kept in an EtOH bath for 7 days and then dried at room temperature. Finally, the dried gel was calcined in ambient air at 1123 K for 12 h using a heating rate of 2 K min^{-1}. For comparison, an equivalent, purely mesoporous sample (denoted as Ni/Al_2O_3-meso) was prepared as stated above, but without PEG-900k added in the gelation solution."[236] The obtained calcined sample is denoted as Ni/Al_2O_3-h.

To study the calcination of the dried gels, a dried gel sample was obtained without performing the calcination step after drying, denoted as Ni/Al_2O_3-dr. Furthermore, a Ni free Al_2O_3 sample was synthesized to study differences during calcination compared to Ni/Al_2O_3. "For the Al_2O_3-dr sample, the same procedure as for Ni/Al_2O_3 was applied with the following amounts of chemicals: 7.726 g $AlCl_3 \cdot 6\,H_2O$, 0.1613 g PEO, 5.762 g of PO. The resulting molar ratio of $n_M\,/\,n_{EtOH}\,/\,n_{H_2O}\,/\,n_{PEO}$ is $1\,/\,5.4\,/\,30.1\,/\,5.6 \cdot 10^{-6}$ and n_M/n_{PO} ratio was 3.1. The sample Al_2O_3-dr was furthermore calcined at 1223 K (ambient air) for 12 h (2 K min^{-1}) to obtain the Al_2O_3-h sample."[239]

The Ni/Al_2O_3-h, Al_2O_3-h and Ni/Al_2O_3-dr samples are shown in Figure 3.2.

Ni/Al_2O_3-dr and Al_2O_3-dr were further applied in *in situ* and *ex situ* X-ray ptychography imaging studies in sections 3.4.5, 3.4.6 as well as in X-ray total scattering experiments detailed in section 3.5.2. Furthermore, Ni/Al_2O_3-h was used for coking experiments as detailed in section 3.4.7. The samples are summarized in Table 3.1.

3.1.3 Deposition Precipitation Ni/ZrO_2 Catalysts[5,6]

For systematic studies of thermal catalyst deactivation a designed Ni/ZrO_2 catalyst series was used. The catalysts were prepared by Mariam L. Schulte (Karlsruhe Institute of Technology)

[5] Parts of section 3.1.3 are adapted and taken from: M. L. Schulte, S. Weber, L. Klag, J.-D. Grunwaldt and T. L. Sheppard, "Synchrotron PXRD deconvolutes nickel particle and support changes in Ni/ZrO_2 methanation catalysts", *Catal. Sci. Technol.*, **2022**, *12*, 6069-6083.[240]

[6] Samples were prepared by M. L. Schulte as part of her master thesis.



Figure 3.2: Pictures of the Ni/Al_2O_3-dr (left), Ni/Al_2O_3-h (middle) and Al_2O_3-h (right) catalysts.

as part of her master thesis supervised by me. The aim was to synthesize a series of catalysts with similarly sized Ni particles, but different textural properties and thermal stability of the support. "Ni/ZrO_2 catalysts were prepared using the homogeneous deposition-precipitation method adapted from Mutz *et al.*[53] As support material commercial ZrO_2 pellets (Saint-Gobain) were crushed and thermally aged at different temperatures for 12 h (10 K min^{-1}) resulting in samples Z350 (623 K), Z500 (773 K), Z650 (823 K), Z800 (1073 K) and Z1000 (1273 K). The calcined powders were finely granulated to a mesh size $\leq$100 µm and 1.6 g of each powder was suspended in an aqueous solution (230 mL) of 2.002 g $Ni(NO_3)_2{\cdot}6H_2O$ (Merck 99 %) with 2.906 g of urea (7 eq., Carl Roth, crystalline, 99.6 %), which corresponds to an aimed Ni loading of 20 wt.%. The suspension was stirred for 1 h at room temperature (pH = 4) and afterwards heated to 363 K. The mixture was heated for 18 h under reflux, cooled to room temperature, then stirred for another 1 h (pH = 8). The solid was filtered off, washed three times with 100 mL of deionized water and dried overnight at 383 K. Subsequently, the catalysts were calcined at 773 K for 4 h (10 K min^{-1})."[240] The support series Z350 to Z1000 as well as the calcined Ni containing catalysts are shown in Figure 3.3.

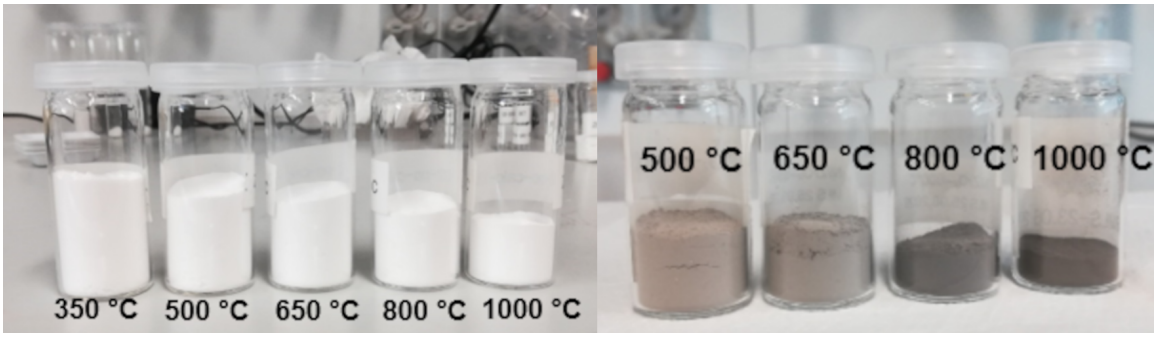


Figure 3.3: Pictures of equal masses of the ZrO_2 support series Z350 to Z1000 (left) and of the calcined Ni/ZrO_2 catalysts NZ500 to NZ1000 (right).

3.1.4 Overview Catalyst Samples

The catalyst samples used within this thesis are summarized in Table 3.1. In addition to the catalysts introduced in sections 3.1.1, 3.1.2 and 3.1.3, a mesoporous Ni/Al_2O_3 catalysts denoted as Ni/Al_2O_3-m was used. The Ni/Al_2O_3-m was prepared by the homogeneous deposition-precipitation described by Mutz *et al.* with a Ni loading of 17 wt.%.[53] For all catalysts in Table 3.1 the section of application together with a short information on the sample is provided. Throughout the thesis the abbreviations provided in Table 3.1 are used.

Table 3.1: Summary of the different catalysts investigated as part of this thesis together with information about the relevant section and optional comments.

Abbreviation	Catalyst type	Section	Comment
SPP2080-IMRC	Ni/Al_2O_3	4.1, 4.2, 4.3	reference catalyst in SPP2080
SPP2080-IMRC-0min	Ni/Al_2O_3	4.2	reference catalyst
SPP2080-IMRC-10min	Ni/Al_2O_3	4.2	core-shell catalyst
SPP2080-IMRC-30min	Ni/Al_2O_3	4.2	core-shell catalyst
SPP2080-IMRC-50min	Ni/Al_2O_3	4.2	core-shell catalyst
Ni/Al_2O_3-h	Ni/Al_2O_3	4.3, 5.2	hierarchically porous catalyst
Ni/Al_2O_3-meso	Ni/Al_2O_3	4.3	mesoporous catalyst
Ni/Al_2O_3-dr	Ni/Al_2O_3	5.1, 5.2	dried gel of Ni/Al_2O_3-h
Ni/Al_2O_3-calc	Ni/Al_2O_3	5.1	calcined Ni/Al_2O_3-dr
Al_2O_3-h	Al_2O_3	5.1, 5.2	hierarchically porous support
Al_2O_3-dr	Al_2O_3	5.1, 5.2	dried gel of Al_2O_3-h
Al_2O_3-calc	Al_2O_3	5.1	calcined Al_2O_3-dr
Ni/Al_2O_3-ha	Ni/Al_2O_3	6.1	activated Ni/Al_2O_3-h
Ni/Al_2O_3-hc	Ni/Al_2O_3	6.1	coked Ni/Al_2O_3-h
Ni/Al_2O_3-m	Ni/Al_2O_3	6.1	mesoporous catalyst
Ni/Al_2O_3-ma	Ni/Al_2O_3	6.1	activated Ni/Al_2O_3-m
Ni/Al_2O_3-mc	Ni/Al_2O_3	6.1	coked Ni/Al_2O_3-m
Z350-Z1000	ZrO_2	6.2	sintered support series
NZ350-NZ1000	Ni/ZrO_2	6.2	calcined catalyst series

3.2 Conventional Catalyst Characterization[7,8]

In the following, information about the conventional characterization methods applied within this thesis is provided. This includes N_2 sorption, Hg porosimetry, He pycnometry, inductively coupled plasma optical emission spectrometry, elemental analysis, laboratory powder X-ray diffraction, diffuse reflectance ultraviolet-visible spectroscopy and temperature-programmed reduction.

N_2 Sorption

N_2 sorption experiments of the hierarchically porous Ni/Al_2O_3 samples were carried out by Ken Luca Abel (Universität Leipzig) as described in the following. "N_2 sorption studies were performed with a Sorptomatic 1990 (Porotec) for Ni/Al_2O_3 samples and on a BELSORP-miniX (MICROTRAC MRB) for the other samples. Calcined samples were degassed for at least 4 h at 523 K, while the dried gel samples were treated at at 373 K, <10 Pa for >48 h. The treatment of the dried gels before N_2 sorption leads to a mass loss of ≈20 %. The adsorption and desorption isotherms were recorded at 77 K and analyzed using the ASiQwin software (Quantachrome Instruments) for Ni/Al_2O_3 and BELMaster software (MICROTRAC MRB) for other samples. The total pore volume (V_{P,tot,N_2}) was determined at $p/p_0 \geq 0.95$."[237]
For the SPP2080-IMRC catalyst, "N_2 sorption experiments were conducted on a BELSORP-miniX equipment. Samples were degassed at 523 K for at least 6 h. The adsorption and desorption isotherms were recorded at 77 K and analyzed using the BELSORP BELMasterTM software (V_{P,tot,N_2} determined at $p/p_0 \geq 0.99$).
"Specific surface area (A_{BET}) and pore width distribution (w_{P,N_2}) were determined by the BET method[242] ($p/p_0 = 0.05 - 0.30$, adsorption branch) and BJH method[243] (desorption branch), respectively. An experimental error of 5 % is expected for specific surface area, specific pore volume, and pore width."[241]
For the ZrO_2 and Ni/ZrO_2 series A_{BET} and V_{P,tot,N_2} were obtained using a BELSORP-mini II system (Microtrac) using the BET method.[242] The measurements were performed by Dr. Eduardo Barbosa and Dr. Sumeet Kale (Karlsruhe Institute of Technology). All samples were

[7] Parts of section 3.2 are adapted and taken from: S. Weber, K. L. Abel, R. T. Zimmermann, X. Huang, J. Bremer, L. K. Rihko-Struckmann, D. Batey, S. Cipiccia, J. Titus, D. Poppitz, C. Kübel, K. Sundmacher, R. Gläser and T. L. Sheppard, "Porosity and Structure of Hierarchically Porous Ni/Al_2O_3 Catalysts for CO_2 Methanation", *Catalysts*, **2020**, *10*, 1471[236]; S. Weber, A. Diaz, M. Holler, A. Schropp, M. Lyubomirskiy, K. L. Abel, M. Kahnt, A. Jeromin, S. Kulkarni, T. F. Keller, R. Gläser, T. L. Sheppard, "Evolution of Hierarchically Porous Nickel Alumina Catalysts Studied by X-ray Ptychography", *Adv. Sci.*, **2022**, *9*, 2105432.[237]; M. L. Schulte, S. Weber, L. Klag, J.-D. Grunwaldt and T. L. Sheppard, "Synchrotron PXRD deconvolutes nickel particle and support changes in Ni/ZrO_2 methanation catalysts", *Catal. Sci. Technol.*, **2022**, *12*, 6069-6083[240] and S. Weber, R. T. Zimmermann, J. Bremer, K. L. Abel, D. Poppitz, N. Prinz, J. Ilsemann, S. Wendholt, Q. Yang, R. Pashminehazar, F. Monaco, P. Cloetens, X. Huang, C. Kübel, E. Kondratenko, M. Bauer, M. Bäumer, M. Zobel, R. Gläser, K. Sundmacher and T. L. Sheppard, "Digitalization in Catalysis Research: Towards a Holistic Description of a Ni/Al_2O_3 Reference Catalyst for CO_2 Methanation", *ChemCatChem*, **2022**, *14* e202101878.[241]

[8] Information about contributions from others are provided for each method separately.

degassed at 573 K for 2 h under vacuum before N_2 sorption measurements.

Hg Porosimetry

Hg porosimetry measurements of all Ni/Al_2O_3 catalyst samples in this thesis were performed in the groups of Prof. Roger Gläser and Prof. Dirk Enke by Ken Luca Abel (Universität Leipzig). For the Ni/ZrO_2 catalyst series the measurements were carried out by Maximilian Franz in the group of Prof. Dirk Enke (Universität Leipzig). "Hg porosimetry analysis was conducted on a Pascal 140 (ThermoScientific, Waltham, MA, USA) for data points from pressures up to 250 kPa and a Pascal 440 (ThermoScientific, Waltham, MA, USA) for data points from pressures between 250 kPa to 400 MPa. The contact angle used was 140 ° with a surface tension of 0.48 $N\,m^{-1}$. The pore width was calculated by the Washburn equation.[244] The meso- and macropore widths with the maximum differential pore volume were referred to as modal mesopore width ($w_{P,meso}$) and modal macropore width ($w_{P,macro}$), respectively. An experimental error of 5 % was expected for specific pore volumes and pore widths."[236]

He Pycnometry

He pycnometry experiments as part of this thesis were carried out in the the group of Prof. Roger Gläser by Ken Luca Abel (Universität Leipzig). "He pycnometry was performed on a Pycnomatic ACT EVO instrument (Porotec, Hofheim am Taunus, Germany) at room temperature. For analysis, at least 10 pulses of He with a gas pressure of 2 bar were used. The final skeletal density (ρ_{skel}) was calculated by taking the average value of four consecutive measurements. An experimental error of 0.002 $g\,cm^{-3}$ was expected for the skeletal density. The total porosity (ϵ_{tot}) of the sample was calculated from eq. 3.1 using the ρ_{skel}, determined via He pycnometry, and the total specific pore volume ($V_{P,tot}$), determined from Hg porosimetry. The meso- and macroporosity were calculated likewise, using the specific mesopore and specific macropore volume in the numerator, respectively."[236]

$$\epsilon_{tot} = \frac{V_{P,tot}}{V_{P,tot} + \frac{1}{\rho_{skel}}} \cdot 100\% \tag{3.1}$$

Inductively Coupled Plasma Optical Emission Spectrometry

Inductively coupled plasma optical emission spectrometry (ICP-OES) measurements of selected catalyst samples discussed in this work were performed by Heike Rudzik in the group of Prof. Roger Gläser (Universität Leipzig). The analysis was performed to determine the elemental catalyst composition focusing on the metal concentration. "ICP-OES was conducted using a Optima 8000 instrument (Perkin Elemer Waltham, MA, USA) equipped with a Scott/crossflow sample injection system. Samples were dissolved in a mixture of hydrofluoric (47-51 wt.%,

Normatom, VWR, Radnor, PA, USA), nitric (67-90 wt.%, Normatom, VWR, Radnor, PA, USA), and hydrochloric acid (34-37 wt.%, Normatom, VWR, Radnor, PA, USA) in an Multiwave 3000 (Anton Paar, Graz, Austria) microwave prior to analysis."[236]

Elemental Analysis

Elemental analysis in terms of carbon (C), hydrogen (H) and nitrogen (N) elemental analysis (CHN) was carried out for selected samples discussed in section 5.1 to obtain information about organic compounds or solvent residues, especially for dried gel samples. The measurements were performed by Manuela Roßberg in the group of Prof. Berthold Kersting (Universität Leipzig). "Carbon (C), hydrogen (H) and nitrogen (N) elemental analysis (CHN) was performed using a Vario EL MICRO element analyzer (Heraeus). Samples were crimped in aluminum containers and analyzed via heat extraction."[237]

Laboratory Powder X-ray Diffraction

General crystalline phase and size analysis of the catalysts discussed in this thesis was performed by laboratory powder X-ray diffraction (PXRD). For the Ni/Al_2O_3-h sample, "PXRD patterns were recorded using a G670 Guinier-Geometry diffractometer (Huber SE, Berching, Germany) equipped with an image plate detector. Reflections were recorded between $2\theta = 4$ to $100\,^\circ$ using Cu-Kα radiation ($\lambda = 0.15406\,\mathrm{nm}$), with a step size of $0.005\,^\circ$ and an irradiation time of 15 min."[236] The measurements were performed by Sebastian Geisler (Universität Leipzig).
In case of ZrO_2 and Ni/ZrO_2, "crystalline phases and crystallite sizes (L_{vol}) of the catalysts were studied (...) using a PANalytical X'Pert PRO diffractometer with Ni-filtered Cu Kα radiation ($\lambda = 1.54060\,\text{Å}$) for 2θ = 5-80 $^\circ$ ($0.625\,^\circ$ steps with $1.6\,\mathrm{s\,step^{-1}}$)."[240] Those measurements were performed by Mariam L. Schulte (Karlsruhe Institute of Technology). The detailed analysis of all laboratory PXRD data was performed similarly to SPXRD experiments using Rietveld analysis[245, 246] by myself as detailed later in section 3.5.1.

Diffuse Reflectance Ultraviolet-Visible Spectroscopy

"Diffuse reflectance ultraviolet-visible (DRUV/vis) spectroscopy was conducted on a Lambda 650S UV/vis spectrometer (Perkin Elmer Waltham, MA, USA) equipped with a 150 mm Ulbricht sphere. Spectra were recorded in the range between 200 to 800 nm with 1 nm step size and 2 nm slit width."[236] The DRUV/vis spectroscopy experiments in this thesis were performed by Ken Luca Abel in the group of Prof. Roger Gläser (Universität Leipzig).

Temperature-Programmed Reduction

Temperature-programmed reduction (TPR) experiments as part of this thesis were performed by Dr. Tanya Wolff in the group of Prof. Kai Sundmacher (Max Planck Institute for Dynamics of

Complex Technical Systems Physical and Chemical Foundations of Process Engineering, Magdeburg). "TPR of catalysts was conducted using the ChemStarPx+ equipment (Quantachrome Instruments, Boynton Beach, FL, USA). Then, 100 mg sample were loaded in a quartz U-tube. First, the sample was heated in a He flow at 423 K for 30 min and subsequently cooled to 323 K. The reduction was performed using 10 % H_2 in Ar (50 cm^3 (STP) / min). The temperature was raised using a ramp rate of 10 K min^{-1} to 1173 K and held at this level for 30 min. To remove moisture formed during reduction, effluents were sent through a silica gel water trap before reaching the detector. H_2 consumption was measured continuously using a thermal conductivity detector (TCD). Cooling was performed in He flow. Finally, a pulse calibration with H_2 was performed at 373 K. The loop volume was 528 µL and Ar was used as carrier flow."[236]

3.3 Catalyst Treatment and Testing

3.3.1 Tubular Quartz Glass Reactor[9,10]

The hierarchically porous Ni/Al_2O_3-h, Ni/Al_2O_3-meso and SPP2080-IMRC catalysts were investigated regarding their catalytic activity in CO_2 methanation. The tests were carried out by Ronny T. Zimmermann, Markus Ikert, Dr. Liisa K. Rihko-Struckmann in the group of Prof. Kai Sundmacher (Otto-von-Guericke University Magdeburg, Max Planck Institute for Dynamics of Complex Technical Systems Physical and Chemical Foundations of Process Engineering, Magdeburg). "Catalytic experiments were performed in an automated lab-scale catalyst testing unit equipped with a tubular quartz glass reactor (inner diameter: 8 mm). The reactor was operated at atmospheric pressure with 100 mg catalyst samples diluted with SiC (carborundum powder, coarse, 46 grit, abcr GmbH, Karlsruhe, Germany) in a ratio of 1:9. The nonpelletized samples were reduced *in situ* prior to the catalytic experiments in a H_2/He mixture. The SPP2080-IMRC sample was reduced at 673 K for 8 h using a mixture of $\dot{V}_{H_2} / \dot{V}_{He} = 1$, with a total gas flow of 120 $cm^3\,min^{-1}$. The Ni/Al_2O_3-h sample was reduced at either 923 K or 1123 K for 2 h using a mixture of $\dot{V}_{H_2} / \dot{V}_{He} = 0.05$, with a total gas flow of 120 $cm^3\,min^{-1}$. The catalytic activity was determined at temperatures of 573 K, 623 K, and 673 K under steady-state conditions after 7 h (673 K), 10 h (623 K), and 13 h (573 K) on stream, respectively. The feed gas consisted of a gas mixture of $\dot{V}_{H_2} / \dot{V}_{CO_2} / \dot{V}_{He} = 4 / 1 / 5$ with a total gas flow rate of 200 $cm^3\,min^{-1}$, respectively. Then, 24 online gas chromatography (GC) measurements were taken (time about 2 h) under each set of conditions after each temperature change and equilibration time, while the last ten measurements were used for calculation of CO_2 conversion and CH_4 selectivity. Water was separated from the reactor effluent with a membrane unit and was not analyzed. No other

[9] Parts of section 3.3.1 are adapted and taken from: S. Weber, K. L. Abel, R. T. Zimmermann, X. Huang, J. Bremer, L. K. Rihko-Struckmann, D. Batey, S. Cipiccia, J. Titus, D. Poppitz, C. Kübel, K. Sundmacher, R. Gläser and T. L. Sheppard, "Porosity and Structure of Hierarchically Porous Ni/Al_2O_3 Catalysts for CO_2 Methanation", *Catalysts*, **2020**, *10*, 1471.[236]

[10] Catalytic testing experiments were performed by R. T. Zimmermann, J. Bremer and L. K. Rihko-Struckmann.

carbon-containing analytes were detected apart from CH_4, CO_2, and CO, which were, therefore, used for the overall carbon mass balance. The CO_2 conversion and CH_4 selectivity (both in %) were calculated from the last 10 GC measurements, as defined in eq. 3.2 and eq. 3.3."[236]

$$X_{CO_2} = \frac{c_{CH_4,out} + c_{CO,out}}{c_{CH_4,out} + c_{CO,out} + c_{CO_2,out}} \cdot 100\% \tag{3.2}$$

$$S_{CH_4} = \frac{c_{CH_4,out}}{c_{CH_4,out} + c_{CO,out}} \cdot 100\% \tag{3.3}$$

3.3.2 Stainless Steel Tubular Fixed-bed Reactor[11,12]

Catalytic testing of the Ni/ZrO_2 series was performed in a laboratory setup originally build up by Dr. Benjamin Mutz at IKFT, Karlsruhe Institute of Technology. The experiments were carried out by Mariam L. Schulte with support from Dr. Marc-André Serrer as part of her master thesis supervised by me. Furthermore, the SPP2080-IMRC catalyst sample applied in imaging experiments was treated in this setup accordingly. "The catalytic performance of the catalysts was studied in a continuous flow setup with a stainless steel tubular fixed-bed reactor (length = 410 mm, inner diameter d_i = 7 mm, outer diameter d_o = 9.5 mm)(Figure 3.4), described in previous work.[53] The catalyst bed (length = 30 to 35 mm) contained 300 mg of catalyst (sieve fraction 300-450 μm) diluted in 1.15 g of SiC (210 μm, Carborundum, VWR Chemicals). The spare void of the reactor was densely packed with SiC (500 μm) and the different layers were separated with quartz glass wool. Thermocouples (K-Type) were placed in front and behind the catalyst bed for automated temperature control, using the average temperature of the front and end positions. Gases were dosed using mass flow controllers (Bronkhorst) calibrated using a gas flow meter (Bios DryCal Definer 220, MesaLabs). Gaseous product analysis was performed by gas chromatography (GC) using an Agilent 490 micro gas chromatograph (μ-GC) (Channel 1: 10 m PoraPLOT Q, 0.25 mm diameter, carrier gas He; Channel 2: 10 m mole sieve column with 5 Å, 0.25 mm diameter, carrier gas Ar). The experimental setup is shown in Figure 3.4 Prior to each reaction, the catalysts were activated in the reactor in a 50 % H_2/N_2 mixture (both purity 99.9999 % from Air Liquide) (600 mL min^{-1}) at 773 K for 2 h. After cooling to reaction temperature, the gas feed was changed to 10 % CO_2/40 % H_2/N_2 (CO_2 purity 99.995 % from Air Liquide) resulting in a weight hourly space velocity ($WHSV$) of 60 L g_{cat}^{-1} h^{-1}. The catalytic performance was tested at three different temperatures (250 °C, 350 °C and 400 °C) and a hold time of 1 h each to obtain stable catalytic activity."[240]

[11] Parts of section 3.3.2 are adapted and taken from: M. L. Schulte, S. Weber, L. Klag, J.-D. Grunwaldt and T. L. Sheppard, "Synchrotron PXRD deconvolutes nickel particle and support changes in Ni/ZrO_2 methanation catalysts", *Catal. Sci. Technol.*, **2022**, *12*, 6069-6083.[240]

[12] Catalytic experiments were performed by M. L. Schulte as part of the master thesis with support from M.-A. Serrer.



Figure 3.4: Picture of the stainless steel tubular fixed-bed reactor setup used for catalytic experiments of the Ni/ZrO_2 catalysts series.

The conversion of CO_2 was calculated analogous to earlier measurements by Mutz *et al.*[53] using N_2 as internal standard (eq. 3.4).

$$X_{CO_2} = 1 - \frac{c^{out}_{CO_2} \cdot c^{in}_{N_2}}{c^{in}_{CO_2} \cdot c^{out}_{N_2}} \tag{3.4}$$

The selectivity of CH_4 and CO was calculated according to eq. 3.5.

$$S_i = \frac{c_i}{c_{CH_4} + c_{CO}} \tag{3.5}$$

The yield of CH_4 and CO was determined by multiplication of the conversion of CO_2 and the selectivity of component i (eq. 3.6).

$$Y_i = X_{CO_2} \cdot S_i \tag{3.6}$$

The equation used for the calculation of TOF is depicted in equation (eq. 3.7). Hereby, $V^{in}_{CO_2}$ is the flow rate of CO_2 ($60\,mL\,min^{-1}$), Y_{CH_4} is the CH_4 yield and V_m is the ideal molar gas volume.

$$TOF = \frac{V^{in}_{CO_2} \cdot Y_{CH_4}}{V_m \cdot n_{active}} \tag{3.7}$$

Here, n_{active} which was calculated according to equation (eq. 3.8) containing the variables of mass (m), molar mass (M), metal loading (L) and dispersion (D) of Ni. All except for the dispersion are known.

$$n_{active} = \frac{m \cdot L \cdot D}{M} \tag{3.8}$$

The dispersion D was calculated out of its relation with the Sauter diameter (d_{SA}) and atomic diameter d_{At} (eq. 3.9).[247] For Ni the atomic diameter of 124.6 pm was used.[248]. The Sauter diameter can be calculated out of the volume (V) and the surface area (A) of a sphere with the crystallite sizes obtained by PXRD. Since from TEM no statistic relevant particle distribution and sizes could be obtained, and XRD represents the average size it is used for the TOF calculations.

$$d_{SA} = \frac{6V}{A} \tag{3.9}$$

$$\frac{d_{VA}}{d_{At}} = \frac{3.32}{D} \tag{3.10}$$

3.3.3 Quartz Glass Microreactor Setup and Artificial Coking Studies[13,14]

A portable capillary microreactor setup with quartz glass capillaries based on the design of Grunwaldt *et al.*[249] was applied in this thesis for different *in situ* and *operando* experiments as well as sample treatments. This includes artificial coking experiments of Ni/Al_2O_3-h and Ni/Al_2O_3-m catalysts with *operando* Raman spectroscopy (section 3.4.7, 6.1), studies of the calcination of Ni/Al_2O_3-dr and Al_2O_3-dr samples by *in situ* X-ray total scattering (section 3.5.2, 5.2) as well as thermal deactivation studies of the Ni/ZrO_2 catalyst series (section 3.5.1, 6.2). The microreactor setup generally consists of the capillary holder with a quartz glass capillary, which is glued gas tight into the holder using a steel reinforced epoxy resin. Furthermore, a custom made gas-dosing system of mass flow controllers (Bronkhorst) available in the group of Prof. Jan-Dierk Grunwaldt or in the XRM group of Dr. Thomas Sheppard is used for gas dosing containing a 4-way valve (VICI) for fast gas switches. On-line gas analysis is performed with an OMNI-Star GSD 320 mass spectrometer (MS) (Pfeiffer Vacuum). The microreactor setup is heated with hot-air blowers: LE MINI SENSOR KIT (Leister Technologies) for artificial coking and thermal deactivation studies or a hot-air blower available at the beamline in case of the

[13] Parts of section 3.3.3 are adapted and taken from: S. Weber, D. Batey, S. Cipiccia, M. Stehle, K. L. Abel, R. Gläser and T. L. Sheppard, "Hard X-Ray Nanotomography for 3D Analysis of Coking in Nickel-Based Catalysts", *Angew. Chem. Int. Ed.*, **2021**, *60*, 21722-21777.[239]

[14] *Operando* Raman spectroscopy experiments were assisted by M. Stehle.

calcination studies. A temperature calibration of the hot-air blowers is performed using Type-K thermocouples inside an empty capillary prior to experiments. The microreactor setup is shown in Figure 3.5 for the combination with Raman spectroscopy, but can be similarly applied for studies using X-rays instead.

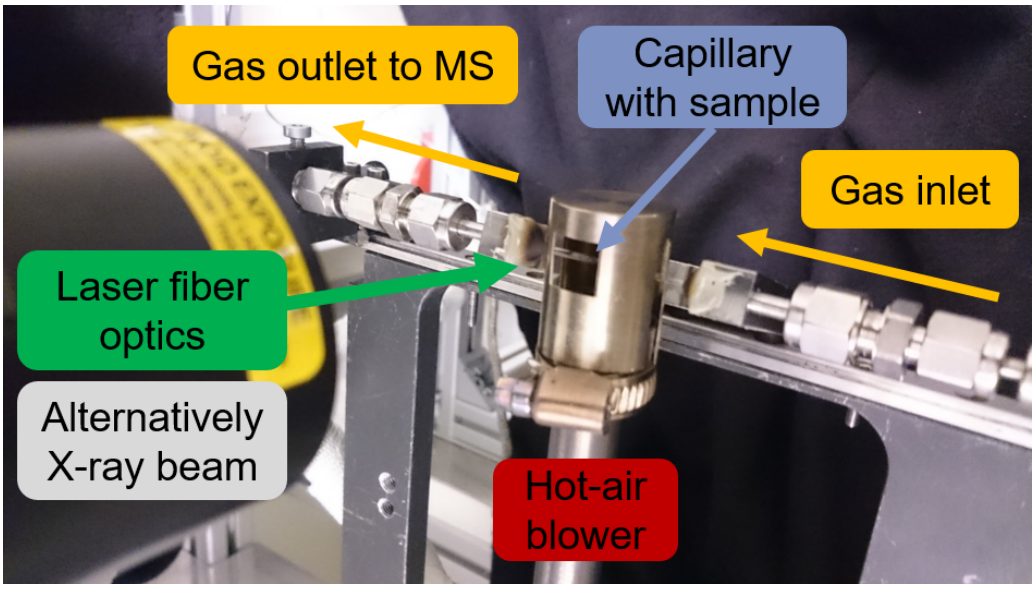


Figure 3.5: Picture of the microreactor setup combined with *operando* Raman spectroscopy as used for the artificial coking experiments.

For artificial coking studies on the Ni/Al_2O_3-h and Ni/Al_2O_3-m (section 3.4.7, 6.1) samples were treated as described following. "Generally, 4 to 5 mg of the Ni/Al_2O_3-h and Ni/Al_2O_3-m sample (100 to 200 µm sieve fraction) were placed into 1.5 mm quartz glass capillaries (Wjm - Glas Müller GmbH) and fixed with quartz wool resulting in a bed length of about 7 mm. A constant total gas flow of 20 mL min^{-1} and atmospheric pressure was used in the experiments. All catalysts were first activated (blue area) and shortly tested under reaction conditions (green area) as shown in Figure 3.6. The activated samples Ni/Al_2O_3-ma and Ni/Al_2O_3-ha were obtained after reaction conditions. The coked samples Ni/Al_2O_3-mc and Ni/Al_2O_3-hc were subsequently treated with an artificial coking procedure (*c.f.* section 6.1, Figure 6.2, orange area). The reaction and artificial coking conditions were exactly the same for both catalyst systems, while the activation procedure differed, because a higher temperature for Ni reduction is required for the Ni/Al_2O_3-h system due to incorporation of Ni into the Al_2O_3 structure see section 4.3.[236] The Ni/Al_2O_3-m samples were activated by heating to 773 K catalyst bed temperature with a ramp of 20 K min^{-1} in 25 % H_2 / 75 % He (v/v). Subsequently, the reactor was cooled to 673 K with 20 K min^{-1} under activation conditions before switching to reaction conditions. The Ni/Al_2O_3-h were activated by heating to 973 K with a ramp of 20 K min^{-1} in 25 % H_2 / 75 % He (v/v) with a subsequent heating to 1023 K and cooling to 673 K with 20 K min^{-1}, before switching to reaction conditions.

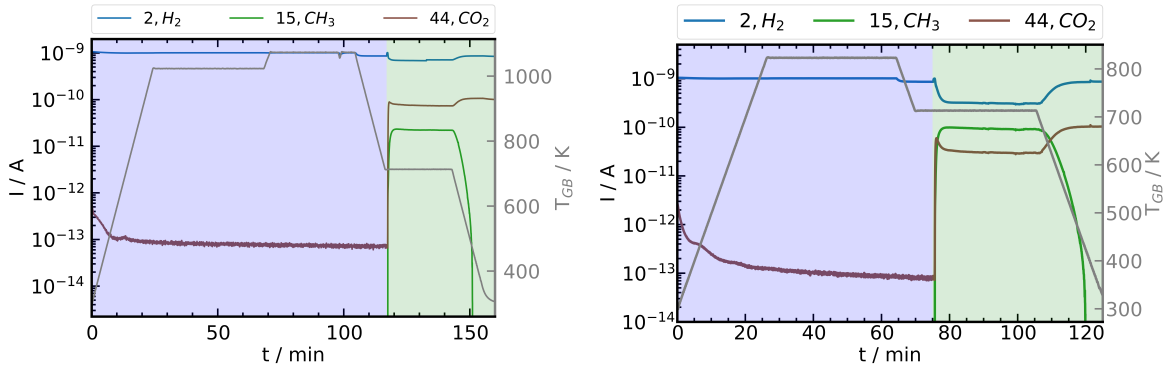


Figure 3.6: Temperature and selected MS data for the activated samples Ni/Al_2O_3-ha (left) and Ni/Al_2O_3-ma (right) with activation conditions (blue) and reaction conditions (green). The estimated X_{CO_2} under reaction conditions are ≈30 % and ≈70 % for Ni/Al_2O_3-ha and Ni/Al_2O_3-ma, respectively. [239] Available under the terms and conditions of the Creative Commons Attribution 4.0 license (CC BY 4.0, `https://creativecommons.org/licenses/by/4.0/`), Copyright ©2021

For both systems, reaction conditions of 20 % H_2 / 5 % CO_2 / 75 % He (v/v) were applied for 30 min at 673 K. The artificial coking conditions for Ni/Al_2O_3-mc and Ni/Al_2O_3-hc were 4 % CH_4 / 96 % He (v/v) at 673 K for 30 min similar to a previous study by Mutz *et al.*[86] The selected on-line mass spectrometry traces corresponding to H_2^+ ($m/z = 2$), CH_3^+ ($m/z = 15$) and CO_2^+ ($m/z = 44$) and the temperature for the coked and activated samples are shown in section 6.1, Figure 6.2 and Figure 3.6, respectively. From the mass spectrometry data of the activated samples, the CO_2 conversion during reaction conditions can be estimated, based on the baseline after cooling in reaction gas mixture and the intensity during reaction conditions as shown in the following equation:

$$X_{CO_2} = \left(1 - \frac{I_{CO_2,reaction}}{I_{CO_2,baseline}}\right) \cdot 100\% \tag{3.11}$$

For the artificially coked samples during the described experiments, *in situ / operando* Raman spectroscopy was performed. An inVia Raman spectrometer (Renishaw) with a frequency doubled Nd:YAG laser (532 nm, about 100 mW laser power at the source) was used. The laser beam was focused on the capillary by a video and optical fiber probe (Renishaw) with a long working distance objective. Spectra were acquired with 50 % laser power over a range of 100-2000 cm^{-1} with a 2400 lines mm^{-1} grating and an acquisition time of 10 s per spectra. Raman spectra were analyzed using WiRE 4.4 software (Renishaw). The data treatment consisted of cosmic ray removal, truncation, and baseline subtraction, while for sample Ni/Al_2O_3-hc a normalization was applied after cosmic ray removal to reduce the influence of the strong fluorescence effects observed at high temperatures. The data was averaged by binning two spectra to create (...) 2D heat maps (...)."[239] The *operando* Raman spectroscopy experiments were supported by Dr. Matthias Stehle.

3.4 Imaging Experiments

3.4.1 Overview Tomography Experiments

In the following Table 3.2 the tomography experiments performed as part of this thesis are summarized. This includes information about the used catalysts according to Table 3.1 together with information about the technique and relevant sections for the discussion of the results. The institutes, where electron tomography (section 3.4.2) and X-ray microtomography (section 3.4.3) experiments were performed are provided. Furthermore, information about the used beamlines for X-ray nanoimaging studies is summarized with respective details for the methods discussed in the upcoming sections 3.4.5, 3.4.6, 3.4.7 and 3.4.8.

Table 3.2: Summary of the different tomography experiments performed as part of this thesis. Electron tomography (ET), X-ray microtromography (µ-XCT), *in situ* 2D X-ray ptychography (XRP), ptychographic X-ray computed tomography (PXCT) and holgraphic X-ray tomography (HXCT). For X-ray nanoimaging experiments the respective beamlines are noted and for ET and µ-XCT the institutes where the studies were done.

Sample	Method	Beamline	Section	Comment
SPP2080-IMRC	µ-XCT	IAM-ET (KIT)	4.1	calcined catalyst
SPP2080-IMRC	HXCT	ID16A-NI	4.1	spent catalyst
SPP2080-IMRC-ET1	ET	INT (KIT)	4.1	spent catalyst
SPP2080-IMRC-ET2	ET	INT (KIT)	4.1	spent catalyst
SPP2080-IMRC-0min	µ-XCT, PXCT	cSAXS	4.2, 4.1	calcined catalyst
SPP2080-IMRC-10min	µ-XCT	IAM-ET (KIT)	4.2	-
SPP2080-IMRC-30min	µ-XCT	IAM-ET (KIT)	4.2	-
SPP2080-IMRC-50min	µ-XCT	IAM-ET (KIT)	4.2	-
Ni/Al_2O_3-h-ET1	ET	INT (KIT)	4.3	-
Ni/Al_2O_3-h-ET2	ET	INT (KIT)	4.3	-
Ni/Al_2O_3-dr	PXCT, XRP	cSAXS, P06	5.1	dried gel of Ni/Al_2O_3-h
Ni/Al_2O_3-calc	PXCT	cSAXS	5.1	calcined Ni/Al_2O_3-dr
Al_2O_3-dr	PXCT	cSAXS	5.1	dried gel of Al_2O_3-h
Al_2O_3-calc	PXCT	cSAXS	5.1	calcined Al_2O_3-dr
Ni/Al_2O_3-ha	PXCT	i13-1	6.1, 4.3*	activated Ni/Al_2O_3-h
Ni/Al_2O_3-hc	PXCT	i13-1	6.1	coked Ni/Al_2O_3-h
Ni/Al_2O_3-ma	PXCT	i13-1	6.1	activated Ni/Al_2O_3-m
Ni/Al_2O_3-mc	PXCT	i13-1	6.1	coked Ni/Al_2O_3-m

* Ni/Al_2O_3-ha in section 4.3 denoted as Ni/Al_2O_3-h

3.4.2 Electron Microscopy Experiments[15,16]

Scanning Electron Microscopy

Scanning electron microscopy (SEM) experiments of the SPP2080-IMRC catalyst discussed in section 4.1 were performed in the group of Prof. Roger Gläser by Dr. David Poppitz (Universität Leipzig). "SEM imaging was performed with a Leo 1530 instrument from Zeiss company operated at 5 kV acceleration voltage and equipped with an Everhart-Thornley and inlens detector for secondary electron detection. The spheres were cut and fixed on SEM sample holder with conductive carbon glue. For conductivity the samples were sputtered with gold using a Balzers MED 010 sputter coater."[241]
For the analysis of core-shell catalysts discussed in section 4.2 SEM was performed as following described by Ronny T. Zimmermann in the group of Prof. Kai Sundmacher (Otto-von-Guericke University Magdeburg, Max Planck Institute for Dynamics of Complex Technical Systems Physical and Chemical Foundations of Process Engineering, Magdeburg). "Samples for cross-sections are embedded in transparent epoxy resin, ground manually under water cooling (grit 180 to grit 2500), polished semi-automatically using polycrystalline diamond suspension (3 µm) and water-based lubricant for 8 min at 15 N and finished semi-automatically using alumina suspension (0.06 µm) for 3 min at 15 N. During preparation, the height of the samples is measured using a Nikon Digimicro MS-11C to ensure a centrical surface for SEM investigations. After preparation, samples are sputter-coated with gold. SEM analyses are performed using a FEI Scios DualBeam (ThermoFisher Scientific, Waltham, MA, USA) microscope equipped with a TEAM Trident system (EDAX, AMETEK GmbH, Weiterstadt, Germany). Secondary electron (SE) and backscattered electron (BSE) contrast are used to image topography and microstructure. EDS is performed for integral and local analyses of the chemical composition."[235]

Scanning Transmission Electron Microscopy and Electron Tomography

Scanning transmission electron microscopy (STEM) and electron tomography (ET) experiments in this thesis were performed for the SPP2080-IMRC (section 4.1) and Ni/Al_2O_3-h (section 4.3 catalysts. STEM and ET measurements were performed together with Xiaohui Huang in the group of Prof. Christian Kübel at the Institute of Nanotechnology (INT), Karlsruhe Institute of Technology. Tomographic reconstructions for the Ni/Al_2O_3-h samples were done by Xiaohui

[15] Parts of section 3.4.2 are adapted and taken from: S. Weber, K. L. Abel, R. T. Zimmermann, X. Huang, J. Bremer, L. K. Rihko-Struckmann, D. Batey, S. Cipiccia, J. Titus, D. Poppitz, C. Kübel, K. Sundmacher, R. Gläser and T. L. Sheppard, "Porosity and Structure of Hierarchically Porous Ni/Al_2O_3 Catalysts for CO_2 Methanation", *Catalysts*, **2020**, *10*, 1471[236], S. Weber, R. T. Zimmermann, J. Bremer, K. L. Abel, D. Poppitz, N. Prinz, J. Ilsemann, S. Wendholt, Q. Yang, R. Pashminehazar, F. Monaco, P. Cloetens, X. Huang, C. Kübel, E. Kondratenko, M. Bauer, M. Bäumer, M. Zobel, R. Gläser, K. Sundmacher and T. L. Sheppard, "Digitalization in Catalysis Research: Towards a Holistic Description of a Ni/Al_2O_3 Reference Catalyst for CO_2 Methanation", *ChemCatChem*, **2022**, *14*, e202101878.[241] and R. T. Zimmermann, S. Weber, J. Bremer, V. Idakiev, R. Pashminehazar, T. L. Sheppard, L. Mörl and K. Sundmacher, "Core-Shell Catalyst Pellets for Effective Reaction Heat Management", *Chem. Eng. J.*, **2023**, *457*, 140921.[235]

[16] Information about contributions from others are provided for each method separately.

Huang.
"STEM and ET experiments on the SPP2080-IMRC were performed on a Thermo Fisher Scientific Themis 300 equipped with probe corrector and operated at 300 kV in STEM mode with a convergence angle of 21.5 mrad, a nominal beam diameter of 0.1 nm and a beam current of 154 pA. STEM and ET analysis were performed on a spent catalyst sample after activation (2 h, 773 K, 25 % H_2 / 75 % He) and catalytic testing at three different temperatures (523, 623, 673 K) with increasing temperature steps (each 1 h, 20 % H_2 / 5 % CO_2 / 75 % He). The catalyst was tested in a continuous flow type laboratory reactor as described in section 3.3.2. Eight different high-angle annular dark field (HAADF)-STEM images were used for particle size analysis with magnifications in the range of 2.75 to 5.50 Mx. Particle size analysis was performed using ImageJ.[250] A Gaussian blurred background of the image was subtracted from the original image to allow for threshold-based Ni particle labeling. The contours of identified Ni particles were checked with the original images to manually remove artifacts and incorrectly identified labels. The area of the particles was determined, and the particle size was approximated assuming spherical particles for in total 875 labeled particles.
Samples for ET were ground in an agate mortar and suspended in EtOH to add a droplet of the suspension on a 100 x 400-mesh carbon-coated Cu-TEM grid (Quantifoil Micro Tools GmbH) with a support film thickness of 10-20 nm. Subsequent to drying under atmospheric conditions for 30 min, 6 nm diameter Au colloidal particles were added. ET measurements were performed with a Fischione 2020 tomography holder (Fischione Instruments). Tilt series of HAADF-STEM images were acquired for two particles with the Xplore3D software 3.1 (FEI Company) over a tilt range of -74 to 76 ° (-68 to 76 ° used for reconstruction) for SPP2080-IMRC-ET1 and -66 to 78 ° (-60 to 74 ° used for reconstruction) for SPP2080-IMRC-ET2 in 2 ° increments. The tilt series was aligned using IMOD[251] with 20 Au particles as fiducial markers, their position was manually refined, allowing for refinement of image rotation and magnification. The mean residual alignment errors were 0.20 and 0.18 nm for SPP2080-IMRC-ET1 and SPP2080-IMRC-ET2, respectively. After 100 iterations of a simultaneous iterative reconstruction technique (SIRT),[252] the reconstructions were denoised using the “Median 3D” and “Enhance Local Contrast (ELAHE)” plugins of ImageJ.[250] After applying 10 iterations of discrete algebraic reconstruction technique (DART)[253] implemented in the “TomoJ” plugin,[254] the final reconstructions were obtained. The reconstructed isotropic voxel sizes are 0.29 nm (SPP2080-IMRC-ET1) 0.58 nm (SPP2080-IMRC-ET2)."[241]
Samples for ET of the Ni/Al_2O_3-h catalyst were prepared similar as above using Au colloidal particles (6.5 nm diameter). "ET measurements of the Ni/Al_2O_3-h sample were performed using a Fischione 2020 tomography holder (Fischione Instruments, Export, PA, USA), on a Titan 80–300 (FEI Company, Hillsboro, OR, USA) microscope with an acceleration voltage of 300 kV in STEM mode. Tilt series of high-angle annular dark field STEM images were collected for two particles with the Xplore3D software 3.1 (FEI Company, Hillsboro, OR, USA) over a tilt range of -72 to 76 ° for Ni/Al_2O_3-h-ET1 and -74 to 78 ° for Ni/Al_2O_3-h-ET2, with an increment of 2 °. Alignment

of the tilt series was performed in IMOD,[251] by tracking 20 Au particles as fiducial markers, manually refining their position, enabling refinement of magnification and image rotation, and grouping tilt angles every three tilts without applying a distortion correction. A mean residual alignment error of 0.34 and 0.48 pixels was obtained for Ni/Al_2O_3-h-ET1 and Ni/Al_2O_3-h-ET2, respectively. After applying a SIRT[252] with 100 iterations to the aligned projection series, the reconstructions were denoised by employing the ImageJ[250] plugins Filters/Median 3D and ELAHE. Final reconstructions were obtained by ten iterations of DART[253] using TomoJ plugin in Fiji[250, 254]. The reconstructed tomograms had a final isotropic voxel size of 0.94 nm for Ni/Al_2O_3-h-ET1 and 0.64 nm for Ni/Al_2O_3-h-ET2."[236]

3.4.3 X-ray Microtomography[17]

X-ray microtomography (µ-XCT) measurements were performed on whole pellets of the SPP2080-IMRC, SPP2080-IMRC-0min, SPP2080-IMRC-10min, SPP2080-IMRC-30min and SPP2080-IMRC-50min samples by Dr. Reihaneh Pashminehazar and Dr. Thomas L. Sheppard at an instrument available at the Institute for Applied Materials - Electrochemical Technologies (IAM-ET) of the Karlsruhe Institute of Technology. Tomographic reconstruction of the data was done by Dr. Reihaneh Pashminehazar. "µ-XCT analysis was performed using a Zeiss Xradia Versa 520 X-ray microscope (Pleasanton, United States). The sample was scanned using a 4X objective lens in binning 2 mode with a tungsten X-ray source. The instrument was operated at 40 kV and 76 µA, employing a low energy filter to optimize transmission and signal to noise ratio. The chosen setting provided an optical magnification of 3.95 and voxel size of 2.67 µm (SPP2080-IMRC) and 2.85 µm (SPP2080-IMRC-0min, SPP2080-IMRC-10min, SPP2080-IMRC-30min and SPP2080-IMRC-50min). The sample was scanned within the entire range of 0-360 ° and 2041 images were acquired with an exposure time of 1000 ms per image. The scanning time highly depends on number of recorded projections and exposure time. This parameter setting let to a scanning time around 2 h. Reconstructions were done manually with a commercial software package (Zeiss XMReconstructor), which uses an algorithm based on standard filtered back-projection. The procedure for manual reconstruction consists of two main steps: finding the correct value for center of rotation and the beam hardening constant. The center shift value is the amount, in pixels, that the axis of rotation is offset from the detector's center column. Images with incorrect center shift are unfocused and blurry, while images with correct center shift are focused and clear, with clean edge features. Beam hardening effect results in non-uniform intensity signals in reconstructed views where the sample density remains the same. Therefore,

[17] Parts of section 3.4.3 are adapted and taken from: S. Weber, R. T. Zimmermann, J. Bremer, K. L. Abel, D. Poppitz, N. Prinz, J. Ilsemann, S. Wendholt, Q. Yang, R. Pashminehazar, F. Monaco, P. Cloetens, X. Huang, C. Kübel, E. Kondratenko, M. Bauer, M. Bäumer, M. Zobel, R. Gläser, K. Sundmacher and T. L. Sheppard, "Digitalization in Catalysis Research: Towards a Holistic Description of a Ni/Al_2O_3 Reference Catalyst for CO_2 Methanation", *ChemCatChem*, **2022**, *14*, e202101878[241] and R. T. Zimmermann, S. Weber, J. Bremer, V. Idakiev, R. Pashminehazar, T. L. Sheppard, L. Mörl and K. Sundmacher, "Core-Shell Catalyst Pellets for Effective Reaction Heat Management", *Chem. Eng. J.*, **2023**, *457*, 140921.[235]

in order to reduce this artifact, the proper correction constant should be selected and performed on a focused image."[241]

3.4.4 Sample Preparation for X-ray Nanoimaging[18,19]

Sample preparation for X-ray nanoimaging experiments, i.e., X-ray ptychography and X-ray holotomography studies, generally required the use of a dual beam focused-ion beam (FIB, Ga^+ ions), scanning electron microscope (SEM) instrument (FIB/SEM) equipped with a micro-manipulator. This is due to the small sample diameters ≈50 µm required for X-ray nanoimaging. Samples for *ex situ* X-ray nanotomography studies were prepared with a Strata 400 S FIB/SEM (FEI Company) available at the Institute of Nanotechnology (INT), Karlsruhe Institute of Technology. The sample preparation was partially supported by Dr. Sabine Schlabach (INT, Karlsruhe Institute of Technology). Al tomography pins, e.g., as shown in Figure 3.7, were used for X-ray holotomography and X-ray ptychography experiments of SPP2080-IMRC, Ni/Al_2O_3-h, Ni/Al_2O_3-ha, Ni/Al_2O_3-hc and Ni/Al_2O_3-ma, Ni/Al_2O_3-mc. Cu tomography pins (Figure 3.7) of the OMNY design[255] were applied for X-ray ptychography experiments of the SPP2080-IMRC, Ni/Al_2O_3-dr, Ni/Al_2O_3-calc, Al_2O_3-dr and Al_2O_3-calc samples.



Figure 3.7: Pictures of the Al pins (left) and Cu pins of the OMNY design[255](right) used to mount samples for X-ray nanotomography experiments.

A suitable particle of the samples was attached to the micro-manipulator of the FIB/SEM instrument by Pt-deposition and afterwards transferred and glued to the tip of the tomography pins by Pt-deposition. This process is illustrate for one example in Figure 3.8. The FIB

[18] Parts of section 3.4.4 are adapted and taken from: S. Weber, A. Diaz, M. Holler, A. Schropp, M. Lyubomirskiy, K. L. Abel, M. Kahnt, A. Jeromin, S. Kulkarni, T. F. Keller, R. Gläser, T. L. Sheppard, "Evolution of Hierarchically Porous Nickel Alumina Catalysts Studied by X-ray Ptychography", *Adv. Sci.*, **2022**, *9*, 2105432.[237]

[19] Sample preparation of the wedge-like structure of the Ni/Al_2O_3-dr was performed by A. Jeromin, S. Kulkarni and T. F. Keller.

preparation time was kept to a minimum to avoid excessive contamination of the sample by Pt or Ga.

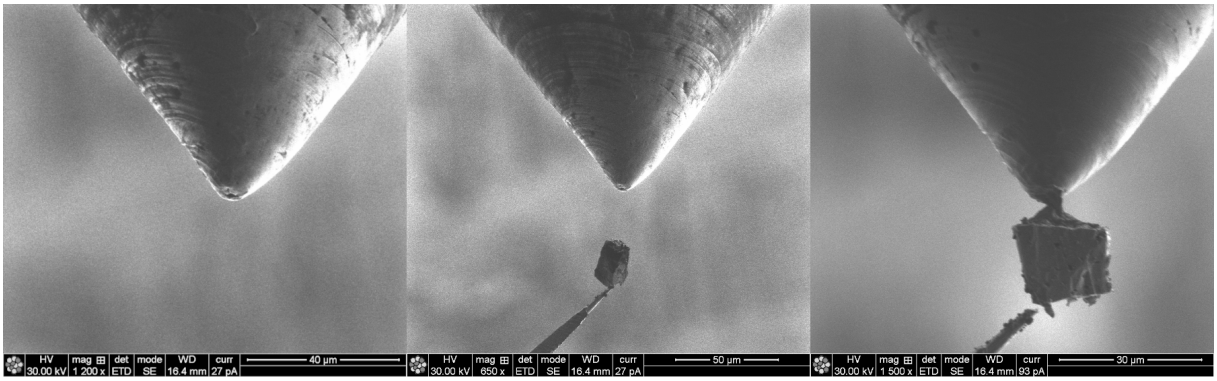


Figure 3.8: Illustration of the sample mounting process for X-ray nanotomography experiments. Empty pin (left), sample attached to the micro-manipulator by Pt-deposition (middle), sample glued to the pin by Pt-deposition and disconnected from the micro-manipulator (right).

The FIB/SEM sample preparation with more demanding sample requirements in case of *in situ* experiments (section 3.4.5) was performed by Arno Jeromin and Satishkumar Kulkarni together with Dr. Thomas F. Keller at DESY Nanolab (Hamburg). "Wedge-shaped samples for *in situ* X-ray ptychography were prepared from a starting powder particle of the dried gel (Ni/Al_2O_3-dr) at a dual beam FIB/SEM instrument[256] via micromanipulation with Ga^+ ions. The Ga ion beam current was 5 nA at a voltage of 30 kV. After lift-off of a cuboidal specimen, the sample was mounted on a FIB grid holder and trimmed from all sides to the final wedge-shape to allow for X-ray and TEM analysis on the same sample. For the final surface cleaning and polishing a voltage of 30 kV and a low current of 1 nA was used. After the final preparation the wedge-shaped sample was transferred to a micro-electro-mechanical systems (MEMS) based Wildfire Nano-Chip (DENSsolutions) and glued using ion beam induced deposition (IBID) of a Pt precursor material. Before the sample was attached to the MEMS chip, the SiN membrane on the hole was removed by the ion beam. SEM images were taken at 2 kV at an electron current of 0.1 nA using a secondary electron Everhart-Thornley (ETD) detector in normal and side view with a sample tilt of 0 ° and 52 °, respectively."[237] The preparation process for the wedge-shaped samples is illustrated in Figure 3.9. SEM images of all samples studied in this thesis are provided in the relevant sections of the appendix A 8.

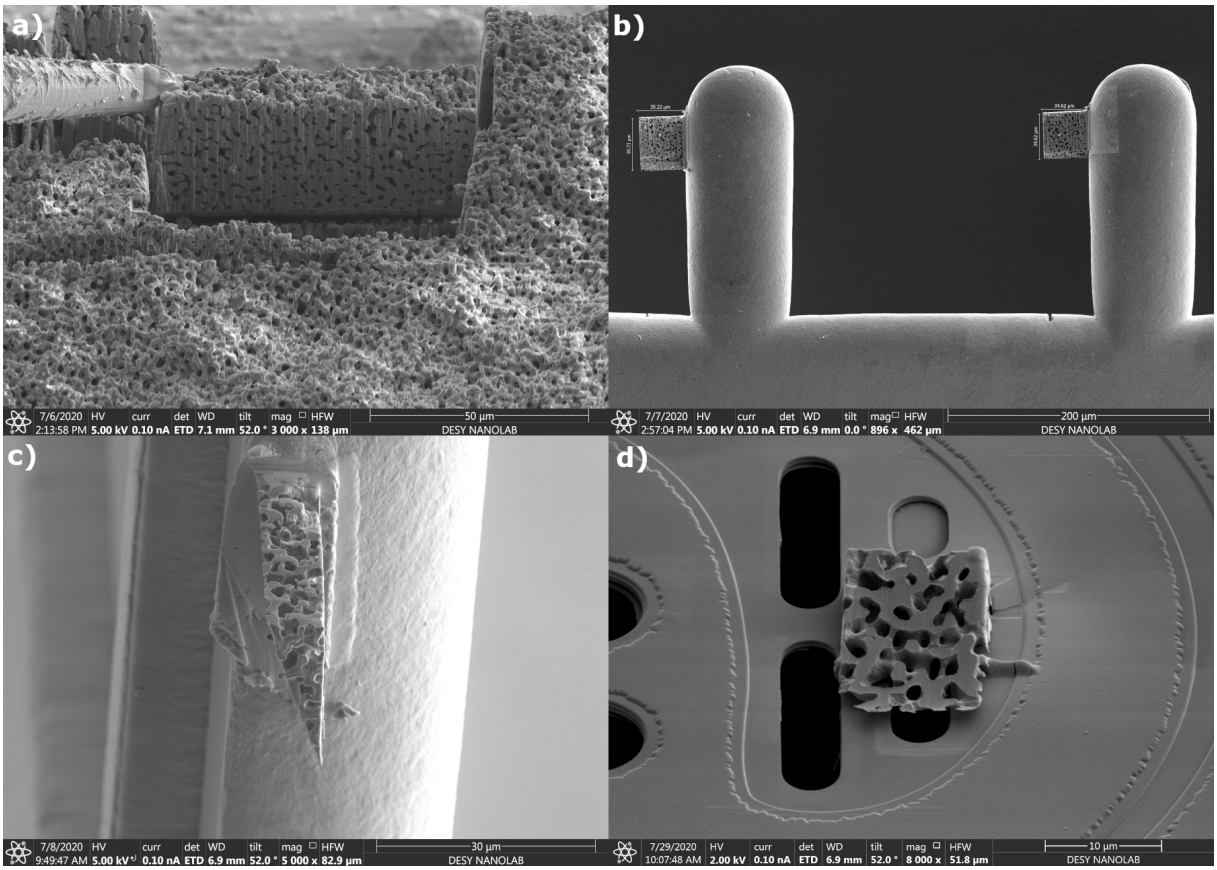


Figure 3.9: Illustration of the sample preparation process for the wedge-shaped sample. (a) larger cut-out from the powder, (b) two cuboidal specimen mounted to a FIB grid holder, (c) trimmed sample on the FIB grid holder and (d) wedge-shaped sample mounted on the MEMS chip by Pt-deposition.

3.4.5 *In Situ* 2D X-ray Ptychography[20,21]

The *in situ* 2D X-ray ptychographic imaging (XRP) was performed with the PtyNAMi setup at the Nanoprobe endstation of beamline P06 of the Deutsches Elektronen-Synchrotron DESY (Hamburg, Germany).[257] The measurements were performed together with Dr. Andreas Schropp, Dr. Mikhail Lyubomirskiy (both Deutsches Elektronen-Synchrotron DESY, Hamburg) and Dr. Maik Kahnt (MAX IV Laboratory, Lund, Sweden), who also assisted with the ptychographic reconstructions. The PtyNAMi setup allows for flexible sample environments for X-ray ptychography studies with nanosized hard X-ray beams. In the present case the nanoreactor developed by Dr. Yakub Fam as reported in ref.[234] was used. "The setup consists of the nanoreactor as *in situ* cell shown in Figure 3.10. The *in situ* cell contains the MEMS based Wildfire Nano-Chip (DENSsolutions) for electrical heating of the mounted sample. The heating is controlled with a

[20] Parts of section 3.4.5 are adapted and taken from: S. Weber, A. Diaz, M. Holler, A. Schropp, M. Lyubomirskiy, K. L. Abel, M. Kahnt, A. Jeromin, S. Kulkarni, T. F. Keller, R. Gläser, T. L. Sheppard, "Evolution of Hierarchically Porous Nickel Alumina Catalysts Studied by X-ray Ptychography", *Adv. Sci.*, **2022**, *9*, 2105432.[237]

[21] *In situ* 2D X-ray ptychography experiments and ptychographic reconstructions were performed together with A. Schropp, M. Lyubomirskiy and M. Kahnt.

Digiheater temperature controller box (DENSsolutions). The cell further has a gas inlet and outlet, with the outlet connected to an on-line mass spectrometer (MS), OMNI-Star GSD 320 (Pfeiffer Vacuum). The gas dosing was controlled by a custom made gas-dosing system of mass flow controllers (Bronkhorst). For further details regarding specifications of the *in situ* cell, the reader is referred to ref.[234]

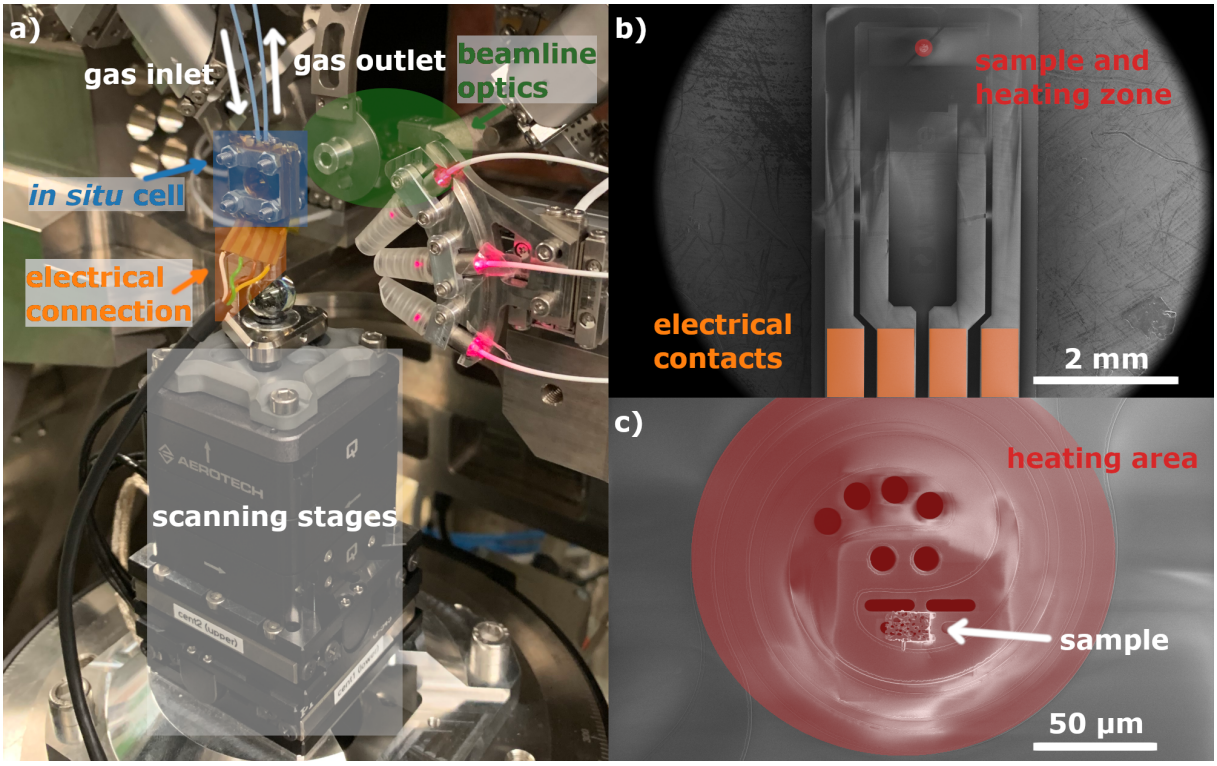


Figure 3.10: "Illustration of the samples setup and MEMS chip used for *in situ* X-ray ptychography experiment. (a) nanoreactor *in situ* cell mounted at the beamline as used during the experiments, the outlet is connected to an online mass spectrometer. (b) SEM overview image of the MEMS chip, which is located inside the *in situ* cell of (a). (c) SEM image of the heating zone of the MEMS chip with the sample located on one of the chip windows."[237] Available under the terms and conditions of the Creative Commons Attribution 4.0 license (CC BY 4.0, `https://creativecommons.org/licenses/by/4.0/`), Copyright ©2022

The *in situ* XRP experiments were carried out at an energy of 12 keV. The beam was focused by two sets of 1D focusing diamond lenses in cross geometry, while the sample was scanned out of focus with an effective spot size of ≈ 1.4 µm on the sample. Far field diffraction patterns were acquired using an EIGER X 4M (Dectris) detector with 2070 x 2167 pixels and a pixelsize of 75 µm. The sample to detector distance was 3.398 m. Before the *in situ* experiments, the sample was aligned and test scans performed under a constant He flow at room temperature. During *in situ* XRP studies, projections of the sample were obtained for a field of view (FOV) of about 18 x 14 µm (horizontal x vertical) with a step size of 0.7 µm and an exposure time of 0.3 s step^{-1}.

The acquisition of one projections required in total about 11 min.
In the *in situ* experiments the Ni/Al_2O_3 sample was studied under three different conditions: (i) calcination, (ii) activation and (iii) reaction conditions. A total gas flow of $2\,mL\,min^{-1}$ was dosed to the *in situ cell*. The gas compositions for each condition are summarized in Table 3.3. The *in situ* experiment was carried out as following starting from the dried gel Ni/Al_2O_3 sample mounted on the MEMS chip:

- calcination, heating from 303 K to 873 K (30 K steps), holding at 873 K for ≈1 h
- activation, heating from 873 K to 1073 K (50 K steps), holding at 1073 K for ≈1 h, cooling to 673 K
- reaction, at 673 K for ≈1 h, cooling to 303 K (30 K steps)

During the *in situ* experiment the gas composition was constantly analyzed by monitoring the following mass to charge ratios with the assigned compounds in brackets: 2 (H_2), 4 (He), 15 (CH_4), 16 (O_2), 18 (H_2O), 28 (CO,N_2), 32 (O_2), 40 (Ar), 44 (CO_2) as shown in Figure 8.12. It should be noted that the MS requires a total flow of $\approx 5\,mL\,min^{-1}$. As the total gas flow during the *in situ* studies was only $2\,mL\,min^{-1}$, the MS constantly sucked air from the exhaust, which is indicated by the increased Ar and CO/N_2 during the *in situ* experiments. Ptychographic reconstruction of

Table 3.3: Gas composition during the different conditions of the *in situ* XRP experiments of sample Ni/Al_2O_3. A total gas flow of $2\,mL\,min^{-1}$ was used during the *in situ* studies.

condition	He / $mL\,min^{-1}$	O_2 / $mL\,min^{-1}$	H_2 / $mL\,min^{-1}$	CO_2 / $mL\,min^{-1}$
calcination	1.6	0.4	-	-
activation	1.5	-	0.5	-
reaction	1.5	-	0.4	0.1

the *in situ* XRP experiments was carried out using an ePIE based algorithm.[258] The diffraction patterns were cropped to 512 x 512 pixels for reconstruction. For each, 1000 iterations of the algorithm were applied. The resulting reconstructed pixel size is 18.6 nm.
The phase contrast projections were further processed using the software ImageJ/Fiji.[250] The phase contrast projections were aligned using the template matching and slice alignment plugin by Tseng *et al.*[259] The open windows of the MEMS-chip above the sample were used as reference for the alignment to avoid any influence of sample changes during the experiment. The width of the sample during the *in situ* experiment was measured manually at a characteristic feature that could be identified in all projections as indicated by the arrows in section 5.1, Figure 5.3.
The resolution of the *in situ* XRP experiment was estimated by Fourier ring correlation (FRC)[260] of the last two projections. For FRC the final projections were cropped to 600 x 600 pixels. The results of the FRC analysis are shown in Figure 8.13 with an estimated resolution of 67.2 nm using the 1/2 bit threshold criterion.[261]"[237]

3.4.6 Ptychographic X-ray Computed Tomography at cSAXS[22,23]

Ptychographic X-ray computed tomography (PXCT) studies of the Ni/Al_2O_3-dr,-calc, Al_2O_3-dr,-calc and SPP2080-IMRC-0min where performed at the coherent small angle X-ray scattering (cSAXS) beamline of the Swiss Light Source at the Paul Scherrer Institute (Villigen, Switzerland). The beamline allows for optimized acquisition of PXCT in reasonably short time with high resolution due to a very automatized workflow. The PXCT experiments as well as ptychographic and tomographic reconstructions were performed together with Dr. Ana Diaz and Dr. Mirko Holler (Paul Scherrer Institut, Villigen, Switzerland). "The flexible tomography nanoimaging endstation (flOMNI)[183, 262] was used for the measurements. The experiments were carried out at room temperature with a constant N_2 stream around the sample. PXCT were measured at an energy of 6.2 keV. A Fresnel zone plate (fabricated at the Laboratory for Micro- and Nanotechnology at the Paul Scherrer Institute in Villigen, Switzerland) with a diameter of 200 µm was used to obtain an illumination size on the sample of about 4 µm, while the sample was measured 1.5 mm out of the zone plate focus point. Far-field diffraction patterns were acquired with an in-vacuum EIGER 1.5 M detector (Detector group at the Paul Scherrer Institute in Villigen, Switzerland) with 75 µm pixel size and a sample to detector distance of 5.235 m. For each sample the total tomogram was divided into evenly distributed interlaced sub-tomograms covering a total angular range from 0 to 180 ° in a so-called binary decomposition.[263] Each projection was acquired with the respective field of view (FOV) in x (horizontal) and y (vertical) using a Fermat spiral trajectory[264]. An acquisition time of 25 ms was used for each scanning point. The detailed measurement parameters for each experiment are summarized in Table 3.4. For the experiments, first PXCT of the dried gel samples as shown in Figure 8.11 were measured. After finishing a tomography scan, the sample was removed from the beamline and calcined mounted on the pin in an external muffle furnace LE 1/11 (Nabertherm). The sample was heated under flowing air with 10 K min^{-1} to 823 K for 15 min at the highest temperature. A higher heating temperature on the pins is not possible due to reaction of the Cu-pin with air as observed for heating an empty pin to 873 K with 10 K min^{-1} for 2 h. After treatment in the muffle furnace the sample was measured again by PXCT, denoted as the calcined sample.

For ptychographic reconstruction, a region of 700 x 700 pixels (reconstructed pixels size 19.9 nm) and 500 x 500 pixels (reconstructed pixels size 27.9 nm) of the acquired diffraction patterns was used. The obtained reconstructed pixel sizes of the projections were 19.9 nm for Ni/Al_2O_3-dr, Al_2O_3-calc, SPP2080-IMRC and Ni/Al_2O_3-calc, 27.9 nm for Al_2O_3-dr. 300 iterations of the difference map algorithm [163] followed by 300 iterations of maximum likelihood refinement

[22] Parts of section 3.4.6 are adapted and taken from: S. Weber, A. Diaz, M. Holler, A. Schropp, M. Lyubomirskiy, K. L. Abel, M. Kahnt, A. Jeromin, S. Kulkarni, T. F. Keller, R. Gläser, T. L. Sheppard, "Evolution of Hierarchically Porous Nickel Alumina Catalysts Studied by X-ray Ptychography", *Adv. Sci.*, **2022**, *9*, 2105432.[237]

[23] Tomography experiments as well as ptychographic and tomographic reconstructions were performed together with A. Diaz and M. Holler.

Table 3.4: Measurement parameters for each PXCT experiment performed at cSAXS.

	Ni/Al_2O_3		Al_2O_3		SPP2080-IMRC
	-dr	-calc	-dr	-calc	-0min
FOV x / µm	60	48	21	20	36
FOV y / µm	10	10	11	10	10
step size / µm	1.2	1.0	1.2	1.2	1.0
no. sub-tomograms / 1	8⋆	8	16	8	8
no. projections / 1	1000	1200	800	500	1100
angular step sub-tomogram / °	1.44	1.20	3.60	2.88	1.31
estimated dose / 10^7 Gy	1.58	2.60	1.65	0.704	8.88
total acquisition time / h	11	11.5	5	2.5	16.5

⋆ last 6 sub-tomograms used for tomographic reconstruction

[265, 266] were used to reconstruct the projections. The obtained 2D projection series of the complex-valued transmission of the sample was first aligned according to Guizar-Sicairos *et al.* and Odstrčil *et al.*[267, 268] The series was aligned in the following steps: (i) cross-correlation, (ii) mass fluctuation based vertical alignment and (iii) tomographic consistency alignment[269]. The aligned phase projection series was subsequently tomographically reconstructed with a filtered-back projection algorithm employing a Ram-Lak filter. The resulting tomogram with the refractive index decrement ($\delta(r)$) contrast was used for further analysis. The electron density ($N_e(r)$) tomogram can be calculated from the $\delta(r)$ tomogram as described in eq. 3.24 and section 3.4.9. 3D Fourier shell correlation (FSC) was used to estimate the resolution of the obtained tomograms.[261] The tomogram dataset was divided in two independent subtomograms with double angular spacing, which were reconstructed individually. On these two independent reconstructed tomograms FSC was performed to estimate the effective resolution using the ½ bit threshold criterion.[261] The FSC analysis for the Ni/Al_2O_3 and Al_2O_3 samples are shown in Figures 8.14,8.15, respectively.

Potential X-ray beam induced sample changes of the dried gels was checked during the tomographic reconstructions. For Ni/Al_2O_3-dr slight sample changes were observed for the first two sub-tomograms. This is also indicated by comparing the resolution from FSC analysis of the reconstructed tomograms using 6 (91.2 nm, Figures 8.14) or 8 (102.7 nm) sub-tomograms. Therefore the first two subtomograms of Ni/Al_2O_3-dr were excluded to reconstruct the final tomogram. In case of Al_2O_3-dr the FSC analysis of tomographic reconstructions of the first 8 (51.6 nm) and the full 16 (49.6 nm, Figures 8.15) sub-tomograms revealed not such pronounced changes. Therefore, all 16 sub-tomograms were used to obtain the final tomographic reconstructions. For the calcined samples no X-ray beam induced changes could be identified, which indicates that the samples changes could be related to the organic and solvent residues."[237]

3.4.7 Ptychographic X-ray Computed Tomography at I13-1[24,25]

PXCT measurements were performed at the coherence branch I13-1 beamline of the Diamond Light Source (Oxford, UK). [270, 271] The studies were done together with Dr. Darren Batey and Dr. Silvia Cipiccia, who additionally assisted the ptychographic reconstruction of the experimental data. "The experiments were carried out at a photon energy of 9.7 keV with a beam size of 5 µm diameter on the sample. The far-field diffraction patterns were recorded with a MerlinX detector with a Quad system of 512 x 512 pixels (pixel size 55 µm) at a sample to detector distance of 4.13 m. For the measurement of each tomogram, 1000 2D projections over an angular range of 180 ° (0.18 ° step^{-1}) were recorded with different fields of view as summarized in Table 3.5. The total acquisition time for the samples ranged from 11 h to 19 h depending on the field of view. Ptychographic reconstructions with 400 iterations were done with the PtyREX package[272] based on the ePIE algorithm[258] to obtain a 2D projection series of the complex object transmission function, which contains information about the amplitude and phase shift. The reconstructions were performed on a cropped detector area of 256 x 256 pixels, which corresponds to a pixel size of 37.5 nm in the reconstructed projections. No modes, no upsampling and no position correction were performed.

Table 3.5: Measurement parameters for each PXCT experiment performed at I13-1.

	Ni/Al_2O_3-m		Ni/Al_2O_3-h	
	activated (ma)	coked (mc)	activated (ha)	coked (hc)
FOV x / µm	33	38	40	54
FOV y / µm	16	12	22	16
step size / µm	1.0	1.0	1.0	1.0
no. projections / 1	1000	1000	1000	1000
total acquisition time / h	12	11	19	18

The obtained 2D-projection series were aligned and tomographically reconstructed using the MATLAB script provided by Odstrčil *et al.*[267, 268] The projection series was aligned by the following steps: (i) crosscorrelation, (ii) vertical alignment based on mass fluctuation and (iii) tomographic consistency alignment[269] as described in ref.[268] The tomograms were reconstructed using a filtered-back projection algorithm implemented in ref.[268] with a Ram-Lak

[24] Parts of section 3.4.7 are adapted and taken from: S. Weber, D. Batey, S. Cipiccia, M. Stehle, K. L. Abel, R. Gläser and T. L. Sheppard, "Hard X-Ray Nanotomography for 3D Analysis of Coking in Nickel-Based Catalysts", *Angew. Chem. Int. Ed.*, **2021**, *60*, 21722-21777.[239] and S. Weber, K. L. Abel, R. T. Zimmermann, X. Huang, J. Bremer, L. K. Rihko-Struckmann, D. Batey, S. Cipiccia, J. Titus, D. Poppitz, C. Kübel, K. Sundmacher, R. Gläser and T. L. Sheppard, "Porosity and Structure of Hierarchically Porous Ni/Al_2O_3 Catalysts for CO_2 Methanation", *Catalysts*, **2020**, *10*, 1471[236]

[25] PXCT experiments and ptychographic reconstruction in this section were performed together with D. Batey and S. Cipiccia.

filter. The obtained tomograms contain information about the complex refractive index $\delta(r)$, from which the electron density N_e can be calculated as described in refs.[156, 157] and shown eq. 3.24. The obtained N_e was offset individually for all samples to the mean value of air in close proximity to the particle. More details regarding the offset are provided in section3.4.9. The resolution of the obtained tomograms was estimated by 3D Fourier shell correlation (FSC).[261, 268] For FSC the full dataset was divided in half to obtain two independent subtomograms with double angular spacing, which were then reconstructed individually. The FSC was then performed on the two reconstructed subtomograms using the 1/2-bit criterion as a threshold.[261] The FSC curves are shown for the samples in Figure 8.28 and Figure 8.29. The estimated resolution ranges from 74 nm to 83 nm. It should be noted that in the Ni/Al_2O_3-m system some phase vortices artifacts are present, which are indicated by line features/streaks, e.g. N_e tomogram slice Figure 6.4. The artifacts may influence the alignment of the projection series and the quantitativeness of the N_e. Therefore, the Ni/Al_2O_3-m system is only presented (...) and discussed as supporting indication to the results of the Ni/Al_2O_3-h system (...). In case these artifacts are only caused by nonconvergence of the ptychographic reconstruction and not due to physical reasons, a recently reported "VortRem" algorithm[273] or strategies as reported in ref.[274, 275] or in the Toupy package[276] might be able to remove them. The origin of those artifacts might be pronounced edge like features or the strong absorbing residues of the Pt-gluing, which cannot be prevented in the chosen sample preparation by FIB-SEM."[239]

3.4.8 Holographic X-ray Computed Tomography[26,27]

Holographic X-ray computed tomography (HXCT) experiments were performed on a spent SPP2080-IMRC catalyst particle after testing as described in section 3.4.2 and shown in Figure 8.1. HXCT were obtained at the ID16A-NI beamline of the European Synchrotron Radiation Facility (ESRF). The remote access measurements were carried out by Dr. Federico Monaco and Dr. Peter Cloetens, who also did the tomographic reconstructions. "The experiment was performed at high energy (17.1 keV) ensuring the transmission of the X-ray across the sample and thus allowing the reconstruction of a large field of view. Two multilayer coated Kirkpatrick-Baez (KB) mirrors are used to focus the X-ray beam down to $\approx 23(\mathrm{h})\,\mathrm{x}\,37(\mathrm{v})$ nanometers.[277] This unique nanometric focus size is coupled with very high photon flux (up to $1013\,\mathrm{photons\,s^{-1}}$), high monochromaticity ($\Delta E/E \approx 1\,\%$) and high spatial coherence thanks to the large propagation distance between the source and the experimental hutch. The 3D reconstruction was obtained using holographic X-ray computed tomography (HXCT).[159] (...) The projections are obtained with

[26] Parts of section 3.4.8 are adapted and taken from: S. Weber, R. T. Zimmermann, J. Bremer, K. L. Abel, D. Poppitz, N. Prinz, J. Ilsemann, S. Wendholt, Q. Yang, R. Pashminehazar, F. Monaco, P. Cloetens, X. Huang, C. Kübel, E. Kondratenko, M. Bauer, M. Bäumer, M. Zobel, R. Gläser, K. Sundmacher and T. L. Sheppard, "Digitalization in Catalysis Research: Towards a Holistic Description of a Ni/Al_2O_3 Reference Catalyst for CO_2 Methanation", *ChemCatChem*, **2022**, *14*, e202101878[241]

[27] The HXCT measurements and tomographic reconstructions thereof were performed by F. Monaco and P. Cloetens.

the sample out-of-focus and the radiographs consist in the magnified near-field in-line holograms of the sample (Fresnel diffraction) containing the information of the phase shift induced by the materials on the X-ray beam. Moreover, taking advantage of the geometric magnification effect of the divergent cone beam, it is possible to select the voxel size in the final reconstruction by changing the relative distance between the sample and the X-ray focal plane. For the tomography reconstruction, 1800 radiographies are acquired over 180 ° with an exposure time of 0.25 s at four different sample-to-focus positions along the optical axis. This longitudinal diversity allows to enhance the final resolution of the volume thanks to the increase of information.[278] Moreover, for each angle, random in-plane motions of the samples are added to avoid ring-shaped artifacts in the final 3D volume.[279] Once the projections have been acquired, flat-field correction is applied to all the images and the radiographies of the 2nd, 3rd, and 4th distances are resized via interpolation to match the pixel size of the 1st distance, which determines the voxel size in the final reconstruction (25 nm). Afterwards, the resized projections at the four distances are carefully aligned to each other[280] and the 2D phase map for each angle is determined from the four aligned projections by using an iterative phase-retrieval procedure implemented in GNU Octave.[281, 282] The final tomographic reconstruction is obtained by using the filtered back-projection (FBP) algorithm on the aligned phase maps. This last step is performed using the PyHST software package developed at the ESRF.[283] The final volume is a 3D map in which the value in each voxel is a quantitative representation of the real part of the local refractive index decrement (δ), which is proportional to the electron density.[157] The spatial resolution in the final 3D volume has been measured by analyzing the edge profile at the interface between two material phases. The measured data have been fitted with a hyperbolic tangent function and a 10 %-90 % criterion was applied to determine the physical resolution in the volume.[183] The same procedure has been applied on different interfaces to be statistically representative. Using this methodology, a mean value of ≈94 nm was found whereas the best value was ≈54 nm corresponding to approximately two voxels *c.f.* Figure 8.2."[241]

3.4.9 Image Analysis of Tomography Data[28]

General Image Analysis

The image analysis of the tomography experiments summarized in Table 3.2 is generally performed using the image analysis software Avizo 9.7.0 (FEI SAS, Thermo Fisher Scientific). The software allows to handle, analyze and visualize large data sets, which were for the reconstructed tomograms up to 30 GB in size. Further statistical analysis and visualization of graphs were performed by own written Python scripts using NumPy[284], matplotlib[285] and seaborn[286] libraries. Image analysis for the different imaging experiments might differ depending on the information that should be retrieved or the applied method itself. However, a generalized workflow often consists of the following steps:

- cropping of the tomogram, if too much air or artifacts are present
- filtering/binning of the tomograms, if necessary to reduce the influence of artifacts or improve signal-to-noise ratio
- segmentation of the grey-scale tomograms into different image labels
- operations to remove artifacts from segmentation if required
- quantitative analysis of the labels obtained from segmentation, which might include derivation and quantification of sophisticated network models

Each of those steps can influence the final outcome of the image analysis and has to be performed carefully. Therefore, the detailed information about the image analysis steps are following provided for each of the later discussed results and discussion sections of this thesis. The result of the quantitative label analysis or derived pore network models were then applied for the porosity characterization.

Section 5.1

(PXCT of samples Ni/Al_2O_3-dr, Ni/Al_2O_3-calc, Al_2O_3-dr and Al_2O_3-calc.)

[28] Parts of section 3.4.9 are adapted and taken from: S. Weber, A. Diaz, M. Holler, A. Schropp, M. Lyubomirskiy, K. L. Abel, M. Kahnt, A. Jeromin, S. Kulkarni, T. F. Keller, R. Gläser, T. L. Sheppard, "Evolution of Hierarchically Porous Nickel Alumina Catalysts Studied by X-ray Ptychography", *Adv. Sci.*, **2022**, *9*, 2105432.[237]; S. Weber, D. Batey, S. Cipiccia, M. Stehle, K. L. Abel, R. Gläser and T. L. Sheppard, "Hard X-Ray Nanotomography for 3D Analysis of Coking in Nickel-Based Catalysts", *Angew. Chem. Int. Ed.*, **2021**, *60*, 21722-21777.[239]; S. Weber, K. L. Abel, R. T. Zimmermann, X. Huang, J. Bremer, L. K. Rihko-Struckmann, D. Batey, S. Cipiccia, J. Titus, D. Poppitz, C. Kübel, K. Sundmacher, R. Gläser and T. L. Sheppard, "Porosity and Structure of Hierarchically Porous Ni/Al_2O_3 Catalysts for CO_2 Methanation", *Catalysts*, **2020**, *10*, 1471[236]; S. Weber, R. T. Zimmermann, J. Bremer, K. L. Abel, D. Poppitz, N. Prinz, J. Ilsemann, S. Wendholt, Q. Yang, R. Pashminehazar, F. Monaco, P. Cloetens, X. Huang, C. Kübel, E. Kondratenko, M. Bauer, M. Bäumer, M. Zobel, R. Gläser, K. Sundmacher and T. L. Sheppard, "Digitalization in Catalysis Research: Towards a Holistic Description of a Ni/Al_2O_3 Reference Catalyst for CO_2 Methanation", *ChemCatChem*, **2022**, *14*, e202101878[241] and R. T. Zimmermann, S. Weber, J. Bremer, V. Idakiev, R. Pashminehazar, T. L. Sheppard, L. Mörl and K. Sundmacher, "Core-Shell Catalyst Pellets for Effective Reaction Heat Management", *Chem. Eng. J.*, **2023**, *457*, 140921.[235]

"(...) For the analysis of the N_e tomograms, the whole sample particle volume was masked from the surrounding air to obtain the particle label by using the *lasso* and *interpolation* tools within the segmentation editor of the software. The particle label was then further segmented by *thresholding* into pore, material and contamination labels (*c.f.* Figure 5.4). The pore label was separated into individual pores by the *separate objects* function to obtain the separated pores label. An *opening* module was applied on the separated pores to remove single voxel artefacts from the separation (*c.f.* Figure 5.5).
(...) The pore label was further analyzed by applying an *auto skeleton* module to retrieve a pore network model of the macropores within the particle. Quantitative information about the pore network model were obtained by applying the *spatial graph statistics* module. The resulting spatial graph of the pore network model contains several sub-graphs. The sub-graphs consist of nodes, which are connected by segments. For all samples in this study one main spatial graph was obtained and the detailed analysis is limited to these main graphs. Other detected graphs consisted only of few pore nodes and segments located at the surface of the particle volume, which were assigned to surface artefacts. The presence of one main graph additionally confirms the presence of a well connected macropore structure in all samples. The statistical analysis of the main spatial graphs provides information about the coordinates of each node and its coordination number (CN). Furthermore, for each segment tortuosity (τ), cylindrical radius (r_{pore}) / diameter (d_{pore}), volume (V_{pore}) and orientation information can be retrieved."[237] Details regarding the further analysis of the skeleton pore network models are provided in the appendix section 8.4.

Section 6.1

(PXCT of samples Ni/Al_2O_3-ha, Ni/Al_2O_3-hc, Ni/Al_2O_3-ma and Ni/Al_2O_3-mc.)
The analysis for both systems was performed identically despite the present artifacts in Ni/Al_2O_3-m. "First the particle was masked from the surroundings using the *lasso* and *interpolation* tools. With that a label for the whole measured particle was obtained, which is referred to as the masked particle volume. Subsequently, the masked particle volume was segmented into catalyst body, pore and contamination labels based on *thresholding*. The contamination observed is attributed to Ga or Pt deposition during the sample preparation for PXCT and is quite localized at certain positions of the particle exterior. The volume rendering of the contamination labels for the Ni/Al_2O_3-h and the Ni/Al_2O_3-m samples are shown in Figure 8.31 and 8.33 and the catalyst body labels in Figure 8.30 and 8.32, respectively. (...)"[239]

Section 4.1

(µ-XCT, HXCT and ET of samples SPP2080-IMRC, SPP2080-IMRC-ET1 and SPP2080-IMRC-ET2.)
"First the tomograms were masked from the surrounding air by *thresholding*, *lasso* and *interpolation* tools of the segmentation editor to obtain a whole particle label. Afterwards, the

particle label was segmented by *thresholding* into solid and pore labels (for ET *thresholding* is performed only to assign the labels). *Closing* and *opening* modules were used to remove segmentation artifacts as indicated in brackets from the solid (ET1: closing 1 px, opening 1 px; ET2: closing 1 px, opening 1 px; HXCT: opening 1 px) and pore labels (ET1: opening 3 px; ET2: opening 2 px; HXCT: opening 1 px). The pore label was further separated into individual labeled pores using the *separate objects* module (ET1: skeleton-aggressive, marker extent = 1 px; ET2: skeleton-aggressive, marker extent = 1 px; HXCT: chamfer-conservative, marker extent = 1 px)."[241]
PXCT data for a particle of SPP2080-IMRC-0min was analyzed accordingly to PXCT of Ni/Al_2O_3-dr, Ni/Al_2O_3-calc, Al_2O_3-dr and Al_2O_3-calc without derivation of a skeleton based pore network model.

Section 4.3
(PXCT and ET of samples Ni/Al_2O_3-ha, Ni/Al_2O_3-h-ET1 and Ni/Al_2O_3-h-ET2.)
"For the DART-reconstructed ET data, the material was first segmented using *thresholding*. Then, the object was masked using the *lasso* and *interpolation* tools to separate pores from background. For the masked object, the pores were labeled by *thresholding*. (...) To analyze individual pores, the pores' label was separated into individual pores by (...) the *separate objects* module. An *opening* module was used afterwards to remove point artifacts of the pore separation.
(...) For the reconstructed PXCT data, first the Pt residues from sample preparation were cropped (...). Then a *non-local means filter* was applied on the grey scale images. This was followed by masking the material and pores from the background using the *convex hull* module. Subsequently, the masked imaged was separated into pores and material by *thresholding*. This simple segmentation was possible due to sufficient contrast in electron density between air in the pores and the Ni/Al_2O_3-ha material."[236]

Section 4.2
(µ-XCT of samples SPP2080-IMRC-0min, SPP2080-IMRC-10min, SPP2080-IMRC-30min and SPP2080-IMRC-50min.)
"For µ-XCT analysis of the core shell catalysts, first a subvolume was extracted to remove glue from sample mounting and surrounding empty air parts of the volume. Then the tomogram was filtered using a *non-local means filter*. The filtered tomogram was then segmented by *thresholding* into surrounding air and particle labels, which was followed by masking out the surrounding air. As the grey value intensity between the shell and the core does not allow a direct segmentation based on *thresholding*, a gradient image was computed on the masked tomogram. The gradient image results in a strong contrast between the core and shell of the particle. This allowed to segment the masked tomogram in the segmentation editor into core, core-pores, shell and shell-pores labels by *thresholding* and *filling* operations and alternate working on the gradient and filtered grey scale images."[235]

Imaging Based Pore Structure Analysis

The tomography results after general image analysis as described before can be used to retrieve quantitative information about the pore structures of the samples. This is differentiated into analysis of the porosity (ϵ) and pore size distribution. The labels retrieved from the general image processing were analyzed by the *label analysis* module to retrieve the following label informations, solid/material (Volume3D, Area3D, BaryCenterX, BaryCenterY, BaryCenterZ), total pores (Volume3D, Area3D), separated pores (Area3D, d_{eq}, Volume3D, Sphericity, Length3D, Width3D, AspectRatio, BaryCenterX, BaryCenterY, BaryCenterZ). For the analysis of the porosity of a tomogram (ϵ_{tomo}) the following general eq. 3.12 is used:

$$\epsilon_{tomo} = \frac{V_P}{V_P + V_{mlabel}} \tag{3.12}$$

with V_P as the total pore volume and V_{mlabel} the total volume of the solid/material. For PXCT and HXCT data ϵ_{tomo} is defined as the macroporosity (ϵ_M, eq. 3.13) as the resolution of both techniques allows to investigate the overall macropore space.

$$\epsilon_M = \frac{V_{M,P}}{V_{M,P} + V_{mlabel}} \tag{3.13}$$

The total porosity (ϵ_{tot}) is the sum of ϵ_M and the mesoporosity ϵ_m:

$$\epsilon_{tot} = \epsilon_M + \epsilon_m \tag{3.14}$$

The ϵ_m can be expressed as:

$$\epsilon_m = \frac{V_{m,P}}{V_{m,P} + V_{M,P} + V_S} \tag{3.15}$$

with V_S as the true solid volume. It should be noted that V_{mlabel} in case of PXCT or HXCT still contains mesopores that are not resolved and detected as shown in eq. 3.16.

$$V_{mlabel} = V_{m,P} + V_S \tag{3.16}$$

Therefore, the differentiation between V_{mlabel} and V_S is required. However, the porosity of the solid/material label (ϵ_{mat}) of PXCT and HXCT data can be described as:

$$\epsilon_{mat} = \frac{V_{m,P}}{V_{mlabel}} \tag{3.17}$$

If ϵ_{mat} and ϵ_M are known, ϵ_m can be retrieved as following:

$$\epsilon_m = \frac{\epsilon_{mat}}{1 + \left(\frac{\epsilon_M}{1-\epsilon_M}\right)} \tag{3.18}$$

Information about ϵ_{mat} can be obtained by two ways: (I) combination of PXCT or HXCT with ET or (II) quantitative electron density analysis of the PXCT or HXCT data. For (I) the ϵ_{tomo} from ET is ϵ_{mat} of the PXCT or HXCT data. ϵ_{mat} might be obtained from an average of ϵ_{tomo} of the ET if multiple particles are studied. In case of (II), ϵ_{mat} can be retrieved from N_e analysis as described in detail later in eq. 3.27

The Avizo software offers different possibilities to retrieve pore size distributions. The simplest approximation is to analyze the separated pore label assuming spherical pores. Thus an equivalent spherical pore diameter (d_{eq}) is obtained, which is calculated from the individual pore volume ($V_{P,ind}$):

$$d_{eq} = \sqrt[3]{\frac{6V_{P,ind}}{\pi}} \tag{3.19}$$

This approximation works well for spherical or close to spherical pores, otherwise it tends to overestimate the pore size or rather probes the pore body than the pore entrance.
A second option to retrieve information about the pore sizes is the use of the skeleton based pore network models. The analysis of the spatial graphs of those skeleton networks provides information about the cylindrical r_{pore}/d_{pore} of each segment. Similar to Hg porosimetry, this method is more sensitive towards the pore throats than the pore body.
Furthermore, Avizo has a *generate pore network model* module, which can be applied on the separated pore label and results in information about the size of cylindrical throats (d_{throat}) connecting the pores.
For the analysis of the pore size distributions, d_{eq}, d_{pore} or d_{throat} are weighted by the relative volume (V_{rel}, eq. 3.20) or individual porosity ($\epsilon_{P,ind}$, eq. 3.21) of the pores or segments.

$$V_{rel} = \frac{V_{P,ind}}{V_{P,tot}} \tag{3.20}$$

$$\epsilon_{P,ind} = \frac{V_{P,ind}}{V_{P,tot} + V_{mlabel}} \tag{3.21}$$

This weighting allows a comparison with the results of conventional porosity characterization methods, i.e., N_2 sorption, Hg porosimetry and He pycnometry, which all work on a volume weighting base.

Imaging Based Shell Thickness Analysis

For the core-shell catalyst particles SPP2080-IMRC-0min, SPP2080-IMRC-10min, SPP2080-IMRC-30min and SPP2080-IMRC-50min, µ-XCT is used to study the shell thickness. The quantitative analysis is performed on the labels (core, core-pores, shell and shell-pores) as result of the general image analysis. "The thickness of the shell can be estimated in different ways from the analysis of the tomograms. Assuming an ideal sphere for the whole particle and core of

the catalyst the thickness can be either approximated based on the measured external surface (A_{surf}) of the Particle label and the volume of the filled shell ($V_{shell,filled}$):

$$\delta_{A,V} = \sqrt{\frac{A_{surf}}{4\pi}} - \left(\left(\sqrt{\frac{A_{surf}}{4\pi}} \right)^3 - \frac{V_{shell,filled}}{4\pi} \right)^{1/3} \tag{3.22}$$

or by subtracting the d_{eq} of the filled core from the overall particle:

$$\delta_d = \frac{d_{eq,particle} - d_{eq,core}}{2} \tag{3.23}$$

From the combined shell and shell-pores labels an inner and outer surface was computed, from which the shell thickness (δ_{shell}) was retrieved. The inner surface represents the surface of the filled catalyst core and the outer surface the surface of the overall particle. δ_{shell} is the shortest distance between each surface points and provides a detailed representation of the thickness distribution of the coating."[235]

Electron Density Analysis

The quantitative electron density (N_e) information from PXCT in this thesis can be applied to retrieve sub-resolution information about the mesoporosity or about coking. Following the derivation of ϵ_{mat}, which is required to calculate ϵ_m is described as well as the analysis of coking based on N_e.
ϵ_{mat} and ϵ_m were derived for samples Ni/Al_2O_3-dr, Ni/Al_2O_3-calc, Al_2O_3-dr, Al_2O_3-calc and SPP2080-IMRC-0min. "The electron density (N_e) of the PXCT was obtained from the phase contrast tomograms as described in ref.[156, 157] and in the following equation:

$$N_e(r) = \frac{2\pi \cdot \delta(r)}{\lambda^2 \cdot r_0} \tag{3.24}$$

with λ as the wavelength and r_0 as the classical electron radius. From the N_e tomograms the mass density ρ tomograms can be calculated as adapted from ref.[157]:

$$\rho(r) = \frac{N_e(r) \cdot M}{N_A \cdot Z_{UC}} \tag{3.25}$$

$$\rho = N_e \cdot f_{mass} \tag{3.26}$$

with M as the molar mass of the unit cell, N_A as Avogadro's constant and Z_{UC} as the number of electrons per unit cell, which are defined as the mass density factor (f_{mass}). The N_e of the

solid/material label with f_{mass} can be used to calculate the mesoporosity ϵ_m of the sample particle. First the porosity of only the material label can be calculated as following:

$$\epsilon_{mat} = 1 - \frac{N_{e,mode} \cdot f_{mass}}{\rho_{theo}} \tag{3.27}$$

The mode of the N_e distribution of the whole solid/material label is used to approximate the average material porosity ϵ_{mat}, while knowledge about the theoretical mass density ρ_{theo} is required. The information about ρ_{theo} can be either retrieved as the X-ray density of the unit cell for the case a crystal structure of the material is known or approximated by experimental measurement of the skeletal density using He pycnometry. The N_e based ϵ_{mat} can be readily used to calculate ϵ_m if ϵ_M is known from quantitative label analysis.
The N_e mode was determined from the normalized N_e distribution of the material labels as shown in Figure 8.16 and Figure 8.5 and summarized in Table 8.4. From the mode the respective ϵ_{mat} was calculated according to eq. 3.27, with f_{mass} and ρ_{theo} as summarized in Table 8.4. For the dried and calcined states the same chemical formula were assumed for each system as $Ni_{0.43}Al_2O_4$ (Ni/Al_2O_3), Al_2O_3 and $Ni_{0.17}Al_2O_4$ (SPP2080-IMRC-0min), respectively. f_{mass} were calculated according to eq. 3.25, 3.26, assuming a defect spinel structures for both systems. ρ_{theo} for the Ni containing samples was determined by He pycnometry, as no exact crystal structure for the sample composition is known. For Al_2O_3, ρ_{theo} is the X-ray density based on the crystal structure of γ-Al_2O_3 as retrieved from ref.[100]"[237]

The analysis of coking for samples Ni/Al_2O_3-ha, Ni/Al_2O_3-hc, Ni/Al_2O_3-ma and Ni/Al_2O_3-mc based on N_e was performed as described following. "The segmented masked particle volume and catalyst body labels are further used to analyze the N_e distribution in the tomograms. The masked particle volume was increased by 10 times applying the *growth selection* function of the segmentation editor to further mask out influence of the material. With another 10 times *growth selection* an air shell around the particle label with a thickness of about 300 nm (ca. 10 voxel) was selected. For this shell the N_e histogram of the surrounding air was computed and the N_e offset was determined from the maximum of the histogram as summarized for each sample in Table 8.8. The offset was then applied to the N_e. The resulting N_e histograms of the complete tomograms after offset are shown in Figure 8.34. These tomograms were used for further analysis.
To obtain spatially-resolved information about N_e, first the slice dependent histogram of N_e was computed for the masked particle volume. The mean N_e and the corresponding variance σ^2 are shown in Figure 8.35. One can clearly identify in both cases pronounced changes of the mean N_e starting from slice number 200. These pronounced changes can be attributed to larger parts of contamination due to Pt, which originates from sample mounting on the measurement pins. Therefore, a slice range from 1 to 200 was selected for further analysis of N_e and slices with contaminant were discarded.
(...)

For a thresholding based segmentation into coked and active parts of the catalyst body the N_e was normalized for the catalyst body label as shown in Figure 8.36. For Ni/Al_2O_3-m the maximum of the Ni/Al_2O_3-mc sample was used as segmentation threshold, while for Ni/Al_2O_3-h the point at higher N_e from which the distributions differed was chosen as the segmentation threshold. The thresholds are summarized in Table 8.8. This threshold-based segmentation is prone to errors, which limits a quantitative analysis.
The potential errors of the segmentation were checked by propagating the N_e threshold to higher N_e values for the activated and coked samples as shown in Figure 8.38 and Figure 8.39 for Ni/Al_2O_3-h and Ni/Al_2O_3-m, respectively."[239]

3.5 Synchrotron X-ray Diffraction Experiments

3.5.1 *Operando* Synchrotron Powder X-ray Diffraction[29,30]

Synchrotron powder X-ray diffraction experiments (SPXRD) were performed on the ZrO_2 and Ni/ZrO_2 samples described in section 3.1.3. The experiments were designed and supervised by myself, while measurements were carried out by Mariam L. Schulte, Linda Klag and Dr. Thomas L. Sheppard (Karlsruhe Institute of Technology) with support from Dr. Nicola Casati, Michael Lange (Paul Scherrer Institute, Villigen, Switzerland) at the X04SA-MS beamline of the Swiss Light Source (Paul Scherrer Institute).[287] "An X-ray energy of 30.5 keV ($\lambda = 0.406739$ Å) was used to ensure high transmission of the samples, which is required due to the strongly absorbing ZrO_2 support. 2D diffraction patterns were acquired with a Pilatus 6M detector, which were azimuthally integrated using the Dioptas software.[288]
Operando SPXRD studies were carried out using a quartz capillary (WJM-Glas Müller GmbH) microreactor setup of 1.0 mm diameter, as described in section 3.3.3.[249] About 4 mg of the undiluted calcined catalyst (sieve fraction 100-200 µm) resulting in a bed length of ≈4 mm was used for each experiment. (...) It should be noted that an online temperature control was used during the whole experiment, but the recording of the temperature values failed due to an error in the control software. A LaB_6 NIST 640b standard was measured inside of a 1.0 mm quartz capillary as a calibrant for 2θ scale and to retrieve an instrumental profile function.
The initial calcined catalyst was first activated in a total flow of 10 mL min^{-1} of 25 % H_2/He at 773 K for 2 h (...) with a heating rate of 10 K min^{-1}. Afterwards, it was cooled to 673 K and switched to reaction conditions of 5 % CO_2/20 % H_2/He to determine the initial activity of the catalyst sample at reaction step R1 for 30 min. Subsequently, the catalysts underwent three artificial thermal deactivation cycles with 5 K min^{-1} ramps and a holding time of 15 min

[29] Parts of section 3.3.2 are adapted and taken from: M. L. Schulte, S. Weber, L. Klag, J.-D. Grunwaldt and T. L. Sheppard, "Synchrotron PXRD deconvolutes nickel particle and support changes in Ni/ZrO_2 methanation catalysts", *Catal. Sci. Technol.*, **2022**, *12*, 6069-6083.[240]
[30] SPXRD measurements were carried out by M. L. Schulte, L. Klag and T. L. Sheppard with support from N. Casati, Michael Lange.

at temperatures of 773 K, 848 K and 898 K, under reaction conditions. In between each cycle, changes in catalyst activity were studied at 673 K labelled as reaction steps R2, R3 and R4. Afterwards, the sample was cooled to room temperature with 10 K min^{-1}. Diffraction patterns were measured with 9 s acquisition time during activation and final cool-down as well as 3 s during reaction conditions and artificial thermal deactivation cycles.
The on-line MS data was used to estimate the conversion of CO_2 (X_{CO_2}) and H_2 (X_{H_2}) during *operando* SPXRD. X_i for the respective m/z ratio and thus component i is calculated according to eq. 3.28:

$$X_i = \left(1 - \frac{I_{i,norm}}{I_{i,norm,baseline}}\right) \cdot 100\% \tag{3.28}$$

with the normalized ion current ($I_{i,norm}$) as the ion current of trace i normalized to the He trace. The $I_{i,norm,baseline}$ is retrieved after cooling down to room temperature at the end of each experiment under reaction conditions (...). To compare relative changes of the conversion during the cycles, X_i is normalized by the initial $X_{i,R1}$ at R1:

$$X_{i,rel} = \frac{X_i}{X_{i,R1}} \tag{3.29}$$

"[240]

3.5.2 *In Situ* X-ray Total Scattering[31]

X-ray total scattering experiments were performed at beamline P21.1 of PETRA III (DESY, Hamburg). The measurements were supported by Linda Klag, Srashtasrita Das (Karlsruhe Institute of Technology) and Ken L. Abel (Universität Leipzig) as well as Dr. Ann-Christin Dippel, Dr. Olof Gutowski, Dr. Soham Bannerjee and Philipp Glaevecke (DESY, Hamburg). Diffraction patterns were acquired at an energy of 102 keV (wavelength of 0.1215 Å) using a Perkin Elmer XRD1621 detector. A micro-reactor setup as described in section 3.3.3 was used. The experimental setup at the beamline is illustrated in Figure 3.11. About 4 mg catalyst sample (sieve fraction 100-200 µm) were measured in 1 mm diameter quartz glass capillaries (WJM-Glas, Berlin, Germany) resulting in bed lengths of about 6 mm. The exposure time during *in situ* experiments was 1 s per pattern, while 10 diffraction patterns were averaged. For *ex situ* measurements 60 patterns were summed with a total exposure time of 60 s. A Ni powder sample (Alfa Aesar, APS 3-7 micron, 99.9 % metal basis) was measured as calibration standard inside a capillary, while an empty capillary was measured accounting for sample container and environmental contributions. Diffraction patterns were corrected by subtracting the reference measurement before analysis. The collected diffraction patterns were integrated using the software pyFAI.[289]

[31] The X-ray total scattering experiments were supported by L. Klag, S. Das, K. L. Abel, A.-C. Dippel, O. Gutowski, S. Bannerjee and P. Glaevecke.

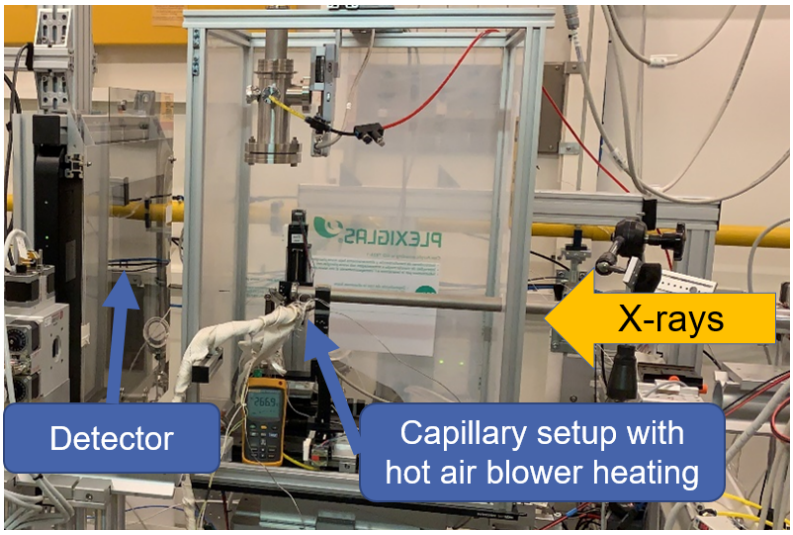


Figure 3.11: Picture of the experimental setup used for *in situ* total scattering experiments at beamline P21.1.

Structural changes during calcination of the dried gel samples Ni/Al_2O_3-dr and Al_2O_3-dr were investigated by *in situ* experiments. The samples were studied under a total gas flow of 10 mL 10 %O_2/He. They were heated to 923 K with a ramp of 10 K min^{-1} and hold for 1 h before cooling down to room temperature with 20 K min^{-1}. In addition to the *in situ* experiments, already calcined Ni/Al_2O_3-h and Al_2O_3-h were studied *ex situ*.

3.5.3 (S)PXRD, Rietveld and PDF Analysis[32]

Rietveld Analysis

Rietveld analysis[245, 246] in this thesis was generally performed using Topas (v.6, Bruker AXS).[290] For refinements of (S)PXRD, a LaB_6 NIST 640b standard was used to derive an instrumental profile function. The profile function was described empirically by a pseudo-Voigt Thompson-Cox Hastings peak shape and the peak shape parameters from the instrumental profile were fixed for refinements of samples. Crystallite size (L_{vol}) and strain (η) information were retrieved by micro-structure analysis using the double-Voigt approach by Balzar as implemented in Topas.[291] For Rietveld refinements literature structure models as summarized in Table 3.6 were applied. Sequential Rietveld analysis was carried out by adapting templates available from the Topas wiki webpage.[292] More details about refinement parameters are provided in the respective discussion section or corresponding appendix information.

[32] Parts of section 3.5.3 are adapted and taken from: M. L. Schulte, S. Weber, L. Klag, J.-D. Grunwaldt and T. L. Sheppard, "Synchrotron PXRD deconvolutes nickel particle and support changes in Ni/ZrO_2 methanation catalysts", *Catal. Sci. Technol.*, **2022**, *12*, 6069-6083.[240]

Table 3.6: Structural models from literature used for Rietveld refinements.

Structure	Space group	Reference	Section
$\gamma-Al_2O_3$	$Fd\bar{3}m$ (227)	[100]	4.3
$\gamma-Al_2O_3$	$Fd\bar{3}m$ (227)	[293]	5.2
$\gamma-AlO(OH)$	$Amam$ (63)	[294]	5.2
$NiAl_2O_4$	$Fd\bar{3}m$ (227)	[97]	4.3
t-ZrO_2	$P4_2/nmc$ (137)	[295]	6.2
m-ZrO_2	$P2_1/c$ (14)	[296]	6.2
Ni	$Fm\bar{3}m$ (225)	[297]	6.2
NiO	$R\bar{3}mH$ (166)	[298]	5.2, 6.2

For the thermal deactivation studies discussed in section 3.5.1 and 6.2, the following detailed analysis of crystallite sizes was performed. "An average $L_{vol,avg}$ of the catalyst is defined as following:

$$L_{vol,avg} = \sum L_{vol,i} \cdot \omega_i \tag{3.30}$$

with $L_{vol,i}$ as the crystallite size of the respective phase i and ω_i as the mass fraction of this phase. Additionally, the relative $L_{vol,rel,i}$ of component i in reference to R1 ($L_{vol,i,R1}$) and its difference $\Delta L_{vol,rel,i}$ are calculated as following:

$$L_{vol,rel,i} = \frac{L_{vol,i}}{L_{vol,i,R1}} \tag{3.31}$$

$$\Delta L_{vol,rel,i} = \left(\frac{L_{vol,i}}{L_{vol,i,R1}} - 1 \right) \cdot 100\% \tag{3.32}$$

For spherical particles, L_{vol} can be used with the density (ρ) to calculate the specific surface area (SSA):

$$SSA = \frac{6000}{L_{vol} \cdot \rho} \tag{3.33}$$

However, in practical cases and upon phase changes ρ also changes, which cannot be determined during *in situ* or *operando* SPXRD experiments. Therefore, SSA is approximated by fitting eq. 3.34 with the fitting parameters a and b to the measured A_{BET} and respective $L_{vol,avg}$ in the initial state of the catalysts, i.e., taking into account the presence of ZrO_2 and NiO phases."[240]

$$SSA = \frac{a}{L_{vol,avg}} + b \tag{3.34}$$

Pair Distribution Function Analysis

From the diffraction data obtained from the total scattering experiments in section 3.5.2 the reduced pair distribution function (PDF, $G(r)$, eq. 3.35) can be retrieved.[299, 300]

$$G(r) = \frac{2}{\pi} \int_{Q_{min}}^{Q_{max}} F(Q) sin(Qr) dQ = 4\pi r \left[\rho(r) - \rho_0\right] \tag{3.35}$$

In eq. 3.35 the Q term represents the reciprocal-space scattering, while $\rho(r)$ is the real-space pair density. $G(r)$ represents the probability to find pair of atoms, which are separated by a distance r. Contrary to Bragg diffraction, e.g., as performed in the 3.5.1, not only the atoms inside of a crystallographic unit cell, but all atoms inside of the probed volume can be analyzed. Therefore, PDF is also sensitive and can provide information towards amorphous structures.[299–301]
The calculation of $G(r)$ was performed using PDFgetX3 software.[302] First, the diffraction patterns were corrected for the capillary and setup background. The PDF is obtained for a Fourier transformation range of $Q_{min} = 0.5\,\text{Å}^{-1}$ to $Q_{max} = 20.0\,\text{Å}^{-1}$.
The structural analysis of the PDF data is performed using DiffPy-cmi.[303] Preliminary PDF fitting was performed using initial structural models from Milligan *et al.* for $\gamma-$AlO(OH)[294] and Smrčok *et al.* for $\gamma-Al_2O_3$.[293] Lattice parameters and isotropic thermal displacement parameters were refined along with a spherical particles size (p_{size}) assumption for dampening of the PDF.

4 Porosity and Textural Characterization of Catalysts by Imaging on Different Length Scales

Technical porous catalysts show features on several length scales as illustrated in Figure 1.9. The pore structure of catalysts controls the transport of molecules within the catalyst particles and therefore strongly determines the catalyst performance. Therefore, a detailed understanding of the pore structure is important. Furthermore, the possibility to prepare optimized pore structures is a valuable tool towards new catalysts with improved catalytic performance. As discussed in section 1.4, hierarchically porous materials can exhibit improved mass transport properties.
However, as reviewed in the introduction sections 1.4 and 1.5.2 there are several open challenges in the characterization of porous catalysts. Conventionally applied gas sorption and Hg porosimetry typically only probe the bulk sample volume and retrieve 1D or 0D information and detailed pore network models or direct confirmation of hierachical structures are hardly accessible.
Advanced 3D imaging methods were shown in case studies to allow for porosity characterization on different length scales as reviewed in section 1.5. For a full understanding of all relevant length scales (*c.f.* Figure 1.9), a combination of different imaging methods is required, which was only shown in few selected case studies, mainly on model systems or with premature porosity analysis (*c.f.* section 1.5). As part of this chapter different aspects regarding the advantage of advanced imaging methods for porosity characterization of catalysts will be discussed.
In section 4.1 the multiscale challenge and requirement to combine different methods is illustrated for the Ni/Al_2O_3 reference catalyst SPP2080-IMRC, an industrial catalyst. Furthermore, limitations of conventional porosity characterization methods to elucidate the true pore structure are shown in this respect. In section 4.2, the macroscopic shell structure of core-shell catalysts based on the SPP2080-IMRC are investigated. The core-shell particles are designed according to simulations for an optimized catalyst particle and reactor concept allowing for dynamic process operation of CO_2 methanation (*c.f.* section 1.2.5). This is complemented in section 4.3 with studies on a tailored hierarchically porous Ni/Al_2O_3 catalyst. These include conventional porosity and structural investigation, imaging based porosity characterization and the usage of derived mass transport descriptors in simulation of the macrokinetic properties.

4.1 Conventional vs. Imaging Methods for Pore Structure Analysis[1,2]

4.1.1 Introduction

As outlined in the introduction chapter sections 1.3, 1.4 and 1.5.2, there are open challenges in the characterization of catalyst pore structures by advanced and conventional imaging methods. Considering the multiple length scales relevant in catalysis (*c.f.* Figure 1.9) a combination of methods is required. In this section an industrially supplied Ni/Al_2O_3 catalyst (SPP2080-IMRC), which is used as a reference catalyst in the SPP2080 DynaKat priority program of the German Research Foundation (DFG)[304] and was supplied by the group of Prof. Kai Sundmacher (Otto-von-Guericke University Magdeburg, Max Planck Institute for Dynamics of Complex Technical Systems Physical and Chemical Foundations of Process Engineering, Magdeburg), is exploited by conventional and advanced imaging methods for porosity characterization.
The aim of this section is to provide an example for the requirement to combine imaging methods and to highlight the various length scales that can be probed by different methods. Furthermore, the results of imaging based porosity characterization are compared with conventional methods, i.e., N_2 sorption, Hg porosimetry and He pycnometry. As the SPP2080-IMRC is applied as a reference catalyst, a fundamental knowledge about the pore structure is necessary as a basis to understand mass transport and related macrokinetic properties. Those information are a requirement for future simulation and modulation studies, which describe the mass transport properties. Furthermore, the catalyst is aimed to be used to create a future "digital twin" in the frame of digitization efforts in catalysis research, e.g., NFDI4CAT.[305]
"The SPP2080-IMRC catalyst particles are of approximately spherical shape as illustrated in the SEM image Figure 4.1 (cut half sphere) and the micro-X-ray computed tomogram (µ-XCT) of a single catalyst particle in Figure 4.3 or as previously shown in Figure 3.1. The particles have a spherical diameter of about 2.5 mm. The SEM images in Figure 4.1 indicate the presence of spherical macropores (Figure 4.1b) and mesopores (Figure 4.1c) in the material."[241]

[1] Parts of section 4.1 are adapted and taken from: S. Weber, R. T. Zimmermann, J. Bremer, K. L. Abel, D. Poppitz, N. Prinz, J. Ilsemann, S. Wendholt, Q. Yang, R. Pashminehazar, F. Monaco, P. Cloetens, X. Huang, C. Kübel, E. Kondratenko, M. Bauer, M. Bäumer, M. Zobel, R. Gläser, K. Sundmacher and T. L. Sheppard, "Digitalization in Catalysis Research: Towards a Holistic Description of a Ni/Al_2O_3 Reference Catalyst for CO_2 Methanation", *ChemCatChem*, **2022**, *14*, e202101878.[241] Available under the terms and conditions of the Creative Commons Attribution 4.0 license (CC BY 4.0, `https://creativecommons.org/licenses/by/4.0/`), Copyright ©2022.

[2] K. L. Abel, D. Poppitz and R. Gläser (Universität Leipzig) provided SEM images, N_2 sorption, Hg porosimetry and He pycnometry analysis. R. T. Zimmermann, J. Bremer and K. Sundmacher (Otto von Guericke University Magdeburg and Max Planck Institute for Dynamics of Complex Technical Systems, Magdeburg) provided the catalyst sample. R. Pashminehazar (ITCP, Karlsruhe Institute of Technology (KIT)) performed the µ-XCT measurements and corresponding tomographic reconstructions. F. Monaco and P. Cloetens (ESRF - the European Synchrotron) performed the HXCT experiments and corresponding tomographic reconstructions. X. Huang and C. Kübel (INT, Karlsruhe Institute of Technology (KIT) and Technische Universität Darmstadt) performed the electron microscopy measurements.

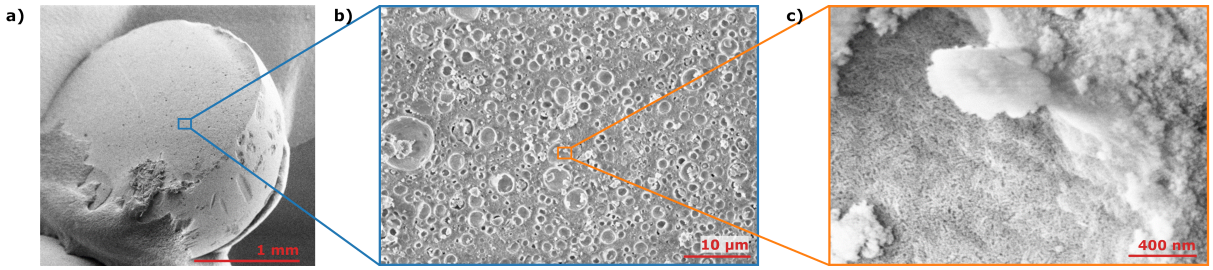


Figure 4.1: "SEM images of a cut half sphere of the SPP2080-IMRC. (a) overview of the cut half sphere, (b) magnified view indicating presence of spherical macropores, (c) further magnification indicates presence of mesopores in the material."[241] Available under the terms and conditions of the Creative Commons Attribution 4.0 license (CC BY 4.0, `https://creativecommons.org/licenses/by/4.0/`), Copyright ©2022.

4.1.2 Conventional Porosity Characterization

The pore structure of SPP2080-IMRC was first investigated by conventional porosity analysis methods, which study the bulk sample volume, i.e., N_2 sorption (Figure 4.2a,b) and Hg porosimetry (Figure 4.2c) (*c.f.* section 3.2 for experimental details). "The catalyst was investigated in

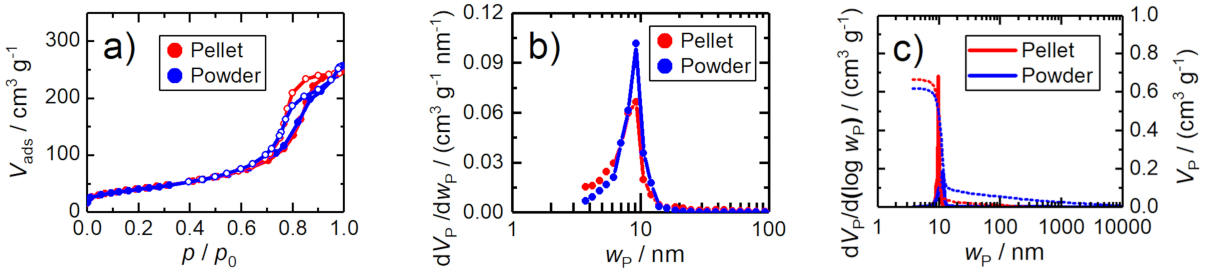


Figure 4.2: "Conventional porosity data of SPP2080-IMRC pellet and powder samples; (a) N_2 sorption isotherms, (b) pore width distribution from N_2 sorption; (c) pore width distribution (solid lines) and cumulative specific pore volume (dashed lines) from Hg porosimetry."[241] Available under the terms and conditions of the Creative Commons Attribution 4.0 license (CC BY 4.0, `https://creativecommons.org/licenses/by/4.0/`), Copyright ©2022.

powder form in addition to porosimetry of the whole pellet (*c.f.* Figure 3.1), to distinguish any influence of sample preparation on the macropores structures observed previously by SEM (Figure 4.1b). N_2 sorption isotherms of both pellet and powder (Figure 4.2a) can be described as type IV isotherms with a H1 hysteresis according to IUPAC classification,[133] typical for mesoporous materials. A narrow pore width distribution is found by both methods, with maxima at 9.2 nm (both samples, N_2 sorption), 9.6 nm and 10.4 nm (pellet and powder sample, Hg porosimetry), respectively. The smaller pore width determined by N_2 sorption compared to Hg porosimetry can be explained by the systematic underestimation of the BJH method used in N_2 sorption for measuring mesopores <20 nm.[135] Notably, the N_2 sorption isotherms in Figure 4.2a do not reach a plateau at high p/p_0 values, indicating the presence of some additional pore volume. Apart from this, conventional porosimetry methods characterize the SPP2080-IMRC as essentially

mesoporous, given the lack of distinct pore volume in the range of 50–10000 nm as probed by Hg porosimetry (Figure 4.2c). Complementary porosity values based on skeletal densities as measured by He pycnometry are given together with quantitative data from conventional porosity analysis in Table 4.1 and 4.3.

Table 4.1: Specific surface area (A_{BET}), specific pore volume (V_P), pore width (w_P), specific mesopore volume ($V_{P,meso}$), specific macropore volume ($V_{P,macro}$), mesopore width ($w_{P,meso}$), macropore width ($w_{P,macro}$), mesoporosity (ϵ_m), macroporosity (ϵ_M), skeletal density (ρ_{skel}) and total porosity (ϵ_{tot}) of SPP2080-IMRC pellet and powder samples, determined via conventional porosimetry.

		Pellet	Powder
N_2 sorption	A_{BET} / $m^2\,g^{-1}$	149	144
	V_P / $cm^3\,g^{-1}$	0.38	0.40
	w_P / nm	9.2	9.2
Hg porosimetry	$V_{P,meso}$ / $cm^3\,g^{-1}$	0.64	0.55
	$V_{P,tot}$ / $cm^3\,g^{-1}$	0.65	0.62
	$w_{P,meso}$ / nm	9.6	10.4
	$w_{P,macro}$ / nm	n.a.*	n.a.*
	ϵ_m / %	69.3	61.9
	ϵ_M / %	1.1	7.9
He pycnometry	ρ_{skel} / $g\,cm^{-3}$	3.663	3.734
	ϵ_{tot} / %	70.4	69.8

* not applicable

Despite the good agreement of N_2 sorption and Hg porosimetry data in terms of the pore width of SPP2080-IMRC, the specific pore volume determined by these methods exhibit large differences (Table 4.1). For both pellet and powder, the total pore volume from Hg porosimetry is more than 0.2 $cm^3\,g^{-1}$ larger when compared to the specific pore volume from N_2 sorption. These large differences indicate the presence of substantial network effects. Studying such network effects is in principle possible with Hg porosimetry by, for example, an analysis of the extrusion curve with varying dwell time at each data point.[135] However, this is tedious and results may be influenced by Hg remaining in the pores after each intrusion/extrusion analysis cycle. As the SEM images indicate the presence of macropores within the material, which were not found by conventional methods, the pore system of SPP2080-IMRC was additionally studied using 3D imaging techniques. In principle, analysis of the SEM images (e.g. Figure 4.1b) can also be used to estimate the macropore diameter, but this is limited to 2D information and depends on precise bisection of each macropore into a hemisphere, which is a disadvantage compared to the applied tomographic techniques."[241]

4.1.3 Tomography-Based Porosity Characterization

Complementary to the conventional porosity characterization, a multiscale imaging investigation of the porosity using different tomography methods was performed. To cover relevant length scales from nm to mm as shown in Figure 4.3, laboratory X-ray microtomography (µ-XCT, *c.f.* section 3.4.3), synchrotron radiation-based holographic X-ray computed tomography (HXCT, *c.f.* section 3.4.8) and electron tomography (ET, *c.f.* section 3.4.2) were combined as feasible methods. The retrieved quantitative results describing the pore structure from the tomography methods are summarized in Table 4.2 and 4.3.

"The µ-XCT of a whole SPP2080-IMRC particle shown in Figure 4.3a,b exhibits an isotropic voxel size of 2.67 µm. Therefore, the overall particle shape and large macropores can be studied by µ-XCT. Figure 4.3b shows the segmentation of the SPP2080-IMRC particle into porous solid (grey) and pores (orange) labels based on thresholding. The identified macro- pores are isolated and of spherical shape, as shown in Figure 4.3b. The porosity (ϵ) weighted equivalent spherical diameter (d_{eq}) distribution of the pores is plotted in Figure 4.3c. The general definitions of ϵ and d_{eq} for the tomograms are provided in eq. 3.12 and 3.19. The calculated porosity derived from µ-XCT is 0.7 %. This indicates that only few macropores with diameters above 3 µm are present in the sample, distributed rather homogeneously within the particle volume. However, as indicated by the SEM images (Figure 4.1) and the small porosity contribution in Figure 4.3c, smaller macropores are expected to be present. Therefore, the low resolution limit of µ-XCT is not enough to study the whole relevant macropore range.

Table 4.2: Isotropic voxel size, porosity (ϵ_{tomo}), the equivalent spherical pore diameter (d_{eq}) and cylindrical pore throat diameter (d_{throat}) for each of the acquired tomograms.

	µ-XCT	HXCT	PXCT	ET1	ET2
Isotropic voxel size / nm	2670	25	19.9	0.29	0.58
ϵ_{tomo} / %	0.7	24.2	30.5	56.4	58.4
d_{eq} / nm	$13691 \pm 10919^{\sharp}$	1433 ± 475	1460 ± 520	16 ± 7	24 ± 9
d_{throat} / nm	n.a.*	n.a.*	n.a.*	12 ± 7	15 ± 7

* not applicable, $^{\sharp}$ determined but not representative data due to limited resolution and small contribution to the overall porosity

To study macropores in the nm to the lower µm range, HXCT was performed on a crushed particle (diameter about 50 µm, *c.f.* Figure 8.1) of the SPP2080-IMRC after testing in CO_2 methanation reaction. The resulting HXCT volume data is shown in Figure 4.3d–f, with an isotropic voxel size of 25 nm. The estimated mean resolutions by fitting with a hyperbolic tangent function and by an edge-profile analysis (*c.f.* Figure 8.2) were ca. 94 nm and 54 nm, respectively. One can clearly identify the spherically shaped macropores of the catalyst, while different macropore sizes can be readily observed in Figure 4.3e,f. The ϵ weighted distribution of d_{eq} as plotted in Figure 4.3g

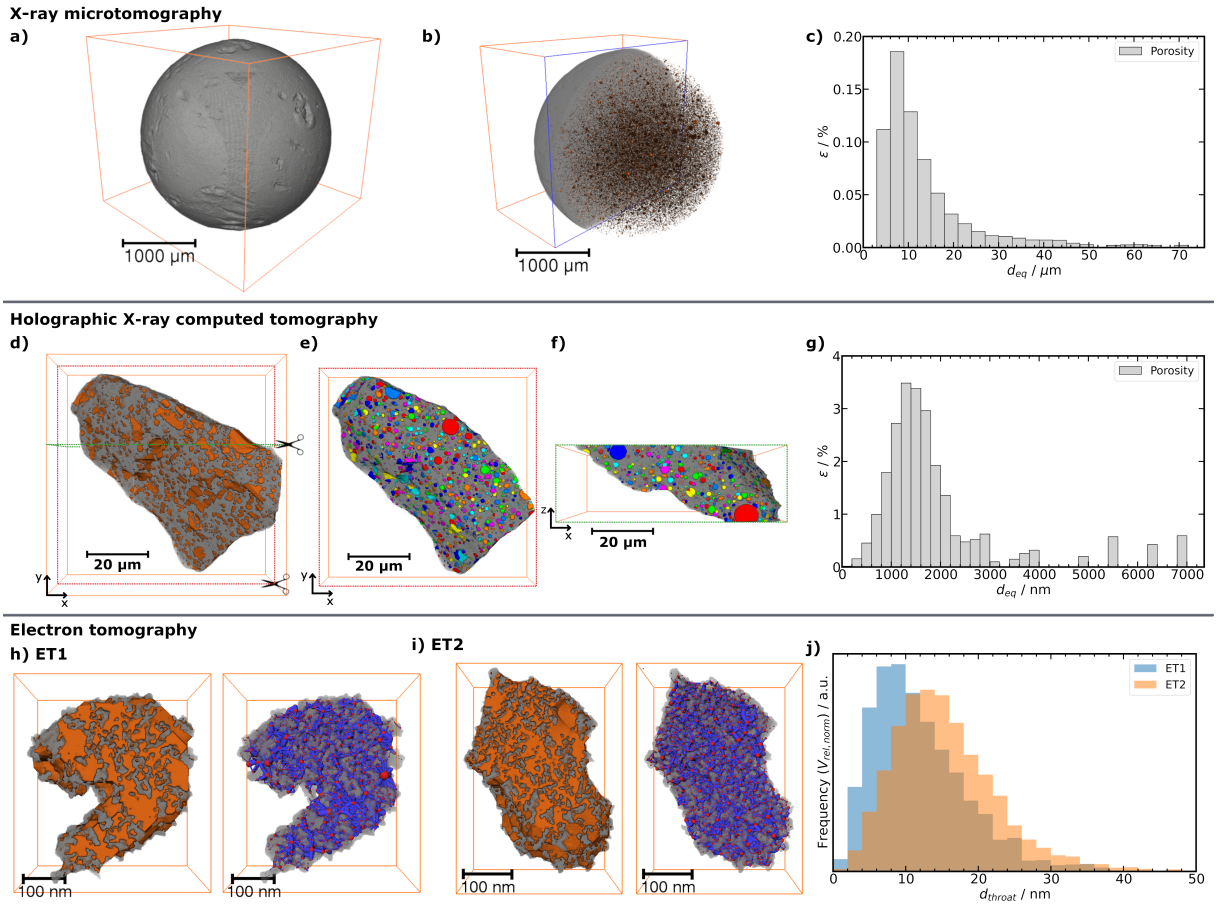


Figure 4.3: "Characterization of the pore structure of the SPP2080-IMRC catalyst by X-ray microtomography (µ-XCT, a-c), holographic X-ray computed tomography (HXCT, d-g) and electron tomography (ET, h-j). (a) volume rendering of the SPP2080-IMRC particle studied by µ-XCT, (b) illustration of the porous solid (grey) and pores (orange) labels after segmentation, with a cut of the porous solid label to highlight the pores, (c) porosity (ϵ) weighted distribution of the equivalent spherical pore diameter (d_{eq}) of the macropores identified by µ-XCT. (d) volume rendering of segmented HXCT data with nanoporous solid (grey) and pores (orange) labels, (e,f) cuts through the volume with individually labelled pores (8-bit color code) and nanoporous solid (grey) showing isolated spherical macropores, (g) porosity (ϵ) weighted distribution of d_{eq} of the pores identified by HXCT. (h,i) volume rendering of ET data from two different sample particles (ET1, ET2), each showing the whole particle with solid (grey) and pores (orange) labels and derived pore network models with solid (grey), individual pores (red) and connecting pore throats (blue), (j) throat volume weighted distribution of the pore throat diameter (d_{throat}) of the ETs." [241] Available under the terms and conditions of the Creative Commons Attribution 4.0 license (CC BY 4.0, `https://creativecommons.org/licenses/by/4.0/`), Copyright ©2022.

reveals a mean d_{eq} of $1.43 \pm 0.48\,\mu m$, while the overall porosity derived from the HXCT data is 24.2 %, which is defined as the macroporosity (ϵ_M) obtained by 3D imaging (see Table 4.3). This clearly shows that the majority of macropores on the basis of volume are in the pore size range of about 0.5 to 2.5 µm (Figure 4.3g). The pores observed previously by µ-XCT are only a few larger macropores contributing relatively little to the particle porosity, which are also found as outliers within the HXCT porosity analysis (Figure 4.3g). It should be further noted that the macropores seem to be well separated in the HXCT data, similarly to the µ-XCT data.
To study the presence of mesopores (<50 nm), ET was carried out on two particles (SPP2080-IMRC-ET1 and SPP2080-IMRC-ET2, diameters about 400 nm) of the SPP2080-IMRC, which were selected and crushed after testing in CO_2 methanation reaction (*c.f.* section 3.3.2). The resulting ET volumes are shown in Figure 4.3h,i for SPP2080-IMRC-ET1 and SPP2080-IMRC-ET2, with isotropic voxel sizes of 0.29 nm and 0.58 nm, respectively. Contrary to the µ-XCT and HXCT results, a connected mesopore network was found in both ET volumes as shown in Figure 4.3h,i with the total pores label (orange). The mesopores identified by ET show no clear spherical shapes, which limits the representativeness of the d_{eq} analysis of separated pores applied previously for µ-XCT and HXCT. Therefore, a pore network model of separated individually labelled pores (Figure 4.4a,b) connected by pore throats was derived. The throat volume weighted

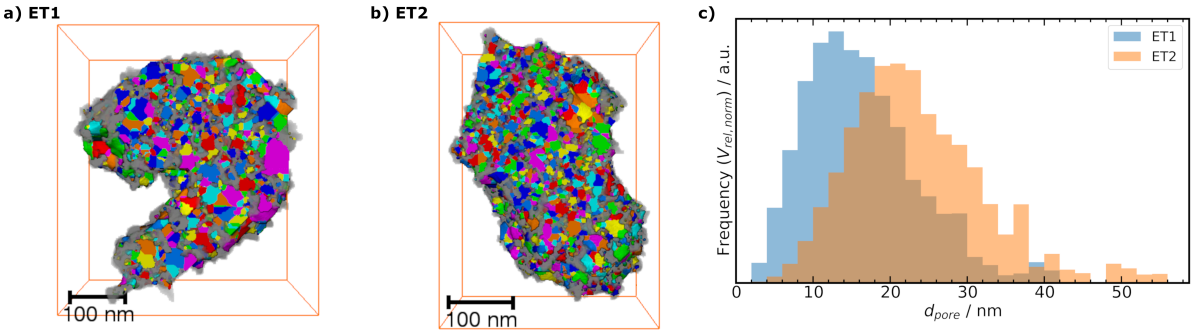


Figure 4.4: "Volume rendering of separated individually labelled pores (8-bit color code) of (a) SPP2080-IMRC-ET1 and (b) SPP2080-IMRC-ET2 with solid label (gray), (c) pore volume weighted d_{eq} distribution of the pores in the extended pore network models (Figure 3 main paper) based on the separated individually labelled pores." [241] Available under the terms and conditions of the Creative Commons Attribution 4.0 license (CC BY 4.0, `https://creativecommons.org/licenses/by/4.0/`), Copyright ©2022.

distributions (d_{throat}) of the derived pore network models are plotted in Figure 4.3j for both ET. Mean d_{throat} values of 12 ± 7 nm and 15 ± 7 nm were found for the mesopore network in particles SPP2080-IMRC-ET1 and SPP2080-IMRC-ET2, respectively. These values can be compared with the mean d_{eq} values, which were larger with 16 ± 7 nm and 24 ± 8 nm for SPP2080-IMRC-ET1 and SPP2080-IMRC-ET2, respectively (Figure 4.4c, Table 4.2). This confirms the overestimation of pore diameter by the d_{eq} spherical pore assumption for mesopores found by ET, validating use of the pore throat values as an alternative. The ϵ values of SPP2080-IMRC-ET1 and SPP2080-IMRC-ET2 are 56.4 % and 58.4 %, respectively. The average of the mean d_{throat} of the

two ET volumes is taken as the mesopore width ($w_{P,meso}$), while the mesoporosity (ϵ_m) of 43.5 % was calculated using the average of the ϵ_{tomo} for SPP2080-IMRC-ET1 and SPP2080-IMRC-ET2, and considering the nanoporous solid of the HXCT volume to have that porosity."[241]
In addition to the combined imaging on spent SPP2080-IMRC catalyst samples, PXCT (*c.f.* section 3.4.6) was performed on a calcined SPP2080-IMRC particle. The sample (diameter about 30 µm) mounted on the tomography pin is shown in the SEM image in Figure 8.3. The volume rendering of the PXCT are shown in Figure 4.5a,b illustrating the material label (grey) and the separated pores (8-bit color code). The estimated resolution of the PXCT by FSC analysis is 40.2 nm (*c.f.* Figure 8.4).

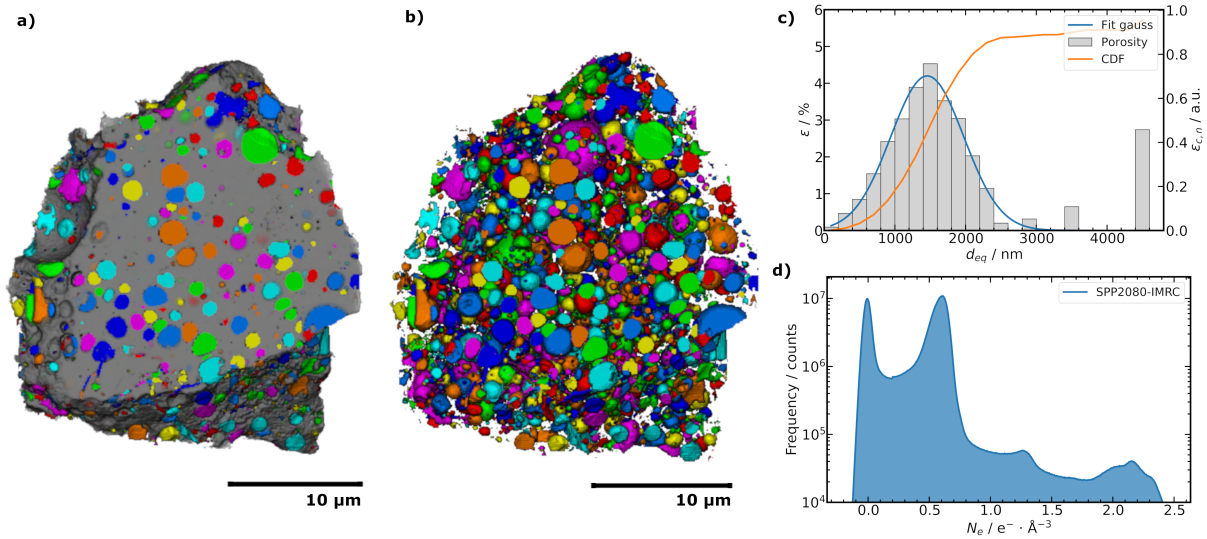


Figure 4.5: "Volume renderings of the PXCT showing (a) the material (grey) and pore (8-bit color code) labels and in (b) only the labelled pores. (c) Porosity (ϵ) weighted distribution of the equivalent spherical pore diameter (d_{eq}) of the pores. (d) Electron density (N_e) distribution of the whole particle."[235] Available under the terms and conditions of the Creative Commons Attribution 4.0 license (CC BY 4.0, `https://creativecommons.org/licenses/by/4.0/`), Copyright ©2023.

Similar to the previously presented HXCT results, also PXCT on the calcined catalyst reveals spherically shaped macropores. The calculated ϵ_M from image analysis according to eq. 3.13 with 30.5 % is larger compared to the HXCT value (Table 4.2 and 4.3). "The porosity weighted distribution of d_{eq} is shown in Figure 4.5c with a Gaussian fit resulting in a mean d_{eq} of 1.46 ± 0.52 µm for the macropores."[235] This value is very similar to the one from HXCT as summarized in Table 4.2 and 4.3. As for HXCT, the resolution of the PXCT is not sufficient to resolve the mesopores of the catalyst. However, PXCT provides quantitative information about the electron density (N_e) as shown in Figure 4.5d. As described in detail in section 3.4.9, N_e can be applied to retrieve information about ϵ_m despite the mesopores cannot be directly resolved. The mode of the N_e distribution of the material label (*c.f.* Figure 8.5) is 0.602 e^- Å^{-3}. The ρ_{skel} of the calcined SPP2080-IMRC sample was determined by He pycnometry as 3.5567 g cm^{-3}.

Using those values and information on the elemental composition, the porosity of the material label (ϵ_{mat}) can be calculated according to eq. 3.25, 3.26 and 3.27. The obtained ϵ_{mat} is 42.6 %. Using the relation shown in eq. 3.18 the ϵ_m can be calculated from ϵ_{mat} to be 26.6 %. ϵ_m and ϵ_M sum up to a ϵ_{tot} of 60.1 %, which is slightly lower compared to the multiscale imaging approach (Table 4.3).
PXCT allows to analyze the macropore size and macroporosity together with the mesoporosity in a single experiment. Therefore, especially the limited sample volume from ET can be circumvented. However, for an analysis of the mesopore size the application of ET is inevitable if the resolution of PXCT is not sufficient to reveal all mesopores.

4.1.4 Comparison of Conventional and Tomography-Based Porosity Characterization

In Table 4.3 the porosity characterization results of the conventional methods and from tomography studies are summarized. "The present case clearly illustrates the importance and power of

Table 4.3: Results of the porestructure analysis of SPP2080-IMRC by conventional characterization (N_2 sorption, Hg porosimetry and He pycnometry) and tomography methods. For conventional characterization whole catalysts pellets and a crushed sievefraction as powder (100–300 µm) were studied. The calculated parameters are specific surface area(A_{BET}), pore width by N_2 sorption (w_{P,N_2}), mesopore width ($w_{P,meso}$), macropore width ($w_{P,macro}$), mesoporosity (ϵ_m), macroporosity (ϵ_M) and total porosity (ϵ_{tot}).

	Pellet	Powder	Tomography	PXCT
A_{BET} / $m^2\,g^{-1}$	149	144	n.a.*	n.a.*
w_{P,N_2} / nm	9.2	9.2	n.a.*	n.a.*
$w_{P,meso}$ / nm	9.6	10.4	14 ± 7^a	n.a.*
$w_{P,macro}$ / µm	n.a.*	n.a.*	1.43 ± 0.48^b	1.46 ± 0.52
ϵ_m / %	69.3	61.9	43.5^c	29.6
ϵ_M / %	1.1	7.9	24.2^b	30.5
ϵ_{tot} / %	70.4	69.8	65.7^c	60.1

* not applicable, ^{a} averaged ET, ^{b} HXCT, ^{c} combined averaged ET and HXCT

applying advanced imaging techniques in addition to conventional methods when attempting to characterize the pore structure of catalysts. Conventional methods, i.e., N_2 sorption and Hg porosimetry failed to reveal significant presence of macropores within the SPP2080-IMRC, neither in pellet nor powder form. While the obtained total porosities (ϵ_{tot}, Table 4.3) are well in agreement for conventional and imaging-based characterization, the distribution of pore sizes constituting the total porosity were very different. Tomography studies showed significant presence of macropores accounting to a macroporosity of 24.2 % (multiscale tomography), which was not found by N_2 sorption and Hg porosimetry. This might be explained by the isolated nature of the spherical macropores identified by imaging studies, which most presumably are connected to each other by a mesopore network as observed by ET. This would additionally explain the agreement of the ϵ_{tot} between tomography and conventional methods, as especially

Hg porosimetry probes the pore opening rather than the pore body.[135] The d_{throat} analysis of the ET data is close to the values found by conventional characterization methods and thus $w_{P,meso}$ (Table 4.3) matches quite well between the methods. However, the d_{eq} analysis of the ET results in significantly larger pore sizes, which might be explained by incorrect assumption of spherical pore shapes, or sensitivity to the pore body rather than the pore throat. This is contrary to mathematical assumptions of the conventional methods, while such differences between tomography and conventional characterization have been reported previously.[236] In general, differences of the results obtained by tomography and conventional characterization of catalyst pore structures are commonly known,[212, 236, 306–308] while the present example in this study is an extreme case. However, if the SPP2080-IMRC should serve as a reference material and to create a "digital twin" of the material, a detailed and correct knowledge of the pore structure is inevitably needed. An incorrect pore model would result in inaccurate descriptions of heat and mass transport in the "digital twin", which would further complicate reaction kinetics studies based on comparing modelling and empirical data.

As shown here, roughly 33 % of the total porosity would be incorrectly defined by relying only on conventional methods, i.e., N_2 sorption or Hg porosimetry. In this respect, it can be concluded that relying only on conventional analysis and reporting or using only mean values of parameters such as mean pore diameter will not provide sufficient detail to allow creation of an accurate digital model for a given material in the future. However, the same is arguably also true for advanced pore characterization techniques when applied individually to complex hierarchically porous samples. For example, ET completely fails in this example to characterize macropore or large mesopore structures, since these are on the same length scale as the entire sample body which can feasibly be measured when using electrons as the probe. On the other hand, even hard X-ray nanotomography methods such as HXCT or PXCT applied at the most modern synchrotron light sources available cannot currently provide sufficient resolution to analyze small mesopores or micropores.

The logical conclusion is that the complementary characteristics and applicable length scales of different tomographic methods should optimally be combined to produce an accurate description of porosity in complex samples (*c.f.* Figure 1.9). As advanced imaging techniques are only local techniques compared to the conventional ones, a careful sample selection is required ensuring highest possible representativity of the selected sample compared to average information from conventional methods."[241] In the present case the sample volume probed by HXCT is significantly larger compared to PXCT, which why ϵ_M from HXCT is considered more representative and is used for comparison. However, PXCT showed the great potential to retrieve sub-resolution information from hard X-ray nanotomography methods in case of quantitative information on the N_e. This has great potential in future applications, as the very limited sample volume of ET experiments can be circumvented at least for the determination of ϵ_m. For direct analysis of mesopores in terms of their size, the resolution has to be improved.

As a future perspective, the data and information from tomography studies on the pore structures

might be applied in digital models of the catalyst. "The generation of a "digital twin" based on ET analysis using also information like connectivity or constrictivity was recently reported for the mesopore network of porous silica, although only as a model system.[309] Based on the tomographic characterization future development of sophisticated pore network models, e. g., creation of imaging based mathematical models,[309] resistor networks,[310] or others are possible but out of scope of this work. (...) The pore network models that can be obtained from imaging studies can be applied for a detailed description of mass transport phenomena in the catalyst, allowing different levels of complexity.[308]"[241]

4.1.5 Particle Size from Transmission Electron Microscopy

Considering the different important length scales in catalysis research (*c.f.* Figure 1.9) even smaller features than macro- or mesopores are important. This smallest relevant length scale are mainly the active sites of the catalyst, where adsoprtion and desorption of reactants and products as well as the reaction itself takes place. To directly analyze the active sites by imaging methods, essentially only TEM techniques are feasible. TEM methods can be either applied to estimate particle sizes of metal nanoparticles or in HR-TEM mode also the morphology of single nanoparticles can be studied. "The Ni particle size of the SPP2080-IMRC was investigated by TEM as shown in Figure 4.6. For TEM studies, a spent catalyst sample after testing in CO_2

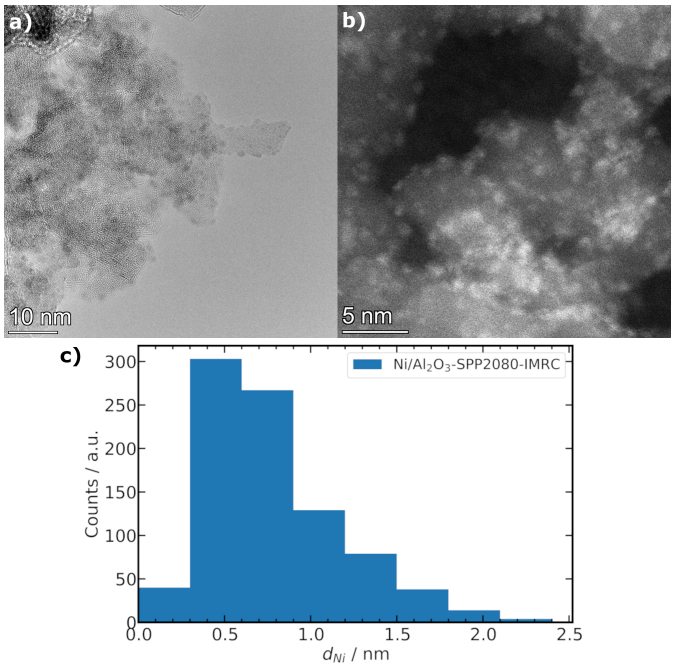


Figure 4.6: "a) Brightfield (BF)-TEM and (b) HAADF-STEM images of the SPP2080-IMRC after testing in CO_2 methanation reaction showing small Ni nanoparticles. (c) Ni particle size distribution (total of 875 Ni particles) for the analysis of eight different HAADF-STEM images."[241] Available under the terms and conditions of the Creative Commons Attribution 4.0 license (CC BY 4.0, `https://creativecommons.org/licenses/by/4.0/`), Copyright ©2022.

methanation reaction conditions up to 673 K was studied (*c.f.* section 3.3.2). In Figure 4.6a,b the exemplary brightfield (BF) and HAADF-STEM images clearly show the presence of small Ni] nanoparticles with diameters below 2 nm. 875 Ni particles were analyzed using eight different HAADF-STEM images resulting in the Ni particle size distribution shown in Figure 4.6c and a calculated mean Ni particle size of $0.8\,\text{nm} \pm 0.4\,\text{nm}$ in the SPP2080-IMRC after catalytic testing."[241] However, despite the high number of analyzed particles in the present case, TEM allows only for very local information about the catalyst and representativity is a general issue of this method (*c.f.* Figure 1.9).

4.1.6 Conclusions

In this section the porosity of the SPP2080-IMRC reference catalyst was characterized by conventional (N_2 sorption, Hg porosimetry and Hepycnometry) as well as advanced imaging methods (µ-XCT, HXCT, PXCT and ET). The SPP2080-IMRC is an ideal showcase of an industrially applied catalyst, as it contains relevant porosity and textural features from the pores in the nm to pellet in the mm scale. The presented porosity investigations highlight limitations of conventional methods in understanding the true pore structure of catalysts. Only the combined advanced imaging methods (here µ-XCT, HXCT, PXCT and ET) revealed the significant presence of macropores in the material (roughly 1/3 of the overall porosity). Conventional methods would have characterized the catalyst as essentially mesoporous with a uniform pore size distribution. Combined tomography instead revealed a bimodal pore size distribution of isolated macropores, which are connected by mesopores.

However, challenges of the tomography methods were also highlighted mainly related towards sample representativity, which can be related to a trade-off between sample size and resolution (*c.f.* Figure 1.9). Therefore, it can be concluded that for detailed understanding of pore structures by imaging methods generally a combination of different techniques is suggested. Especially for efforts towards the creation of "digital twins" of catalysts in digitization efforts, such detailed porosity characterization is recommended to complement and cross check results from conventional methods. The "digital twin" would be a detailed mathematical model of the catalyst, which provides a holistic description about its structure and performance directly applicable in modeling studies. A major drawback of the advanced methods is the small sample throughput compared to the conventional ones, which might currently limit a routine application. Promising future perspectives are quantitative information on the electron density by hard X-ray nanotomography methods, as shown here for PXCT, which enables to retrieve sub-resolution information. Usually, this information would only be available by electron tomography methods on very limited sample volumes, with sample diameters of two to three orders of magnitude smaller than for hard X-ray nanotomography. However, a major drawback of the X-ray nanotomography methods is the small sample throughput compared to the conventional or laboratory ones, which currently limits routine application.

4.2 Shell Thickness Analysis of Designed Core-Shell Catalysts[3,4]

4.2.1 Introduction

As discussed in detail in the introduction section 1.2.5 a core-shell catalyst particle design consisting of an active catalyst core and an inert shell is a promising approach to improve the performance of CO_2 methanation catalysts. In the simulation studies by Zimmermann *et al.*[114, 115] this macroscopic particle design is introduced to allow a better control of hot-spot formation and thermal runaway behavior in industrial scale reactors, especially during load changes. The task of the inert shell is to artificially introduce a mass transport limitation layer. As shown in Figure 1.8 at higher reaction temperatures, i.e., in hot-spots the reaction can be controlled by the mass transport properties of the catalyst particles, because the mass transport becomes the rate limiting step. Despite the theoretical studies, which can optimize the shell parameters, like thickness or porosity, the preparation and characterization of this particle design is not trivial. In this section core-shell catalyst particles are studied, which were prepared by coating of the SPP2080-IMRC catalyst pellets via fluidized bed coating as described in section 3.1.1 by Ronny T. Zimmermann, Dr. Jens Bremer and Dr.-Ing. Vesselin Idakiev from the groups of Prof. Kai Sundmacher (Otto von Guericke University Magdeburg and Max Planck Institute for Dynamics of Complex Technical Systems Process Systems Engineering, Magdeburg) and Prof. Lothar Mörl (Otto von Guericke University Magdeburg). The porosity of the SPP2080-IMRC acting as the active core was thoroughly investigated and discussed in the previous section 4.1. Here, the focus is to understand the influence of the coating time on the shell thickness as an important design parameter and to verify the presence of a closed shell. For this purpose, µ-XCT was applied on SPP2080-IMRC pellets with different coating times as detailed in section 3.1.1 and 3.4.3.

4.2.2 Shell Thickness Analysis

The SPP2080-IMRC catalyst used as active core is denoted as SPP2080-IMRC-0min. Furthermore, three different core-shell catalysts were studied with coating duration of 10, 30 and 50 min, which are labeled as SPP2080-IMRC-10min, SPP2080-IMRC-30min and SPP2080-IMRC-50min, respectively. As shown in the SEM images of the four catalysts in Figure 4.7, a clear difference between the catalyst core and shell can be observed. Similar as in the previous section 4.1 the presence of the spherically shaped macropores in the core can be observed. The core and shell

[3] Parts of section 4.2 are adapted and taken from: R. T. Zimmermann, S. Weber, J. Bremer, V. Idakiev, R. Pashminehazar, T. L. Sheppard, L. Mörl and K. Sundmacher, "Core-Shell Catalyst Pellets for Effective Reaction Heat Management", *Chem. Eng. J.*, **2023**, *457*, 140921.[235] Available under the terms and conditions of the Creative Commons Attribution 4.0 license (CC BY 4.0, `https://creativecommons.org/licenses/by/4.0/`), Copyright ©2023.

[4] R. T. Zimmermann, J. Bremer and K. Sundmacher (Otto von Guericke University Magdeburg and Max Planck Institute for Dynamics of Complex Technical Systems, Magdeburg) and V. Idakiev, L. Mörl (Otto von Guericke University Magdeburg) provided the core-shell catalysts discussed in this section. R. T. Zimmermann, J. Bremer and K. Sundmacher further provided the SEM images. R. Pashminehazar performed the µ-XCT measurements and tomographic reconstructions thereof.

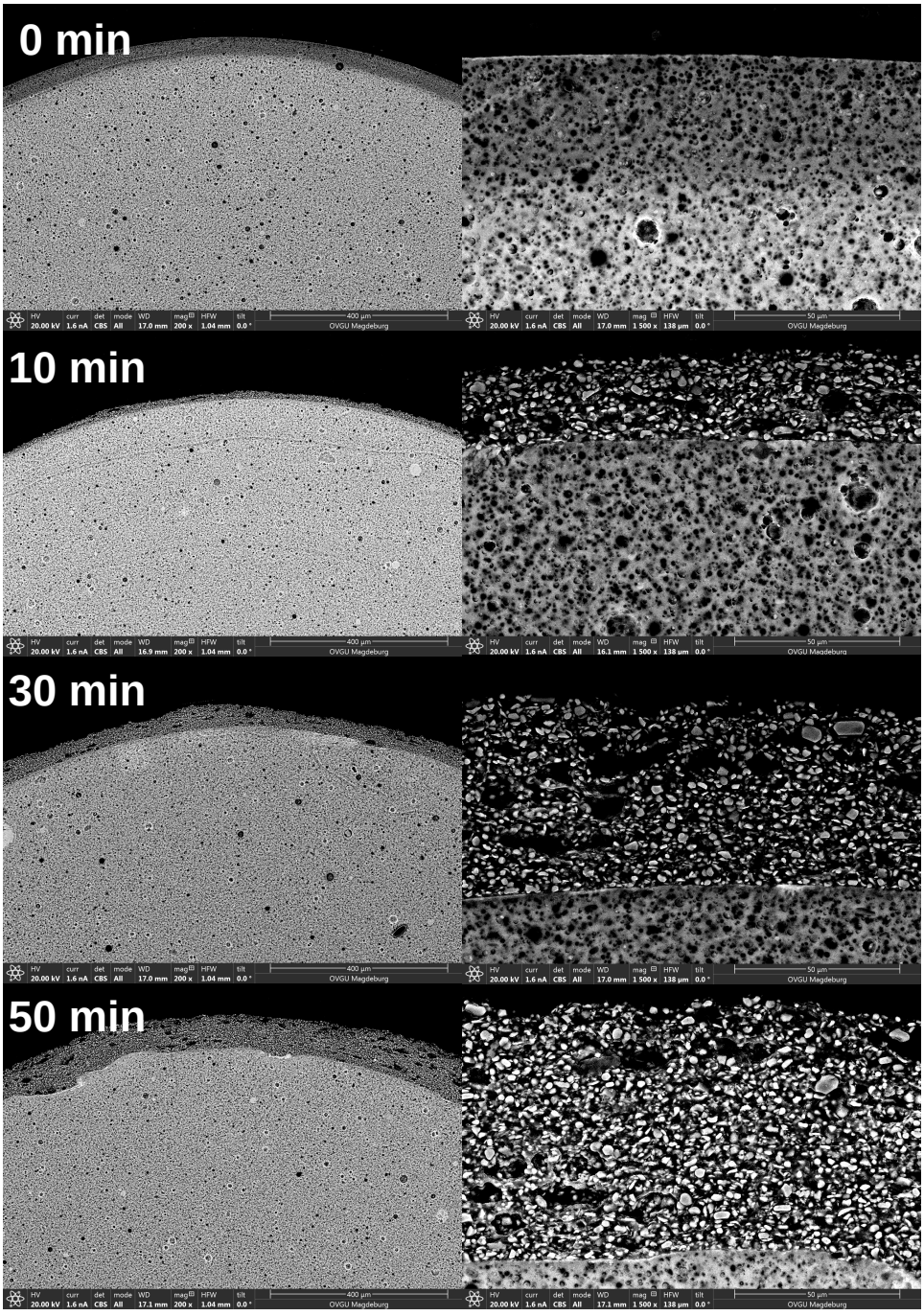


Figure 4.7: "SEM images of calcined samples taken after coating times of 0, 10, 30 and 50 min."[235] Available under the terms and conditions of the Creative Commons Attribution 4.0 license (CC BY 4.0, `https://creativecommons.org/licenses/by/4.0/`), Copyright ©2023.

are separated quite distinct with a different microstructure of the shell compared to the core. The shell thickness is increasing with coating time of the catalysts, while larger void spaces in the shell can be observed for all coating times. Generally, it is possible to retrieve quantitative information about the thickness of the shell from those SEM images. However, the SEM image is only limited to very local information from one cross section of the catalyst. This strongly restricts the information content from this analysis and information whether a homogeneously closed shell was obtained is hardly possible at all.
For this purpose, µ-XCT studies were performed on the four different catalyst samples. "The µ-XCT volume renderings of the four scanned catalyst pellets (after 0, 10, 30, and 50 min coating duration) are shown in Figure 4.8a,d,g,j with isotropic voxel sizes of 2.85 µm, respectively. The obtained µ-XCT were segmented into different labels for further quantitative image analysis as described in section 3.4.9. The retrieved labels in Figure 4.8a,d,g,j represent the core of the catalyst (grey) with the core-pores (green) as well as the shell (blue) with the shell-pores (orange).
The resolution of the µ-XCT is not sufficient for a full analysis of the porosity as shown previously in section 4.1. However, in the present case it can provide a qualitative measure on the differences between the core and shell and their respective contribution to the overall resolved porosity. As the voxel size and measurement parameters are identical for all µ-XCT, this comparison is possible and observed differences can be carefully discussed. Furthermore, larger voids in the shell as indicated by the SEM images (Figure 4.7) can be identified. The porosity distributions of the µ-XCT depending on the d_{eq} of the detected pores are shown in Figure 4.8b,e,h,k for each coating time. It can be observed, that the contribution by the shell to the overall resolved porosity is increasing with longer coating times. The obtained porosity and mean d_{eq} values for the µ-XCT are summarized in Table 4.4.

In particular, the contribution of the shell porosity to the ϵ_{tot} is increasing with longer coating time, while the observed $d_{eq,shell}$ of the pores in the shell are not changing significantly. In the distribution of the ϵ weighted d_{eq} depending on the distance to the catalyst pellet center (d_{center}) the two different pore labels, core-pores and shell-pores, can be readily identified. The measured d_{eq} for the shell-pores are larger compared to the core-pores. The resolvable d_{eq} distribution of the core is quite homogeneous and similar for all four samples. However, the resolution of the chosen µ-XCT method is not sufficient for a complete analysis of the catalyst pore structure, which ranges from few nm up to several µm and thus requires a combination of different imaging techniques as shown in section 4.1. It is rather sufficient to identify larger outliers of the macrcoporosity being present in the catalysts.
In addition to a qualitative comparison of measurable porosity and pore diameters, µ-XCT was used to analyze the thickness of the coated shell. (...) µ-XCT allows for a 3D analysis of the shell as shown in Figure 4.9 for three different coating times (10, 30, and 50 min).

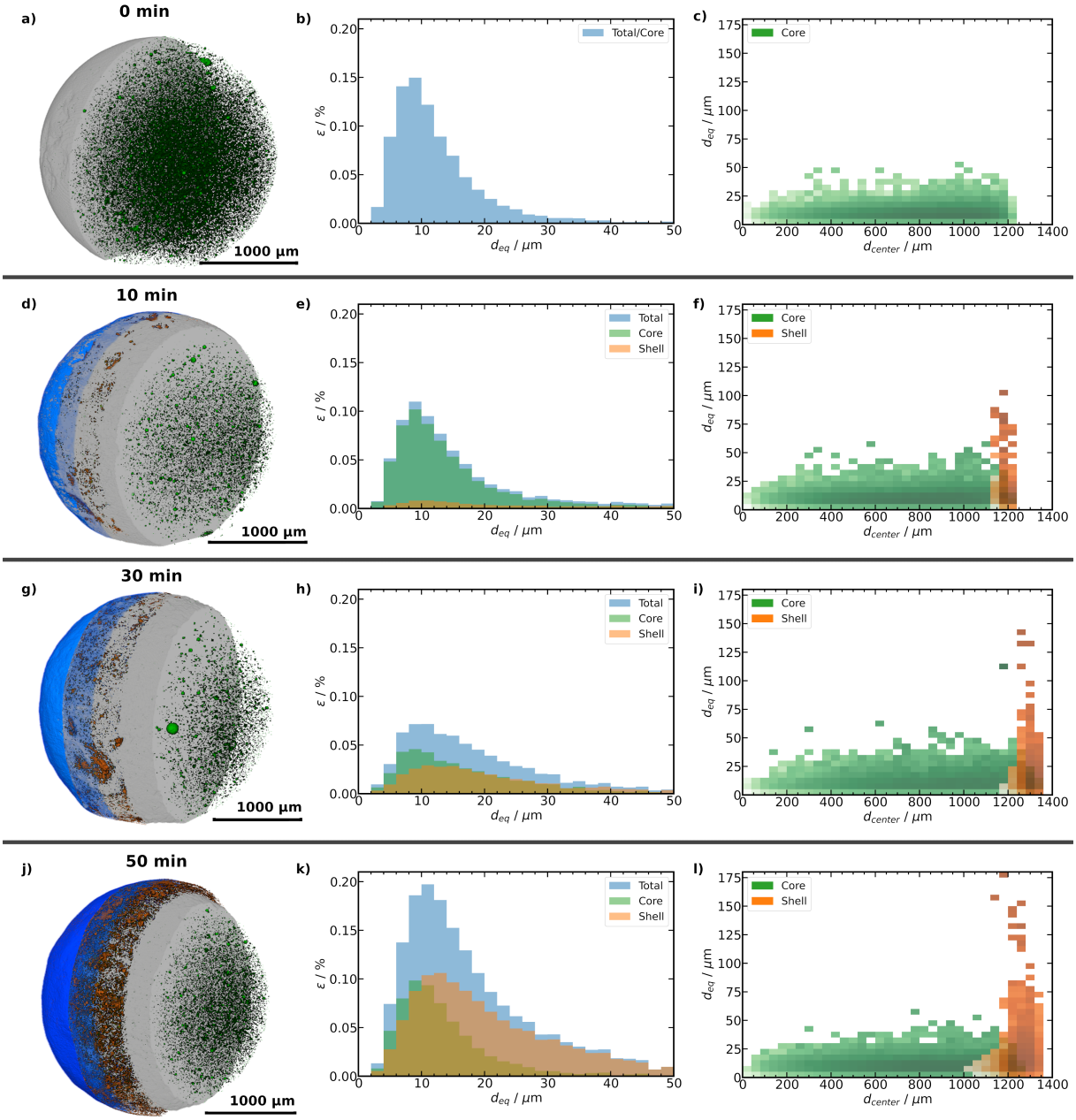


Figure 4.8: "XCT volume renderings of selected whole catalyst pellets with different coating times, (a) 0 min, (d) 10 min, (g) 30 min, and (j) 50 min showing each the segmented labels for the catalyst core (grey), core-pores (green), shell (blue), and shell-pores (orange). The volume renderings are cut at certain positions to highlight the different labels being present. (b,e,h,k) show the porosity depending on d_{eq} separated into total-porosity (blue), core-porosity (green) and shell-porosity (orange) for the respective samples. (c,f,i,l) show the volume weighted 2D histograms of d_{eq} depending on d_{center} distinguished into core-pores (green) and shell-pores (orange)."[235] Available under the terms and conditions of the Creative Commons Attribution 4.0 license (CC BY 4.0, `https://creativecommons.org/licenses/by/4.0/`), Copyright ©2023.

Table 4.4: Quantitative information about the porosity and shell thickness retrieved from image analysis of the XCT for the studied samples.

coating time / min	0	10	30	50
ϵ_{tot} / %	0.9	0.8	0.8	2.1
$\epsilon_{core,tot}$ / %	0.9	0.6	0.4	0.6
ϵ_{core} / %	0.9	0.7	0.4	0.8
$\epsilon_{shell,tot}$ / %	n.a.*	0.2	0.4	1.5
ϵ_{shell} / %	n.a.*	6.4	5.7	7.5
$d_{eq,core}$ / µm	7 ± 4	8 ± 5	9 ± 5	8 ± 4
$d_{eq,shell}$ / µm	n.a.*	11 ± 11	11 ± 9	11 ± 9
δ_{shell} / µm	n.a.*	15 ± 12	40 ± 17	105 ± 31
$\delta_{A,V}$ / min	n.a.*	11	33	90
δ_d / min	n.a.*	14	38	96

* not applicable

The cuts through the µ-XCT volumes in Figure 4.9a-c illustrate the increasing shell thickness with increasing coating duration. In a simple approximation of spheres the coating thickness can be estimated via two approaches. First, a spherical filled shell can be assumed and thus the exterior surface of this shell, used to calculate the thickness of the shell $\delta_{A,V}$ as shown in eq. 3.22. Second, assuming two spheres, the filled core and the overall filled pellet, the difference of the equivalent spherical diameters of those spheres (eq. 3.23) can be used to approximated a shell thickness δ_d. The obtained thickness values for the two approximations are summarized in Table 4.4. However, drawbacks of this analysis are that an error estimation is hardly possible, the results are only strictly valid for ideal spheres and no information whether a shell is closed or homogeneous can be retrieved.

To investigate the thickness of the shell in more detail, two surfaces where computed, one for the filled catalyst core and one for exterior of the filled shell. Cuts through the rendering of the surfaces are shown in Figure 4.9d-f. It can be observed that for 10 min coating time no closed shell was obtained, while for 30 min coating time the thickness increased and only few voids in the shell still remained. After 50 min coating duration, a completely closed shell with increased shell thickness could be observed. The information whether there are open parts in the shell and to which extend is hardly possible with any other technique than tomography studies and detailed analysis of those. Furthermore, the shortest distance of the exterior surface of the shell to the surface of the filled core was computed for each surface point. The resulting distributions of the shell thickness δ_{shell} are presented in Figure 4.9g-i. The distributions clearly show the increased shell thickness with increasing coating time and allow to retrieve a mean δ_{shell} value together with its standard deviation as summarized in Table 4.4. It was found that within the standard deviation the δ_{shell} values match quite well the δ_d and $\delta_{A,V}$ values of the ideal spherical

approximations. The mean δ_{shell} increased from about 15 µm after 10 min, over 40 µm after 30 min and 105 µm after 50 min coating time."[235]

4.2.3 Conclusions

In summary, it was shown how µ-XCT can be employed to characterize the thickness of core-shell catalyst particles with a potentially promising performance for dynamic reactor operation of the CO_2 methanation reaction as suggested in simulation studies.[114, 115] It was shown that only starting with a coating time of 30 min a closed shell could be obtained. This was contrary to the SEM images, highlighting the advantage of 3D charcterization methods over their 2D counterparts or alternatives. The exact analysis of the shell thickness and whether a closed shell is present is hardly possible with any other method on the present core-shell catalysts than µ-XCT. The correct knowledge about the shell properties is important to understand the future performance of the catalysts in catalytic experiments. Furthermore, the results can be readily applied to tailor the synthesis of the core-shell catalysts in terms of the coating thickness.
A detailed study of the pore structure of the shell was not possible with the achievable resolution of µ-XCT. While exact information about the macro- and mesoporosity of the shell are important for future simulation studies, this requires hard X-ray nanotomography or electron tomography studies as shown in the previous section 4.1 or illustrated in Figure 1.9. In this respect only hard X-ray nanotomography is feasible to study a selected sample size in the range of the shell thickness.
As the measurement time for a single tomogram presented here is on the time scale of about 2 h, laboratory µ-XCT is feasible for a more routine application in catalyst characterization. Furthermore, as illustrated in Figure 1.9 packed beds might be studied containing tens of catalyst particles with similar resolution at once. This outlook might provide a showcase for more routine application of X-ray tomography characterization in catalysis research.

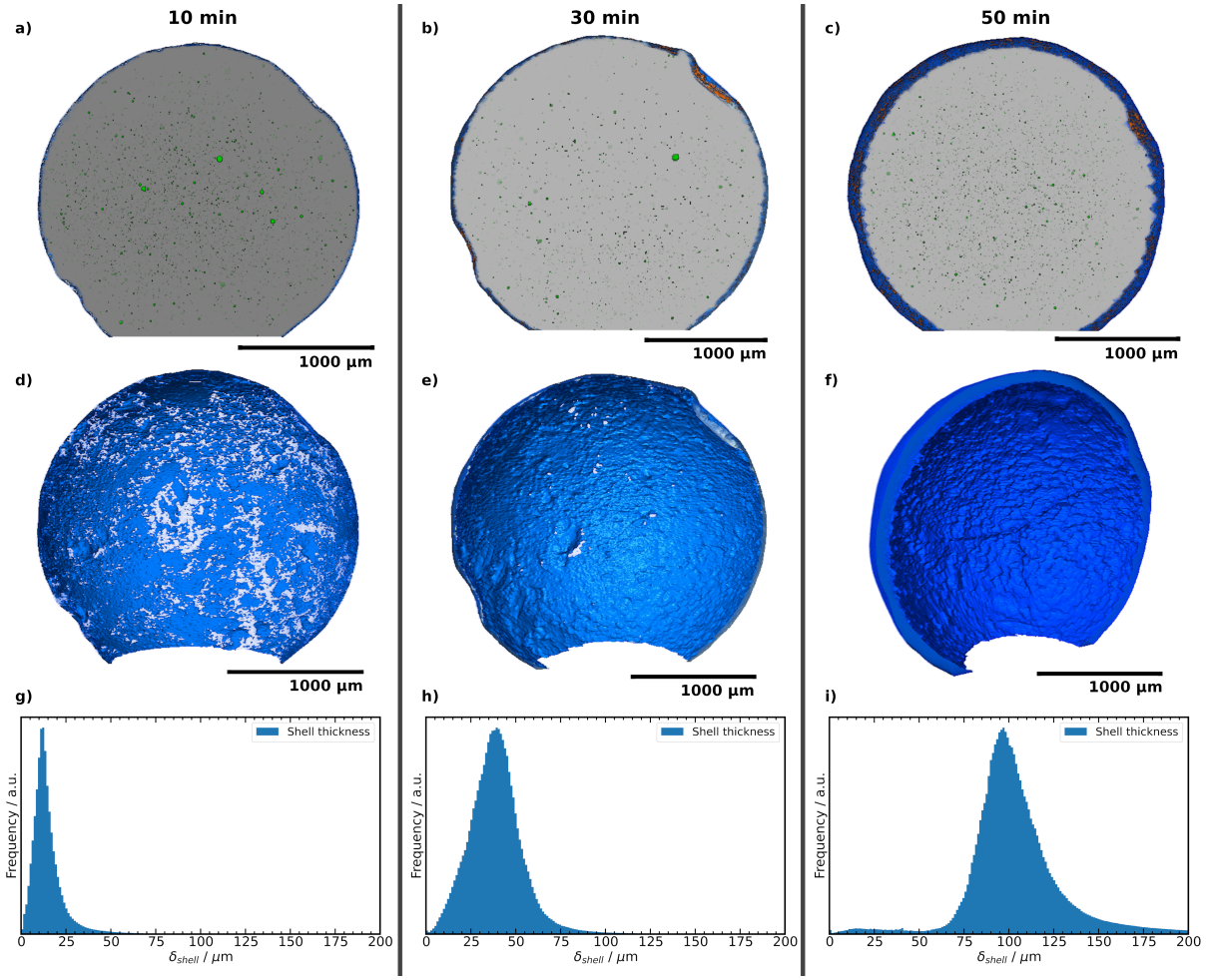


Figure 4.9: "Analysis of the shell thickness based on XCT depending on the coating time. (a-c) show cuts through the middle of the volume renderings with core (gray), core-pores (green), shell (blue) and shell-pores (orange) labels. (d-f) show a cut through surface renderings of the filled shell. (g-i) show the shell thickness distribution."[235] Available under the terms and conditions of the Creative Commons Attribution 4.0 license (CC BY 4.0, `https://creativecommons.org/licenses/by/4.0/`), Copyright ©2023.

4.3 Hierarchically Porous Catalysts for CO_2 Methanation[5,6]

4.3.1 Introduction

As presented in section 4.1 and 4.2 advanced tomography characterization methods are helpful tools to understand textural properties of catalysts. The focus in the previous sections was only on the characterization of those properties. As outlined in the introduction section 1.2.5, mass transport properties are a crucial parameter for the performance of methanation catalysts. In section 4.2 designed core-shell catalyst particles were characterized, which utilize mass transport limitations to provide less sensitivity of the catalyst particle towards load changes in dynamic process operation. This mass transport limitations are intended in the inert shell, but not the active core.[114, 115] Ideally, such limitations should be absent in the active core for increased catalyst performance.

To improve the mass transport inside the active core, tailored hierarchical pore structures are a promising option as presented in the introduction section 1.4 and in ref.[123–128] For the SPP2080-IMRC in section 4.1 only a bimodal pore size distribution of isolated macropores that are connected by mesopores was found, but not a hierarchical pore structure connecting mesopores to a macropore network. Therefore, a tailored hierachically porous Ni/Al_2O_3 catalyst (denoted as Ni/Al_2O_3-h) prepared by Ken Luca Abel in the group of Prof. Roger Gläser (Universität Leipzig) is presented as a promising candidate for improved mass transport properties. As for the SP2080-IMRC reference sample and reviewed in section 1.2, Ni/Al_2O_3 catalysts are commonly applied for CO_2 methanation. With Al_2O_3 typically being present as $\gamma-Al_2O_3$ transition form, these catalysts are essentially of mesoporous nature with pore sizes in the range of 2 to 10 nm.[48, 49, 311] Despite bimodal meso-/macroporous Al_2O_3 are known in literature and can be obtained from sol-gel synthesis,[312](*c.f.* section 1.4) their application in CO_2 methanation were not widely studied. The formation of spinel-type phases is generally challenging for Ni/Al_2O_3, especially for sol-gel synthesized materials.[313, 314] The incorporation of NiO in the defect-spinel structure of $\gamma-Al_2O_3$ to form $NiAl_2O_4$ has been reported to start at calcination temperatures of about 573 to 673 K.[311, 315, 316] Such an incorporation of Ni into $NiAl_2O_4$ would require high reduction temperatures above 1023 K.[311, 317]

[5] Parts of section 4.3 are adapted and taken from: S. Weber, K. L. Abel, R. T. Zimmermann, X. Huang, J. Bremer, L. K. Rihko-Struckmann, D. Batey, S. Cipiccia, J. Titus, D. Poppitz, C. Kübel, K. Sundmacher, R. Gläser and T. L. Sheppard, "Porosity and Structure of Hierarchically Porous Ni/Al_2O_3 Catalysts for CO_2 Methanation", *Catalysts*, **2020**, *10*, 1471.[236] Available under the terms and conditions of the Creative Commons Attribution 4.0 license (CC BY 4.0, `https://creativecommons.org/licenses/by/4.0/`), Copyright ©2020.

[6] K. L. Abel, J. Titus, D. Poppitz and R. Gläser (Universität Leipzig) provided the synthesis of the materials, DRUV/vis spectroscopy results, PXRD measurements, N_2 sorption, Hg porosimetry, He pycnometry, ICP-OES analysis and TPR results. R. T. Zimmermann, J. Bremer, L. K. Rihko-Struckmann and K. Sundmacher (Otto von Guericke University Magdeburg and Max Planck Institute for Dynamics of Complex Technical Systems, Magdeburg) provided catalytic testing results and macrokinetic simulations. Together with X. Huang and C. Kübel (INT, Karlsruhe Institute of Technology (KIT) and Technische Universität Darmstadt) the ET experiments were performed and tomographic reconstruction thereof. D. Batey and S. Cipiccia (Diamond Light Source) supported the PXCT experiments and ptychographic reconstructions

To explore the potential application of the sol-gel synthesized Ni/Al_2O_3-h catalyst in CO_2 methanation, a thorough investigation of the structural and textural properties of the catalysts is presented. First the synthesis and structural characterization are discussed, followed by catalytic testing data. Furthermore, conventional and imaging based characterization of the porosity is presented. Finally, simulation studies on macrokinetics for the catalyst are compared to a purely mesoporous sample (Ni/Al_2O_3-meso) to evaluate the potential benefits of a hierarchical pore structure, which were performed by Ronny T. Zimmermann and Dr. Jens Bremer in the group of Prof. Kai Sundmacher (Otto-von-Guericke University Magdeburg, Max Planck Institute for Dynamics of Complex Technical Systems Physical and Chemical Foundations of Process Engineering, Magdeburg).

4.3.2 Synthesis and Structural Characterization

The Ni/Al_2O_3-h catalyst with a hierarchical meso- and macropore structure, which was prepared in Leipzig, is based on the route by Herwig *et al.*[238] First, a general characterization of the material was performed in Leipzig including inductively coupled plasma optical emission spectrometry (ICP-OES), powder X-ray diffraction (PXRD) measurements, DRUV/vis spectroscopy and H_2 temperature-programmed reduction (TPR) (*c.f.* section 3.2). According to ICP-OES analysis, the Ni mass fraction was determined as 18.0 wt.% for Ni/Al_2O_3-h. The crystallographic structure of the calcined Ni/Al_2O_3-h sample was analyzed by Rietveld refinement of PXRD data obtained from Leipzig to understand the influence of the co-gelation synthesis procedure on the resulting structure. "For the synthesis of Ni/Al_2O_3-h, the formation of a $NiAl_2O_4$ spinel phase was already known,[238] while crystallographic details were not reported yet. However, this is important to properly understand the material as $NiAl_2O_4$ is a spinel structure and most transition polymorphs of Al_2O_3, e.g., γ or $\eta-Al_2O_3$, are typically described as defect-spinel structures.[96, 98–100] As Ni/Al_2O_3-h is synthesized by co-gelation, an initially homogeneous distribution of Ni and Al can be expected. This raises the question of whether an Al_2O_3 transition form, NiO or $NiAl_2O_4$ as reported by Herwig *et al.*, is obtained upon calcination. [238] From a qualitative analysis of the PXRD one can already exclude the formation of crystalline NiO. To get more insights into the formation of the Al_2O_3 transition form or $NiAl_2O_4$ Rietveld refinement was applied. The resulting patterns for two different refinements of the same PXRD data set are shown in Figure 4.10a,b.

An initial approach for the refinement was to use structure models of $\gamma-Al_2O_3$ by Zhou *et al.* and $NiAl_2O_4$ by O'Neill *et al.* without refinement of atomic parameters, which is shown in Figure 4.10a.[97, 100] Compared to this, Figure 4.10b shows another refinement with the same structural models as above, but with refinement of occupancy of the Al positions of the $\gamma-Al_2O_3$ transition form. From the refined patterns, one can directly see that the occupancy refinement (Figure 4.10b) led to a better fit compared to fixed occupancies (Figure 4.10a). Other potentially

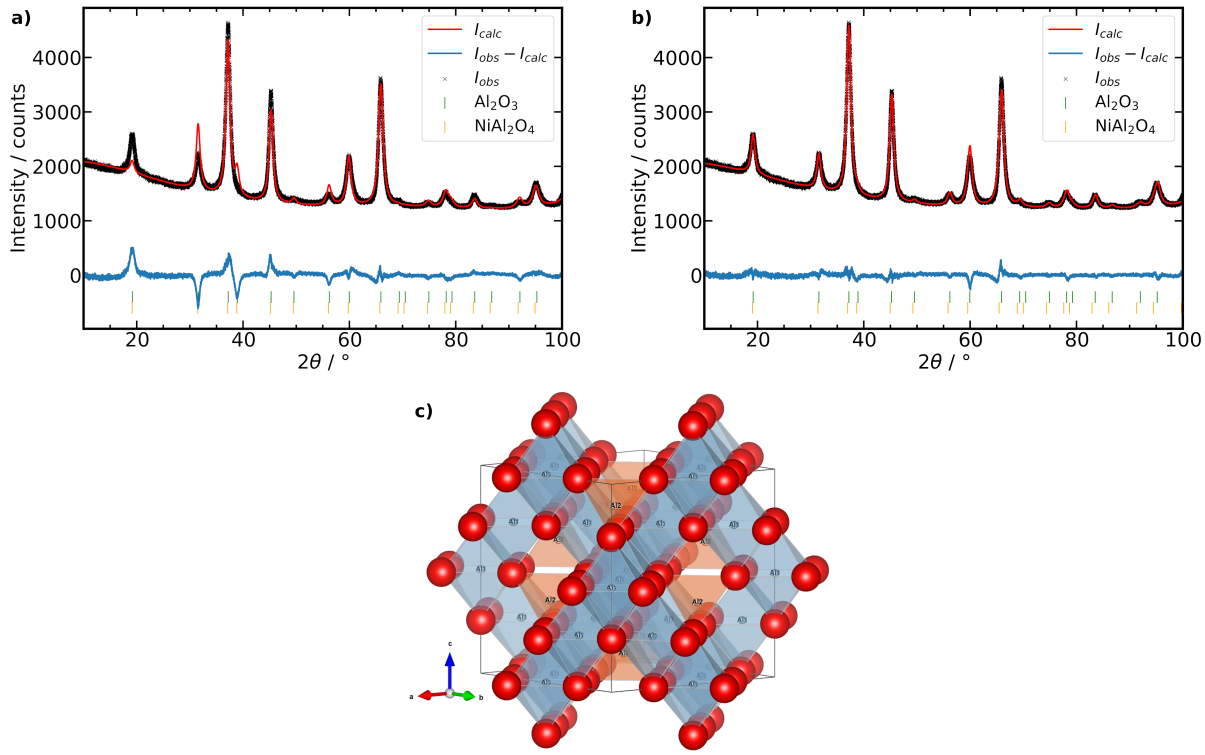


Figure 4.10: "Rietveld refinements of PXRD of Ni/Al_2O_3-h: (a) fixed Al occupancies of the Al_2O_3 phase according the literature model; (b) refined Al occupancies of the Al_2O_3 phase; (c) representation of the Al_2O_3 structure based on the Rietveld refinement with refined Al occupancies for Ni/Al_2O_3-h. O (red), octahedral Al1 (blue), tetrahedral Al2 (orange), Al3 position is not shown for enhanced visibility of the octahedral and tetrahedral sites."[236] Available under the terms and conditions of the Creative Commons Attribution 4.0 license (CC BY 4.0, `https://creativecommons.org/licenses/by/4.0/`), Copyright ©2020.

matching Al_2O_3 transition forms such as $\eta-Al_2O_3$ by Zhou *et al.* were also tested for refinement but led to worse results.[100] The results obtained from the Rietveld refinements are summarized for both refinements in the appendix Table 8.1. The observed better fit was also confirmed by the R_{wp} and GoF fit criteria of the refinement. For both refinements, the main phase was the Al_2O_3 transition form with a phase fraction of 95.5 wt.% versus 84.3 wt.% for the refined occupancy vs. the fixed one. In both cases, the crystallite sizes obtained by microstructure analysis were similar and resembled nanocrystalline materials of around 7 nm size for the Al_2O_3 transition form as well as for $NiAl_2O_4$. The nanocrystalline nature is typical for Al_2O_3 transition forms.[98, 99]
The focus of the refinement results was on the occupancy of the Al positions. For a better structural understanding, the Al_2O_3 structure is illustrated in Figure 4.10c. The O position of the Al_2O_3 phase was fixed as it is generally reported that in all defect-spinel type Al_2O_3 transition forms (γ-, η-, $\theta-Al_2O_3$) this position is fully occupied and the transition forms can be described by different Al occupancies of the octahedral and tetrahedral voids of the O sublattice.[99, 100] In Figure 4.10c, the octahedral voids of the Al1 position are shown in blue and the tetrahedral

voids of the Al2 position are orange. For clarity, the Al3 position is not shown, while it resembled a distorted octahedral position. In comparison with both refinements, the occupancy of the tetrahedral void was equal with 0.84 in the literature-reported structure and 0.839(4) in the refinement. However, the distorted Al3 position in the analysis with refined occupancy was strongly decreased compared to the literature structure this position is considered as barely occupied. As the Ni/Al_2O_3-h material was prepared via co-gelation, a homogeneous distribution of Ni was expected. However, the refined Al1 occupancy showed an increased occupation with 1.156(7) compared to the literature value of 0.58. This indicates that Ni was not only present in the $NiAl_2O_4$ spinel phase, but also present in the octahedral void of the Al_2O_3 transition form. This higher occupancy indicates an increased electron density in the octahedral void, which could be caused by a mixed occupancy of this position by Al and Ni, as in the ideal $NiAl_2O_4$ structure. A refinement of a mixed occupancy is limited by the data quality and requires further studies. This is partially supported by results from DRUV/vis spectroscopy, as shown in Figure 4.11. In

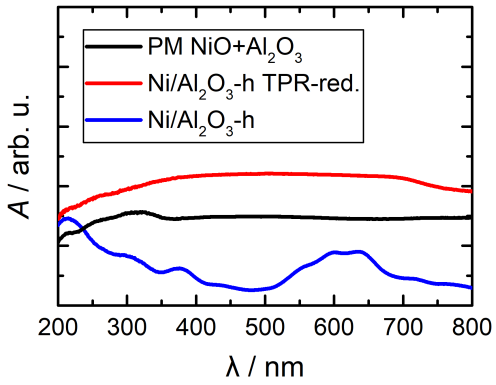


Figure 4.11: "DRUV/vis spectra of a physical mixture of NiO and γ-Al_2O_3 (PM, in black), H_2-TPR-reduced Ni/Al_2O_3-h (TPR-red., in red) and Ni/Al_2O_3-h after calcination (in blue)."[236] Available under the terms and conditions of the Creative Commons Attribution 4.0 license (CC BY 4.0, `https://creativecommons.org/licenses/by/4.0/`), Copyright ©2020.

several literature sources, the absorption band at around 380 nm was assigned to octahedrally coordinated Ni^{2+}, while the bands at about 550 to 650 nm were assigned to tetrahedrally coordinated Ni^{2+} within the $NiAl_2O_4$ structure.[316, 318–320] Therefore, both coordination environments of Ni^{2+} should be present within the Ni/Al_2O_3-h sample. Rietveld refinement indicates that Ni^{2+} was already integrated into the Al_2O_3 transition form by occupying the octahedral Al1 site, while the formation of $NiAl_2O_4$ secondary phase can be also observed. The incorporation of Ni already into the Al_2O_3 transition form upon calcination resembled a potential problem regarding the reducibility of the material. However, based on the current results, a detailed structural knowledge about the incorporation pathway was missing and needs to be investigated.

The H_2-TPR curves for Ni/Al_2O_3-h are shown in Figure 4.12a. The reduction of NiO typically occurs between 473 K and 573 K, depending on the particle size, support material, and confinement

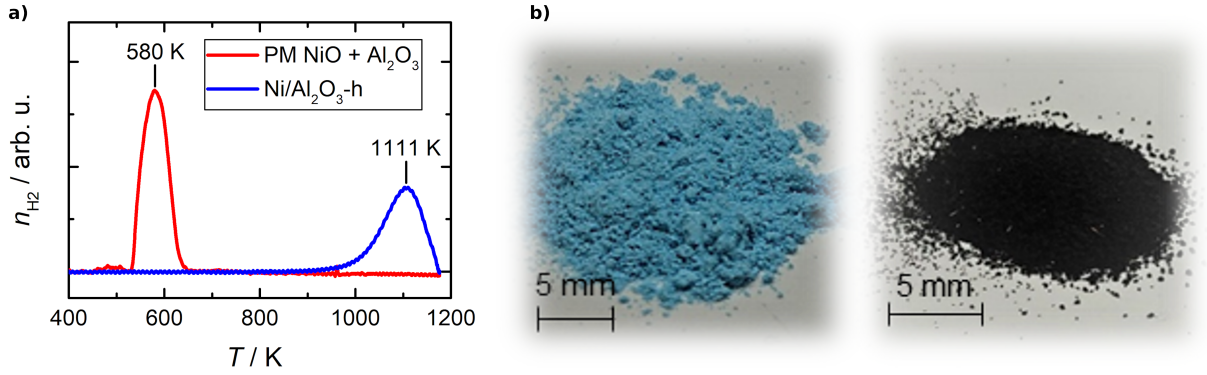


Figure 4.12: "(a) H_2-TPR curves of Ni/Al_2O_3-h and a physical mixture of NiO and Al_2O_3 (ω_{Ni} = 16.3 wt.%); (b) photographs of Ni/Al_2O_3-h prior to (blue) and after reduction by H_2-TPR (black)."[236] Available under the terms and conditions of the Creative Commons Attribution 4.0 license (CC BY 4.0, `https://creativecommons.org/licenses/by/4.0/`), Copyright ©2020.

within pores.[321, 322] Consistently, a physical mixture (PM) of NiO powder and the Ni-free xerogel support showed a reduction peak with maximum at 580 K (Figure 4.12a). Compared to this mixture, the maximum reduction temperature (T_{red}) of Ni/Al_2O_3-h was 1111 K. This remarkably higher T_{red} was likely caused by the incorporation of Ni into the Al_2O_3 or the $NiAl_2O_4$ structure (Figure 4.10, *c.f.* Table 8.1),[321] and has been suggested by Herwig et al.[238] and Titus et al.[323] for Ni/Al_2O_3 xerogel catalysts. Within the Al_2O_3 or the $NiAl_2O_4$ structure, Ni^{2+} is strongly bound within the framework of the crystal, which hampers its reduction to Ni^0. The H_2 consumption during TPR of Ni/Al_2O_3-h amounted to 1800 µmol g^{-1}, which represented a reduction of only 59 % of the Ni atoms based on ICP-OES results, when NiO was assumed to react with H_2 in a 1:1 molar ratio. This shows that even the high temperatures of up to 1173 K were not enough to fully reduce Ni within the sample. Nevertheless, reduction during TPR resulted in color change of the powder from blue to black (Figure 4.12b), indicative of the transformation of Ni^{2+} to Ni^0, consistent with UV-vis spectroscopy results (Figure 4.11)."[236]

4.3.3 Catalytic Measurements

The catalytic activity in the methanation of CO_2 with H_2 was studied for the Ni/Al_2O_3−h catalyst reduced at two temperatures in Leipzig (Figure 4.13). The catalytic testing was performed in the group of Prof. Kai Sundmacher (Otto-von-Guericke University Magdeburg, Max Planck Institute for Dynamics of Complex Technical Systems Physical and Chemical Foundations of Process Engineering, Magdeburg) as described in section 3.3.1. The activity of the catalysts was compared to the reference catalyst SPP2080-IMRC from section 4.1. "The activity studies were performed to determine whether the necessary harsh activation conditions of the material resulted in a functional catalyst for CO_2 methanation. A substantial increase of the CO_2 conversion was found if Ni/Al_2O_3-h was reduced at 1123 K compared to 923 K (Figure 4.13a), while the CH_4 selectivity increased significantly to >90 % (Figure 4.13b). This finding is conclusive with the

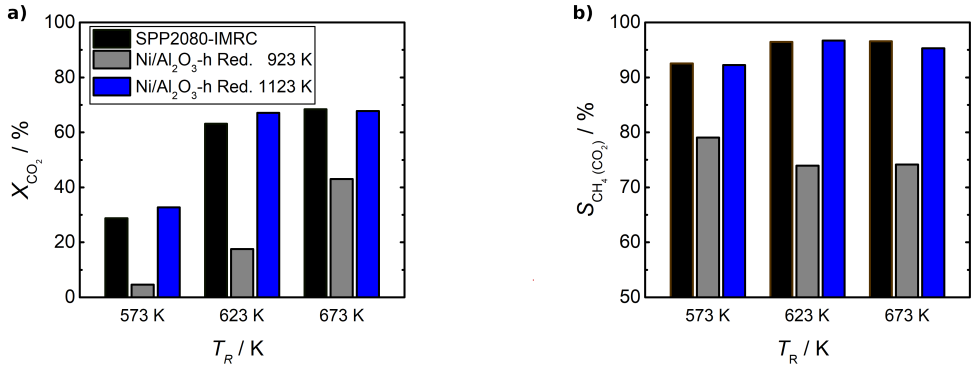


Figure 4.13: "CO_2 conversion (a) and selectivity for CH_4 (b) in the methanation of CO_2 over the reference catalyst SPP2080-IMRC and Ni/Al_2O_3-h, reduced at 923 K or 1123 K after 7-13 h on stream. The volume ratio of reactive gases was $\dot{V}_{H_2}/\dot{V}_{CO_2} = 4/1$."[236] Available under the terms and conditions of the Creative Commons Attribution 4.0 license (CC BY 4.0, `https://creativecommons.org/licenses/by/4.0/`), Copyright ©2020.

results obtained from H_2-TPR (Figure 4.12a), in which the temperature of 923 K represented the onset of the catalyst reduction, whereas 1123 K was close to the maximum H_2 consumption. Therefore, it is reasonable to assume that increasing the reduction temperature to 1123 K led to a significantly larger fraction of Ni atoms being reduced to the elemental state and, thus, becoming active. This resulted in a significant enhancement of the CO_2 conversion and the CH_4 selectivity since Ni^0 was mainly responsible for the hydrogenation activity of the catalyst.[60, 324] When reduced at 1123 K, the CO_2 conversion of 67 % obtained for the Ni/Al_2O_3-h catalyst at a reaction temperature of 623 K and 673 K was higher than ≈38 % (623 K) and ≈49 % (673 K) for the 20 wt.% Ni/ZrO_2 catalysts studied by Martínez *et al.* under similar catalytic conditions, although the CH_4 selectivity of >99 % reported by Martínez *et al.* is higher than the values obtained in this study.[47] The Ni/Al_2O_3-h catalyst reduced at 1123 K is also comparable with the SPP2080-IMRC catalyst in terms of CO_2 conversion and CH_4 selectivity (Figure 4.13). However, given both the substantially higher reduction temperature and Ni loading, the Ni/Al_2O_3-h catalyst did not compete with the SPP2080-IMRC catalyst in terms of activity. Furthermore, it should be noted that comparison of catalysts here based on conversion is shown purely as a qualitative method to determine whether or not the catalyst was active following synthesis of the hierarchical pore system. To quantitatively compare effectiveness or efficiency of the various catalysts in the future, further kinetic studies are required including consideration of metal loading, dispersion, turnover, and presence of mass transport phenomena over a range of conditions."[236]

4.3.4 Tomographic Studies

Similar to section 4.1 a multiscale tomography characterization was performed for a detailed analysis of the pore structure of the hierarchically meso-/macroporous Ni/Al_2O_3-h catalyst. For

this purpose ET at INT, KIT and PXCT at beamline I13-1 of the Diamond Light Source were combined as detailed in section 3.4.2 and 3.4.7. "The volume renderings for the PXCT and both discrete algebraic reconstruction technique (DART)-reconstructed ETs are shown in Figure 4.14. For the PXCT volumes in Figure 4.14a, the upper part of the tomogram was cropped to remove Pt traces from the sample preparation (*c.f.* section 3.4.9). The reconstructed tomogram had a voxel size of [37.5] nm and an effective spatial resolution of [78] nm, estimated by Fourier shell correlation (FSC, Figure 8.28 (left)) as implemented in the reconstruction script of Odstrčil *et al.*[268] The measured particle had a maximum diameter of about 25 µm. The sample size and the resolution allowed obtaining information about the whole macropore space of the material. The two DART-reconstructed ET volumes of the Ni/Al_2O_3-h catalyst are visualized in Figure 4.14b,c, respectively. The measured particles had a diameter of about 450 nm for Ni/Al_2O_3-h-ET1 and 400 nm for Ni/Al_2O_3-h-ET2, while the obtained voxel size after simultaneous iterative reconstruction technique (SIRT) and DART reconstruction was 0.92 nm and 0.64 nm for Ni/Al_2O_3-h-ET1 and Ni/Al_2O_3-h-ET2, respectively. The sample size and resolution of the ET volumes allowed to investigate the mesopores of the material, though on a limited volume of the sample. The effective resolutions for Ni/Al_2O_3-h-ET1 and Ni/Al_2O_3-h-ET2 were estimated as 4.2 nm and 5.6 nm based on the 10–90 % rise distance analysis of an edge feature in the SIRT reconstructed tomogram (*c.f.* Figure 8.6,8.7).

For all three tomograms shown in Figure 4.14, image analysis was performed as described in section 3.4.9 to obtain labels for the material (blue, white), the total pore space (orange), and separated individually labeled pores (8-bit color coding). For all three tomograms, a slice through the volume is shown to illustrate the total pore space together with the separated pores. The combination of PXCT and ET was essential to cover all relevant length scales of the pore system ranging from mesopores (2 nm to 50 nm) up to macropores in the µm range, similar to the studies on the SPP2080-IMRC in section 4.1.[180, 187] The different length scales between PXCT and ET are illustrated by the black box in Figure 4.14, and the ET volume can be considered as a zoom into the material label identified by PXCT. In the PXCT volume (Figure 4.14a), one can see a well-connected macropore network, while the mesopores of the material are not resolved [with the resolution of 78 nm]. However, by applying ET one can resolve the mesopores present inside the material label of the PXCT, as shown in Figure 4.14b,c. The mesopores formed a connected network, similar to the macropores. Based on this multiscale analysis, one can justify the application of the term "hierarchical" for the pore system, as the macropores formed an overall connected system as shown by PXCT, with the mesopores identified by ET connected to this macropore network."[236] This is different compared to the SPP2080-IMRC in section 4.1, which only exhibited a bimodal pore size distribution.

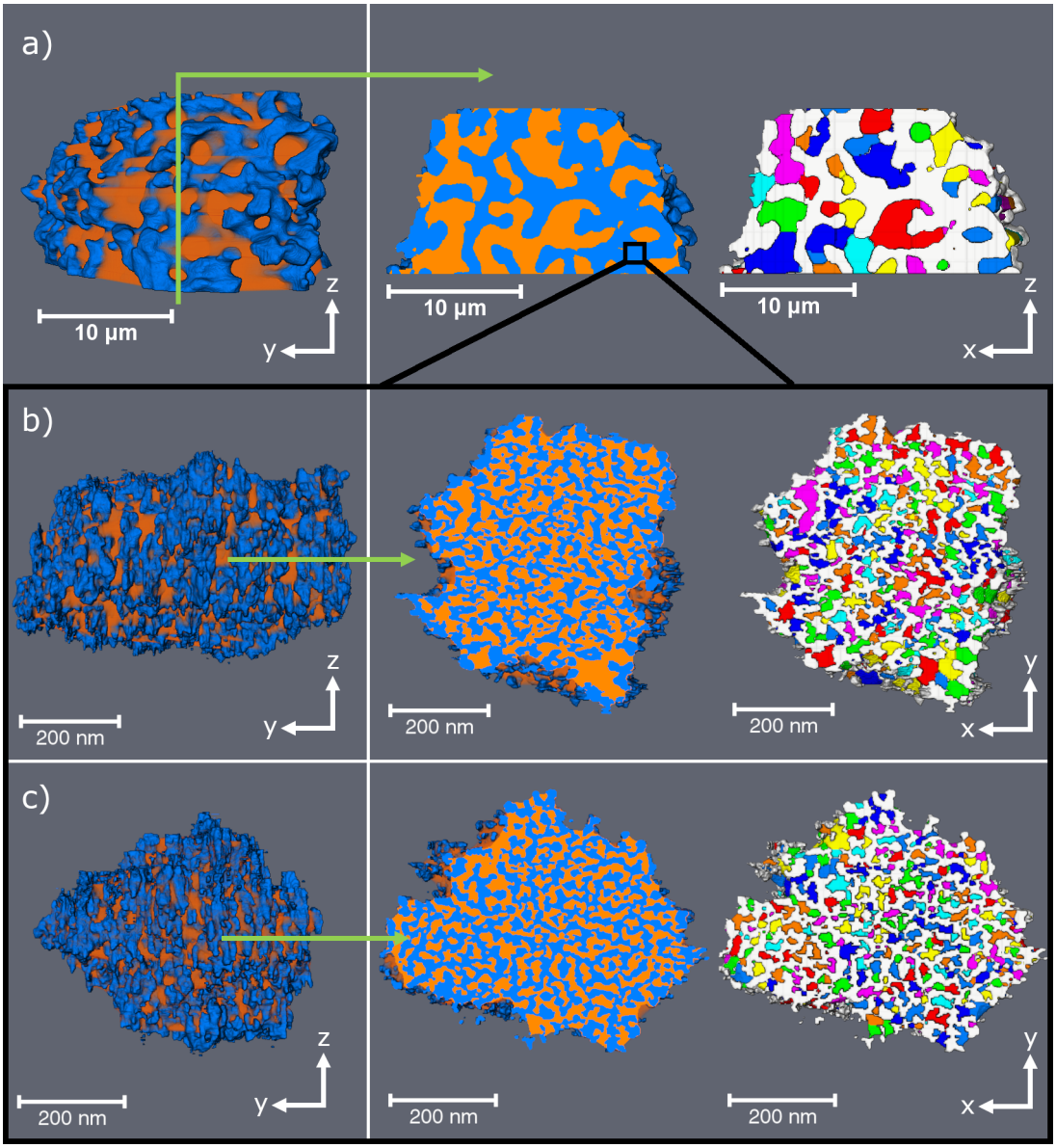


Figure 4.14: "(a) A 3D volume rendering of the PXCT of a Ni/Al_2O_3-h particle along the x-axis together with a slice thorough the xz-plane and the same slice with separated pores. (b) Ni/Al_2O_3-h-ET1 and (c) Ni/Al_2O_3-h-ET2: 3D volume rendering of the DART-reconstructed tomograms along the x-axis together with a slice of the xy-plane, and the same slice with individually labelled pores. The material label is denoted in blue or white, the pore label is shown in orange, and the individually separated pores are illustrated in 8-bit color coding. The position of the slices within the volume is indicated by the green arrow. The different length scales of PXCT and ET are illustrated by the black box in (a)."[236] Available under the terms and conditions of the Creative Commons Attribution 4.0 license (CC BY 4.0, `https://creativecommons.org/licenses/by/4.0/`), Copyright ©2020.

4.3.5 Porosity Analysis

The porosity analysis of the tomograms was performed as described in section 3.4.9. "The separated pores (8-bit color code), total pore (orange), and material (blue) labels for both the ET and PXCT volumes were quantitatively analyzed to retrieve porosity descriptors for the Ni/Al_2O_3-h catalyst. From the label analysis using the Avizo software information such as volume and surface area for the material and total pore labels, as well as the equivalent pore diameter d_{eq} (*c.f.* section 3.4.9, eq. 3.19) for each individual pore label were retrieved, as shown in Figure 4.14a–c for the PXCT and ET volumes, respectively. The rounded total pore $V_{p,tot}$ and material volumes $V_{s,tot}$ are listed in Table 4.5 together with the total porosity ϵ_{tomo} of each tomogram.

Table 4.5: Results obtained from the quantitative pore analysis based on image analysis of the Ni/Al_2O_3-h catalyst. Rounded total *material* volume $V_{s,tot}$, *total pore* volume $V_{p,tot}$, porosity of the measured tomograms ϵ_{tomo}, weighted mean pore diameter $d_{eq,w}$, and fitted mean pore diameter $d_{eq,f}$ for the Ni/Al_2O_3-h-ET1, Ni/Al_2O_3-h-ET2, and PXCT.

Tomogram	ET1	ET2	PXCT
$V_{s,tot}$ / µm^3	$28,898.3 \cdot 10^{-6}$	$22,374.8 \cdot 10^{-6}$	1952.39
$V_{p,tot}$ / µm^3	$25,402.1 \cdot 10^{-6}$	$16,795.3 \cdot 10^{-6}$	1684.09
ϵ_{tomo} / %	46.8	42.9	46.3
$d_{eq,w}$ / nm	37.4 ± 1.2	29.2 ± 1.3	2545 ± 2.3
$d_{eq,f}$ / nm	36.2	27.9	2522

All three tomograms show a porosity larger than 40 %. With respect to the resolution, ϵ_{tomo} of the PXCT is defined as the macroporosity ϵ_M of the Ni/Al_2O_3-h catalyst based on image analysis. To calculate the total porosity ϵ_{tot} of the material based on the tomography studies, the mesoporosity visible by ET must also be included. Therefore, the porosity of the material label (ϵ_{mat}) in PXCT was assumed to further contain the average of the porosity values obtained from ET, which was 44.9 %. Taking into account this extra porosity for the PXCT results, a ϵ_{tot} of 70.4 % was obtained. Based on this ϵ_{tot}, the mesoporosity ϵ_m of the Ni/Al_2O_3-h catalyst based on the tomography analysis was 24.1 %.

In addition to the porosity information, one can extract information about the pore size distribution from the tomograms. The frequency of the occurrence of each pore diameter for the three tomograms is shown in the appendix Figure 8.8. For the PXCT volumes, one can observe a unimodal pore size distribution based on the frequency analysis with a maximum around 2 µm. The frequency-based pore distribution indicates a bimodal pore size distribution for the ET volumes with a maximum around 3 nm and another at around 22 nm to 25 nm. Based on the qualitative analysis of the ET, the small pores around 2 nm to 6 nm can be mainly assigned to isolated pores or artefacts from the pore separation that were not removed by the "Opening"

module or caused by the limited effective resolution. These were not considered to contribute to the total porosity. The larger mesopores represent the measurable pores of the connected pore system. To investigate the contribution of different pore sizes toward the pore volume, the porosity of each individual pore was calculated by eq. 3.21, and the sum of the individual porosities was plotted depending on d_{eq}, as shown in Figure 4.15 for (a) ET1, (b) ET2, and (c) PXCT.

The obtained pore size distributions were analyzed to obtain the weighted numerical mean

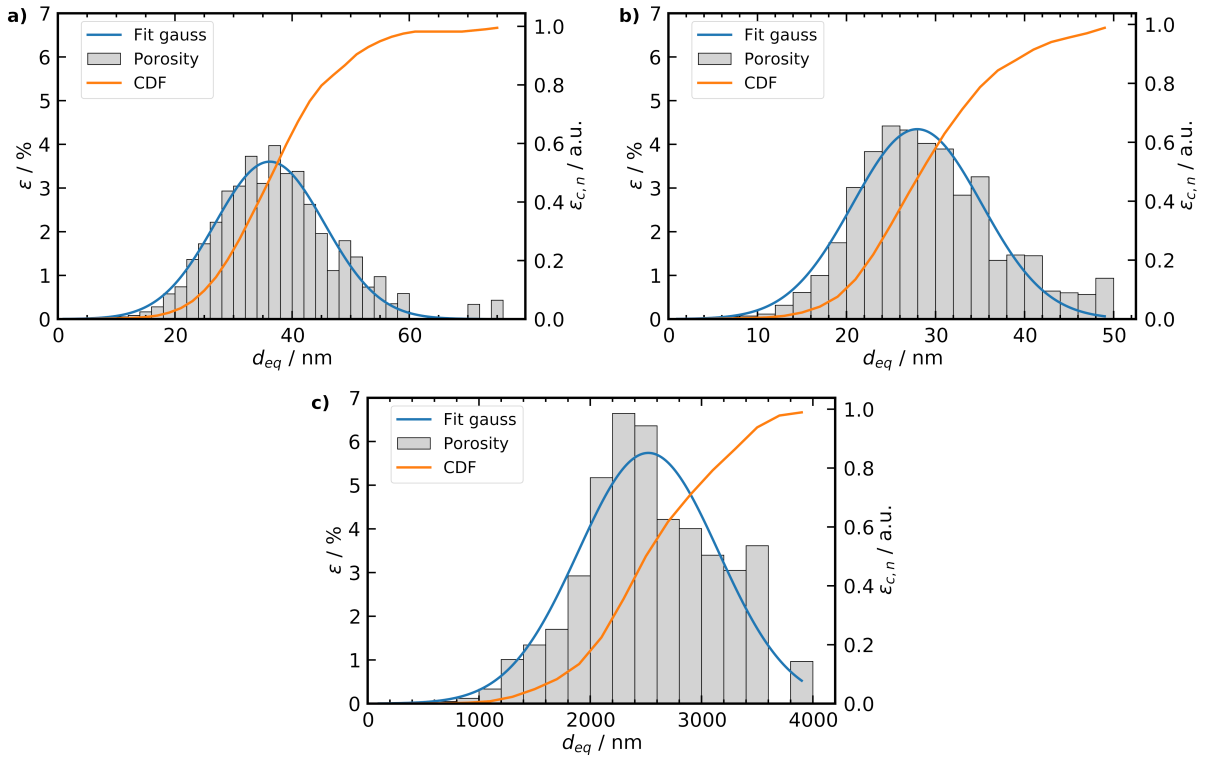


Figure 4.15: "Sum of individual porosities ϵ (grey) depending on d_{eq} as obtained from image analysis of the three tomograms (a) Ni/Al_2O_3-h-ET1, (b) Ni/Al_2O_3-h-ET2, and (c) PXCT of the Ni/Al_2O_3-h catalysts together with the normalized cumulative distribution function of the porosity $\epsilon_{c,n}$ (orange) and a fitted Gaussian distribution function (blue)."[236] Available under the terms and conditions of the Creative Commons Attribution 4.0 license (CC BY 4.0, `https://creativecommons.org/licenses/by/4.0/`), Copyright ©2020.

pore diameter $d_{eq,w}$ as well as the fitted mean pore diameter $d_{eq,f}$ from the Gaussian fit. Both mean pore diameter values for all three tomograms are summarized in Table 4.5. The difference between $d_{eq,w}$ and $d_{eq,f}$ was used to estimate the error of the mean pore diameter, while, for further discussion, the values of $d_{eq,w}$ were used. For Ni/Al_2O_3-h-ET1 and Ni/Al_2O_3-h-ET2 $d_{eq,w}$ of 37.4 ± 1.2 nm and 29.2 ± 1.3 nm were obtained, respectively. These values represent mesopores in the Ni/Al_2O_3-h catalyst, while no significant amount of macropores could be detected by ET. The absence of meaningful macropore data may be due to the limited size of the sample, which can be investigated by ET (e.g., 450 nm diameter), which can potentially be the same order of

magnitude as a single large macropore (*c.f.* Figure 1.9). The average of $d_{eq,w}$ of Ni/Al_2O_3-h-ET1 and Ni/Al_2O_3-h-ET2 is the mean mesopore diameter $d_{eq,meso}$ of 33.3 ± 4.1 nm of the Ni/Al_2O_3-h catalyst determined from tomography analysis.

The mean pore diameter for the macroporosity $d_{eq,macro}$ was similarly determined from the pore size distribution of the PXCT data as 2545 ± 23 nm. While no significant porosity contribution of macropores below 1 µm can be observed, the majority of the macropores ranged from 1 µm up to 3.5 µm, resembling a narrow macropore distribution and, thus, a relatively homogenous pore system. Compared to the study of Tariq *et al.* on a hierarchical Al_2O_3 material, a much higher macro- and mesoporosity for the Ni/Al_2O_3-h catalysts and a narrower pore size distribution were found, especially for the macropore space.[212] Furthermore, by the combination of PXCT with ET all relevant length scales for the hierarchical pore system of the Ni/Al_2O_3-h catalyst could be covered with only two techniques, instead of a combination of ET (limited sample volume), dual-beam FIB imaging (destructive), and µ-CT (low spatial resolution). PXCT is particularly notable for allowing exceptional spatial resolutions for a hard X-ray imaging method, which can therefore be applied to extended sample volumes in the micron scale. Here the combination of ET and PXCT enabled to detect pores ranging from about 2 nm to 80 nm (ET) up to 4 µm (PXCT).

The textural properties of Ni/Al_2O_3-h were also studied using well-established characterization techniques, i.e., N_2 sorption and Hg porosimetry by Ken Luca Abel in the group of Prof. Roger Gläser (Universität Leipzig). For these conventional techniques, a purely mesoporous Ni/Al_2O_3-meso sample, prepared via the same method but without addition of PEO, was used for comparison. The Ni/Al_2O_3-meso sample contained a similar amount of 18.6 wt.% Ni as the Ni/Al_2O_3-h. According to the IUPAC definition,[133] the N_2 sorption isotherms displayed in Figure 4.16a can be classified as type IV isotherms with a H1 hysteresis, indicating mesoporous materials. Indeed, narrow pore width distributions (Figure 4.16b) with maxima at 8.3 nm and 10.3 nm were

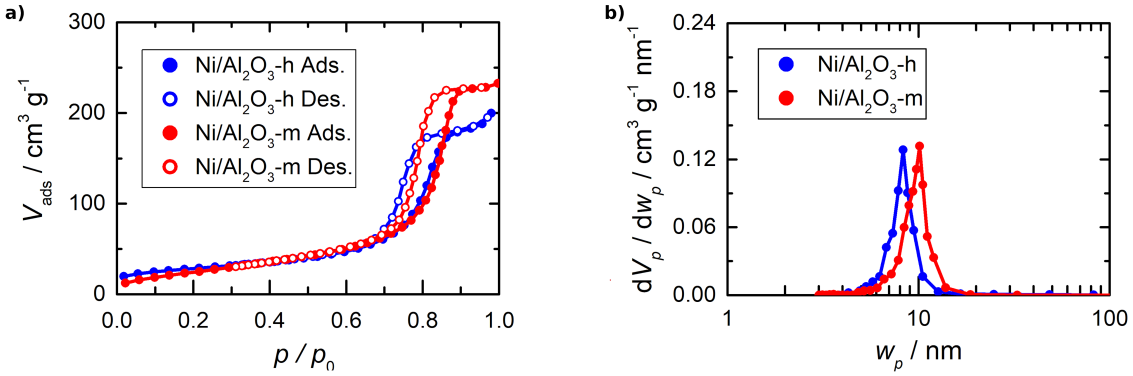


Figure 4.16: "N_2 sorption isotherms (a) and Barrett-Joyner-Halenda (BJH) pore width distribution (b) of Ni/Al_2O_3-h and Ni/Al_2O_3-meso denoted as Ni/Al_2O_3-m."[236] Available under the terms and conditions of the Creative Commons Attribution 4.0 license (CC BY 4.0, `https://creativecommons.org/licenses/by/4.0/`), Copyright ©2020.

obtained, respectively. The different mesopore widths for these materials were most likely caused by the influences of the polymerization-induced phase separation on the gelation process, which was induced in Ni/Al_2O_3-h but not in Ni/Al_2O_3-meso.
The existence of mesopores within Ni/Al_2O_3-h and Ni/Al_2O_3-meso was also confirmed with Hg porosimetry (Figure 4.17). Additionally, Ni/Al_2O_3-h exhibited macropores with a narrow

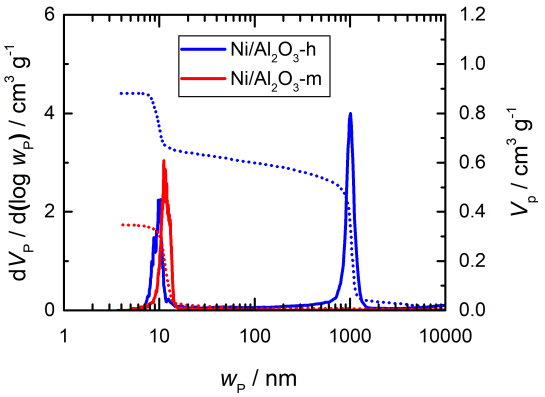


Figure 4.17: "Pore width distribution (solid lines) and cumulative specific pore volume (dashed lines) of Ni/Al_2O_3-h and Ni/Al_2O_3-meso denoted as Ni/Al_2O_3-m, determined by Hg porosimetry."[236] Available under the terms and conditions of the Creative Commons Attribution 4.0 license (CC BY 4.0, `https://creativecommons.org/licenses/by/4.0/`), Copyright ©2020.

width distribution around 1000 nm. This illustrates the bimodal nature of the pore system with distinct meso- and macropore regimes. Approximately two-thirds of the specific total pore volume of Ni/Al_2O_3-h was contributed by macropores, with the remaining third from the mesopores (Table 4.6).

Both mesopore width and specific mesopore volume of Ni/Al_2O_3-h and Ni/Al_2O_3-meso are comparable to the values obtained by Herwig *et al.*,[238] though lower values for macropore width and higher values for specific macropore volume were reported. However, the Ni loading (3.4 wt.%, 23 wt.%, and 33 wt.%) and the amount of PEO used during gelation, both of which were found to have a large impact on the macropore formation,[238] are different from this current work. A Ni mass fraction of 18 wt.% was chosen since this is a common Ni loading for CO_2 methanation catalysts.[47, 325] Therefore, the comparability of the macropore systems of the materials prepared here with those from Herwig *et al.*[238] is limited. The pore widths w_P of Ni/Al_2O_3-h and Ni/Al_2O_3-meso determined from Hg porosimetry were 1–2 nm higher and the specific mesopore volume was slightly lower compared to the results from N_2 sorption (Table 4.6). This may be due to an inaccurate representation of the smaller mesopores (<10 nm) by Hg porosimetry at high pressure, which results in a higher impact of connectivity effects.[326] Thus, within the mesopore range, Hg intrusion could rather represent a more pore throat width distribution compared to a rather pore body width distribution for N_2 sorption, as suggested by Rijfkogel *et al.*[327] or as discussed in section 4.1. To experimentally determine the porosity of

Table 4.6: Specific surface area (A_{BET}) and pore volume (V_P) from N_2 sorption, specific pore mesopore volume ($V_{P,meso}$), specific total pore volume ($V_{P,tot}$), mesopore width ($w_{P,meso}$), macropore width ($w_{P,macro}$), mesoporosity (ϵ_m) and macroporosity (ϵ_M), skeletal density (ρ), and total porosity (ϵ_{tot}) from He pycnometry, and mean mesopore diameter ($d_{eq,meso}$), mean macropore diameter ($d_{eq,macro}$), and porosity information from tomography analysis for calcined Ni/Al_2O_3-h and Ni/Al_2O_3-meso

	Ni/Al_2O_3-h	Ni/Al_2O_3-meso
N_2 sorption		
A_{BET} / $m^2\ g^{-1}$	99	108
V_P / $cm^{-3}\ g^{-1}$	0.31	0.37
w_P / nm	8.3	10.3
Hg porositmetry		
$V_{P,meso}$ / $cm^{-3}\ g^{-1}$	0.26	0.33
$V_{P,tot}$ / $cm^{-3}\ g^{-1}$	0.88	0.35
$w_{P,meso}$ / nm	10.3	11.2
$w_{P,macro}$ / nm	1012	-
ϵ_m / %	23.0	55.8
ϵ_M / %	55.0	3.4
He pycnometry		
ρ / g cm^{-3}	4.028	4.144
ϵ_{tot} / %	78.0	59.1
Tomography		
$d_{eq,meso}$ / nm	33.3 ± 4.1	
$d_{eq,macro}$ / nm	2545 ± 23	
ϵ_m / %	24.1	
ϵ_M / %	46.3	
ϵ_{tot} / %	70.4	

the Ni/Al_2O_3 xerogels, He pycnometry was performed and combined with the Hg porosimetry results according to eq. 3.1. The skeletal density of Ni/Al_2O_3-h and Ni/Al_2O_3-meso was similar (Table 4.6), with that of Ni/Al_2O_3-h being slightly lower, possibly due to a higher degree of pores inaccessible to Hg. Notably, a porosity of 59 % was obtained for the purely mesoporous Ni/Al_2O_3-meso. The introduction of PEO during gelation, which generates a substantial amount of macropores, then gave rise to an increase in porosity to 78 % for Ni/Al_2O_3-h.

To compare the results of the porosity analysis of Ni/Al_2O_3-h for the different techniques, the focus is on the pore size distributions and porosity values obtained by the standard techniques and imaging methods. The total porosity ϵ_{tot} from He pycnometry and Hg porosimetry was 78.0 %, with a macroporosity of $\epsilon_M = 55.0$ % and a mesoporosity of $\epsilon_m = 23.0$ %. The combined values obtained from the tomography studies were 70.4 % for ϵ_{tot}, 46.3 % for ϵ_M, and 24.1 % for ϵ_m. The macroporosity determination via both methods seemed to be in a similar range, with a difference

of 7.4 %. This behavior with similar macroporosity differences between X-ray tomography and Hg porosimetry characterization was also found by Andersson *et al.* and Tariq *et al.*[212, 328] Compared to the macroporosity determination, the difference between the mesoporosity values obtained from conventional techniques and the imaging techniques was even smaller, with only 1.1 %. Tariq *et al.* reported the major discrepancy in porosity determination for the mesoporosity analysis of Hg porosimetry compared to ET.[212] However, in the present case, the mesoporosity information matched well. The reason for the differences in the study of Tariq *et al.* is that, there, pores below 10 nm diameter could not be properly resolved.[212] This shows that the accuracy of quantitative porosity analysis by tomographic methods is directly linked to the spatial resolution, and it is, therefore, crucial to report on the spatial resolution during such investigations.
Aside from the porosity values, the $w_{P,macro}$ by Hg porosimetry with 1.012 µm was smaller than the $d_{eq,macro}$ determined via PXCT with 2.545 µm. Hg porosimetry is known from literature to overestimate small pore sizes in the macropore range on the costs of larger pore sizes.[212, 329–331] This can be explained considering that Hg porosimetry probes the pore throat size / pore opening size by using the Washburn equation,[244] while with image analysis using the PXCT data the equivalent diameter assuming spherical pores within the material according to eq. 3.19 is retrieved. In addition to the $w_{P,macro}$, the $w_{P,meso}$ of the mesopores determined by Hg porosimetry or N_2 sorption ranged from 10.3 to 8.3 nm, respectively, and was much smaller than the average 33.3 ± 4.1 nm obtained from ET. This difference can be explained, again, by the different pore size definitions as for macropores. On the other hand, the presence of a hierarchical pore network is difficult to elucidate unambiguously by conventional methods, like N_2 sorption, Hg porosimetry, and He pycnometry. From the visual inspection of the pore structure from the segmented tomography data Figure 4.14, it can be concluded that the Ni/Al_2O_3-h catalyst exhibits a well-connected macropores' network, while the mesopores are located within the solid material label of the PXCT. This represents a hierarchical pore system as the macropores form a parent-connected network from which the mesopores are originating. This clearly shows the advantage of imaging methods in performing quantitative and meaningful pore structure analysis, as not only pore sizes and porosity can be analyzed, but also more complex pore network models can be retrieved and co-located in 3D space.[308]"[236]

4.3.6 Macrokinetics

To make valuable use of the detailed porosity characterization and to estimate the potential benefits of the hierarchically porous material, model-based macrokinetic simulations were performed by Ronny T. Zimmermann and Dr. Jens Bremer in the group of Prof. Kai Sundmacher (Otto-von-Guericke University Magdeburg, Max Planck Institute for Dynamics of Complex Technical Systems Physical and Chemical Foundations of Process Engineering, Magdeburg). The simulation results for the Ni/Al_2O_3-h catalyst are compared with a purely mesoporous sample Ni/Al_2O_3-meso. The detailed information on the macrokinetic modelling can be found in

the supplementary information of ref.[236] "This model-based investigation aimed to evaluate the relevant conditions in CO_2 methanation where a tailored hierarchical pore system might be advantageous in terms of mass-transport properties, compared to a conventional purely mesoporous material. The calculated diffusion coefficients ($D_{CO_2,eff}$) based on PXCT data and Hg-intrusion data are given in Table 4.7 at industrially occurring CO_2 methanation conditions.

Table 4.7: Pore network data based on tomography and Hg porosimetry measurements as well as calculated effective diffusion coefficients of CO_2 of a stoichiometric mixture $x_{H_2}/x_{CO_2} = 4/1$ at 600 K and 10 bar.

Sample	Data Set	ϵ_M / %	d_M / nm	ϵ_m / %	d_m / nm	$D_{CO_2,eff}$ / m^2 g^{-1}
Ni/Al_2O_3-h	Tomography	46.3	2545	24.1	33.3	$5.89 \cdot 10^{-6}$
Ni/Al_2O_3-h	Hg poros.	55.0	1012	23.0	10.3	$6.67 \cdot 10^{-6}$
Ni/Al_2O_3-meso	Hg poros.	n.a.[a]	n.a.[a]	55.8	11.2	$5.74 \cdot 10^{-7}$

[a] not applicable

According to these results, the introduction of the macroporous network into the porous catalyst material increased the effective diffusion coefficient by more than one order of magnitude. The reason for this is that in the macropores' molecular diffusion was the main diffusion mechanism, while in the mesopores, Knudsen diffusion prevailed. Thus, much higher catalyst effectiveness factors are expected to be present for a catalyst pellet with hierarchical pore system of industrially relevant size at high temperatures.

To underline this statement, the effective reaction rates as well as effectiveness factors for a spherical catalyst pellet of 2.5 mm diameter based on the pore network properties given in Table 4.7 were calculated. The results are shown in the Arrhenius plots in Figure 4.18. On the one hand, it is evident that mass transport limitations in the exclusively mesoporous sample started at about 550 K. On the other hand, mass transport limitations for the hierarchically porous sample started at about 650 K to 675 K, depending on the data set. However, it has to be noted, that this effect was not solely based on the increased diffusion coefficient in the hierarchically porous material but also on the lower intrinsic reaction rate. This is due to the lower mesoporosity of the hierarchically porous sample, in comparison to the exclusively mesoporous sample. Based on the observed potential mass-transfer limitations from the macrokinetic simulations, further kinetic studies on the Ni/Al_2O_3-h and Ni/Al_2O_3-meso samples should be carried out to experimentally validate whether a hierarchical pore system is superior in terms of minimizing mass transport phenomena, compared to a purely mesoporous material."[236]

Extrapolating the findings of the macrokinetic simulations towards the SPP2080-IMRC in section 4.1 and the core-shell particle design in section 4.2, a hierarchically porous active catalyst core might be promising to further improve the core-shell design.

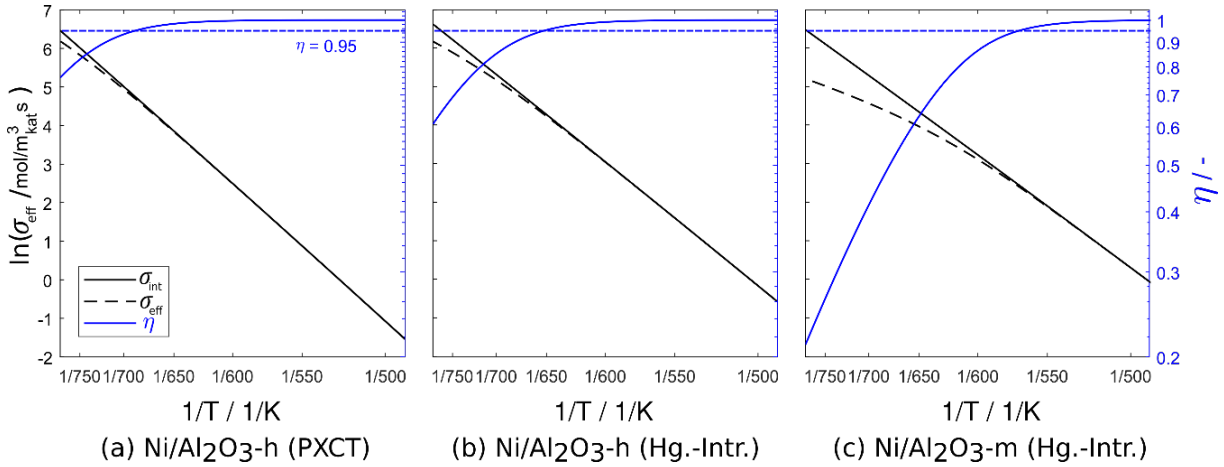


Figure 4.18: "Arrhenius plots of effective and intrinsic reaction rates as well as catalysts effectiveness factor η based on pore network properties given in Table 4.7 for a catalyst pellet of 2.5 mm diameter. (a) Ni/Al_2O_3-h (tomography), (b) Ni/Al_2O_3-h (Hg porosimetry) and (c) Ni/Al_2O_3-m (Hg porosimetry). All plots were calculated at $p_{surf,CO_2} = 2$ bar, $p_{surf,H_2} = 8$ bar and $p_{surf,H_2O} = p_{surf,H_2O} = 0$ bar."[236] Available under the terms and conditions of the Creative Commons Attribution 4.0 license (CC BY 4.0, `https://creativecommons.org/licenses/by/4.0/`), Copyright ©2020.

4.3.7 Conclusions

In this section a hierarchically porous Ni/Al_2O_3 catalyst (Ni/Al_2O_3-h) was characterized as a potential catalyst candidate with improved mass transport properties for CO_2 methanation. The Ni/Al_2O_3-h showed superior performance in macrokinetic simulations compared to a purely mesoporous sample in terms of its effectiveness factor. Especially at higher reaction temperatures above 550 K mass transfer limitation are less severe for the hierarchically porous catalyst. Based on this findings an application of a hierarchically porous active core in the core-shell design of section 4.2 is an interesting option to further improve the performance of Ni-based catalysts in dynamic CO_2 methanation. However, there is probably quite some room to improve the catalyst activity based on first testing results.

A key information required as input for the macrokinetic simulations is exact knowledge about the pore structure of the catalyst. Furthermore, the hierarchical nature of the meso-/macropores structure had to be proven. Similar to section 4.1 it was shown that a combination of different imaging methods, here ET and PXCT, is required to analyze the different pore length scales being present in Ni/Al_2O_3-h. PXCT allowed to cover the whole macropore space, while ET was required to analyze the mesopores of the catalyst. Based on the combined advanced imaging characterization a truly hierarchical pore structure of meso- and macropores was identified, which is difficult to decide by conventional methods. In future studies, the tomographic data can be applied for detailed modeling of pore networks and might facilitate a knowledge-driven tailoring of the pore structure.

One drawback of the synthesis procedure via sol-gel method was found to be Ni incorporation

into the $\gamma-Al_2O_3$ structure and partial formation of $NiAl_2O_4$. This required high reduction temperatures ($\approx$1123 K) in order to reduce Ni^{2+} to Ni^0 for catalyst activation. To understand and possibly avoid the incorporation of Ni more detailed knowledge about the synthesis procedure of the catalyst is required. A decreased necessary reduction temperature is potentially a requirement for a future application of the material at the typically lower temperatures of CO_2 methanation at 523–773 K. The detailed understanding of sample changes during the last synthesis step - the calcination - will be the focus of the next chapter 5.
Additionally, this section showed that the combination of different disciplines, i.e., synthesis, characterization and modeling is essential for a later rational design of porous catalyst materials. The presented Ni/Al_2O_3-h is an interesting case study for future extensive studies of kinetics and associated mass transport phenomena to confirm simulation results. Furthermore, understanding textural (*c.f.* section 5.1) and structural (*c.f.* section 5.2) changes of the material during calcination are required for a future knowledge-based tailoring of the catalyst material and its preparation.

5 Understanding the Synthesis of Catalysts with Tailored Pore Structures

In the present chapter the synthesis of the hierarchically porous Ni/Al_2O_3-h catalyst as presented in section 4.3 is studied. First, the application of hard X-ray ptychography is shown in understanding the evolution of the pore structure during calcination of the dried gels in section 5.1. This allows to study textural changes of the dried gels during calcination, but no information about structural atomic changes. Therefore, in section 5.2 X-ray total scattering with PXRD and PDF analysis are applied in studying structural changes of the dried gels during calcination. This provides initial information about different phases and their transformation processes during calcination. Therefore, the chapter highlights the complexity in understanding textural and structural changes of catalysts during their synthesis. However, a detailed knowledge thereof is required for a future knowledge-based catalyst designed or tuning of material preparation. *In situ* hard X-ray techniques are highlighted in this chapter as powerful tools to unravel different samples states during the selected calcination step of the sol-gel synthesis of the hierarchically porous Ni/Al_2O_3-h catalyst.

5.1 Following the Porosity Evolution by X-ray Ptychography[1,2]

5.1.1 Introduction

In section 4.3 a hierarchically porous Ni/Al_2O_3 catalyst was presented as a promising candidate to improve mass transport properties of Ni/Al_2O_3 catalysts applied in CO_2 methanation. As reviewed in the introduction section 1.4, hierarchically meso-/macroporous catalysts are generally thought to be able to improve the transport of molecules in porous catalysts. Often the connected macropore network is referred to as a transport network connected to mesopores, where the actual reaction mainly takes place. The Ni/Al_2O_3-h material in section 4.3 was prepared via a modified sol-gel method, which is generally a promising synthesis route towards hierarchically porous materials as reviewed in section 1.4.

However, the synthesis procedure often relies on extensive trial and error approaches in order to tune the final pore structure. Control over the latter is a requirement to design an optimal pore structure for application of such hierarchical catalysts. For example, the active core in the core-shell design of section 4.2 might be improved in its performance in case a hierarchical pore structure is present, as in the active core ideally no mass transport limitations should be present.[114, 115] The sol-gel method usually consists of five steps, all of them can influence the final pore structure of the catalyst: (i) sol formation by hydrolysis and partial condensation, (ii) gel formation by polycondensation, (iii) gel aging, (iv) gel drying and (v) stabilization, typically via calcination.[143, 146, 147] Here, the aim is to focus on the influence of the last step of the synthesis, the calcination as it can induce many changes to porosity, pore sizes, crystallization, sintering, partial or even complete structural collapse. As reviewed in the introduction section 1.4, conventional methods, i.e., N_2-sorption, Hg porosimetry and He pycnometry are very limited in their application on fragile samples, which is likely the case for the dried gel state. Furthermore, they do not allow at all to follow changes of the pore structure as they occur.

Therefore, in the present section the application of *in situ* 2D X-ray ptychography (XRP) imaging and *ex situ* ptychographic X-ray computed tomography (PXCT) is exploited to understand the evolution of pore structures during calcination. As illustrated in Figure 5.1, *in situ* XRP and *ex situ* PXCT are applied complementary to each other to study the changes of the dried gel of the Ni/Al_2O_3-h sample presented in section 4.3 and a comparable Al_2O_3-h sample without Ni

[1] Parts of section 5.1 are adapted and taken from: S. Weber, A. Diaz, M. Holler, A. Schropp, M. Lyubomirskiy, K. L. Abel, M. Kahnt, A. Jeromin, S. Kulkarni, T. F. Keller, R. Gläser, T. L. Sheppard, "Evolution of Hierarchically Porous Nickel Alumina Catalysts Studied by X-ray Ptychography", *Adv. Sci.*, **2022**, *9*, 2105432.[237] Available under the terms and conditions of the Creative Commons Attribution 4.0 license (CC BY 4.0, `https://creativecommons.org/licenses/by/4.0/`), Copyright ©2022.

[2] K. L. Abel and R. Gläser (Universität Leipzig) provided the synthesis of the materials, N_2 sorption, Hg porosimetry, He pycnometry and elemental analysis. A. Diaz and M. Holler (Paul Scherrer Institut, Villigen PSI) supported the PXCT experiments along with the ptychographic and tomographic reconstruction. A. Schropp, M. Lyubomirskiy (Deutsches Elektronen-Synchrotron DESY, Hamburg) and M. Kahnt (MAX IV Laboratory, Lund) supported *in situ* XRP experiments and ptychographic reconstruction. A. Jeromin, S. Kulkarni and T. F. Keller (Deutsches Elektronen-Synchrotron DESY, Hamburg) prepared the wedge-shaped sample for *in situ* XRP experiments by FIB/SEM.

addition. In addition to the advanced imaging studies, conventional porosity characterization by N_2-sorption, Hg porosimetry, and He pycnometry are shown.

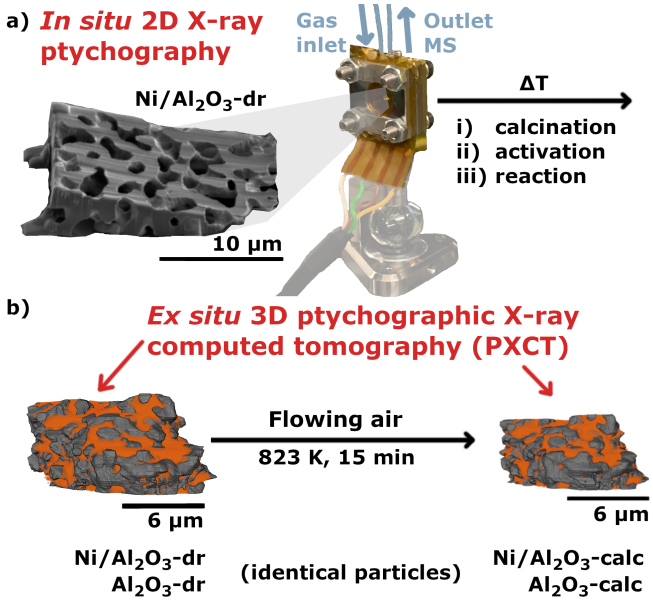


Figure 5.1: "Overview of experiments performed. (a) *in situ* 2D X-ray ptychography of the dried gel Ni/Al_2O_3-dr sample during calcination, activation, and reaction conditions in a nanoreactor setup. (b) Illustration of sample particles, which are placed on Cu-pins for *ex situ* 3D ptychographic tomography experiments. Tomography data was acquired first on the dried gels (Ni/Al_2O_3-dr and Al_2O_3-dr), and again on the identical samples following calcination in a muffle furnace (Ni/Al_2O_3-calc and Al_2O_3-calc)."[237] Available under the terms and conditions of the Creative Commons Attribution 4.0 license (CC BY 4.0, `https://creativecommons.org/licenses/by/4.0/`), Copyright ©2022.

5.1.2 Synthesis and Characterization of Hierarchically Porous Nickel Alumina Catalysts

The preparation of the hierarchically porous Ni/Al_2O_3 and Al_2O_3 catalysts was performed similar to section 4.3 by Ken Luca Abel in the group of Prof. Roger Gläser (Universität Leipzig). The route was adapted from previous studies, reporting bimodal meso- and macroporous structures by sol-gel synthesis with polymerization induced phase separation in ref.[238, 312] or as detailed in the experimental section 3.1.2. "Briefly, chloride salts of Al and Ni were homogeneously mixed with poly(ethylene oxide) (PEO) in an ethanolic solution. Polymerization and phase separation were induced by addition of propylene oxide (PO) to obtain the wet gels, which were then dried and subsequently calcined.[236, 238, 312] The dried gel samples discussed in this study (Ni/Al_2O_3-dr and Al_2O_3-dr) were separated from the main synthesis batch after drying, and therefore represent the catalyst state without subsequent treatment steps such as calcination, activation, or catalytic testing (...).

Elemental analysis (C,H,N, *c.f.* Table 8.2) revealed the presence of organic compounds and water in the dried gels, this was assigned to polymer or solvent residues from the synthesis and was not

found in the calcined samples. Hg porosimetry studies (Figure 5.2, *c.f.* Figure 8.9 and Table 8.3) of the dried gel and calcined samples showed that only macropores (≈1 µm) were significantly present in the dried gels, while additional mesopores (≈10 nm) were conclusively identified only in the calcined samples. The mode of the macropore width ($w_{P,M,Hg}$) decreased after calcination

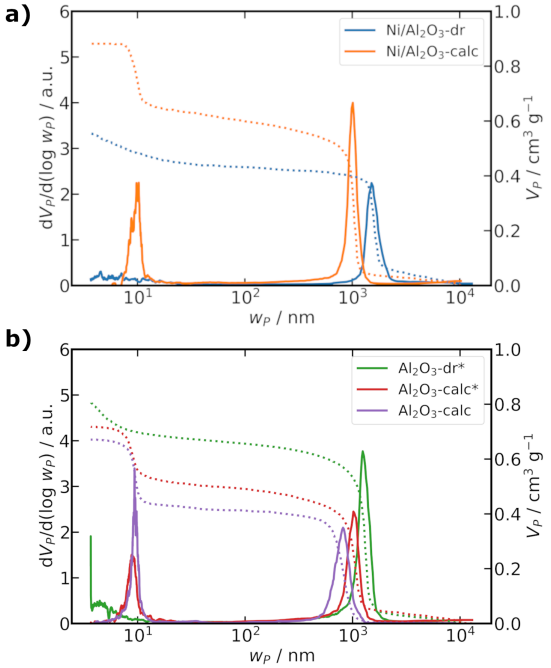


Figure 5.2: "Hg porosimetry data for the (a) Ni/Al_2O_3 and (b) Al_2O_3 samples as dried gel and calcined. Al_2O_3-dr* and Al_2O_3-calc* are from a different sample batch than used for imaging studies. The solid lines show the pore width distribution as ($dV_P/d(log\, w_P)$) and the dashed lines the cumulative specific pore volume (V_P)."[237] Available under the terms and conditions of the Creative Commons Attribution 4.0 license (CC BY 4.0, `https://creativecommons.org/licenses/by/4.0/`), Copyright ©2022.

from 1.5 µm to 1.0 µm in Ni/Al_2O_3, and from 1.2 µm to 1.0 µm in $Al_2O_3{}^\star$. It should be noted that Hg porosimetry studies to compare the dried gel and calcined state of Al_2O_3 were carried out on a different sample batch than for the X-ray imaging studies (indicated by an asterisk *). This was done due to an insufficient amount of sample remaining from the X-ray imaging batch to allow both Hg porosimetry and N_2 sorption, rather only Hg porosimetry on the X-ray imaging batch was performed (Al_2O_3-calc). To compensate for this, a new batch of dried gel sample (Al_2O_3-dr*) was made by the same exact preparation procedure and examined by Hg porosimetry before and after calcination (Al_2O_3-calc*). This might influence the absolute pore width values, as $w_{P,M,Hg}$ for the same Al_2O_3-calc batch as the X-ray imaging studies was 0.82 µm, compared to 1.0 µm for the new batch (Al_2O_3-calc*). Furthermore, small mesopore contributions (< 10 nm) were found for Al_2O_3-dr at $w_{P,M,Hg}$ close to the resolution limit of Hg porosimetry. The A_{BET} increased from 5 $m^2\,g^{-1}$ (Ni/Al_2O_3-dr) to 99 $m^2\,g^{-1}$ (Ni/Al_2O_3-calc) after calcination, while a decrease from 128 $m^2\,g^{-1}$ (Al_2O_3-dr) to 91 $m^2\,g^{-1}$ (Al_2O_3-calc) was observed."[237]

5.1.3 *In Situ* X-ray Ptychography

As a next step, the evolution of the Ni/Al_2O_3-dr dried gel sample was investigated during calcination, activation, and reaction conditions by *in situ* XRP as detailed in section 3.4.5. *In situ* XRP allows to follow textural changes almost in real time as they occur, contrary to *post mortem* analysis by gas sorption or Hg porosimetry. For the *in situ* experiments, a wedge-like structure of Ni/Al_2O_3-dr was prepared by Arno Jeromin and Satishkumar Kulkarni together with Dr. Thomas F. Keller at DESY Nanolab (Hamburg) as shown in Figure 5.3f *via* focused-ion beam (FIB) milling.[256] The wedge-like sample was mounted on a micro-electro-mechanical systems (MEMS) Wildfire Nano-Chip (DENSsolutions, Delft, Netherlands) by gluing using ion-beam-induced deposition (IBID) of a Pt precursor inside the FIB system *c.f.* Figure 3.9, 8.10. Scanning electron microscopy (SEM) images indicated sample dimensions of length ≈18 µm, width ≈13 µm and maximum thickness of ≈5 µm. "The Ni/Al_2O_3-dr sample on the MEMS chip was placed in a nanoreactor (*c.f.* Figure 3.10),[234] which was mounted on the stage of the PtyNAMi setup at the Nanoprobe endstation of beamline P06 of the Deutsches Elektronen Synchrotron DESY (Hamburg, Germany).[257] *In situ* XRP studies were carried out employing three different gas conditions: (i) calcination (20 % O_2/He), (ii) activation (25 % H_2/He) and (iii) reaction (20 % H_2/5 % CO_2/He) with a constant total gas flow of 2 mL min^{-1} (*c.f.* Table 3.3). During *in situ* XRP the outlet gas composition was monitored by online mass spectrometry (MS) (Figure 5.3d). For further details on the *in situ* XRP experiments *c.f.* section 3.4.5 and MS data in Figure 8.12.

Figure 5.3a shows the phase contrast image of the initial state of the Ni/Al_2O_3-dr sample at 303 K under He atmosphere, with spatial resolution estimated to be 67.2 nm via Fourier ring correlation (FRC) (*c.f.* Figure 8.13).[260] The macropore system can be readily identified, in agreement with the SEM images recorded during FIB preparation (Figure 5.3f, Figure 8.10, Figure 3.9). The sample was then heated in 30 K steps up to 873 K under calcination conditions and held for ≈1 h at 873 K. At each temperature step a ptychographic projection was recorded with an acquisition time of ≈11 min under isothermal conditions, while during longer holding times multiple projections were recorded. The sample was visibly shrinking during the entire calcination period, which can be readily observed comparing the image at the final stage of the calcination (Figure 5.3b) with the initial state (Figure 5.3a). (...) The width of the sample was analyzed by aligning to a clearly identifiable feature as indicated by the arrow in Figure 5.3a-c, with the evolution of the width shown in Figure 5.3e. During calcination the width decreased from 12.9 µm to 10.7 µm by about 17 %. The most pronounced changes occurred in the temperature range from about 400 K to 800 K. The calcination was followed by activation conditions in 50 K steps up to 1073 K and a holding time of ≈1 h at 1073 K. The sample further contracted during activation, indicating continuing minor sample changes but less severe compared to those seen during calcination. The width from the initial dried gel to the activated state decreased by

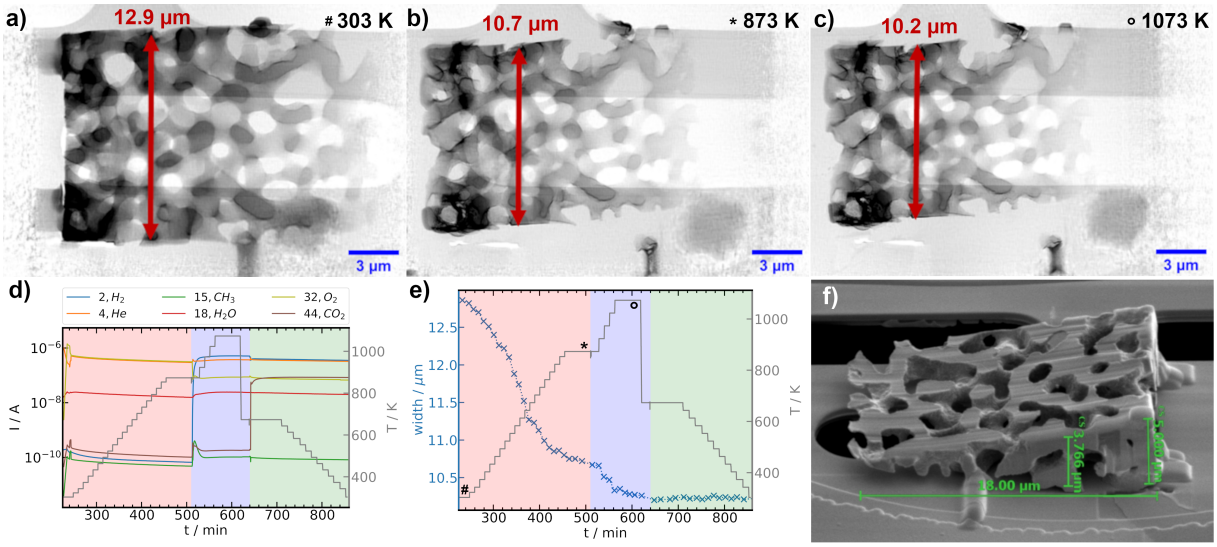


Figure 5.3: "*In situ* XRP experiments for Ni/Al_2O_3. (a-c) Ptychographic reconstructions with 18.6 nm pixel size, MEMS chip and windows (bright) visible in the background; (a) initial state of the dried gel ('#', 100 % He); (b) after calcination at 873 K ('⋆', 20 % O_2/He); (c) after activation at 1073 K ('∘', 25 % H_2/He), total gas flow 2 mL min^{-1}; (d) selected MS traces and temperature (red box - calcination, blue - activation and green - reaction conditions (20 % H_2/5 % CO_2/He)); (e) sample width measured at the characteristic feature as indicated by the red arrow in (a-c) with identical conditions as in (d); (f) SEM image before the experiment, the width is based on a single point measurements at each temperature at the identified characteristic feature."[237] Available under the terms and conditions of the Creative Commons Attribution 4.0 license (CC BY 4.0, `https://creativecommons.org/licenses/by/4.0/`), Copyright ©2022.

about 20 % from 12.9 µm to 10.2 µm. After cooling to 673 K and switching to reaction conditions, no further significant change of sample width was observed. The observed sample changes are consistent with bulk *ex situ* observations during laboratory synthesis of hierarchically porous Ni/Al_2O_3, where monoliths were typically found to shrink about 15 % in width from the dried gel to the calcined state. Despite the observed volume shrinkage, the macropore network stayed qualitatively intact during the whole *in situ* experiment in terms of the overall connectivity and general shape. However, no quantification is possible from only 2D projection images. During the whole *in situ* experiment the outlet gas was analyzed confirming the applied gas composition was present at the sample as indicated by the colored regions in Figure 5.3d,e. However, the amount of sample and thus evolution of gaseous products in the experiment (which would constitute an *operando* study) was too low to be detected via online MS analysis.

The *in situ* XRP studies show the potential of XRP for studying extended sample volumes (several µm) with sub-100 nm resolution under well defined temperature and gas conditions. Comparable results from SEM or FIB-SEM imaging are not feasible, due to insensitivity to the bulk sample or destruction of the sample, respectively. Likewise the sample volume probed here using hard X-ray imaging is orders of magnitude larger than could be studied with transmission electron microscopy (TEM), due to electron beam attenuation. While *in situ* XRP studies in catalysis

science were already reported before for sintering experiments on model systems[233, 234], here the application to retrieve textural information of the evolution of an applied catalyst system under different gas compositions and temperature steps is shown. In principal the setup would also allow for missing wedge tomography acquisition, which enables to retrieve 3D quantitative information from *in situ* experiments.[234] This is in principle analogous to TEM-tomography, although permitting much larger sample volumes due to the low attenuation of hard X-rays compared to electrons. However, the required time for acquisition of a limited angle tomogram in the used experimental configuration would have taken too long ($\approx 24\,h$ per tomogram). Despite measuring changes of the sample width, deriving further quantitative information about the pore structure is not feasible based on 2D projection data. Further PXCT experiments were therefore performed.

In principle, any structural changes of the sample leading to changes in electron density can be investigated by XRP. For Ni/Al_2O_3 this could be exemplary the reduction of NiO to Ni during catalyst activation. However, the achieved 2D resolution of about 67 nm is not sufficient to directly resolve any large Ni particles which may be formed by sintering or aggregation during or after the activation step. Generally, changes in electron density can also be observed even if single individual features such as Ni particles cannot be directly resolved, as it will be presented for coking studies in section 6.1.[239] In the present case, a quantitative analysis of the electron density is limited due to the tilting of the sample upon thermal treatment, which would require to account for changes of the sample thickness that cannot be directly obtained from only 2D projections. In summary, the ability to resolve structural changes in 2D can be challenging on extended 3D samples and is limited by the achieved 2D resolution and potential textural changes."[237]

5.1.4 *Ex Situ* Ptychographic X-ray Computed Tomography

The *in situ* XRP allowed to follow the sample changes of the dried gel under well-defined temperature and gas conditions, but the quantification of observed sample changes is limited. Therefore, complementary 3D spatially-resolved PXCT experiments were performed to retrieve quantitative measures for the pore structure changes during the calcination step of the Ni/Al_2O_3-h and Al_2O_3-h samples. This includes information about porosity and pore sizes, but also whether the pore network or the electron density of the nanoporous solid are changing. "Suitable particles of Ni/Al_2O_3-dr and Al_2O_3-dr were mounted on Cu tomography pins of the OMNY design[255] by gluing using IBID of a Pt precursor gas inside the FIB-SEM as described in section 3.4.4. The mounted particles had a diameter of $\approx$50 µm and $\approx$15 µm for Ni/Al_2O_3-dr and Al_2O_3-dr, respectively, as shown by SEM (*c.f.* Figure 8.11). PXCT studies were performed at cSAXS beamline of the Swiss Light Source (Paul Scherrer Institut, Villigen, Switzerland) using the flOMNI endstation at an energy of 6.2 keV.[183, 262] For experimental details see section 3.4.6 and Table 3.4. After initial PXCT scans of the dried gels, the samples were removed from

the beamline and calcined in a muffle furnace. The samples on the pins were heated to 823 K with a rate of 10 K min^{-1} under flowing air with a holding time of 15 min at 823 K. It should be noted that higher temperatures during calcination were not possible due to ablation of the Cu-pins, which happens above 873 K and would contaminate the sample. After the calcination step, comparable regions of the exact same particles were studied again by PXCT, denoted as Ni/Al_2O_3-calc and Al_2O_3-calc.
The resulting phase contrast tomograms of Ni/Al_2O_3-dr and Ni/Al_2O_3-calc have voxel sizes of 19.9 nm and 27.9 nm and estimated resolutions by Fourier shell correlation (FSC)[261] of 91.2 nm and 55.6 nm, respectively (*c.f.* Figure 8.14). For Al_2O_3-dr and Al_2O_3-calc the voxel sizes are 27.9 nm and 19.9 nm with estimated FSC resolutions of 49.6 nm and 40.9 nm, respectively (*c.f.* Figure 8.15). Each PXCT acquisition was performed by sequential acquisition of subtomograms. This allowed to check for and exclude potential beam damage effects, by comparing slices with neighboring projection angle recorded at time intervals of ≈20-60 min, depending on the sample (*c.f.* section 3.4.6). The 3D N_e distribution of the reconstructed PXCT tomograms was retrieved from the phase contrast tomograms (*c.f.* section 3.4.6) as described in ref.[156, 157] Selected slices of the resulting N_e tomograms are shown in Figure 5.4(a3-d3).

For image analysis of all PXCT data, the whole particles were first masked from the surrounding air. Then the particle volumes were segmented by thresholding into pores (orange), material (gray) and contamination (green) labels based on N_e (Figure 5.4(a1-d1)). The contamination mainly consists of Pt complexes deposited during FIB preparation, or from redeposition of a mixture of materials (sample, Cu pin) which can occur during ion beam milling. These contaminants were easily identified and excluded from further analysis of porosity. The obtained pore labels of all samples were additionally transformed into global skeleton networks, which are used as pore network models as shown in Figure 5.4(a2-d2). Additionally, the pore labels were separated into individual pores as shown in Figure 5.5a,b,d,e with an 8-bit color code for Ni/Al_2O_3-dr, Ni/Al_2O_3-calc, Al_2O_3-dr and Al_2O_3-calc, respectively. For details regarding image analysis and processing steps *c.f.* section 3.4.9. The different labels and pore network models were then used to quantify the pore structure of the samples."[237]

5.1.5 3D Pore Structure Characterization by PXCT Image Analysis

"A connected macropore network can be directly identified in all four tomography datasets (Figure 5.4). The spatial resolution (≈50 to 90 nm) of the tomograms is not sufficient to directly resolve mesopores within the samples,[236, 238, 312] and as similar shown in sections 4.1 and 4.3 before. However, PXCT can quantify such features indirectly by N_e analysis discussed in the following section and already presented for the SPP2080-IMRC in section 4.1. The presence of mesopores in the calcined samples was expected from Hg porosimetry shown above, as well as from the multiscale studies in section 4.3 on an activated Ni/Al_2O_3-h sample. Quantitative

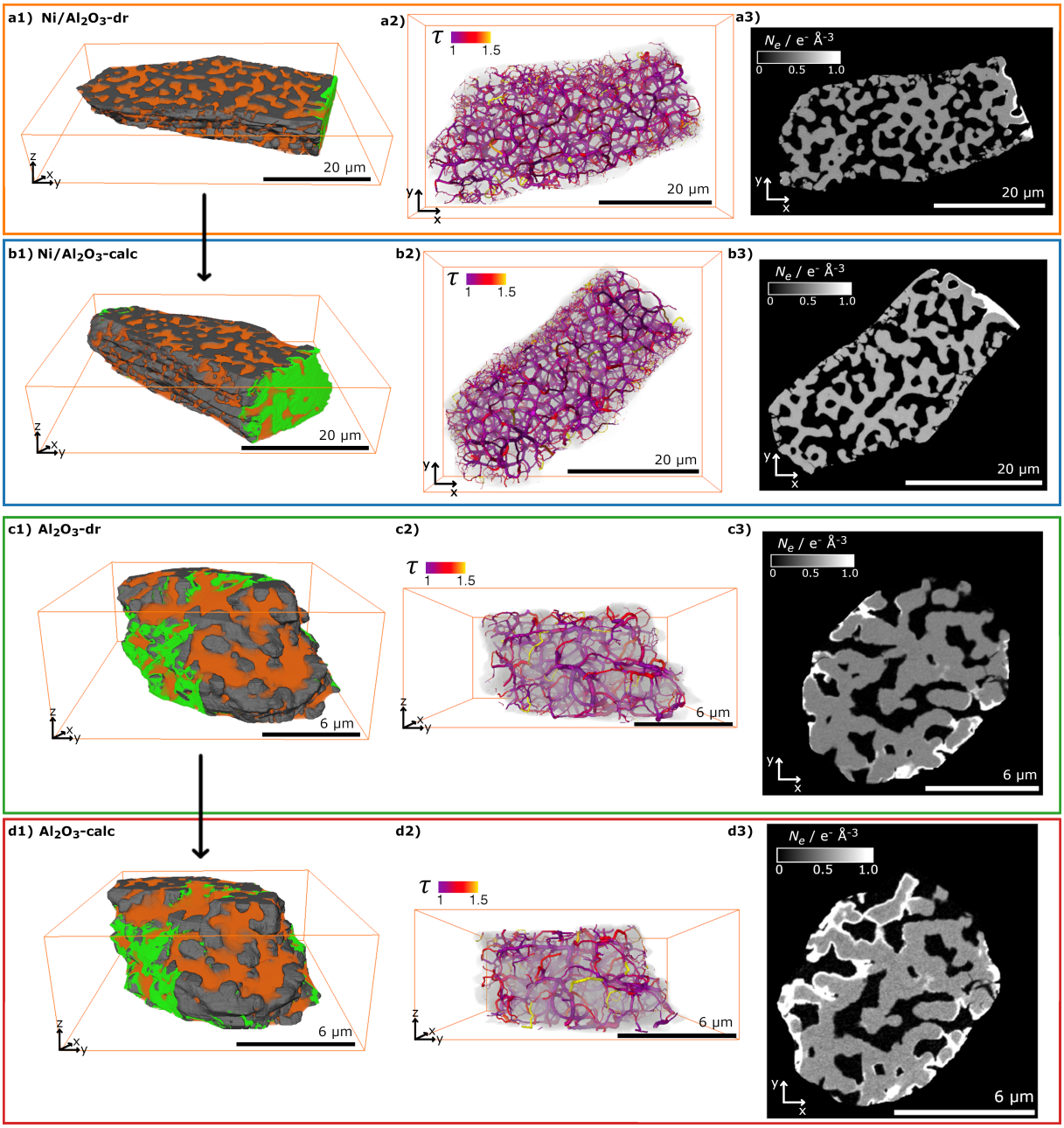


Figure 5.4: "PXCT volume renderings with labeling for (a1) Ni/Al_2O_3-dr, (b1) Ni/Al_2O_3-calc, (c1) Al_2O_3-dr, and (d1) Al_2O_3-calc, showing "material" (gray), "pores" (orange), and "contamination" (green) labels, with reconstructed voxel sizes (a,d) 19.9 nm and (b,c) 27.9 nm. (a2-d2) Pore network models derived from PXCT data, colormap representing segment tortuosity (τ), with segment size proportional to pore radius (r_{pore}). (a3-d3) Selected slices of PXCT volumes with grayscale N_e in $e^- Å^{-3}$. The calcined samples (b3,d3) were measured after heating the dried gels (a3,c3) in air at 823 K (10 K min^{-1}) for 15 min."[237] Available under the terms and conditions of the Creative Commons Attribution 4.0 license (CC BY 4.0, `https://creativecommons.org/licenses/by/4.0/`), Copyright ©2022.

label analysis of the pore and material labels (Figure 5.4(a1-d1)) allowed to determine the label volumes and to calculate the macroporosity (ϵ_M) of the measured particle volumes (*c.f.* section 3.4.9 for details). The porosity analysis results are summarized in Table 5.1 for all samples. The determined ϵ_M for Ni/Al_2O_3-dr showed only a minor increase after calcination to Ni/Al_2O_3-calc, while both states showed comparable macroporosity as in the previous PXCT study of the same material after activation ($\epsilon_M = 46.3\,\%$, *c.f.* section 4.3).[236] For Al_2O_3-dr the ϵ_M slightly decreased after calcination to Al_2O_3-calc. For both catalyst types, the N_e slices of similar particle regions showed significant volume shrinkage comparable to the *in situ* XRP experiments (Figure 5.4(a3-d3), note difference in scale bars).

Table 5.1: Summary of pore characterization based on PXCT data, including: macroporosity (ϵ_M), mesoporosity (ϵ_m), total porosity (ϵ_{tot}), mean equivalent spherical pore diameter of separated pores ($\overline{d}_{eq}$), mean pore diameter of skeleton-based pore network model ($\overline{d}_{pore}$), mean length of skeleton segments ($\overline{l}_{cu,pore}$), mean tortuosity of skeleton segments ($\overline{\tau}$), mean coordination number of all nodes in skeleton network ($\overline{CN}$), mean coordination number of branching nodes in skeleton network ($\overline{CN}_{br}$).

	Ni/Al_2O_3		Al_2O_3	
	dried	calcined	dried	calcined
ϵ_M / %	43.9	44.5	34.9	33.6
ϵ_m / %	29.4	23.4	34.3	30.1
ϵ_{tot} / %	73.3	67.9	69.2	63.7
$\overline{d}_{eq}$ / µm	2.54 ± 0.65	2.43 ± 0.66	1.54 ± 0.41	1.19 ± 0.31
$\overline{d}_{pore}$ / µm	1.36 ± 0.44	1.17 ± 0.39	0.57 ± 0.20	0.47 ± 0.17
$\overline{l}_{cu,pore}$ / µm	1.64 ± 1.02	1.51 ± 0.83	1.03 ± 0.55	0.85 ± 0.49
$\overline{\tau}$ / 1	1.1 ± 0.1	1.1 ± 0.3	1.1 ± 0.1	1.1 ± 0.1
$\overline{CN}$ / 1	2.3 ± 1.0	2.6 ± 1.0	2.6 ± 1.0	2.4 ± 1.0
$\overline{CN}_{br}$ / 1	3.1 ± 0.3	3.1 ± 0.4	3.1 ± 0.4	3.1 ± 0.3

The macropore structure can be further characterized by the equivalent spherical pore diameter (d_{eq}, *c.f.* eq. 3.19) of the individually labeled pores (Figure 5.5). The porosity-weighted d_{eq} distribution for Ni/Al_2O_3 and Al_2O_3 are shown in Figure 5.5c,f, respectively. From these distributions, the mean $\overline{d}_{eq}$ was extracted (Table 5.1). The $\overline{d}_{eq}$ slightly decreased from Ni/Al_2O_3-dr to Ni/Al_2O_3-calc after calcination, showing comparable values to the activated catalyst studied previously ($\overline{d}_{eq} = 2.55 \pm 0.2\,\mu m$, *c.f.* section 4.3).[236] For Al_2O_3, the decrease of $\overline{d}_{eq}$ was more pronounced after calcination, also clearly visible in the d_{eq} distribution (Figure 5.5f).
As d_{eq} is only a strictly correct assumption for spherical pores and in our case rather represents the pore body of the macropores, the macropore shape and structure were further characterized using a skeleton based pore network model (*c.f.* section 3.4.9 and appendix section 8.4 for details). The retrieved pore network models consist of connected spatial graphs, constructed from pore nodes connected to each other via pore segments. The pore network models for Ni/Al_2O_3-dr,

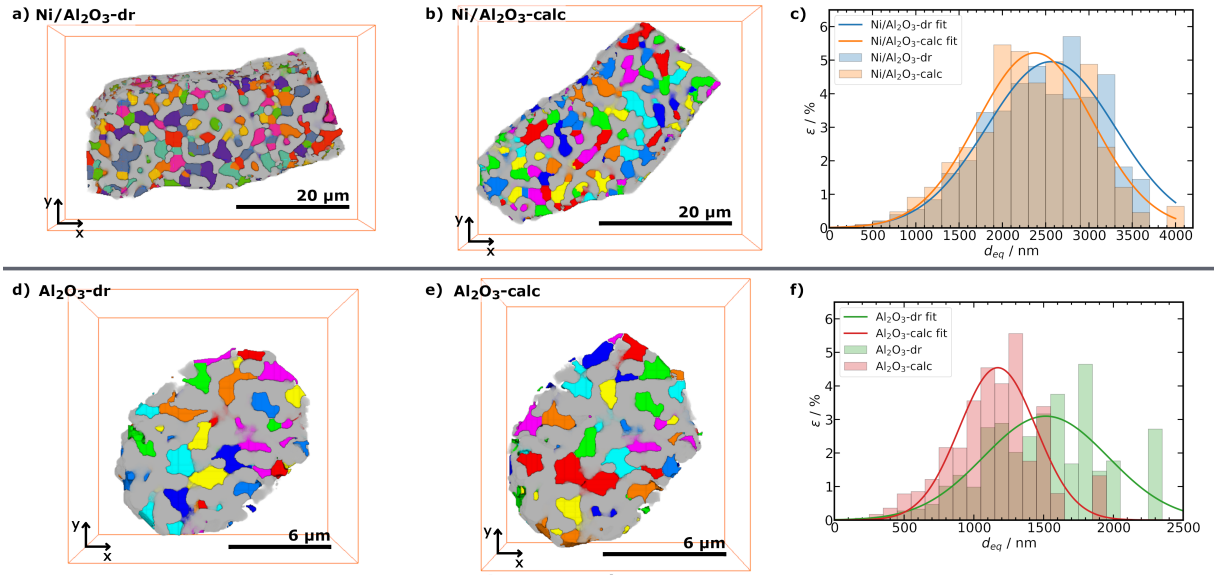


Figure 5.5: "Equivalent spherical diameter (d_{eq}) analysis of separated pore labels from PXCT. Volume renderings of pores (8-bit color code) and material (gray) labels for (a) Ni/Al_2O_3-dr, (b) Ni/Al_2O_3-calc, (d) Al_2O_3-dr and (e) Al_2O_3-calc. Porosity (ϵ) depending on d_{eq} and Gaussian fit for (c) Ni/Al_2O_3 (d_{eq} binning of 200 nm, number of analyzed pores: Ni/Al_2O_3-dr 971 and Ni/Al_2O_3-calc 880) and (f) Al_2O_3 (d_{eq} binning of 100 nm, number of analyzed pores: Al_2O_3-dr 217 and Al_2O_3-calc 265)."[237] Available under the terms and conditions of the Creative Commons Attribution 4.0 license (CC BY 4.0, `https://creativecommons.org/licenses/by/4.0/`), Copyright ©2022.

Ni/Al_2O_3-calc, Al_2O_3-dr and Al_2O_3-calc are plotted in (Figure 5.4(a2-d2)). A single primary spatial graph (i.e. a fully connected network of pore segments) was identified for all samples, which confirms the presence of a well-connected macropore structure in each case. Further analysis was restricted to this main graph, therefore excluding any outlying or disconnected features, e.g., at the external particle boundary. For each pore segment, a cylindrical macropore radius/diameter (r_{pore}/d_{pore}), segment volume, segment tortuosity (τ), and segment length ($l_{cu,pore}$) can be retrieved. For each node, the location in the particle, coordination number, and thus amount of terminating and branching nodes, can be analyzed. The location of nodes and segments is defined here by the distance to the gravimetric center of the particle volume (d_{center}), while the segment coordinates are approximated as the center point of the connected nodes. Statistical analysis results of the pore network models are shown in Figure 5.6a-c for Ni/Al_2O_3 and Figure 5.6d-f for Al_2O_3, respectively.

Figure 5.6a,d shows the r_{pore} distribution of each segment relative to d_{center} for Ni/Al_2O_3 and Al_2O_3, with scatter sizes indicating normalized relative segment volume ($V_{rel,norm}$). For both samples, calcination generally led to a decrease in the macropore radii (r_{pore}) and appeared to indicate particle volume shrinkage, with a higher density of segments observed at lower d_{center} values after calcination. The significance of the segment r_{pore} distribution was tested

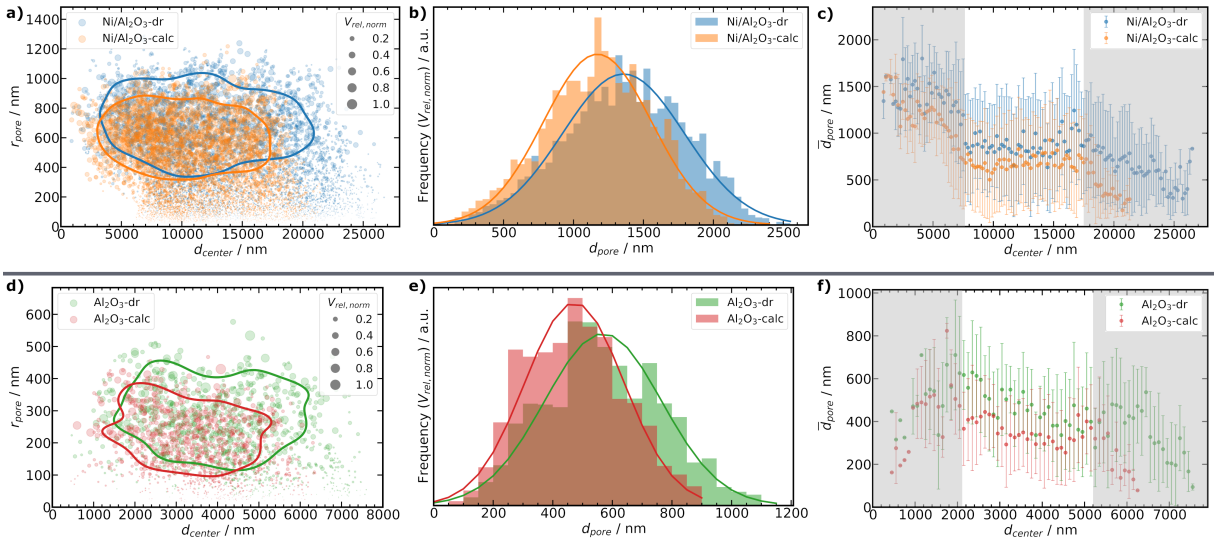


Figure 5.6: "Characterization based on pore network models in Figure 5.4(a2-d2). (a,d) pore radius (r_{pore}) depending on distance to the particle center (d_{center}), with scatter size showing relative normalized pore volume ($V_{rel,norm}$) for Ni/Al_2O_3 and Al_2O_3, respectively. Contours represent the $V_{rel,norm}$ weighted probability to enclose 75 % of all pores (*c.f.* section 3.4.9, number of segments as pores: Ni/Al_2O_3-dr 6415, Ni/Al_2O_3-calc 5654, Al_2O_3-dr 1078, and Al_2O_3-calc 1119). (b,e) $V_{rel,norm}$ weighted pore diameter (d_{pore}) distribution for Ni/Al_2O_3 and Al_2O_3, respectively. (c,f) Dependence of mean pore diameter ($\overline{d}_{pore}$) on d_{center} for Ni/Al_2O_3 (d_{center} binning 200 nm) and Al_2O_3 (d_{center} binning 100 nm), respectively. Data is shown as mean values with standard deviation as errorbars. Shaded regions indicate low statistical relevance defined by qualitative inspection of the volumes (surface and core artifacts)."[237] Available under the terms and conditions of the Creative Commons Attribution 4.0 license (CC BY 4.0, `https://creativecommons.org/licenses/by/4.0/`), Copyright ©2022.

by performing a kernel density estimation (KDE) of the volume weighted 2D histograms (*c.f.* Figure 8.20, 8.21) as implemented in the python seaborn package[286]. The resulting KDE-contours enclose 75 % of the volume weighted segments highlighting differences between the dried gel and calcined states. The decrease in macropore radii is additionally highlighted by the $V_{rel,norm}$ weighted distribution of d_{pore} shown in Figure 5.6b,e for Ni/Al_2O_3 and Al_2O_3. The mean macropore diameter ($\overline{d}_{pore}$) calculated from the spatial graphs therefore also decreased after calcination for both catalysts as expected (Table 5.1). Furthermore, the volume shrinkage observed previously during the *in situ* XRP studies and on visual inspection of the PXCT data was also confirmed (Figure 5.6a,d). In addition to the overall d_{pore} distribution, Figure 5.6c,f highlights the dependence of $\overline{d}_{pore}$ on d_{center} for each catalyst system. Small and large d_{center} values indicated by the shaded region in Figure 5.6c,f, were not considered statistically relevant due to limited sampling volume, and likelihood of anomalous values at the external particle boundary. In general and particularly for Ni/Al_2O_3, a quite homogeneous $\overline{d}_{pore}$ distribution was observed independent of position within the particle as defined by d_{center}. This further supports the presence of a homogeneous and well-ordered macropore structure in each sample. The distribution of $\overline{d}_{pore}$ relative to d_{center} did not change significantly following calcination.

In addition to quantification of porosity characteristics, further information is readily available from tomographic image analysis, which cannot be directly retrieved from N_2 sorption or Hg porosimetry analysis. For example, segment tortuosity (τ) and coordination number of the nodes (CN) can be derived (Table 5.1). Here the mean coordination number $\overline{CN}$ of the nodes was between 2.3 to 2.6 for all samples. As these values are strongly influenced by terminal nodes at the particle exterior, the mean coordination number including only branched nodes ($\overline{CN}_{br}$) is also reported (Table 5.1), which is more sensitive to potential internal changes of the pore structure compared to $\overline{CN}$. $\overline{CN}_{br}$ was 3.1 for all four samples. The average segment tortuosity ($\overline{\tau}$) was 1.1 for all four samples. As the segments are short compared to the sample volume investigated by PXCT, $\overline{\tau}$ should not be mistaken for macroscopic tortuosity, which is typically employed for diffusion calculations.[332] However, τ can be used to search for specific regions in the pore network that might form a bottleneck for mass transport in such highly connected pore structures. Therefore, $\overline{CN}$ and $\overline{\tau}$ were analyzed regarding their dependence on d_{center} as shown in Figure 8.17, 8.18, respectively. No significant changes were observed for either catalyst system between dried gel and calcined states. This supports the results from the overall mean values of $\overline{CN}$, $\overline{CN}_{br}$ and $\overline{\tau}$ confirming a homogeneous macropore structure. Furthermore, this quantitatively confirms the observations made during the *in situ* XRP experiments, indicating no obvious pore opening, closing, or disruption of the macropore network."[237]

5.1.6 Electron Density Analysis of PXCT Data

"Direct quantification of the pore structure based on image analysis is generally restricted to the spatial resolution of the measurement. Here, PXCT offered sufficient spatial resolution (ca. 50 to 90 nm) for detailed analysis of the majority of macropores. On the other hand, direct quantification of mesopore features below the spatial resolution limit was neither feasible nor statistically meaningful. However, an advantage of PXCT compared to other tomographic imaging methods is that quantitative information about the local N_e can be obtained, which is indicative of the material composition at each sampling point regardless of the exact spatial resolution.[156–158, 183] The overall N_e histogram of the whole particle volumes measured by PXCT is shown in Figure 5.7a,d for Ni/Al_2O_3 and Al_2O_3, respectively. Three main features were observed and labeled, corresponding to the image segmentation procedure discussed previously: $N_e \approx 0\,e^-\,Å^{-3}$ as air/macropores (pores label), $N_e \approx 0.5$ to $0.55\,e^-\,Å^{-3}$ as nanoporous material (material label), and $N_e > 0.9\,e^-\,Å^{-3}$ labeled as contamination from sample preparation. Already in the overall N_e distribution (Figure 5.7a,d), and individual N_e slices (Figure 5.4(a3-d3)) of the whole particle volume, a significant shift of the material label peak to higher values of ≈ 0.6 to $0.65\,e^-\,Å^{-3}$ was observed after calcination of the dried gels for both catalyst systems. This may indicate a densification of the nanoporous material, also supported by an increase of the skeletal density (ρ_{skel}) observed by He pycnometry after calcination of the dried gel samples (*c.f.* Table 8.3). Figure 5.7b,e shows the slice dependent analysis of the mean electron density ($\overline{N}_e$)

of the whole particle volume for Ni/Al_2O_3 and Al_2O_3, respectively. Slice dependent analysis allows for easy identification and exclusion of regions with strong contamination from further analysis.[239]

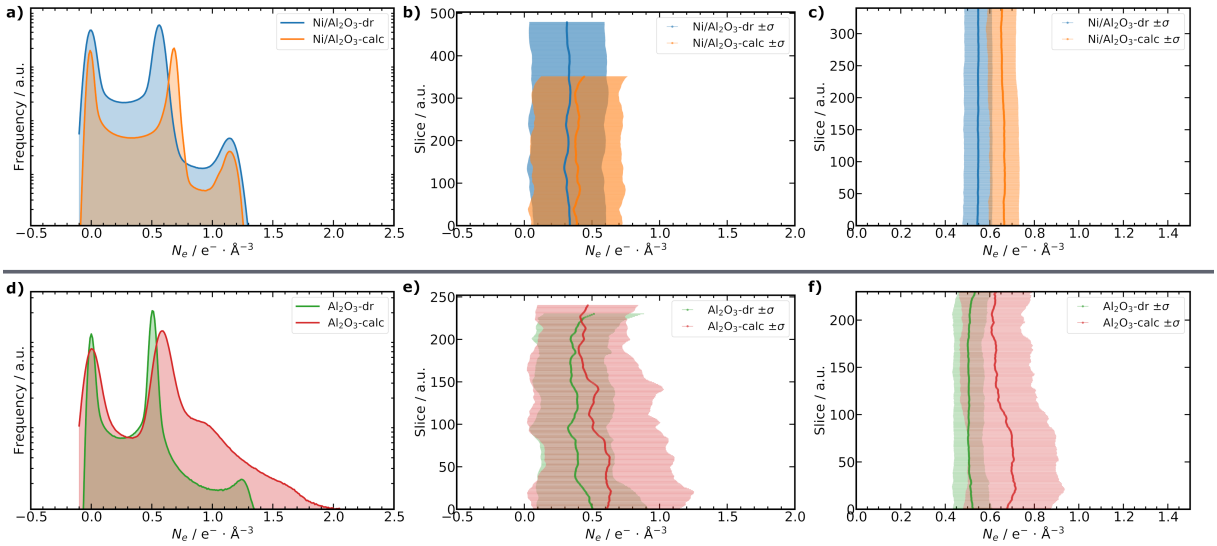


Figure 5.7: "Electron density (N_e) analysis of PXCT data. (a,d) N_e distribution for the whole particle volumes of Ni/Al_2O_3 and Al_2O_3, respectively. (b,e) Slice dependent analysis of the mean N_e with standard deviation (σ) as errorbars for the whole particle volume of Ni/Al_2O_3 and Al_2O_3, respectively. (c,f) Selected slice range analysis of the mean N_e with σ as errorbars only for the segmented material label of the nanoporous solid for Ni/Al_2O_3 and Al_2O_3, respectively."[237] Available under the terms and conditions of the Creative Commons Attribution 4.0 license (CC BY 4.0, `https://creativecommons.org/licenses/by/4.0/`), Copyright ©2022.

For the segmented material label, the overall N_e distribution is shown in Figure 8.16 and the slice dependent analysis of $\overline{N}_e$ in Figure 5.7c,f for Ni/Al_2O_3 and Al_2O_3, respectively. For Ni/Al_2O_3, a homogeneous and significant shift of $\overline{N}_e$ is found for the selected slice range (Figure 5.7c). In the case of Al_2O_3, a similar significant shift of $\overline{N}_e$ was observed (Figure 5.7f), while the $\overline{N}_e$ of Al_2O_3-calc was not as homogeneous as for Ni/Al_2O_3-calc. This can be partly attributed to the smaller sample volume of the Al_2O_3 particle compared to Ni/Al_2O_3 and thus stronger influence of the surface structure accompanied with surface defects and artefacts. Furthermore, some increased formation of contaminant species was observed after calcination of Al_2O_3 (Figure 5.4(d3)) probably originating from the tip of the Cu sample pin, which was not found for Ni/Al_2O_3. Nevertheless, both systems confirm an increase in N_e for the material label, corresponding to a densification of the nanoporous solid after calcination.

With prior knowledge about the chemical composition, the observed N_e can be converted into observed mass density (ρ),[156, 157] in order to indirectly measure porosity even below the spatial resolution limit of the measurement. This was similar performed and already shown for the SPP2080-IMRC discussed in section 4.1 and is detailed in section 3.4.9. The porosity of the

material label (ϵ_{mat}) can be derived by comparing the observed (ρ) and theoretical mass density (ρ_{theo}). Subsequently, ϵ_{mat} was used to calculate the mesoporosity (ϵ_m) and total porosity (ϵ_{tot}) of the samples, with ϵ_{tot} as the sum of ϵ_M and ϵ_m. The theoretical density of the structures can be obtained from a known crystal structure or approximated experimentally as ρ_{skel} by He pycnometry (*c.f.* Table 8.4). For Al_2O_3, ρ_{theo} was taken as the X-ray density of a reported γ-Al_2O_3 structure,[100] and for Ni/Al_2O_3 ρ_{theo} was defined as ρ_{skel} determined experimentally by He pycnometry. The mode of the N_e distribution of the material label (*c.f.* Table 8.4) was then used to calculate ϵ_{mat}, from which ϵ_m and ϵ_{tot} were derived (Table 5.1). An exact chemical composition of the dried gel materials Al_2O_3-dr and Ni/Al_2O_3-dr is unknown, as these probably still contain organic and solvent residues as shown by CHN-analysis. For simplification and in order to calculate ρ, the chemical composition of the dried gels was approximated by the known structures of the calcined samples ($Ni_{0.43}Al_2O_4$, γ-Al_2O_3).[236, 238, 312] It is therefore important to note that only for the calcined states do the above porosity values correspond to true porosity. Since ϵ_{mat}, ϵ_m and ϵ_{tot} are calculated based on sub-resolution information, i.e., local N_e of the material label, therefore the porosity values of the dried gels are influenced by organic and solvent residues, potential intermediate Al_2O_3 and Ni/Al_2O_3 structures or blocked pores which cannot be directly resolved. In this respect, mesoporosity values are described as an "apparent" ϵ_m for the dried gels, which can only be carefully compared to conventional pore characterization methods. In more detail, the "apparent" ϵ_m for the dried gels from PXCT can hardly resolve or distinguish between accessible or inaccessible porosity, as it is a sub-resolution information. This is contrary to conventional methods, i.e., Hg porosimetry and N_2 sorption, which indeed can only resolve accessible pores to the respective probe species (Hg or N_2). Therefore, ϵ_m from PXCT experiments and conventional methods can only be strictly compared for the calcined samples. In the calcined samples, ϵ_m is not influenced anymore by solvent or organic residues, which might fill the mesopores in the dried gel state making them inaccessible for conventional methods. Nevertheless, this information provides valuable and potentially quantitative insights into sample changes occurring during calcination.

On calcination of Ni/Al_2O_3-dr to form Ni/Al_2O_3-calc, ϵ_m decreased from 29.4 % to 23.4 % and ϵ_{tot} from 73.3 % to 67.9 %. A similar trend was also observed for Al_2O_3-dr to Al_2O_3-calc, where ϵ_m decreased from 34.3 % to 30.1 % and ϵ_{tot} from 69.2 % to 63.7 %. Thus, during calcination a significant densification of the nanoporous solid occurs for both systems. ϵ_m of Ni/Al_2O_3-calc is well in line with the value of 24.1 % previously reported by electron tomography on the activate Ni/Al_2O_3-h sample in section 4.3, where direct imaging of mesopores is feasible due to much higher spatial resolution than PXCT.[236] It is important to note however, that electron tomography is restricted to samples with several orders of magnitude smaller volume than can be measured with hard X-ray tomography. Particularly for hierarchically porous or complex catalysts, X-ray microscopy potentially provides a more representative view of the sample structure. The derived ϵ_m is also in agreement with the previously shown Hg porosimetry combined with He pycnometry (*c.f.* section 4.3).[236] However, conventional porosimetry techniques probe only the bulk sample

and cannot provide spatially-resolved data comparable to that produced by tomography. The agreement with electron tomography and Hg porosimetry therefore validates the quantitative N_e based porosity analysis enabled here by PXCT, even if the resolution is currently not high enough to directly visualize mesopores in the sample."[237]

5.1.7 Pore Structure Evolution During Calcination

"The deconvolution of different processes occurring during synthesis and treatment of hierarchical materials (e.g. by calcination) and their influence on the final pore structure is challenging to unravel. In previous work, Tokudome *et al.* proposed that mesopores were generated during calcination by crystallization of alumina, as they were not detected by Hg porosimetry in the dried gels.[312] In the current study, the presence of macropores in Al_2O_3-dr and Ni/Al_2O_3-dr was found by Hg porosimetry, which was shown by PXCT, XRP, and SEM imaging to be an ordered and connected macropore network. While the resolution of PXCT obtained here was not sufficient to study mesopores directly, N_e analysis revealed an apparent ϵ_m of about 29 % and 34 % for Al_2O_3-dr and Ni/Al_2O_3-dr, respectively. From these results it may be concluded that the mesopore system is probably already pre-organized in the dried gels, but filled with solvent or polymer species, while exact knowledge about the precursors oxide structure is missing.
During calcination, PXCT and *in situ* XRP revealed an extensive overall volume shrinkage accompanied with a densification of the nanoporous solid, which is also in line with observations during calcination in the laboratory synthesis. While *in situ* XRP could monitor the changes occurring in real time under controlled gas and temperature conditions, PXCT was required to quantify these changes in terms of pore structure. Based on PXCT, the sample macroporosity was almost constant during calcination, while the mesoporosity and total porosity decreased for both systems (see Table 5.1). A decrease was also observed for both d_{eq} and d_{pore} after calcination based on PXCT. $w_{P,M,Hg}$ obtained from Hg porosimetry showed the same trend for Ni/Al_2O_3 and a similar sample of Al_2O_3 compared to the imaging studies. N_2 sorption analysis of Al_2O_3-dr revealed presence of mesopores in the dried gel, while a mild thermal treatment at 373 K was carried out before the experiment. The heat treatment can be sufficient to already remove solvent or H_2O from the dried gel leading to changes of the sample. For Ni/Al_2O_3-dr no significant mesopores were identified by N_2 sorption. This obviously illustrates a major drawback of conventional methods compared to PXCT in studying sol-gel materials in the intermediate stages of synthesis. While in PXCT such method related changes can be identified by analysis of the acquired subtomograms, which revealed some X-ray beam induced sample changes for the dried gel samples in the beginning of the measurement as described in the experimental procedure (*c.f.* section 3.4.6).
The advantages of X-ray tomography based pore characterization compared to Hg porosimetry to derive quantitative pore structure descriptors has been reported in several studies.[211, 212, 236, 306–308, 328] In the present work $\overline{CN}_{br}$ is 3.1 for all four studied samples, from which it

can be concluded that during calcination no major changes of the connectivity of the macropore network occur. This is furthermore supported by the analysis of the segment τ and that for all PXCT data sets only one major spatial graph was identified to represent the pore network. The scanning of the same particles of Al_2O_3 and Ni/Al_2O_3 as dried gels and after calcination of these gels allows to directly compare the results for both states. This eliminates the challenge of selecting a representative sample particle, which is a common problem for imaging methods as illustrated in the introduction Figure 1.9. Changes of macropores upon thermal treatment investigated by X-ray microtomography have been reported in literature.[333–335] However, the resolution of X-ray microtomography can only cover larger macropores and not all relevant macropore length scales. PXCT as shown in this study enables to routinely study materials with sub 50 nm resolution on tens of µm sample sizes, in the current implementation.
The experimental strategy shown here can be generally employed to study textural and structural changes of materials with high spatial resolution, for example during thermal treatment as shown here. *In situ* XRP can be currently performed in 2D experiments, while a future extension into 3D studies is feasible. This allows to actually follow the evolution of porous materials during their synthesis and to elucidate the influence of different process steps that are typically required. The method is not only limited to the sol-gel strategy discussed in this work, but can be readily extended to templating, casting or other self-assembly strategies which are common in literature.[125, 127, 136–145] On the other hand, a combination with *ex situ* PXCT allows to directly retrieve quantitative 3D spatially-resolved textural and structural information about different states of the synthesis. Additionally, combining X-ray ptychography with other contrast modes, like X-ray fluorescence, X-ray diffraction or X-ray absorption spectroscopy can lead to further complementary insights into the studied material as already presented in the introduction section 1.5."[237]

5.1.8 Conclusions

The present section showed how advanced hard X-ray imaging methods, i.e., X-ray ptychography allow to follow the evolution of the pore structure of a hierarchically porous Ni/Al_2O_3 catalyst during calcination of the dried gels. The hierarchical pore structure was already confirmed in section 4.3 by a combination of PXCT and ET with conventional methods. Conventional porosity analysis methods, like gas sorption and Hg porosimetry do not allow do understand changes of the pore structures while they take place as they cannot be applied *in situ*. Furthermore, their application on fragile sample states, like the dried gels can be challenging and the methods can be regarded as invasive. However, detailed knowledge about porosity formation is required in order to be able to tailor the pore structure in a knowledge-based catalyst design.
In this section, *in situ* 2D X-ray ptychography imaging allowed to follow the sample changes under very controlled gas and temperature conditions during calcination, activation and reaction conditions of the dried gel from the Ni/Al_2O_3-h previously discussed in section 4.3. This is

combined with a quantification of those changes, which were retrieved by performing PXCT on identical particles in the dried gel state and after calcination. Significant shrinkage of the macropore diameter was found from the dried gel to the calcined state, while the connectivity of the macropore network kept unchanged and the macropore network was already formed in the dried gel state. Additionally, PXCT allowed to retrieve information about the local electron density changes of the sample during calcination, revealing a densification of the nanoporous solid containing the mesopores. Therefore, a decrease of the apparent mesoporosity during calcination was observed. Hard X-ray ptychography was shown as an emerging technique allowing for detailed understanding of the evolution of textural properties of catalysts, which can also be applied to other systems or synthesis routes. The approach might be applied also in other fields of material science, e.g., adsorbents or membranes.

An open challenge is the unknown exact atomic structural evolution from the dried gel during calcination. This information cannot be directly provided by X-ray ptychography, being one limitation in the sub-resolution analysis of the mesoporosity based on the electron density, which requires knowledge about present atomic/crystalline structures. Therefore, complementary structural methods, i.e., X-ray total scattering, to understand the sample evolution during calcination are applied in the following section 5.2.

5.2 Resolving Structural Changes During Calcination by X-ray Total Scattering[3]

5.2.1 Introduction

In the previous section 5.1 the evolution of the pore structure of hierarchically porous Ni/Al_2O_3 and Al_2O_3 catalysts was presented. On the one hand, this highlighted strong textural changes of the samples from the dried gels towards the calcined samples. On the other hand, the resolution and contrast mode of X-ray ptychography does not allow to retrieve information about changes of the atomic structure of the catalysts. Furthermore, as illustrated in Figure 1.9, X-ray ptychography is a very localized method, which at present can only probe small sample volumes. However, detailed understanding also on changes of the atomic configuration during calcination and for larger sample volumes are required for future knowledge-based tailored synthesis.[336] As already reviewed for spatially-resolved characterization methods and different X-ray probes in the introduction sections 1.5.1, 1.5.3, Figure 1.11, there are hard X-ray methods allowing to retrieve atomic structure information, e.g., XRD, XAS, PDF. Those methods have to be ideally applied while the synthesis is performed, i.e., *in situ* to gain knowledge about different potential intermediates formed during synthesis, which might influence the final material.[336]
As discussed with changes of the electron density during calcination in section 5.1, knowledge about the atomic configuration is important to retrieve true mesoporosity and not only an apparent mesoporosity information. Furthermore, in section 4.3 the incorporation of Ni into the $\gamma-Al_2O_3$ structure was found, which should be ideally prevented for enhanced reducibility of the catalyst. In the present section, *in situ* X-ray total scattering experiments during calcination of dried gels of Ni/Al_2O_3-h and Al_2O_3-h samples were performed. The combined powder X-ray diffraction (PXRD) and pair distribution function (PDF) analysis allows to retrieve information about local and long range ordered structures.[299–301] Therefore, it is possible to investigate (nano-)crystalline as well as amorphous structures and their transformation during the calcination process. An understanding of those transformation processes is complementary important to the studies on the porosity formation presented in section 5.1. The combined understanding of textural and structural (atomic scale) changes is important for a fundamental knowledge of the sample changes of the dried gels during calcination. The results presented in this section provide some initial information about structural phase transformations during calcination.

5.2.2 *In Situ* Calcination Followed by PXRD

X-ray total scattering experiments were performed at an energy of 102 keV (wavelength of 0.1215 Å) at beamline P21.1 of the Deutsches Elektronen Synchrotron DESY (Hamburg, Germany), which

[3]X-ray total scattering measurements were assisted and supported by L. Klag, S. Das (ITCP, Karlsruhe Institute of Technology (KIT)), K. L. Abel (Universität Leipzig), A.-C. Dippel, O. Gutowski, S. Bannerjee and P. Glaevecke (Deutsches Elektronen-Synchrotron DESY, Hamburg)

allowed to retrieve both, PXRD and PDF data of the samples as detailed in the experimental section 3.5.2. The *in situ* calcination of the dried gels Ni/Al_2O_3-dr and Al_2O_3-dr was performed under a total gas flow of 10 mL 10 %O_2/He. In this section, first the *in situ* PXRD results are briefly presented together with the on-line gas analysis, while *in situ* PDF data is presented in the following section 5.2.3.

Figure 5.8 shows the on-line mass spectrometry (MS) data together with a 2D map of the averaged PXRD (10 s average, *c.f.* section 3.5.2) for the Ni/Al_2O_3 sample starting from the dried gel Ni/Al_2O_3-dr. The PXRD data is corrected for background contributions from the setup and capillary as detailed in section 3.5.2. In the beginning of the *in situ* calcination a

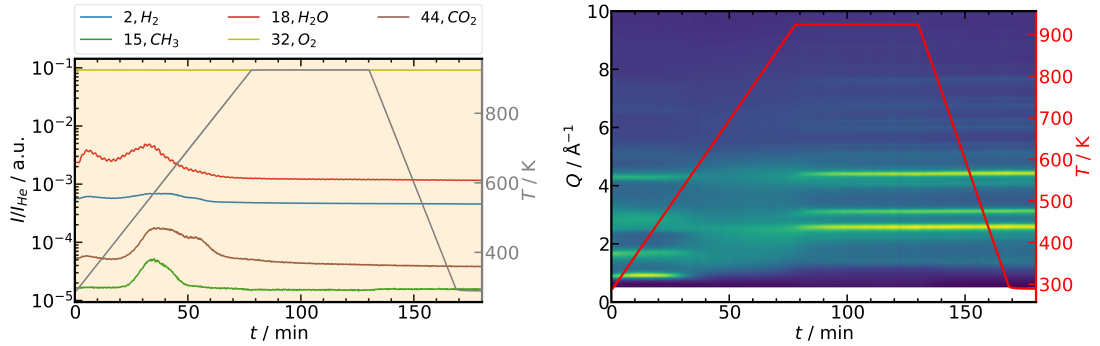


Figure 5.8: On-line mass spectrometry data (left) and 2D map of the *in situ* PXRD (right) acquired during calcination of the dried gel Ni/Al_2O_3-dr sample. Total gas flow of 10 mL 10 %O_2/He.

nanocrystalline structure is present, which might be explained by a Boehmite type AlO(OH) structure ($\gamma-$AlO(OH)).[96, 294] Similar, this is observed for the Ni free sample as shown in Figure 5.9. The MS data acquired during *in situ* calcination of both dried gels reveals formation

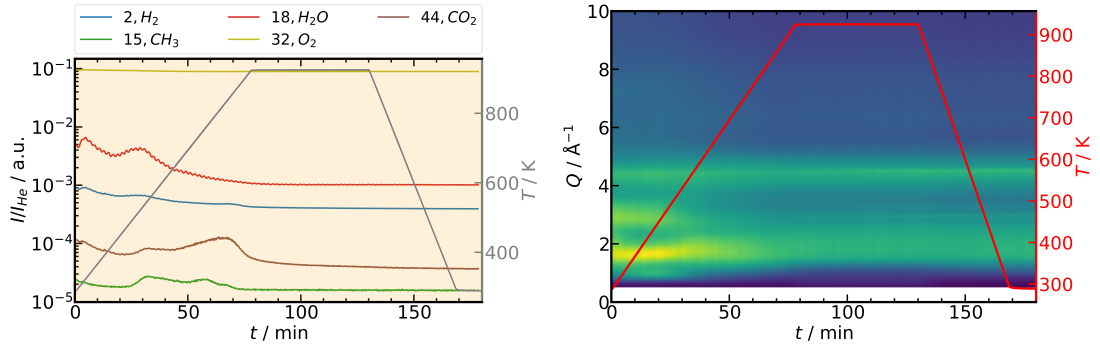


Figure 5.9: On-line mass spectrometry data (left) and 2D map of the *in situ* PXRD (right) acquired during calcination of the dried gel Al_2O_3-dr sample. Total gas flow of 10 mL 10 %O_2/He.

of H_2O and species related to organic compounds (CO_2, CH_3 signals) during heating (Figure 5.8, 5.9). Remarkably, a rather distinct early H_2O signal can be observed at temperatures of a about 373 K, which might correspond to evaporated H_2O that was present inside the dried gels. A second H_2O and peaks related to organic compounds can be observed at higher temperatures starting

at about 573 K. Interestingly, those fit to the temperature at which also the nanocrystalline $\gamma-$AlO(OH) reflexes vanish and the PXRD shows only amorphous contributions (Figure 5.8, 5.9).

The initial $\gamma-$AlO(OH) structure differs for the two dried gels, which can be readily observed in the Rietveld refinements of Ni/Al_2O_3-dr and Al_2O_3-dr for the scan numbers 1 as shown in Figure 5.10, 5.11, respectively. For Ni/Al_2O_3-dr the $\gamma-$AlO(OH) appears to be more

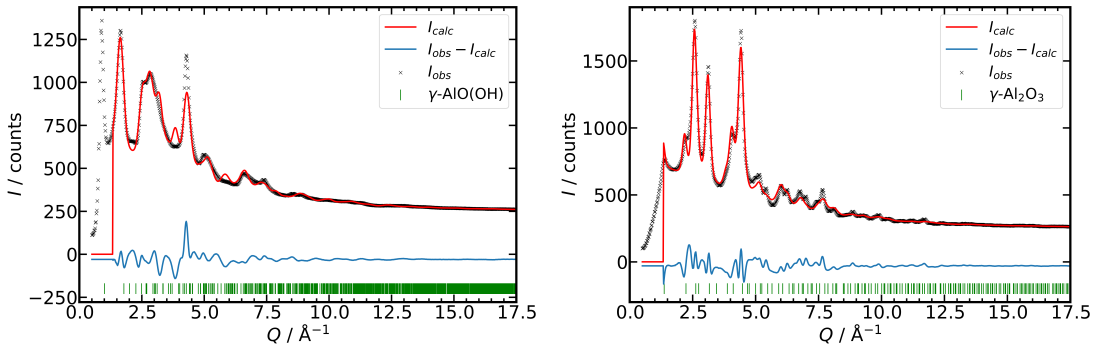


Figure 5.10: Rietveld refinement of the scan number 1 (left) representing the dried gel Ni/Al_2O_3-dr and 1050 (right) showing the calcined state Ni/Al_2O_3-calc after *in situ* calcination. (*c.f.* Table 8.5, 8.6)

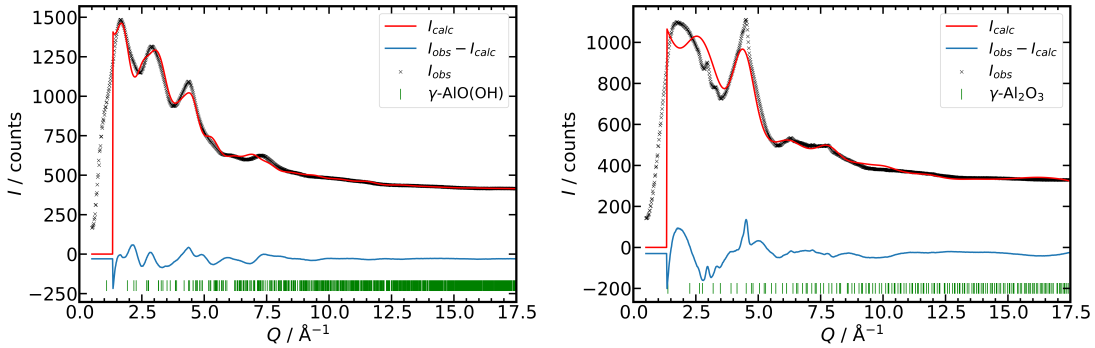


Figure 5.11: Rietveld refinement of the scan number 1 (left) representing the dried gel Al_2O_3-dr and 1050 (right) showing the calcined state Al_2O_3-calc after *in situ* calcination. (*c.f.* Table 8.5, 8.6)

crystalline, which is also confirmed by the microstructure analysis as part of the Rietveld analysis (*c.f.* Table 8.5). The crystallite size L_{vol} is with 2.15 ± 0.04 nm larger than 1.090 ± 0.019 nm for Al_2O_3-dr. Additionally, the lattice parameters differ strongly with Ni/Al_2O_3-dr showing an enlarged unit cell compared to Al_2O_3-dr (*c.f.* Table 8.5). However, due to the strong nanocrystalline nature of the presumable $\gamma-$AlO(OH) phase, the refinement quality is limited towards reliable structural information. Therefore, the results are discussed as observed trends. During further heating in the *in situ* experiment, the appearance of a new crystalline phase can be observed for Ni/Al_2O_3, which is denoted as Ni/Al_2O_3-calc. The phase formation coincidences with reaching the final calcination temperature of 923 K. It should be noted that higher temperature could not be reached reliably with the employed experimental configuration. In case of Al_2O_3, a

slight increase in intensity and potentially sharpening of the reflex at $\approx 4.5\,\text{Å}^{-1}$ can be observed, with this final state denoted as Al_2O_3-calc. However, no distinct crystallization as for Ni/Al_2O_3-calc was found.
Rietveld refinement for selected scans of Ni/Al_2O_3-calc and Al_2O_3-calc are presented in Figure 5.10 and 5.11, respectively (*c.f.* Table 8.6). Ni/Al_2O_3-calc could be properly described by a defect $\gamma-Al_2O_3$ structure based on the model from Smrčok *et al.*.[293] Similar to refinements of the laboratory data on calcined Ni/A_2O_3-h presented in section 4.3, Al occupancies were attempted to be refined. This was also tried for Al_2O_3-calc, which indeed allowed a refinement, but due to the nanocrystalline nature those results should be only discussed carefully and the refinement quality is very limited. For Ni/Al_2O_3-calc the refined L_{vol} is $6.0 \pm 0.6\,\text{nm}$, while for Al_2O_3-calc it is $0.632 \pm 0.015\,\text{nm}$. On the one hand, this illustrates the nanocrystalline nature of Al_2O_3-calc, otherwise with a unit cell size of 7.8636 Å this resembles almost only a single unit cell showing the limitation of PXRD and Rietveld refinement to properly analyze this state of the material. Therefore, complementary PDF analysis was performed to obtain further insides into the dried gel and calcined states as well as the amorphous transition phase.

5.2.3 *In Situ* Calcination Followed by PDF

The zoomed 2D maps showing the evolution of the PDF during the *in situ* calcination of Ni/Al_2O_3-dr and Al_2O_3-dr are presented in Figure 5.12 (*c.f.* Figure 8.25 for extended r range). Similar to

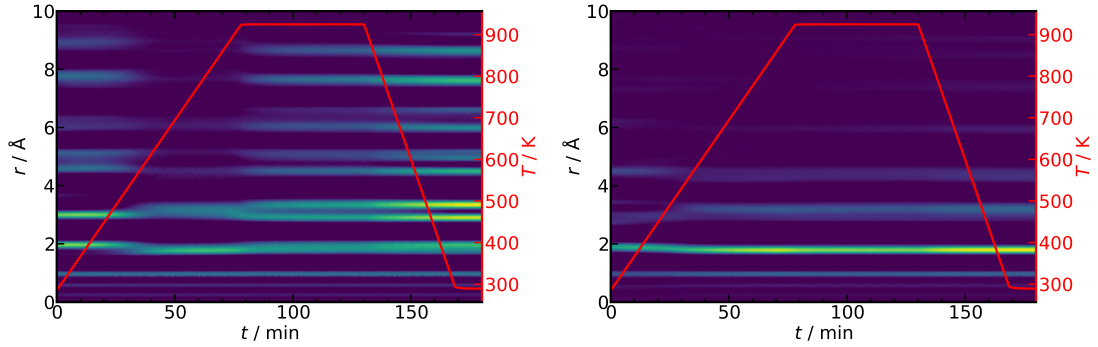


Figure 5.12: 2D maps of the *in situ* PDF for a zoomed r range acquired during calcination of the dried gels Ni/Al_2O_3-dr (left) and Al_2O_3-dr (right). Total gas flow of 10 mL 10 %O_2/He.

the PXRD data, PDF reveals the transition from the initial nanocrystalline $\gamma-$AlO(OH) phase into a rather amorphous structure at about 573 K. Comparing Ni/Al_2O_3-dr and Al_2O_3-dr, it appears that the $\gamma-$AlO(OH) phase is far more ordered in case of the Ni containing samples. However, also for Al_2O_3-dr changes in the same temperature range of the structural order can be observed, but not as pronounced. The initial dried gel states at scan number 1 and the final calcined states at scan number 1050 were used in preliminary structural refinements of the PDF data using the same initial structural models for $\gamma-$AlO(OH) (dried gel) and $\gamma-Al_2O_3$ (calcined) as for Rietveld refinement of PXRD. The PDF fittings are presented for Ni/Al_2O_3 and Al_2O_3 in

Figure 5.13 and 5.14,respectively (*c.f.* Table 8.5, 8.6).

In the refinements, the differences in atomic order can be readily observed. Al_2O_3-dr only shows

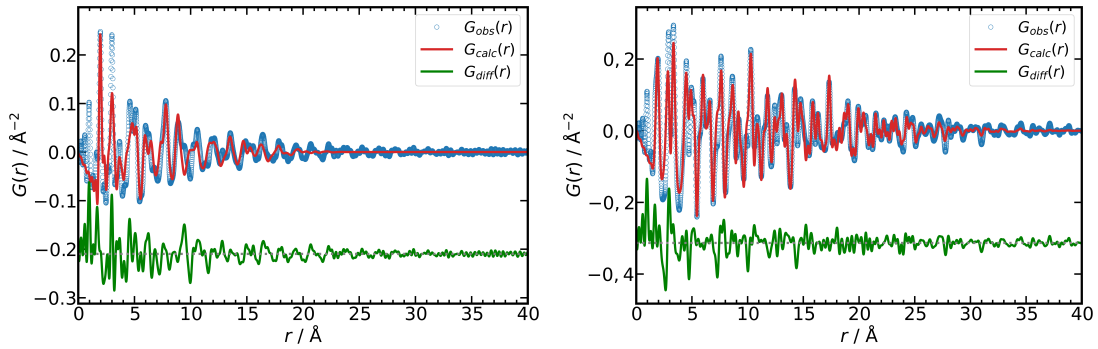


Figure 5.13: PDF refinement of the scan number 1 (left) representing the dried gel Ni/Al_2O_3-dr and 1050 (right) showing the calcined state Ni/Al_2O_3-calc after *in situ* calcination. (*c.f.* Table 8.5, 8.6)

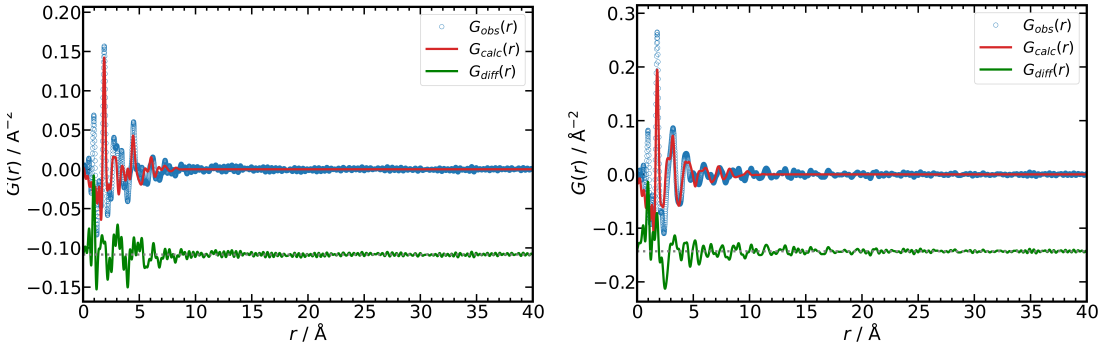


Figure 5.14: PDF refinement of the scan number 1 (left) representing the dried gel Al_2O_3-dr and 1050 (right) showing the calcined state Al_2O_3-calc after *in situ* calcination. (*c.f.* Table 8.5, 8.6)

contributions from a few coordination shells below ≈1 nm. On the other hand, Ni/Al_2O_3-dr exhibits some kind of order up to ≈2 nm. In both cases initial fitting attempts were only performed using the $\gamma-$AlO(OH) structure model by Milligan *et al.*[294] However, it can be observed that these fitted models do not yet describe the present structures fully or contributions of secondary phases might be present that could not be identified yet.

After calcination, the PDF fit for Al_2O_3-calc still reveals solely short range order compared to Ni/Al_2O_3-calc. Fitting was performed only with the crystalline structure model for $\gamma-Al_2O_3$.[293] For Ni/Al_2O_3-calc the fitting describes the structure quite well, although especially in the close coordination some deviations can still be observed. This might indicate either not correctly described occupancies, as those were kept fixed contrary to PXRD or an unidentified secondary phase. The $\gamma-Al_2O_3$ model can also be applied for Al_2O_3-calc, but for the small crystalline domain size the correct description might be doubtful, despite the first coordination shells seem to be described by the model.

The PDF fits reveal spherical particles sizes of 2.46(5) nm and 4.32(1) nm for Ni/Al_2O_3-dr and

Ni/Al_2O_3-calc, respectively. While for Al_2O_3-dr and Al_2O_3-calc the obtained values were 0.93(2) and 1.14(3) nm, respectively. This supports the findings of the Rietveld analysis of the PXRD described in the previous section 5.2.2 on the higher nanocrystalline nature of the Al_2O_3 samples compared to Ni/Al_2O_3. As the temperature reached during *in situ* studies was limited and especially for Al_2O_3 no crystallization was observed, the laboratory calcined samples Al_2O_3-h and Ni/Al_2O_3-h were measured *ex situ* and are discussed in the following section.

5.2.4 Discussion of Structural Analysis by PXRD and PDF

As presented in the previous two sections, *in situ* PXRD and PDF allowed to reveal phase transformations occurring during calcination. The Rietveld analysis and PDF fitting results for the laboratory calcined *ex situ* measured samples (calcination temperature 1123 K) are shown in Figure 5.15 and 5.16, respectively.

The structures are in both cases described by a $\gamma-Al_2O_3$ structural model as for Ni/Al_2O_3-calc

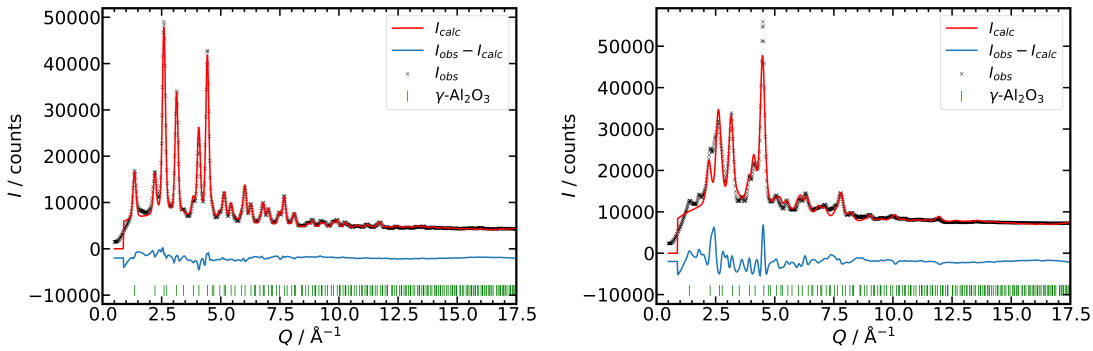


Figure 5.15: *Ex situ* Rietveld analysis of the PXRD for the calcined Ni/Al_2O_3-h (left) and Al_2O_3-h (right) samples. (*c.f.* Table 8.7)

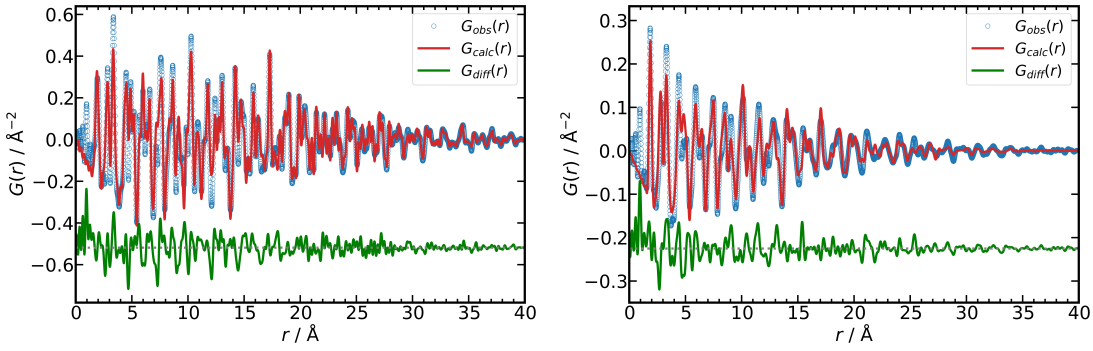


Figure 5.16: *Ex situ* fitting results of the PDF for the calcined Ni/Al_2O_3-h (left) and Al_2O_3-h (right) samples. (*c.f.* Table 8.7)

and Al_2O_3-calc (*c.f.* Table 8.7).[293] Similar to those, Ni/Al_2O_3-h exhibts a significant larger L_{vol} = 5.21(4) nm and p_{size} = 7.9(2) nm compared to Al_2O_3-h with L_{vol} = 2.96(6) nm and

p_{size} = 4.32(8) nm. The Rietveld refinements describe the Ni/Al_2O_3-h quite well as shown in Figure 5.15, while in the PDF analysis significant deviations can be still be observed. It should be noted that for the PXRD analysis refinement of the occupancy of the Al positions was attempted, but the results should be treated carefully. As summarized in the appendix Table 8.7 a significantly higher occupancy of Al positions for the Ni/Al_2O_3-h sample compared to Al_2O_3-h was found. This might indicate the incorporation of Ni into the defect-spinel structure of $\gamma-Al_2O_3$ as already suggested in the laboratory PXRD Rietveld analysis of the material in section 4.3. However, the refined occupancies are significantly higher compared to the *in situ* calcined Ni/Al_2O_3-calc sample, which cannot be explained by the analysis so far. For the PDF analysis occupancies were fixed, while for both Ni/Al_2O_3-h and Al_2O_3-h undescribed contributions can be found in the PDF fitting.
In case of Ni/Al_2O_3 the L_{vol} values for Ni/Al_2O_3-h and Ni/Al_2O_3-calc are similar, while the p_{size} is larger for Ni/Al_2O_3-calc. This might indicate that despite a 200 K higher temperature during calcination no strong increase in crystallite size is observed. For Al_2O_3 the values for Al_2O_3-calc are significantly larger than for Al_2O_3-calc highlighting that the crystallization did not took place. As L_{vol} and p_{size} for the *in situ* and *ex situ* are larger for Ni/Al_2O_3 compared to Al_2O_3, Ni might be discussed in a role to facilitate the crystallization of the defect-spinel type $\gamma-Al_2O_3$ structure. This might finally lead to partial formation of a $NiAl_2O_4$ spinel structure.

5.2.5 Conclusions

Generally, the *in situ* and *ex situ* PXRD and PDF analysis results are of preliminary nature and further data analysis and studies are required to support the current findings and reveal more details. Nevertheless, some conclusions on the phase transformation processes during calcination can be derived. For both systems, Ni/Al_2O_3 and Al_2O_3, a nanocrystalline $\gamma-AlO(OH)$ like structure was identified in the dried gel states and no separate crystalline Ni containing phases were found. Upon calcination the sample turned amorphous, while PDF revealed significant distances of atomic pairs only up to 4 Å , which indicates the presence of cluster type intermediates. However, further studies involving probably molecular spectroscopy, X-ray absorption spectroscopy and theoretic structure modeling are required to unravel those. For Ni/Al_2O_3 the formation of a $\gamma-Al_2O_3$ like structure could be observed in the *in situ* experiments beginning with the final calcination temperature of about 923 K, which was not found for Al_2O_3. Together with the larger crystallite (L_{vol}) and particle (p_{size}) sizes, also of the starting $\gamma-AlO(OH)$ like structure, this might indicate that Ni influences the crystallization tendency of the material. This might be related to the incorporation of Ni into the defect-spinel like $\gamma-Al_2O_3$ structure or already partial formation of $NiAl_2O_4$. However, a direct proof of those hypotheses requires additional studies.
One advantage of the X-ray total scattering experiments compared to X-ray nanoimaging studies (*c.f.* sections 4.3 and 5.1) was the larger probed sample volume of roughly 1 mm^3, which allows a higher representativity. Principally, it would also be possible to perform the experiments in a

spatially-resolved way as discussed in section 1.5. In the present case it was assumed that the powder like material in the dried gel state was homogeneous, while especially for monolithic or shaped samples this might not be valid, which would require a spatially-resolved analysis of the calcination. In summary, the initial results on the structural evolution of the Ni/Al_2O_3 and Al_2O_3 during calcination revealed at least two occuring phase transformations. For tailored synthesis procedures detailed knowledge about such processes is required, but not trivial to retrieve even with advanced synchrotron-based methods as shown here. Hard X-ray based methods as reviewed in section 1.5 and illustrated in Figure 1.11 offer a broad toolbox for this purpose including spatially-resolved XRD-CT and PDF-CT. Furthermore, the potential Ni incorporation was discussed similar to section 4.3 along with a potential promotion of crystallization by Ni. Future studies on the structural evolution of the sol-gel based materials are therefore emphasized and require additional complementary characterization methods and theory.

6 Revealing Catalyst Deactivation with Hard X-rays

In the previous chapters, the multiscale approach of imaging methods relevant for porosity characterization (*c.f.* chapter 4) or the understanding of textural and structural changes during catalyst synthesis (*c.f.* chapter 5) were presented. For a practical application of catalysts, knowledge about deactivation pathways is equally important. Several relevant deactivation mechanism for Ni-based methanation catalysts were reviewed in section 1.2.3.
As part of the present chapter, selected deactivation mechanisms of Ni-based catalysts employed in CO_2 methanation are investigated. First, coking that might cause deactivation in certain operation conditions is discussed in section 6.1 for the hierarchically porous Ni/Al_2O_3-h catalyst from section 4.3 together with a purely mesoporous sample for comparison. The aim of this section is to reveal the location of coke spatially-resolved in 3D, which is a basis for future tailoring of the catalysts pore structures to withstand coking. For this purpose, ptychographic X-ray computed tomography as an advanced imaging method is applied on artificially coked and activated catalyst samples. Furthermore, in section 6.2 a designed series of Ni/ZrO_2 catalysts with systematic differing textural support properties is investigated by *operando* synchrotron-based powder X-ray diffraction during artificial thermal aging. This combination allows to deconvolute various deactivation phenomena with a focus on support and metal nanoparticle sintering, which is hardly possible to reveal with conventional characterization methods. Detailed knowledge about the deactivation mechanism is crucial to increase catalyst stability and thus performance.

6.1 Coke Localization Unraveled by X-ray Ptychography[1,2]

6.1.1 Introduction

As reviewed in the introduction section 1.2.3 several possible deactivation phenomena might occur for Ni-based catalysts employed in CO_2 methanation. Among those, coking is commonly reported and might be generally relevant for reactions involving carbonaceous species.[38, 40, 60] Despite under ideal stoichiometric CO_2 methanation conditions it is rather unlikely to play a major role, mixed CO/CO_2 methanation or dynamic operation of the reactor might lead to operation conditions that enhance coke formation. In this respect, detailed understanding of the coke formation is important to be able to improve the catalyst stability and performance. Often the coke formation is related to coverage of active sites or blocking of pores.[92, 337–340] Hence, the introduction of hierarchically meso-/macropores structures has been suggested to improve catalyst stability and performance as the introduced larger macropores can help to mitigate pore blocking.[341, 342] However, there is often missing understanding where the coke is exactly formed in the porous catalyst particles, which is a requirement to tailor such pore structures and needs a spatially-resolved characterization.

"Commonly applied methods to investigate catalyst coking mainly retrieve bulk information, such as amount and elemental composition of coke.[339, 340] This is partly due to the difficulty in separating or distinguishing different coke species on the solid catalyst. On the other hand, with microscopy or other 2D spatially-resolved characterization methods (e.g. FTIR or Raman spectroscopy), no separation is needed and coke can be studied directly on the catalyst surface. There are only few techniques reported to extend spatially-resolved characterization to 3D space, which can provide a more representative view of sample structure. These include electron microscopy (EM),[343, 344] atom probe tomography (APT)[345] and soft X-ray scanning transmission microscopy (STXM).[346] A main drawback of the above methods is that they only cover limited length scales, while coking is a relevant phenomenon from the mesopore up to the whole particle or even the reactor scale. Ideally, high spatial resolution over extended sample length scales should be combined in a single measurement, or complementary methods should be used to include information from different scales (*c.f.* Figure 1.9 and section 1.3,1.5). This is especially important for materials with hierarchical meso- and macropore systems (or other heterogeneous samples), where the pore system itself ranges from nm to µm and the catalyst particles may range from µm to cm as presented in the previous sections 4.3 and 5.1. EM and

[1] Parts of section 6.1 are adapted and taken from: S. Weber, D. Batey, S. Cipiccia, M. Stehle, K. L. Abel, R. Gläser and T. L. Sheppard, "Hard X-Ray Nanotomography for 3D Analysis of Coking in Nickel-Based Catalysts", *Angew. Chem. Int. Ed.*, **2021**, *60*, 21722-21777.[239] Available under the terms and conditions of the Creative Commons Attribution 4.0 license (CC BY 4.0, `https://creativecommons.org/licenses/by/4.0/`), Copyright ©2021.

[2] D. Batey and S. Cipiccia (Diamond Light Source) supported the PXCT experiments and ptychographic reconstructions. M. Stehle (ITCP, Karlsruhe Institute of Technology (KIT)) assisted the Raman spectroscopy experiments. K. L. Abel, J. Titus, D. Poppitz and R. Gläser (Universität Leipzig) provided the synthesis of the materials.

APT provide high-resolution data in the nm range, but on limited and localized sample volumes. STXM can cover nm to µm and can directly provide information about the carbon species by X-ray absorption spectroscopy at the C-K-edge, but with soft X-rays this is limited to relatively thin samples due to strong attenuation of the transmitted beam."[239]
As presented previously in section 4.1 and 5.1, PXCT allows to retrieve quantitative information about the local electron density (N_e) on extended sample volumes of tens of µm with sub 50 nm resolution. If coke is formed inside the pores of catalysts, this leads principally to changes in N_e. In a recent study, X-ray holotomography was shown to locate coke formation in 60 µm diameter FCC particles with ≈200 nm resolution. However, the contrast approach there was only sensitive to relative changes of N_e in an arbitrary unit scale, without an exact physical unit for N_e.[197] Therefore, in the present section the potential of PXCT to unravel the location of coke in artificially coked samples of the hierarchically porous Ni/Al_2O_3-h catalyst and a purely mesoporous sample Ni/Al_2O_3-m is exploited.
As illustrated in Figure 6.1, for both systems activated and artificially coked samples are investigated. The artificial coking step is thereby followed by Raman spectroscopy to qualitatively confirm the coking.

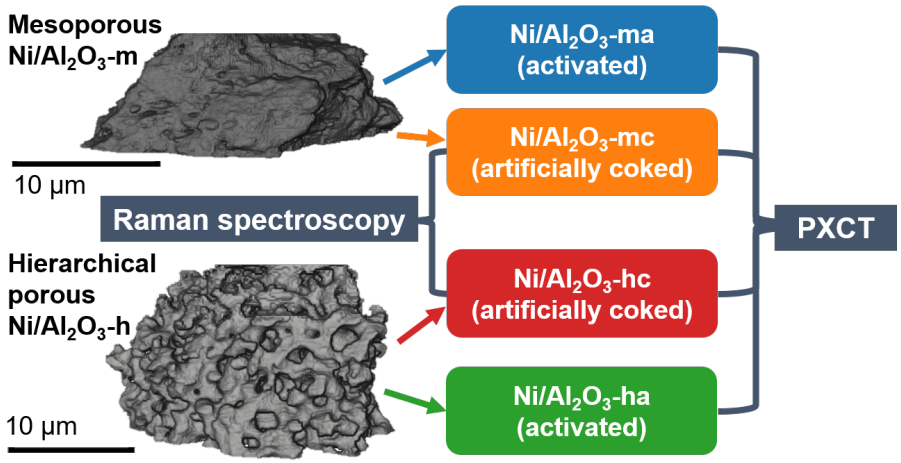


Figure 6.1: "Experiments to study coke formation on two Ni/Al_2O_3 catalysts with different pore structures. Treatments consisted of activation, reaction conditions and additional artificial coking (see Supporting Information). The coking was followed by *operando* Raman spectroscopy. All samples were then investigated by PXCT."[239] Available under the terms and conditions of the Creative Commons Attribution 4.0 license (CC BY 4.0, `https://creativecommons.org/licenses/by/4.0/`), Copyright ©2021.

6.1.2 Artificial Coking Treatment and Raman Spectroscopy

The two catalyst systems studied here were prepared via two different routes as detailed in the experimental section 3.1 (*c.f.* Table 3.1) to obtain the hierarchically meso-/macroporous Ni/Al_2O_3-h and purely mesoporous Ni/Al_2O_3-m. The catalysts exhibit a similar Ni content of

17 wt.% for Ni/Al_2O_3-m and 18 wt.% for Ni/Al_2O_3-h, while the hierarchically porous sample was already part of investigations in sections 4.3, 5.1 and 5.2 and the mesoporous sample was provided by Dr. Marc-André Serrer (Karlsruhe Institute of Technolgy (KIT)). The samples were treated in a quartz capillary setup (*c.f.* Figure 3.5) to obtain an activated and artificially coked sample of each, as illustrated in Figure 6.1 and detailed in the experimental section 3.3.3. "Briefly, all samples were first activated in 25 % H_2 / He (V_{tot} = 20 mL min^{-1}), followed by 30 min of CO_2 methanation reaction conditions 20 % H_2 / 5 % CO_2 / He (V_{tot} = 20 mL min^{-1}, 673 K), resulting in the activated catalyst samples Ni/Al_2O_3-ma and Ni/Al_2O_3-ha (*c.f.* Figure 3.6). Catalytic activity was quantified during this process by online mass spectrometry (*c.f.* Figure 3.6).
In a separate experiment, artificial coking conditions of 4 % CH_4 / He (V_{tot} = 20 mL min^{-1}, 673 K, 30 min) were then applied, similar as reported by Mutz *et al.*[86] Treatment of artificially coked samples Ni/Al_2O_3-mc and Ni/Al_2O_3-hc was monitored by *operando* Raman spectroscopy, confirming the formation of carbonaceous species. Figure 6.2 shows online mass spectrometry data and temperature profiles for the artificially coked samples together with 2D plots of the *operando* Raman spectra. Neither sample showed significant Raman bands before artificial coking. Upon artificial coking, formation of typical carbon bands was observed and assigned

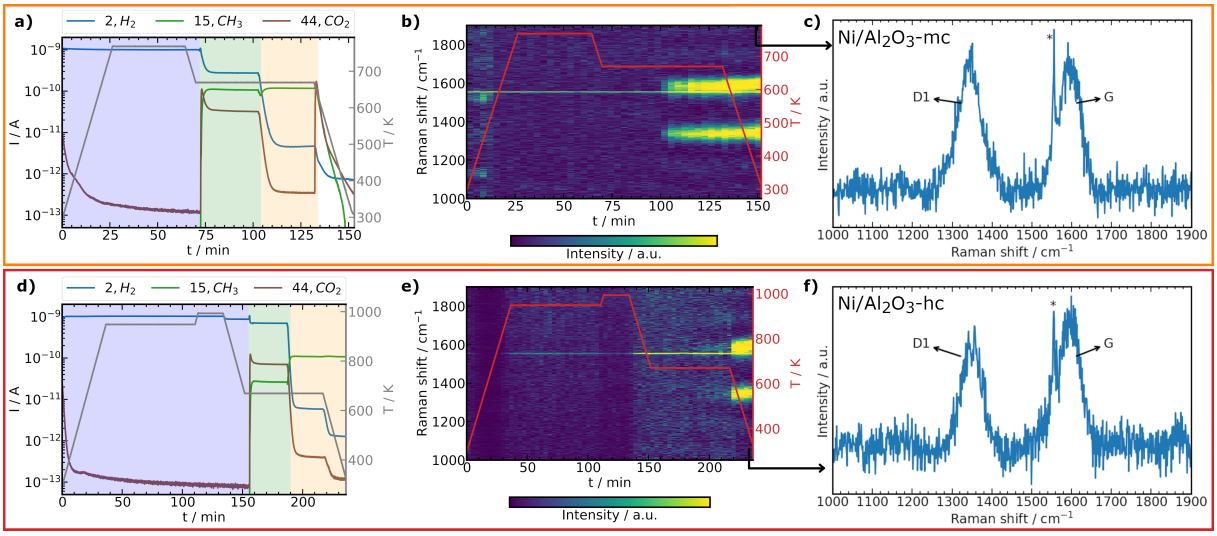


Figure 6.2: "*Operando* Raman spectroscopy of Ni/Al_2O_3-mc (a–c) and Ni/Al_2O_3-hc (d–f). (a,d) selected mass spectrometry traces during activation (blue), reaction (green) and artificial coking (orange) with temperature (T, gray); cooling in He (white). (b,e) 2D plots of Raman spectra (2 x binned) with the last spectra highlighted in (c,f) showing formation of carbon (D1 and G bands). * Line feature at 1557 cm^{-1} in (b,c,e,f) corresponds to O_2 from air.[347]."[239] Available under the terms and conditions of the Creative Commons Attribution 4.0 license (CC BY 4.0, `https://creativecommons.org/licenses/by/4.0/`), Copyright ©2021.

to carbonaceous species for Ni/Al_2O_3-mc (Figure 6.2b,c) and Ni/Al_2O_3-hc (Figure 6.2e,f). The D1 band (≈1340 cm^{-1}) originating from the vibration of disordered graphitic lattice (A_{1g} symmetry), and the G band originating from ideal graphitic lattice vibrations with E_{2g} symmetry (≈1590 cm^{-1}) were detected.[86, 348, 349] The presence of carbonaceous species was therefore

confirmed by *operando* Raman spectroscopy for both Ni/Al_2O_3-mc and Ni/Al_2O_3-hc, but as a bulk characterization this provides limited information about the location of coke species in the particles."[239]

6.1.3 Ptychographic X-ray Computed Tomography Analysis

"Samples Ni/Al_2O_3-ma, Ni/Al_2O_3-mc, Ni/Al_2O_3-ha and Ni/Al_2O_3-hc were then investigated by PXCT to study the distribution of carbonaceous species within the catalyst particles. From catalyst powders obtained after treatment, suitable particles of each sample with diameters of about 30 to 50 µm were selected and mounted on Al tomography pins using a dual-beam focused ion beam scanning electron microscope (FIB-SEM) *c.f.* Figure 8.26,8.27."[239] PXCT experiments were performed at beamline I13-1 of the Diamond Light Source as detailed in the experimental section 3.4.7. The FSC estimated resolution of the tomograms ranges from 74 to 83 nm (*c.f.* Figure 8.28, 8.29). The obtained N_e density contrast tomograms for Ni/Al_2O_3-h and Ni/Al_2O_3-m are shown in Figure 6.3 and Figure 6.4, respectively.
The results for the Ni/Al_2O_3-m samples are only discussed carefully and presented supportive to Ni/Al_2O_3-h due to artifacts from reconstructions. "Especially for the Ni/Al_2O_3-mc sample some phase artifacts could not be resolved, which may influence the projection alignment and obtained N_e values, therefore limiting the reliability of the coking analysis. This issue did not affect the Ni/Al_2O_3-h data which can be discussed reliably. For N_e analysis, the particles were first masked from the surrounding air to obtain a label of the whole catalyst particle. The obtained particle label was further segmented by thresholding into pores (orange), catalyst body (gray) and contamination (green) labels (Figure 6.3, 6.4; *c.f.* Figure 8.30–8.33). The contamination originates from Pt used during FIB preparation of the samples on the tomography pins, which could be easily segmented due to relatively high N_e and discarded from further analysis. One can

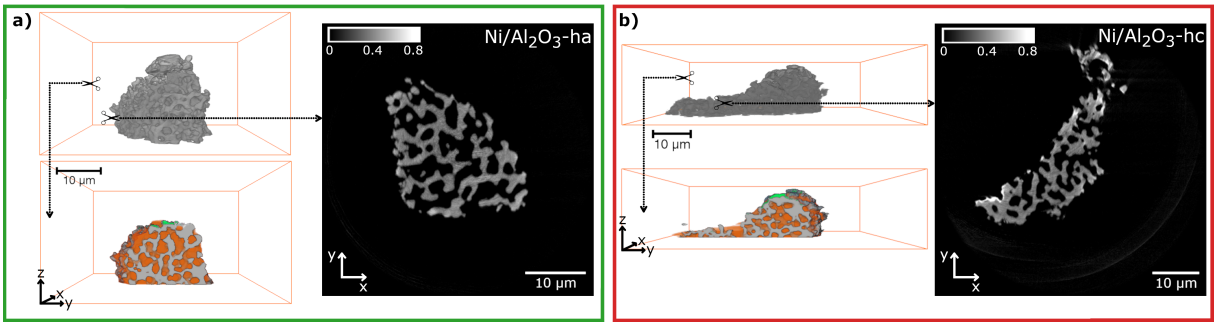


Figure 6.3: "PXCT of activated catalyst Ni/Al_2O_3-ha (a) and artificially coked catalyst Ni/Al_2O_3-hc (b). Each reconstructed volume (gray) is shown with a cut through the middle, illustrating the segmented and labeled tomograms (gray = nanoporous catalyst body, orange = pores, green = contamination) and a grayscale N_e image of a typical slice through the volume (color bar in N_e / e^{-3} $Å^{-3}$, N_e offset to 0 with respect to air close to the sample (*c.f.* section 3.4.9 and Table 8.8)."[239] Available under the terms and conditions of the Creative Commons Attribution 4.0 license (CC BY 4.0, `https://creativecommons.org/licenses/by/4.0/`), Copyright ©2021.

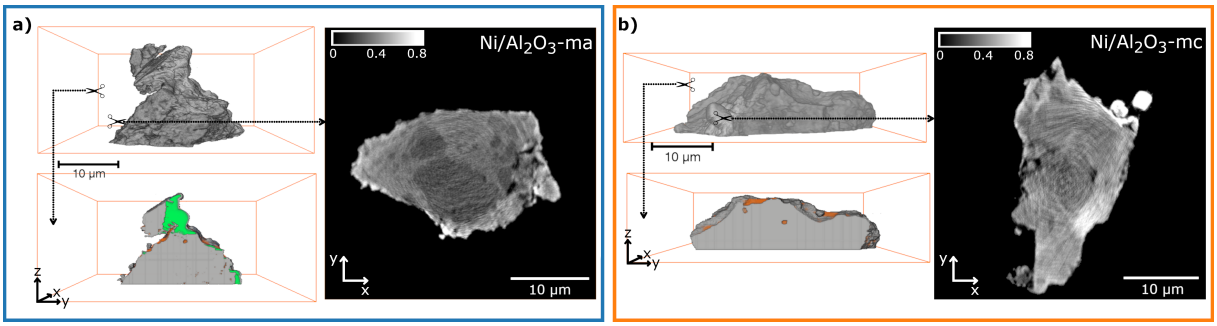


Figure 6.4: "PXCT of activated catalyst Ni/Al_2O_3-ma (a) and artificially coked catalyst Ni/Al_2O_3-mc (b). Each reconstructed volume (gray) is shown with a cut through the middle, illustrating the segmented and labeled tomograms (gray = nanoporous catalyst body, orange = pores, green = contamination) and a grayscale N_e image of a typical slice through the volume (color bar in N_e / e^{-3} Å^{-3}, N_e offset to 0 with respect to air close to the sample (*c.f.* section 3.4.9 and Table 8.8)."[239] Available under the terms and conditions of the Creative Commons Attribution 4.0 license (CC BY 4.0, `https://creativecommons.org/licenses/by/4.0/`), Copyright ©2021.

clearly observe the different pore structures of the two systems. For Ni/Al_2O_3-h (Figure 6.3) a connected macropore network can be observed, while for Ni/Al_2O_3-m (Figure 6.4) only few voids within the particles are present."[239] The hierarchically porous nature of sample Ni/Al_2O_3-ha was extensively presented in sections 4.3 and 5.1. On the other hand, the mesoporous structure of Ni/Al_2O_3-m was reported in earlier studies based on conventional methods.[53] "In Ni/Al_2O_3-hc no clear coke formation inside the macropores or voids was detected (Figure 6.3b). While the resolution obtained (ca. 80 nm) was not sufficient to directly visualize the presence and location of coke by thresholding and image segmentation, this is a common limitation of all current hard X-ray microscopy methods."[239]

6.1.4 Electron Density Analysis to Reveal Coke Location

As the resolution of PXCT was not high enough to directly detect coking, its advantage is the provision of quantitative information about N_e. Similar to section 5.1 where a densification of the nanoporous solid of a dried gel Ni/Al_2O_3-h during calcination was observed, the N_e can be analyzed for changes during coking. "This property was used to objectively evaluate coke formation in terms of variation in N_e within the sample, but is in principle additionally sensitive to sample elemental composition, bonding, atomic configuration, and other fine structural variations. Figure 6.5a and Figure 6.6a show the global N_e distribution within whole particles of Ni/Al_2O_3-h and Ni/Al_2O_3-m, respectively. Prior to analysis, N_e was offset to 0 with respect to air in close proximity to the sample (for details *c.f.* section 3.4.9 and Table 8.8).

A peak around 0.0 e^- Å^{-3} was assigned to air in the macropores or voids, while a second peak with maxima around 0.4 e^- Å^{-3} corresponds to the nanoporous catalyst body, and peaks at higher N_e values to Pt contamination. In the case of Ni/Al_2O_3-hc (Figure 6.5a) no clear shift of the N_e mode for the artificially coked sample was detected compared to the Ni/Al_2O_3-ha sample.

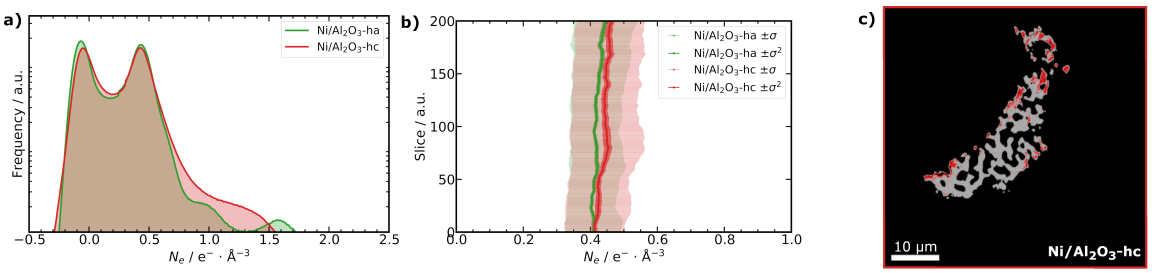


Figure 6.5: "Global electron density distribution from PXCT of the activated and artificially coked catalyst particle labels of Ni/Al_2O_3-h (a). Mean, standard deviation (σ) and variance (σ^2) in N_e of the segmented catalyst body label in a selected slice range (b). Segmented tomogram slice of Ni/Al_2O_3-hc (c) showing less electron dense (gray, assigned to activated catalyst body) and higher density (red, assigned to coked catalysts body) regions by binary thresholding of the normalized N_e distribution (*c.f.* Figure 8.36, Table 8.8). The reliability of the thresholding-based segmentation was tested for different thresholds (*c.f.* Figure 8.38)."[239] Available under the terms and conditions of the Creative Commons Attribution 4.0 license (CC BY 4.0, `https://creativecommons.org/licenses/by/4.0/`), Copyright ©2021.

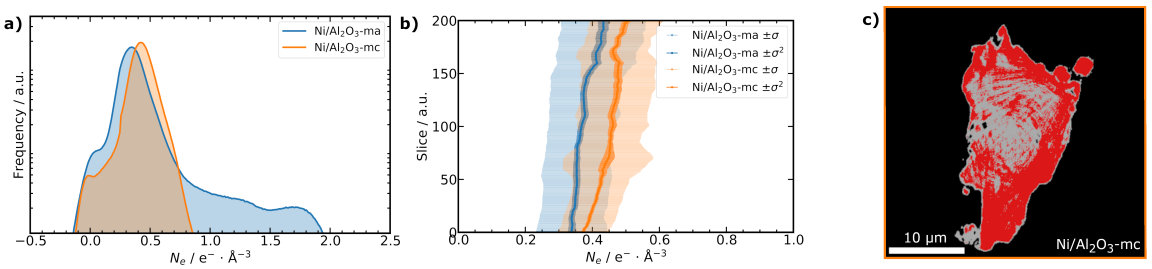


Figure 6.6: "Global electron density distribution from PXCT of the activated and artificially coked catalyst particle labels of Ni/Al_2O_3-m (a). Mean, standard deviation (σ) and variance (σ^2) in N_e of the segmented catalyst body label in a selected slice range (b). Segmented tomogram slice of Ni/Al_2O_3-mc (c) showing less electron dense (gray, assigned to activated catalyst body) and higher density (red, assigned to coked catalysts body) regions by binary thresholding of the normalized N_e distribution (*c.f.* Figure 8.36, Table 8.8). The reliability of the thresholding-based segmentation was tested for different thresholds (*c.f.* Figure 8.39)."[239] Available under the terms and conditions of the Creative Commons Attribution 4.0 license (CC BY 4.0, `https://creativecommons.org/licenses/by/4.0/`), Copyright ©2021.

However, the appearance of a slight shoulder at higher N_e values was observed as highlighted in the normalized N_e of the catalyst body labels (see Figure 8.36). As *operando* Raman spectroscopy revealed clear evidence of coking under the applied conditions, the appearing shoulder at increased N_e was assigned to coke formation within the nanoporous catalyst body of Ni/Al_2O_3-hc. It should be noted that in principle, N_e is sensitive to any variation of local chemical structure or bond/atom arrangement. This constitutes a powerful characterization potential, but also requires caution in interpretation. Relative increases in N_e may result not only from coke-filled pores, but also effects such as pore collapse, sintering of active metal, crystallographic changes in catalyst support, or other such effects. Since the treatments of Ni/Al_2O_3-ha and Ni/Al_2O_3-hc performed in the capillary setup differ only by the artificial coking step, which was lower in temperature than that of the initial activation, it can be reasonably concluded that changes in N_e observed are most likely a result of coking.

For finer spatially-resolved statistical analysis of the tomography data, the dependence of the mean N_e of the whole particle label on specific tomogram slices was checked (*c.f.* Figure 8.35). Regions with strong Pt contamination can be easily identified and excluded, so further analysis was limited to slices 1 to 200. The slice-dependent analysis of the mean N_e of the Ni/Al_2O_3-h samples shows an increase of the N_e for the coked sample (Figure 6.5b, *c.f.* Table 8.8). The mode of the N_e is almost identical for the Ni/Al_2O_3-ha and Ni/Al_2O_3-hc samples (*c.f.* Figure 8.37), but the standard deviation (σ) clearly shows the increased contribution mainly from higher N_e regions for Ni/Al_2O_3-hc and thus significant increase of N_e (Figure 6.5b, *c.f.* Figure 8.37). As the slice-dependent analysis only provides information along the z-direction of the tomograms, the tomograms were further segmented based on the normalized N_e distribution of the catalyst body labels to estimate the location of more prevalent coking (*c.f.* Figure 8.36). For thresholding-based segmentation a clearly recognizable feature was chosen. The point of the normalized N_e distribution of the *catalyst body* label from which Ni/Al_2O_3-hc differed from Ni/Al_2O_3-ha (*c.f.* Figure 8.36) was selected. The resulting further segmented *catalyst body* labels for Ni/Al_2O_3-hc are shown in Figure 6.5c, separated into an activated and coked catalyst body label based on the chosen thresholds (*c.f.* Table 8.8). It can be observed that the coke label is stronger distributed at the exterior of the particle, from which we postulate that coking may start in mesopores at the exterior of the catalyst particles and further progress to the center with increasing reaction time. This is furthermore supported by comparing multiple higher thresholds for the activated and coked samples (*c.f.* Figure 8.38). It should be noted that this comparison is of qualitative nature based on the N_e and the resolution is not high enough to clearly identify single voxels of coking. A similar gradient of the N_e during coke formation was also found in FCC catalysts particles studied with X-ray holotomography.[197] However, further detailed experiments at different coking stages are required to validate this conclusion.

The same analysis was also performed for the Ni/Al_2O_3-m system. A similar trend was found for the PXCT of the Ni/Al_2O_3-m samples, with an even more pronounced shift of the N_e upon coking (Figure 6.6, *c.f.* Figure 8.35, 8.36, 8.37, 8.39, Table 8.8). However, due to existing phase vortices artifacts, especially in Ni/Al_2O_3-mc, that might influence the projection alignment and N_e values, those results should not be regarded as conclusive but rather only as indicative. The artifacts in question may occur due to distinct edge like or strong absorbing features in the sample and are a general challenge in ptychographic reconstruction of thick samples. Recently, an algorithm called "VortRem" was reported to remove such artifacts caused by non-convergence of the ptychographic reconstruction.[273] This readily shows potential limitations of PXCT depending on the studied samples, and the requirement of a careful sample selection and preparation in future studies.

In a crucial advantage over bulk measurements, PXCT can not only characterize, but directly visualize the results of deactivation phenomena with sub-100 nm resolution in 3D space within the catalyst particle. By the nature of N_e , which is in principle unique to each distinct configuration of atoms in 3D space, chemical distinction of coke species depending on the N_e as suggested by Vesely *et al.* may be possible in future, since graphitic coke or activated carbon exhibit different

N_e.[197] However, for such a distinction to be accurate higher spatial resolution is indispensable to more precisely assign N_e within the 3D sample structure. For this reason, PXCT is positioned as the ideal technique to drive catalysis research forward, having shown astonishing progress during only a decade since its invention.[156]."[239]

6.1.5 Conclusions

In summary, PXCT was presented in this section as an emerging technique to study catalyst deactivation in a spatially-resolved manner. Similar to the studies on the pore structure of the SPP2080-IMRC or porosity formation of Ni/Al_2O_3-h in sections 4.1 or 5.1, respectively, the quantitative local N_e information was shown to provide sub-resolution information about the sample. PXCT enables to study deactivation on whole catalysts grains of tens of µm in size with sub 100 nm resolution as shown here. For both catalyst systems, the purely mesoporous and hierarchically meso-/macroporous samples, coking appears to take place in the mesopores of the catalysts starting from the exterior of the catalyst grains. However, to validate this interpretation, future studies of different coking stages are required.
A limitation of PXCT was shown in terms of the reliability of the data in case of reconstruction artifacts, which were found for Ni/Al_2O_3-m. Therefore, it can be concluded that sample preparation and data processing have to be performed carefully and might exhibit challenges for non-ideal samples. As N_e is not only sensitive towards coking, but in general towards samples changes that lead to differences in density, the presented approach might be feasible to study other deactivation effects like composite formation, sintering or collapse of mesoporous structures. All of those are potentially relevant for CO_2 methanation with Ni-based catalysts as reviewed in section 1.2.3. In this respect, future improvements in resolution are important to better distinguish overlapping features in the N_e distribution. This might enable a true quantitative labeling of coked areas and not only qualitative conclusions on the location of coke as shown here.
However, the limited sample volume by X-ray nanoimaging methods might be challenging. In this respect, *in situ* studies as presented in section 5.1 are emphasized which can at least reduce the influence of sample selection.

6.2 Deconvolution of Thermal Deactivation Phenomena by X-ray Diffraction[3,4]

6.2.1 Introduction

In the previous section 6.1, the location of coke as a deactivation pathway was investigated by PXCT. However, in a practical application it is not regarded as the major deactivation pathway (*c.f.* section 1.2.3). As reviewed in the introduction section 1.2.3, thermal deactivation is rather expected the major deactivation phenomena for Ni-based catalysts applied in CO_2 methanation. In general, for exothermic catalytic processes a reliable heat management is a fundamental requirement to ensure catalyst stability and safe process operation. Thermal deactivation might lead in this respect to morphological changes, mixed oxide formation of metal nanoparticles and the support as well as sintering of metal nanoparticles or the support as it was illustrated in Figure 1.6. However, the variety of potential changes makes it difficult to distinguish those as they can occur simultaneously or together with other deactivation phenomena, e.g., poisoning or fouling (*c.f.* Figure 1.6). Though, detailed knowledge about the deactivation is required for knowledge-based design of catalysts with increased thermal stability.
Due to the strong tendency towards hot-spot formation in CO_2 methanation as presented in section 1.2.3 (*c.f.* Figure 1.7), it is an ideal model reaction to study thermal deactivation of catalysts. As shown in the introduction section 1.2.3 thermal activation of different Ni/Al_2O_3 catalysts is related to sintering of Ni nanoparticles, mixed oxide formation or textural changes of the support. However, the reviewed studies were not able to deconvolute the different effects as characterization of the catalysts is typically performed *post mortem* and *ex situ*. Nevertheless, a general conclusion from the literature knowledge is that both support and metal nanoparticle can change upon thermal aging and strongly influence the stability of Ni-based catalysts applied in CO_2 methanation.
In the present section, *operando* synchrotron-based powder X-ray diffraction (SPXRD) is applied to unravel different deactivation pathways during artificial thermal aging of a designed series of Ni/ZrO_2 catalysts. As illustrated in Figure 6.7, the catalyst series was prepared from the same ZrO_2 support material, which was calcined at different temperatures before Ni deposition. With this systematic approach, the catalysts should exhibit different thermal stability of the support material, while Ni particles should be similar in all samples. This allows to observe different deactivation pathways upon thermal deactivation regarding changes of Ni nanoparticles and the ZrO_2 support, which helps to deconvolute deactivation phenomena. Similarly to section 5.2,

[3]Parts of section 6.1 are adapted and taken from: M. L. Schulte, S. Weber, L. Klag, J.-D. Grunwaldt and T. L. Sheppard, "Synchrotron PXRD deconvolutes nickel particle and support changes in Ni/ZrO_2 methanation catalysts", *Catal. Sci. Technol.*, **2022**, *12*, 6069-6083.
[4]M. L. Schulte (Karlsruhe Institute of Technology (KIT)) performed the catalyst synthesis and testing together with general catalyst characterization as part of her master thesis supervised by me. M. L Schulte, L. Klag and T. L. Sheppard carried out the SPXRD measurements. Data analysis of SPXRD experiments and conceptualization of the project was carried out by myself.

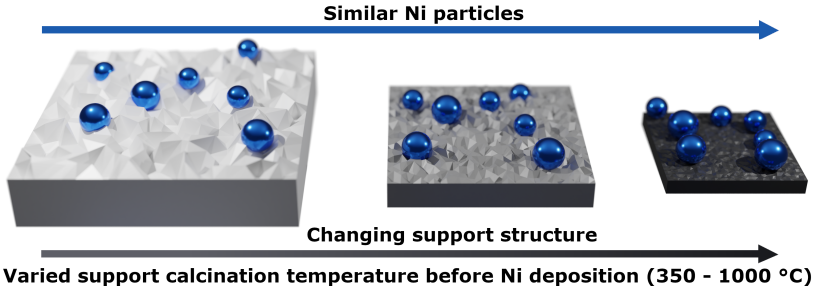


Figure 6.7: "Illustration of the initially prepared Ni/ZrO_2 catalysts applied in artificial thermal aging experiments. Before Ni deposition the ZrO_2 support was calcined at different temperatures to alter the support textural properties (surface area, pore volume) and to vary the thermal stability of the support. Ni blue, ZrO_2 grey, the grey color gradient illustrates changing textural properties of the support."[240] Available under the terms and conditions of the Creative Commons Attribution 3.0 license (CC BY 3.0, `https://creativecommons.org/licenses/by/3.0/`), Copyright ©2022.

the applied *operando* SPXRD experiments can reveal textural and structural changes of the support and Ni nanoparticles, which allows to derive a structure-deactivation relationship for the Ni/ZrO_2 catalyst series.

6.2.2 Synthesis of Catalysts with Varying Support Texture

"A series of five ZrO_2 supports was synthesized with different calcination temperatures ranging from 623 K to 1273 K (supports Z350 to Z1000, *c.f.* section 3.1.3, Figure 3.3, Table 8.9). Following Ni deposition, the resulting Ni/ZrO_2 catalysts were named accordingly as NZ350 to NZ1000 (Table 6.1). The aim was to prepare a catalyst series with distinct textural properties of the support (e.g. A_{BET}, V_P) dependent only on one parameter – the support structure by varying calcination temperature (Figure 6.7). In addition, the supported Ni particles were intended to exhibit a similar initial size distribution across all catalysts.
The synthesized catalysts were first characterized by various methods to study the structural and textural properties as summarized in Figure 6.8 and Table 6.1. The support textural properties

Table 6.1: Overview of the characterization results for the different as-prepared calcined Ni/ZrO_2 catalysts. Additionally, $L_{vol,Ni}$, D and TOF for the spent catalysts after testing in CO_2 methanation at 673 K is reported.

Catalysts	ω_{Ni} / wt.%	A_{BET} / $m^2\ g^{-1}$	V_p / $cm^3\ g^{-1}$	L_{vol,ZrO_2} / nm	$L_{vol,NiO}$ / nm	$L_{vol,Ni}$ / nm	D / %	TOF / s^{-1}
NZ350	14.1	66	0.23	10.4	10.7	34	11.0	$2.3 \cdot 10^{-2}$
NZ500	13.2	53	0.14	13.6	9.6	32	11.2	$1.8 \cdot 10^{-2}$
NZ650	14.7	33	0.070	23	10.3	26	12.9	$1.2 \cdot 10^{-2}$
NZ800	15.2	26	0.055	45	8.1	31	11.5	$7.7 \cdot 10^{-3}$
NZ1000	14.7	18	0.056	95	7.9	29	11.8	$2.6 \cdot 10^{-3}$

were studied by N_2 physisorption to gain information about the surface area (A_{BET}) and the

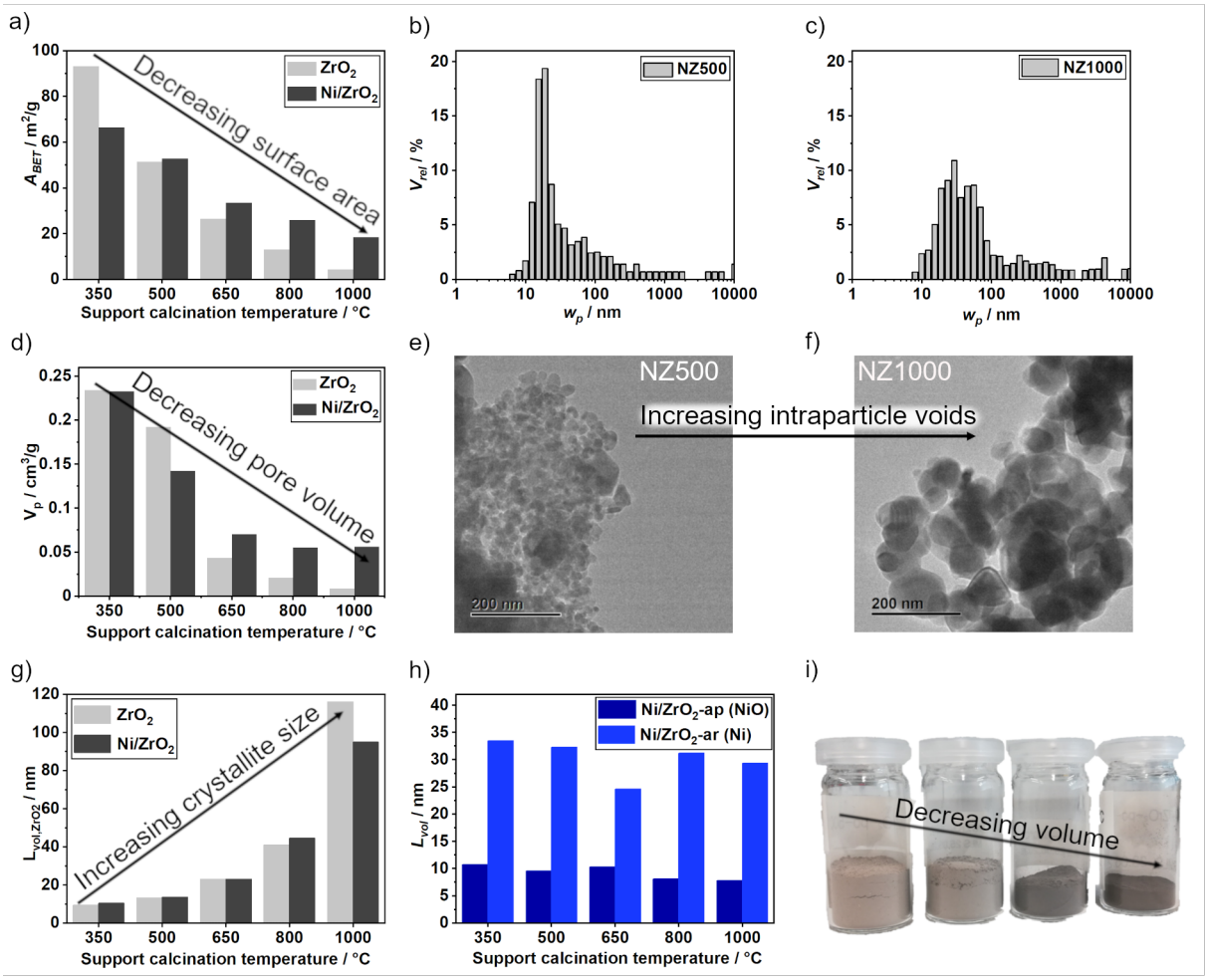


Figure 6.8: "(a) A_{BET} obtained by N_2 physisorption of the pure calcined supports (light grey) and as-prepared catalysts (dark grey). (b,c) Pore width (w_P) distribution obtained by MIP for as-prepared calcined NZ500 and NZ1000. (d) V_P obtained by N_2 physisorption of the pure calcined supports (light grey) and as-prepared catalysts (dark grey). (e,f) TEM images of the catalysts NZ500 and NZ1000 after CO_2 methanation. (g) ZrO_2 crystallite sizes (L_{vol,ZrO_2}) of the pure calcined supports (ligth grey) and as-prepared catalysts (dark grey). (h) Crystallite size L_{vol} for NiO of the as-prepared catalysts (Ni/ZrO_2-ap) and Ni of the spent catalysts after CO_2 methanation (Ni/ZrO_2-ar). (i) An equal mass of the as-prepared catalysts NZ500, NZ650, NZ800 and NZ1000 showing volume loss and color change."[240] Available under the terms and conditions of the Creative Commons Attribution 3.0 license (CC BY 3.0, https://creativecommons.org/licenses/by/3.0/), Copyright ©2022.

pore volume (V_p) (*c.f.* Table 8.9). A steady decrease in A_{BET} from $93\,m^2g^{-1}$ for the support calcined at 623 K to $5\,m^2g^{-1}$ for the support calcined at 1273 K was observed (Figure 6.8a, light grey). The V_p changed analogously from $0.23\,cm^3g^{-1}$ to $0.009\,cm^3g^{-1}$ with increasing calcination temperature (*c.f.* Table 8.9). The as-prepared Ni/ZrO_2 catalysts exhibited similar tendencies as the pure supports. A decrease in A_{BET} from $66\,m^2g^{-1}$ to $18\,m^2g^{-1}$ (Figure 6.8a, dark grey) and in V_p from $0.23\,cm^3g^{-1}$ to $0.056\,cm^3g^{-1}$ were observed with increasing calcination temperature of the initial support (Table 6.1). An increased density and therefore decrease in volume of the ZrO_2 powders with higher support calcination temperatures was visually apparent following synthesis (Figure 6.8i , *c.f.* Figure 3.3), which correlates with the N_2 physisorption results. In general, the A_{BET} values increased following Ni deposition, excluding for the NZ350 catalyst. The relatively large decrease in A_{BET} between Z350 ($93\,m^2g^{-1}$) and NZ350 ($66\,m^2g^{-1}$) can be explained by the subsequent calcination of all catalysts at 773 K after Ni deposition. For all catalysts except NZ350, 773 K was an equal or lower temperature treatment than during the initial support calcination step prior to Ni deposition, and would therefore not be expected to induce significant changes in the support. Notably for the NZ350 catalyst A_{BET} ($66\,m^2g^{-1}$) and V_p ($0.23\,cm^3g^{-1}$) remained higher than for NZ500 ($52\,m^2g^{-1}$, $0.14\,cm^3g^{-1}$). At higher support calcination temperatures (923–1273 K) the catalysts exhibited larger A_{BET} and V_p than the pure support, which can be explained by additional contribution of the nickel to the surface area and pore volume. The A_{BET} of the catalysts is comparable to other Ni/ZrO_2 catalysts in literature. Everett *et al.* reported $66\,m^2g^{-1}$ (calcined at 773 K) for a 5 wt.% Ni/ZrO_2 catalyst with commercial m-ZrO_2 from Saint-Gobain.[350] Martinez *et al.* presented surface areas of 53 and $19\,m^2g^{-1}$ for 20 wt.% Ni/ZrO_2 catalysts (calcined at 773 K) with mixed ZrO_2 phases (m-ZrO_2 and t-ZrO_2).[47] Pandey *et al.* reported Ni and Ni−Fe supported on m-ZrO_2 (calcined at 773 K) with surface areas between 34 and $23\,m^2g^{-1}$.[351]

The pore structure of the as-prepared catalysts was further studied by mercury intrusion porosimetry (MIP) (*c.f.* Figure 8.40–8.44). The w_P distribution for NZ500 and NZ1000 are depicted in Figure 6.8b,c. A shift to larger mean w_P values (from 17 nm to 43 nm) was observed with rising calcination temperature. In addition, TEM analysis showed growth and agglomeration of the support particles during the aging process, leading to the formation of intraparticle voids (Figure 6.8e,f). For the NZ1000 catalyst, the support structure mainly consists of large agglomerated particles with no visible internal porosity. Compared to NZ1000, the NZ500 catalyst has smaller particles, which seem to be packed more densely. Hence, an increase of intraparticles voids with rising support calcination temperature can be observed combined with particle growth, explaining the w_P changes from MIP. This further substantiates the N_2 physisorption results which showed a strong decrease of surface area, and the visually apparent increase in density of supports calcined at higher temperature.

The trend of increasing support particle sizes can further be confirmed with laboratory powder X-Ray diffraction (PXRD). The PXRD for the calcined supports, as-prepared and spent catalysts are shown in in the appendix Figure 8.45–8.48. For the support almost all reflections can be

assigned to m-ZrO_2 with small contributions of t-ZrO_2 for the supports Z25 and Z350 (*c.f.* Figure 8.45, 8.46). The t-ZrO_2 phase is not detected in NZ350, which might be related to the calcination after Ni deposition. By using Rietveld refinement, the crystallite sizes (L_{vol}) of ZrO_2 for the pure support and the catalysts were determined (*c.f.* Table 8.10–8.15). The zirconia crystallite size (L_{vol,ZrO_2}) increased for the pure support together with temperature from ≈10 nm (Z350) to ≈116 nm (Z1000) (Figure 6.8d, light grey, *c.f.* Table 8.10). For the catalysts (dark grey) a similar trend with increasing L_{vol,ZrO_2} from ≈10 nm (NZ350) to ≈95 nm (NZ1000) was observed (Figure 6.8d, Table 6.1). The difference in L_{vol,ZrO_2} for Z1000 (116 nm) and NZ1000 (95 nm) could be due to support changes during the synthesis and/or calcination after Ni deposition. In summary, the textural properties A_{BET} and V_P decreased, whereas L_{vol,ZrO_2} increased with rising support calcination temperature. Therefore, the temperature can be used as a single parameter to adjust the textural properties of the initial supports prior to Ni deposition.
Despite the textural differences of the supports, it was aimed to have similar Ni loading and particle size across the catalyst series. Elemental analysis showed that all catalysts have a comparable Ni loading of ≈13–15 wt.% (Figure 6.8g, Table 6.1). The crystallite sizes of NiO (as-prepared catalysts) and Ni (spent catalysts) were investigated using PXRD. A comparable $L_{vol,NiO}$ for all as-prepared catalysts of ≈10 nm was determined (Figure 6.8h, light blue). After the reaction, $L_{vol,Ni}$ was ≈32 nm for all catalysts except NZ650 (26 nm) (Figure 6.8h, dark blue). The crystallite growth from 10 to 32 nm could be due to agglomeration during reduction and/or reaction. The size of Ni crystallites is comparable to other Ni/ZrO_2 catalysts reported in literature. Pandey *et al.*[351] reported $L_{vol,Ni}$ of 58 nm for a 10 wt.% Ni/ZrO_2 catalyst and Ren *et al.*[352] 34 nm for a 30 wt.% Ni/ZrO_2 catalyst.
For a 17 wt.% Ni/Al_2O_3 catalyst, which was synthesized with the same method used in this study, $L_{vol,Ni}$ of 5.7 nm was reported.[53, 71] However the different support material (Al_2O_3) limits comparability to this study, while tuning the Ni particle size towards lower values is not the focus of the present work. A common technique to obtain particle size distributions is TEM/STEM. However, the obtained contrast between ZrO_2 and Ni was too low to distinguish these from each other, which did not allow for reasonable particle size analysis using TEM/STEM. Therefore, EDX mapping was applied for specific areas of selected catalysts (*c.f.* Figure 8.49–8.52). Both large (≥100 nm) and small Ni particles (10-30 nm) were found for all catalysts by EDX. With the large Ni particles, the number of obtained images was not sufficient to retrieve statistically meaningful particle size distributions. Therefore, solely PXRD is used to quantitatively estimate the particle/crystallite size based on structural refinement. In conclusion, a catalyst series (NZ350–1000) with similar Ni centers was obtained based on ZrO_2 supports with varying textural properties. This series allows to further investigate the activity and stability of the catalysts depending on the support properties."[240]

6.2.3 Catalyst Testing Results

"The catalytic activity in CO_2 methanation was monitored at three reaction temperatures (T_r: 523 K, 623 K, 673 K) (Figure 6.9a). At 523 K between 1 to 8 % X_{CO_2} was reached, which is far

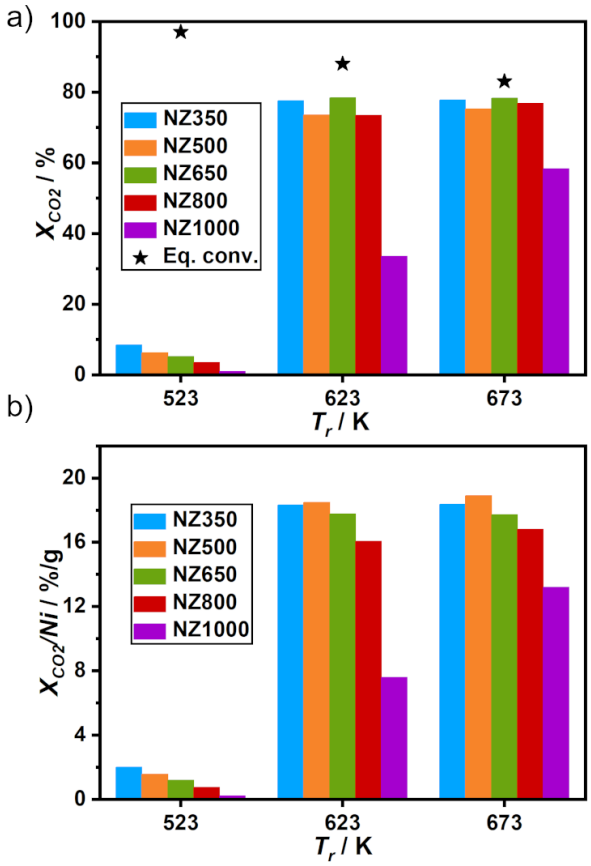


Figure 6.9: "Catalytic activity of the Ni/ZrO_2 series in CO_2 methanation at 523 K, 623 K and 673 K. (a) CO_2 conversion (X_{CO_2}) with equilibrium conversion (black stars). (b) X_{CO_2} normalized to the Ni amount in the reactor."[240] Available under the terms and conditions of the Creative Commons Attribution 3.0 license (CC BY 3.0, `https://creativecommons.org/licenses/by/3.0/`), Copyright ©2022.

below the equilibrium conversion of 97 % and therefore suitable for probing catalyst stability.[45] A trend of decreasing X_{CO_2} with increasing calcination temperature of the support could be observed during reaction at 523 K. At higher temperatures (623 K, 673 K) no specific trend was observed, except for the strong decrease in activity for NZ1000. At 623 K conversions between 73 % and 78 % were obtained for NZ350 to NZ800 and 33 % for NZ1000. At 673 K the NZ1000 catalyst showed an increase in activity with 58 % X_{CO_2}, whereas the rest of the series achieved similar X_{CO_2} as for 623 K (≈78 %), close to equilibrium conversion (Figure 6.9a, black stars). For better comparison of the activity data, the conversion was normalized to the Ni amount of the tested catalyst (Figure 6.9b). With the normalization a similar trend to the one observed at 523 K can be found also at higher temperatures for the catalysts NZ800 and NZ1000, exhibiting decreasing activity compared to NZ350, NZ500 and NZ650. For the latter no clear trend can be

found.
All catalysts exhibited 100 % selectivity towards CH_4 at 523 K (*c.f.* Figure 8.53). With increase of T_r, the formation of CO slightly increases. CO formation is probably due to the reverse water gas shift (RWGS) reaction, which is endothermic and therefore more favored at higher temperatures.[45] The catalysts showed almost no differences in CH_4 selectivity depending on the support calcination temperature except for NZ1000. At 623 K CH_4 selectivity decreased from 99 % (NZ350) to 86 % (NZ1000), while at 673 K 97 % (NZ350) to 84 % (NZ1000) was found. The decline in S_{CH_4} is accompanied with a rise in S_{CO} from 1 % (NZ350) to 14 % (NZ1000) at 623 K and from 3 % (NZ350) to 16 % (NZ1000) at 673 K. A similar phenomena was observed by Beierlein *et al.* by applying rapid aging tests on Ni/Al_2O_3 catalysts.[87] They could observe an increase in S_{CO} for samples aged at higher temperatures. Zhao *et al.*[353] used different combustion methods to synthesize 15 wt.% Ni/ZrO_2 catalysts and tested them in CO_2 methanation. They obtained 1–15 % X_{CO_2} at 523 K, 40–80 % at 623 K and 60–82 % at 673 K. The selectivity towards CH_4 was 100 % at 523 K and at higher temperatures a slight decrease (93 %) for some catalysts was observed.
For better comparison with literature the turnover frequency (TOF) was calculated (*c.f.* section 3.3.2, eq. 3.7) for T_r of 523 K with X_{CO_2} far below the thermodynamic equilibrium (Table 6.1). The dispersion D was calculated using the $L_{vol,Ni}$ obtained from Rietveld refinements of the spent samples. For all catalysts a similar D ranging from 11 to 12 % was determined (Table 6.1). The calculated TOF values ranged between $2.3{\cdot}10^{-2}\,s^{-1}$ for NZ350 and $2.6{\cdot}10^{-3}\,s^{-1}$ for NZ1000 (Table 6.1). Tan *et al.*[354] reported a comparable TOF of $3.8{\cdot}10^{-3}\,s^{-1}$ at 473 K for a 12 wt.% Ni/ZrO_2 catalyst with similar X_{CO_2}, as at 523 K reported here. The value is similar to NZ1000 at 523 K with $2.6{\cdot}10^{-3}\,s^{-1}$, which showed the lowest activity in this series compared to NZ350 with a nearly one order of magnitude higher TOF of $2.3{\cdot}10^{-2}\,s^{-1}$. Jia *et al.*[355] obtained a TOF value of $4.0{\cdot}10^{-2}\,s^{-1}$ for a 10 wt.% Ni/ZrO_2 catalyst at 508 K which is similar to NZ350. At 473 K the group of Liu *et al.*[356] found a TOF of $4.9{\cdot}10^{-3}\,s^{-1}$ with a similar X_{CO_2} as for 523 K in this study. In conclusion, the activity of the catalysts can be influenced by the support calcination temperature, while showing comparable performance to literature values. Notably, the loading, dispersion, and crystallite size of nickel was similar for all catalysts. A decrease in X_{CO_2} and TOF with rising aging temperature can be observed, especially at T_r of 523 K. Following activity tests, the stability of the catalyst during thermal aging experiments was further investigated to distinguish between deactivation caused by changes of the support or Ni particles."[240]

6.2.4 *Operando* Synchrotron Powder X-ray Diffraction Experiments (SPXRD)

"*Operando* SPXRD studies were carried out for the Ni/ZrO_2 catalyst series to investigate various potential deactivation mechanisms. Distinctions in catalyst thermal stability were expected due to the different initial calcination temperatures of the ZrO_2 supports prior to Ni deposition, and the observed differences in catalytic performance depending on the support properties. The

experimental setup and applied temperature profile are shown in Figure 6.10a,b, respectively. The acquired MS data for the samples are shown in the appendix Figures 8.55, 8.57, 8.59, 8.61,

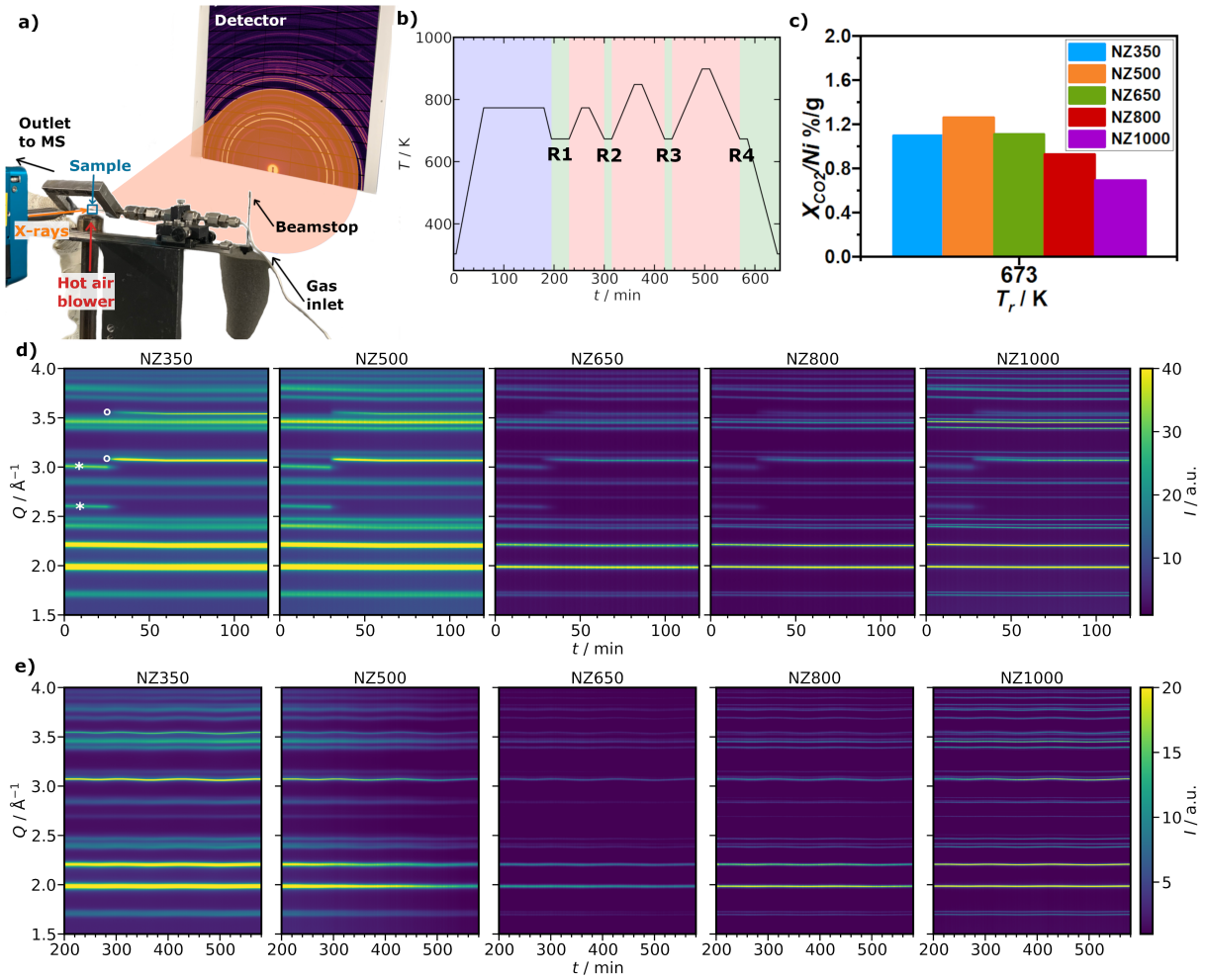


Figure 6.10: "(a) Scheme of the used experimental setup at the beamline. (b) Overview of the experimental conditions during *operando* SPXRD experiments with activation in 25 % H_2/He (blue), reaction conditions 5 % CO_2/20 % H_2/He (green) and thermal deactivation cycles under reaction conditions (red) with each reaction condition step labelled as R1-4. (c) CO_2 conversion normalized by the Ni mass inside the reactor of the *operando* SPXRD at reaction step R1. (d) 2D overview plots of the diffraction patterns showing the Ni (○) formation from NiO (⋆) during activation of the five samples as well as (e) under reaction conditions and thermal deactivation cycles showing no crystalline phase changes."[240] Available under the terms and conditions of the Creative Commons Attribution 3.0 license (CC BY 3.0, `https://creativecommons.org/licenses/by/3.0/`), Copyright ©2022.

8.63. All catalysts were first activated in 25 %H_2/He at 773 K for 2 h with the SPXRD results shown in Figure 6.10d. During activation the NiO reflexes completely vanish and Ni reflexes appear in the same temperature region (≈470 to 520 K) for all five samples.
The activation was followed by switching to reaction conditions 5 %CO_2/20 %H_2/He at 673 K for 30 min, which is labelled as the first reaction step R1. R1 is used to determine the initial activity of the catalysts based on the determined X_{CO_2} and X_{H_2} (*c.f.* Figure 8.56, 8.58, 8.60, 8.62, 8.64).

The X_{CO_2}/Ni is shown in Figure 6.10c. The activity differences between the samples show comparable trends to those found during laboratory testing (Figure 6.9). R1 was followed by artificial thermal deactivation cycles (Figure 6.10b), with temperatures of 773 K, 848 K and 898 K. After each cycle the activity of the catalysts was measured again at 673 K for 15 min, labelled as reaction steps R2, R3 and R4, respectively. This allows to determine catalyst deactivation depending on three different applied temperatures. During thermal deactivation cycles no changes of the crystalline phase composition were found as shown by the SPXRD in Figure 6.10e. Minor changes of the reflex positions (Figure 6.10e), can be attributed to temperature induced lattice expansion or contraction, which matches the temperature program applied to the capillary."[240]

6.2.5 Crystallite Size Changes During *Operando* SPXRD

"In general, textural properties such as surface area are strongly connected to catalyst performance. In particular adsorption of reactants or products takes place on the surface, but the available surface area is also linked to stabilization of metal nanoparticles. The specific surface area (SSA) can be calculated from particle sizes as shown in eq. 3.33, where for crystalline compounds the particle size can be approximated by the crystallite size. However, this relation is only valid for spherical particles. In the present case, two distinct crystalline phases are present, which limits the definition of an overall particle size based on the crystallite sizes as required for eq. 3.33. Additionally, exact knowledge about ρ is hardly possible during *operando* experiments due to textural changes of the sample, which might lead to density changes. Therefore, in a first step an average crystallite size ($L_{vol,avg}$) is calculated for the catalysts in the initial calcined state based on eq. 3.30 taking into account L_{vol,ZrO_2} and $L_{vol,NiO}$. Details on the respective refinements are provided in section 3.5.3 and appendix section 8.7. This $L_{vol,avg}$ is then correlated to A_{BET} (Figure 6.11a), which is available for the catalysts in the initial state. This correlation is fitted by eq. 3.34, which is similar to eq. 3.33 without the requirement of knowing the exact value of ρ and approximating it *via* a fitting parameter. The fitting results are shown in Figure 6.11a with the theoretical curve for pure monoclinic ZrO_2 (eq. 3.33, $\rho = 5.86\,\mathrm{g\,cm^{-3}}$[296]) showing a similar trend.

Based on the fitted values it is possible to calculate the SSA of the catalysts during the *operando* SPXRD experiments using $L_{vol,avg}$ of the ZrO_2 and Ni phases present after activation. However, it should be noted that the values are an approximation as the correlation was obtained for the calcined state and not the activated state. Nevertheless, as all catalysts show a very similar phase composition and no crystalline phase changes occur during reaction conditions and thermal deactivation cycles, SSA can be approximated in this way to unravel textural changes of the catalysts. The same correlation was also studied for the pure supports as shown in appendix Figure 8.77, resulting in similar fit values supporting the correlation approach. The SSA starting from R1 evolves differently for the catalysts as shown in Figure 6.11b. As for A_{BET} analysis (Figure 6.8a), it can be observed that the initial SSA of the catalysts (at $t = 200$ min) decreases

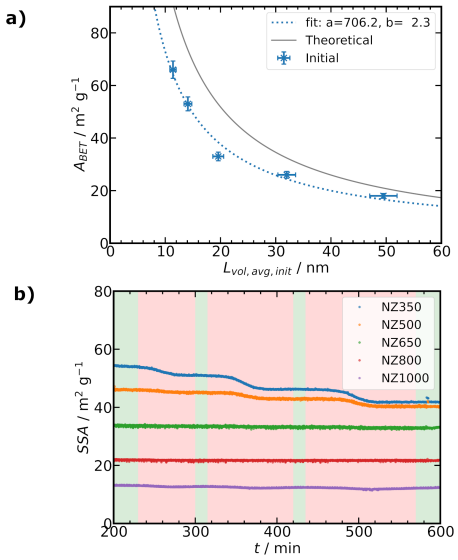


Figure 6.11: "(a) Fitted correlation (blue dotted line) of the measured A_{BET} to $L_{vol,avg}$ (blue crosses, mass fraction weighted average of L_{vol,ZrO_2} and $L_{vol,NiO}$) initially at the start of the *operando* SPXRD experiments based on eq. 3.34 with fitting variables a and b, error bars estimated as 5 % standard deviation. Theoretical relation of A_{BET} and L_{vol} for spherical particles based on eq. 3.33 (grey line). (b) Changes of SSA during reaction conditions and thermal deactivation cycles of the *operando* SPXRD experiments as calculated from $L_{vol,avg}$ (mass fraction weighted average of L_{vol,ZrO_2} and $L_{vol,Ni}$) and the fit values from (a) according eq. 3.34 (shaded areas as Figure 6.10b)."[240] Available under the terms and conditions of the Creative Commons Attribution 3.0 license (CC BY 3.0, `https://creativecommons.org/licenses/by/3.0/`), Copyright ©2022.

with increasing calcination temperature of the ZrO_2 support before Ni deposition. The initial SSA for all catalysts is lower compared to the A_{BET} values of the initial calcined samples (Table 6.1), which can be attributed to the increased crystallite sizes of Ni compared to NiO by a factor of ≈ 3 (...). For NZ350 a pronounced step-wise decrease of the SSA can be observed, with each step related to one of the thermal deactivation cycles. NZ500 exhibits a decrease only significantly with the second and third thermal deactivation step, while NZ650, NZ800 and NZ1000 show no significant reduction of SSA following the thermal deactivation cycles.
Besides the study of the overall textural changes based on the calculated SSA, Rietveld refinement together with microstructural analysis allows to investigate crystallite size changes of each crystalline phase. Figure 6.12a,b show the evolution of the selected (111) reflex for ZrO_2 and Ni phases during *operando* SPXRD, respectively. The different peak shapes of the ZrO_2 (111) reflection (Figure 6.12a) illustrate the different ZrO_2 crystallite sizes depending on the calcination temperature of the support prior to Ni deposition. A representative pattern during each of the reaction steps R1 to R4 is highlighted. For NZ350 and NZ500 significant changes of the reflex depending on the reaction step can be observed, which are more pronounced for NZ350. This indicates crystallite growth of the ZrO_2 phase during thermal deactivation cycles. For NZ650, NZ800 and NZ1000 no significant variation of the reflex can be directly observed. In the case of the

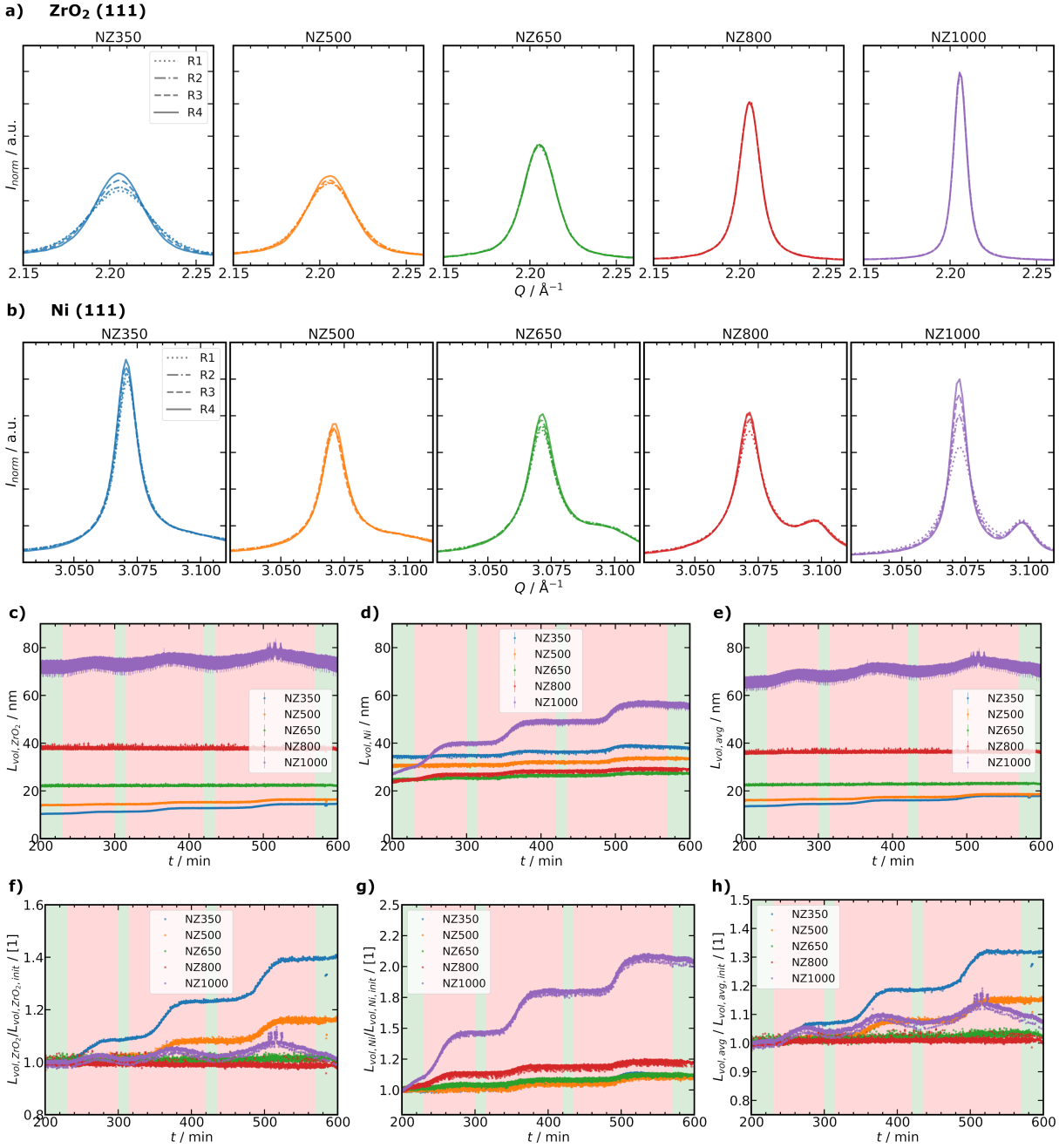


Figure 6.12: "(a) Changes of the ZrO_2 (111) reflex during thermal deactivation cycles highlighted by R1, R2, R3 and R4 steps, (b) analogous changes of the Ni (111) reflex. Evolution of different crystallite sizes obtained from sequential Rietveld refinements for the different catalysts during *operando* SPXRD experiments: (c) L_{vol,ZrO_2}, (d) $L_{vol,Ni}$ and (e) $L_{vol,avg}$ (mass fraction weighted average of L_{vol,ZrO_2} and $L_{vol,Ni}$). Relative changes of L_{vol} normalized to the initial reaction step R1 according eq. 3.31: (f) ZrO_2 phase, (g) Ni phase and (h) average crystallite size of the catalysts. Shaded areas as Figure 6.10b."[240] Available under the terms and conditions of the Creative Commons Attribution 3.0 license (CC BY 3.0, `https://creativecommons.org/licenses/by/3.0/`), Copyright ©2022.

Ni (111) reflex (Figure 6.12b), all samples show significant changes depending on the reaction step. The variations become more pronounced with higher calcination temperature of the ZrO_2 support. Additionally to the qualitative description of the peak shape, a microstructural refinement as part of Rietveld refinement of the SPXRD provides quantitative information about crystallite size changes during the thermal deactivation cycles. Figure 6.12c-e show the evolution of L_{vol,ZrO_2}, $L_{vol,Ni}$ and the mass fraction weighted average $L_{vol,avg}$ of both, respectively. Complementary to the absolute values, Figure 6.12f-h show the relative changes compared to the initial reaction step R1, respectively, indicating sequential changes during the subsequent thermal aging cycles. L_{vol,ZrO_2} depends on the calcination temperature of the support prior to Ni deposition and ranges from about 9 nm to 70 nm in the initial reaction step R1. During thermal deactivation cycles a step-wise increase of L_{vol,ZrO_2} can be observed for each temperature step for NZ350. Although all catalysts were initially activated for 2 h at 773 K, for NZ350 a crystallite growth can be observed already at the first thermal deactivation temperature of 773 K. For NZ500 a significant increase of the crystallite size is only detected with the second and third thermal deactivation steps. The catalysts NZ650, NZ800 and NZ1000 show no significant increase of L_{vol,ZrO_2} during those cycles. The reversible increase of L_{vol,ZrO_2} of NZ1000 during the thermal deactivation cycles (Figure 6.12c,f) might be explained by larger crystalline domains due to lattice expansion or reversible ordering/disordering, but the differences are small compared to the refinement error and could also be caused by refinement artifacts. The evolution of $L_{vol,Ni}$ is contrary compared to the ZrO_2 phase. The initial $L_{vol,Ni}$ at reaction step R1 range from about 25 to 35 nm for the different catalysts (Figure 6.12d). For NZ350, NZ500 and NZ650, the $L_{vol,Ni}$ only slightly increased with thermal deactivation after the second reaction step R2 (Figure 6.12d,g). This is different for the NZ800 and NZ1000 samples where $L_{vol,Ni}$ already increased with the first thermal deactivation step, while the behavior is most pronounced for NZ1000. The changes can be also observed for the $L_{vol,avg}$ in Figure 6.12e,h. As $L_{vol,avg}$ represents the mass fraction weighted average for ZrO_2 and Ni it mainly reflects changes of the ZrO_2 phase. Therefore, here the NZ350 and NZ500 samples show the most pronounced changes. On the other hand, it can be observed that the strong changes of $L_{vol,Ni}$ result in a significant increase of the $L_{vol,avg}$ for NZ1000. The strong Ni crystallite size increase in NZ1000 might be explained that the support reached such a small SSA that Ni particle growth is strongly favored. In contrast, NZ650 and NZ800 were as a whole less impacted by the thermal deactivation procedure.
In summary, the crystallite size changes during thermal deactivation cycles could be quantified and show for NZ350 and NZ500 mainly changes of L_{vol,ZrO_2}, while for NZ800 and NZ1000 especially changes of $L_{vol,Ni}$ were observed."[240]

6.2.6 Correlation of Crystallite Size and Thermal Deactivation

"The conversion of CO_2 and H_2 obtained from MS analysis were used to determine the activity of the catalysts during *operando* SPXRD. The absolute values for X_{CO_2} and X_{H_2} at the different

reaction steps R1-4 are shown in appendix Figure 8.65 and 8.66, respectively. The initial conversions for the catalysts at R1 are in the range of 57 to 67 %. Therefore, it can be reasonably assumed that the reaction is performed far from thermodynamic equilibrium conditions or full conversion (≈ 80 %, Figure 6.9a), which is a prerequisite to detect possible catalyst deactivation. The changes of X_{CO_2} and X_{H_2} in comparison to the initial activity at R1 (ΔX) are shown in Figure 6.13a,d, respectively. All studied catalysts show a step-wise deactivation during the

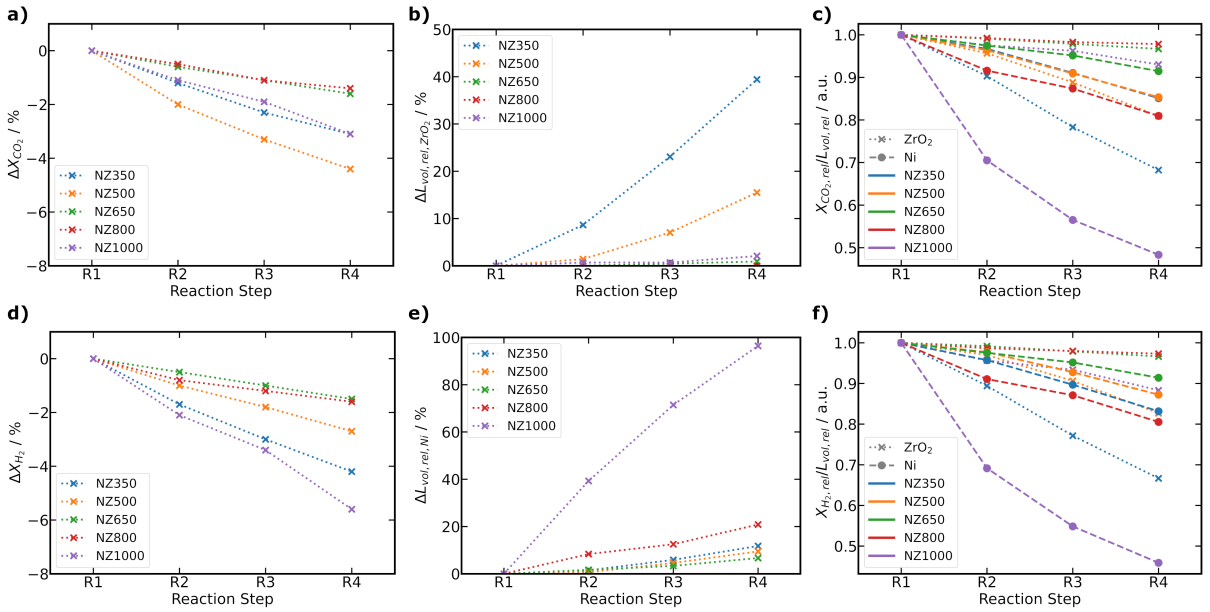


Figure 6.13: "(a) Changes of the X_{CO_2} for each reaction step as difference to the initial activity at R1. (b) Relative changes $\Delta L_{vol,rel,ZrO_2}$ of the ZrO_2 crystallite size according eq. 3.32 depending on the reaction step referenced to R1. (c) Relative CO_2 conversion $X_{CO_2,rel}$ (eq. 3.29) divided by the relative crystallite size $L_{vol,rel}$ (eq. 3.31) for Ni and ZrO_2 phases. (d) Changes of the X_{H_2} for each reaction step as difference to the initial activity at R1. (e) Relative changes $\Delta L_{vol,rel,Ni}$ of the Ni crystallite size according eq. 3.32 depending on the reaction step with R1 as reference. (f) Relative H_2 conversion $X_{H_2,rel}$ (eq. 3.29) divided by the relative crystallite size $L_{vol,rel}$ (eq. 3.31) for Ni and ZrO_2 phases."[240] Available under the terms and conditions of the Creative Commons Attribution 3.0 license (CC BY 3.0, `https://creativecommons.org/licenses/by/3.0/`), Copyright ©2022.

thermal deactivation cycles. Therefore, the deactivation can be clearly related to the temperature applied during each of the cycles. Less pronounced deactivation occurs for the NZ650 and NZ800 catalysts, which suffer a loss of ≈1 % in X_{CO_2} and X_{H_2} after thermal deactivation cycles. The other three catalysts lost more than 2 % in X_{CO_2} and X_{H_2}, while there are differences in the extent of activity loss between X_{CO_2} and X_{H_2}.

Besides the activity differences, the changes of L_{vol,rel,ZrO_2} and $L_{vol,rel,Ni}$ in reference to the initial reaction step R1 are shown in Figure 6.13b,e, respectively. The L_{vol,rel,ZrO_2} of NZ350 is increased by about 40 % and for NZ500 by about 17 % compared to the initial values at R1, while the other three catalysts show only minor changes of the L_{vol,rel,ZrO_2} after thermal deactivation cycles of less than 3 %. This is different for $L_{vol,rel,Ni}$, where NZ1000 shows an increase of almost

100 % followed by the NZ800 sample of ≈20 %. The other three samples show increases of ≈10 % or below.
To estimate the influence of the different L_{vol} changes on catalyst deactivation, the relative conversions ($X_{CO_2,rel}$, $X_{H_2,rel}$, eq. 3.29) are correlated with the relative crystallite sizes ($L_{vol,rel,i}$ eq. 3.31) with respect to the initial reaction step R1 in Figure 6.13c,f, respectively. This correlation analysis allows to retrieve information regarding which of the two phases might have a stronger influence on catalyst deactivation. For both evaluated conversions, the strongest observed correlations are for the the changes of $L_{vol,Ni}$ of the NZ1000 catalyst, followed by the correlations of L_{vol,ZrO_2} for NZ350. In general, it can be observed that there is a greater correlation between $L_{vol,Ni}$ and the conversions for NZ1000, NZ800 and NZ650. This is different for NZ350 and NZ500, where the correlation of L_{vol,ZrO_2} with the conversions is larger than $L_{vol,Ni}$."[240]

6.2.7 Overall Discussion of the Thermal Deactivation

"The five different studied catalysts essentially differ by the calcination temperature and as consequence surface area and pore volume of the ZrO_2 support prior to Ni deposition, while the following calcination and activation steps are identical for all samples. In addition, the initial properties of the active metal Ni particles in terms of loading, dispersion, and crystallite size were similar for all catalysts following synthesis and calcination. As observed in the *operando* SPXRD the activity trends of the catalysts after activation at R1 are similar compared to laboratory tests, showing decreasing activity with higher calcination temperature of the support, especially for NZ1000. The activated catalysts at R1 are mainly distinguished by their L_{vol,ZrO_2}, while the $L_{vol,Ni}$ is in a comparable range for all catalysts with minor differences. The $L_{vol,Ni}$ is relatively large at around 30 nm. Therefore, it can be reasonably assumed that no major differences in the reaction mechanism depending on the Ni particle size as shown by Vogt *et al.*[70] are present as the kind of surface sites are similar and deactivation as reported by Mutz *et al.*[81] should be negligible. The resulting activity should mainly depend on the available active surface area of the catalysts.
Typically, the active surface area and the specific surface area of catalysts are determined *via* gas sorption methods in *post mortem* analysis.[133, 357] However, an application of those under *operando* conditions is hardly possible. Contrary to this, PXRD with microstructural refinement as shown here allows to determine textural changes of the ZrO_2 support and Ni nanoparticles as long as there are no complex phase changes occurring during thermal deactivation. In the present case, the five catalysts show different crystallite size changes and deactivation behavior depending on the calcination temperature of the support. The most pronounced catalyst deactivation was observed for NZ350, NZ500 and NZ1000 catalysts (Figure 6.13a,d), while for those three samples also the strongest crystallite size changes were found. For NZ350 and NZ500, mainly an increase of L_{vol,ZrO_2} and thus sintering of the support was detected, while for NZ1000 the $L_{vol,Ni}$ is

much larger and thus Ni particle sintering occured. Based on the correlation analysis shown in Figure 6.13c,f the major reason for catalyst deactivation might be divided into: (i) dominant changes of the ZrO_2 support, (ii) dominant changes of the Ni phase and (iii) an intermediate region with both effects as schematically illustrated in Figure 6.14.

Despite that all catalysts were activated at 773 K for 2 h, NZ350, NZ500 and NZ1000 show a

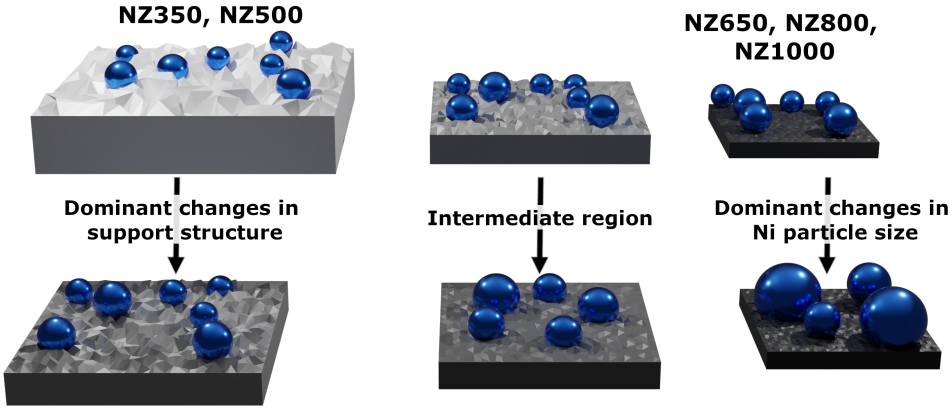


Figure 6.14: "Summary of the different proposed deactivation mechanism found by *operando* SPXRD. NZ350 and NZ500 show predominant ZrO_2 sintering and NZ650, NZ800 and NZ1000 dominant Ni sintering and an expected intermediate region as origin of deactivation. Ni blue, ZrO_2 grey. The grey color gradient illustrates changing textural properties of the support associated to a decrease in surface area and pore volume due to sintering."[240] Available under the terms and conditions of the Creative Commons Attribution 3.0 license (CC BY 3.0, `https://creativecommons.org/licenses/by/3.0/`), Copyright ©2022.

slight deactivation after only 15 min at 773 K under reaction conditions. The deactivation of NZ350 and NZ500 can be mainly related to textural changes of the ZrO_2 support. For NZ650, NZ800 and NZ1000 sintering of Ni particles appears to be the main reason for deactivation, with NZ650 and NZ800 showing highest stability among the tested samples. The stability of NZ650 and NZ800 might be related to the calcination temperature of the support, which were higher than the deactivation temperatures. The deactivation due to Ni sintering can be explained by a decrease in the active metal surface area. Literature studies have discussed changes of Ni nanoparticles, the support material and a complex interplay of the effects as reasons for deactivation.[51, 87, 95, 101] However, deconvolution of these effects was not previously possible due to entirely *post mortem* analysis and thus the missing link with activity data provided by *operando* analysis as shown here. The sintering of the ZrO_2 support as shown in the present work might influence the catalyst stability in different ways. For Ni/ZrO_2 the associative mechanism for CO_2 methanation would require CO_2 adsorbates on the ZrO_2 support to take part in the reaction.[38, 42, 60] Therefore the amount of CO_2 adsorbed on the support is lower with decreasing support surface area leading to lower catalytic activity. Furthermore, it is possible that the textural changes of the support result in blocking of active Ni surface sites.

Additionally, SPXRD did not reveal formation of bulk NiO species and the quantitative phase

analysis from Rietveld refinement matches the values obtained from elemental analysis. Thus, a fully reduced state of Ni throughout the experiment was assumed. The formation of surface NiO cannot be fully excluded by the applied methods, however due to the relatively large and similar Ni particle sizes in the catalyst series, similar redox properties are assumed for all catalysts. Possible deactivation due to formation of surface oxide species, if this occurs, should therefore be similar for all five catalysts due to identical reaction conditions. The significant quantity of H_2 in the feed makes formation of NiO species unlikely in any case, also according to previous studies using *operando* XAS.[71, 80–82] In this case, NiO was only significantly present during H_2-dropout tests. However, to unravel the different potential effects in more detail, further kinetic and spectroscopic studies of the active and deactivated catalysts would be required. In the present study, the focus was on presenting SPXRD as a single powerful and relatively routinely available method to differentiate thermal deactivation effects sensitive towards textural and crystallographic changes under *operando* conditions, with the possibility to distinguish support and metal nanoparticle changes."[240]

6.2.8 Conclusions

In this section, a designed series of five different Ni/ZrO_2 catalysts with different textural support properties, but similar Ni sites, was presented for systematic investigation of thermal catalyst deactivation. This deactivation pathway is strongly associated to hot-spot formation (*c.f.* section 1.2.3 and Figure 1.7), which might be even enhanced during dynamic process operation of the CO_2 methanation (*c.f.* section 1.2.4). Conventional laboratory characterization proved a decrease in specific surface area depending on the support calcination temperature prior to Ni deposition. The obtained catalysts showed comparable activity based on the estimated TOF as other Ni/ZrO_2 catalysts in literature, while all samples showed similar Ni nanoparticles with crystallite sizes of ≈30 nm. Therefore, the catalysts essentially differ by the textural properties of the support adjusted by the calcination temperature, making them a suitable model system for thermal deactivation studies.
For this purpose, *operando* SPXRD experiments with artificial thermal aging cycles were carried out. The catalysts in the series showed different deactivation behavior with the samples NZ350, NZ500 and NZ1000 showing strongest activity loss and NZ650 and NZ800 the least. During thermal deactivation cycles no crystalline phase changes were observed. However, significant changes of crystallite sizes either of the support or metal nanoparticles could be identified, with their extend depending on the respective catalyst. The crystallite size changes of the ZrO_2 support correlated with the support calcination temperature. The catalyst series can be distinguished into NZ350 and NZ500 showing mainly deactivation due to support changes, while NZ650, NZ800 and NZ1000 show dominant Ni crystallite size changes. The differences in deactivation might be explained by loss in specific metal surface area in case of dominant Ni sintering, while for support sintering loss of CO_2 adsorption sites due to decrease in support surface area or blocking

of accessible metal surface area are a possible explanation (*c.f.* section 1.2.2). However, those assumptions have to be verified by more detailed kinetic and spectroscopic studies.
The presented results in this section highlight the importance to deconvolute different deactivation mechanisms in a systematic way. Here, *operando* SPXRD was shown as an ideal tool to follow crystalline phases as well as microstructural changes, from which textural properties can be derived. Accessing these sample changes during deactivation is taking place, i.e., *in situ* or *operando*, is hardly possible with conventionally applied methods to derive textural properties. However, this is required to derive structure-deactivation relationships as presented here based on *operando* SPXRD experiments. Similar, to *in situ* X-ray total scattering studies including PXRD analysis of the calcination of the hierarchically porous Ni/Al_2O_3-h catalyst in section 5.2, the present example highlights the various application possibilities of hard X-ray methods to understand the evolution of the catalyst structure. The presented approach can be expanded towards *in situ* spatially-resolved studies, which are especially interesting for heterogeneous samples like the designed core-shell catalysts that allow a dynamic process operation as discussed in section 1.2.5 and 4.2. XRD-CT or PDF-CT studies would allow to obtain information on the atomic structure with µm-sized spatial resolution as reviewed for selected examples in *c.f.* section 1.5 or shown in Figure 1.16 and 1.17.

7 Conclusions and Outlook

Advanced characterization methods are important to derive structure-function relationships in heterogeneous catalysis. This is fundamental for a future knowledge-based design of catalysts with improved performance and stability. As part of this thesis, various hard X-ray-based methods were exploited for a detailed understanding of the structural and textural properties of Ni-based catalysts with potential application in CO_2 methanation. Especially, synchrotron-based high resolution X-ray nanotomography and diffraction techniques were used to retrieve a holistic view on the catalyst structure and changes thereof during synthesis and deactivation. Different hard X-ray methods can be applied either in 0D/1D or spatially-resolved in 2D/3D, with the various contrasts allowing for many complementary information on the sample as illustrated in the introduction Figure 1.11. Therefore, hard X-ray methods are regarded as an universal toolbox, with the methods applied in the present thesis illustrated and summarized in Figure 7.1.

A major challenge in the spatially-resolved application of hard X-ray methods to understand

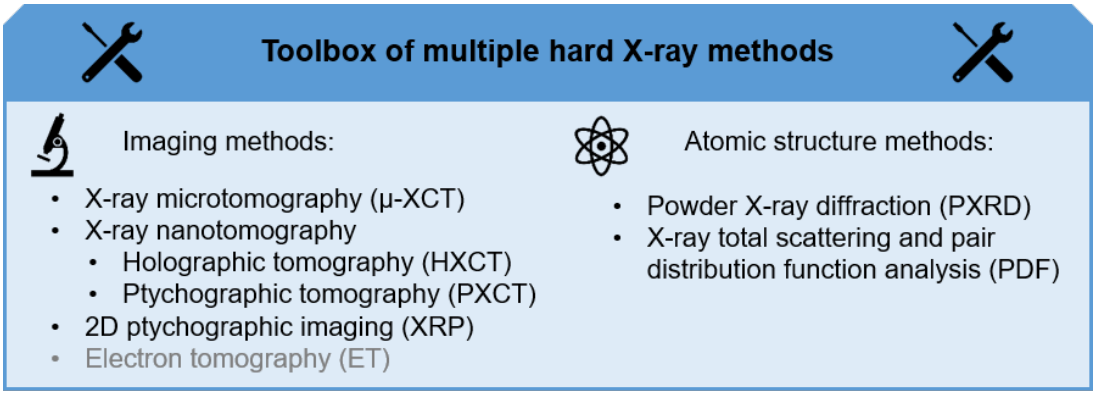


Figure 7.1: Overview of the different hard X-ray methods applied throughout this thesis, which are considered as a toolbox for advanced catalyst characterization. The methods are sorted into imaging and atomic structure methods. For completeness electron tomography is listed.

catalyst structures in 3D are the multiple relevant length scales from sub-nm to m (*c.f.* Figure 1.9). A main focus in this thesis was the multiscale analysis of the porosity and textural properties of applied Ni-based catalyst systems for CO_2 methanation as summarized in Figure 7.2. In studies of a Ni/Al_2O_3 reference catalyst (SPP2080-IMRC), the requirement of the combination of different imaging methods to cover all relevant length scales in heterogeneous catalysis was illustrated. X-ray microtomography (µ-XCT), X-ray nanotomography (holographic X-ray computed tomography (HXCT) and ptychographic X-ray computed tomography (PXCT))

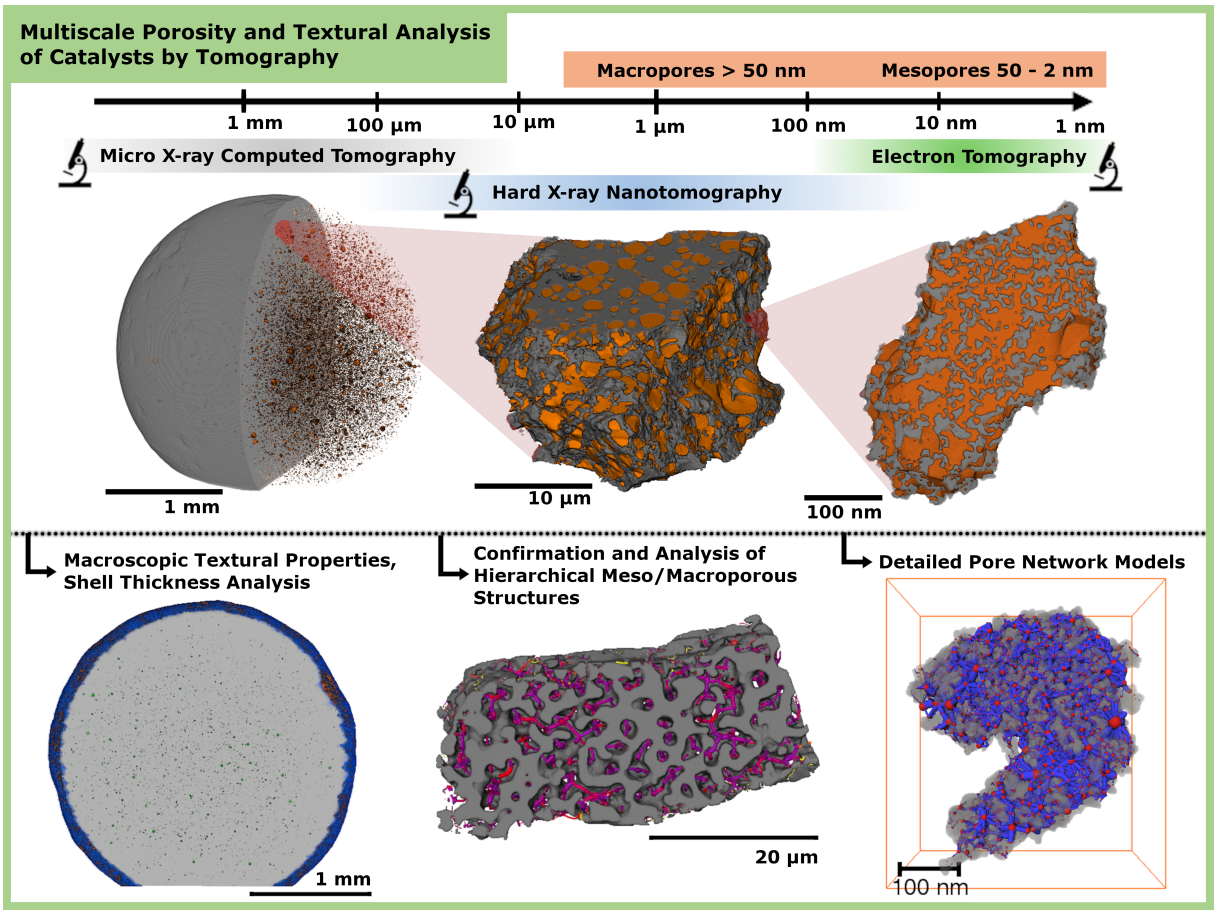


Figure 7.2: Illustration of the results of the advanced multiscale porosity and textural characterization by imaging methods. In this respect, the covered length scales within this thesis are shown together with some main results that could be derived from the application of the imaging techniques.

along with electron tomography (ET) allowed to reveal the meso-/macropore structure of the SPP2080-IMRC, thereby covering length scales from mm to nm. Essentially, µ-XCT could only provide an overview of the sample, but not resolve significant porosity. The macropores could be fully analyzed by HXCT or PXCT, while on a limited sample volume ET could provide information on the mesopores, illustrating the trade-off between sample size, imaging resolution and representativity as shown in Figure 7.2. Although this was mainly reported for model systems before, it has been rarely applied on technical catalysts as presented here and has to be carefully considered in all imaging studies. As an important result, the combined imaging approach was found to be superior compared to conventional porosity analysis methods, i.e., gas sorption or intrusion methods. The latter could not reveal significant presence of macropores, although accounting for about 1/3 of the total porosity as proven by multiscale imaging studies. The exceeding potential of advanced imaging methods in porosity and textural analysis of catalysts compared to conventional methods, also to retrieve complex detailed pore network models, was not reported in this extend before. In future, those results could be readily applied in the

simulation of mass transport properties directly on the true pore structure including measures for tortuosity or pore connectivity. Additionally, the powerful potential of PXCT to retrieve 3D quantitative information about the local electron density and its unexplored utilization to retrieve sub-resolution information on textural properties was presented. With sufficient general knowledge about the chemical structure and composition of a material, the analysis of the electron density allowed to retrieve sub-resolution information about the mesoporosity, which usually requires ET on much smaller sample volumes, prone to be not representative for the overall sample. However, without structural knowledge this is limited to only qualitative information.
One challenge in CO_2 methanation is the possibility for a dynamic process operation in the frame of fluctuating renewable energy supply, which for current state-of-the-art catalysts, e.g., the SPP2080-IMRC, leads to hot-spot formation and thermal runaway scenarios. In this respect, a designed core-shell catalyst particle from the group of Prof. Kai Sundmacher (Magdeburg) is suggested to significantly reduce the thermal sensitivity by controlling catalyst performance *via* mass transport limitations from an inert shell around an active core (SPP2080-IMRC). The thorough µ-XCT characterization of the shell thickness and homogeneity revealed that both depended on the coating duration during sample preparation in a fluidized-bed. Well-controlled textural properties of the shell are crucial for effective mass transport limitations. It was highlighted that a minimum coating time (30 min) was necessary to achieve a homogeneously closed shell, which was not known from SEM imaging. Furthermore, the thickness of the shell and presence of larger void spaces was retrieved and quantified as an important future design parameter. For detailed knowledge on the shell porosity additional hard X-ray nanotomography studies are emphasized. An advantage of laboratory µ-XCT compared to X-ray nanotomography is its wider availability. Therefore, similar studies like on the shell-thickness can be routinely applied in the manufacturing of complex heterogeneous catalyst designs. Here, µ-XCT is also not only limited to spherical samples like often applied dynamic light scattering, but allows for free sample morphology. Furthermore, scanning of whole catalyst beds is feasible, which drastically enhances sample statistics and representativity.
To increase catalyst activity, e.g., in the active core of the previous design, mass transport limitations should be ideally absent. Hierarchically meso-/macroporous catalysts are often proposed to increase mass transport in the catalysts. Therefore, a sol-gel synthesized hierarchically porous Ni/Al_2O_3 catalyst (Ni/Al_2O_3-h) from the group of Prof. Gläser (Leipzig) was studied as a promising candidate. The true hierarchical nature of the pore structure of Ni/Al_2O_3-h could be proven by combined PXCT and ET as illustrated in Figure 7.2. Similar to the SPP2080-IMRC, PXCT revealed a connected macropore structure, while ET could be used to study the mesopores. This is not directly possible by conventional porosity analysis methods, i.e., gas sorption of Hg porosimetry. As the introduction and presence of a hierarchical pore structure is generally believed to enhance mass transport in the catalysts, initial macrokinetic simulations were reported confirming an improved effectiveness factor compared to a purely mesoporous catalyst. This shows a direct utilization of tomographic data in simulation studies, while future

more sophisticated modeling studies directly on the tomographic data can be valuable, which is currently not established. However, an experimental confirmation thereof requires future detailed kinetic experiments. The catalytic activity of Ni/Al_2O_3-h was tested in CO_2 methanation, while a high reduction temperature (>1100 K) was required for catalyst activation. By initial Rietveld analysis of powder X-ray diffraction (PXRD), diffuse reflectance UV/Vis spectroscopy and temperature-programmed reduction, it was concluded that the incorporation of Ni into the $\gamma-Al_2O_3$-like structure results in limited reducibilty at low temperatures. This requires a more detailed knowledge about the preparation of the Ni/Al_2O_3-h catalyst, which might allows to synthesize tailored materials with better reducibilty at low temperatures.

Therefore, *in situ* experiments are required, which can unravel sample transformations as they occur providing a holistic understanding of catalyst synthesis. The calcination of the Ni/Al_2O_3-h system at 873 K as last synthesis step was chosen, because it can involve many changes of the material. For the Ni/Al_2O_3-h, especially the evolution of the pore structure and of the atomic structure are of interest as depicted in Figure 7.3 *In situ* X-ray ptychography imaging

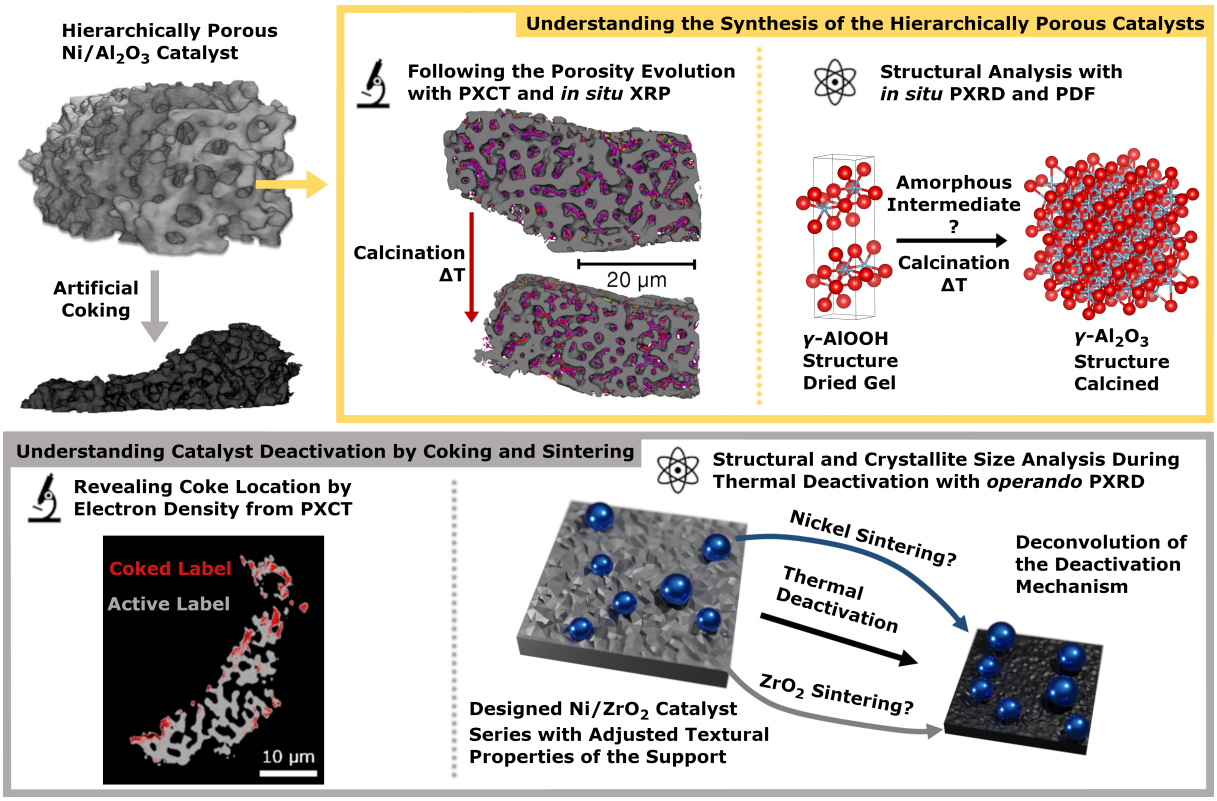


Figure 7.3: Overview on the experiments using hard X-ray methods to understand the synthesis of the hierarchically porous Ni/Al_2O_3-h catalyst broadly discussed in this thesis. Furthermore, potential relevant deactivation phenomena for CO_2 methanation were studied using hard X-ray imaging (coking) or hard X-ray methods for atomic structural information (thermal deactivation).

in 2D allowed to follow the morphological changes during calcination, activation and under

reaction conditions with a resolution of about 67 nm. A volume shrinkage of ca. 17 % could be estimated during calcination, while 2D imaging did not enable for further quantification. Therefore, complementary PXCT studies on identical particles of Ni/Al_2O_3-h and a Ni-free sample were performed in dried gel and calcined states. The quantification of the PXCT revealed a reduction of the macropore diameter during calcination and further confirmed the volume shrinkage. The analysis of the electron density showed a densification of the catalysts during calcination, which was attributed to a reduction of the apparent mesoporosity. Though, the true mesoporosity value was only obtained reliably for the calcined state as the exact dried gel and intermediate structures were unknown. As PXCT cannot provide direct information on atomic structures of the material, complementary structural investigations of the sample changes during calcination are necessary.
To reveal those structural changes during calcination of the dried gels, *in situ* X-ray total scattering experiments were performed. Those allowed to simultaneously obtain PXRD data and by transformation thereof the pair distribution function (PDF). The presence of a nanocrystalline $\gamma-$AlO(OH)-like structure was found for the initial dried gel state, while the Ni containing sample exhibited larger crystallite/particle sizes. During calcination, the dried gels became amorphous, while PDF could reveal atom pairs only for a small range significantly up to about 5 Å highlighting the short-range order. The amorphization was additionally accompanied with the detection of traces found by MS that can be related to the decomposition of organic compounds, probably originating from the used porogen and solvent in the synthesis. At a calcination temperature of 923 K the Ni/Al_2O_3-h sample showed the formation of a $\gamma-Al_2O_3$-like structure, while the temperature was not sufficient for a crystallization of the Ni-free sample. Premature Rietveld analysis indicated the incorporation of Ni into the $\gamma-Al_2O_3$-like structure. Therefore, two phase transformation processes during calcination were found, which cannot be resolved by a single method. However, the structural analysis requires further information and more detailed evaluation together with future theoretical and experimental studies. Those should focus especially on understanding the intermediate amorphous structure along with the suggested incorporation pathway of Ni into the $\gamma-Al_2O_3$-like structure. For this purpose also complementary other hard X-ray methods (*c.f.* Figure 1.11) like X-ray absorption spectroscopy can be valuable. The future goal should be to lower the required reduction temperature of Ni by adapting the synthesis procedure while sustaining the hierarchical pore structure.

Besides understanding of catalyst synthesis, a detailed knowledge about deactivation phenomena is important for a future knowledge-based catalyst design. Here, coking and thermal deactivation were selected as two relevant deactivation pathways in CO_2 methanation over Ni-based catalysts as illustrated in Figure 7.3. As coking can lead to blocking of pores or the active sites, the location thereof inside the catalyst particles is important to know. However, this is hardly possible using established conventional techniques for the analysis of coke species. The potential of PXCT in revealing the 3D-location of coke in whole catalyst grains is exploited for artificially coked

Ni/Al_2O_3-h and a purely mesoporous catalyst. The coke formation was qualitatively confirmed by Raman spectroscopy during the artificial coking treatment. The electron density information from PXCT on activated and coked samples was then applied to unravel catalyst coking, as an increase in electron density could be observed. A thresholding based image analysis approach suggested that the coking occurs in mesopores of the catalyst starting at the exterior of the catalyst grains. However, more studies at different coking stages are required for confirmation. This might involve *in situ* X-ray ptychography experiments similar to the porosity evolution during calcination, which can be feasible to locate coke species during their formation.
Compared to coking, thermal deactivation is considered as the major deactivation pathway of Ni-based catalysts in CO_2 methanation. Thermal deactivation can lead to morphological changes, mixed oxide formation of metal nanoparticles and the support as well as sintering of metal nanoparticles or the support, which are usually beyond the current achievable resolution of hard X-ray nanoimaging methods. Therefore, complementary *operando* synchrotron PXRD experiments on a designed series of Ni/ZrO_2 catalysts were performed to obtain atomic and micro-structural information. The catalyst series exhibited similar Ni metal sites in terms of loading and crystallite size, while they differed by the calcination temperature of the support prior to Ni deposition. The catalysts showed different textural properties, essentially related to the support surface area and the calcination temperature as single parameter. Therefore, the series was an ideal model system to systematically differentiate deactivation mechanisms during thermal aging, which can be hardly distinguished by conventional *post mortem* characterization. *Operando* PXRD experiments during artificial thermal aging cycles at three different temperatures revealed changes of the crystallite size of the support and metal nanoparticles depending on the support calcination temperature, while no crystalline phase changes were observed. Thereby, crystallite size changes were assumed to be proportionally correlated to textural properties of the catalysts and corresponding crystalline phases. It was found that catalysts calcined at temperatures of 623 and 773 K before Ni deposition mainly deactivated due to sintering of the ZrO_2 support. On the other hand, for catalysts with supports calcined at 923, 1073 and 1273 K a correlation of the deactivation with Ni sintering was revealed. Therefore, *operando* PXRD was presented as an ideal method to investigate structural and textural (crystallite size) changes, which allowed to deconvolute different deactivation phenomena. In future, the extension of the analysis into 3D space using *in situ* XRD-CT or PDF-CT is feasible, especially to understand the deactivation of advanced catalysts designs, e.g., the core-shell concept, which exhibit a non-uniform 3D structure.

Within this thesis the potential of different hard X-ray techniques, with a focus on modern synchrotron-based methods, was presented to elucidate structural and textural properties of catalysts from the pellet down to the atomic scale. Several complementary imaging techniques, e.g., phase-contrast imaging, diffraction or spectroscopic methods (*c.f.* Figure 1.11) have to be combined to obtain a holistic understanding of catalyst structure, synthesis and deactivation. In such a multimodal approach, superior information content compared to conventionally applied

characterization techniques is accessible. The presented results for the use of advanced imaging techniques for porosity and textural characterization emphasize a more wide application on industrially-relevant catalyst samples. In future work, this valuable data can be applied to improve the synthesis of the catalysts to increase catalyst performance and stability based on fundamental knowledge. Furthermore, extended mathematical models for simulation studies based on the advanced characterization methods are emphasized and can be developed. The combination of different X-ray contrast modes for multidimensional characterization of catalysts presents a powerful future research trend to reveal structure-function relationships in very detail. Beyond the shown results focusing on textural and porosity analysis, different length scales can be covered by application of complementary contrasts, e.g., PXRD/PDF for atomic length scales combined with phase contrast imaging for resolution imaging in the tens or hundreds of nanometer scale. This multimodal approach would provide even more detailed information and can be expected as a future trend in 3D characterization of catalysts. Ideally, this would finally lead to new materials or catalyst designs for CO_2 methanation providing enhanced low-temperature activity, allowing for dynamic catalyst operation in the framework of fluctuating renewable energy supply or better resistance towards deactivation.

For hard X-ray nanoimaging methods a general future challenge is to further develop *in situ* and *operando* capabilities, which are required for true structure-function relationships. The *ex situ* PXCT studies of coking as part of this thesis should be ideally performed *in situ*. Principally, the presented *in situ* X-ray ptychography setup would allow for acquisition of tomograms, but the currently feasible acquisition time (more than 12 h per tomogram) prevents a practical application. Generally, the current availability of hard X-ray nanoimaging methods is a critical point, which only allows to study few selected samples. Therefore, possibilities to perform *in situ* X-ray nanotomography in shorter time are required, which is strongly related to developments of 4^{th} generation synchrotron sources, detector technology, beamline hardware and software solutions.[158, 358, 359] In this respect, the presented X-ray nanotomography methods are expected to reach sub 10 nm resolution on a routine base in the near future or much faster acquisition of tomograms, ideally in less than one hour. This would allow to either study more samples at the same time, which would provide better sample statistics or to approach length scales currently only feasible for electron tomography. Therefore, current borders in the trade-off between sample size vs. resolution vs. representativity can be expanded, but will still present an unavoidable challenge in imaging-based characterization.

In future, the application of imaging results in chemical engineering should be further exploited, which is essentially related to advanced data analysis, derivation of mathematical models and potential development of "digital twins" of catalysts. Overall, it can be expected that synchrotron-based hard X-ray methods will play an important role towards a holistic spatially- and time-resolved understanding of catalyst as a basis for a future knowledge-based catalysts design – still a "holy grail" in catalysis research. This will provide a strong contribution towards a more sustainable future society with catalysis as a key technology.

Bibliography

[1] J. Hansen, M. Sato, P. Kharecha, G. Russell, D. W. Lea, M. Siddall, "Climate change and trace gases", *Philos. Trans. R. Soc. A* **2007**, *365*, 1925–1954.

[2] O. Hoegh-Guldberg, D. Jacob, M. Taylor, T. G. Bolaños, M. Bindi, S. Brown, I. A. Camilloni, A. Diedhiou, R. Djalante, K. Ebi, F. Engelbrecht, J. Guiot, Y. Hijioka, S. Mehrotra, C. W. Hope, A. J. Payne, H.-O. Pörtner, S. I. Seneviratne, A. Thomas, R. Warren, G. Zhou, "The human imperative of stabilizing global climate change at 1.5 °C", *Science* **2019**, *365*, eaaw6974.

[3] H. Pörtner, D. Roberts, H. Adams, C. Adler, P. Aldunce, E. Ali, R. Ara Begum, R. Betts, R. Bezner Kerr, R. Biesbroek, J. Birkmann, K. Bowen, E. Castellanos, G. Cissé, A. Constable, W. Cramer, D. Dodman, S. Eriksen, A. Fischlin, M. Garschagen, B. Glavovic, E. Gilmore, M. Haasnoot, S. Harper, T. Hasegawa, B. Hayward, Y. Hirabayashi, M. Howden, K. Kalaba, W. Kiessling, R. Lasco, J. Lawrence, M. Lemos, R. Lempert, D. Ley, T. Lissner, S. Lluch-Cota, S. Loeschke, S. Lucatello, Y. Luo, B. Mackey, S. Maharaj, C. Mendez, K. Mintenbeck, M. Moncassim Vale, M. Morecroft, A. Mukherji, M. Mycoo, T. Mustonen, J. Nalau, A. Okem, J. Ometto, C. Parmesan, M. Pelling, P. Pinho, E. Poloczanska, M.-F. Racault, D. Reckien, J. Pereira, A. Revi, S. Rose, R. Sanchez-Rodriguez, E. Schipper, D. Schmidt, D. Schoeman, R. Shaw, C. Singh, W. Solecki, L. Stringer, A. Thomas, E. Totin, C. Trisos, D. Viner, M. van Aalst, M. Wairiu, R. Warren, P. Yanda, Z. Zaiton Ibrahim, *Climate change 2022: impacts, adaptation and vulnerability*, IPCC, **2022**.

[4] A. Raza, A. Razzaq, S. S. Mehmood, X. Zou, X. Zhang, Y. Lv, J. Xu, "Impact of Climate Change on Crops Adaptation and Strategies to Tackle Its Outcome: A Review", *Plants* **2019**, *8*, 34.

[5] I. Monasterolo, "Climate Change and the Financial System", *Annu. Rev. Resour. Econ.* **2020**, *12*, 299–320.

[6] J. Patz, D. Campbell-Lendrum, T. Holloway, J. A. Foley, "Impact of regional climate change on human health.", *Nature* **2005**, *438*, 310–317.

[7] J. Cronin, G. Anandarajah, O. Dessens, "Climate change impacts on the energy system: a review of trends and gaps.", *Clim. Change* **2018**, *151*, 79–93.

[8] K. Solaun, E. Cerdá, "Climate change impacts on renewable energy generation. A review of quantitative projections", *Renew. Sust. Energ. Rev.* **2019**, *116*, 109415.

[9] *Paris Agreement to the United Nations Framework Convention on Climate Change*, United Nations, **2015**.

[10] International Energy Agency, Global CO_2 emissions by sector, 2019, `https://www.iea.org/reports/greenhouse-gas-emissions-from-energy-overview`, Accessed: 2022-03-24.

[11] International Energy Agency, Renewables Information: Overview, 2019, `https://www.iea.org/reports/renewables-information-overview/supply`, Accessed: 2022-03-24.

[12] *Erneuerbare Energien in Zahlen - Nationale und internationale Entwicklung im Jahr 2019*, Bundesministerium für Wirtschaft und Energie (BMWi), **2020**.

[13] Bundesministerium für Wirtschaft und Energie (BMWi), Eröffnungsbilanz Klimaschutz, `https://www.bmwi.de/Redaktion/DE/Downloads/Energie/220111_eroeffnungsbilanz_klimaschutz.pdf?__blob=publicationFile&v=22`, Accessed: 2022-03-24.

[14] Energy-Charts by Fraunhofer Institute for Solar Energy Systems ISE, `https://www.energy-charts.info/charts/power/chart.htm?c=DE&stacking=stacked_absolute_area`, Accessed: 2022-02-22.

[15] entsoe Transparency Platform, Actual Generation per Production Type, `https://transparency.entsoe.eu/generation/r2/actualGenerationPerProductionType/show`, Accessed: 2022-02-22.

[16] *Erneuerbare Energien in Deutschland Daten zur Entwicklung im Jahr 2019*, Umweltbundesamt, **2020**.

[17] T. Bocklisch, "Hybrid energy storage approach for renewable energy applications", *J. Energy Storage* **2016**, *8*, 311–319.

[18] A. A. Kebede, T. Kalogiannis, J. Van Mierlo, M. Berecibar, "A comprehensive review of stationary energy storage devices for large scale renewable energy sources grid integration", *Renew. Sust. Energ. Rev.* **2022**, *159*, 112213.

[19] S. Ould Amrouche, D. Rekioua, T. Rekioua, S. Bacha, "Overview of energy storage in renewable energy systems", *Int. J. Hydrog. Energy* **2016**, *41*, 20914–20927.

[20] T. Schaaf, J. Grünig, M. R. Schuster, T. Rothenfluh, A. Orth, "Methanation of CO_2 - storage of renewable energy in a gas distribution system", *Energy Sustain. Soc.* **2014**, *4*, 2.

[21] F. Schüth, "Chemical Compounds for Energy Storage", *Chem. Ing. Technol.* **2011**, *83*, 1984–1993.

[22] R. Dittmeyer, R. Schoof, "Chemische Energieträger über Power-to-X: Kompakte integrierte Systeme und klassische Großanlagen", *Chem. Ing. Tech.* **2020**, *92*, 1157–1158.

[23] R. Daiyan, I. MacGill, R. Amal, "Opportunities and Challenges for Renewable Power-to-X", *ACS Energy Lett.* **2020**, *5*, 3843–3847.

[24] Z. Chehade, C. Mansilla, P. Lucchese, S. Hilliard, J. Proost, "Review and analysis of demonstration projects on power-to-X pathways in the world", *Int. J. Hydrog. Energy* **2019**, *44*, 27637–27655.

[25] J. Burre, D. Bongartz, L. Brée, K. Roh, A. Mitsos, "Power-to-X: Between Electricity Storage, e-Production, and Demand Side Management", *Chem. Ing. Tech.* **2020**, *92*, 74–84.

[26] M. Bailera, P. Lisbona, L. M. Romeo, S. Espatolero, "Power to Gas projects review: Lab, pilot and demo plants for storing renewable energy and CO_2", *Renew. Sust. Energ. Rev.* **2017**, *69*, 292–312.

[27] R. Dittmeyer, M. Klumpp, P. Kant, G. Ozin, "Crowd oil not crude oil", *Nat. Commun.* **2019**, *10*, 1818.

[28] C. Finn, S. Schnittger, L. J. Yellowlees, J. B. Love, "Molecular approaches to the electrochemical reduction of carbon dioxide", *Chem. Commun.* **2012**, *48*, 1392–1399.

[29] C. Costentin, M. Robert, J.-M. Savéant, "Catalysis of the electrochemical reduction of carbon dioxide", *Chem. Soc. Rev.* **2013**, *42*, 2423–2436.

[30] K. F. Kalz, R. Kraehnert, M. Dvoyashkin, R. Dittmeyer, R. Gläser, U. Krewer, K. Reuter, J.-D. Grunwaldt, "Future Challenges in Heterogeneous Catalysis: Understanding Catalysts under Dynamic Reaction Conditions", *ChemCatChem* **2017**, *9*, 17–29.

[31] D. Haeseldonckx, W. D'haeseleer, "The use of the natural-gas pipeline infrastructure for hydrogen transport in a changing market structure", *Int. J. Hydrog. Energy* **2007**, *32*, 1381–1386.

[32] V. Tietze, D. Stolten, "Comparison of hydrogen and methane storage by means of a thermodynamic analysis", *Int. J. Hydrog. Energy* **2015**, *40*, 11530–11537.

[33] A. Amid, D. Mignard, M. Wilkinson, "Seasonal storage of hydrogen in a depleted natural gas reservoir", *Int. J. Hydrog. Energy* **2016**, *41*, 5549–5558.

[34] *Position Paper Utilisation and Storage of CO_2*, DECHEMA Gesellschaft für Chemische Technik und Biotechnologie e.V. and Verband der Chemischen Industrie e.V., **2009**.

[35] *Technologien für Nachhaltigkeit und Klimaschutz - Chemische Prozesse und stoffliche Nutzung von CO_2*, (Eds.: A. Bazzanella, D. Krämer), DECHEMA Gesellschaft für Chemische Technik und Biotechnologie e.V., **2017**.

[36] P. Sabatier, J. B. Senderens, "Nouvelle syntheses du methane.", *C. R. Acad. Sci.* **1902**, *134*, 514–516.

[37] P. Sabatier, The Method of Direct Hydrogenation by Catalysis - Nobel Lecture, `https://www.nobelprize.org/prizes/chemistry/1912/sabatier/biographical/`, Accessed: 2018-12-12, **1912**.

[38] S. Rönsch, J. Schneider, S. Matthischke, M. Schlüter, M. Götz, J. Lefebvre, P. Prabhakaran, S. Bajohr, "Review on methanation - From fundamentals to current projects", *Fuel* **2016**, *166*, 276–296.

[39] J. Gao, Q. Liu, F. Gu, B. Liu, Z. Zhong, F. Su, "Recent advances in methanation catalysts for the production of synthetic natural gas", *RSC Adv.* **2015**, *5*, 22759–22776.

[40] M. Younas, L. Loong Kong, M. J. Bashir, H. Nadeem, A. Shehzad, S. Sethupathi, "Recent Advancements, Fundamental Challenges, and Opportunities in Catalytic Methanation of CO_2", *Energy Fuels* **2016**, *30*, 8815–8831.

[41] M. A. Aziz, A. A. Jalil, S. Triwahyono, A. Ahmad, "CO_2 methanation over heterogeneous catalysts: Recent progress and future prospects", *Green Chem.* **2015**, *17*, 2647–2663.

[42] P. Frontera, A. Macario, M. Ferraro, P. L. Antonucci, "Supported catalysts for CO_2 methanation: A review", *Catalysts* **2017**, *7*, 59.

[43] L. Li, W. Zeng, M. Song, X. Wu, G. Li, C. Hu, "Research Progress and Reaction Mechanism of CO_2 Methanation over Ni-Based Catalysts at Low Temperature: A Review", *Catalysts* **2022**, *12*, 244.

[44] C. Lv, L. Xu, M. Chen, Y. Cui, X. Wen, Y. Li, C. E. Wu, B. Yang, Z. Miao, X. Hu, Q. Shou, "Recent Progresses in Constructing the Highly Efficient Ni Based Catalysts With Advanced Low-Temperature Activity Toward CO_2 Methanation", *Front. Chem.* **2020**, *8*, 1–32.

[45] J. Gao, Y. Wang, Y. Ping, D. Hu, G. Xu, F. Gu, F. Su, "A thermodynamic analysis of methanation reactions of carbon oxides for the production of synthetic natural gas", *RSC Adv.* **2012**, *2*, 2358–2368.

[46] Web of Sciece, Database search for "(Ni) AND (methanation) AND (CO_2)", `https://www.webofscience.com`, Accessed: 2022-03-28.

[47] J. Martínez, E. Hernández, S. Alfaro, R. L. Medina, G. V. Aguilar, E. Albiter, M. A. Valenzuela, "High selectivity and stability of nickel catalysts for CO_2 Methanation: Support effects", *Catalysts* **2019**, *9*, 24.

[48] J. Lin, C. Ma, J. Luo, X. Kong, Y. Xu, G. Ma, J. Wang, C. Zhang, Z. Li, M. Ding, "Preparation of Ni based mesoporous Al_2O_3 catalyst with enhanced CO_2 methanation performance", *RSC Adv.* **2019**, *9*, 8684–8694.

[49] S. Rahmani, M. Rezaei, F. Meshkani, "Preparation of highly active nickel catalysts supported on mesoporous nanocrystalline γ-Al_2O_3 for CO_2 methanation", *J. Ind. Eng. Chem.* **2014**, *20*, 1346–1352.

[50] Q. Pan, J. Peng, T. Sun, S. Wang, S. Wang, "Insight into the reaction route of CO_2 methanation: Promotion effect of medium basic sites", *Catal. Commun.* **2014**, *45*, 74–78.

[51] F. Koschany, D. Schlereth, O. Hinrichsen, "On the kinetics of the methanation of carbon dioxide on coprecipitated $NiAl(O)_x$", *Appl. Catal. B. Environ.* **2016**, *181*, 504–516.

[52] M. Cai, J. Wen, W. Chu, X. Cheng, Z. Li, "Methanation of carbon dioxide on Ni/ZrO_2-Al_2O_3 catalysts: Effects of ZrO_2 promoter and preparation method of novel ZrO_2-Al_2O_3 carrier", *J. Nat. Gas Chem.* **2011**, *20*, 318–324.

[53] B. Mutz, M. Belimov, W. Wang, P. Sprenger, M.-A. Serrer, D. Wang, P. Pfeifer, W. Kleist, J.-D. Grunwaldt, "Potential of an alumina-supported Ni_3Fe catalyst in the methanation of CO_2: Impact of alloy formation on activity and stability", *ACS Catal.* **2017**, *7*, 6802–6814.

[54] B. Mutz, H. Carvalho, W. Kleist, J.-D. Grunwaldt, "Dynamic transformation of small Ni particles during methanation of CO_2 under fluctuating reaction conditions monitored by operando X-ray absorption spectroscopy", *J. Phys. Conf. Ser.* **2016**, *712*, 012050.

[55] J. Lin, C. Ma, Q. Wang, Y. Xu, G. Ma, J. Wang, H. Wang, C. Dong, C. Zhang, M. Ding, "Enhanced low-temperature performance of CO_2 methanation over mesoporous Ni/Al_2O_3-ZrO_2 catalysts", *Appl. Catal. B Environ.* **2019**, *243*, 262–272.

[56] F. Ocampo, B. Louis, L. Kiwi-Minsker, A. C. Roger, "Effect of Ce/Zr composition and noble metal promotion on nickel based $Ce_xZr_{1-x}O_2$ catalysts for carbon dioxide methanation", *Appl. Catal. A Gen.* **2011**, *392*, 36–44.

[57] P. A. Aldana, F. Ocampo, K. Kobl, B. Louis, F. Thibault-Starzyk, M. Daturi, P. Bazin, S. Thomas, A. C. Roger, "Catalytic CO_2 valorization into CH_4 on Ni-based ceria-zirconia. Reaction mechanism by operando IR spectroscopy", *Catal. Today* **2013**, *215*, 201–207.

[58] S. Hwang, U. G. Hong, J. Lee, J. H. Baik, D. J. Koh, H. Lim, I. K. Song, "Methanation of Carbon Dioxide over Mesoporous Nickel-M-Alumina (M = Fe, Zr, Ni, Y, and Mg) Xerogel Catalysts: Effect of Second Metal", *Catal. Lett.* **2012**, *142*, 860–868.

[59] A. I. Tsiotsias, N. D. Charisiou, I. V. Yentekakis, M. A. Goula, "Bimetallic Ni-based Catalysts for CO_2 Methanation: A Review", *Nanomaterials* **2021**, *11*, 28.

[60] B. Miao, S. S. K. Ma, X. Wang, H. Su, S. H. Chan, "Catalysis mechanisms of CO_2 and CO methanation", *Catal. Sci. Technol.* **2016**, *6*, 4048–4058.

[61] A. Westermann, B. Azambre, M. Bacariza, I. Graça, M. Ribeiro, J. Lopes, C. Henriques, "Insight into CO_2 methanation mechanism over Ni/USY zeolites: An operando IR study", *Appl. Catal. B Environ.* **2015**, *174-175*, 120–125.

[62] C. V. Miguel, A. Mendes, L. M. Madeira, "Intrinsic kinetics of CO_2 methanation over an industrial nickel-based catalyst", *J. CO2 Util.* **2018**, *25*, 128–136.

[63] J. R. Rostrup-Nielsen, K. Pedersen, J. Sehested, "High temperature methanation. Sintering and structure sensitivity", *Appl. Catal. A Gen.* **2007**, *330*, 134–138.

[64] C. Schild, A. Wokaun, R. A. Koeppel, A. Baiker, "CO_2 hydrogenation over nickel/zirconia catalysts from amorphous precursors: On the mechanism of methane formation", *J. Phys. Chem.* **1991**, *95*, 6341–6346.

[65] H. Takano, Y. Kirihata, K. Izumiya, N. Kumagai, H. Habazaki, K. Hashimoto, "Highly active Ni/Y-doped ZrO_2 catalysts for CO_2 methanation", *Appl. Surf. Sci.* **2016**, *388*, 653–663.

[66] A. Solis-Garcia, J. F. Louvier-Hernandez, A. Almendarez-Camarillo, J. C. Fierro-Gonzalez, "Participation of surface bicarbonate, formate and methoxy species in the carbon dioxide methanation catalyzed by ZrO_2-supported Ni", *Appl. Catal. B Environ.* **2017**, *218*, 611–620.

[67] H. Muroyama, Y. Tsuda, T. Asakoshi, H. Masitah, T. Okanishi, T. Matsui, K. Eguchi, "Carbon dioxide methanation over Ni catalysts supported on various metal oxides", *J. Catal.* **2016**, *343*, 178–184.

[68] J. Guilera, J. Del Valle, A. Alarcón, J. A. Díaz, T. Andreu, "Metal-oxide promoted Ni/Al_2O_3 as CO_2 methanation micro-size catalysts", *J. CO2 Util.* **2019**, *30*, 11–17.

[69] Y. X. Pan, C. J. Liu, Q. Ge, "Effect of surface hydroxyls on selective CO_2 hydrogenation over Ni_4/γ-Al_2O_3: A density functional theory study", *J. Catal.* **2010**, *272*, 227–234.

[70] C. Vogt, E. Groeneveld, G. Kamsma, M. Nachtegaal, L. Lu, C. J. Kiely, P. H. Berben, F. Meirer, B. M. Weckhuysen, "Unravelling structure sensitivity in CO_2 hydrogenation over nickel", *Nat. Catal.* **2018**, *1*, 127–134.

[71] M. A. Serrer, A. Gaur, J. Jelic, S. Weber, C. Fritsch, A. H. Clark, E. Saraçi, F. Studt, J.-D. Grunwaldt, "Structural dynamics in Ni-Fe catalysts during CO_2 methanation-role of iron oxide clusters", *Catal. Sci. Technol.* **2020**, *10*, 7542–7554.

[72] C. H. Bartholomew, "Mechanisms of catalyst deactivation", *Appl. Catal. A Gen.* **2001**, *212*, 17–60.

[73] M. D. Argyle, C. H. Bartholomew, "Heterogeneous catalyst deactivation and regeneration: A review", *Catalysts* **2015**, *5*, 145–269.

[74] R. P. Struis, T. J. Schildhauer, I. Czekaj, M. Janousch, S. M. Biollaz, C. Ludwig, "Sulphur poisoning of Ni catalysts in the SNG production from biomass: A TPO/XPS/XAS study", *Appl. Catal. A: Gen.* **2009**, *362*, 121–128.

[75] B. Legras, V. V. Ordomsky, C. Dujardin, M. Virginie, A. Y. Khodakov, "Impact and detailed action of sulfur in syngas on methane synthesis on Ni/γ-Al_2O_3 catalyst", *ACS Catal.* **2014**, *4*, 2785–2791.

[76] E. J. Erekson, C. H. Bartholomew, "Sulfur poisoning of nickel methanation catalysts. II. Effects of H_2S concentration, CO and H_2O partial pressures and temperature on reactivation rates", *Appl. Catal.* **1983**, *5*, 323–336.

[77] W. Fitzharris, J. Katzer, W. Manogue, "Sulfur deactivation of nickel methanation catalysts", *J. Catal.* **1982**, *76*, 369–384.

[78] J. R. Rostrup-Nielsen, K. Pedersen, "Sulfur poisoning of Boudouard and methanation reactions on nickel catalysts", *J. Catal.* **1979**, *59*, 395–404.

[79] J. Engbæk, O. Lytken, J. H. Nielsen, I. Chorkendorff, "CO dissociation on Ni: The effect of steps and of nickel carbonyl", *Surf. Sci.* **2008**, *602*, 733–743.

[80] B. Mutz, H. W. P. Carvalho, S. Mangold, W. Kleist, J.-D. Grunwaldt, "Methanation of CO_2: Structural response of a Ni-based catalyst under fluctuating reaction conditions unraveled by operando spectroscopy", *J. Catal.* **2015**, *327*, 48–53.

[81] B. Mutz, A. M. Gänzler, M. Nachtegaal, O. Müller, R. Frahm, W. Kleist, J.-D. Grunwaldt, "Surface oxidation of supported Ni particles and its impact on the catalytic performance during dynamically operated methanation of CO_2", *Catalysts* **2017**, *7*, 279.

[82] M. A. Serrer, K. F. Kalz, E. Saraci, H. Lichtenberg, J.-D. Grunwaldt, "Role of Iron on the Structure and Stability of $Ni_{3.2}Fe/Al_2O_3$ during Dynamic CO_2 Methanation for P2X Applications", *ChemCatChem* **2019**, *11*, 5018–5021.

[83] C. H. Bartholomew, "Carbon Deposition in Steam Reforming and Methanation", *Catal. Rev.* **1982**, *24*, 67–112.

[84] J. G. McCarty, H. Wise, "Hydrogenation of surface carbon on alumina-supported nickel", *J. Catal.* **1979**, *57*, 406–416.

[85] I. Czekaj, F. Loviat, F. Raimondi, J. Wambach, S. Biollaz, A. Wokaun, "Characterization of surface processes at the Ni-based catalyst during the methanation of biomass-derived synthesis gas: X-ray photoelectron spectroscopy (XPS)", *Appl. Catal. A Gen.* **2007**, *329*, 68–78.

[86] B. Mutz, P. Sprenger, W. Wang, D. Wang, W. Kleist, J.-D. Grunwaldt, "Operando Raman spectroscopy on CO_2 methanation over alumina-supported Ni, Ni_3Fe and $NiRh_{0.1}$ catalysts: Role of carbon formation as possible deactivation pathway", *Appl. Catal. A* **2018**, *556*, 160–171.

[87] D. Beierlein, D. Häussermann, Y. Traa, E. Klemm, "Rapid Aging as a Key to Understand Deactivation of Ni/Al_2O_3 Catalysts Applied for the CO_2 Methanation", *Catal. Lett.* **2021**, *1*, 3.

[88] M. A. Serrer, M. Stehle, M. L. Schulte, H. Besser, W. Pfleging, E. Saraci, J.-D. Grunwaldt, "Spatially-Resolved Insights Into Local Activity and Structure of Ni-Based CO_2 Methanation Catalysts in Fixed-Bed Reactors", *ChemCatChem* **2021**, *13*, 3010–3020.

[89] J. Bremer, K. Sundmacher, "Operation range extension via hot-spot control for catalytic CO_2 methanation reactors", *Reac. Chem. Eng.* **2019**, *4*, 1019–1037.

[90] J. Xu, G. F. Froment, "Methane steam reforming, methanation and water-gas shift: I. Intrinsic kinetics", *AIChE J.* **1989**, *35*, 88–96.

[91] S. Abelló, C. Berrueco, D. Montané, "High-loaded nickel-alumina catalyst for direct CO_2 hydrogenation into synthetic natural gas (SNG)", *Fuel* **2013**, *113*, 598–609.

[92] *Handbook of Heterogeneous Catalysis*, 2nd Edition, (Eds.: G. Ertl, H. Knözinger, F. Schüth, J. Weitkamp), Wiley-VCH, Weinheim, **2008**.

[93] J. Sehested, A. Carlsson, T. V. Janssens, P. L. Hansen, A. K. Datyey, "Sintering of nickel steam-reforming catalysts on $MgAl_2O_4$ spinel supports", *J. Catal.* **2001**, *197*, 200–209.

[94] J. Sehested, J. A. Gelten, S. Helveg, "Sintering of nickel catalysts: Effects of time, atmosphere, temperature, nickel-carrier interactions, and dopants", *Appl. Catal. A Gen.* **2006**, *309*, 237–246.

[95] C. Mebrahtu, S. Perathoner, G. Giorgianni, S. Chen, G. Centi, F. Krebs, R. Palkovits, S. Abate, "Deactivation mechanism of hydrotalcite-derived Ni-AlO_x catalysts during low-temperature CO_2 methanation via Ni-hydroxide formation and the role of Fe in limiting this effect", *Catal. Sci. Technol.* **2019**, *9*, 4023–4035.

[96] K. Wefers, C. Misra, *Oxides and hydroxides of aluminum*, *Vol. 19*, Alcoa Laboratories Pittsburgh, **1987**.

[97] H. S. C. O'Neill, W. A. Dollase, C. R. Ross, "Temperature dependence of the cation distribution in nickel aluminate ($NiAl_2O_4$) spinel: a powder XRD study", *Phys. Chem. Minerals* **1991**, *18*, 302–319.

[98] S. J. Smith, S. Amin, B. F. Woodfield, J. Boerio-Goates, B. J. Campbell, "Phase progression of γ-Al_2O_3 nanoparticles synthesized in a solvent-deficient environment", *Inorg. Chem.* **2013**, *52*, 4411–4423.

[99] I. Levin, D. Brandon, "Metastable alumina polymorphs: Crystal structures and transition sequences", *J. Am. Ceram. Soc.* **1998**, *81*, 1995–2012.

[100] R.-S. Zhou, R. L. Snyder, "Structures and transformation mechanisms of the η, γ and θ transition aluminas", *Acta Cryst. B* **1991**, *47*, 617–630.

[101] S. Ewald, M. Kolbeck, T. Kratky, M. Wolf, O. Hinrichsen, "On the deactivation of Ni-Al catalysts in CO_2 methanation", *Appl. Catal. A Gen.* **2019**, *570*, 376–386.

[102] M. A. Bañares, "Operando methodology: Combination of in situ spectroscopy and simultaneous activity measurements under catalytic reaction conditions", *Catal. Today* **2005**, *100*, 71–77.

[103] R. Portela, S. Perez-Ferreras, A. Serrano-Lotina, M. A. Bañares, "Engineering operando methodology: Understanding catalysis in time and space", *Front. Chem. Sci. Eng.* **2018**, *12*, 509–536.

[104] I. L. Buurmans, B. M. Weckhuysen, "Heterogeneities of individual catalyst particles in space and time as monitored by spectroscopy", *Nat. Chem.* **2012**, *4*, 873–886.

[105] M. Iglesias González, H. Eilers, G. Schaub, "Flexible Operation of Fixed-Bed Reactors for a Catalytic Fuel Synthesis – CO_2 Hydrogenation as Example Reaction", *Energy Technol.* **2016**, *4*, 90–103.

[106] D. Schlereth, O. Hinrichsen, "A fixed-bed reactor modeling study on the methanation of CO_2", *Chem. Eng. Res. Des.* **2014**, *92*, 702–712.

[107] K. H. G. Rätze, J. Bremer, L. T. Biegler, K. Sundmacher, "Physics-Based Surrogate Models for Optimal Control of a CO_2 Methanation Reactor", *Comput. Aided Chem. Eng.* **2017**, *40*, 127–132.

[108] J. Bremer, K. H. G. Rätze, K. Sundmacher, "CO_2 methanation: Optimal start-up control of a fixed-bed reactor for power-to-gas applications", *AIChE J.* **2017**, *63*, 23–31.

[109] S. K. Mazidi, M. T. Sadeghi, M. A. Marvast, "Optimization of Fischer-Tropsch Process in a Fixed-Bed Reactor Using Non-uniform Catalysts", *Chem. Eng. Technol.* **2013**, *36*, 62–72.

[110] H. Wu, Q. Yuan, B. Zhu, "An experimental investigation of optimal active catalyst distribution in nonisothermal pellets", *Ind. Eng. Chem. Res.* **1988**, *27*, 1169–1174.

[111] H. Wu, Q. Yuan, B. Zhu, "An experimental study of optimal active catalyst distribution in pellets for maximum selectivity", *Ind. Eng. Chem. Res.* **1990**, *29*, 1771–1776.

[112] R. Aris, *The Mathematical Theory of Diffusion and Reaction in Permeable Catalysts: The theory of the steady state*, *Vol. 1*, Clarendon Press, **1975**.

[113] M. Morbidelli, A. Gavriilidis, A. Varma, *Catalyst Design: Optimal Distribution of Catalyst in Pellets, Reactors, and Membranes*, Cambridge University Press, **2001**.

[114] R. T. Zimmermann, J. Bremer, K. Sundmacher, "Optimal catalyst particle design for flexible fixed-bed CO_2 methanation reactors", *Chem. Eng. J.* **2020**, *387*, 123704.

[115] R. T. Zimmermann, J. Bremer, K. Sundmacher, "Load-flexible fixed-bed reactors by multi-period design optimization", *Chem. Eng. J.* **2021**, *428*, 130771.

[116] B. M. Weckhuysen, "Chemical imaging of spatial heterogeneities in catalytic solids at different length and time scales", *Angew. Chem. Int. Ed.* **2009**, *48*, 4910–4943.

[117] J.-D. Grunwaldt, J. B. Wagner, R. E. Dunin-Borkowski, "Imaging Catalysts at Work: A Hierarchical Approach from the Macro- to the Meso- and Nano-scale", *ChemCatChem* **2013**, *5*, 62–80.

[118] S. Das, R. Pashminehazar, S. Sharma, S. Weber, T. L. Sheppard, "New Dimensions in Catalysis Research with Hard X-Ray Tomography", *Chem. Ing. Tech.* **2022**, *94*, 1591–1610.

[119] W. Schwieger, A. G. Machoke, T. Weissenberger, A. Inayat, T. Selvam, M. Klumpp, A. Inayat, "Hierarchy concepts: Classification and preparation strategies for zeolite containing materials with hierarchical porosity", *Chem. Soc. Rev.* **2016**, *45*, 3353–3376.

[120] S. Mitchell, N. L. Michels, K. Kunze, J. Pérez-Ramírez, "Visualization of hierarchically structured zeolite bodies from macro to nano length scales", *Nat. Chem.* **2012**, *4*, 825–831.

[121] A. Urakawa, "Trends and advances in Operando methodology", *Cur. Opin. Chem. Eng.* **2016**, *12*, 31–36.

[122] J. Rouquerol, D. Avnir, C. W. Fairbridge, D. H. Everett, J. H. Haynes, N. Pernicone, J. D. F. Ramsay, K. S. Sing, K. Unger, "Recommendations for the characterization of porous solids", *Pure Appl. Chem.* **1994**, *66*, 1739–1758.

[123] S. Gheorghiu, M. O. Coppens, "Optimal Bimodal Pore Networks for Heterogeneous Catalysis", *AIChE J.* **2004**, *50*, 812–820.

[124] M. O. Coppens, *Structured Catalysts and Reactors*, 2nd ed., (Eds.: A. Cybulski, J. A. Moulijin), Taylor & Francis Group, LLC, Boca Raton, FL, USA, **2006**, pp. 779–805.

[125] C. M. Parlett, K. Wilson, A. F. Lee, "Hierarchical porous materials: Catalytic applications", *Chem. Soc. Rev.* **2013**, *42*, 3876–3893.

[126] P. Trogadas, M. M. Nigra, M. O. Coppens, "Nature-inspired optimization of hierarchical porous media for catalytic and separation processes", *New J. Chem.* **2016**, *40*, 4016–4026.

[127] P. Trogadas, V. Ramani, P. Strasser, T. F. Fuller, M. O. Coppens, "Hierarchically Structured Nanomaterials for Electrochemical Energy Conversion", *Angew. Chem. Int. Ed.* **2016**, *55*, 122–148.

[128] L. B. McCusker, F. Liebau, G. Englehardt, "Nomenclature of structural and compositional characteristics of ordered microporous and mesoporous materials with inorganic hosts (IUPAC recommendations 2001): Physical chemistry Division commision on colloid and surface chemistry including catalysis", *Pure Appl. Chem.* **2001**, *73*, 381–394.

[129] G. Wang, M. O. Coppens, "Calculation of the optimal macropore size in nanoporous catalysts and its application to DeNO$_x$ catalysis", *Ind. Eng. Chem. Res.* **2008**, *47*, 3847–3855.

[130] A. Kriete in *Visualization in Biomedical Computing*, *Vol. 1131*, (Eds.: K. Höhne, R. Kikinis), Springer, Berlin, Heidelberg, **1996**, pp. 399–404.

[131] V. Eppell, B. A. McClurg, J. M. Bunker, "A four level road hierarchy for network planning and management", *Proceedings of the 20th ARRB Conference* **2001**, 1–7.

[132] J. Rouquerol, G. Baron, R. Denoyel, H. Giesche, J. Groen, P. Klobes, P. Levitz, A. V. Neimark, S. Rigby, R. Skudas, K. Sing, M. Thommes, K. Unger, "Liquid intrusion and alternative methods for the characterization of macroporous materials (IUPAC technical report)", *Pure Appl. Chem.* **2012**, *84*, 107–136.

[133] M. Thommes, K. Kaneko, A. V. Neimark, J. P. Olivier, F. Rodriguez-Reinoso, J. Rouquerol, K. S. Sing, "Physisorption of gases, with special reference to the evaluation of surface area and pore size distribution (IUPAC Technical Report)", *Pure Appl. Chem.* **2015**, *87*, 1051–1069.

[134] K. A. Cychosz, R. Guillet-Nicolas, J. García-Martínez, M. Thommes, "Recent advances in the textural characterization of hierarchically structured nanoporous materials", *Chem. Soc. Rev.* **2017**, *46*, 389–414.

[135] C. Schlumberger, M. Thommes, "Characterization of Hierarchically Ordered Porous Materials by Physisorption and Mercury Porosimetry – A Tutorial Review", *Adv. Mater. Interfaces* **2021**, *8*, 2002181.

[136] X. Y. Yang, Y. Li, A. Lemaire, J. G. Yu, B. L. Su, "Hierarchically structured functional materials: Synthesis strategies for multimodal porous networks", *Pure Appl. Chem.* **2009**, *81*, 2265–2307.

[137] P. Colombo, C. Vakifahmetoglu, S. Costacurta, "Fabrication of ceramic components with hierarchical porosity", *J. Mater. Sci.* **2010**, *45*, 5425–5455.

[138] A. Inayat, B. Reinhardt, H. Uhlig, W. D. Einicke, D. Enke, "Silica monoliths with hierarchical porosity obtained from porous glasses", *Chem. Soc. Rev.* **2013**, *42*, 3753–3764.

[139] Y. Liu, J. Goebl, Y. Yin, "Templated synthesis of nanostructured materials", *Chem. Soc. Rev.* **2013**, *42*, 2610–2653.

[140] A. Stein, B. E. Wilson, S. G. Rudisill, "Design and functionality of colloidal–crystal-templated materials – chemical applications of inverse opals", *Chem. Soc. Rev.* **2013**, *42*, 2763–2803.

[141] C. Triantafillidis, M. S. Elsaesser, N. Hüsing, "Chemical phase separation strategies towards silica monoliths with hierarchical porosity", *Chem. Soc. Rev.* **2013**, *42*, 3833–3846.

[142] A. Walcarius, "Mesoporous materials and electrochemistry", *Chem. Soc. Rev.* **2013**, *42*, 4098–4140.

[143] A. Feinle, M. S. Elsaesser, N. Hüsing, "Sol-gel synthesis of monolithic materials with hierarchical porosity", *Chem. Soc. Rev.* **2016**, *45*, 3377–3399.

[144] Y. Wang, H. Arandiyan, J. Scott, A. Bagheri, H. Dai, R. Amal, "Recent advances in ordered meso/macroporous metal oxides for heterogeneous catalysis: A review", *J. Mater. Chem. A* **2017**, *5*, 8825–8846.

[145] L. Wu, Y. Li, Z. Fu, B. L. Su, "Hierarchically structured porous materials: Synthesis strategies and applications in energy storage", *Natl. Sci. Rev.* **2020**, *7*, 1667–1701.

[146] A. E. Danks, S. R. Hall, Z. Schnepp, "The evolution of 'sol-gel' chemistry as a technique for materials synthesis", *Mater. Horiz.* **2016**, *3*, 91–112.

[147] L. L. Hench, J. K. West, "The Sol-Gel Process", *Chem. Rev.* **1990**, *90*, 33–72.

[148] M. Berger, J. Hubbell, S. Seltzer, J. Chang, J. Coursey, R. Sukumar, D. Zucker, K. Olsen, "XCOM: photon cross sections database", *NIST Standard Reference Database 8* **2010**, DOI 10.18434/T48G6X.

[149] L. Mino, E. Borfecchia, J. Segura-Ruiz, C. Giannini, G. Martinez-Criado, C. Lamberti, "Materials characterization by synchrotron x-ray microprobes and nanoprobes", *Rev. Mod. Phys.* **2018**, *90*, 25007.

[150] A. Sakdinawat, D. Attwood, "Nanoscale X-ray imaging", *Nat. Photon.* **2010**, *4*, 840–848.

[151] F. M. F. de Groot, E. de Smit, M. M. van Schooneveld, L. R. Aramburo, B. M. Weckhuysen, "In-situ Scanning Transmission X-Ray Microscopy of Catalytic Solids and Related Nanomaterials", *ChemPhysChem* **2010**, *11*, 951–962.

[152] In *Elements of Modern X-ray Physics*, John Wiley & Sons, Ltd, Chichester, **2011**, Chapter 2, pp. 29–67.

[153] F. Meirer, B. M. Weckhuysen, "Spatial and temporal exploration of heterogeneous catalysts with synchrotron radiation", *Nat. Rev. Mater.* **2018**, *3*, 324–340.

[154] J.-D. Grunwaldt, C. G. Schroer, "Hard and soft X-ray microscopy and tomography in catalysis: Bridging the different time and length scales", *Chem. Soc. Rev.* **2010**, *39*, 4741–4753.

[155] M. A. Newton, M. Di Michiel, D. Ferri, M. Fernàndez-Garcia, A. M. Beale, S. D. Jacques, P. J. Chupas, K. W. Chapman, "Catalytic Adventures in Space and Time Using High Energy X-rays", *Catal. Surv. Asia* **2014**, *18*, 134–148.

[156] M. Dierolf, A. Menzel, P. Thibault, P. Schneider, C. M. Kewish, R. Wepf, O. Bunk, F. Pfeiffer, "Ptychographic X-ray computed tomography at the nanoscale", *Nature* **2010**, *467*, 436–439.

[157] A. Diaz, P. Trtik, M. Guizar-Sicairos, A. Menzel, P. Thibault, O. Bunk, "Quantitative x-ray phase nanotomography", *Phys. Rev. B Condens. Matter* **2012**, *85*, 020104.

[158] F. Pfeiffer, "X-ray ptychography", *Nat. Photon.* **2018**, *12*, 9–17.

[159] P. Cloetens, W. Ludwig, J. Baruchel, D. Van Dyck, J. Van Landuyt, J. P. Guigay, M. Schlenker, "Holotomography: Quantitative phase tomography with micrometer resolution using hard synchrotron radiation x rays", *Appl. Phys. Lett.* **1999**, *75*, 2912–2914.

[160] J. M. Rodenburg, H. M. Faulkner, "A phase retrieval algorithm for shifting illumination", *Appl. Phys. Lett.* **2004**, *85*, 4795–4797.

[161] H. M. Faulkner, J. M. Rodenburg, "Movable aperture lensless transmission microscopy: A novel phase retrieval algorithm", *Phys. Rev. Lett.* **2004**, *93*, 023903.

[162] J. M. Rodenburg, A. C. Hurst, A. G. Cullis, B. R. Dobson, F. Pfeiffer, O. Bunk, C. David, K. Jefimovs, I. Johnson, "Hard-X-ray lensless imaging of extended objects", *Phys. Rev. Lett.* **2007**, *98*, 034801.

[163] P. Thibault, M. Dierolf, A. Menzel, O. Bunk, C. David, F. Pfeiffer, "High-Resolution Scanning X-ray Diffraction", *Science* **2008**, *321*, 379–382.

[164] R. Caulkin, X. Jia, C. Xu, M. Fairweather, R. A. Williams, H. Stitt, M. Nijemeisland, S. Aferka, M. Crine, A. Léonard, D. Toye, P. Marchot, "Simulations of structures in packed columns and validation by x-ray tomography", *Ind. Eng. Chem. Res.* **2009**, *48*, 202–213.

[165] J. von Seckendorff, K. Achterhold, F. Pfeiffer, R. Fischer, O. Hinrichsen, "Experimental and numerical analysis of void structure in random packed beds of spheres", *Powder Technol.* **2021**, *380*, 613–628.

[166] E. Bianchi, T. Heidig, C. G. Visconti, G. Groppi, H. Freund, E. Tronconi, "Heat transfer properties of metal foam supports for structured catalysts: Wall heat transfer coefficient", *Catal. Today* **2013**, *216*, 121–134.

[167] E. Bianchi, G. Groppi, W. Schwieger, E. Tronconi, H. Freund, "Numerical simulation of heat transfer in the near-wall region of tubular reactors packed with metal open-cell foams", *Chem. Eng. J.* **2015**, *264*, 268–279.

[168] C. Sinn, G. R. Pesch, J. Thöming, L. Kiewidt, "Coupled conjugate heat transfer and heat production in open-cell ceramic foams investigated using CFD", *Int. J. Heat Mass Transf.* **2019**, *139*, 600–612.

[169] M. Sadeghi, M. Mirdrikvand, G. R. Pesch, W. Dreher, J. Thöming, "Full-field analysis of gas flow within open-cell foams: comparison of micro-computed tomography-based CFD simulations with experimental magnetic resonance flow mapping data", *Exp. Fluids* **2020**, *61*, 124.

[170] P. Kočí, M. Isoz, M. Plachá, A. Arvajová, M. Václavík, M. Svoboda, E. Price, V. Novák, D. Thompsett, "3D reconstruction and pore-scale modeling of coated catalytic filters for automotive exhaust gas aftertreatment", *Catal. Today* **2019**, *320*, 165–174.

[171] L. Joss, R. Pini, "3D Mapping of Gas Physisorption for the Spatial Characterisation of Nanoporous Materials", *ChemPhysChem* **2019**, *20*, 524–528.

[172] X. Ou, X. Zhang, T. Lowe, R. Blanc, M. N. Rad, Y. Wang, N. Batail, C. Pham, N. Shokri, A. Garforth, P. Withers, X. Fan, "X-ray micro computed tomography characterization of cellular SiC foams for their applications in chemical engineering", *Mater. Charact.* **2017**, *123*, 20–28.

[173] W. Curtis Conner, S. W. Webb, P. Spanne, K. W. Jones, "Use of x-ray microscopy and synchrotron microtomography to characterize polyethylene polymerization particles", *Macromolecules* **1990**, *23*, 4742–4747.

[174] M. A. Ferrero, R. Sommer, P. Spanne, K. W. Jones, W. Curtis Conner, "X-ray microtomography studies of nascent polyolefin particles polymerized over magnesium chloride-supported catalysts", *J. Polym. Sci. A: Polym. Chem.* **1993**, *31*, 2507–2512.

[175] J.-D. Grunwaldt, B. Kimmerle, A. Baiker, P. Boye, C. G. Schroer, P. Glatzel, C. N. Borca, F. Beckmann, "Catalysts at work: From integral to spatially resolved X-ray absorption spectroscopy", *Catal. Today* **2009**, *145*, 267–278.

[176] E. K. Gibson, M. W. Zandbergen, S. D. Jacques, C. Biao, R. J. Cernik, M. G. O'Brien, M. Di Michiel, B. M. Weckhuysen, A. M. Beale, "Noninvasive spatiotemporal profiling of the processes of impregnation and drying within Mo/Al_2O_3 catalyst bodies by a combination of x-ray absorption tomography and diagonal offset Raman spectroscopy", *ACS Catal.* **2013**, *3*, 339–347.

[177] H. Silva, M. G. Nielsen, E. M. Fiordaliso, C. D. Damsgaard, C. Gundlach, T. Kasama, I. B. Chorkendorff, D. Chakraborty, "Synthesis and characterization of Fe-Ni/γ-Al_2O_3 egg-shell catalyst for H_2 generation by ammonia decomposition", *Appl. Catal. A Gen.* **2015**, *505*, 548–556.

[178] J. Pura, P. Kwaśniak, D. Jakubowska, J. Jaroszewicz, J. Zdunek, H. Garbacz, J. Mizera, M. Gierej, Z. Laskowski, "Investigation of degradation mechanism of palladium-nickel wires during oxidation of ammonia", *Catal. Today* **2013**, *208*, 48–55.

[179] G. Hofmann, A. Rochet, E. Ogel, M. Casapu, S. Ritter, M. Ogurreck, J.-D. Grunwaldt, "Aging of a Pt/Al_2O_3 exhaust gas catalyst monitored by quasi in situ X-ray micro computed tomography", *RSC Adv.* **2015**, *5*, 6893–6905.

[180] J. Becher, T. L. Sheppard, Y. Fam, S. Baier, W. Wang, D. Wang, S. Kulkarni, T. F. Keller, M. Lyubomirskiy, D. Brueckner, M. Kahnt, A. Schropp, C. G. Schroer, J.-D. Grunwaldt, "Mapping the Pore Architecture of Structured Catalyst Monoliths from Nanometer to Centimeter Scale with Electron and X-ray Tomographies", *J. Phys. Chem. C* **2019**, *123*, 25197–25208.

[181] A. Hart, "Microstructural Investigation of Coke Deposition in Pelleted Catalyst during Downhole Catalytic Upgrading of Heavy Crude Oil Using Porosimetry and X-ray Computed Tomography", *Catal. Lett.* **2021**, *151*, 1788–1795.

[182] W. Kaltner, K. Lorenz, B. Schillinger, A. Jentys, J. A. Lercher, "Using tomography for exploring complex structured emission control catalysts", *Catal. Lett.* **2010**, *134*, 24–30.

[183] M. Holler, A. Diaz, M. Guizar-Sicairos, P. Karvinen, E. Färm, E. Härkönen, M. Ritala, A. Menzel, J. Raabe, O. Bunk, "X-ray ptychographic computed tomography at 16 nm isotropic 3D resolution", *Sci. Rep.* **2014**, *4*, 3857.

[184] J. C. da Silva, K. Mader, M. Holler, D. Haberthür, A. Diaz, M. Guizar-Sicairos, W. C. Cheng, Y. Shu, J. Raabe, A. Menzel, J. A. van Bokhoven, "Assessment of the 3-D pore structure and individual components of preshaped catalyst bodies by X-ray imaging", *ChemCatChem* **2015**, *7*, 413–416.

[185] J. Ihli, R. R. Jacob, M. Holler, M. Guizar-Sicairos, A. Diaz, J. C. da Silva, D. Ferreira Sanchez, F. Krumeich, D. Grolimund, M. Taddei, W. C. Cheng, Y. Shu, A. Menzel, J. A. van Bokhoven, "A three-dimensional view of structural changes caused by deactivation of fluid catalytic cracking catalysts", *Nat. Commun.* **2017**, *8*, 809.

[186] J. Ihli, A. Diaz, Y. Shu, M. Guizar-Sicairos, M. Holler, K. Wakonig, M. Odstrcil, T. Li, F. Krumeich, E. Müller, W. C. Cheng, J. A. van Bokhoven, A. Menzel, "Resonant Ptychographic Tomography Facilitates Three-Dimensional Quantitative Colocalization of Catalyst Components and Chemical Elements", *J. Phys. Chem. C* **2018**, *122*, 22920–22929.

[187] Y. Fam, T. L. Sheppard, A. Diaz, T. Scherer, M. Holler, W. Wang, D. Wang, P. Brenner, A. Wittstock, J.-D. Grunwaldt, "Correlative Multiscale 3D Imaging of a Hierarchical Nanoporous Gold Catalyst by Electron, Ion and X-ray Nanotomography", *ChemCatChem* **2018**, *10*, 2858–2867.

[188] T. Weissenberger, R. Leonhardt, B. A. Zubiri, M. Pitínová-Štekrová, T. L. Sheppard, B. Reiprich, J. Bauer, R. Dotzel, M. Kahnt, A. Schropp, C. G. Schroer, J.-D. Grunwaldt, J. L. Casci, J. Čejka, E. Spiecker, W. Schwieger, "Synthesis and Characterisation of Hierarchically Structured Titanium Silicalite-1 Zeolites with Large Intracrystalline Macropores", *Chem. Eur. J.* **2019**, *25*, 14430–14440.

[189] J. Ihli, L. Bloch, F. Krumeich, K. Wakonig, M. Holler, M. Guizar-Sicairos, T. Weber, J. C. da Silva, J. A. van Bokhoven, "Hierarchical Structure of NiMo Hydrodesulfurization Catalysts Determined by Ptychographic X-Ray Computed Tomography", *Angew. Chem. Int. Ed.* **2020**, *59*, 17266–17271.

[190] F. Meirer, D. T. Morris, S. Kalirai, Y. Liu, J. C. Andrews, B. M. Weckhuysen, "Mapping metals incorporation of a whole single catalyst particle using element specific X-ray nanotomography", *J. Am. Chem. Soc.* **2015**, *137*, 102–105.

[191] F. Meirer, S. Kalirai, J. N. Weker, Y. Liu, J. C. Andrews, B. M. Weckhuysen, "Agglutination of single catalyst particles during fluid catalytic cracking as observed by X-ray nanotomography", *Chem. Commun.* **2015**, *51*, 8097–8100.

[192] H. Yamada, T. Tagawa, S. Nagao, S. Kato, "Investigation of gas diffusion phenomena in porous catalyst support pellets based on microstructure", *Catal. Today* **2021**, *375*, 30–35.

[193] L. R. Aramburo, Y. Liu, T. Tyliszczak, F. M. de Groot, J. C. Andrews, B. M. Weckhuysen, "3D nanoscale chemical imaging of the distribution of aluminum coordination environments in zeolites with soft X-ray microscopy", *ChemPhysChem* **2013**, *14*, 496–499.

[194] J. Wu, X. Zhu, D. A. Shapiro, J. R. Lee, T. Van Buuren, M. M. Biener, S. A. Gammon, T. T. Li, T. F. Baumann, A. P. Hitchcock, "Four-Dimensional Imaging of ZnO-Coated Alumina Aerogels by Scanning Transmission X-ray Microscopy and Ptychographic Tomography", *J. Phys. Chem. C* **2018**, *122*, 25374–25385.

[195] M. J. Werny, R. Valadian, L. M. Lohse, A.-L. Robisch, S. Zanoni, C. Hendriksen, B. M. Weckhuysen, F. Meirer, "X-ray nanotomography uncovers morphological heterogeneity in a polymerization catalyst at multiple reaction stages", *Chem Catal.* **2021**, *1*, 1413–1426.

[196] K. W. Bossers, R. Valadian, J. Garrevoet, S. V. Malderen, R. Chan, N. Friederichs, J. Severn, A. Wilbers, S. Zanoni, M. K. Jongkind, B. M. Weckhuysen, F. Meirer, "Heterogeneity in the Fragmentation of Ziegler Catalyst Particles during Ethylene Polymerization Quantified by X-ray Nanotomography", *J. Am. Chem. Soc. Au* **2021**, *1*, 852–864.

[197] M. Veselý, R. Valadian, L. Merten Lohse, M. Toepperwien, K. Spiers, J. Garrevoet, E. T. Vogt, T. Salditt, B. M. Weckhuysen, F. Meirer, "3-D X-ray Nanotomography Reveals Different Carbon Deposition Mechanisms in a Single Catalyst Particle", *ChemCatChem* **2021**, *13*, 2494–2507.

[198] M. Hirose, N. Ishiguro, K. Shimomura, N. Burdet, H. Matsui, M. Tada, Y. Takahashi, "Visualization of Heterogeneous Oxygen Storage Behavior in Platinum-Supported Cerium-Zirconium Oxide Three-Way Catalyst Particles by Hard X-ray Spectro-Ptychography", *Angew. Chem. Int. Ed.* **2018**, *57*, 1474–1479.

[199] Z. Gao, M. Odstrcil, S. Böcklein, D. Palagin, M. Holler, D. F. Sanchez, F. Krumeich, A. Menzel, M. Stampanoni, G. Mestl, J. A. van Bokhoven, M. Guizar-Sicairos, J. Ihli, "Sparse ab initio x-ray transmission spectrotomography for nanoscopic compositional analysis of functional materials", *Sci. Adv.* **2021**, *7*, eabf6971.

[200] K. W. Bossers, R. Valadian, S. Zanoni, R. Smeets, N. Friederichs, J. Garrevoet, F. Meirer, B. M. Weckhuysen, "Correlated X-ray Ptychography and Fluorescence Nano-Tomography on the Fragmentation Behavior of an Individual Catalyst Particle during the Early Stages of Olefin Polymerization", *J. Am. Chem. Soc.* **2020**, *142*, 3691–3695.

[201] B. Apeleo Zubiri, J. Wirth, D. Drobek, S. Englisch, T. Przybilla, T. Weissenberger, W. Schwieger, E. Spiecker, "Correlative Laboratory Nano-CT and 360° Electron Tomography of Macropore Structures in Hierarchical Zeolites", *Adv. Mater. Interf.* **2021**, *8*, 2001154.

[202] J. Wirth, S. Englisch, D. Drobek, B. Apeleo Zubiri, M. Wu, N. Taccardi, N. Raman, P. Wasserscheid, E. Spiecker, "Unraveling structural details in Ga-Pd SCALMS systems using correlative nano-CT, 360° electron tomography and analytical TEM", *Catalysts* **2021**, *11*, 810.

[203] Y. S. Zhang, X. Lu, R. E. Owen, G. Manos, R. Xu, F. R. Wang, W. C. Maskell, P. R. Shearing, D. J. Brett, "Fine structural changes of fluid catalytic catalysts and characterization of coke formed resulting from heavy oil devolatilization", *Appl. Catal. B Environ.* **2020**, *263*, 118329.

[204] J. Zečević, K. P. de Jong, P. E. de Jongh, "Progress in electron tomography to assess the 3D nanostructure of catalysts", *Curr. Opin. Solid State Mater. Sci.* **2013**, *17*, 115–125.

[205] H. Friedrich, P. E. de Jongh, A. J. Verkleij, K. P. de Jong, "Electron tomography for heterogeneous catalysts and related nanostructured materials", *Chem. Rev.* **2009**, *109*, 1613–1629.

[206] D. Stoeckel, C. Kübel, K. Hormann, A. Höltzel, B. M. Smarsly, U. Tallarek, "Morphological analysis of disordered macroporous-mesoporous solids based on physical reconstruction by nanoscale tomography", *Langmuir* **2014**, *30*, 9022–9027.

[207] C. J. Gommes, H. Friedrich, M. Wolters, P. E. de Jongh, K. P. de Jong, "Quantitative characterization of pore corrugation in ordered mesoporous materials using image analysis of electron tomograms", *Chem. Mater.* **2009**, *21*, 1311–1317.

[208] J. P. Tessonnier, O. Ersen, G. Weinberg, C. Pham-Huu, D. S. Su, R. Schlögl, "Selective deposition of metal nanoparticles inside or outside multiwalled carbon nanotubes", *ACS Nano* **2009**, *3*, 2081–2089.

[209] O. Daoura, G. Fornasieri, M. Boutros, N. El Hassan, P. Beaunier, C. Thomas, M. Selmane, A. Miche, C. Sassoye, O. Ersen, W. Baaziz, P. Massiani, A. Bleuzen, F. Launay, "One-pot prepared mesoporous silica SBA-15-like monoliths with embedded Ni particles as selective and stable catalysts for methane dry reforming", *Appl. Catal. B Environ.* **2021**, *280*, 119417.

[210] G. Prieto, J. Zečević, H. Friedrich, K. P. De Jong, P. E. De Jongh, "Towards stable catalysts by controlling collective properties of supported metal nanoparticles", *Nat. Mater.* **2013**, *12*, 34–39.

[211] F. Tariq, P. D. Lee, R. Haswell, D. W. McComb, "The influence of nanoscale microstructural variations on the pellet scale flow properties of hierarchical porous catalytic structures using multiscale 3D imaging", *Chem. Eng. Sci.* **2011**, *66*, 5804–5812.

[212] F. Tariq, R. Haswell, P. D. Lee, D. W. McComb, "Characterization of hierarchical pore structures in ceramics using multiscale tomography", *Acta Mater.* **2011**, *59*, 2109–2120.

[213] S. R. Bare, M. E. Charochak, S. D. Kelly, B. Lai, J. Wang, Y. C. K. Chen-Wiegart, "Characterization of a fluidized catalytic cracking catalyst on ensemble and individual particle level by X-ray micro- and nanotomography, micro-X-ray fluorescence, and micro-X-ray diffraction", *ChemCatChem* **2014**, *6*, 1427–1437.

[214] S. Kalirai, U. Boesenberg, G. Falkenberg, F. Meirer, B. M. Weckhuysen, "X-ray Fluorescence Tomography of Aged Fluid-Catalytic-Cracking Catalyst Particles Reveals Insight into Metal Deposition Processes", *ChemCatChem* **2015**, *7*, 3674–3682.

[215] S. W. Price, K. Ignatyev, K. Geraki, M. Basham, J. Filik, N. T. Vo, P. T. Witte, A. M. Beale, J. F. Mosselmans, "Chemical imaging of single catalyst particles with scanning μ-XANES-CT and μ-XRF-CT", *Phys. Chem. Chem. Phys.* **2015**, *17*, 521–529.

[216] P. Sprenger, T. L. Sheppard, J. P. Suuronen, A. Gaur, F. Benzi, J.-D. Grunwaldt, "Structural evolution of highly active multicomponent catalysts for selective propylene oxidation", *Catalysts* **2018**, *8*, 356.

[217] M. Gambino, M. Veselý, M. Filez, R. Oord, D. Ferreira Sanchez, D. Grolimund, N. Nesterenko, D. Minoux, M. Maquet, F. Meirer, B. M. Weckhuysen, "Nickel Poisoning of a Cracking Catalyst Unravelled by Single-Particle X-ray Fluorescence-Diffraction-Absorption Tomography", *Angew. Chem. Int. Ed.* **2020**, *59*, 3922–3927.

[218] T. L. Sheppard, S. W. Price, F. Benzi, S. Baier, M. Klumpp, R. Dittmeyer, W. Schwieger, J.-D. Grunwaldt, "In Situ Multimodal 3D Chemical Imaging of a Hierarchically Structured Core@Shell Catalyst", *J. Am. Chem. Soc.* **2017**, *139*, 7855–7863.

[219] P. H. Ho, W. de Nolf, F. Ospitali, A. Gondolini, G. Fornasari, E. Scavetta, D. Tonelli, A. Vaccari, P. Benito, "Coprecipitated-like hydrotalcite-derived coatings on open-cell metallic foams by electrodeposition: Rh nanoparticles on oxide layers stable under harsh reaction conditions", *Appl. Catal. A Gen.* **2018**, *560*, 12–20.

[220] C. G. Schroer, M. Kuhlmann, T. F. Günzler, B. Lengeler, M. Richwin, B. Griesebock, D. Lützenkirchen-Hecht, R. Frahm, E. Ziegler, A. Mashayekhi, D. R. Haeffner, J.-D. Grunwaldt, A. Baiker, "Mapping the chemical states of an element inside a sample using tomographic x-ray absorption spectroscopy", *Appl. Phys. Lett.* **2003**, *82*, 3360–3362.

[221] D. S. Wragg, M. G. O'Brien, M. Di Michiel, F. Lønstad-Bleken, "Rietveld analysis of computed tomography and its application to methanol to olefin reactor beds", *J. Appl. Cryst.* **2015**, *48*, 1719–1728.

[222] M. G. O'Brien, S. D. Jacques, M. Di Michiel, P. Barnes, B. M. Weckhuysen, A. M. Beale, "Active phase evolution in single Ni/Al_2O_3 methanation catalyst bodies studied in real time using combined μ-XRD-CT and μ-absorption-CT", *Chem. Sci.* **2012**, *3*, 509–523.

[223] S. D. Jacques, M. Di Michiel, A. M. Beale, T. Sochi, M. G. O'Brien, L. Espinosa-Alonso, B. M. Weckhuysen, P. Barnes, "Dynamic x-ray diffraction computed tomography reveals real-time insight into catalyst active phase evolution", *Angew. Chem. Int. Ed.* **2011**, *50*, 10148–10152.

[224] S. D. Jacques, M. Di Michiel, S. A. Kimber, X. Yang, R. J. Cernik, A. M. Beale, S. J. Billinge, "Pair distribution function computed tomography", *Nat. Commun.* **2013**, *4*, 2536.

[225] B. M. Weckhuysen, "Determining the active site in a catalytic process: Operando spectroscopy is more than a buzzword", *Phys. Chem. Chem. Phys.* **2003**, *5*, 4351–4360.

[226] A. M. Beale, S. D. Jacques, E. K. Gibson, M. Di Michiel, "Progress towards five dimensional diffraction imaging of functional materials under process conditions", *Coord. Chem. Rev.* **2014**, *277*, 208–223.

[227] A. Vamvakeros, S. D. Jacques, M. Di Michiel, D. Matras, V. Middelkoop, I. Z. Ismagilov, E. V. Matus, V. V. Kuznetsov, J. Drnec, P. Senecal, A. M. Beale, "5D operando tomographic diffraction imaging of a catalyst bed", *Nat. Commun.* **2018**, *9*, 4751.

[228] A. Vamvakeros, D. Matras, S. D. Jacques, M. Di Michiel, S. W. Price, P. Senecal, M. A. Aran, V. Middelkoop, G. B. Stenning, J. F. W. Mosselmans, I. Z. Ismagilov, A. M. Beale, "Real-time multi-length scale chemical tomography of fixed bed reactors during the oxidative coupling of methane reaction", *J. Catal.* **2020**, *386*, 39–52.

[229] A. Vamvakeros, D. Matras, S. D. Jacques, M. di Michiel, V. Middelkoop, P. Cong, S. W. Price, C. L. Bull, P. Senecal, A. M. Beale, "Real-time tomographic diffraction imaging of catalytic membrane reactors for the oxidative coupling of methane", *Catal. Today* **2021**, *364*, 242–255.

[230] J. Becher, D. F. Sanchez, D. E. Doronkin, D. Zengel, D. M. Meira, S. Pascarelli, J.-D. Grunwaldt, T. L. Sheppard, "Chemical gradients in automotive Cu-SSZ-13 catalysts for NO_x removal revealed by operando X-ray spectrotomography", *Nat. Catal.* **2021**, *4*, 46–53.

[231] J. Becher, S. Weber, D. F. Sanchez, D. E. Doronkin, J. Garrevoet, G. Falkenberg, D. M. Meira, S. Pascarelli, J.-D. Grunwaldt, T. L. Sheppard, "Sample environment for operando hard x-ray tomography – an enabling technology for multimodal characterization in heterogeneous catalysis", *Catalysts* **2021**, *11*, 459.

[232] J. Villanova, R. Daudin, P. Lhuissier, D. Jauffrès, S. Lou, C. L. Martin, S. Labouré, R. Tucoulou, G. Martínez-Criado, L. Salvo, "Fast in situ 3D nanoimaging: a new tool for dynamic characterization in materials science", *Mater. Today* **2017**, *20*, 354–359.

[233] S. Baier, A. Wittstock, C. D. Damsgaard, A. Diaz, J. Reinhardt, F. Benzi, J. Shi, T. Scherer, D. Wang, C. Kübel, C. G. Schroer, J.-D. Grunwaldt, "Influence of gas atmospheres and ceria on the stability of nanoporous gold studied by environmental electron microscopy and: In situ ptychography", *RSC Adv.* **2016**, *6*, 83031–83043.

[234] Y. Fam, T. L. Sheppard, J. Becher, D. Scherhaufer, H. Lambach, S. Kulkarni, T. F. Keller, A. Wittstock, F. Wittwer, M. Seyrich, D. Brueckner, M. Kahnt, X. Yang, A. Schropp, A. Stierle, C. G. Schroer, J.-D. Grunwaldt, "A versatile nanoreactor for complementary in situ X-ray and electron microscopy studies in catalysis and materials science", *J. Synchrotron Rad.* **2019**, *26*, 1769–1781.

[235] R. T. Zimmermann, S. Weber, J. Bremer, V. Idakiev, R. Pashminehazar, T. L. Sheppard, L. Mörl, K. Sundmacher, "Core-Shell Catalyst Pellets for Effective Reaction Heat Management", *Chem. Eng. J.* **2023**, *457*, 140921.

[236] S. Weber, K. L. Abel, R. T. Zimmermann, X. Huang, J. Bremer, L. K. Rihko-Struckmann, D. Batey, S. Cipiccia, J. Titus, D. Poppitz, C. Kübel, K. Sundmacher, R. Gläser, T. L. Sheppard, "Porosity and structure of hierarchically porous Ni/Al_2O_3 catalysts for CO_2 methanation", *Catalysts* **2020**, *10*, 1471.

[237] S. Weber, A. Diaz, M. Holler, A. Schropp, M. Lyubomirskiy, K. L. Abel, M. Kahnt, A. Jeromin, S. Kulkarni, T. F. Keller, R. Gläser, T. L. Sheppard, "Evolution of Hierarchically Porous Nickel Alumina Catalysts Studied by X-Ray Ptychography", *Adv. Sci.* **2022**, *9*, 2105432.

[238] J. Herwig, J. Titus, J. Kullmann, N. Wilde, T. Hahn, R. Gläser, D. Enke, "Hierarchically structured porous spinels via an epoxide-mediated sol-gel process accompanied by polymerization-induced phase separation", *ACS Omega* **2018**, *3*, 1201–1212.

[239] S. Weber, D. Batey, S. Cipiccia, M. Stehle, K. L. Abel, R. Gläser, T. L. Sheppard, "Hard X-ray Nanotomography for 3D Analysis of Coking in Nickel-based Catalysts", *Angew. Chem. Int. Ed.* **2021**, *60*, 21722–21777.

[240] M. L. Schulte, S. Weber, L. Klag, J.-D. Grunwaldt, T. L. Sheppard, "Synchrotron PXRD deconvolutes nickel particle and support changes in Ni/ZrO_2 methanation catalysts", *Catal. Sci. Technol.* **2022**, *12*, 6069–6083.

[241] S. Weber, R. T. Zimmermann, J. Bremer, K. L. Abel, D. Poppitz, N. Prinz, J. Ilsemann, S. Wendholt, Q. Yang, R. Pashminehazar, F. Monaco, P. Cloetens, X. Huang, C. Kübel, E. Kondratenko, M. Bauer, M. Bäumer, M. Zobel, R. Gläser, K. Sundmacher, T. L. Sheppard, "Digitization in Catalysis Research: Towards a Holistic Description of a Ni/Al_2O_3 Reference Catalyst for CO_2 Methanation", *ChemCatChem*, *14*, e202101878.

[242] S. Brunauer, P. H. Emmett, E. Teller, "Adsorption of Gases in Multimolecular Layers", *J. Am. Chem. Soc.* **1938**, *60*, 309–319.

[243] E. P. Barrett, L. G. Joyner, P. P. Halenda, "The Determination of Pore Volume and Area Distributions in Porous Substances. I. Computations from Nitrogen Isotherms", *J. Am. Chem. Soc.* **1951**, *73*, 373–380.

[244] E. W. Washburn, "The Dynamics of Capillary Flow.", *Phys. Rev.* **1921**, *17*, 273–283.

[245] H. M. Rietveld, "Line profiles of neutron powder-diffraction peaks for structure refinement", *Acta Crystallogr.* **1967**, *22*, 151–152.

[246] H. M. Rietveld, "A profile refinement method for nuclear and magnetic structures", *J. Appl. Crystallogr.* **1969**, *2*, 65–71.

[247] A. Borodziński, M. Bonarowska, "Relation between crystallite size and dispersion on supported metal catalysts", *Langmuir* **1997**, *13*, 5613–5620.

[248] *Lehrbuch der anorganischen Chemie*, 102nd ed., (Eds.: A. F. Holleman, E. Wiberg, N. Wiberg), de Gruyter, Berlin [u.a.], **2007**.

[249] J.-D. Grunwaldt, M. Caravati, S. Hannemann, A. Baiker, "X-ray absorption spectroscopy under reaction conditions: Suitability of different reaction cells for combined catalyst characterization and time-resolved studies", *Phys. Chem. Chem. Phys.* **2004**, *6*, 3037–3047.

[250] J. Schindelin, I. Arganda-Carreras, E. Frise, V. Kaynig, M. Longair, T. Pietzsch, S. Preibisch, C. Rueden, S. Saalfeld, B. Schmid, J.-Y. Tinevez, D. J. White, V. Hartenstein, K. Eliceiri, P. Tomancak, A. Cardona, "Fiji: an open-source platform for biological-image analysis", *Nat. Methods* **2012**, *9*, 676–682.

[251] J. R. Kremer, D. N. Mastronarde, J. R. McIntosh, "Computer visualization of three-dimensional image data using IMOD", *J. Struct. Biol.* **1996**, *116*, 71–76.

[252] P. Gilbert, "Iterative methods for the three-dimensional reconstruction of an object from projections", *J. Theor. Biol.* **1972**, *36*, 105–117.

[253] K. Batenburg, S. Bals, J. Sijbers, C. Kübel, P. Midgley, J. Hernandez, U. Kaiser, E. Encina, E. Coronado, G. Van Tendeloo, "3D imaging of nanomaterials by discrete tomography", *Ultramicroscopy* **2009**, *109*, 730–740.

[254] C. Messaoudil, T. Boudier, C. O. S. Sorzano, S. Marco, "TomoJ: tomography software for three-dimensional reconstruction in transmission electron microscopy", *BMC Bioinformatics* **2007**, *8*, 288.

[255] M. Holler, J. Raabe, R. Wepf, S. H. Shahmoradian, A. Diaz, B. Sarafimov, T. Lachat, H. Walther, M. Vitins, "OMNY PIN - A versatile sample holder for tomographic measurements at room and cryogenic temperatures", *Rev. Sci. Instrum.* **2017**, *88*, 113701.

[256] A. Stierle, T. F. Keller, H. Noei, V. Vonk, R. Roehlsberger, "DESY NanoLab", *JLSRF* **2016**, *2*, A76.

[257] A. Schropp, R. Dohrmann, S. Botta, D. Bruckner, M. Kahnt, M. Lyubomirskiy, C. Ossig, M. Scholz, M. Seyrich, M. E. Stuckelberger, P. Wiljes, F. Wittwer, J. Garrevoet, G. Falkenberg, Y. Fam, T. L. Sheppard, J.-D. Grunwaldt, C. G. Schroer, "PtyNAMi: Ptychographic nano-analytical microscope", *J. Appl. Cryst.* **2020**, *53*, 957–971.

[258] A. M. Maiden, J. M. Rodenburg, "An improved ptychographical phase retrieval algorithm for diffractive imaging", *Ultramicroscopy* **2009**, *109*, 1256–1262.

[259] Q. Tseng, E. Duchemin-Pelletier, A. Deshiere, M. Balland, H. Guilloud, O. Filhol, M. Theńy, "Spatial organization of the extracellular matrix regulates cell-cell junction positioning", *PNAS* **2012**, *109*, 1506–1511.

[260] N. Banterle, K. H. Bui, E. A. Lemke, M. Beck, "Fourier ring correlation as a resolution criterion for super-resolution microscopy", *J. Struct. Biol.* **2013**, *183*, 363–367.

[261] M. van Heel, M. Schatz, "Fourier shell correlation threshold criteria", *J. Struct. Biol.* **2005**, *151*, 250–262.

[262] M. Holler, J. Raabe, A. Diaz, M. Guizar-Sicairos, C. Quitmann, A. Menzel, O. Bunk, "An instrument for 3D x-ray nano-imaging", *Rev. Sci. Instrum.* **2012**, *83*, 073703.

[263] A. Kaestner, B. Münch, P. Trtik, L. Butler, "Spatiotemporal computed tomography of dynamic processes", *Opt. Eng.* **2011**, *50*, 123201.

[264] X. Huang, H. Yan, R. Harder, Y. Hwu, I. K. Robinson, Y. S. Chu, "Optimization of overlap uniformness for ptychography", *Optics Express* **2014**, *22*, 12634.

[265] M. Guizar-Sicairos, J. R. Fienup, "Phase retrieval with transverse translation diversity: a nonlinear optimization approach", *Opt. Express* **2008**, *16*, 7264.

[266] P. Thibault, M. Guizar-Sicairos, "Maximum-likelihood refinement for coherent diffractive imaging", *New J.Phys.* **2012**, *14*, 063004.

[267] M. Guizar-Sicairos, A. Diaz, M. Holler, M. S. Lucas, A. Menzel, R. A. Wepf, O. Bunk, "Phase tomography from x-ray coherent diffractive imaging projections", *Opt. Express* **2011**, *19*, 21345.

[268] M. Odstrčil, M. Holler, J. Raabe, M. Guizar-Sicairos, "Alignment methods for nanotomography with deep subpixel accuracy", *Opt. Express* **2019**, *27*, 36637.

[269] M. Guizar-Sicairos, J. J. Boon, K. Mader, A. Diaz, A. Menzel, O. Bunk, "Quantitative interior x-ray nanotomography by a hybrid imaging technique", *Optica* **2015**, *2*, 259.

[270] C. Rau, D. Batey, S. Cipiccia, X. Shi, S. Marathe, M. Storm, A. J. Bodey, M.-C. Zdora, "New imaging opportunities at the DIAMOND beamline I13L", *Proc. SPIE* **2019**, 31.

[271] D. Batey, S. Cipiccia, X. Shi, S. Williams, K. Wanelik, A. Wilson, S. Pérez-Tamarit, P. Cimavilla, M. A. Ródriguez-Pérez, C. Rau, "Coherence Branch at I13, DLS: The Multiscale, Multimodal, Ptycho-tomographic End Station", *Microsc. Microanal.* **2018**, *24*, 42–43.

[272] D. Batey, PhD Thesis, University of Sheffffield, **2014**.

[273] I. Zanette, R. Clare, D. Eastwood, C. Venkata, F. Pfeiffer, P. Cloetens, P. Thibault, "Phase-Vortex Removal for Quantitative X-Ray Nanotomography with Near-Field Ptychography", *Phys. Rev. Appl.* **2020**, *14*, 064078.

[274] J. C. da Silva, P. Trtik, A. Diaz, M. Holler, M. Guizar-Sicairos, J. Raabe, O. Bunk, A. Menzel, "Mass Density and Water Content of Saturated Never-Dried Calcium Silicate Hydrates", *Langmuir* **2015**, *31*, 3779–3783.

[275] A. Cuesta, A. G. De la Torre, I. Santacruz, P. Trtik, J. C. da Silva, A. Diaz, M. Holler, M. A. G. Aranda, "Chemistry and Mass Density of Aluminum Hydroxide Gel in Eco-Cements by Ptychographic X-ray Computed Tomography", *J. Phys. Chem. C* **2017**, *121*, 3044–3054.

[276] J. C. da Silva, Toupy, `https://toupy.readthedocs.io/en/latest/index.html`, Accessed: 2022-04-19.

[277] C. Morawe, R Barrett, P Cloetens, B Lantelme, J.-C. Peffen, A Vivo, "Graded multilayers for figured Kirkpatrick-Baez mirrors on the new ESRF end station ID16A", **2015**, *9588*, 8–14.

[278] S. Zabler, P. Cloetens, J.-P. Guigay, J. Baruchel, M. Schlenker, "Optimization of phase contrast imaging using hard x rays", *Rev. Sci. Instrum.* **2005**, *76*, 073705.

[279] M. Hubert, A. Pacureanu, C. Guilloud, Y. Yang, J. C. da Silva, J. Laurencin, F. Lefebvre-Joud, P. Cloetens, "Efficient correction of wavefront inhomogeneities in X-ray holographic nanotomography by random sample displacement", *Appl. Phys. Lett.* **2018**, *112*, 203704.

[280] L. Weber, A. Hänsch, U. Wlfram, A. Pacureanu, P. Cloetens, F. Peyrin, S. Rit, M. Langer, "Registration of phase-contrast images in propagation-based X-ray phase tomography", *J. Microsc.* **2018**, *269*, 36–47.

[281] P. Cloetens, W. Ludwig, E. Boller, L. Helfen, L. Salvo, R. Mache, M. Schlenker, "Quantitative phase contrast tomography using coherent synchrotron radiation", *SPIE 4503 Dev. X-ray Tomogr. III* **2002**, *4503*, 82–91.

[282] B. Yu, L. Weber, A. Pacureanu, M. Langer, C. Olivier, P. Cloetens, F. Peyrin, "Evaluation of phase retrieval approaches in magnified X-ray phase nano computerized tomography applied to bone tissue", *Opt. Express* **2018**, *26*, 11110–11124.

[283] A. Mirone, E. Brun, E. Gouillart, P. Tafforeau, J. Kieffer, "The PyHST2 hybrid distributed code for high speed tomographic reconstruction with iterative reconstruction and a priori knowledge capabilities", *Nucl. Instrum. Methods Phys. Res. B* **2014**, *324*, 1st International Conference on Tomography of Materials and Structures, 41–48.

[284] C. R. Harris, K. J. Millman, S. J. van der Walt, R. Gommers, P. Virtanen, D. Cournapeau, E. Wieser, J. Taylor, S. Berg, N. J. Smith, R. Kern, M. Picus, S. Hoyer, M. H. van Kerkwijk, M. Brett, A. Haldane, J. F. del Río, M. Wiebe, P. Peterson, P. Gérard-Marchant, K. Sheppard, T. Reddy, W. Weckesser, H. Abbasi, C. Gohlke, T. E. Oliphant, "Array programming with NumPy", *Nature* **2020**, *585*, 357–362.

[285] J. D. Hunter, "Matplotlib: A 2D graphics environment", *Comput. Sci. Eng.* **2007**, *9*, 90–95.

[286] M. L. Waskom, "seaborn: statistical data visualization", *J. Open Source Softw.* **2021**, *6*, 3021.

[287] P. R. Willmott, D. Meister, S. J. Leake, M. Lange, A. Bergamaschi, M. Böge, M. Calvi, C. Cancellieri, N. Casati, A. Cervellino, Q. Chen, C. David, U. Flechsig, F. Gozzo, B. Henrich, S. Jäggi-Spielmann, B. Jakob, I. Kalichava, P. Karvinen, J. Krempasky, A. Lüdeke, R. Lüscher, S. Maag, C. Quitmann, M. L. Reinle-Schmitt, T. Schmidt, B. Schmitt, A. Streun, I. Vartiainen, M. Vitins, X. Wang, R. Wullschleger, "The Materials Science beamline upgrade at the Swiss Light Source", *J. Synchrotron Rad.* **2013**, *20*, 667–682.

[288] C. Prescher, V. B. Prakapenka, "DIOPTAS: a program for reduction of two-dimensional X-ray diffraction data and data exploration", *High Press. Res.* **2015**, *35*, 223–230.

[289] J. Kieffer, D. Karkoulis, "PyFAI, a versatile library for azimuthal regrouping", *J. Phys. Conf. Ser.* **2013**, *425*, 202012.

[290] DIFFRAC.SUITE TOPAS - XRD Software Bruker, `https://www.bruker.com/de/products/x-ray-diffraction-and-elemental-analysis/x-ray-diffraction/xrd-software/topas.html`, accessed on 2020-10-08.

[291] D. Balzar, "Voigt Function Model in Diffraction-Line Broadening Analysis", *International Union of Crystallography Monographs on Crystallography* **1999**, *10*, 94–126.

[292] Topas Wiki, `http://topas.dur.ac.uk/topaswiki/doku.php?id=topas`, accessed on 2021-10-18.

[293] L. Smrčok, V. Langer, J Křest'an, "γ-Alumina: a single-crystal X-ray diffraction study", *Acta Cryst. C* **2006**, *62*, i83–i84.

[294] W. O. Milligan, J. L. McAtee, "Crystal structure of γ-AlOOH and γ-ScOOH", *J. Phys. Chem.* **1956**, *60*, 273–277.

[295] B. Bondars, G. Heidemane, J. Grabis, K. Laschke, H. Boysen, J. Schneider, F. Frey, "Powder diffraction investigations of plasma sprayed zirconia", *J. Mater. Sci.* **1995**, *30*, 1621–1625.

[296] D. K. Smith, W. Newkirk, " The crystal structure of baddeleyite (monoclinic ZrO_2) and its relation to the polymorphism of ZrO_2", *Acta Crystallogr.* **1965**, *18*, 983–991.

[297] J. Rouquette, J. Haines, G. Fraysse, A. Al-Zein, V. Bornand, M Pintard, P. Papet, S. Hull, F. Gorelli, "High-pressure structural and vibrational study of $PbZr_{0.40}Ti_{0.60}O_3$", *Inorg. Chem.* **2008**, *47*, 9898–9904.

[298] D. Rodic, V. Spasojevic, V. Kusigerski, R. Tellgren, H. Rundlof, "Magnetic ordering in polycrystalline $Ni_xZn_{1-x}O$ Solid Solutions", *Phys. Status Solidi B Basic Res.* **2000**, *218*, 527–536.

[299] C. L. Farrow, S. J. L. Billinge, "Relationship between the atomic pair distribution function and small-angle scattering: implications for modeling of nanoparticles", *Acta Cryst. A* **2009**, *65*, 232–239.

[300] E. Takeshi, S. J. Billinge in *Underneath the Bragg Peaks*, (Eds.: T. Egami, S. J. Billinge), Pergamon Materials Series, Pergamon, **2012**, pp. 55–111.

[301] M. W. Terban, S. J. L. Billinge, "Structural Analysis of Molecular Materials Using the Pair Distribution Function", *Chem. Rev.* **2022**, *122*, 1208–1272.

[302] P. Juhás, T. Davis, C. L. Farrow, S. J. Billinge, "PDFgetX3: a rapid and highly automatable program for processing powder diffraction data into total scattering pair distribution functions", *J. Appl. Cryst.* **2013**, *46*, 560–566.

[303] P. Juhás, C. L. Farrow, X. Yang, K. R. Knox, S. J. Billinge, "Complex modeling: A strategy and software program for combining multiple information sources to solve ill posed structure and nanostructure inverse problems", *Acta Cryst. A* **2015**, *71*, 562–568.

[304] DFG Priority Program SPP 2080 "Catalysts and reactors under dynamic conditions for energy storage and conversion", `https://www.itcp.kit.edu/spp2080/english/index.php`, Accessed: 2022-04-23.

[305] NFDI4Cat - NFDI für Wissenschaften mit Bezug zur Katalyse, `https://nfdi4cat.org/`, Accessed: 2022-04-24.

[306] S. H. Lee, W. S. Chang, S. M. Han, D. H. Kim, J. K. Kim, "Synchrotron X-ray nanotomography and three-dimensional nanoscale imaging analysis of pore structure-function in nanoporous polymeric membranes", *J. Mem. Sci.* **2017**, *535*, 28–34.

[307] E. Gregorová, T. Uhlířová, W. Pabst, P. Diblíková, I. Sedlářová, "Microstructure characterization of mullite foam by image analysis, mercury porosimetry and X-ray computed microtomography", *Ceram. Int.* **2018**, *44*, 12315–12328.

[308] Q. Xiong, T. G. Baychev, A. P. Jivkov, "Review of pore network modelling of porous media: Experimental characterisations, network constructions and applications to reactive transport", *J. Contam. Hydrol.* **2016**, *192*, 101–117.

[309] B. Prifling, M. Neumann, D. Hlushkou, C. Kübel, U. Tallarek, V. Schmidt, "Generating digital twins of mesoporous silica by graph-based stochastic microstructure modeling", *Comput. Mater. Sci.* **2021**, *187*, 1–21.

[310] Y. Liu, F. Meirer, C. M. Krest, S. Webb, B. M. Weckhuysen, "Relating structure and composition with accessibility of a single catalyst particle using correlative 3-dimensional micro-spectroscopy", *Nat. Commun.* **2016**, *7*, 12634.

[311] R. Daroughegi, F. Meshkani, M. Rezaei, "Enhanced activity of CO_2 methanation over mesoporous nanocrystalline Ni/Al_2O_3 catalysts prepared by ultrasound-assisted co-precipitation method", *Int. J. Hydrogen Energy* **2017**, *42*, 15115–15125.

[312] Y. Tokudome, K. Fujita, K. Nakanishi, K. Miura, K. Hirao, "Synthesis of monolithic Al_2O_3 with well-defined macropores and mesostructured skeletons via the sol-gel process accompanied by phase separation", *Chem. Mater.* **2007**, *19*, 3393–3398.

[313] M. Zangouei, A. Z. Moghaddam, M. Arasteh, "The influence of nickel loading on reducibility of NiO/Al_2O_3 catalysts synthesized by sol-gel method", *Chem. Eng. Res. Bull.* **2010**, *14*, 97–102.

[314] D. Li, Y. Li, X. Liu, Y. Guo, C.-W. Pao, J.-L. Chen, Y. Hu, Y. Wang, "$NiAl_2O_4$ Spinel Supported Pt Catalyst: High Performance and Origin in Aqueous-Phase Reforming of Methanol", *ACS Catal.* **2019**, *9*, 9671–9682.

[315] E. Kiš, R. Marinković-Nedučin, G. Lomić, G. Bošković, D. Obadović, J. Kiurski, P. Putanov, "Structural and textural properties of the NiO/Al_2O_3 catalyst", *Polyhedron* **1998**, *17*, 27–34.

[316] S. Sengupta, K. Ray, G. Deo, "Effects of modifying Ni/Al_2O_3 catalyst with cobalt on the reforming of CH_4 with CO_2 and cracking of CH_4 reactions", *Int. J. Hydrogen Energy* **2014**, *39*, 11462–11472.

[317] S. V. Moghaddam, M. Rezaei, F. Meshkani, "Surfactant-Free Sol–Gel Synthesis Method for the Preparation of Mesoporous High Surface Area $NiO–Al_2O_3$ Nanopowder and Its Application in Catalytic CO_2 Methanation", *Energy Technol.* **2020**, *8*, 1900778.

[318] R. López-Fonseca, C. Jiménez-González, B. de Rivas, J. I. Gutiérrez-Ortiz, "Partial oxidation of methane to syngas on bulk $NiAl_2O_4$ catalyst. Comparison with alumina supported nickel, platinum and rhodium catalysts", *Appl. Catal. A Gen.* **2012**, *437-438*, 53–62.

[319] P. Kim, Y. Kim, H. Kim, I. K. Song, J. Yi, "Synthesis and characterization of mesoporous alumina with nickel incorporated for use in the partial oxidation of methane into synthesis gas", *Appl. Catal. A Gen.* **2004**, *272*, 157–166.

[320] B. Scheffer, J. J. Heijeinga, J. A. Moulijn, "An electron spectroscopy and x-ray diffraction study of nickel oxide/alumina and nickel-oxide-tungsten trioxide/alumina catalysts", *J. Phys. Chem.* **1987**, *91*, 4752–4759.

[321] C. Li, Y.-W. Chen, "Temperature-programmed-reduction studies of nickel oxide/alumina catalysts: effects of the preparation method", *Thermochim. Acta* **1995**, *256*, 457–465.

[322] X. Xu, L. Li, F. Yu, H. Peng, X. Fang, X. Wang, "Mesoporous high surface area NiO synthesized with soft templates: Remarkable for catalytic CH_4 deep oxidation", *Mol. Catal.* **2017**, *441*, 81–91.

[323] T. J., K. J., H. J., E. D., W. N., G. R., "Dry reforming of methane over a Ni spinel with bimodal porosity", *DGMK Tagungsbericht* **2015**, 225–232.

[324] L. R. Winter, R. Chen, X. Chen, K. Chang, Z. Liu, S. D. Senanayake, A. M. Ebrahim, J. G. Chen, "Elucidating the roles of metallic Ni and oxygen vacancies in CO_2 hydrogenation over Ni/CeO_2 using isotope exchange and in situ measurements", *Appl. Catal. B Environ.* **2019**, *245*, 360–366.

[325] Y. Ma, J. Liu, M. Chu, J. Yue, Y. Cui, G. Xu, "Cooperation Between Active Metal and Basic Support in Ni-Based Catalyst for Low-Temperature CO_2 Methanation", *Catal. Lett.* **2020**, *150*, 1418–1426.

[326] W. Conner, S. Christensen, H. Topsøe, M. Ferrero, A. Pullen, "The Estimation of Pore-network Dimensions and Structure: Analysis of Sorption and Comparison with Porosimetry", *Stud. Surf. Sci. Catal.* **1994**, *87*, 151–163.

[327] L. S. Rijfkogel, B. Ghanbarian, Q. Hu, H.-H. Liu, "Clarifying pore diameter, pore width, and their relationship through pressure measurements: A critical study", *Mar. Pet. Geol.* **2019**, *107*, 142–148.

[328] L. Andersson, A. C. Jones, M. A. Knackstedt, L. Bergström, "Three-dimensional structure analysis by X-ray micro-computed tomography of macroporous alumina templated with expandable microspheres", *J. Eur. Ceram.* **2010**, *30*, 2547–2554.

[329] S. Diamond, "Mercury porosimetry. An inappropriate method for the measurement of pore size distributions in cement-based materials", *Cem. Concr. Res.* **2000**, *30*, 1517–1525.

[330] N. M. N. Alford, A. A. Rahman, "An assesment of porosity and pore sizes in hardened cement pastes", *J. Mater. Sci.* **1981**, *16*, 3105–3114.

[331] H. Seong, S. Choi, K. E. Matusik, A. L. Kastengren, C. F. Powell, "3D pore analysis of gasoline particulate filters using X-ray tomography: impact of coating and ash loading", *J. Mater. Sci.* **2019**, *54*, 6053–6065.

[332] L. Shen, Z. Chen, "Critical review of the impact of tortuosity on diffusion", *Chem. Eng. Sci.* **2007**, *62*, 3748–3755.

[333] K. Y. Kim, T. S. Yun, K. P. Park, "Evaluation of pore structures and cracking in cement paste exposed to elevated temperatures by X-ray computed tomography", *Cem. Concr. Res.* **2013**, *50*, 34–40.

[334] J. Samei, M. Amirmaleki, M. Shirinzadeh Dastgiri, C. Marinelli, D. E. Green, "In-situ X-ray tomography analysis of the evolution of pores during deformation of AlSi10Mg fabricated by selective laser melting", *Mater. Lett.* **2019**, *255*, 126512.

[335] T. Hondo, Z. Kato, K. Yasuda, F. Wakai, S. Tanaka, "Coarse pore evolution in dry-pressed alumina ceramics during sintering", *Adv. Powder Technol.* **2016**, *27*, 1006–1012.

[336] H. Kohlmann, "Looking into the Black Box of Solid-State Synthesis", *Eur. J. Inorg. Chem.* **2019**, *2019*, 4174–4180.

[337] P. Forzatti, L. Liettie, "Catalyst deactivation", *Catal. Today* **1999**, *52*, 165–181.

[338] J. Hagen, *Industrial Catalysis: A Practical Approach*, 3rd Edition, Wiley-VCH, Weinheim, **2015**.

[339] M. Guisnet, P. Magnoux, "Coking and deactivation of zeolites. Influence of the Pore Structure", *Appl. Catal.* **1989**, *54*, 1–27.

[340] M. Guisnet, P. Magnoux, "Organic chemistry of coke formation", *Appl. Catal. A* **2001**, *212*, 83–96.

[341] P. Mougin, M. Pons, J. Villermaux, "Reaction and Diffusion at an Artificial Fractal Interface: Evidence for a new Diffusional Regime", *Chem. Eng. Sci.* **1996**, *51*, 2293–2302.

[342] G. Wang, M. O. Coppens, "Rational design of hierarchically structured porous catalysts for autothermal reforming of methane", *Chem. Eng. Sci.* **2010**, *65*, 2344–2351.

[343] J. R. Rostrup-Nielsen, *Catalysis: Science and Technology Volume 5*, (Eds.: J. Anderson, M. Boudart), Springer-Verlag Berlin Heidelberg, Berlin, **1984**.

[344] E. Tracz, R. Scholz, T. Borowiecki, "High-resolution electron microscopy study of the carbon deposit morphology on nickel catalysts", *Appl. Catal.* **1990**, *66*, 133–148.

[345] J. E. Schmidt, J. D. Poplawsky, B. Mazumder, Ö. Attila, D. Fu, D. A. de Winter, F. Meirer, S. R. Bare, B. M. Weckhuysen, "Coke Formation in a Zeolite Crystal During the Methanol-to-Hydrocarbons Reaction as Studied with Atom Probe Tomography", *Angew. Chem. Int. Ed.* **2016**, *55*, 11173–11177.

[346] I. K. van Ravenhorst, C. Vogt, H. Oosterbeek, K. W. Bossers, J. G. Moya-Cancino, A. P. van Bavel, A. M. van der Eerden, D. Vine, F. M. de Groot, F. Meirer, B. M. Weckhuysen, "Capturing the Genesis of an Active Fischer–Tropsch Synthesis Catalyst with Operando X-ray Nanospectroscopy", *Angew. Chem. Int. Ed.* **2018**, *57*, 11957–11962.

[347] F. Pauer, J. Kipfstuhl, W. Kuhs, "Raman spectroscopic study on the spatial distribution of nitrogen and oxygen in natural ice clathrates and their decomposition to air bubbles", *Geophys. Res. Lett.* **1996**, *23*, 177–180.

[348] A. Ferrari, J. Robertson, "Interpretation of Raman spectra of disordered and amorphous carbon", *Phys. Rev. B* **2000**, *61*, 95–107.

[349] A. Sadezky, H. Muckenhuber, H. Grothe, R. Niessner, U. Pöschl, "Raman microspectroscopy of soot and related carbonaceous materials: Spectral analysis and structural information", *Carbon* **2005**, *43*, 1731–1742.

[350] O. E. Everett, P. C. Zonetti, O. C. Alves, R. R. de Avillez, L. G. Appel, "The role of oxygen vacancies in the CO_2 methanation employing Ni/ZrO_2 doped with Ca", *Int. J. Hydrog. Energy* **2020**, *45*, 6352–6359.

[351] D. Pandey, G. Deo, "Effect of support on the catalytic activity of supported Ni-Fe catalysts for the CO_2 methanation reaction", *J. Ind. Eng. Chem.* **2016**, *33*, 99–107.

[352] J. Ren, X. Qin, J. Z. Yang, Z. F. Qin, H. L. Guo, J. Y. Lin, Z. Li, "Methanation of carbon dioxide over Ni-M/ZrO_2 (M = Fe, Co, Cu) catalysts: Effect of addition of a second metal", *Fuel Process. Technol.* **2015**, *137*, 204–211.

[353] K. Zhao, W. Wang, Z. Li, "Highly efficient Ni/ZrO_2 catalysts prepared via combustion method for CO_2 methanation", *J. CO2 Util.* **2016**, *16*, 236–244.

[354] J. Tan, J. Wang, Z. Zhang, Z. Ma, L. Wang, Y. Liu, "Highly dispersed and stable Ni nanoparticles confined by MgO on ZrO_2 for CO_2 methanation", *Appl. Surf. Sci.* **2019**, *481*, 1538–1548.

[355] X. Jia, X. Zhang, N. Rui, X. Hu, C. jun Liu, "Structural effect of Ni/ZrO_2 catalyst on CO_2 methanation with enhanced activity", *Appl. Catal. B: Environ.* **2019**, *244*, 159–169.

[356] Z. Liu, X. Ding, R. Zhu, Y. Li, Y. Wang, W. Sun, D. Wang, L. Wu, L. Zheng, "Investigation on the Effect of Highly Active Ni/ZrO_2 Catalysts Modified by MgO-Nd_2O_3 Promoters in CO_2 Methanation at Low Temperature Condition", *ChemistrySelect* **2022**, *7*, e202103774.

[357] M. Králik, "Adsorption, chemisorption, and catalysis", *Chem. Pap.* **2014**, *68*, 1625–1638.

[358] C. G. Schroer, I. Agapov, W. Brefeld, R. Brinkmann, Y. C. Chae, H. C. Chao, M. Eriksson, J. Keil, X. Nuel Gavaldà, R. Röhlsberger, O. H. Seeck, M. Sprung, M. Tischer, R. Wanzenberg, E. Weckert, "PETRA IV: the ultralow-emittance source project at DESY", *J. Synchrotron Rad.* **2018**, *25*, 1277–1290.

[359] P. F. Tavares, S. C. Leemann, M. Sjöström, Å. Andersson, "The MAX IV storage ring project", *J. Synchrotron Rad.* **2014**, *21*, 862–877.

[360] R. Delhez, T. H. De Keijser, J. I. Langford, D. Louër, E. J. Mittemeijer, E. J. Sonneveld, "Crystal imperfection broadening and peak shape in the Rietveld method", *The Rietveld Method (IUCR Book Series)* **1993**, 132.

[361] V. Honkimäki, P. Surotti, "Effects of instrument function, crystallite size and strain on reflection profiles", *Defect and Microstructure Analysis by Diffraction (IUCR Book Series)* **1999**.

8 Appendix A

8.1 Conventional vs. Imaging Methods for Pore Structure Analysis

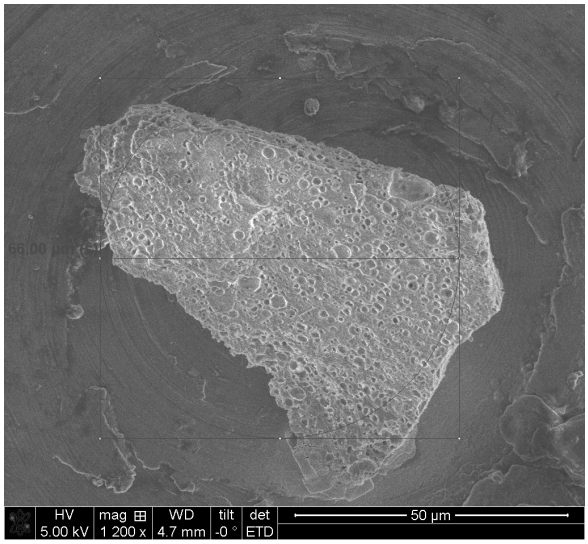


Figure 8.1: SEM image of the SPP2080-IMRC particle mounted on a pure Al pin for HXCT measurements.[241] Available under the terms and conditions of the Creative Commons Attribution 4.0 license (CC BY 4.0, `https://creativecommons.org/licenses/by/4.0/`), Copyright ©2022.

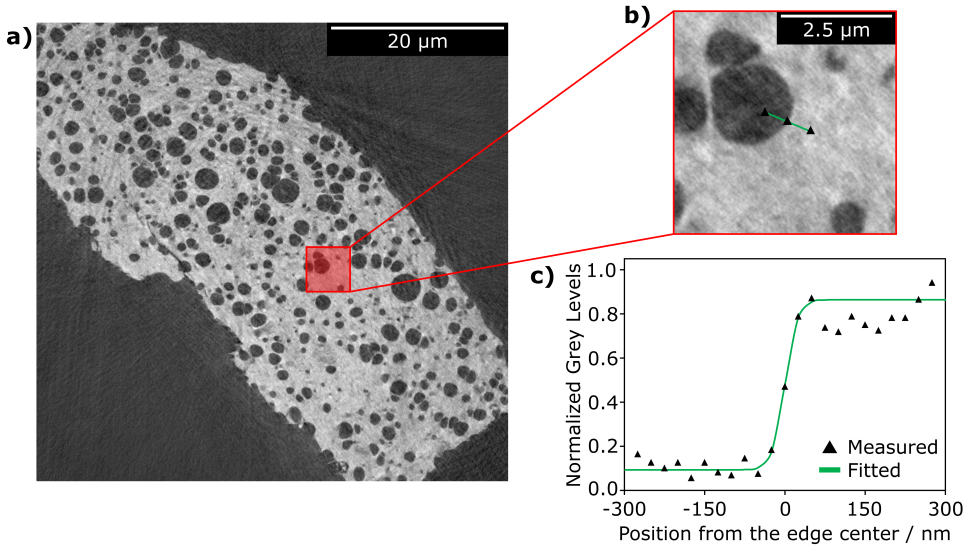


Figure 8.2: Determination of the physical resolution in the HXCT reconstruction. a) xy slice extracted from the 3D volume. b) Zoom on the interface between the matrix and the void. c) Normalized grey level profile at the interface.[241] Available under the terms and conditions of the Creative Commons Attribution 4.0 license (CC BY 4.0, `https://creativecommons.org/licenses/by/4.0/`), Copyright ©2022.

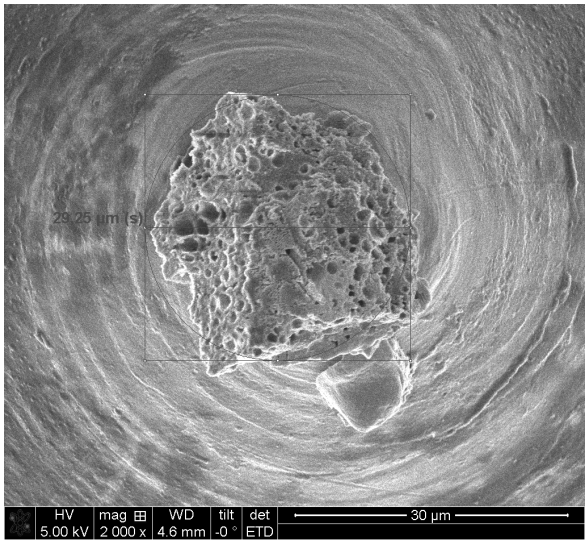


Figure 8.3: SEM image of the mounted catalyst particle from the SPP2080-IMRC-0min sample on top of the Cu-pin for PXCT measurements.[235] Available under the terms and conditions of the Creative Commons Attribution 4.0 license (CC BY 4.0, `https://creativecommons.org/licenses/by/4.0/`), Copyright ©2023.

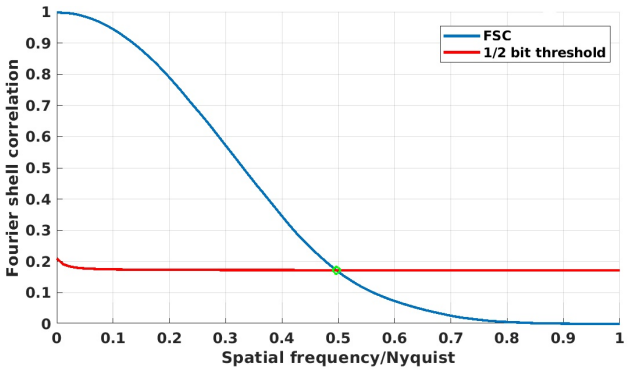


Figure 8.4: FSC analysis to estimate the resolution of the obtained tomogram. The estimated resolution according the 1/2-bit criterion is 40.2 nm.[235] Available under the terms and conditions of the Creative Commons Attribution 4.0 license (CC BY 4.0, `https://creativecommons.org/licenses/by/4.0/`), Copyright ©2023.

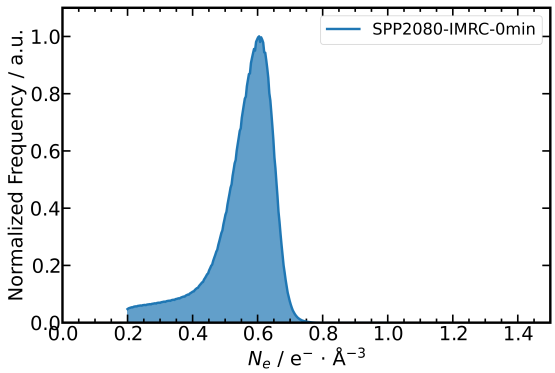


Figure 8.5: Normalized electron density distribution of the SPP2080-IMRC-0min material label obtained form PXCT.

8.2 Shell Thickness Analysis of Designed Core-Shell Catalysts

8.3 Hierarchically Porous Catalysts for CO_2 Methanation

Table 8.1: Structural parameters obtained from Rietveld analysis for the refinements of Ni/Al_2O_3-h with refined and fixed occupancies of the Al positions of the Al_2O_3 phase.

	Refined Al occupancies				Fixed Al occupancies			
R_{exp} / %	2.49				2.49			
R_{wp} / %	2.05				4.87			
GoF / %	0.82				1.96			
Phase	Al_2O_3			$NiAl_2O_4$	Al_2O_3			$NiAl_2O_4$
Space group	$Fd\bar{3}m$			$Fd\bar{3}m$	$Fd\bar{3}m$			$Fd\bar{3}m$
ω / wt.%	95.50(13)			4.50(13)	84.29(12)			15.71(12)
L_{vol} / nm	6.933(19)			7.41(13)	7.03(7)			6.77(6)
a / Å	8.0133(2)			8.0604(11)	8.0080(6)			8.0305(9)
Phase	Al_2O_3				Al_2O_3			
Atom	x	y	z	occ	x	y	z	occ
O1	0.25470	0.25470	0.25470	1	0.25470	0.25470	0.25470	1
Al1	1/2	1/2	1/2	1.156(7)	1/2	1/2	1/2	0.58
Al2	1/8	1/8	1/8	0.839(4)	1/8	1/8	1/8	0.84
Al3	0.02720	0.02720	0.02720	0.0133(13)	0.02720	0.02720	0.02720	0.17
Phase	$NiAl_2O_4$				$NiAl_2O_4$			
Atom	x	y	z	occ	x	y	z	occ
O	0.25490	0.25490	0.25490	1	0.25490	0.25490	0.25490	1
Al1	1/2	1/2	1/2	1	1/2	1/2	1/2	1
Al2	1/8	1/8	1/8	1	1/8	1/8	1/8	1
Ni1	1/2	1/2	1/2	1	1/2	1/2	1/2	1
Ni2	1/8	1/8	1/8	1	1/8	1/8	1/8	1

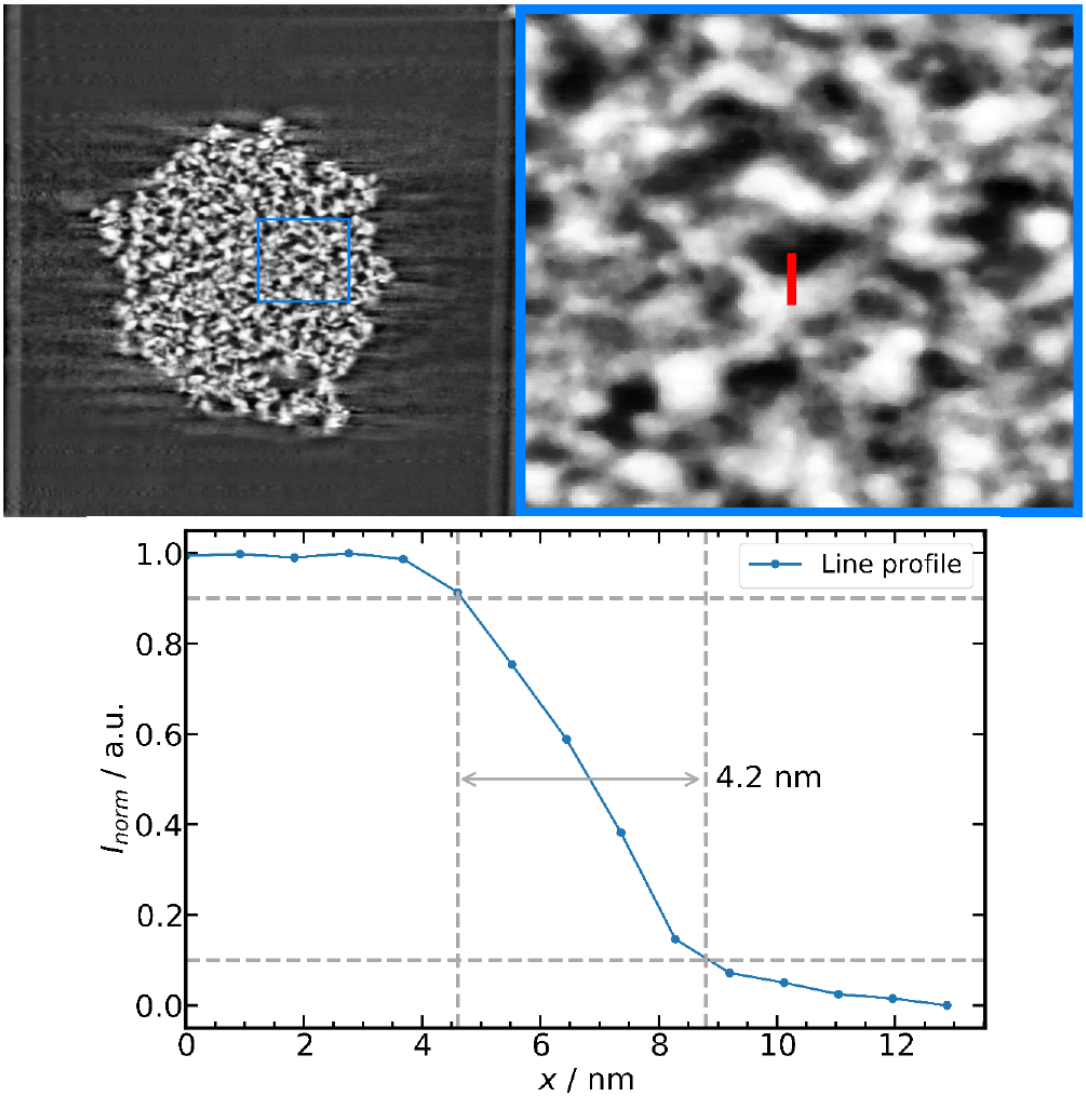


Figure 8.6: Selected slice of the SIRT reconstructed Ni/Al_2O_3-h-ET1. The blue box depicts the area shown zoomed for the line profile (red) analysis to estimate the resolution of the tomogram. The estimated resolution by the 10 %-90 % criteria for the selected line profile is 4.2 nm.[236] Available under the terms and conditions of the Creative Commons Attribution 4.0 license (CC BY 4.0, `https://creativecommons.org/licenses/by/4.0/`), Copyright ©2020.

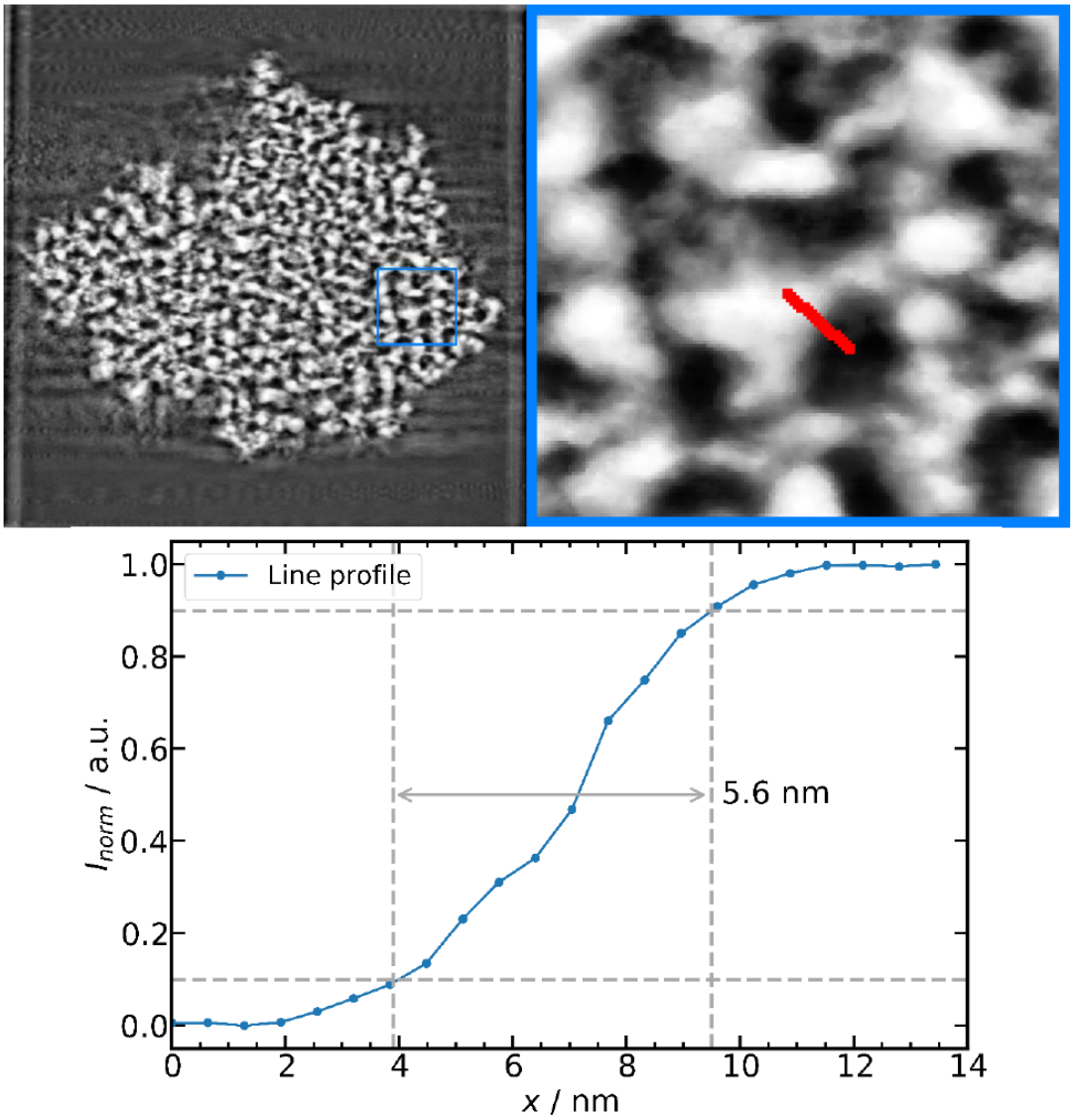


Figure 8.7: Selected slice of the SIRT reconstructed Ni/Al_2O_3-h-ET2. The blue box depicts the area shown zoomed for the line profile (red) analysis to estimate the resolution of the tomogram. The estimated resolution by the 10 %-90 % criteria for the selected line profile is 5.6 nm.[236] Available under the terms and conditions of the Creative Commons Attribution 4.0 license (CC BY 4.0, `https://creativecommons.org/licenses/by/4.0/`), Copyright ©2020.

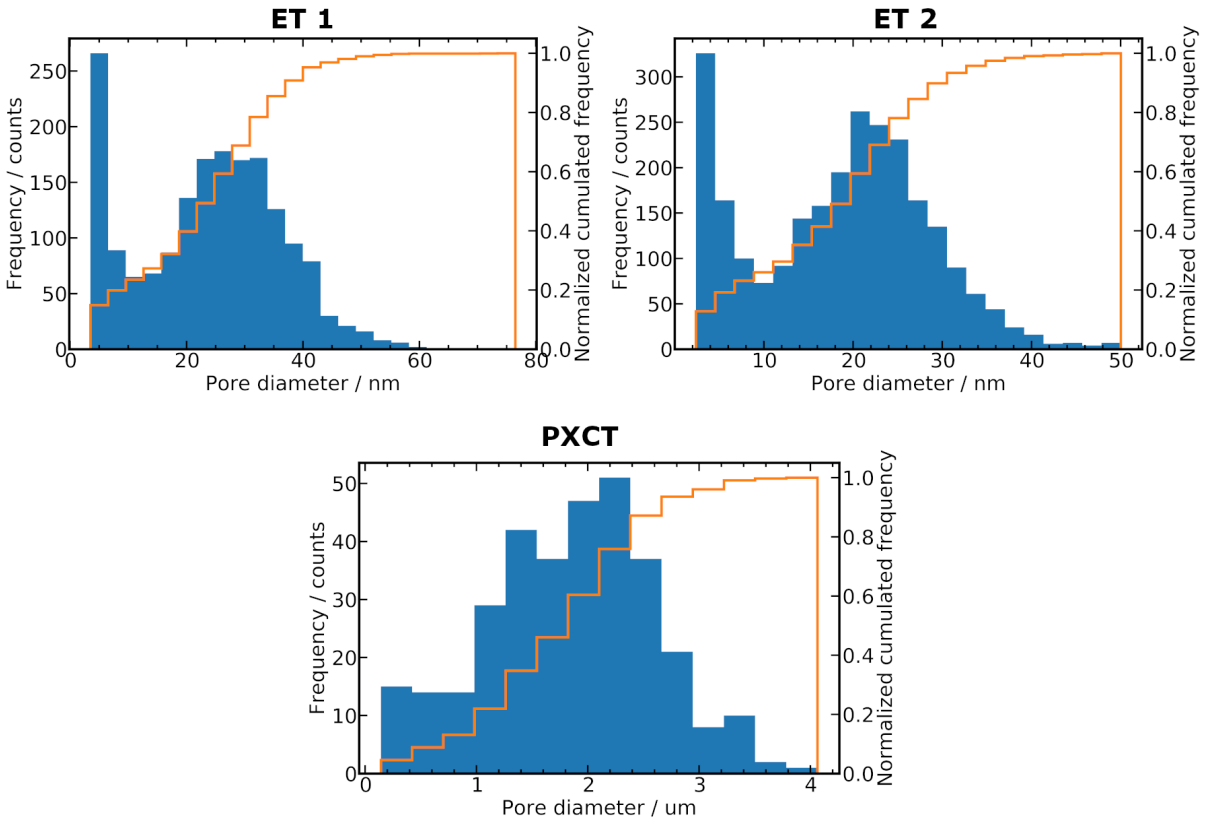


Figure 8.8: Frequency distribution of different pore diameters obtained from the label analysis of the separated pores from the ET and PXCT experiments of the Ni/Al_2O_3-h catalyst.[236] Available under the terms and conditions of the Creative Commons Attribution 4.0 license (CC BY 4.0, `https://creativecommons.org/licenses/by/4.0/`), Copyright ©2020.

8.4 Following the Porosity Evolution by X-ray Ptychography

Table 8.2: Results of the CHN-analyis of the dried gel samples and corresponding samples calcined in the laboratory.

Sample	weighed portion / mg	N / wt.%	C / wt.%	H / wt.%
Ni/Al_2O_3-dr	21.021	0.00	3.40	4.76
	22.077	0.00	3.44	4.73
	23.003	0.00	3.40	4.67
Ni/Al_2O_3-calc	11.660	0.00	0.17	0.56
	11.408	0.00	0.18	0.59
	10.800	0.00	0.20	0.57
Al_2O_3-dr	16.618	0.00	1.73	4.74
	16.832	0.00	1.73	4.82
	16.554	0.00	1.74	4.84
Al_2O_3-calc	23.195	0.00	0.07	0.56
	22.926	0.00	0.09	0.59
	22.369	0.00	0.09	0.57

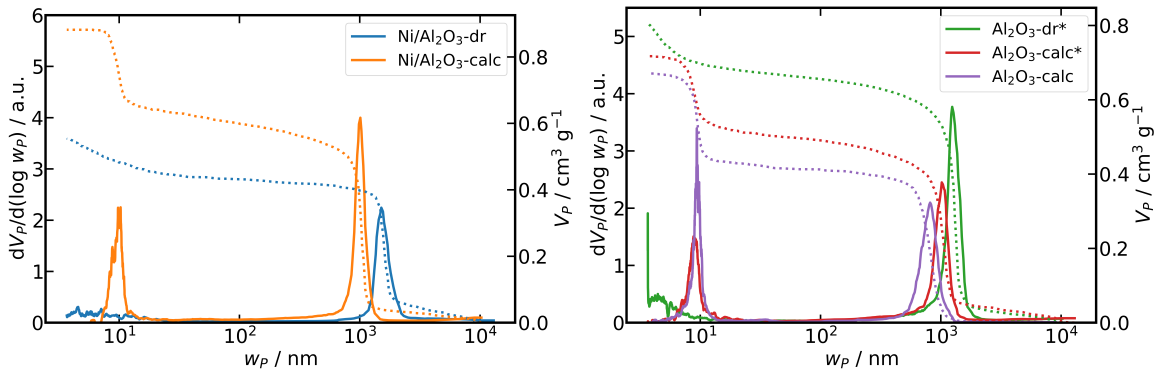


Figure 8.9: Hg porosimetry data for the Ni/Al_2O_3 (left) and Al_2O_3 (right) samples as dried gel and calcined. Al_2O_3-dr* and Al_2O_3-calc* are from a different sample batch than used for imaging studies.[237] Available under the terms and conditions of the Creative Commons Attribution 4.0 license (CC BY 4.0, `https://creativecommons.org/licenses/by/4.0/`), Copyright ©2022.

Table 8.3: Conventional pore characterization results.

	Ni/Al_2O_3		Al_2O_3			
	dried	calcined[a]	dried	calcined	dried⋆	calcined⋆
A_{BET} / $m^2\ g^{-1}$	5	99	128	91	-	-
V_{P,tot,N_2} / $cm^3\ g^{-1}$	0.02	0.31	0.22	0.24	-	-
w_{P,N_2} / nm	8.8	8.3	4.0	9.2	-	-
$V_{P,tot,Hg}$ / $cm^3\ g^{-1}$	0.56	0.88	-	0.67	0.80	0.71
$V_{P,m,Hg}$ / $cm^3\ g^{-1}$	0.12	0.26	-	0.26	0.13	0.21
$V_{P,M,Hg}$ / $cm^3\ g^{-1}$	0.44	0.62	-	0.41	0.67	0.50
$w_{P,m,Hg}$ / nm	n.a.[b]	10.3	-	9.4	3.7[c]	9.2
$w_{P,M,Hg}$ / µm	1.5	1.0	-	0.82	1.2	1.0
ρ_{skel} / $g\ cm^{-3}$	1.944	4.028	-	3.351	1.918	3.351
$\epsilon_{gen,tot}$ / %	52.1	78.0	-	55.0	60.5	70.4
$\epsilon_{gen,m}$ / %	11.2	23.0	-	26.8	9.8	20.8
$\epsilon_{gen,M}$ / %	40.9	55.0	-	42.3	50.7	49.6

[a] values of the calcined Ni/Al_2O_3 sample from ref.[236]
[b] not applicable
[c] pore width smaller than 3.7 nm not detectable
⋆ different sample batch than used for imaging studies

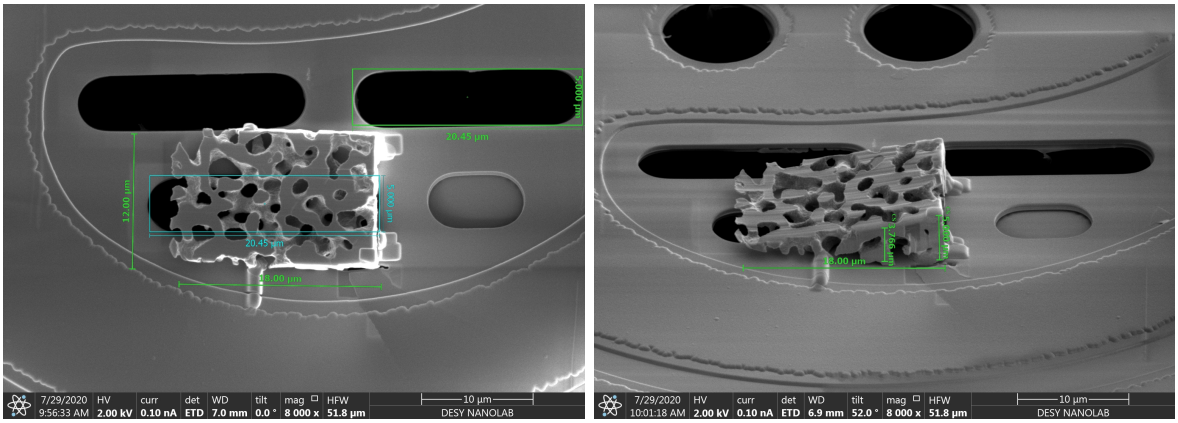


Figure 8.10: SEM images of the wedge-shaped samples used for the *in situ* X-ray ptychography (XRP) experiment. Normal view (left) and tilted view (right) of the FIB-prepared specimen that were prepared from the dried gel (Ni/Al_2O_3-dr) are shown to see all relevant dimensions.[237] Available under the terms and conditions of the Creative Commons Attribution 4.0 license (CC BY 4.0, `https://creativecommons.org/licenses/by/4.0/`), Copyright ©2022.

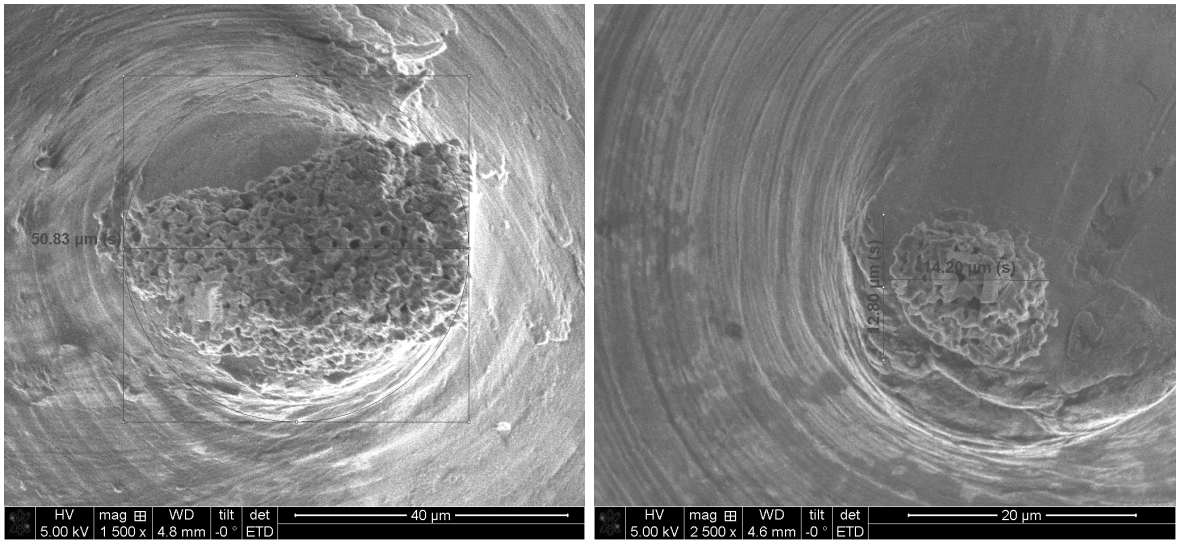


Figure 8.11: Top view SEM images of the dried gel samples mounted on the Cu-pins for PXCT experiments with the Cu-pins below the sample, left: [Ni/Al_2O_3-dr], right: [Al_2O_3-dr].[237] Available under the terms and conditions of the Creative Commons Attribution 4.0 license (CC BY 4.0, `https://creativecommons.org/licenses/by/4.0/`), Copyright ©2022.

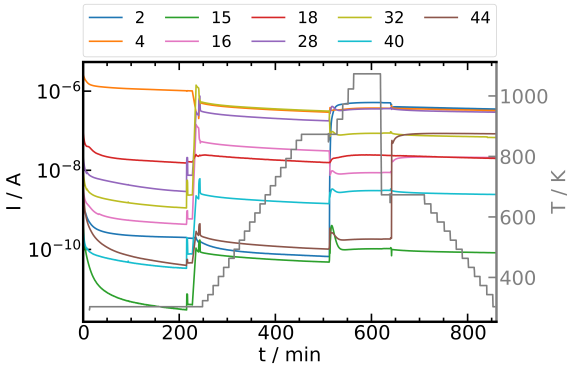


Figure 8.12: Mass spectrometry data as mass to charge ratio (m/z) constantly monitored during the *in situ* XRP experiments of the [Ni/Al_2O_3-dr] sample together with the MEMS-chip readout temperature.[237] Available under the terms and conditions of the Creative Commons Attribution 4.0 license (CC BY 4.0, `https://creativecommons.org/licenses/by/4.0/`), Copyright ©2022.

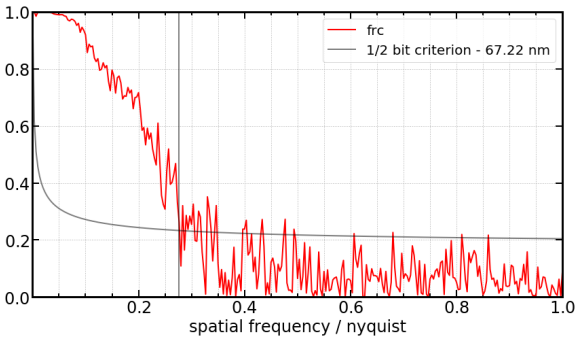


Figure 8.13: FRC analysis of the last two projections for the *in situ* XRP experiment of the Ni/Al_2O_3 sample. Reconstructed pixel size 18.6 nm, estimated 1/2 bit threshold resolution is 67.2 nm for a 600 x 600 pixel cropped area of the sample.[237] Available under the terms and conditions of the Creative Commons Attribution 4.0 license (CC BY 4.0, `https://creativecommons.org/licenses/by/4.0/`), Copyright ©2022.

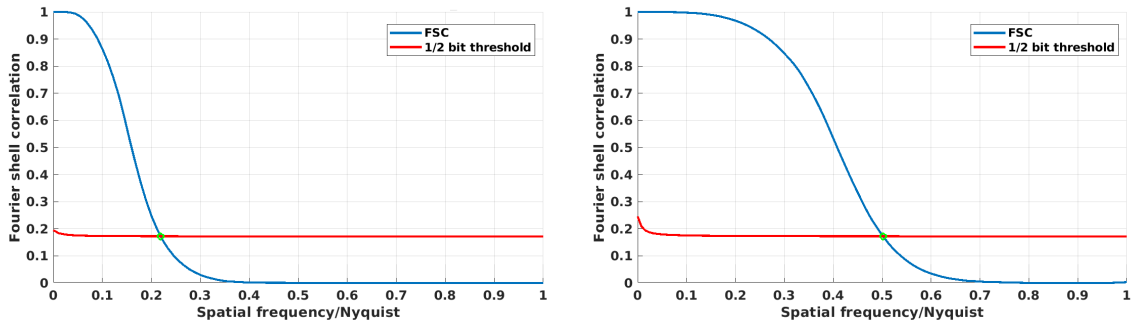


Figure 8.14: FSC analysis of the PXCT of the Ni/Al_2O_3 samples. Left: Ni/Al_2O_3-dr reconstructed voxel size 19.9 nm, estimated resolution 91.2 nm, right: Ni/Al_2O_3-calc reconstructed voxel size 27.9 nm, estimated resolution 55.6 nm.[237] Available under the terms and conditions of the Creative Commons Attribution 4.0 license (CC BY 4.0, `https://creativecommons.org/licenses/by/4.0/`), Copyright ©2022.

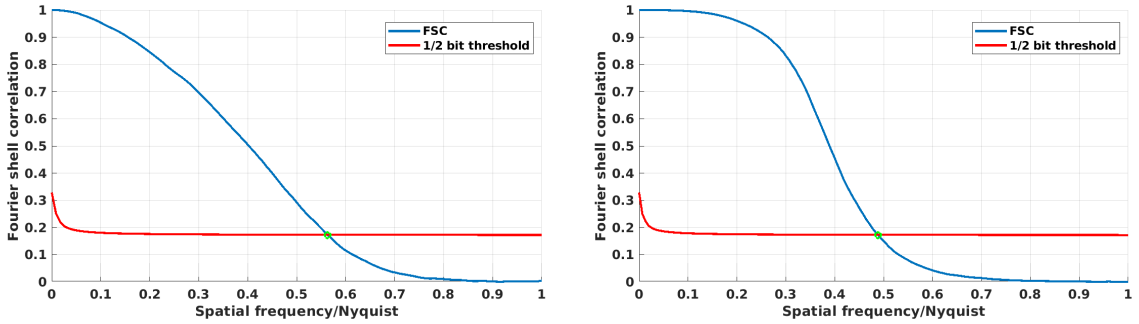


Figure 8.15: FSC analysis of the PXCT of the Al_2O_3 samples. Left: Al_2O_3-dr reconstructed voxel size 27.9 nm, estimated resolution 49.6 nm, right: Al_2O_3-calc reconstructed voxel size 19.9 nm, estimated resolution 40.9 nm.[237] Available under the terms and conditions of the Creative Commons Attribution 4.0 license (CC BY 4.0, `https://creativecommons.org/licenses/by/4.0/`), Copyright ©2022.

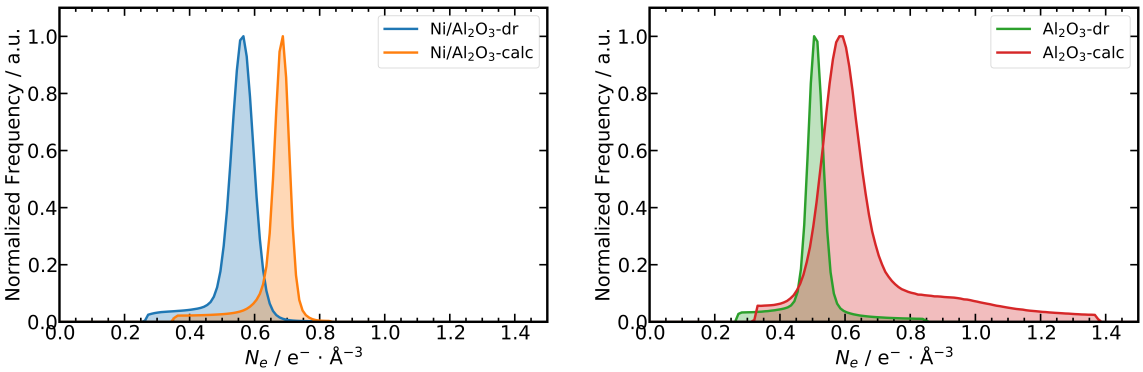


Figure 8.16: Electron density (N_e) distribution for the material label of the dried and calcined samples, left: Ni/Al_2O_3, right: Al_2O_3.[237] Available under the terms and conditions of the Creative Commons Attribution 4.0 license (CC BY 4.0, `https://creativecommons.org/licenses/by/4.0/`), Copyright ©2022.

Further information from the pore network model

"The pore network model obtained from the spatial graph analysis in Avizo provides further measures about the pore system that can be relevant in respect of mass transport properties. For an analysis of the location of nodes and pores (segments) within the particle, the center is defined as the gravity center of the whole *particle* label. With the coordinates of the gravity center we can calculate the distance to center (d_{center}) for each node and segment. As a segment connects two nodes, the coordinates of the segment is approximated as the middle point of the vector directly connecting the nodes. Average measures depending on d_{center} were computed for binned spherical shells of 200 nm and 100 nm thickness for Ni/Al_2O_3 and Al_2O_3, respectively. The average coordination number ($\overline{CN}$) of the nodes depending on d_{center} are shown in Figure 8.17.

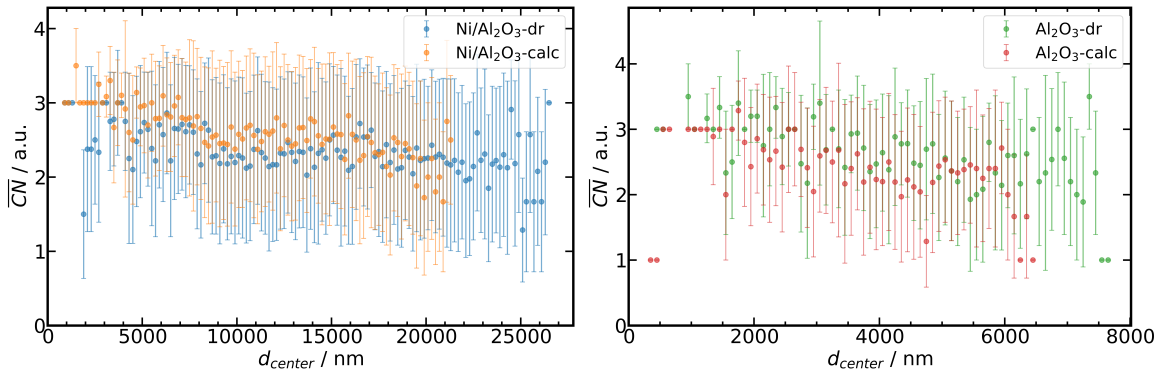


Figure 8.17: Average coordination number ($\overline{CN}$) of the nodes with standard deviation (σ) as errorbars depending on the distance to the particle center (d_{center}), left: Ni/Al_2O_3 (d_{center} binning 200 nm), right: Al_2O_3 (d_{center} binning 100 nm).[237] Available under the terms and conditions of the Creative Commons Attribution 4.0 license (CC BY 4.0, `https://creativecommons.org/licenses/by/4.0/`), Copyright ©2022.

Besides $\overline{CN}$, the average tortuosity ($\overline{\tau}$) of the segments was analyzed depending on d_{center} as shown in Figure 8.18. Additionally, the distribution of the tortuosity τ weighted by the volume of the respective segment is shown in Figure 8.19. It should be noted that the discussed τ represents single segments and not a whole path through the particle. Therefore we refer this τ as a microscopic tortuosity. However, with more detailed pore network analysis whole paths through the sample can be analyzed to retrieve a macroscopic tortuosity. For both systems Ni/Al_2O_3 and Al_2O_3 no significant differences of $\overline{CN}$ and $\overline{\tau}$ between the dried gel and calcined samples can be identified. Also the analysis of $\overline{CN}$ and $\overline{\tau}$ in respect to d_{center} shows no significant trends in regions that are statistically trustful. It should be noted that the for statistical analysis artefacts might arise very close to the particle center and particle surface. This can be clearly observed in Figure 8.17 for $\overline{CN}$ close to the center. These are mainly caused by undersampling, which can also be identified by missing error bars pointing out single values in the respective analyzed shell.

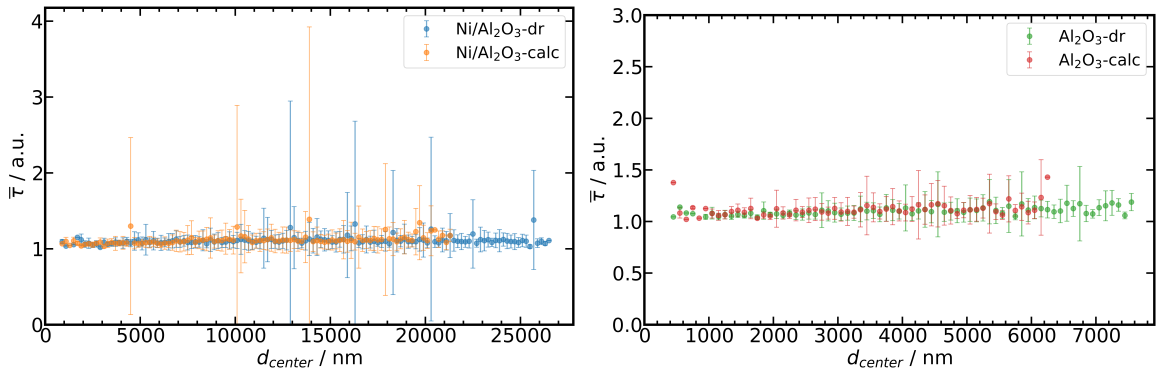


Figure 8.18: Average tortuosity ($\overline{\tau}$) of the segments with standard deviation (σ) as errorbars depending on the distance to the particle center (d_{center}), left: Ni/Al_2O_3 (d_{center} binning 200 nm), right: Al_2O_3 (d_{center} binning 100 nm).[237] Available under the terms and conditions of the Creative Commons Attribution 4.0 license (CC BY 4.0, `https://creativecommons.org/licenses/by/4.0/`), Copyright ©2022.

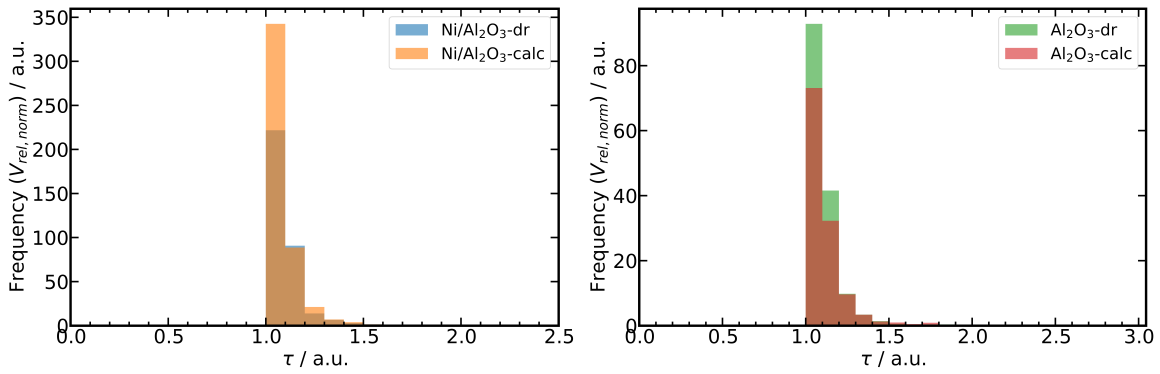


Figure 8.19: Segment tortuosity (τ) distribution weighted by the normalized segment volume ($V_{rel,norm}$), left: Ni/Al_2O_3, right: Al_2O_3.[237] Available under the terms and conditions of the Creative Commons Attribution 4.0 license (CC BY 4.0, `https://creativecommons.org/licenses/by/4.0/`), Copyright ©2022.

Additionally to the analysis of $\overline{CN}$ and $\overline{\tau}$, the distribution of r_{pore} was analyzed depending on d_{center}. A 2D histogram of the relative normalized volume ($V_{rel,norm}$) weighted r_{pore} distribution was computed. Furthermore, a kernel density estimate (KDE) was computed of the 2D histogram as implemented in the seaborn python library.[286] With the KDE a contour was calculated enclosing 75 % of the volume weighted pores. The 2D histograms together with the 75 % contours are shown in Figure 8.20,8.21 for Ni/Al_2O_3 andAl_2O_3, respectively.

To show the potential and amount of information available in PXCT studies of pore structures, we further performed a correlation analysis of the normalized pore volume ($V_{rel,norm}$), r_{pore}, d_{center} and τ. The results of the correlation analysis is shown in Figure 8.22, 8.23 for Ni/Al_2O_3 and Al_2O_3, respectively. The scatter plots of the correlation analysis contain 4D information (2 axes, scatter size and scatter color) and can be used to identify potential clusters with certain properties within the studied particles. Exemplary, for τ (scatter color) no obvious clusters can

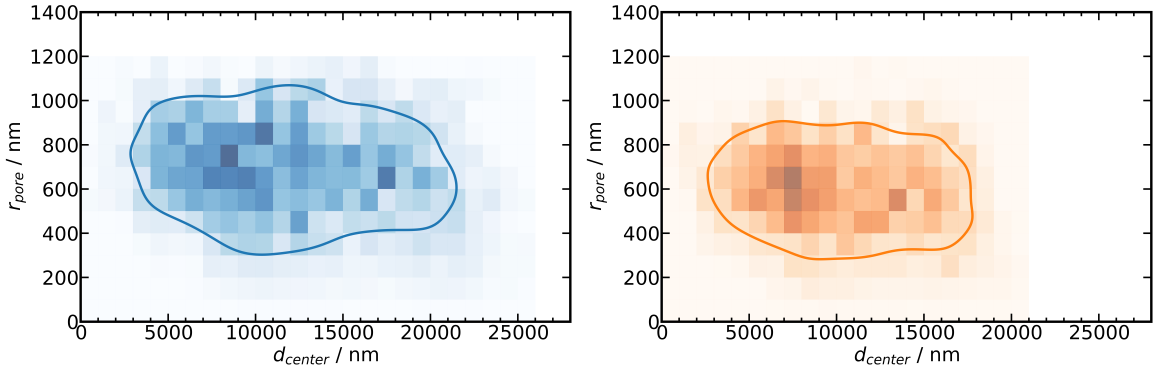


Figure 8.20: 2D histogram of the volume ($V_{rel,norm}$) weighted segment based pore radius r_{pore} distribution for binning of $r_{pore} = 100\,\text{nm}$ and $d_{center} = 1000\,\text{nm}$ together with the KDE based 75 % contour, left: Ni/Al_2O_3-dr, right: Ni/Al_2O_3-calc.[237] Available under the terms and conditions of the Creative Commons Attribution 4.0 license (CC BY 4.0, `https://creativecommons.org/licenses/by/4.0/`), Copyright ©2022.

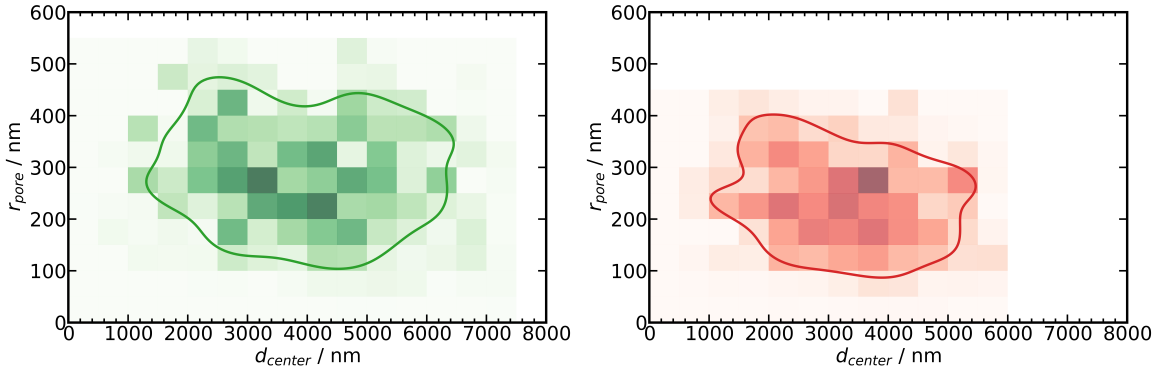


Figure 8.21: 2D histogram of the volume ($V_{rel,norm}$) weighted segment based pore radius r_{pore} distribution for binning of $r_{pore} = 50\,\text{nm}$ and $d_{center} = 500\,\text{nm}$ together with the KDE based 75 % contour, left: Al_2O_3-dr, right: Al_2O_3-calc.[237] Available under the terms and conditions of the Creative Commons Attribution 4.0 license (CC BY 4.0, `https://creativecommons.org/licenses/by/4.0/`), Copyright ©2022.

be observed, as already indicated by the analysis of $\overline{\tau}$ depending on d_{center} shown in Figure 8.18. The correlation analysis might unravel correlation, which might not be easily identified in common x-y data representation."[237]

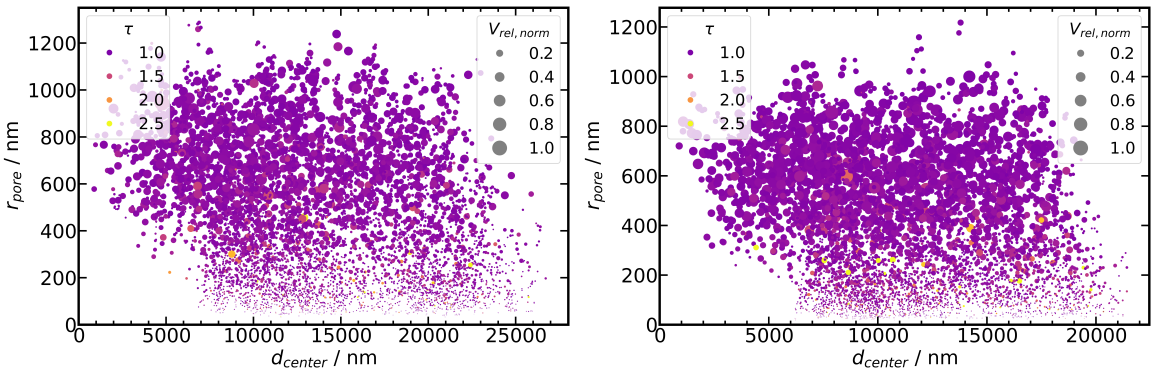


Figure 8.22: Scatter plot for correlation analysis of the segments radius (r_{pore}), distance to particle center (d_{center}) with the normalized segment volume ($V_{rel,norm}$, scatter size) and segment tortuosity (τ, scatter color), left: Ni/Al_2O_3-dr, right: Ni/Al_2O_3-calc.[237] Available under the terms and conditions of the Creative Commons Attribution 4.0 license (CC BY 4.0, `https://creativecommons.org/licenses/by/4.0/`), Copyright ©2022.

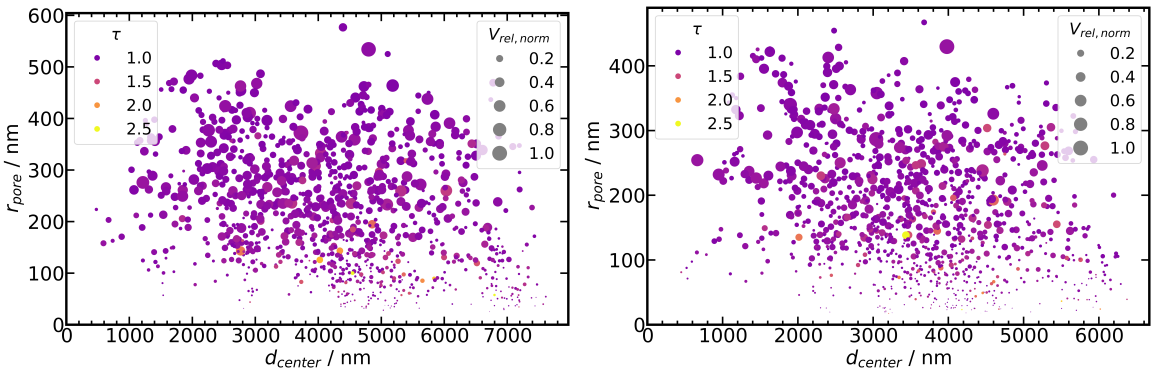


Figure 8.23: Scatter plot for correlation analysis of the segments radius (r_{pore}), distance to particle center (d_{center}) with the normalized segment volume ($V_{rel,norm}$, scatter size) and segment tortuosity (τ, scatter color), left: Al_2O_3-dr, right: Al_2O_3-calc.[237] Available under the terms and conditions of the Creative Commons Attribution 4.0 license (CC BY 4.0, `https://creativecommons.org/licenses/by/4.0/`), Copyright ©2022.

Table 8.4: Summarized results of the analysis of the electron density (N_e) distribution of the *material* label of the dried and calcined samples of Ni/Al_2O_3 and Al_2O_3 as well as SPP2080-IMRC-0min. Material label porosity (ϵ_{mat}); mass factor (f_{mass}) and theoretical mass density (ρ_{theo}) used to calculate ϵ_{mat}; mesoporosity (ϵ_m) calculated from ϵ_{mat}, macroporosity (ϵ_M) from image analysis and total porosity (ϵ_{tot}) obtained from image and N_e analysis.

	Ni/Al_2O_3		Al_2O_3		SPP2080-IMRC
	-dr	-calc	-dr	-calc	-0min
mode N_e / e^- $Å^{-3}$	0.561	0..683	0.511	0.591	0.602
ϵ_{mat} / %	52.5	42.2	52.7	45.3	42.6
f_{mass} / 10^{23} g	3.407	3.407	3.386	3.386	3.392
ρ_{theo} / g cm^{-3}	4.028	4.028	3.66	3.66	3.557
ϵ_m / %	29.4	23.4	34.3	30.1	29.6
ϵ_M / %	43.9	44.5	34.9	33.6	30.5
ϵ_{tot} / %	73.3	67.9	69.2	63.7	60.1

8.5 Resolving Structural Changes During Calcination by X-ray Total Scattering

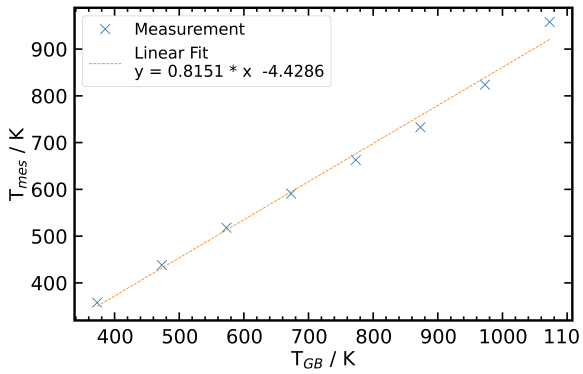


Figure 8.24: Temperature calibration of the hot-air blower used for *in situ* PXRD and PDF experiments.

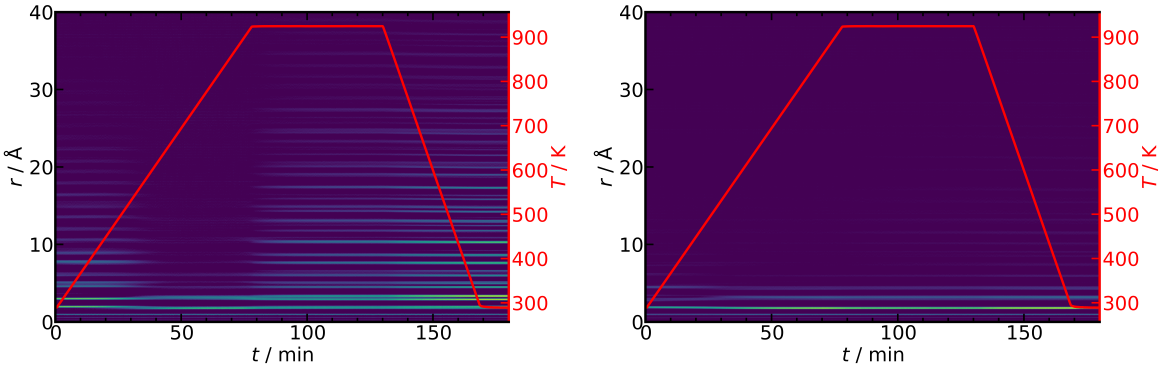


Figure 8.25: 2D maps of the *in situ* PDF acquired during calcination of the dried gels Ni/Al_2O_3-dr (left) and Al_2O_3-dr (right). Total gas flow of 10 mL 10 %O_2/He.

Table 8.5: Rietveld and PDF refinement results for the initial dried gels Ni/Al_2O_3-dr and Al_2O_3-dr during *in situ* calcination (scan number 1). B_{iso} for Rietveld refinements were fixed and did not allowed to be stable refined.

	Ni/Al_2O_3-dr		Al_2O_3-dr	
	PXRD	PDF	PXRD	PDF
phase		$\gamma-AlO(OH)$		
space group		*Amam* (63)		
R_{wp} / %	4.56	n.a.*	2.85	n.a.*
R_w / %	n.a.*	0.59	n.a.*	0.61
GOF / %	0.95	n.a.*	0.72	n.a.*
L_{vol} / nm	2.15(4)	n.a.$^\circ$	1.090(19)	n.a.*
p_{size} / nm	n.a.*	2.46(5)	n.a.*	0.93(2)
a / Å	4.263(7)	4.384(5)	3.969(17)	4.041(8)
b / Å	12.50(3)	12.733(13)	11.50(7)	11.75(4)
c / Å	2.846(5)	2.934(3)	2.844(12)	2.853(6)
$B_{iso}(Al)$ / Å^2	0.3	0.68(7)	0.3	-0.42(15)
$B_{iso}(O)$ / Å^2	0.5	2.44(12)	0.5	2.28(14)

* not applicable

Table 8.6: Rietveld and PDF refinement results for the *in situ* calcined Ni/Al_2O_3-calc and Al_2O_3-calc samples (scan number 1050). B_{iso} for Rietveld refinements were fixed and did not allowed to be stable refined. For Al_2O_3-calc no crystal structure parameters had to be fixed for stable reconstruction.

	Ni/Al_2O_3-calc		Al_2O_3-calc	
	PXRD	PDF	PXRD	PDF
phase		$\gamma-Al_2O_3$		
space group		$Fd\bar{3}m$ (227)		
R_{wp} / %	5.00	n.a.*	5.82	n.a.*
R_w / %	n.a.*	0.41	n.a.*	0.58
GOF / %	1.08	n.a.*	1.33	n.a.*
L_{vol} / nm	6.0(6)	n.a.*	0.632(15)	n.a.*
p_{size} / nm	n.a.*	4.32(1)	n.a.*	1.14(3)
a / Å	7.941(10)	8.0289(8)	7.8636201	7.642(5)
$B_{iso}(Al)$ / Å^2	0.3	0.255(10)	0.3	1.10(7)
$B_{iso}(O)$ / Å^2	4.0(6)	1.76(4)	0.5	7.4(3)
occ_{Al1}	0.63(2)	0.8633	0.8698	0.8633
occ_{Al2}	0.60(3)	0.8160	0.668	0.8160
occ_{Al3}	0.066(7)	0.0280	0.201	0.0280
occ_{Al4}	0.045(3)	0.0190	0.05938	0.0190
occ_{O1}	1	1	1	1

* not applicable

Table 8.7: Rietveld and PDF refinement results for the *ex situ* laboratory calcined samples Ni/Al_2O_3-h and Al_2O_3-h. B_{iso} for Rietveld refinements were fixed and did not allowed to be stable refined.

	Ni/Al_2O_3-h		Al_2O_3-h	
	PXRD	PDF	PXRD	PDF
phase		$\gamma-Al_2O_3$		
space group		$Fd\bar{3}m$ (227)		
R_{wp} / %	3.00	n.a.*	6.20	n.a.*
R_w / %	n.a.*	0.36	n.a.$^\circ$	0.41
GOF / %	2.92	n.a.*	7.04	n.a.*
L_{vol} / nm	5.21(4)	n.a.*	2.96(6)	n.a.*
p_{size} / nm	n.a.*	7.9(2)	n.a.*	4.32(8)
a / Å	8.0046(17)	8.0091(4)	7.863(12)	7.9003(10)
$B_{iso}(Al)$ / Å^2	0.3	0.166(5)	0.3	0.529(18)
$B_{iso}(O)$ / Å^2	0.92(8)	1.69(3)	1.2(3)	1.82(4)
occ_{Al1}	0.937(14)	0.8633	0.87(4)	0.8633
occ_{Al2}	1.22(2)	0.8160	0.66(4)	0.8160
occ_{Al3}	0.040(7)	0.0280	0.200(16)	0.0280
occ_{Al4}	0.0248(18)	0.0190	0.059(6)	0.0190
occ_{O1}	1	1	1	1

* not applicable

8.6 Coke Localization Unraveled by X-ray Ptychography

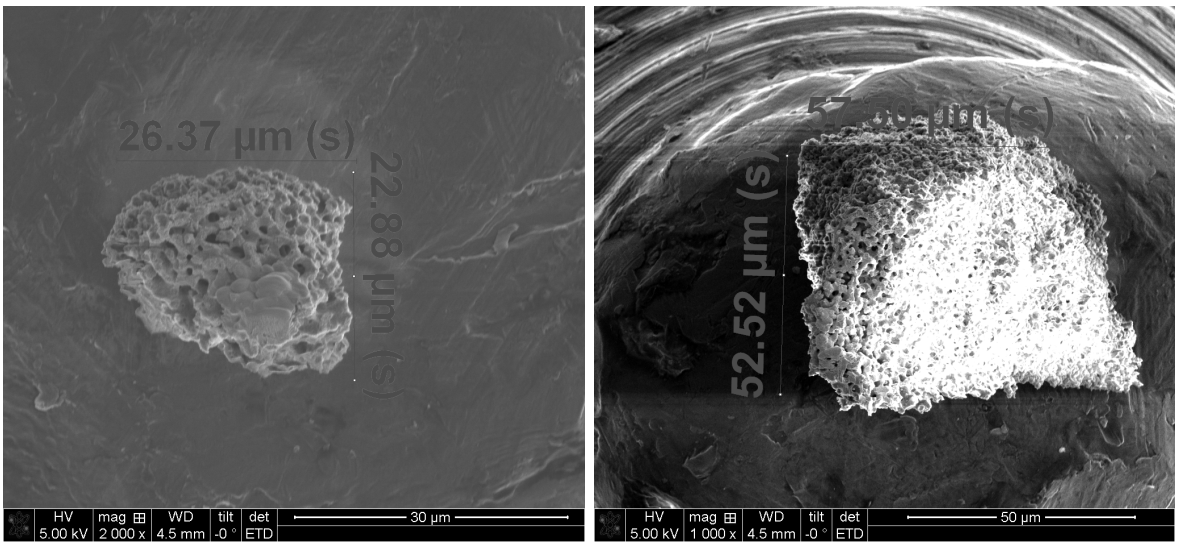


Figure 8.26: Sample Ni/Al_2O_3-h activated (left)[236] coked (right)[239]. Available under the terms and conditions of the Creative Commons Attribution 4.0 license (CC BY 4.0, `https://creativecommons.org/licenses/by/4.0/`), Copyright ©2021.

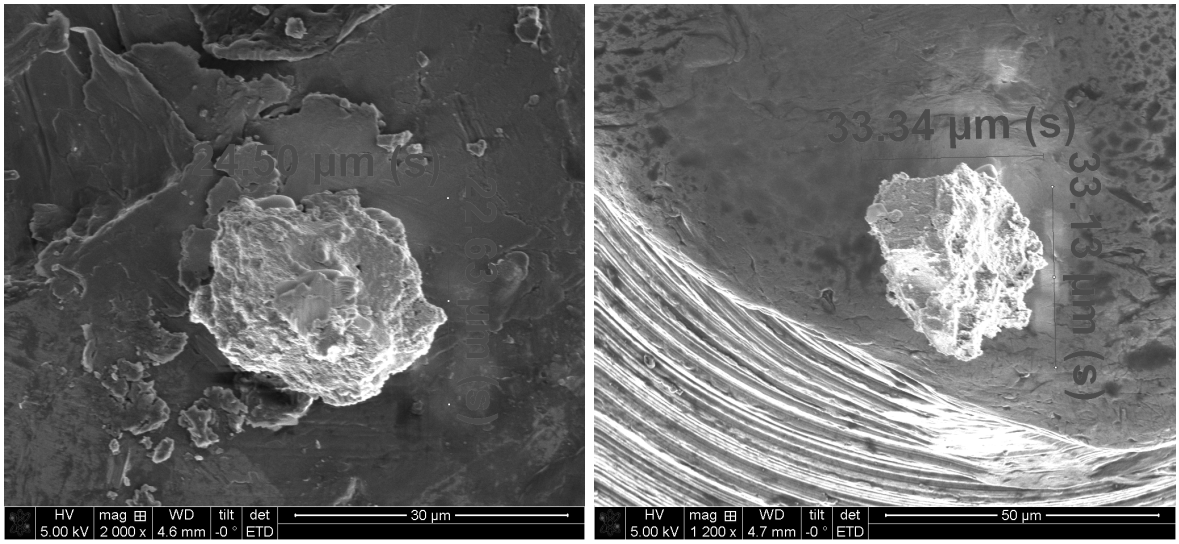


Figure 8.27: Sample Ni/Al_2O_3-m activated (left) coked (right).[239] Available under the terms and conditions of the Creative Commons Attribution 4.0 license (CC BY 4.0, `https://creativecommons.org/licenses/by/4.0/`), Copyright ©2021.

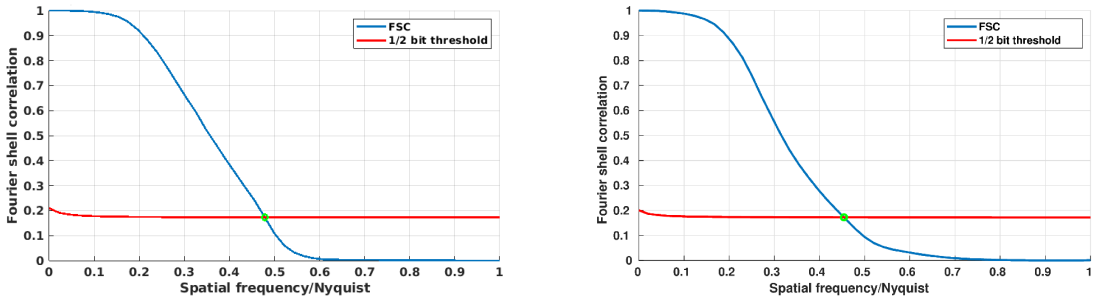


Figure 8.28: FSC analysis of the $NiAl_2O_3$-ha (left) and $NiAl_2O_3$-hc (right), the reconstructed pixel sizes are 37.5 nm and the resolutions from the FSC are 78 nm and 83 nm, respectively.[239] Available under the terms and conditions of the Creative Commons Attribution 4.0 license (CC BY 4.0, `https://creativecommons.org/licenses/by/4.0/`), Copyright ©2021.

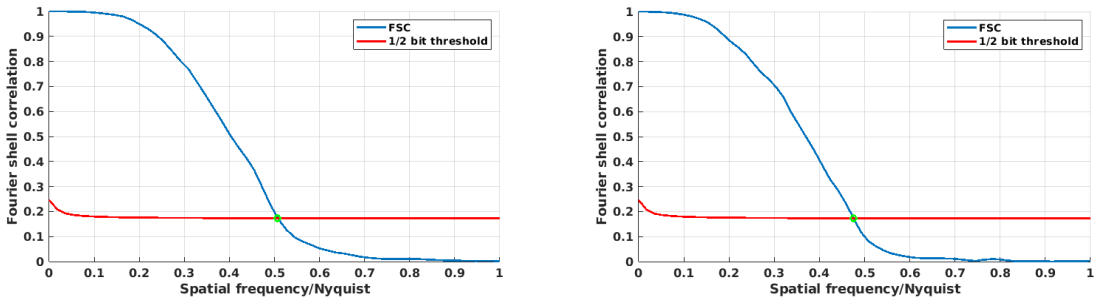


Figure 8.29: FSC analysis of the $NiAl_2O_3$-ma (left) and $NiAl_2O_3$-mc (right), the reconstructed pixel sizes are 37.5 nm and the resolutions from the FSC are 74 nm and 79 nm, respectively.[239] Available under the terms and conditions of the Creative Commons Attribution 4.0 license (CC BY 4.0, `https://creativecommons.org/licenses/by/4.0/`), Copyright ©2021.

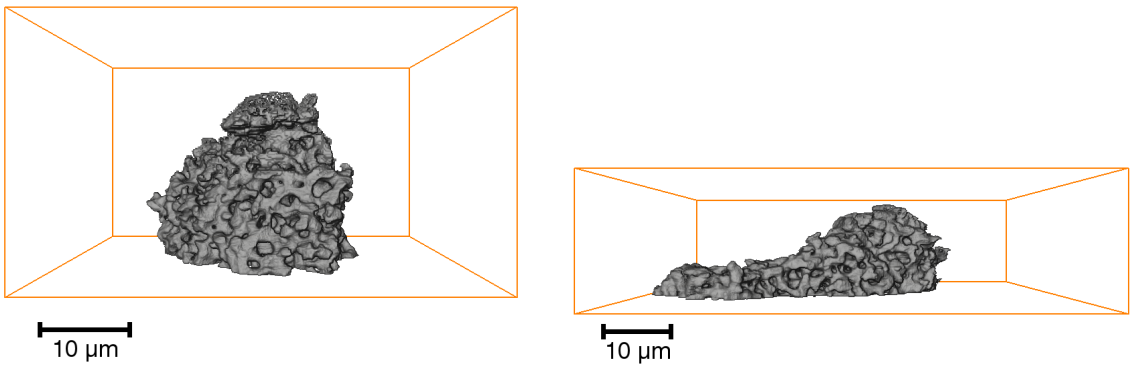


Figure 8.30: Segmented catalyst body label for $NiAl_2O_3$-ha (left) and $NiAl_2O_3$-hc (right).[239] Available under the terms and conditions of the Creative Commons Attribution 4.0 license (CC BY 4.0, `https://creativecommons.org/licenses/by/4.0/`), Copyright ©2021.

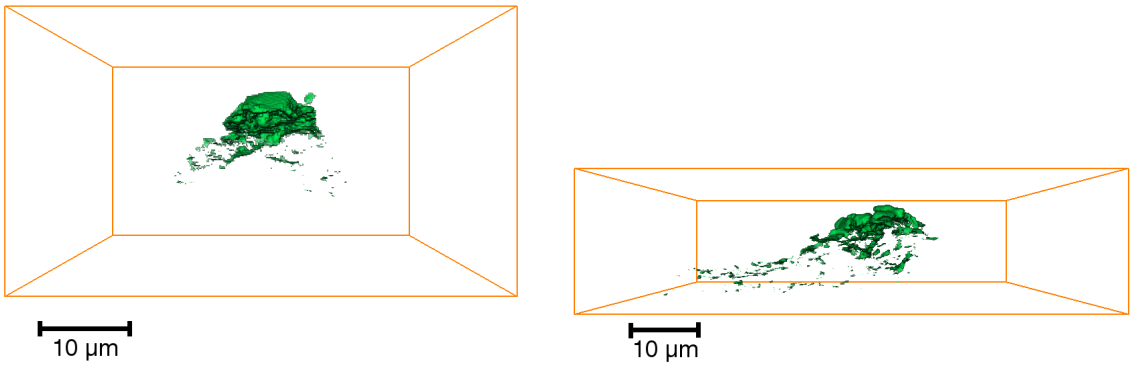


Figure 8.31: Segmented Pt contamination from FIB sample preparation for $NiAl_2O_3$-ha (left) and $NiAl_2O_3$-hc (right).[239] Available under the terms and conditions of the Creative Commons Attribution 4.0 license (CC BY 4.0, `https://creativecommons.org/licenses/by/4.0/`), Copyright ©2021.

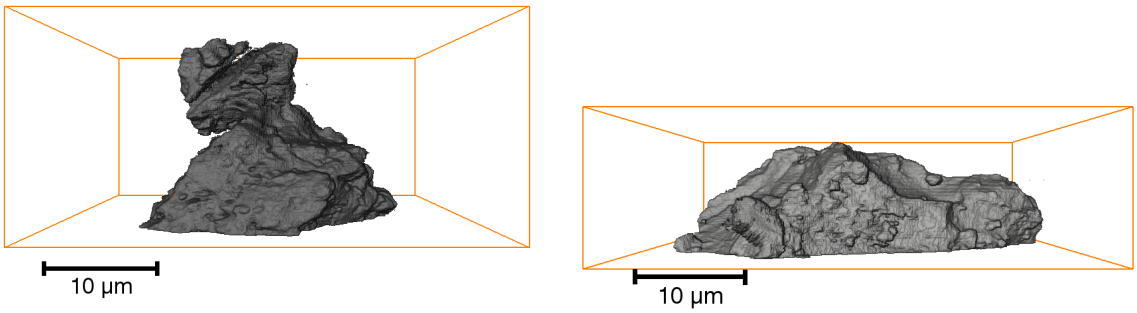


Figure 8.32: Segmented catalyst body label for $NiAl_2O_3$-ma (left) and $NiAl_2O_3$-mc (right).[239] Available under the terms and conditions of the Creative Commons Attribution 4.0 license (CC BY 4.0, `https://creativecommons.org/licenses/by/4.0/`), Copyright ©2021.

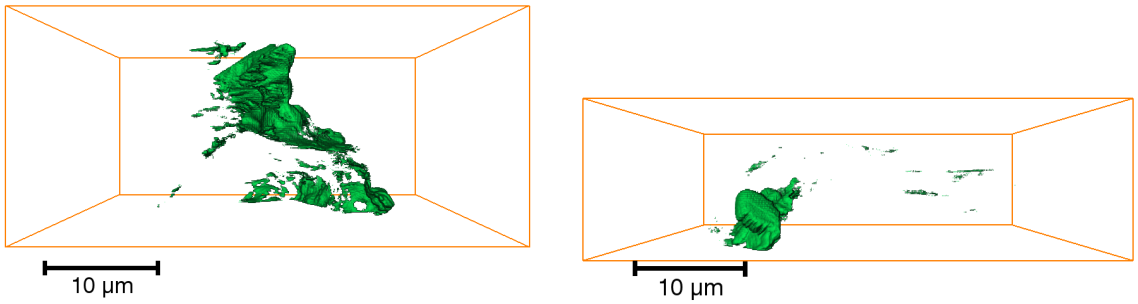


Figure 8.33: Segmented Pt contamination from FIB sample preparation for $NiAl_2O_3$-ma (left) and $NiAl_2O_3$-mc (right).[239] Available under the terms and conditions of the Creative Commons Attribution 4.0 license (CC BY 4.0, `https://creativecommons.org/licenses/by/4.0/`), Copyright ©2021.

Table 8.8: N_e offset values obtained from air in close proximity to the sample and the segmentation threshold to obtain the coked and activated catalyst body labels. Difference values for the slice dependent analysis of the mean N_e of the catalyst body label of the activated and coked samples.

	Ni/Al_2O_3-m		Ni/Al_2O_3-h	
	activated (ma)	coked (mc)	activated (ha)	coked (hc)
N_e offset / $e^- Å^{-3}$	+0.05	+0.075	+0.05	+0.055
N_e threshold segmentation / $e^- Å^{-3}$	-	0.425	-	0.525
Difference N_e(coked) − N_e(activated)				
Mean difference / $e^- Å^{-3}$		0.075		0.021
Max. difference / $e^- Å^{-3}$		0.101		0.038
Min. difference / $e^- Å^{-3}$		0.036		0.001

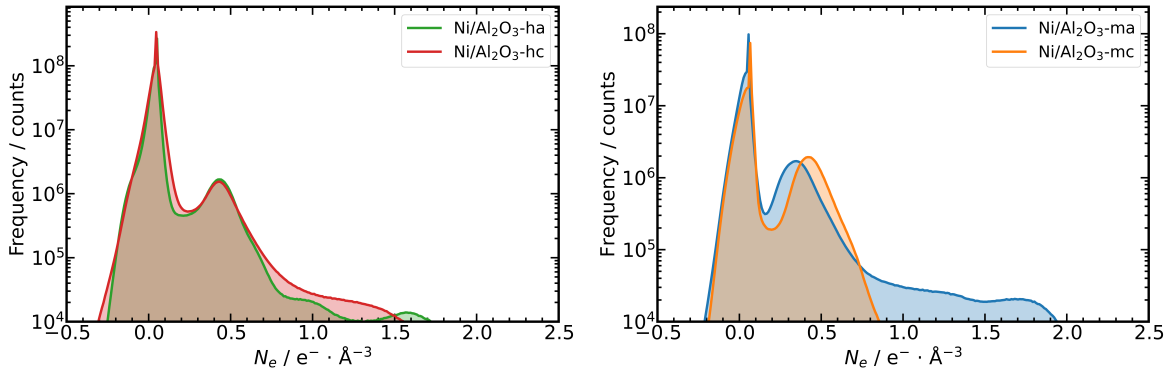


Figure 8.34: Total electron density distribution for the PXCT of samples for $NiAl_2O_3$-h (left) and $NiAl_2O_3$-m (right).[239] Available under the terms and conditions of the Creative Commons Attribution 4.0 license (CC BY 4.0, `https://creativecommons.org/licenses/by/4.0/`), Copyright ©2021.

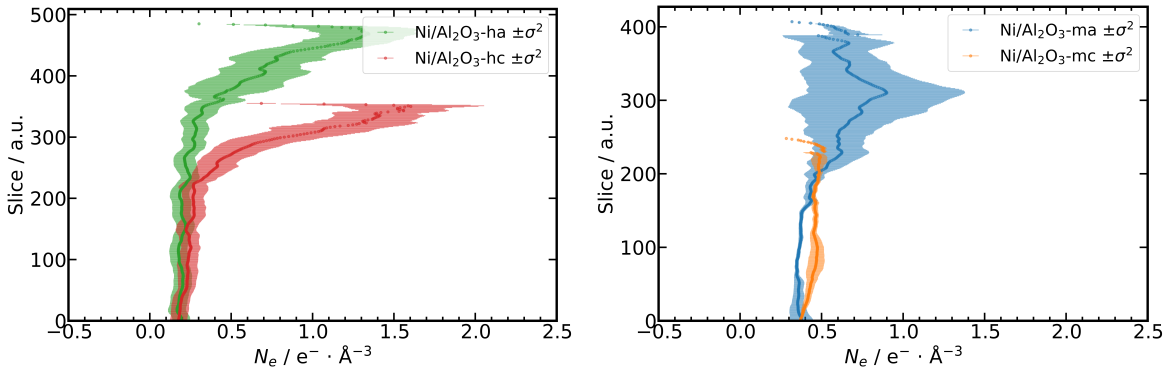


Figure 8.35: Mean electron density with the variance σ^2 for single slices of the masked particle volume of the PXCT of samples $NiAl_2O_3$-h (left) and $NiAl_2O_3$-m (right).[239] Available under the terms and conditions of the Creative Commons Attribution 4.0 license (CC BY 4.0, `https://creativecommons.org/licenses/by/4.0/`), Copyright ©2021.

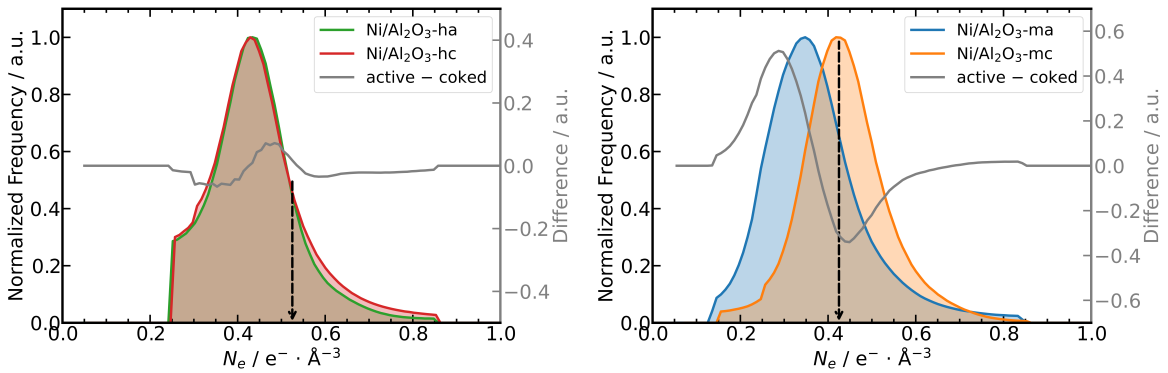


Figure 8.36: Normalized electron density distribution of the masked catalyst body label volume of the PXCT of samples $NiAl_2O_3$-h (left) and $NiAl_2O_3$-m (right) together with the difference curve. The arrow indicates the intersection used as threshold for segmentation.[239] Available under the terms and conditions of the Creative Commons Attribution 4.0 license (CC BY 4.0, `https://creativecommons.org/licenses/by/4.0/`), Copyright ©2021.

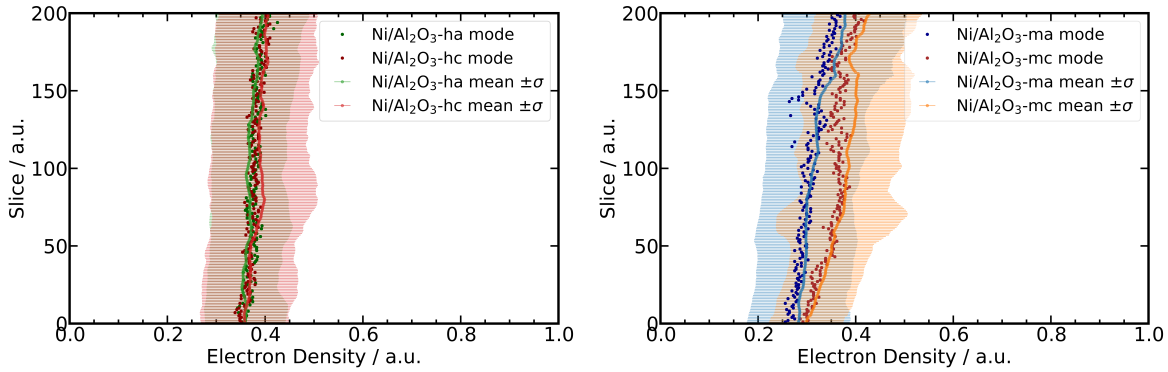


Figure 8.37: Comparison of the mean electron density with the standard deviation σ and mode of the electron density for single slices of the masked catalyst body label of the PXCT of samples $NiAl_2O_3$-h (left) and $NiAl_2O_3$-m (right).[239] Available under the terms and conditions of the Creative Commons Attribution 4.0 license (CC BY 4.0, `https://creativecommons.org/licenses/by/4.0/`), Copyright ©2021.

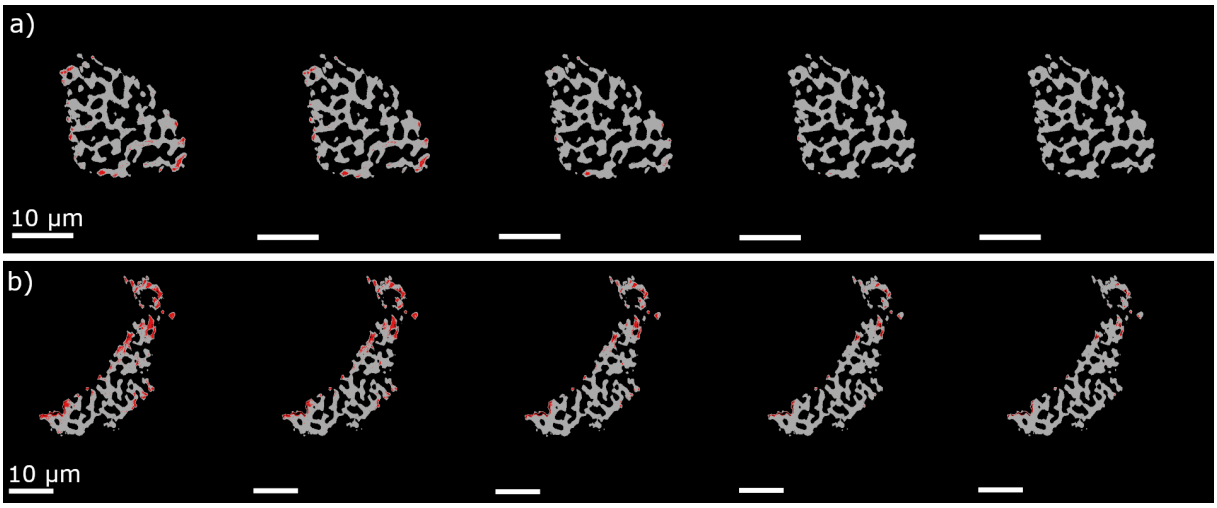


Figure 8.38: Propagation of the N_e threshold used for binary segmentation into activated (gray) and coked (red) catalyst body labels for (a) $NiAl_2O_3$-ha and (b) $NiAl_2O_3$-hc. N_e thresholds from left to right: 0.525, 0.555, 0.605, 0.655, 0.705 e^- $Å^{-3}$. Scale bar 10 µm.[239] Available under the terms and conditions of the Creative Commons Attribution 4.0 license (CC BY 4.0, `https://creativecommons.org/licenses/by/4.0/`), Copyright ©2021.

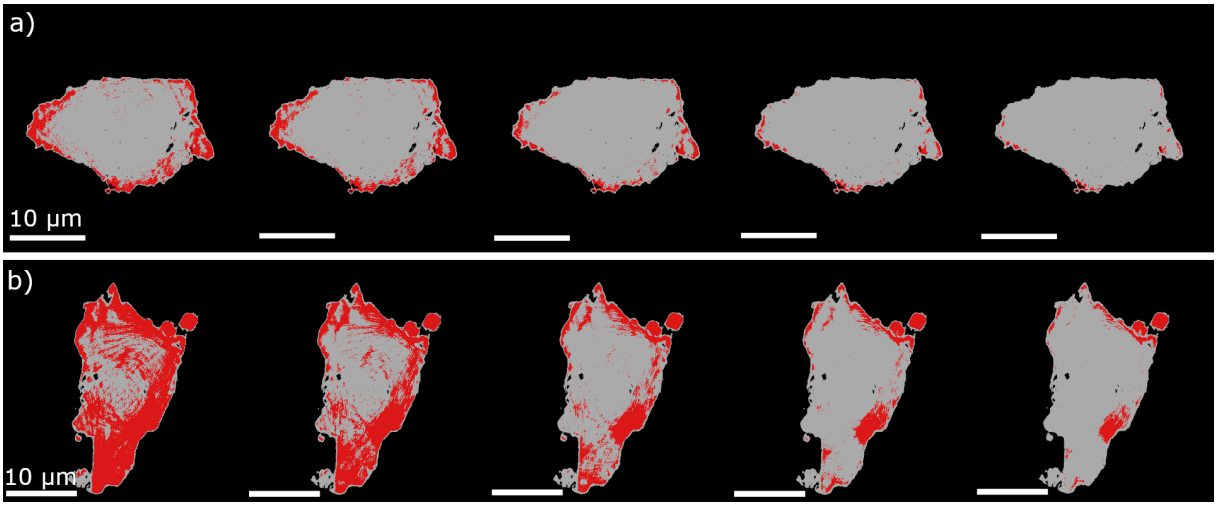


Figure 8.39: Propagation of the N_e threshold used for binary segmentation into activated (gray) and coked (red) catalyst body labels for (a) $NiAl_2O_3$-ma and (b) $NiAl_2O_3$-mc. N_e thresholds from left to right: 0.425, 0.475, 0.525, 0.575, 0.625 e^- $Å^{-3}$. Scale bar 10 µm.[239] Available under the terms and conditions of the Creative Commons Attribution 4.0 license (CC BY 4.0, `https://creativecommons.org/licenses/by/4.0/`), Copyright ©2021.

8.7 Deconvolution of Thermal Deactivation Phenomena by X-ray Diffraction

Table 8.9: Summary of the laboratory characterization results for the different ZrO_2 supports of the study before Ni deposition, with Z25 as supplied.

supports	A_{BET} / $m^2\,g^{-1}$	V_p / $cm^3\,g^{-1}$	$L_{vol}(ZrO_2)$ / nm
Z25	100	0.24	9.5
Z350	93	0.23	9.5
Z500	51	0.19	13
Z650	26	0.043	23
Z800	13	0.021	41
Z1000	5	0.009	116

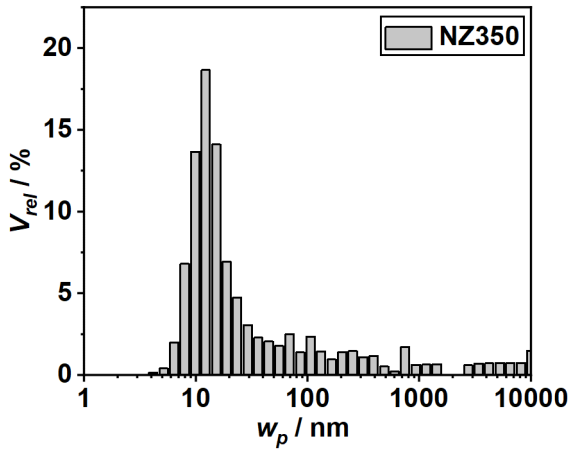


Figure 8.40: Pore width distribution w_P obtained by MIP for NZ350 catalyst.[240] Available under the terms and conditions of the Creative Commons Attribution 3.0 license (CC BY 3.0, `https://creativecommons.org/licenses/by/3.0/`), Copyright ©2022.

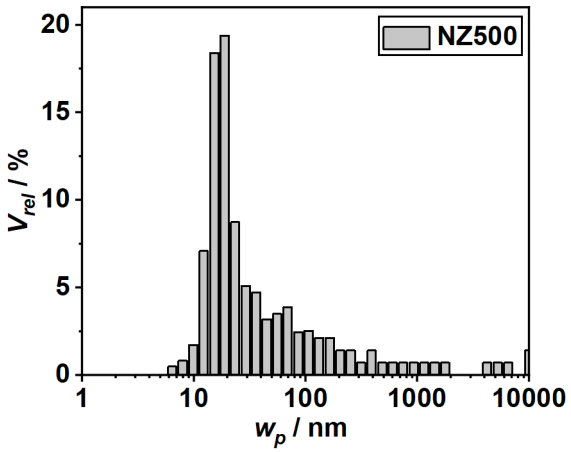


Figure 8.41: Pore width distribution w_P obtained by MIP for NZ500 catalyst.[240] Available under the terms and conditions of the Creative Commons Attribution 3.0 license (CC BY 3.0, `https://creativecommons.org/licenses/by/3.0/`), Copyright ©2022.

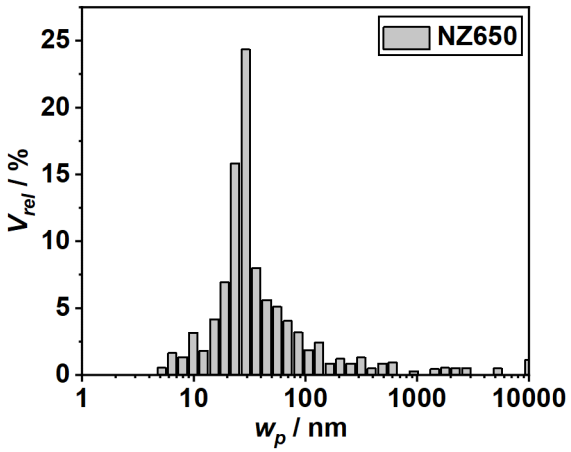


Figure 8.42: Pore width distribution w_P obtained by MIP for NZ650 catalyst.[240] Available under the terms and conditions of the Creative Commons Attribution 3.0 license (CC BY 3.0, `https://creativecommons.org/licenses/by/3.0/`), Copyright ©2022.

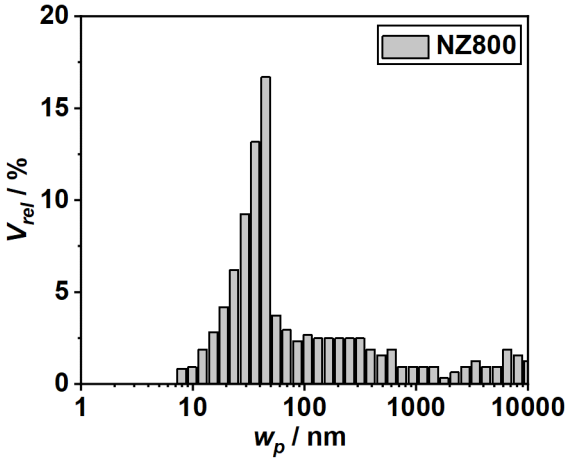


Figure 8.43: Pore width distribution w_P obtained by MIP for NZ800 catalyst.[240] Available under the terms and conditions of the Creative Commons Attribution 3.0 license (CC BY 3.0, `https://creativecommons.org/licenses/by/3.0/`), Copyright ©2022.

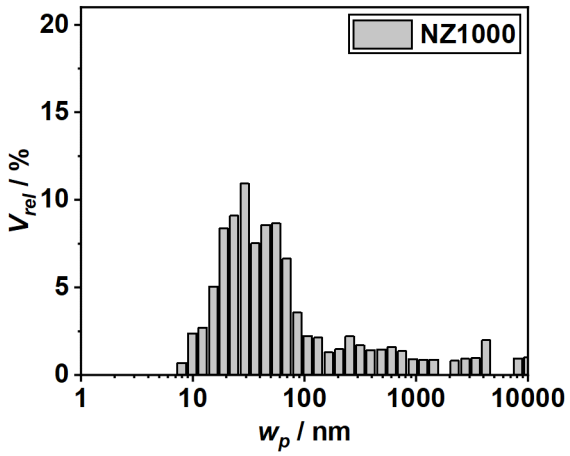


Figure 8.44: Pore width distribution w_P obtained by MIP for NZ1000 catalyst.[240] Available under the terms and conditions of the Creative Commons Attribution 3.0 license (CC BY 3.0, `https://creativecommons.org/licenses/by/3.0/`), Copyright ©2022.

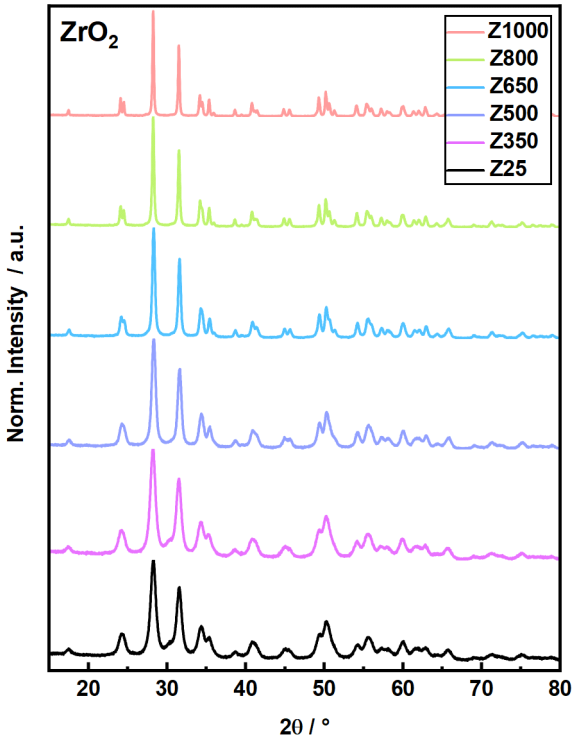


Figure 8.45: XRD patterns of the pure ZrO_2 support prior calcination (Z25) and calcined at temperatures between 523 K and 1273 K (Z350-Z1000). All samples show mainly the presence of m-ZrO_2, while Z25 and Z350 show small contributions of t-ZrO_2 as shown in Figure 8.46 and Table 8.10.[240] Available under the terms and conditions of the Creative Commons Attribution 3.0 license (CC BY 3.0, `https://creativecommons.org/licenses/by/3.0/`), Copyright ©2022.

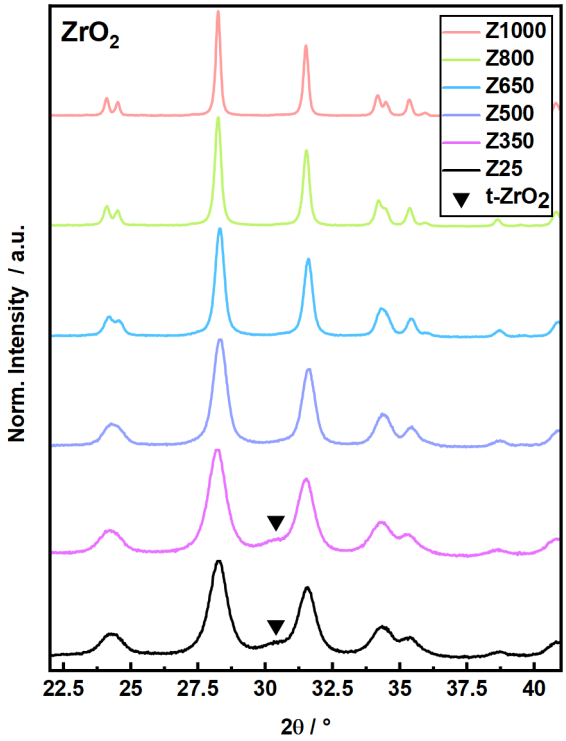


Figure 8.46: Zoomed XRD patterns of Figure 8.45 for the pure ZrO_2 support prior caclination (Z25) and calcined at temperatures between 523 K and 1273 K (Z350-Z1000). The features marked with black triangle can be assigned to t-ZrO_2.[240] Available under the terms and conditions of the Creative Commons Attribution 3.0 license (CC BY 3.0, `https://creativecommons.org/licenses/by/3.0/`), Copyright ©2022.

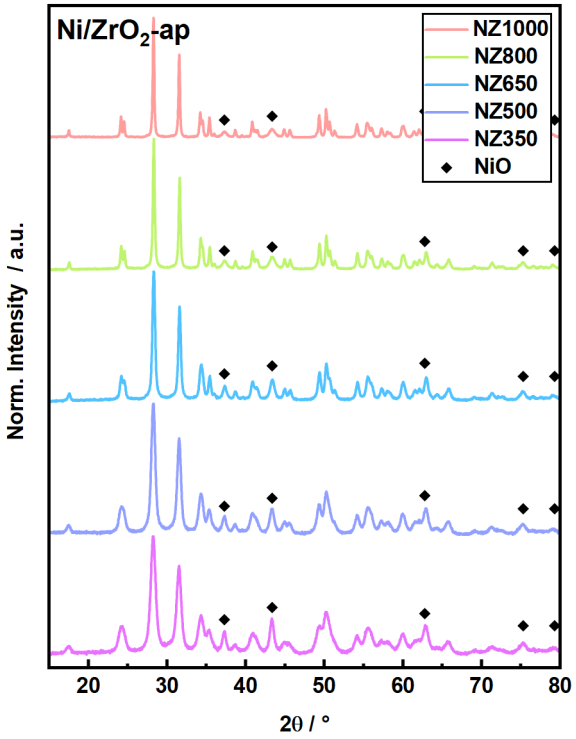


Figure 8.47: XRD patterns of as-prepared Ni/ZrO_2 catalysts (NZ350-NZ1000). The present NiO is marked with black rhombus.[240] Available under the terms and conditions of the Creative Commons Attribution 3.0 license (CC BY 3.0, `https://creativecommons.org/licenses/by/3.0/`), Copyright ©2022.

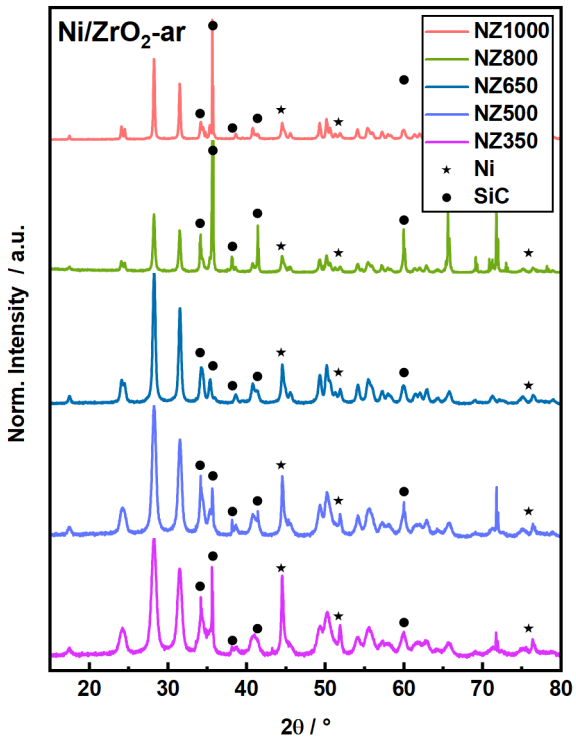


Figure 8.48: XRD patterns of the spent Ni/ZrO_2 catalysts after catalytic tests in CO_2 methanation. The present Ni is marked with black stars and present SiC is marked with black circles. SiC is used as inert material in the reactor and could not be separated completely after reaction.[240] Available under the terms and conditions of the Creative Commons Attribution 3.0 license (CC BY 3.0, `https://creativecommons.org/licenses/by/3.0/`), Copyright ©2022.

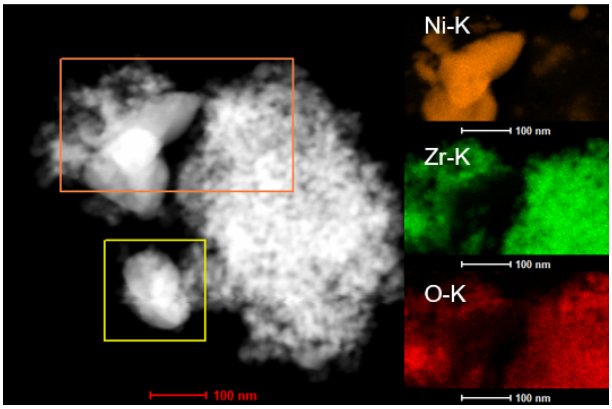


Figure 8.49: STEM images with EDX mapping of NZ500 after CO_2 methanation. The orange box indicates the investigated area with EDX, the yellow one is for drift correction.[240] Available under the terms and conditions of the Creative Commons Attribution 3.0 license (CC BY 3.0, `https://creativecommons.org/licenses/by/3.0/`), Copyright ©2022.

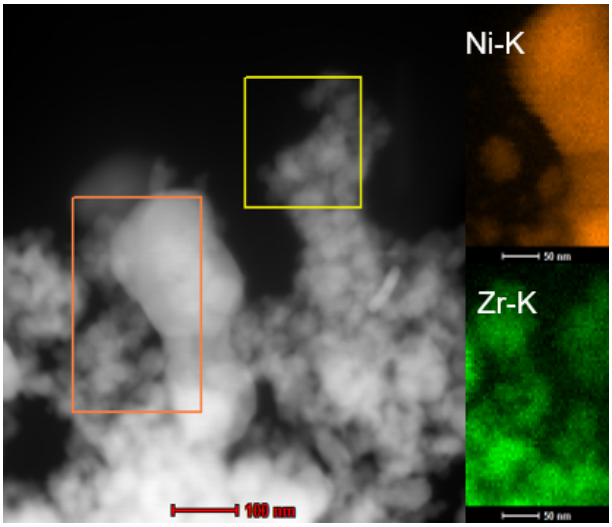


Figure 8.50: STEM images with EDX mapping of NZ650 after CO_2 methanation. The orange box indicates the investigated area with EDX, the yellow one is for drift correction.[240] Available under the terms and conditions of the Creative Commons Attribution 3.0 license (CC BY 3.0, `https://creativecommons.org/licenses/by/3.0/`), Copyright ©2022.

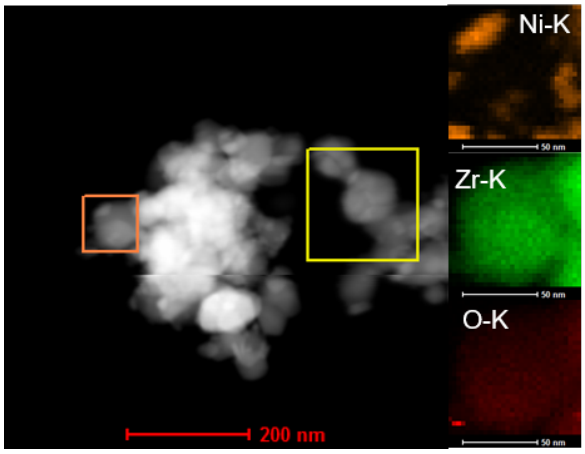


Figure 8.51: STEM images with EDX mapping of NZ1000 after CO_2 methanation. The orange box indicates the investigated area with EDX, the yellow one is for drift correction.[240] Available under the terms and conditions of the Creative Commons Attribution 3.0 license (CC BY 3.0, `https://creativecommons.org/licenses/by/3.0/`), Copyright ©2022.

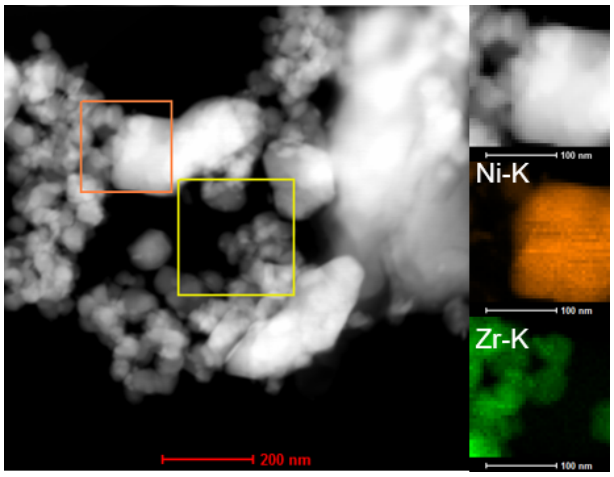


Figure 8.52: STEM images with EDX mapping of NZ1000 after CO_2 methanation. The orange box indicates the investigated area with EDX, the yellow one is for drift correction.[240] Available under the terms and conditions of the Creative Commons Attribution 3.0 license (CC BY 3.0, `https://creativecommons.org/licenses/by/3.0/`), Copyright ©2022.

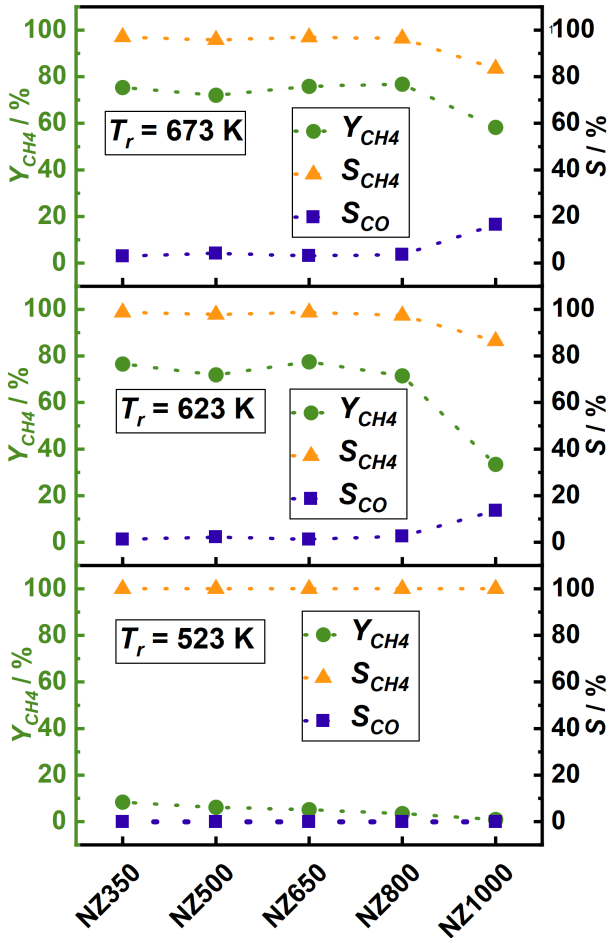


Figure 8.53: Catalytic performance of the Ni/ZrO_2 catalyst series during CO_2 methanation at 523 K, 623 K and 673 K. Calculated CH_4 yield (green, left side) and selectivitiy towards CH_4 (orange) and CO (blue).[240] Available under the terms and conditions of the Creative Commons Attribution 3.0 license (CC BY 3.0, `https://creativecommons.org/licenses/by/3.0/`), Copyright ©2022.

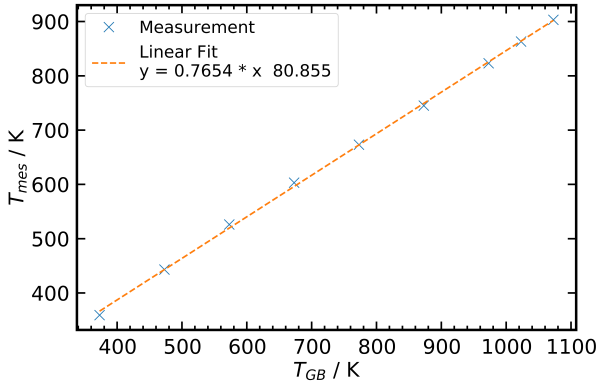


Figure 8.54: Calibration of the hot-air blower temperature T_{GB} with the measured temperature inside an empty quartz capillary T_{mes} using a type-K thermocouple.[240] Available under the terms and conditions of the Creative Commons Attribution 3.0 license (CC BY 3.0, `https://creativecommons.org/licenses/by/3.0/`), Copyright ©2022.

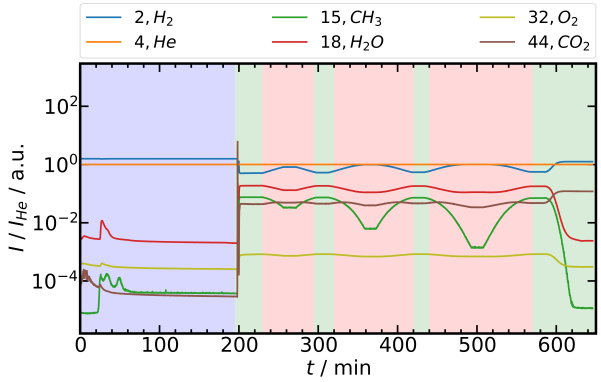


Figure 8.55: Selected MS traces and assigned compounds during *operando* SPXRD experiments of NZ350. All traces were normalized by the He trace. Activation conditions of 25 %H_2/He (blue area), reaction conditions of 5 %CO_2/20 %H_2/He (green area) and thermal deactivation cycles under reaction conditions (red area) with a total gas flow of 10 mL min^{-1}.[240] Available under the terms and conditions of the Creative Commons Attribution 3.0 license (CC BY 3.0, `https://creativecommons.org/licenses/by/3.0/`), Copyright ©2022.

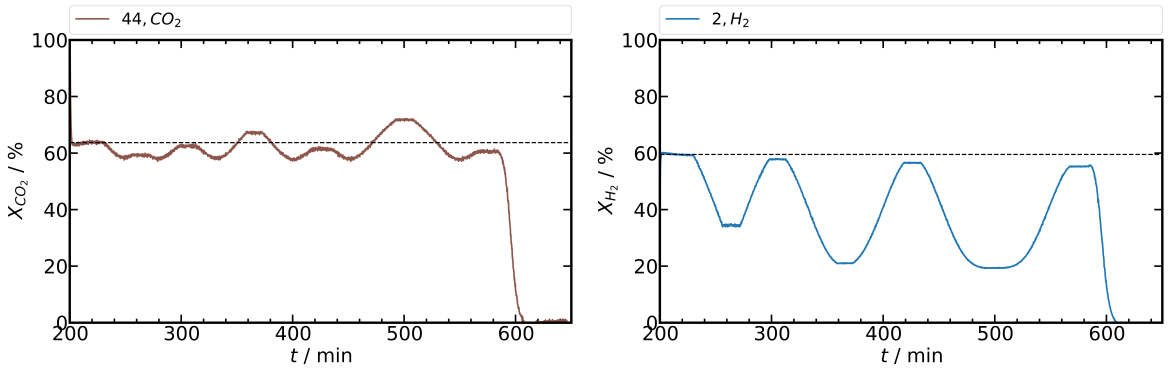


Figure 8.56: CO_2 and H_2 conversion from MS data during *operando* SPXRD experiments of NZ350 under reaction conditions of 5 %CO_2/20 %H_2/He and thermal deactivation cycles under reaction conditions.[240] Available under the terms and conditions of the Creative Commons Attribution 3.0 license (CC BY 3.0, `https://creativecommons.org/licenses/by/3.0/`), Copyright ©2022.

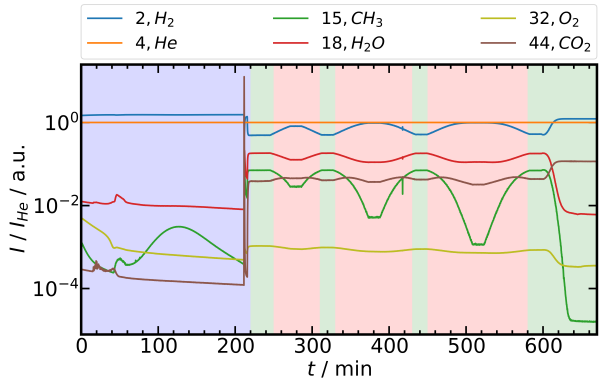


Figure 8.57: Selected MS traces and assigned compounds during *operando* SPXRD experiments of NZ500. All traces were normalized by the He trace. Activation conditions of 25 %H_2/He (blue area), reaction conditions of 5 %CO_2/20 %H_2/He (green area) and thermal deactivation cycles under reaction conditions (red area) with a total gas flow of 10 mL min^{-1}.[240] Available under the terms and conditions of the Creative Commons Attribution 3.0 license (CC BY 3.0, `https://creativecommons.org/licenses/by/3.0/`), Copyright ©2022.

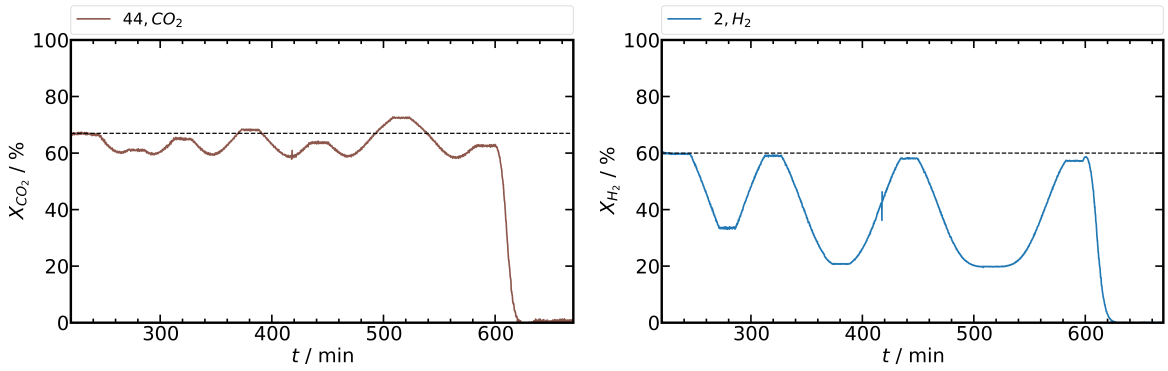


Figure 8.58: CO_2 and H_2 conversion from MS data during *operando* SPXRD experiments of NZ500 under reaction conditions of 5 %CO_2/20 %H_2/He and thermal deactivation cycles under reaction conditions.[240] Available under the terms and conditions of the Creative Commons Attribution 3.0 license (CC BY 3.0, `https://creativecommons.org/licenses/by/3.0/`), Copyright ©2022.

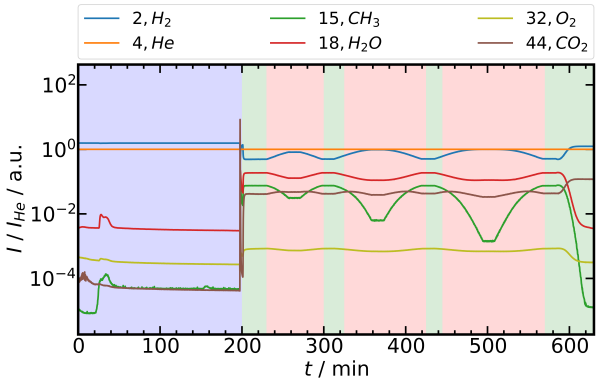


Figure 8.59: Selected MS traces and assigned compounds during *operando* SPXRD experiments of NZ650. All traces were normalized by the He trace. Activation conditions of 25 %H_2/He (blue area), reaction conditions of 5 %CO_2/20 %H_2/He (green area) and thermal deactivation cycles under reaction conditions (red area) with a total gas flow of 10 mL min^{-1}.[240] Available under the terms and conditions of the Creative Commons Attribution 3.0 license (CC BY 3.0, `https://creativecommons.org/licenses/by/3.0/`), Copyright ©2022.

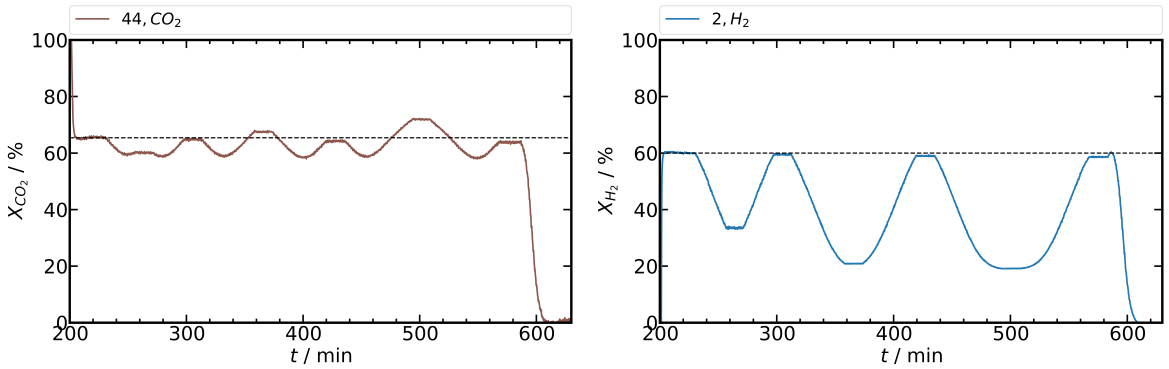


Figure 8.60: CO_2 and H_2 conversion from MS data during *operando* SPXRD experiments of NZ650 under reaction conditions of 5 %CO_2/20 %H_2/He and thermal deactivation cycles under reaction conditions.[240] Available under the terms and conditions of the Creative Commons Attribution 3.0 license (CC BY 3.0, `https://creativecommons.org/licenses/by/3.0/`), Copyright ©2022.

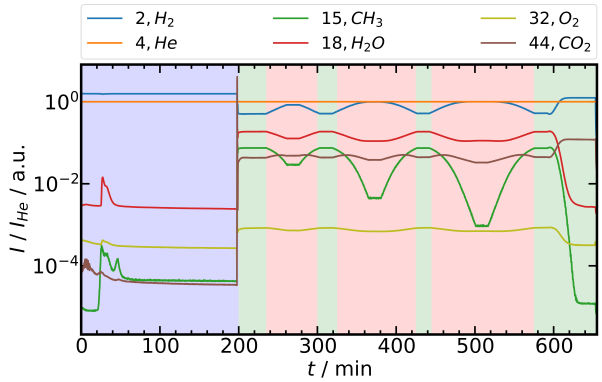


Figure 8.61: Selected MS traces and assigned compounds during *operando* SPXRD experiments of NZ800. All traces were normalized by the He trace. Activation conditions of 25 %H_2/He (blue area), reaction conditions of 5 %CO_2/20 %H_2/He (green area) and thermal deactivation cycles under reaction conditions (red area) with a total gas flow of 10 mL min^{-1}.[240] Available under the terms and conditions of the Creative Commons Attribution 3.0 license (CC BY 3.0, `https://creativecommons.org/licenses/by/3.0/`), Copyright ©2022.

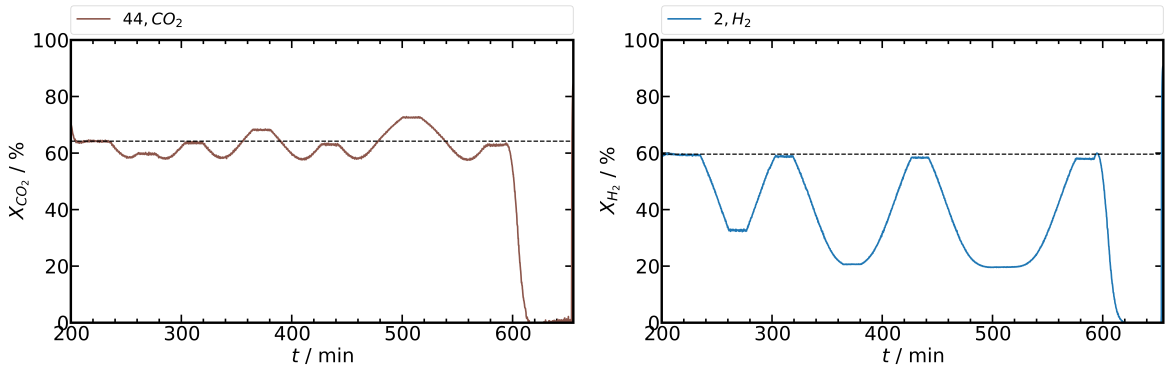


Figure 8.62: CO_2 and H_2 conversion from MS data during *operando* SPXRD experiments of NZ800 under reaction conditions of 5 %CO_2/20 %H_2/He and thermal deactivation cycles under reaction conditions.[240] Available under the terms and conditions of the Creative Commons Attribution 3.0 license (CC BY 3.0, `https://creativecommons.org/licenses/by/3.0/`), Copyright ©2022.

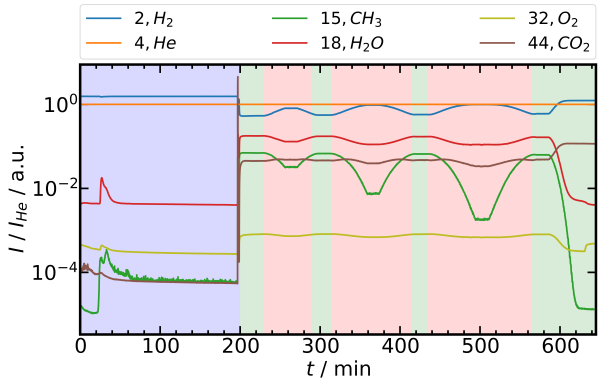


Figure 8.63: Selected MS traces and assigned compounds during *operando* SPXRD experiments of NZ1000. All traces were normalized by the He trace. Activation conditions of 25 %H_2/He (blue area), reaction conditions of 5 %CO_2/20 %H_2/He (green area) and thermal deactivation cycles under reaction conditions (red area) with a total gas flow of 10 mL min^{-1}.[240] Available under the terms and conditions of the Creative Commons Attribution 3.0 license (CC BY 3.0, `https://creativecommons.org/licenses/by/3.0/`), Copyright ©2022.

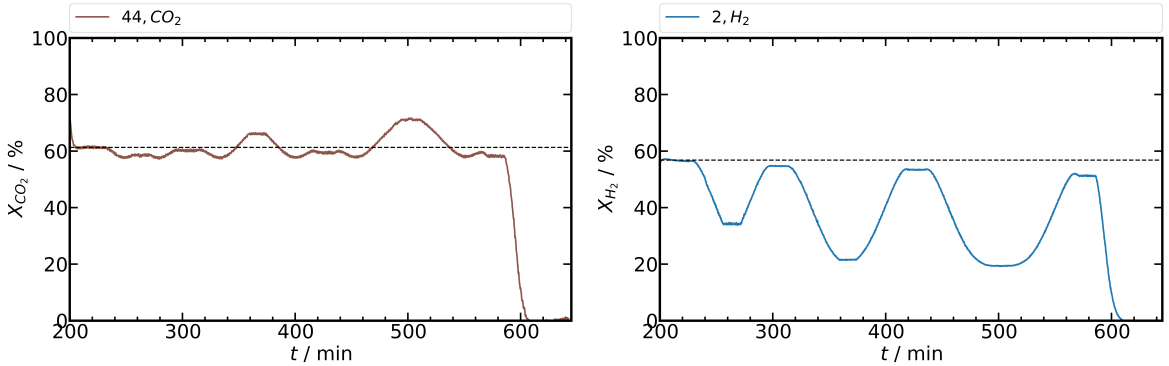


Figure 8.64: CO_2 and H_2 conversion from MS data during *operando* SPXRD experiments of NZ1000 under reaction conditions of 5 %CO_2/20 %H_2/He and thermal deactivation cycles under reaction conditions.[240] Available under the terms and conditions of the Creative Commons Attribution 3.0 license (CC BY 3.0, `https://creativecommons.org/licenses/by/3.0/`), Copyright ©2022.

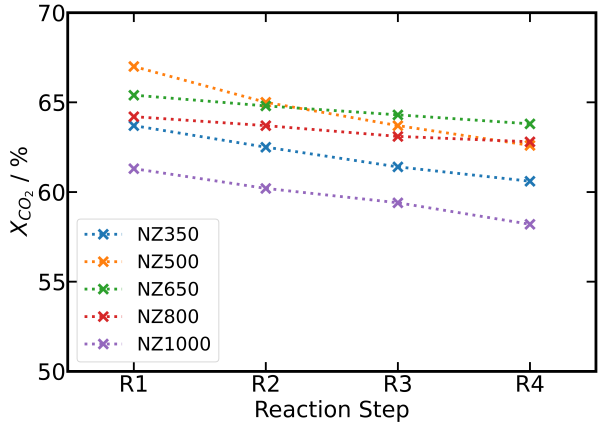


Figure 8.65: CO_2 conversion during *operando* SPXRD experiments depending on the reaction step R1 to R4 for the different catalysts.[240] Available under the terms and conditions of the Creative Commons Attribution 3.0 license (CC BY 3.0, `https://creativecommons.org/licenses/by/3.0/`), Copyright ©2022.

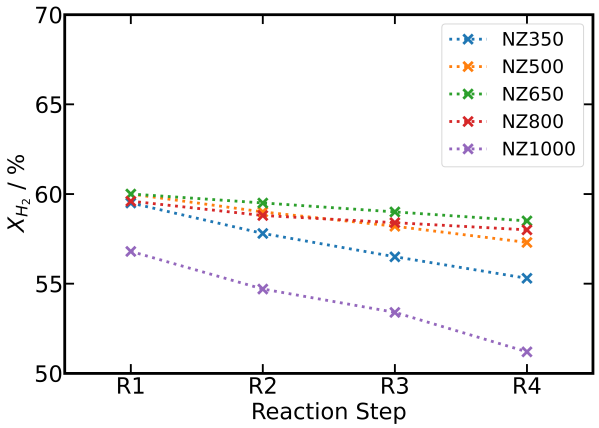


Figure 8.66: H_2 conversion during *operando* SPXRD experiments depending on the reaction step R1 to R4 for the different catalysts.[240] Available under the terms and conditions of the Creative Commons Attribution 3.0 license (CC BY 3.0, `https://creativecommons.org/licenses/by/3.0/`), Copyright ©2022.

Rietveld Refinements

"Rietveld refinements[245, 246] of the measured *operando* SPXRD and laboratory PXRD measurements were performed using Topas (v.6, Bruker AXS).[290] In both cases a measured LaB_6 NIST 640b standard was used to derive an instrumental profile function, described by a pseudo-Voigt Thompson-Cox Hastings peak shape (*operando* SPXRD) or via the fundamental parameters approach for the laboratory diffractometer. A 6^{th} order polynomial was used to describe the background of the diffraction patterns. Refinements of the SPXRD were performed for a Q range of 0.8 to 6.0 $Å^{-1}$. A micro-structure analysis was performed using the double-Voigt approach by Balzar as implemented in Topas to describe crystallite size (L_{vol}) and strain (η).[291] The SPXRD profile of the catalysts were refined by employing each a Lorentzian and Gaussian component for size and strain in case of the monoclinic ZrO_2 phase, while for the Ni and NiO phases the size was described with a Lorentzian and the strain with a Gaussian component. This was required due to the small number of reflections of the Ni and NiO phases in the invesitgate Q space and is a common strategy to prevent parameters running into non-physical values during refinement.[360, 361] The laboratory PXRD are used to compare catalysts before and after testing. The discussion of crystallite size changes and sintering is only based on the SPXRD data The monoclinic ZrO_2 phase was described by the structure reported by Smith *et al.*[296], tetragonal ZrO_2 phase based on a structure by Bondars et al.[295], NiO phase could be described with a structure by Rodic *et al.*[298] and the Ni phase with a structure by Rouquette *et al.*[297] For laboratory PXRD, lattice parameters, micro-structural parameters and atom coordinates were refined, while thermal displacement parameters could not be refined. Results of the refinements of the laboratory PXRD are summarized in Tables 8.10, 8.11, 8.12, 8.13, 8.14, 8.15.
For SPXRD refinements lattice parameters, micro-structural parameters and atom coordinates were refined, while thermal displacement parameters were allowed to be refined restrained an a range of 0 to 5 $Å^2$, with only one B_{iso} parameter used for both O positions. *Ex situ* SPXRD of the pure supports are shown in Figures 8.67, 8.68, 8.69, 8.70, 8.71 and the refinements results are summarized in Table 8.16. For the *operando* SPXRD sequential Rietveld refinements were performed by adapting templates available from the Topas wiki website.[292] Selected refined diffraction patterns of the initial state and the final state after *operando* SPXRD for the catalysts are shown in Figures 8.72, 8.73, 8.74, 8.75, 8.76 with the respective refinement results summarized in Tables 8.17, 8.18, 8.19, 8.20, 8.21. The evolution of the GoF during sequential refinements is shown in Figure 8.78, it should be noted that the abrupt changes can be related to different measurement conditions between activation, reaction conditions and final cool-down. For activation and cool-down the acquisition time was 9 s and for reaction conditions and thermal deactivation cycles 3 s. The sequentially refined lattice parameters for the ZrO_2 phase of the catalysts are shown in Figures 8.79, 8.80, 8.81, 8.82, the B_{iso} in Figures 8.83, 8.84. For the Ni phase the sequentially refined lattice parameter is shown in Figure 8.85 and the B_{iso} in Figure 8.86."[240]

Table 8.10: Rietveld refinement results for the laboratory PXRD of the pure support materials Z350-1000.

support	Z350		Z500	Z650	Z800	Z1000
phase	m-ZrO_2	t-ZrO_2	m-ZrO_2	m-ZrO_2	m-ZrO_2	m-ZrO_2
space group	$P2_1/c$	$P4_2/nmc$	$P2_1/c$	$P2_1/c$	$P2_1/c$	$P2_1/c$
R_{exp} / %	1.92		1.92	1.90	1.92	1.95
R_{wp} / %	2.37		2.79	2.78	2.77	3.29
R_p / %	1.89		2.16	2.17	2.15	2.56
GOF / %	1.23		1.45	1.46	1.44	1.68
ω / wt.%	96.49(10)	3.51(10)	100	100	100	100
L_{vol} / nm	9.45(8)	8.9(4)	13.23(11)	22.9(2)	40.9(5)	116(3)
η /	0.00042(4)	-	0.00015(2)	0.000116(15)	0.000132(10)	0.000324(9)
a / Å	5.1550(4)	3.6110(17)	5.14991(13)	5.15190(15)	5.14954(10)	5.15061(9)
b / Å	5.2123(4)	-	5.20976(14)	5.21400(17)	5.21113(11)	5.20827(10)
c / Å	5.3211(4)	5.169(5)	5.31802(15)	5.32075(18)	5.31963(11)	5.32356(10)
β / °	99.244(4)	-	99.2351(13)	99.2182(15)	99.1995(10)	99.1608(9)
atom parameters m-ZrO_2						
Zr1						
x	0.27711(16)		0.27618(15)	0.27595(13)	0.27592(11)	0.27612(13)
y	0.03992(14)		0.03967(13)	0.03990(11)	0.03990(9)	0.03972(11)
z	0.20932(17)		0.20962(15)	0.20995(12)	0.20964(10)	0.20946(11)
B_{iso} / Å^2	0		0	0	0	0
occ	1		1	1	1	1
O1						
x	0.0722(9)		0.0734(9)	0.0747(7)	0.0746(6)	0.0742(7)
y	0.3274(8)		0.3282(7)	0.3310(6)	0.3323(5)	0.3318(6)
z	0.3467(7)		0.3445(7)	0.3445(6)	0.3445(6)	0.3437(6)
B_{iso} / Å^2	0		0	0	0	0
occ	1		1	1	1	1
O2						
x	0.4508(10)		0.4529(9)	0.4524(7)	0.4511(6)	0.4488(7)
y	0.7554(6)		0.7555(5)	0.7554(5)	0.7553(4)	0.7558(5)
z	0.4771(12)		0.4779(12)	0.4809(10) 0.4806(9)	0.4804(10)	
B_{iso} / Å^2	0		0	0	0	0
occ	1		1	1	1	1
atom parameters t-ZrO_2						
Zr1						
x	3/4		n.a.	n.a.	n.a.	n.a.
y	1/4		n.a.	n.a.	n.a.	n.a.
z	1/4		n.a.	n.a.	n.a.	n.a.
B_{iso} / Å^2	0.48		n.a.	n.a.	n.a.	n.a.
occ	1		n.a.	n.a.	n.a.	n.a.
O1						
x	1/4		n.a.	n.a.	n.a.	n.a.
y	1/4		n.a.	n.a.	n.a.	n.a.
z	0.45450		n.a.	n.a.	n.a.	n.a.
B_{iso} / Å^2	0		n.a.	n.a.	n.a.	n.a.
occ	1		n.a.	n.a.	n.a.	n.a.

Table 8.11: Rietveld refinement results for the laboratory PXRD of the NZ350 catalysts in the initial state and after laboratory CO_2 methanation reaction

	NZ350 initial		NZ350 after	
phase	m-ZrO_2	NiO	m-ZrO_2	Ni
space group	$P2_1/c$	$R\bar{3}m$	$P2_1/c$	$Fm\bar{3}m$
R_{exp} / %	1.51		1.74	
R_{wp} / %	1.86		2.31	
R_p / %	1.45		1.72	
GOF / %	1.24		1.35	
ω / wt.%	82.48(12)	17.52(12)	88.11(10)	11.89(10)
L_{vol} / nm	10.36(11)	10.73(15)	10.08(12)	33.5(7)
η /	0.00044(4)	-	0.00004(5)	-
a / Å	5.1537(4)	2.9622(4)	5.1540(5)	3.5266(2)
b / Å	5.2123(5)	-	5.2118(6)	-
c / Å	5.3201(5)	7.221(2)	5.3205(6)	-
β / °	99.190(4)	-	99.198(5)	-
	Zr1	Ni1	Zr1	Ni 1
x	0.2765(2)	0	0.2759(3)	0
y	0.03882(17)	0	0.0387(2)	0
z	0.2090(2)	0	0.2095(3)	0
B_{iso} / Å^2	0	0	0	0.0058
occ	1	1	1	1
	O1	O1	O1	
x	0.0746(11)	0	0.0775(16)	
y	0.3250(9)	0	0.3324(12)	
z	0.3465(9)	1/2	0.3356(13)	
B_{iso} / Å^2	0	0	0	
occ	1	1	1	
	O2		O2	
x	0.4535(12)		0.4534(16)	
y	0.7545(7)		0.7554(9)	
z	0.4745(15)		0.466(2)	
B_{iso} / Å^2	0		0	
occ	1		1	

Table 8.12: Rietveld refinement results for the laboratory PXRD of the NZ500 catalysts in the initial state and after laboratory CO_2 methanation reaction

	NZ500 initial		NZ500 after	
phase	m-ZrO_2	NiO	m-ZrO_2	Ni
space group	$P2_1/c$	$R\bar{3}m$	$P2_1/c$	$Fm\bar{3}m$
R_{exp} / %	1.53		1.71	
R_{wp} / %	1.96		2.69	
R_p / %	1.52		1.89	
GOF / %	1.28		1.57	
ω / wt.%	83.35(13)	16.65(13)	89.69(11)	10.31(11)
L_{vol} / nm	13.64(14)	9.61(15)	13.32(17)	32.3(8)
η /	0.00028(3)	-	0.00001(4)	-
a / Å	5.1515(3)	2.9623(5)	5.1520(4)	3.52709(19)
b / Å	5.2131(3)	-	5.2119(5)	-
c / Å	5.3196(3)	7.222(3)	5.3214(5)	-
β / °	99.209(3)	-	99.219(4)	-
	Zr1	Ni1	Zr1	Ni 1
x	0.27633(18)	0	0.2770(3)	0
y	0.03958(15)	0	0.0398(2)	0
z	0.21005(17)	0	0.2104(2)	0
B_{iso} / Å^2	0	0	0	0.0058
occ	1	1	1	1
	O1	O1	O1	
x	0.0755(10)	0	0.0682(19)	
y	0.3287(8)	0	0.3365(12)	
z	0.3453(8)	1/2	0.3351(13)	
B_{iso} / Å^2	0	0	0	
occ	1	1	1	
	O2		O2	
x	0.4529(10)		0.463(2)	
y	0.7548(6)		0.7542(9)	
z	0.4769(14)		0.462(2)	
B_{iso} / Å^2	0		0	
occ	1		1	

Table 8.13: Rietveld refinement results for the laboratory PXRD of the NZ650 catalysts in the initial state and after laboratory CO_2 methanation reaction

	NZ650 initial		NZ650 after	
phase	m-ZrO_2	NiO	m-ZrO_2	Ni
space group	$P2_1/c$	$R\bar{3}m$	$P2_1/c$	$Fm\bar{3}m$
R_{exp} / %	1.51		1.54	
R_{wp} / %	1.93		2.02	
R_p / %	1.50		1.56	
GOF / %	1.28		1.31	
ω / wt.%	81.12(13)	18.88(13)	88.17(9)	11.83(9)
L_{vol} / nm	23.0(2)	10.33(14)	22.1(2)	24.6(4)
η /	0.000146(18)	-	0.000046(18)	-
a / Å	5.15214(18)	2.9628(5)	5.15125(18)	3.52715(12)
b / Å	5.2148(2)	-	5.2140(2)	-
c / Å	5.3208(2)	7.230(3)	5.3193(2)	-
β / °	99.2074(17)	-	99.2084(18)	-
	Zr1	Ni1	Zr1	Ni 1
x	0.27616(15)	0	0.27610(16)	0
y	0.03987(12)	0	0.03967(13)	0
z	0.21012(14)	0	0.21001(14)	0
B_{iso} / Å^2	0	0	0	0.0058
occ	1	1	1	1
	O1	O1	O1	
x	0.0748(8)	0	0.0745(8)	
y	0.3314(7)	0	0.3316(7)	
z	0.3442(7)	1/2	0.3426(7)	
B_{iso} / Å^2	0	0	0	
occ	1	1	1	
	O2		O2	
x	0.4507(8)		0.4524(9)	
y	0.7548(5)		0.7547(5)	
z	0.4800(12)		0.4815(14)	
B_{iso} / Å^2	0		0	
occ	1		1	

Table 8.14: Rietveld refinement results for the laboratory PXRD of the NZ800 catalysts in the initial state and after laboratory CO_2 methanation reaction

	NZ800 initial		NZ800 after	
phase	m-ZrO_2	NiO	m-ZrO_2	Ni
space group	$P2_1/c$	$R\bar{3}m$	$P2_1/c$	$Fm\bar{3}m$
R_{exp} / %	1.49		2.33	
R_{wp} / %	1.83		4.55	
R_p / %	1.43		3.11	
GOF / %	1.23		1.96	
ω / wt.%	79.78(14)	20.22(14)	88.0(3)	12.0(3)
L_{vol} / nm	44.5(6)	8.10(11)	34.1(13)	31.2(17)
η /	0.000204(12)	-	0.00000(5)	-
a / Å	5.15138(12)	2.9652(5)	5.1504(4)	3.5280(3)
b / Å	5.21357(13)	-	5.2121(5)	-
c / Å	5.32117(13)	7.221(3)	5.3259(5)	-
β / °	99.1923(11)	-	99.193(4)	-
	Zr1	Ni1	Zr1	Ni 1
x	0.27558(13)	0	0.2758(6)	0
y	0.03936(11)	0	0.0383(4)	0
z	0.20960(12)	0	0.2133(5)	0
B_{iso} / Å^2	0	0	0	0.0058
occ	1	1	1	1
	O1	O1	O1	
x	0.0749(7)	0	0.091(4)	
y	0.3334(6)	0	0.364(2)	
z	0.3437(6)	1/2	0.311(3)	
B_{iso} / Å^2	0	0	0	
occ	1	1	1	
	O2		O2	
x	0.4535(7)		0.458(3)	
y	0.7555(4)		0.7525(19)	
z	0.4788(10)		0.395(3)	
B_{iso} / Å^2	0		0	
occ	1		1	

Table 8.15: Rietveld refinement results for the laboratory PXRD of the NZ1000 catalysts in the initial state and after laboratory CO_2 methanation reaction

	NZ1000 initial		NZ1000 after	
phase	m-ZrO_2	NiO	m-ZrO_2	Ni
space group	$P2_1/c$	$R\bar{3}m$	$P2_1/c$	$Fm\bar{3}m$
R_{exp} / %	1.52		1.71	
R_{wp} / %	2.05		2.66	
R_p / %	1.56		3.05	
GOF / %	1.35		1.56	
ω / wt.%	79.97(16)	20.03(16)	87.19(12)	12.81(12)
L_{vol} / nm	95(2)	7.85(12)	76.4(19)	29.4(7)
η /	0.000322(10)	-	0.000173(13)	-
a / Å	5.15062(10)	2.9544(9)	5.15187(12)	3.52826(11)
b / Å	5.21006(11)	-	5.21112(13)	-
c / Å	5.32250(11)	7.265(5)	5.32425(14)	-
β / °	99.1693(10)	-	99.1672(12)	-
	Zr1	Ni1	Zr1	Ni 1
x	0.27614(14)	0	0.27580(18)	0
y	0.03951(11)	0	0.03902(16)	0
z	0.20946(12)	0	0.20949(16)	0
B_{iso} / Å^2	0	0	0	0.0058
occ	1	1	1	1
	O1	O1	O1	
x	0.0750(7)	0	0.0800(9)	
y	0.3326(6)	0	0.3333(8)	
z	0.3439(6)	1/2	0.3380(9)	
B_{iso} / Å^2	0	0	0	
occ	1	1	1	
	O2		O2	
x	0.4500(7)		0.4460(10)	
y	0.7551(5)		0.7555(6)	
z	0.4820(11)		0.4800(16)	
B_{iso} / Å^2	0		0	
occ	1		1	

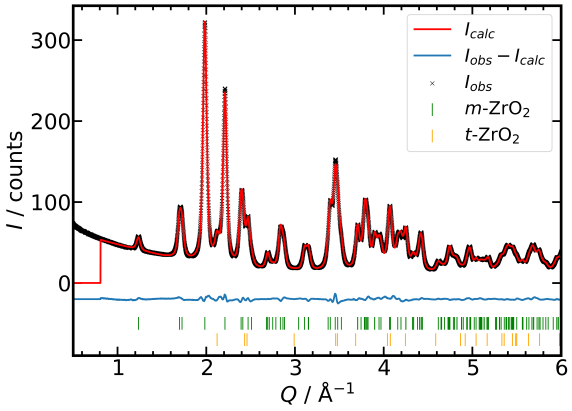


Figure 8.67: Rietveld refinement of the measured *ex situ* SPXRD measurement of Z350.[240] Available under the terms and conditions of the Creative Commons Attribution 3.0 license (CC BY 3.0, `https://creativecommons.org/licenses/by/3.0/`), Copyright ©2022.

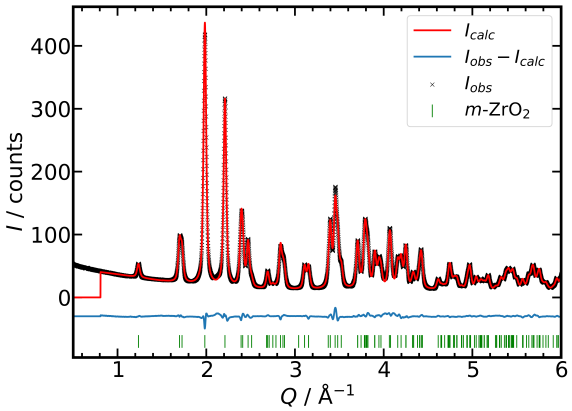


Figure 8.68: Rietveld refinement of the measured *ex situ* SPXRD measurement of Z500.[240] Available under the terms and conditions of the Creative Commons Attribution 3.0 license (CC BY 3.0, `https://creativecommons.org/licenses/by/3.0/`), Copyright ©2022.

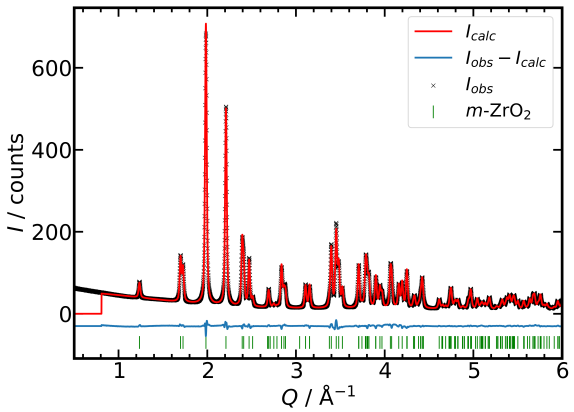


Figure 8.69: Rietveld refinement of the measured *ex situ* SPXRD measurement of Z650.[240] Available under the terms and conditions of the Creative Commons Attribution 3.0 license (CC BY 3.0, `https://creativecommons.org/licenses/by/3.0/`), Copyright ©2022.

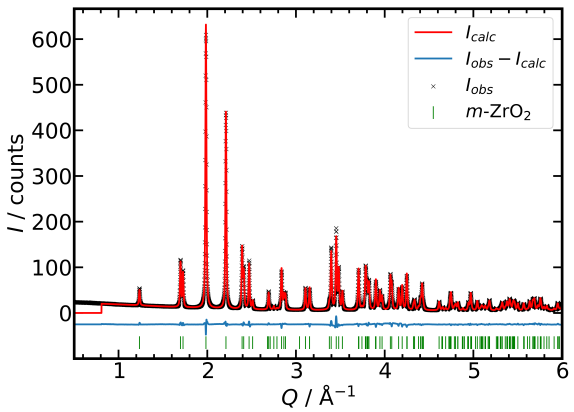


Figure 8.70: Rietveld refinement of the measured *ex situ* SPXRD measurement of Z800.[240] Available under the terms and conditions of the Creative Commons Attribution 3.0 license (CC BY 3.0, `https://creativecommons.org/licenses/by/3.0/`), Copyright ©2022.

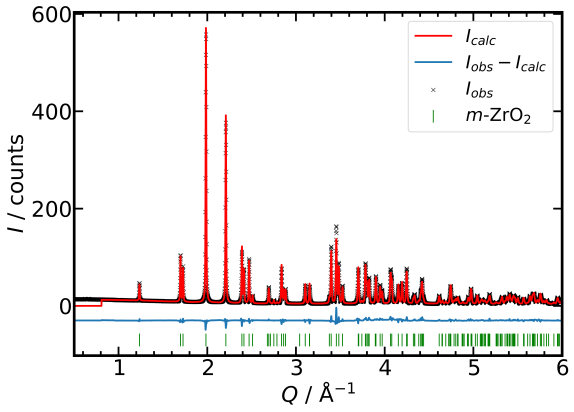


Figure 8.71: Rietveld refinement of the measured *ex situ* SPXRD measurement of Z1000.[240] Available under the terms and conditions of the Creative Commons Attribution 3.0 license (CC BY 3.0, `https://creativecommons.org/licenses/by/3.0/`), Copyright ©2022.

Table 8.16: Rietveld refinement results for the *ex situ* SPXRD of the pure support materials Z350-1000.

support	Z350		Z500	Z650	Z800	Z1000
phase	m-ZrO_2	t-ZrO_2	m-ZrO_2	m-ZrO_2	m-ZrO_2	m-ZrO_2
space group	$P2_1/c$	$P4_2/nmc$	$P2_1/c$	$P2_1/c$	$P2_1/c$	$P2_1/c$
R_{exp} / %	11.50		12.52	12.32	17.76	22.09
R_{wp} / %	2.36		3.39	3.23	4.31	6.91
R_p / %	1.83		2.46	2.46	3.02	5.09
GOF / %	0.21		0.27	0.26	0.24	0.31
ω / wt.%	95.47(14)	4.53(14)	100	100	100	100
L_{vol} / nm	9.63(14)	12.7(12)	13.13(14)	22.8(2)	41.1(6)	98(14)
η /	0.00098(8)	0.0045(2)	0.00069(4)	0.0002(6)	0.00030(2)	0.000624(10)
a / Å	5.1508(2)	3.612(2)	5.14991(13)	5.14873(7)	5.14849(6)	5.14869(6)
b / Å	5.2077(2)	-	5.20976(14)	5.21034(8)	5.20977(6)	5.20551(6)
c / Å	5.3199(3)	5.165(7)	5.31802(15)	5.31735(8)	5.31872(7)	5.32243(6)
β / °	99.254(2)	-	99.2351(13)	99.2197(8)	99.1975(6)	99.1564(6)
atom parameters m-ZrO_2						
Zr1						
x	0.27526(9)		0.27512(7)	0.27524(7)	0.27515(8)	0.27539(9)
y	0.03949(8)		0.03917(6)	0.03971(5)	0.03977(6)	0.03955(8)
z	0.20940(11)		0.20928(8)	0.20913(7)	0.20900(8)	0.20881(8)
B_{iso} / Å^2	0.00(3)		0.000(17)	0.722(14)	0.651(16)	0.000(18)
occ	1		1	1	1	1
O1						
x	0.0748(7)		0.0762(5)	0.0742(4)	0.0750(5)	0.0759(6)
y	0.3229(5)		0.3247(4)	0.3284(4)	0.3297(5)	0.3311(5)
z	0.3472(5)		0.3436(4)	0.3440(4)	0.3451(5)	0.3469(5)
B_{iso} / Å^2	0.00(9)		0.00(7)	0.90(6)	0.91(7)	0.00(7)
occ	1		1	1	1	1
O2						
x	0.4521(7)		0.4492(5)	0.4495(5)	0.4500(5)	0.4500(6)
y	0.7583(5)		0.7583(4)	0.7577(3)	0.7574(4)	0.7571(5)
z	0.4770(7)		0.4788(6)	0.4768(5)	0.4774(6)	0.4792(7)
B_{iso} / Å^2	0.71(10)		0.42(7)	1.60(6)	1.51(7)	0.65(8)
occ	1		1	1	1	1
atom parameters t-ZrO_2						
Zr1						
x	3/4		n.a.	n.a.	n.a.	n.a.
y	1/4		n.a.	n.a.	n.a.	n.a.
z	1/4		n.a.	n.a.	n.a.	n.a.
B_{iso} / Å^2	0.00(13)		n.a.	n.a.	n.a.	n.a.
occ	1		n.a.	n.a.	n.a.	n.a.
O1						
x	1/4		n.a.	n.a.	n.a.	n.a.
y	1/4		n.a.	n.a.	n.a.	n.a.
z	0.417(6)		n.a.	n.a.	n.a.	n.a.
B_{iso} / Å^2	0.0(8)		n.a.	n.a.	n.a.	n.a.
occ	1		n.a.	n.a.	n.a.	n.a.

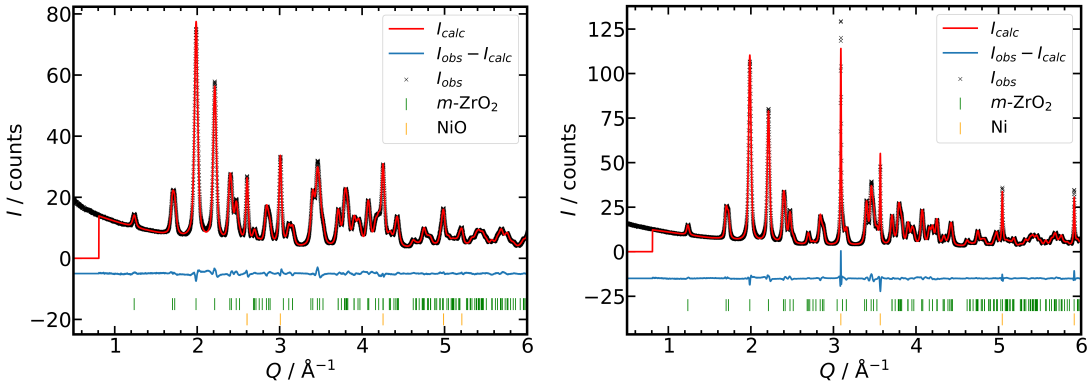


Figure 8.72: Rietveld refinements of the initial state before (left) and after (right) *operando* SPXRD experiments of NZ350.[240] Available under the terms and conditions of the Creative Commons Attribution 3.0 license (CC BY 3.0, `https://creativecommons.org/licenses/by/3.0/`), Copyright ©2022.

Table 8.17: Selected Rietveld refinement results for the NZ350 catalysts in the initial state and after *operando* SPXRD.

	NZ350 initial		NZ350 after	
phase	m-ZrO_2	NiO	m-ZrO_2	Ni
space group	$P2_1/c$	$R\bar{3}m$	$P2_1/c$	$Fm\bar{3}m$
R_{exp} / %	23.11		24.11	
R_{wp} / %	2.76		3.70	
R_p / %	2.09		2.53	
GOF / %	0.12		0.15	
ω / wt.%	81.36(11)	18.64(11)	86.00(6)	14.00(6)
L_{vol} / nm	10.72(16)	13.94(12)	14.80(17)	37.5(2)
η /	0.00092(9)	0.00128(3)	0.00036(14)	0.00000(3)
a / Å	5.1459(2)	2.954(2)	5.14475(11)	3.52195(4)
b / Å	5.2044(2)	-	5.20276(12)	-
c / Å	5.3126(2)	7.234(11)	5.31441(12)	-
β / °	99.219(2)	-	99.2080(13)	-
	Zr1	Ni1	Zr1	Ni 1
x	0.27536(9)	0	0.27528(8)	0
y	0.03901(8)	0	0.03970(6)	0
z	0.20922(10)	0	0.20951(8)	0
B_{iso} / Å^2	0.45(2)	0.76(3)	0.730(19)	0.692(17)
occ	1	1	1	1
	O1	O1	O1	
x	0.0772(6)	0	0.0731(5)	
y	0.3234(5)	0	0.3268(4)	
z	0.3429(5)	1/2	0.3448(4)	
B_{iso} / Å^2	0.08(8)	0.64(7)	0.45(7)	
occ	1	1	1	
	O2		O2	
x	0.4491(7)		0.4488(6)	
y	0.7580(4)		0.7560(4)	
z	0.4767(7)		0.4731(7)	
B_{iso} / Å^2	0.97(9)		1.03(7)	
occ	1		1	

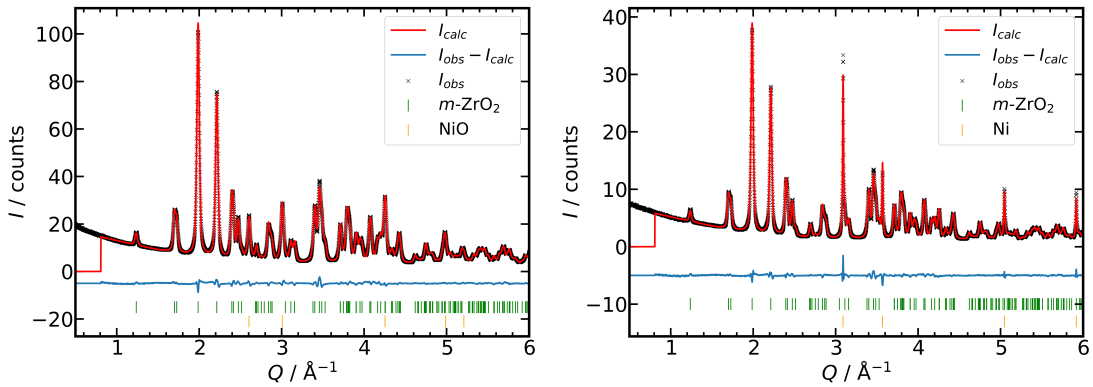


Figure 8.73: Rietveld refinements of the initial state before (left) and after (right) *operando* SPXRD experiments of NZ500.[240] Available under the terms and conditions of the Creative Commons Attribution 3.0 license (CC BY 3.0, `https://creativecommons.org/licenses/by/3.0/`), Copyright ©2022.

Table 8.18: Selected Rietveld refinement results for the NZ500 catalysts in the initial state and after *operando* SPXRD.

	NZ500 initial		NZ500 after	
phase	m-ZrO_2	NiO	m-ZrO_2	Ni
space group	$P2_1/c$	$R\bar{3}m$	$P2_1/c$	$Fm\bar{3}m$
R_{exp} / %	23.04		39.02	
R_{wp} / %	2.71		3.21	
R_p / %	2.09		2.26	
GOF / %	0.12		0.08	
ω / wt.%	82.84(10)	17.16(10)	87.30(10)	12.70(10)
L_{vol} / nm	14.40(18)	12.93(12)	16.2(3)	33.8(4)
η /	0.000(17)	0.00140(3)	0.00047(10)	0.00000(7)
a / Å	5.14426(13)	2.954(3)	5.14338(17)	3.52124(7)
b / Å	5.20459(15)	-	5.20294(19)	-
c / Å	5.31132(15)	7.236(13)	5.3121(2)	-
β / °	99.2223(14)	-	99.221(2)	-
	Zr1	Ni1	Zr1	Ni 1
x	0.27503(8)	0	0.27512(14)	0
y	0.03932(7)	0	0.03980(11)	0
z	0.20917(8)	0	0.20936(14)	0
B_{iso} / Å^2	0.55(2)	0.85(4)	0.74(3)	0.66(3)
occ	1	1	1	1
	O1	O1	O1	
x	0.0742(5)	0	0.0729(9)	
y	0.3266(4)	0	0.3278(7)	
z	0.3439(4)	$^1/_2$	0.3454(7)	
B_{iso} / Å^2	0.42(7)	0.82(7)	0.54(12)	
occ	1	1	1	
	O2		O2	
x	0.4496(6)		0.4499(10)	
y	0.7575(4)		0.7567(7)	
z	0.4789(6)		0.4746(12)	
B_{iso} / Å^2	1.22(7)		1.22(13)	
occ	1		1	

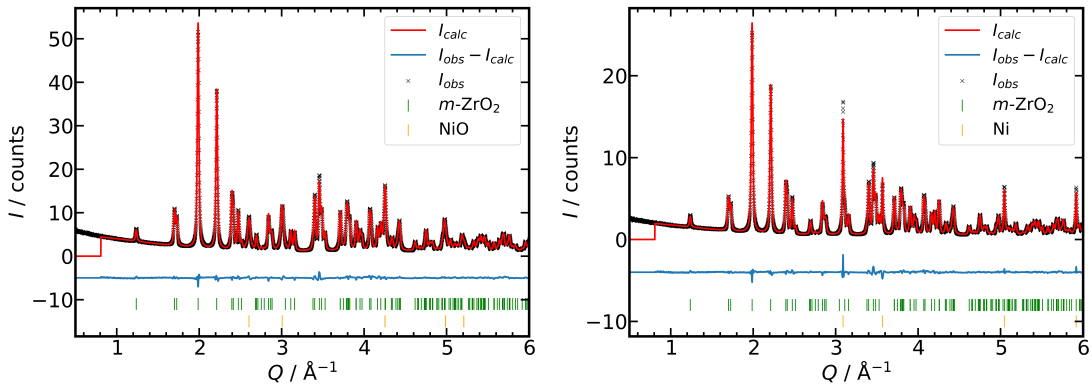


Figure 8.74: Rietveld refinements of the initial state before (left) and after (right) *operando* SPXRD experiments of NZ650.[240] Available under the terms and conditions of the Creative Commons Attribution 3.0 license (CC BY 3.0, `https://creativecommons.org/licenses/by/3.0/`), Copyright ©2022.

Table 8.19: Selected Rietveld refinement results for the NZ650 catalysts in the initial state and after *operando* SPXRD.

	NZ650 initial		NZ650 after	
phase	m-ZrO_2	NiO	m-ZrO_2	Ni
space group	$P2_1/c$	$R\bar{3}m$	$P2_1/c$	$Fm\bar{3}m$
R_{exp} / %	39.72		58.40	
R_{wp} / %	3.15		3.79	
R_p / %	2.38		2.76	
GOF / %	0.08		0.06	
ω / wt.%	81.13(15)	18.87(15)	85.76(13)	14.24(13)
L_{vol} / nm	21.1(4)	12.87(16)	21.4(5)	27.2(4)
η /	0.00042(4)	0.00121(4)	0.00035(6)	0.00000(13)
a / Å	5.14361(12)	2.955(3)	5.14339(16)	3.52193(8)
b / Å	5.20581(14)	-	5.20514(18)	-
c / Å	5.31131(14)	7.236(13)	5.31185(18)	-
β / °	99.2147(13)	-	99.2190(18)	-
	Zr1	Ni1	Zr1	Ni 1
x	0.27514(11)	0	0.27519(16)	0
y	0.03951(9)	0	0.03964(13)	0
z	0.20902(11)	0	0.20910(15)	0
B_{iso} / Å^2	0.00(2)	0.00(5)	0.00(3)	0.00(4)
occ	1	1	1	1
	O1	O1	O1	
x	0.0736(7)	0	0.0728(10)	
y	0.3292(6)	0	0.3299(9)	
z	0.3445(6)	1/2	0.3459(9)	
B_{iso} / Å^2	0.00(9)	0.19(11)	0.00(13)	
occ	1	1	1	
	O2		O2	
x	0.4498(8)		0.4505(11)	
y	0.7573(6)		0.7565(8)	
z	0.4804(9)		0.4796(14)	
B_{iso} / Å^2	0.86(10)		0.45(14)	
occ	1		1	

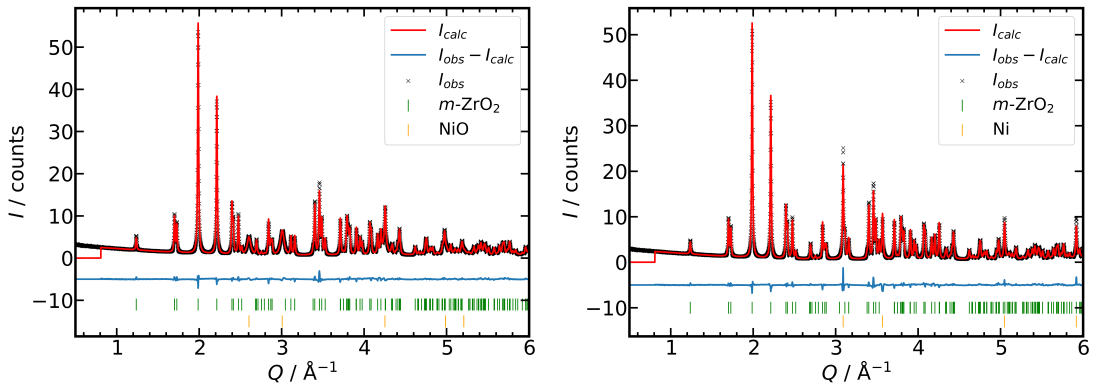


Figure 8.75: Rietveld refinements of the initial state before (left) and after (right) *operando* SPXRD experiments of NZ800.[240] Available under the terms and conditions of the Creative Commons Attribution 3.0 license (CC BY 3.0, `https://creativecommons.org/licenses/by/3.0/`), Copyright ©2022.

Table 8.20: Selected Rietveld refinement results for the NZ800 catalysts in the initial state and after *operando* SPXR.

	NZ800 initial		NZ800 after	
phase	m-ZrO_2	NiO	m-ZrO_2	Ni
space group	$P2_1/c$	$R\bar{3}m$	$P2_1/c$	$Fm\bar{3}m$
R_{exp} / %	50.00		52.34	
R_{wp} / %	4.26		5.18	
R_p / %	3.19		3.72	
GOF / %	0.09		0.10	
ω / wt.%	80.1(3)	19.9(3)	85.25(11)	14.75(11)
L_{vol} / nm	36.1(9)	9.91(16)	35.0(7)	28.9(4)
η /	0.00043(2)	0.00169(6)	0.00034(2)	0.00000(10)
a / Å	5.14135(10)	2.954(16)	5.14115(9)	3.52075(5)
b / Å	5.20473(11)	-	5.20342(10)	-
c / Å	5.30929(11)	7.24(8)	5.31025(10)	-
β / °	99.2067(10)	-	99.2056(10)	-
	Zr1	Ni1	Zr1	Ni 1
x	0.27508(12)	0	0.27532(12)	0
y	0.03962(10)	0	0.03989(10)	0
z	0.20880(12)	0	0.20874(12)	0
B_{iso} / Å^2	0.00(2)	0.00(6)	0.00(3)	0.00(4)
occ	1	1	1	1
	O1	O1	O1	
x	0.0754(8)	0	0.0733(8)	
y	0.3315(7)	0	0.3309(7)	
z	0.3460(7)	1/2	0.3461(7)	
B_{iso} / Å^2	0.26(10)	0.30(13)	0.09(10)	
occ	1	1	1	
	O2		O2	
x	0.4505(8)		0.4504(8)	
y	0.7594(7)		0.7584(7)	
z	0.4777(10)		0.4750(11)	
B_{iso} / Å^2	0.89(11)		0.57(11)	
occ	1		1	

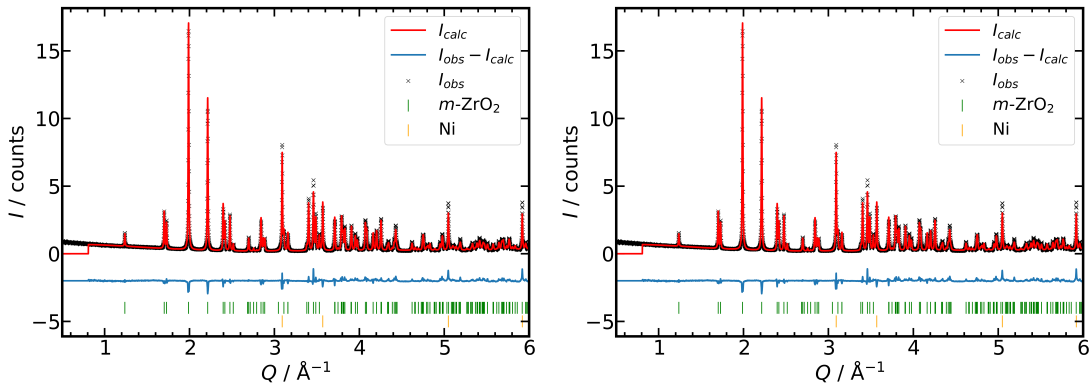


Figure 8.76: Rietveld refinements of the initial state before (left) and after (right) *operando* SPXRD experiments of NZ1000.[240] Available under the terms and conditions of the Creative Commons Attribution 3.0 license (CC BY 3.0, `https://creativecommons.org/licenses/by/3.0/`), Copyright ©2022.

Table 8.21: Selected Rietveld refinement results for the NZ1000 catalysts in the initial state and after *operando* SPXRD.

	NZ1000 initial		NZ1000 after	
phase	m-ZrO_2	NiO	m-ZrO_2	Ni
space group	$P2_1/c$	$R\bar{3}m$	$P2_1/c$	$Fm\bar{3}m$
R_{exp} / %	35.72		102.44	
R_{wp} / %	8.85		9.10	
R_p / %	7.08		7.14	
GOF / %	0.25		0.09	
ω / wt.%	79.8(3)	20.2(3)	84.9(2)	15.1(2)
L_{vol} / nm	60.0(6)	8.9(2)	67.1(10)	53.4(15)
η /	0.000462(7)	0.00101(19)	0.000475(9)	0.00000(8)
a / Å	5.14031(11)	2.955(4)	5.14034(14)	3.51991(7)
b / Å	5.20115(12)	-	5.20045(15)	-
c / Å	5.31061(13)	7.23(2)	5.31118(16)	-
β / °	99.1824(12)	-	99.1816(16)	-
	Zr1	Ni1	Zr1	Ni 1
x	0.27520(19)	0	0.2754(3)	0
y	0.03921(15)	0	0.0395(2)	0
z	0.20866(17)	0	0.2084(2)	0
B_{iso} / Å^2	0.00(3)	0.00(10)	0.00(4)	0.00(7)
occ	1	1	1	1
	O1	O1	O1	
x	0.0743(11)	0	0.0718(16)	
y	0.3343(11)	0	0.3341(15)	
z	0.3478(10)	1/2	0.3477(14)	
B_{iso} / Å^2	0.00(16)	0.0(2)	0.0(2)	
occ	1	1	1	
	O2		O2	
x	0.4514(12)		0.4514(16)	
y	0.7590(9)		0.7596(13)	
z	0.4819(14)		0.477(2)	
B_{iso} / Å^2	0.00(16)		0.0(2)	
occ	1		1	

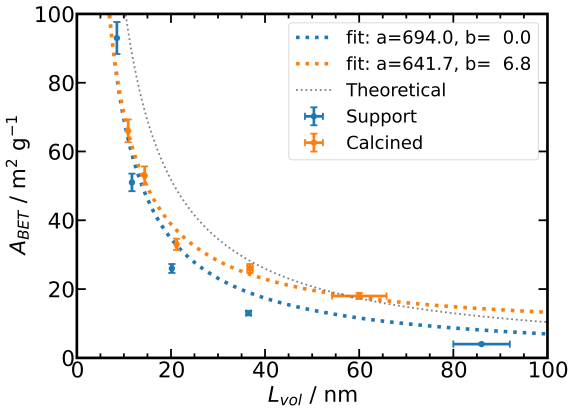


Figure 8.77: Correlation of A_{BET} and L_{vol} of the ZrO_2 phase for the pure supports before Ni deposition (blue) and the as-prepared calcined catalysts (orange).[240] Available under the terms and conditions of the Creative Commons Attribution 3.0 license (CC BY 3.0, `https://creativecommons.org/licenses/by/3.0/`), Copyright ©2022.

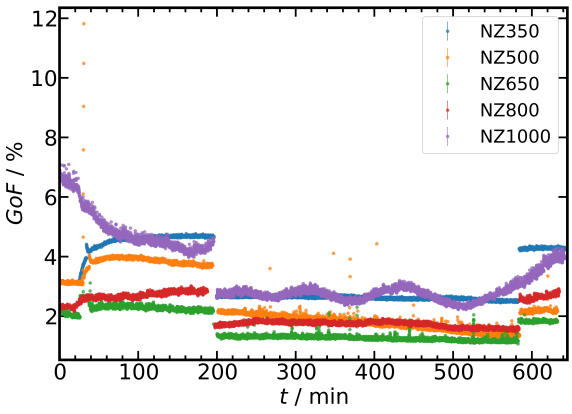


Figure 8.78: *GOF* obtained for the sequential Rietveld refinements. Steps origin in different acquisition time of the SPXRD during activation and final cool-down (9 s) as well as reaction and thermal deactivation cycles (3 s).[240] Available under the terms and conditions of the Creative Commons Attribution 3.0 license (CC BY 3.0, `https://creativecommons.org/licenses/by/3.0/`), Copyright ©2022.

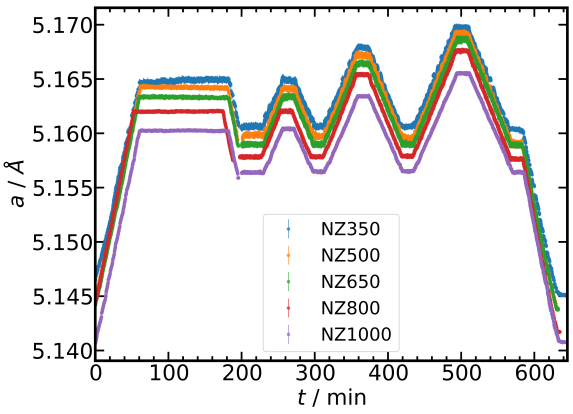


Figure 8.79: ZrO_2 lattice parameter a obtained from the sequential Rietveld refinements.[240] Available under the terms and conditions of the Creative Commons Attribution 3.0 license (CC BY 3.0, `https://creativecommons.org/licenses/by/3.0/`), Copyright ©2022.

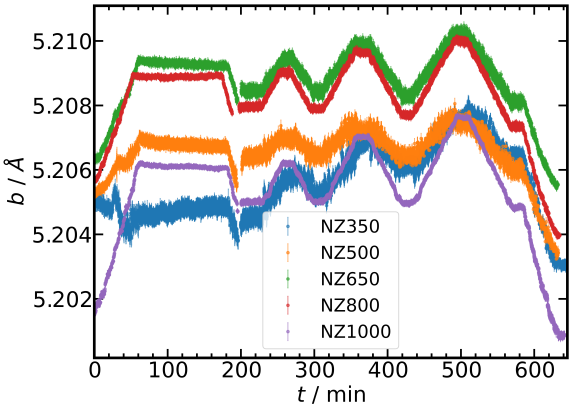


Figure 8.80: ZrO_2 lattice parameter b obtained from the sequential Rietveld refinements.[240] Available under the terms and conditions of the Creative Commons Attribution 3.0 license (CC BY 3.0, `https://creativecommons.org/licenses/by/3.0/`), Copyright ©2022.

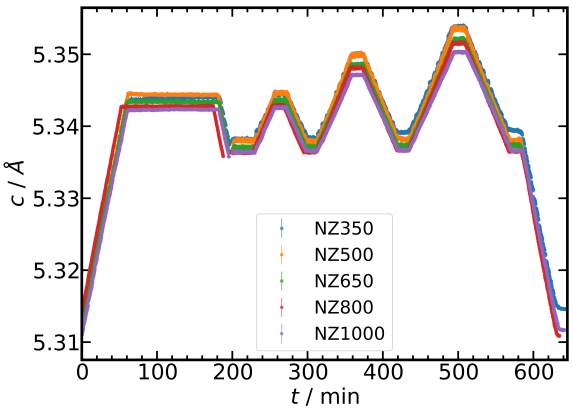


Figure 8.81: ZrO_2 lattice parameter c obtained from the sequential Rietveld refinements.[240] Available under the terms and conditions of the Creative Commons Attribution 3.0 license (CC BY 3.0, `https://creativecommons.org/licenses/by/3.0/`), Copyright ©2022.

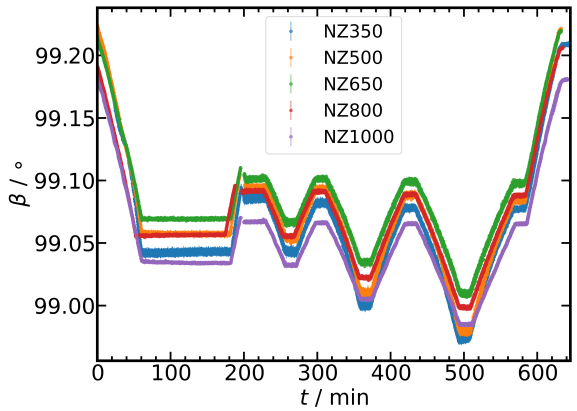


Figure 8.82: ZrO_2 lattice parameter β obtained from the sequential Rietveld refinements.[240] Available under the terms and conditions of the Creative Commons Attribution 3.0 license (CC BY 3.0, `https://creativecommons.org/licenses/by/3.0/`), Copyright ©2022.

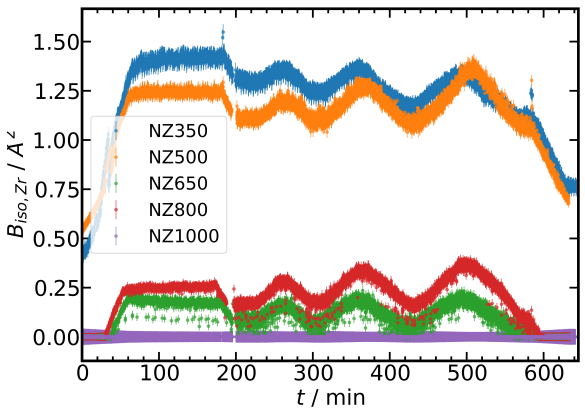


Figure 8.83: ZrO_2 phase B_{iso} for Zr obtained from the sequential Rietveld refinements.[240] Available under the terms and conditions of the Creative Commons Attribution 3.0 license (CC BY 3.0, `https://creativecommons.org/licenses/by/3.0/`), Copyright ©2022.

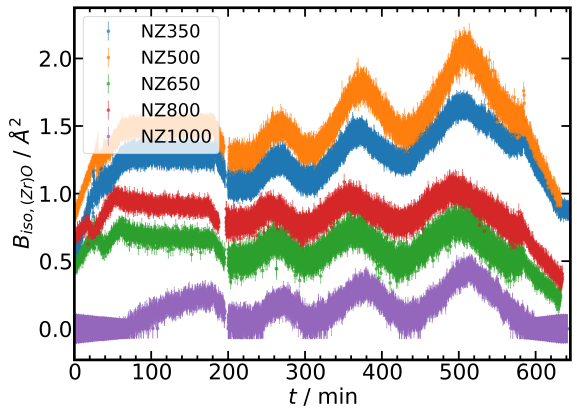


Figure 8.84: ZrO_2 phase B_{iso} for O obtained from the sequential Rietveld refinements.[240] Available under the terms and conditions of the Creative Commons Attribution 3.0 license (CC BY 3.0, `https://creativecommons.org/licenses/by/3.0/`), Copyright ©2022.

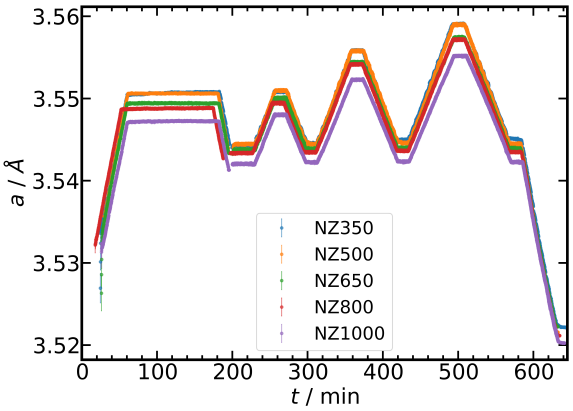


Figure 8.85: Ni lattice parameter a obtained from the sequential Rietveld refinements.[240] Available under the terms and conditions of the Creative Commons Attribution 3.0 license (CC BY 3.0, `https://creativecommons.org/licenses/by/3.0/`), Copyright ©2022.

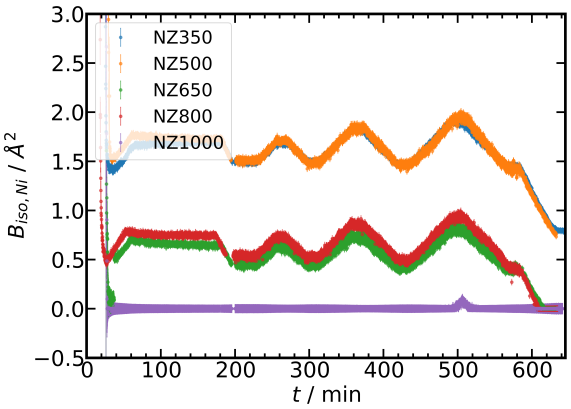


Figure 8.86: Ni phase B_{iso} for Ni obtained from the sequential Rietveld refinements.[240] Available under the terms and conditions of the Creative Commons Attribution 3.0 license (CC BY 3.0, `https://creativecommons.org/licenses/by/3.0/`), Copyright ©2022.

Appendix B

Acknowledgments

The presented results would not have been possible without the help and support of many people. Therefore, parts of the credit are dedicated to all those who were involved directly or indirectly into this work.

First of all, I would like to thank Prof. Dr. Jan-Dierk Grunwaldt and Dr. Thomas L. Sheppard for the possibility of carrying out this highly interesting project at KIT in the XRM subgroup of the Grunwaldt group. Specifically, Prof. Jan-Dierk Grunwaldt is acknowledged for the supervision of the PhD thesis and the leading creation of the DFG priority program SPP2080, which the research of my thesis was part of. Furthermore, your daily excitement about science and research was/is definitely an inspiration. A major thank goes to the direct supervision by Dr. Thomas L. Sheppard. Thereby, I am grateful for the big freedom in performing my research, the continuous trust in my work, all critical questions and scientific discussion. Furthermore, I am glad for your advises regarding proposal and publication writing. Each time, I definitely was able to learn something new, especially further improving my language skills. I think as a group leader and mentor your were and are excellent and I can imagine there will be some bright scientific future lying ahead for you.

Large parts of this work would not have been possible at all without the great collaboration inside the research consortium between Leipzig, Magdeburg and Karlsruhe as part of the SPP2080. In general, I would like to thank here the team from Universität Leipzig consisting of Prof. Dr. Roger Gläser, Ken Luca Abel, Dr. David Poppitz and Dr. Juliane Titus. From the Otto von Guericke University of Mageburg and the Max Planck Institute for Dynamics of Complex Technical Systems Magdeburg, I would like to acknowledge all contributions by Prof. Dr. Kai Sundmacher, Ronny Zimmermann, Dr. Jens Bremer and Dr. Liisa Rihko-Struckmann. Especially the provision of the SPP2080-IMRC reference catalyst to the whole SPP2080 should be highlighted in this regard. I highly appreciated all the fruitful discussions, new and critical ideas and our open regular exchange meetings within our consortium. In more detail, I would like to thank Ken Luca Abel for the synthesis of all the hierarchically porous catalysts presented as part of this study, the provision of the conventional porosity and parts of the conventional laboratory characterization presented in this thesis. Ronny Zimmermann is especially acknowledged for providing macrokinetic simulations on the hierarchically porous catalyst, for the core-shell catalysts based on the SPP2080-IMRC, which were prepared together with Dr. Jens Bremer as well as Dr. Vesselin Idakiev and Prof. Dr. Lothar Mörl (both Otto von Guericke University Magdeburg). Ken and Ronny, I am very grateful for our highly constructive, collaborative and relaxed joint research work and our regular PhD exchange meetings, where we definitely learned how to bring together synthesis, characterization and engineering.

Major parts of this thesis involved various experiments at synchrotron light sources, which would not have been possible without all people supporting these experiments, that are only feasible as a team. In this regard, I would first like to thank all the beamline scientist who contributed to the experiments. At DESY, this includes Dr. Andreas Schropp, Dr. Mikhail Lyubomirskiy, Dr. Maik Kahnt, Dr. Jan Garrevoet, Dr. Michael Stückelberger, Dr. Martin Seyrich, Dr. Ann-Christin Dippel, Dr. Olof Gutowski, Dr. Soham Bannerjee and Philipp Glaevecke. At SLS, this includes Dr. Ana Diaz, Dr. Mirko Holler, Dr. Dario Ferreira Sanchez, Dr. Nicola Pietro Maria Casati and Michael Lange. At DLS, I would like to thank Dr. Darren Batey and Dr. Silvia Cipiccia. For experiments at the ESRF, Dr. Federico Monaco and Dr. Peter Cloetens are acknowledged. Furthermore, I would like to thank Dr. Anna Zimina and Dr. Tim Prüßmann for some initial experiments at the KIT Light Source, which were not presented in this thesis. I really enjoyed the possibilities that I had in performing all the synchrotron experiments with various different contrast modes or techniques. As part of this strong interdisciplinary work, I learned a lot on different X-ray methods as well as the related data analysis and possibilities to understand functional materials. In this respect, I would also like to acknowledge all the people who assisted in my beamtimes including Dr. Thomas Sheppard, Linda Klag, Srashtasrita Das, Mariam Schulte, Dr. Matthias Stehle, Dr. Reihaneh Pashminehazar, Shweta Sharma, Ken Luca Abel, Dr. Johannes Becher, Dr. Marc-André Serrer and Dr. Yakub Fam. I hope despite some night shifts that you might had to do you enjoyed them similarly as me. I wish I sufficiently returned the favor in assisting your experiments, which I always enjoyed to help out. Furthermore, I would like to thank my master student Mariam Schulte for the great work during her thesis time and her help to successfully accomplish the side project on the sintering studies of the Ni/ZrO_2 series.

Regarding electron microscopy studies, I would like to appreciate the support by Xiaohui Huang, Dr. Di Wang, Dr. Wu Wang and Prof. Dr. Christian Kübel. Special thanks should go here to Xiaohui Huang and Prof. Dr. Christian Kübel in respect to all electron tomography studies presented in this work. Furthermore, I would like to thank Dr. Sabine Schlabach for her support during sample preparation via FIB/SEM for X-ray imaging studies. In this respect, I further acknowledge the great work by the team of Arno Jeromin, Satishkumar Kulkarni and Dr. Thomas F. Keller from the DESY Nanolab in preparing the catalyst samples for *in situ* X-ray ptychography experiments. I appreciate some general discussion with Prof. Dr. Mirijam Zobel and Nils Prinz regarding PDF analysis. For the X-ray microtromography experiments presented in this work, I would like to thank Dr. Reihaneh Pashminehazar and Dr. Thomas Sheppard. I am grateful for the initial detailed instruction into the capillary reactor setup for *in situ* and *operando* experiments by Dr. Matthias Stehle and all the help in case of technical issues or questions regarding the Raman and mass spectrometers. I would further like to thank all people involved in the SPP2080 program. The exchange among all PhD students and PostDocs was really great, especially during the possible on-site PhD workshops. Furthermore, I would like

to thank Mariam Schulte, Linda Klag, Dr. Matthias Stehle, Dr. Florian Maurer, Ken Luca Abel, Florian Sachse, Srashtasrita Das, Maximilian Springer and Shweta Sharma for comments and helpful suggestions to improve the first draft of this thesis. For an outside of academia perspective on catalysis research and providing helpful industrial insights, I would like to acknowledge my mentor Dr. Stephan Schunk. Additionally, I am grateful for my previous supervisors and mentors in my Bachelor thesis, Dr. Henry Auer and Prof. Dr. Holger Kohlmann, who strongly inspired me and have woken my interest in large scale research facility experiments.

I want to gratefully acknowledge all the financial support that allowed to perform all the different experiments during my PhD research. This includes the grant for the SPP2080 by the Deutsche Forschungsgemeinschaft (DFG)-406914011. Furthermore, the synchrotron sources DESY, SLS, DLS, ESRF and KIT Light Source are acknowledged for providing the various beamtimes. I thank the funding from the European Union's Horizon 2020 research and innovation programme under grant agreement No 731019 (EUSMI) for the PXCT experiments at cSAXS, SLS. Additionally, FIB/SEM sample preparation and electron microscopy experiments were carried out with the support of the Karlsruhe Nano Micro Facility (KNMF), a Helmholtz Research Infrastructure at Karlsruhe Institute of Technology (KIT) via proposals 2019-022-026980 and 2020-023-028494. Furthermore, I acknowledge KIT and DFG for financing the Raman spectrometer system (INST121384/73-1).

Especially in the time before the Corona pandemic, I would like to express my joy about the great group atmosphere within the AKG and your warm welcome to me. I really enjoyed our regular joined dinner or pub evenings and I hope this spirit will now come back after the pandemic. In this respect, many thanks to Matthias, Marc, Dasha, Linda, Daniel, Flo, Mariam, Sarina, Deniz, Mario, Vasyl and Paolo. Furthermore, the numerous coffee breaks between Marc, Dasha, Linda, Sarina, lately Vera and also Matthias (without coffee) were joyful and helped to keep a great balance also during stressful times. In this regard, I would also like to thank Ken and Max for our endless open discussions about God and the world. The same accounts for the evening/night long video calls with Flo and André. Here, I would like to further thank my close friends Katrin and Sabine from my study times in Leipzig.

Finally, I would like to thank all my friends and family for their continuous support and joyful moments. Especially, I am grateful for the unconditional support by my parents Anja and Lutz. The last two years were strongly brightened by Nicole and especially your help during/after my knee surgery was remarkable.

Curriculum Vitae

Personal Information

Name:	Sebastian Weber
Date of birth:	9^{th} August 1992
Place of birth:	Friedrichroda, Germany

Academic Experience

Since 10/2018:	PhD Researcher Karlsruhe Institute of Technology (KIT), Karlsruhe, Germany Institute of Catalysis Research and Technology (IKFT) Institute for Chemical Technology and Polymer Chemistry (ITCP) Prof. Dr. Jan-Dierk Grunwaldt and Dr. Thomas L. Sheppard
10/2015 – 04/2018:	Master of Science Chemistry (Grade: 1.2, A-level) Universität Leipzig, Leipzig, Germany Master thesis with Prof. Dr. Roger Gläser and Dr. Stephan A. Schunk "Synthesis of Oxide-Based Electrides in an Arc Furnace and their Potential Application in Heterogeneous Catalysis"
08/2017 – 02/2018:	Internship hetcatlab - BASF JointLab, hte GmbH, Heidelberg, Germany
02/2016 – 07/2016:	Semester Abroad Monash University, Melbourne, Australia
10/2012 – 2015:	Bachelor of Science Chemistry (Grade: 1.5, A-level) Universität Leipzig, Leipzig, Germany Bachelor thesis with Prof. Dr. Holger Kohlmann "Synthese und Untersuchung der Reaktivität der Zintl-Phasen EaTt mit Ea = Sr, Ba und Tt = Sn, Pb gegenüber Wasserstoff"
2010:	Abitur Certificate (Grade: 1.7) Arnoldischule Staatliches Gymnasium Gotha, Germany

Extracurricular Activities

02/2019 – 05/2022:	PhD Representative SPP2080
since 05/2017:	International Younger Chemists Network (IYCN) Executive Board Member (03/2018 – 08/2021) Social Media Committee Leader (03/2018 – 08/2021)
since 11/2014:	Young Chemistry Network of the GDCh (JCF) Chair of regional network Leipzig (05/2015 – 07/2017)

Awards and Scholarships

since 08/2018:	BASF Hi-Potential Program
10/2015 – 07/2017:	German Scholarship of the Bayer Foundation
02/2016 – 07/2016:	German Academic Exchange Service (DAAD) – ISAP scholarship
12/2015:	Book award of the Freundeskreis der Fakultät für Chemie und Mineralogie, Universität Leipzig, B. Sc. degree
06/2010:	GDCh-graduate award for the best chemistry exam

Measurement Campaigns at Synchrotron Radiation Facilities[1]

- 03/2022, X-ray diffraction tomography, microXAS, Swiss Light Source, Villigen, Switzerland.
- 12/2021, Powder X-ray diffraction, MS - X04SA, Swiss Light Source, Villigen, Switzerland. (online participation)⋆
- 07/2021, X-ray ptychography imaging, P06-nanoprobe, Deutsches Elektronen Synchrotron, Hamburg, Germany.
- 12/2020, X-ray holotomography and X-ray fluorescence imaging, ID 16, European Synchrotron Radiation Facility, Grenoble, France.⋆
- 10/2020, X-ray total scattering, P21.1, Deutsches Elektronen Synchrotron, Hamburg, Germany.⋆
- 10/2020, X-ray ptychography imaging, cSAXS, Swiss Light Source, Villigen, Switzerland.⋆
- 09/2020, X-ray ptychography imaging, P06-nanoprobe, Deutsches Elektronen Synchrotron, Hamburg, Germany.
- 08/2020, X-ray ptychography imaging, P06-nanoprobe, Deutsches Elektronen Synchrotron, Hamburg, Germany.⋆
- 06/2020, X-ray absorption spectroscopy, CAT-ACT, KIT Light Source, Karlsruhe, Germany.
- 05/2020, X-ray diffraction tomography, P06-microprobe, Deutsches Elektronen Synchrotron, Hamburg, Germany.
- 11/2019, X-ray ptychography imaging, I13-1, Diamond Light Source, Didcot, UK.⋆
- 10/2019, X-ray diffraction tomography, P06-microprobe, Deutsches Elektronen Synchrotron, Hamburg, Germany.
- 10/2019, X-ray diffraction tomography, microXAS, Swiss Light Source, Villigen, Switzerland.
- 10/2019, X-ray ptychography imaging, cSAXS, Swiss Light Source, Villigen, Switzerland.
- 08/2019, X-ray absorption spectroscopy, CAT-ACT, KIT Light Source, Karlsruhe, Germany.
- 07/2019, X-ray absorption spectroscopy, CAT-ACT, KIT Light Source, Karlsruhe, Germany.
- 05/2019, X-ray ptychography imaging, P06-nanoprobe, Deutsches Elektronen Synchrotron, Hamburg, Germany.

[1] Beamtimes part of this thesis marked with ⋆.

- 12/2018, X-ray ptychography imaging, P06-nanoprobe, Deutsches Elektronen Synchrotron, Hamburg, Germany.
- 11/2018, X-ray absorption spectroscopy, CAT-ACT, KIT Light Source, Karlsruhe, Germany.

List of Publications Related to this Thesis

1. R. T. Zimmermann, S. Weber, J. Bremer, V. Idakiev, R. Pashminehazar, T. L. Sheppard, L. Mörl and K. Sundmacher, "Core-Shell Catalyst Pellets for Effective Reaction Heat Management", *Chem. Eng. J.*, **2023**, **457**, 140921.
   Discussed as part of section 4.2 and 4.1.

2. S. Das, R. Pashminehazar, S. Sharma, S. Weber and T. L Sheppard, "New Dimensions in Catalysis Research with Hard X-ray Tomography", *Chem. Ing. Tech.*, **2022**, *94*, 1591-1610.
   Figure as part of chapter 1.

3. M. L. Schulte†, S. Weber†, L. Klag, J.-D. Grunwaldt and T. L. Sheppard, "Synchrotron PXRD deconvolutes nickel particle and support changes in Ni/ZrO_2 methanation catalysts", *Catal. Sci. Technol.*, **2022**, *12*, 6069-6083.[2]
   Discussed as part of section 6.2.

4. S. Weber, R. T. Zimmermann, J. Bremer, K. L. Abel, D. Poppitz, N. Prinz, J. Ilsemann, S. Wendholt, Q. Yang, R. Pashminehazar, F. Monaco, P. Cloetens, X. Huang, C. Kübel, E. Kondratenko, M. Bauer, M. Bäumer, M. Zobel, R. Gläser, K. Sundmacher and T. L. Sheppard, "Digitalization in Catalysis Research: Towards a Holistic Description of a Ni/Al_2O_3 Reference Catalyst for CO_2 Methanation", *ChemCatChem*, **2022**, *14*, e202101878.
   Discussed as part of section 4.1.

5. S. Weber, A. Diaz, M. Holler, A. Schropp, M. Lyubomirskiy, K. L. Abel, M. Kahnt, A. Jeromin, S. Kulkarni, T. F. Keller, R. Gläser, T. L. Sheppard, "Evolution of Hierarchically Porous Nickel Alumina Catalysts Studied by X-ray Ptychography", *Adv. Sci.*, **2022**, *9*, 2105432.
   Discussed as part of section 5.1.

6. S. Weber, D. Batey, S. Cipiccia, M. Stehle, K. L. Abel, R. Gläser and T. L. Sheppard, "Hard X-Ray Nanotomography for 3D Analysis of Coking in Nickel-Based Catalysts", *Angew. Chem. Int. Ed.*, **2021**, *60*, 21722-21777.
   "Harte Röntgen-Nanotomographie zur 3D-Analyse der Verkokung in Nickel-basierten Katalysatoren", *Angew. Chem.*, **2021**, *133*, 21940-21945. (German version)
   Discussed as part of section 6.1.

7. S. Weber, K. L. Abel, R. T. Zimmermann, X. Huang, J. Bremer, L. K. Rihko-Struckmann, D. Batey, S. Cipiccia, J. Titus, D. Poppitz, C. Kübel, K. Sundmacher, R. Gläser and T. L. Sheppard, "Porosity and Structure of Hierarchically Porous Ni/Al_2O_3 Catalysts for CO_2 Methanation", *Catalysts*, **2020**, *10*, 1471.
   Discussed as part of section 4.3.

[2] † equal author contribution

List of Further Publications

1. K. L. Abel, S. Weber, D. Poppitz, J. Titus, T. L. Sheppard and Roger Gläser "Thermally Stable Mesoporous Tetragonal Zirconia Through Surfactant-Controlled Synthesis and Si-Stabilization", *RSC Adv.*, **2022**, *12*, 16875-16885.

2. M. Stehle, A. Gaur, S. Weber, T. L.Sheppard, M. Thomann, A. Fischer and J.-D. Grunwaldt, "Complementary operando insights into the activation of multicomponent selective propylene oxidation catalysts", *J. Catal.*, **2022**, *408*, 339-355.

3. S. Weber and S. A. Schunk, "Reply to Inoue et al. Comment on "Weber et al. Mayenite-Based Electride C12A7e$^-$: A Reactivity and Stability Study. Catalysts 2021, 11, 334"", *Catalysts*, **2021**, *11*, 1155.

4. S. Weber, S. Schäfer, M. Saccoccio, N. Ortner, M. Bertmer, K. Seidel, S. Berendts, M. Lerch, R. Gläser, H. Kohlmann and S. A. Schunk, "Mayenite-Based Electride C12A7e$^-$: A Reactivity and Stability Study", *Catalysts*, **2021**, *11*, 334.

5. S. Weber, S. Schäfer, M. Saccoccio, K. Seidel, H. Kohlmann, R. Gläser and S. A. Schunk, "Mayenite-based electride C12A7e$^-$: an innovative synthetic method via plasma arc melting", *Mater. Chem. Front.*, **2021**, *5*, 1301-1314.

6. J. Becher, S. Weber, D. Ferreira Sanchez, D. E. Doronkin, J. Garrevoet, G. Falkenberg, D. Motta Meira, S. Pascarelli, J.-D. Grunwaldt and T. L. Sheppard, "Sample Environment for Operando Hard X-ray Tomography - An Enabling Technology for Multimodal Characterization in Heterogeneous Catalysis", *Catalysts*, **2021**, *11*, 459.

7. S. Weber, "Seeing is Believing – Understanding Catalyst Function in 3D by Imaging", *ChemViews*, **2020**.

8. D. T. Pournara, G. D. Tormet-González, S. Weber, J. Borges, M. Menche, J. V. Milić, "EYCN and IYCN: Connecting and Empowering Young Chemists Globally", *ChemViews*, **2020**.

9. M.-A. Serrer, A. Gaur, J. Jelic, S. Weber, C. Fritsch, A. H. Clark, E. Saraçi, F. Studt and J.-D. Grunwaldt, "Structural dynamics in Ni-Fe catalysts during CO_2 methanation - role of iron oxide clusters", *Catal. Sci. Technol.*, **2020**, *10*, 7542-7554.

10. H. Auer, S. Weber, T. C. Hansen, D. M. Többens and H. Kohlmann, "Reversible hydrogenation of the Zintl phases BaGe and BaSn studied by in situ diffraction", *Z. Kristallogr.*, **2018**, *233*, 399-409.

11. H. Auer, R. Guehne, M. Bertmer, S. Weber, P. Wenderoth, T. C. Hansen, J. Haase and H. Kohlmann, "Hydrides of Alkaline Earth–Tetrel (AeTt) Zintl Phases: Covalent Tt–H Bonds from Silicon to Tin", *Inorg. Chem.*, **2017**, *56*, 1061-1071.

List of Conference Contributions

* presenting author

1. S. Weber*, K. L. Abel, R. Gläser and T. Sheppard, "Understanding of Catalyst Synthesis and Deactivation in 3D with Xray Ptychography" (oral presentation), *55th Meeting of the German Catalysis Society*, Weimar, Germany, 2022.

2. M. Stehle*, A. Gaur, S. Weber, T. L. Sheppard, M. Thomann, A. Fischer, and J.-D. Grunwaldt, "Monitoring the structural evolution of complex multicomponent catalysts for selective oxidation by correlative *operando* techniques" (poster presentation), *55th Meeting of the German Catalysis Society*, Weimar, Germany, 2022.

3. S. Weber*, A. Diaz, M. Holler, A. Schropp, M. Lyubomirskiy, K. L. Abel, S. Kulkarni, T. F. Keller, Roger Gläser and T. L. Sheppard, "High-resolution Imaging of the Calcination and Porosity Evolution of Ni/Al_2O_3 Catalysts by Ptychographic X-ray Microscopy" (oral presentation), *14th International Conference on Synchrotron Radiation Instrumentation (SRI)*, Online Event, 2022.

4. S. Weber*, A. Schropp, M. Lyubomirskiy, A. Jeromin, S. Kulkarni, T. F. Keller and T. L. Sheppard, "*In situ* Study of the Porosity Evolution of a Hierarchically Porous Catalyst by X-ray Ptychography" (poster presentation), *DESY Photon Science Users' Meeting*, Online Event, 2022.

5. S. Weber*, K. L. Abel, R. Gläser and T. Sheppard, "X-ray Ptychography as a Tool to Understand Catalyst Synthesis and Deactivation in 3D" (pitch/poster presentation), *758th WE-Heraeus-Seminar*, Online Event, 2022. (*poster prize*)

6. J. Titus*, K. L. Abel, O. Kuschel, S. Weber, D. Poppitz, T. Sheppard and R. Gläser, "Control of Textural Properties and Ni Species of Ni-Catalysts Supported on Si-Stabilized ZrO_2" (poster presentation), *758th WE-Heraeus-Seminar*, Online Event, 2022.

7. K. L. Abel*, D. Poppitz, J. Titus, S. Weber, T. L. Sheppard and R. Gläser, "Monolithic Alumina Xerogels with Hierarchical Meso-/Macropore Structure for the Methanation of CO_2" (oral presentation), *5th EuChemS Conference on Green and Sustainable Chemistry (5th EuGSC)*, Online Event, 2021.

8. S. Weber*, D. Batey, S. Cipiccia and T. L. Sheppard, "X-ray Nanotomography Reveals Coking of Nickel-based Catalysts Spatially-Resolved in 3D" (oral presentation), *Wissenschaftsforum Chemie*, Online Event, 2021.

9. S. Weber*, A. Diaz, M. Holler, A. Schropp, M. Lyubomirskiy, K. L. Abel, S. Kulkarni, T. F. Keller, R. Gläser and T. L. Sheppard, "Following Calcination and Porosity Evolution

with Nanometer Resolution by Ptychographic X-ray Microscopy" (oral presentation), *104th Canadian Chemistry Conference and Exhibition, IUPAC CCCE 2021*, Online Event, 2021.

10. K. L. Abel*, S. Weber, D. Poppitz, J. Titus, T. L. Sheppard and R. Gläser, "Thermally Stable Mesoporous Tetragonal Zirconia Through Surfactant-Controlled Synthesis and Si-Stabilization" (poster presentation), *8th Conference of the Federation of European Zeolite Associations (FEZA 2021)*, Online Event, 2021.

11. S. Weber*, K. L. Abel, R. Gläser and T. L. Sheppard, "Unravelling the Pore Structure of a Ni/Al_2O_3 Catalyst by Tomography" (poster presentation), *23rd Frühjahrssymposium*, Online Event, 2021.

12. S. Weber*, K. L. Abel, R. T. Zimmermann, X. Huang, C. Kübel, K. Sundmacher, R. Gläeser and T. L. Sheppard, "Porosity and Structural Analysis of a Hierarchical Porous Ni/Al_2O_3 Catalyst for CO_2 Methanation" (poster presentation), *54th Meeting of the German Catalysis Society*, Online Event, 2021.

13. S. Weber* and S. A. Schunk, "Novel Plasma Synthesis of Mayenite-based Electrides and their Catalytic Application for Ammonia Synthesis" (pitch/poster presentation), *54th Meeting of the German Catalysis Society*, Online Event, 2021.

14. S. Weber* and T. L. Sheppard, "Imaging Pore Structure Evolution of a Hierarchical Porous Ni/Al_2O_3 Catalyst During Calcination" (poster presentation), *3rd SPP2080 Status Meeting*, Online Event, 2021. (*poster prize*)

15. S. Weber* and T. L. Sheppard, "Porosity Analysis of Ni/Al_2O_3 Catalysts by Multi-scale Tomography" (pitch presentation), *5th Annual Workshop on Advances in X-ray Imaging*, Online Event, 2021. (*poster prize*)

16. S. Weber*, "Demanding Sample Environment and Preparation for in situ Ptychographic X-ray Microscopy Studies of Nickel-based Methanation Catalysts " (online oral presentation), *DESY Photon Science Users' Meeting - Satellite Meeting The DESY NanoLab*, Online Event, 2021.

17. S. Weber* and S. A. Schunk, "Novel Plasma Synthesis of Mayenite-Based Electrides and Their Catalytic Application for Ammonia Synthesis" (oral presentation), *Conference on Inorganic Chemistry, GDCh Divisions of Inorganic Chemistry (Wöhler-Vereinigung) and Solid-State Chemistry & Materials Research (Festkörperchemie und Materialforschung*, Online Event, 2020.

18. S. Weber*, K. L. Abel, J. Titus, R. Gläeser, R. T. Zimmermann, K. Sundmacher and T. L. Sheppard, "Investigation of Nickel-based Methanation Catalysts by *Operando* XAS and Tomography Studies" (poster presentation), *17th International Congress on Catalysis*, San Diego, USA, 2020 (event cancelled due to Corona pandemic).

19. S. Weber*, K. L. Abel, J. Titus, R. Gläeser, J.-D. Grunwaldt and T. L. Sheppard, "Structural Analysis of Ni/ZrO_2 Methanation Catalysts by Tomography Methods and *Operando* XAS" (poster presentation), *#CouchCatalysis Online Poster Conference by YEuCat*, Online Event, 2020.

20. S. Weber*, K. L. Abel, J. Titus, R. Gläeser, J.-D. Grunwaldt and T. L. Sheppard, "Structural Analysis of Ni/ZrO_2 Methanation Catalysts by Tomography Methods and *Operando* XAS" (poster presentation), *Virtual Poster Show 53rd Meeting of the German Catalysis Society*, Online Event, 2020.

21. M. Stehle*, A. Gaur, S. Weber, T. L. Sheppard, M. Thomann, A. Fischer, and J.-D. Grunwaldt, "Monitoring the structural evolution of complex multicomponent catalysts for selective oxidation by correlative *operando* techniques" (poster presentation), *53rd Meeting of the German Catalysis Society*, Weimar, Germany, 2020 (event cancelled due to Corona pandemic).

22. S. Weber* and S. A. Schunk, "Novel Plasma Synthesis of Mayenite-Based Electrides and Their Catalytic Application for Ammonia Synthesis" (oral presentation), *53rd Meeting of the German Catalysis Society*, Weimar, Germany, 2020 (event cancelled due to Corona pandemic).

23. S. Weber, R. Pashmineh*, K. L. Abel, J. Titus, R. Gläser, T. L. Sheppard and J.-D. Grunwaldt, "Investigation of Catalyst Materials by Electron Microscopy Methods for 2D and 3D Analysis" (pitch/poster presentation), *KNMF User Meeting*, Karlsruhe, Germany, 2020.

24. S. Weber* and T. L. Sheppard, "Structural Analysis of Ni/ZrO_2 Methanation Catalysts by Tomography Methods and *Operando* XAS" (poster presentation), *2nd SPP2080 Status Meeting*, Leipzig, Germany, 2020.

25. A.Schropp*, D. Brückner, X. Yang, J. Becher, Y. Fam, T. L. Sheppard, S. Weber, J.-D. Grunwaldt and C. G. Schroer, "*In-situ* Hard X-ray Ptychography" (oral presentation), *Workshop on Coherence at ESRF-EBS*, Grenoble, France, 2019.

26. S. Weber*, T. L. Sheppard and J.-D. Grunwaldt, "Multiscale time-and spatially-resolved catalyst characterization with synchrotron radiation" (poster presentation), *BASF International Summer Course*, Ludwigshafen am Rhein, Germany, 2019.

27. S. Weber*, C. Rawlins and W. C. Muganda, "Younger chemists making a positive change" (poster presentation), *21st Frühjahrssymposium*, Bremen, Germany, 2019.

28. Y. Fam*, T. L. Sheppard, J. Becher, S. Weber, S. Kulkarni, T. F. Keller, A. Schropp, F. Wittwer, M. Seyrich, D. Brückner, M. Kahnt, A. Wittstock, A. Stierle, C. G. Schroer

and J.-D. Grunwaldt, "Design of *in situ* cells for 2D/3D X-ray & electron microscopy in catalysis" (poster presentation), *52nd Meeting of the German Catalysis Society*, Weimar, Germany, 2019.

29. Y. Fam*, T. L. Sheppard, J. Becher, S. Weber, S. Kulkarni, T. F. Keller, A. Schropp, F. Wittwer, M. Seyrich, D. Brückner, M. Kahnt, A. Wittstock, C. G. Schroer and J.-D. Grunwaldt, "Nanoreactors for *in situ* X-ray and electron microscopy" (poster presentation), *DESY Photon Science Users' Meeting*, Hamburg, Germany, 2019.

30. S. Weber*, T. John, C. Wulf, W. C. Muganda, B. Schmid and T. Bachmann, "The German Young Chemists' Network - "JungChemikerForum" (JCF)" (oral/poster presentation), *7th EuCheMS Chemistry Congress*, Liverpool, UK, 2018.

31. S. Weber*, E. Llabani, L. Ferrins, F. Lucci, S. Carenco and C. Rawlins, "The Future of Chemistry is Global" (poster presentation), *7th Berliner Chemie Symposium*, Berlin, Germany, 2018.

32. H. Auer, S. Weber* and H. Kohlmann, "Reactions in the AeTt-hydrogen system (Ae=Sr,Ba; Tt=Ge-Pb)" (poster presentation), *GDCh-Wissenschaftsforum Chemie*, Dresden, Germany, 2015.

Eidesstattliche Erklärung

Hiermit versichere ich eidesstattlich, dass ich die vorgelegte Dissertation selbständig angefertigt und keine anderen als die angegebenen Quellen und Hilfsmittel benutzt habe. Die wörtlichen oder inhaltlich übernommenen Stellen wurden als solche kenntlich gemacht. Weiterhin habe ich die Satzung des Karlsruher Instituts für Technologie (KIT) zur Sicherung guter wissenschaftlicher Praxis in der gültigen Fassung beachtet und die Primärdaten gemäß Abs. A (6) gesichert. Die elektronische Version der Arbeit stimmt mit der schriftlichen überein. Die Arbeit wurde in gleicher oder anderer Form keiner anderen Prüfungsbehörde zur Erlangung eines akademischen Grades vorgelegt.

Karlsruhe, den 31.05.2022